U.S. DEPARTMENT OF
ENERGY

Office of
ENERGY EFFICIENCY &
RENEWABLE ENERGY

Batteries

2017 Annual Progress Report

Vehicle Technologies Office

(This page intentionally left blank)

Disclaimer

Acknowledgements

The projects reported in this report were supported through various contracts funded by the U.S. Department of Energy, Vehicle Technologies Office. A list of contributing authors appears in the sections for specific projects in this report.

Acronyms

AABC	Advanced Automotive Batteries Conference
ABA	American Bar Association
ABDT	ANSYS Battery Design Tool
ABMR	Advanced Battery Materials Research
ABR	Applied Battery research
ABRT	Applied Battery Research for Transportation
ACB	Acetylene Carbon Black
ACS	American Chemical Society
ADF-STEM	Annular dark-field – scanning transmission electron microscope
AERTC	Advanced Energy Research and Technology Center (at Stony Brook University)
AFM	Atomic force microscopy
AIBN	Azobisisobutyronitrile
AIMD	*Ab initio* molecular dynamics
AIRSS	*Ab initio* random structure searching
ALABC	Advanced Lead Acid Battery Consortium
ALD	Atomic layer deposition
ALS	Advanced Light Source (facility)
AMR	Annual Merit Review
ANL	Argonne National Laboratory
APS	Advanced Photon Source (laboratory)
ARC	Accelerated rate calorimetry
ARL	Army Research Laboratory
ASI	Area-specific impedance
ASR	Area-specific resistance
ATR	Attenuated total reflection

ATR-FTIR	Attenuated total reflection-Fourier transform infrared spectroscopy
ATR-IR	Attenuated total reflection- infrared spectroscopy
BCC	Body-centered cubic
BCDI	Bragg Coherent Diffraction Imaging
BEAT	Battery Environmental Assessment Tool
BET	Brunauer, Emmett, and Teller (surface area analysis)
BEV	Battery electric vehicle
BF	Bright field
BLI	Beyond Lithium-ion
BMF	Battery manufacturing facility
BMR	(Advanced) Battery Materials Research (program)
BMS	Battery management system
BNL	Brookhaven National Laboratory
BOL	Beginning of life
BP	Budget period
BSD	Berkeley Software Distribution
BSF	Battery scaling factor
BTC	Battery Technology Center
BTFE	Bis(2,2,2-trifluoroethyl) ether
BYU	Brigham Young University
CABS	Consortium for Advanced Battery Simulation
CAD	Computer-aided Design
CAEBAT	Computer-aided engineering of batteries
CAFE	Corporate Average Fuel Economy
CAMP	Cell analysis, modeling, and prototyping (facility)
CARB	California Air Resource Board

CBA	Carbon/binder additive (geometry)
CCD	Charge-coupled device
CCVD	Catalytic chemical vapor deposition
CDFEM	Conformal decomposition finite element method
CE	Coulombic efficiency
CEI	Cathode electrolyte interfaces
CERC	Clean Energy research Center
CF	Carbon fabric
CFM	Complex framework materials
CFN	Center for Functional Nanomaterials
CID	Current interrupt device
CIF	Crystallographic information file
CIP	Contact ion pair
CLP	Cross-linked polymer
CMC	Carboxymethyl cellulose
CNF	Carbon nanofibers
CNT	Carbon nano-tubes
COTS	Commercial-off-the-shelf
CP	Cross-polarization
CPDB	2-cyano-2-propyl benzodithioate
CPE	Constant phase element
CPI	Compact Power Inc.
CPM	Constant potential method
CPMEA	Cross-linked poly(ethylene glycol) methyl ether acrylate
CPS	Counts per second
CRADA	Cooperative research and development agreement

CS	Charge-sustaining
CSE	Chemical Sciences and Engineering (at ANL)
CSWG	Crash Safety Work Group
CTQ	Critical to quality (criteria)
CV	Cyclic voltammetry
CY	Calendar year
DCB	Dichlorobenzene
DCR	Direct current resistance
DD	Deep-dive
DDSA	Directly doped sulfur architecture
DEC	Diethyl carbonate
DEGDBE	Diethyleneglycol dibutylether
DEGDME	Glycol dimethyl ether
DEIM	Discrete empirical interpolation method
DEMS	Differential electrochemical mass spectrometry
DES	Deep eutectic solvent
DFEC	(4R,5S)-4,5-Difluoro-1,3-dioxolan-2-one
DFT	Density function theory
DFTB	Density functional-based tight binding
DI	De-ionized (water)
DMC	Dimethyl carbonate
DME	Dimethyl ether
DMF	Dimethylformamide
DMSO	Dimethylsulfoxide
DNP	Dynamic nuclear polarization
DOD	Depth-of-discharge

DOE	Department of Energy
DOL	Dioxolane
DOS	Density of state
DOT/NHTSA	Department of Transportation/National Highway Traffic Safety Administration
DP	Dry process
DPA	Destructive physical analysis
DPP	Dynamic particle-packing (model)
DSC	Differential scanning calorimetry
DX	(ANSYS) DesignXplorer
EADL	Electrochemical Analysis and Diagnostic Laboratory (at ANL)
EB	Electron beam
EC	Ethylene carbonate
ECM	Equivalent circuit model
ECS	Electrochemical Society
ED	Electrode domain
EDAX	Energy dispersive x-ray spectroscopy mapping
EDM	Electrode-domain model
EDS	Energy dispersive spectroscopy
EDV	Electric Drive Vehicle
EDX	Energy-dispersive x-ray (spectroscopy)
EDXRD	Energy Dispersive X-ray Diffraction
EELS	Electron energy loss spectroscopy
EERE	Energy Efficiency and Renewable Energy (DOE Office)
EES	Electrochemical energy storage
EGDEG/EGDGE	Ethylene glycol diglycidyl ether
EIS	Electrochemical impedance spectroscopy

EM	Electro-mechanical
EMSL	Environmental Molecular Sciences Laboratory
EOL	End of life
EPA	Environmental Protection agency
EPEAT	Electronic product environmental assessment tool
EPR	Electron paramagnetic resonance
EQCM	Electrochemical quartz crystal microbalance
ETEM	Environmental transmission electron microscope
ETMSMC	Ethyl (trimethylsilyl)methyl carbonate
EUCAR	European Council for Automotive Research and Development
EV	Electric vehicle
EVI	Electric vehicle initiative
EVSE	Electric vehicle supply equipment
EXAFS	Extended X-ray absorption fine structure
FCE	First cycle efficiency
FEA	Finite element analysis
FEC	Fluoro ethylene carbonate
FEM	Finite element method
FFT	Fast Fourier-transform
FIB	Focused ion beam
FIR	First cycle irreversible loss
FITR/FTIR	Fourier-transform infrared spectroscopy
FOA	Federal opportunity anouncement
FOM	Figure of merit
FOME	Energy figure of merit
FOMP	Power figure of merit

FSI	Bis(fluorosulfonyl)imide (anion)
FSP	Flame spray pyrolysis
FTIR, FT-IR	Fourier-transform infra-red spectroscopy
FWHM	Full width at half maximum
FY	Fiscal year
GAFF	General AMBER Force Field
GB	Grain boundary
GC	Gas chromatography
GGA	Generalized gradient approximation
GHG	Green-house gases
GITT	Galvanostatic intermittent titration
GPC	Gel permeation chromatography
GPE	Gel polymer electrolyte
GREET	Greenhouse gas regulated energy and emissions and transpiration
GSE	Garnet solid electrolyte
HAADF	High-angle annular dark-field
HE/HV	High energy/high voltage
HEHV	High energy high voltage
HEMR	High-energy mechanochemical reduction
HEV	Hybrid electric vehicle
HEXRD	High energy x-ray diffraction
HF	Hydrofluoric acid
HFDEC	Bis (2,2,2 trifluoroethyl) carbonate
HFE	Hydrofluoroether
HFEC	Bis (2,2,2 trifluoroethyl) carbonate
HFIP	Hexafluoroisopropanol

HFP	Hexafluoropropylene
HGN	Hollow graphene nanocages
HMDS	Hexamethyldisilazane
HMPA	Hexamethylphosphoramide
HOMO	Highest occupied molecular orbital
HOPG	Highly oriented pyrolytic graphite
HP	High power
HPC	High performance computing
HPLC	High-performance liquid chromatography
HPLC	High Pressure Liquid Chromatography
HPPC	Hybrid pulse power characterization
HQ	Hydro-Québec
HRTEM	High-resolution transmission electron microscopy
HT	High temperature
HV	High voltage
HXN	Hard x-ray nano-probe
IAPG	Interagency advanced power group
IBA	International battery materials association
ICE	Internal combustion engine
ICEV	Internal combustion engine vehicle
ICL	Initial capacity loss
ICP	Inductively coupled plasma
ICP-AES	Inductively-coupled plasma-atomic emission spectroscopy
ICP-MS	Inductively-coupled plasma-mass spectroscopy
ID	Intensity of the carbon D-band
IEA	International Energy Agency

IEEE	Institute of Electrical and Electronics Engineers
IHTC	International Heat Transfer Conference
ILA	International Lead Association
INL	Idaho National Laboratory
IPA	Isopropyl alcohol
IR	Infra-red
IRCL	Irreversible capacity loss
ISC	Internal short circuit
JACS	Journal of the American Chemical Society
JCI	Johnson Controls, Incorporated
JES	Journal of the Electrochemical Society
JKR	Johnson-Kendall-Roberts (models)
KPFM	Kelvin probe force microscopy
LBNL	Lawrence Berkeley National Laboratory
LCA	Life cycle analysis
LCD	Levelized cost of driving
LCO	Lithium cobalt oxide
LEDC	Lithium ethylene dicarbonate
LEED	Low energy electron diffraction
LEX-RS	Li-excess disordered (rocksalt) transition metal oxide
LFMO	$Li_2FeMn_3O_8$
LFO	Li_5FeO_4
LFP	Li-iron phosphate
LIB	Lithium-ion battery
LIC	Lithium-ion conducting
LIPON	Lithium phosphorous oxy-nitride

LLATO	$Li_{0.33}La_{0.56}Al_{0.005}Ti_{0.995}O_3$
LLCZN	$Li_{6.8}La_{2.95}Ca_{0.05}Zr_{1.75}Nb_{0.25}O_{12}$
LLS	Layered-layered spinel
LLTO	$(Li,La)TiO_3$
LLZ	$Li_7La_3Zr_2O_{12}$
LLZO	Lithium lanthanum zirconate
LLZT	$Li_{6.5}La_3Zr_{1.5}Ta_{0.5}O_{12}$
LMNO	Lithium manganese nickel oxide
LMO	Lithium manganese oxide
LMR	Lithium manganese-rich (layered cathode material)
LNMO	$LiNi_{0.5}Mn_{0.5}O_2$
LNRO	$Li_{1.2}Ni_{0.2}Mn_{0.6}O_2$
LNTMO	Li-Ni-Ti-Mo oxide
LNTO	Li-Ni-Ti oxide
LOESS	Locally weighted scatter-plot smoother (regression model)
LPR	Linear polarization resistance
LPS	$B\text{-}Li_3PS_4$
LR	Liquids reflectometer
LS	Low spin
LSB	Lithium sulfur batteries
LSHT/LSTH	$Li_{1/8}Sr_{7/16}Hf_{1/9}Ta_{1/4}O_{32}$
LSV	Linear scanning voltammetry
LT	Low temperature
LTO	Lithium titanate, $Li_4Ti_5O_{12}$
LTSR	Low temperature solid-state reduction
LUMO	Lowest unoccupied molecular orbital

MACD	Maximum allowable current density
MAS	Magic angle spinning
MCMB	Mesocarbon micro beads
MD	Molecular dynamics
MERF	Materials Engineering Research Facility
MFCA	Multifunctional cathode additive
MIT	Massachusetts Institute of Technology
MLD	Molecular layer deposition
MPEGA	Methoxy-polyethylene glycol acrylate
MRI	Magnetic resonance imaging
MRL	Manufacturing Readiness Level
MRS	Materials Research Society
MSMD	Multi-scale, multi-domain
MSU	Michigan State University
MTMSMC	Methyl (trimethylsilyl)methyl carbonate
MW	Molecular weight
NASA	National Aeronautics and Space Administration
NCA	$LiNi_{0.8}Co_{0.15}Al_{0.05}O_2$
NCM	$Li_{1+w}[Ni_xCo_yMn_z]1\text{-}wO_2$
NCO	Nickel cobalt oxide
NCSU	North Carolina State University
NDI	Naphthalene diimide
NEB	Nudged elastic band (method)
NETL	National Energy Technology Laboratory
NHTSA	National Highway Transportation Safety Administration
NIST	National Institute of Standards and Technology

NMC	$LiNi_{1/3}Co_{1/3}Mn_{1/3}O_2$
NMF	Non-negative matrix factorization
NMO	Nickel-manganese-oxide
NMP	N-methylpyrrolidone
NMR	Nuclear magnetic resonance
NP	Nano Particles
NR	Neutron reflectometry
NREL	National Renewable Energy Laboratory
NSLS	National Synchrotron Light Source
NSOM	Near-field scanning optical microscopy
OCV	Open circuit voltage
OEM	Original equipment manufacturer
OPLS	Optimized Potential for Liquid Simulation
ORNL	Oak Ridge National Laboratory
ORR	Oxygen reduction reaction
OS	Orgnic solvent
PAA	Polyacrylic acid
PAN	Polyacrylonitrile
PARC	Palo Alto Research Center
PAW	Projected augmented wave
PBE	Ethylene glycol ester
PDF	Pair density function
PDI	Polydispersity index
PDMS	Polydimethylsiloxane
PE	Polyethylene

PEFM	Poly(2,7-9,9-dioctylfluorene-co-2,7-9,9-(di(oxy-2,5,8-trioxadecane)) fluorine-co-2,7-fluorenone-co-2,5-1-methylbenzoic ester)
PEG	Polyethylene glycol
PEGDA	Poly(ethylene glycol) diacrylate
PEGDMA	Poly(ethylene glycol) dimethacrylate
PEO	Polyethyleneoxide
PES	Prop-1-ene-1,3-sultone
PET	Polyethylene terephthalate
PEV	Plug-in electric vehicle
PFG-NMR	Pulsed field gradient nuclear magnetic resonance
PFPE	Perfluoropolyether
PHEV	Plug-in hybrid electric vehicle
PI	Principal investigator
PNNL	Pacific Northwest National Laboratory
PPE	Personal protective equipment
PS	Polystyrene
PSD	Pore size distribution
PTA	Polysulfide trapping agent
PTF	Post-test facility
PTFE	Poly(tetrafluoroethylene) (cathode)
PVAE	Poly(vinyl alcohol-co-ethylene)
PVD	Physical vapor deposition
PVDF	Poly(vinylidenefluoride)
R&D	Research and Development
RAFT	Reversible addition–fragmentation chain transfer (polymerization)
RDE	Rotating disk electrode

RE	Reference electrode
RH	Relative humidity
RIXS	Resonant inelastic x-ray scattering
ROM	Reduced-order model
RPT	Reference performance test
RT	Room temperature
RVE	Representative volume element
SAE	Society of Automotive Engineers
SAED	Selected area electrode diffraction
SBIR	Small Business Innovation Research
SBR	Styrene-butadiene rubber (binder)
SBU	Stony Brook University
SCW	Supercritical water
SDS	Safety data sheet
SE	Solid electrolyte
SEET	Structural, electrical, electrochemical and thermal
SEI	Solid electrolyte interphase
SEM	Scanning electron microscopy
SFM	Sulfur infiltrated framework
SHE	Self-healing elastomer
SHP	Self-healing polymer
SIA	Isomorphous alloy
SIB	Sodium ion batteries
SIMS	Secondary ion mass spectrometry
SLAC	Stanford acceleration laboratory
SLD	Scattering length density

SLDV	Scanning laser doppler vibrometer
SLMP	Stabilized lithium metal powder
SLP	Single layer pouch (cells)
SNL	Sandia National Laboratories
SNS	Spallation Neutron Source
SOA	State of the art
SOC	State of charge
SOFC	Solid oxide fuel cell
SOW	Statement of work
SP	Silly Putty
SPH	Smooth particle hydrodynamics
SQS	Special quasi-random structures
SS	Solid-state
SSE	Solid-state electrolyte
SSIP	Solvent-separated ion pair
SSRL	Stanford Synchroton Radiation Lightsource
SSRM	Solvent-separated ion pair
STDEV	Standard Deviation
STEM	Scanning transmission electron microscopy
STFSI	(4-styrenesulfonyl) (trifluoromethanesulfonyl)imide
STL	StereoLithography
STM	Scanning tunneling microscope
STO	Strontium titanate
STTR	Small Business Technology Transfer Program
STXM	Scanning transmission X-ray microscopy
SUNY	State University of New York

SXAS	Soft x-ray absorption
SXRD	Synchrotron X-ray diffraction
T2M	Technology-to-market
TAC	Technical Advisory Committee
TAMU	Texas A&M University
TBC	Thermal boundary conductance
TBD	To-be-decided
TC	Thermocouple
TCD	Thermal Conductivity Detector
TCL	Tool Command Language
TCP	Technology collaboration program
TD	Transverse direction
TEGDME	Tetraethyleneglycoldimethyl
TEM	Transmission electron microscopy
TERS	Tip-enhanced Raman spectroscopy
TES	Tender-energy x-ray absorption spectroscopy
TEY	Total electron yield
TFSI	Bistriflimide (anion)
TFY	Total fluorescence yield
TGA	Thermal gravimetric analysis
THF	Tetrahydrofuran
TM	Transition metal
TMA	Tri-methyl aluminum
TMS	Trimethylsilyl
TMSF	Trimethylsilyl fluoride
TOF-SIMS	Time-of-flight SIMS

TR-XAS	TR-XRD and absorption
TR-XRD	Time-resolved X-ray diffraction
TTFP	Tris(2,2,2,-trifluoroethyl)phosphite
TVR	Taylor vortex reactor
TXM	Transmission X-ray microscopy
UCL	University College, London
UCSD	University of California, San Diego
UHMW	Ultra-high molecular weight
UHMWPE	Ultra-high molecular weight polyethylene
UHV	Ultra-high vacuum
UI	User interface
UM	University of Michigan
UMD	University of Maryland
UMERC	University of Maryland, Energy Research Center
UPL	Upper potential limit
USABC	United States Advanced Battery Consortium
USCAR	United States Council for Automotive Research
USDRIVE	Driving Research and Innovation for Vehicle efficiency and Energy sustainability
USGS	United States Geological Survey
UTA	University of Texas, Austin
UV	Ultraviolet
UV-VIS	Ultraviolet–visible
UW	University of Washington
VASP	Vienna *ab initio* Simulation Package
VC	Vinylene carbonate
VGCF	Vapor grown carbon fiber

VIBE	Virtual integrated battery environment
VOC	Volatile organic compounds
VTK	Visualization tool kit
VTO	Vehicle Technologies Office
WP	Wet polishing
WPI	Worcester Polytechnic Institute
WVU	West Virginia University
XANES	X-ray absorption near edge structure
XAS	X-ray absorption spectroscopy
XCH	Excited electron and core hole (approach)
XCT	X-ray computed tomography
XFC	Extreme fast charging
XPD	X-ray powder diffraction
XPS	X-ray photoelectron spectroscopy
XRD	X-ray diffraction
XRF	X-ray fluorescence (microscopy)
XRR	X-ray reflectivity

Executive Summary

Introduction

The Vehicle Technologies Office (VTO) of the Department of Energy (DOE) conducts research and development (R&D) on advanced transportation technologies that would reduce the nation's use of imported oil and reduce harmful emissions. Technologies supported by VTO include electric drive components such as advanced energy storage devices (batteries and ultracapacitors), power electronics and electric drive motors, advanced structural materials, energy efficient mobility systems, advanced combustion engines, and fuels. VTO is focused on funding early stage, high-reward/high-risk research to improve critical components needed for more fuel efficient (and consequently, also cleaner-operating) vehicles.

One of the major VTO objectives is to enable U.S. innovators rapidly develop the next generation of technologies that achieve the cost, range, and charging infrastructure necessary for the widespread adoption of PEVs. An important prerequisite for the electrification of the nation's light duty transportation sector is development of more cost-effective, longer lasting, and more abuse-tolerant plug-in electric vehicle (PEV) batteries. One of the ultimate goals of this research, and currently a strong trend in vehicle electrification, is an EV which can provide the full driving performance, convenience, and price of an internal combustion engine (ICE) vehicle. To achieve this, VTO has established the following overarching goal:

> *VTO supports early-stage R&D to identify new battery chemistry and cell technology with the potential to reduce the cost of electric vehicle batteries by more than half to less than $100/kWh and increase the range to 300 miles while decreasing the charge time to less than 15 minutes by 2028.*

The cost target supports a levelized cost of driving (LCD) of a 300-mile BEV at $0.28/mile, which is comparable to that for future ICEs at $0.27/mile. The ultimate cost goal for a 300-mile BEV battery is $80/kWh, which achieves an LCD of $0.26/mile.

During the past year, VTO continued R&D support of PEVs such as plug-in hybrid vehicles, extended range electric vehicles, and all-electric vehicles (EVs), as well as some conventional hybrid vehicle technologies, particularly the 12 volt start/stop hybrid. VTO competitively awards funding through funding opportunity announcement (FOA) selections, and projects are fully funded through the duration of the project in the year that the funding is awarded. Directly-funded work at the national laboratories (also awarded competitively through a lab-call process) is subject to change based on annual appropriations.

Stakeholders for the VTO R&D activities include universities, national laboratories, other government agencies and members of industry including automakers, battery manufacturers, material suppliers, component developers, private research firms, and small businesses. VTO works with key U.S. automakers through the United States Council for Automotive Research (USCAR) – an umbrella organization for collaborative research consisting of the Fiat Chrysler LLC, the Ford Motor Company, and the General Motors Company. Collaboration with automakers through the partnership known as U.S. Driving Research and Innovation for Vehicle Efficiency and Energy Sustainability (US DRIVE) attempts to enhance the relevance and the potential for success of the research portfolio.

This document summarizes the progress of VTO battery R&D projects supported during the fiscal year 2017 (FY 2017). In FY 2017, the DOE VTO battery R&D funding was approximately $101 million. Its R&D focus was on the development of high-energy batteries for PEVs and very high-power devices for hybrid vehicles. The electrochemical energy storage roadmap (which is found at the EERE Roadmap web page http://energy.gov/eere/vehicles/downloads/us-drive-electrochemical-energy-storage-technical-team-roadmap) describes ongoing and planned efforts to develop electrochemical storage technologies for PEVs. To advance battery technology to improve the market penetration of PEVs and hybrid vehicles, the program focuses on overcoming specific technical barriers typically related to the battery's cost, performance, life (both calendar life and cycle life), its tolerance to abusive conditions, and its recyclability/sustainability. Various battery chemistries are being investigated with that aim.

VTO R&D has lowered the cost of EV battery packs to the value of $219/kWh in 2017, representing an ~80% reduction since 2008, yet even further cost reduction in high-energy batteries is necessary for EVs to achieve head-to-head cost competitiveness (without Federal subsidies). In addition, today's batteries also need improvements in such areas as their ability to accept charging at a high rate – termed extreme fast charging (XFC) where this rate approaches 400 kW; and a better ability to operate at low temperatures – so as to enable EVs an all-weather performance and "refueling" convenience similar to ICE vehicles. Research into "enhanced Li-ion" batteries which would provide such functionalities is one of the R&D focus areas. For even further gains in energy density and reduction in cost, VTO is researching both "next gen" chemistries (which employ an alloy anode and/or a high voltage cathode) and beyond lithium-ion (BLI) chemistries (which can employ a lithium metal anode). Current cycle and calendar lives of next gen and BLI chemistries are well short of the goals set for EVs – most cells employing a significant amount of silicon provide only 500 deep discharge cycles and less than two years of calendar life.

To quantify the improvements needed to accelerate large-scale adoption of PEVs and HEVs, performance and cost targets have been established. Some sample targets for EV batteries are shown in Table ES- 1, both at cell level and at system (pack) level.

Table ES- 1: Subset of EV requirements for batteries and cells.

Energy Storage Goals (by characteristic)	Pack Level	Cell Level
Cost @ 100k units/year (kWh = useable energy)	$100/kWh*	$75/kWh*
Peak specific discharge power (30s)	470 W/kg	700 W/kg
Peak specific regen power (10s)	200 W/kg	300 W/kg
Useable specific energy (C/3)	235 Wh/kg*	350 Wh/kg*
Calendar life	15 years	15 years
Deep discharge cycle life	1000 cycles	1000 cycles
Low temperature performance	>70% useable energy @C/3 discharge at -20°C	>70% useable energy @C/3 discharge at -20°C
	*Current commercial cells and packs not meeting the goal	

The batteries R&D effort includes multiple activities, ranging from focused fundamental materials research to prototype battery cell development and testing. It includes, as described above, R&D on BLI and next-gen materials and cell components, as well as that on synthesis and design, and ways to address the high cost. Those activities are organized into several inter-related (and complementary) program elements:

- Advanced Cell and Battery Research and Development
- Advanced Materials Research
- Battery Testing, Analysis, and Design
- Recycling and Sustainability

A short overview of work under each of those program elements is given below.

Advanced Cell and Battery Research and Development

The *Advanced Cell and Battery Research and Development* activity focuses on the development of robust battery cells and modules to significantly reduce battery cost, increase life, and improve performance. This work mainly spans the following general areas:

- United States Advanced Battery Consortium (USABC)-supported battery development & materials R&D (15 projects)
- Advanced processing (nine projects)
- Computer-aided engineering for batteries (CAEBAT) (eight projects)
- High-energy, long-life lithium-ion battery (one project)
- Extreme fast-charging (one project)
- Small business innovative research (SBIR) (multiple Phase I and Phase II projects)

Chapter I of this report describes projects under the *Advanced Cell and Battery Research and Development* activity. A substantial part of this effort occurs in close partnership with the automotive industry, through a cooperative agreement with the USABC. In FY 2017, via the USABC, VTO supported 15 cost-shared contracts with developers to further the development of PEV and HEV batteries and battery components. The estimated DOE share of those USABC contracts (over the life of the contracts) is approximately $25M. These include lower cost, high energy lithium battery technology being developed by **Envia Systems, Amprius, Inc.**, **LG Chem Power, Inc., Farasis Energy and 24M.** As an example, Figure ES- 1 shows an Envia 11 Ah capacity pouch cell undergoing teardown and failure analysis. The development of lithium-ion battery technology for 12V Start-stop microhybrid batteries is being supported through R&D efforts wth **Saft** and **LG Chem Power.** Additional battery technologies are also supported, including two separator technologies being developed by **Celgard**, and **Entek Membranes,** and high capacity anode materials by **Sinode Systems**. Various battery manufacturing, recycling, benchmarking activities are funded at other industry partners (including those at **Farasis Energy, NOHMs Technologies, PPG, Worcester Polytechnic Institute,** and **FEV**).

Figure ES- 1. Images of an 11 Ah capacity pouch cell undergoing teardown and failure analysis

In addition to the USABC projects listed above, VTO also supports battery and material supplier R&D projects which are funded/administered by the National Energy Technology Laboratory (NETL). This report contains an account of nine such *advanced processing* projects. Most strategies for increasing the performance and reducing the cost of lithium-ion batteries have focused on novel battery chemistries, material loading modifications, and increasing electrode thickness. Increasing electrode thickness is a known approach for increasing energy density (and in turn, the overall cell capacity). However, practical thicknesses are constrained by ionic transport limitations that occur with the increased thickness, limiting the cell power. The

Palo Alto Research Center's (PARC) co-extrusion (CoEx) technology is aimed at enabling a substantial improvement in the performance of thick electrodes for lithium-ion chemistries. The project aims to demonstrate CoEx printing technology at EV-relevant scales by assembling large (14 Ah) pouch cells. In another project, conducted by **Group14**, the objective is to develop a new low-cost production process capable of mass-producing silicon-based lithium ion battery anode material that can reach 1000 mAh/g after 1000 cycles and with a cell level cost target of < $125/kWh, validate performance in LIB full cells, and prove the cost basis at pilot scale. Also, a **Miltec** project was recently completed in which a commercial scale system (entitled Miltec CX400) was designed utilizing flexographic printing technology and ultraviolet (UV) curable binder to take advantages of UV technology (which include cost saving, performance improvement, and enhanced safety). The remaining advanced processing projects include another **Miltec** project aimed at UV curing to reduce the manufacturing cost of LIB electrodes; producing low-cost, water-based electrodes via electrodeposition (by **PPG)**; a solvent-less processing of thick electron-beam (EB) cured LIB cathodes at **ORNL**; developing novel electrolytes for high-voltage batteries (at **Silatronix)**; developing a scalable process to fabricate porous silicon (at **Navitas)** (Figure ES- 2); and electrode processing for lithium-ion batteries (at **ORNL)**. The estimated value of those advanced processing projects (over project lifetime) is approximately $16M.

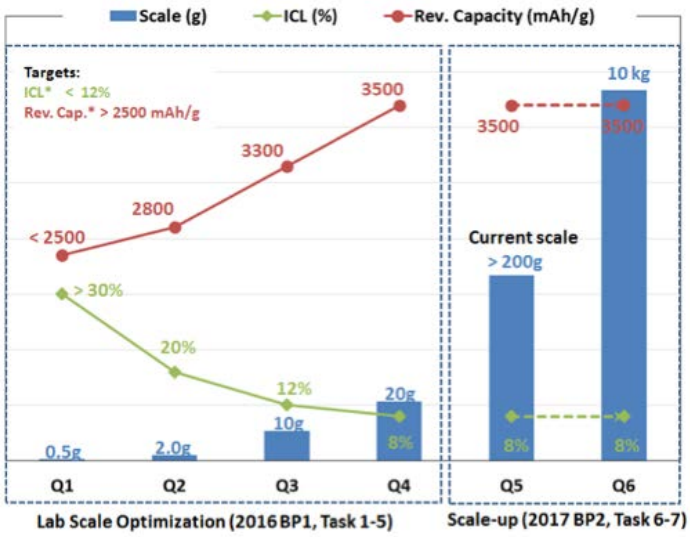

Figure ES- 2. Capacity and ICL both improved during Navitas' material scale up procedures

The advanced cell and battery research activity also includes several projects categorized under the Computer Aided Engineering for Electric-Drive Vehicle Batteries (CAEBAT) Program – which recently evolved into the **Advanced Computer Aided Battery Engineering Consortium** and which seeks to enhance/validate the predictive capability of computationally efficient electrochemical models for thick electrode designs for lower battery cost and increased energy density and mechanical/electrochemical/thermal simulation models of battery physiochemical processes that would take place in the event of a vehicle crash, a possible internal short and thermal runaway – with the objective of providing a better understanding of and enabling safer designs. With the National Renewable Energy Laboratory (NREL) as lead, the Consortium's partner laboratories Argonne National Laboratory (ANL) and Sandia National Laboratories (SNL) perform experimental studies, supported by Purdue University in performing mesoscale modeling. Sample results from the consortium efforts, from a simulation to determine effective electrolyte transport properties in porous electrodes (using geometry from the CT imaging of an actual electrode) are shown in Figure ES- 3.

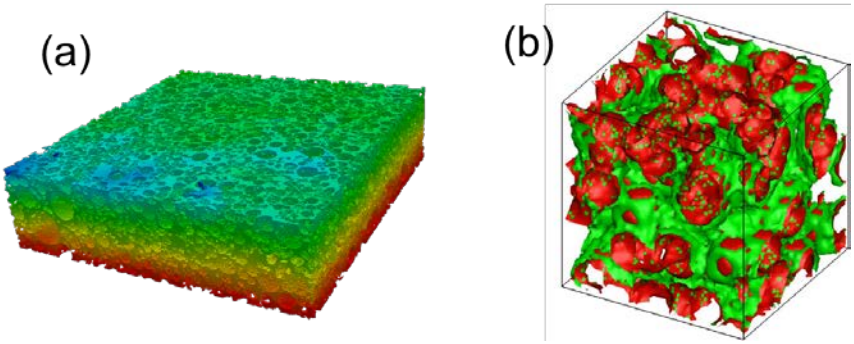

Figure ES- 3. (a) Homogenization simulation to determine effective electrolyte transport properties in porous electrode using geometry from CT imaging of an actual electrode. (b) Stochastic reconstruction of virtual geometry, showing CBA phase (green) on active material matrix (red).

The **consortium for advanced battery simulation** (CABS) is an integrated partnership between Oak Ridge National Laboratory (ORNL), Lawrence Berkeley National Laboratory (LBNL), and SNL. The main cause of battery failure/thermal runaway in crashes involving electric vehicles is believed to be a mechanically induced internal short-circuit. To accurately predict this internal short-circuit, one needs to capture deformed material variations and their influence on transport properties. The associated projects highlight new experiments to develop constitutive relations for mechanical response of constituent materials, effective transport properties for electrochemical behavior of electrodes under deformation, and coupled simulations at layer-resolved scale to predict the behavior of the damaged batteries. The approximate value of the CAEBAT and its follow-on programs is $14M.

To become truly competitive with the internal combustion engine vehicle (ICEV) refueling experience, EV charging times must also dramatically decrease. A research project to understand/enable extreme fast charging (XFC) in enhanced Li-ion systems began in 2017. XFC, or charging an EV at the power rate of up to 400 kW, would decrease vehicle charging times and increase EV utility. To address this issue, a multi-national laboratory team consisting of ANL, Idaho National Laboratory (INL), and NREL engaged with industry stakeholders to identify barriers and opportunities for technology R&D solutions needed to achieve 400 kW charging power levels and combine the findings into a single document for governments and private industries to reference. Industry perspectives on the direction of fast charging were used to develop a technology gap assessment report, which would inform the team on areas that need an extensive literature review, and would assess the economic feasibility of XFC.

VTO also supports several *Small Business Innovation Research* (SBIR) contracts in addition to the R&D described above. These SBIR projects focus on development of new battery materials/components and serve as the source of new ideas and concepts. At the end of chapter I, a section on SBIR projects includes a short list of recent such projects active in FY 2017.

Advanced Materials R&D

The *Advanced Materials Research & Development* activity addresses fundamental issues of materials and electrochemical interactions associated with rechargeable automotive batteries. It develops new/promising materials and it makes use of advanced material models to discover such materials (and their failure modes), utilizing scientific diagnostic tools and techniques to gain insight into the failure process. The researchers belong to various national labs, universities, and industry partners. The work spans mainly two general areas – "next gen" chemistries (which employ an alloy anode and/or a high voltage cathode) and beyond lithium-ion (BLI) chemistries (which employ a lithium metal anode). The projects are distributed as follows:

- Next generation (Next-gen) lithium-ion battery technologies (48 projects)
  - Advanced Electrodes (four projects)
  - Advanced Anodes (eight projects)

  - Advanced Cathodes (13 projects)
  - Diagnostics (nine projects)
  - Modeling Advanced Electrode Materials (six projects)
  - Processing Science (eight projects)

- Beyond lithium-ion battery technologies (29 projects)
  - Metallic Lithium and Solid Electrolytes (11 projects)
  - Lithium sulfur (13 projects)
  - Lithium-Air Batteries (three projects)
  - Sodium-ion batteries (two projects)

The *next generation lithium-ion battery* R&D area's goal is to advance material performances, designs, and processes to significantly improve performance and reduce the cost of Li-ion batteries using an alloy or intermetallic anode and/or high voltage cathode. Specific areas of investigation include high-energy anodes (e.g., those containing silicon or tin), high voltage cathodes, high voltage and non-flammable electrolytes, novel processing technologies, high-energy and low-cost electrode designs, and certain other areas. This work spans a range of US DRIVE activities.

- *Advanced electrode R&D* research includes four projects. **LBNL** is studying inactive components and processing conditions and looking at different binder sources, slurry viscosities, and other parameters to identify physics for a smooth laminate to meet specific performance requirements. **Hydro-Quebec** is developing an electrode architecture-based on nano-Si powders. **MIT** is developing scalable designs and fabrication processes for high density low-tortuosity electrodes.

- *Advanced anodes* R&D includes 8 projects. Four of them, conducted by the five-member National Laboratory Consortium, comprise the **silicon deep-dive program**. Silicon is a viable alternative to graphitic carbon as an electrode in lithium-ion cells and can theoretically store >3,500 mAh/g (i.e., about ten times more than graphite). However, lifetime problems severely limit its use in practical systems – this project is focused on those problems. The consortium tackles the barriers for advanced lithium-ion negative electrodes which would use silicon as the active material. The program performs baseline tests on promising silicon materials in quantities sufficient for electrode preparation within consortium facilities. The other four projects, conducted by various national labs (including NREL, ANL, ORNL, PNNL, and LBNL) and academia/industry partners (including Stanford University and GM) are part of the **silicon electrolyte interface stabilization (SEISta) program** developing a foundational understanding of the formation/evolution of the solid electrolyte interphase on silicon.

- *Advanced cathodes* R&D includes 13 projects. Five of those projects are based at **ANL**, of which three are geared to **enable high-energy/high-voltage cells** via new insights and/or understanding into the failure of present materials/systems. (For example, in one of those projects, an electrolyte based on fluorinated sulfones improved the cycle life of NMC532/Graphite full cells. The performance of the electrolyte additive was evaluated using the high energy high voltage (HEHV) protocol, which predicted the number of cycles that will have 80% capacity retention under the high voltage cycling protocol. The cycle number with 80% capacity retention improved substantially – from 150 cycles with the baseline electrolyte to 400 cycles (Figure ES- 4) in the presence of the new fluorinated electrolyte.) To increase the energy density of lithium-ion batteries, electrochemical cells containing near lithium-stoichiometric, manganese-bearing, nickel-rich layered oxides and graphite-bearing negative electrodes are cycled to higher voltages (>4.35 V) in the Applied Battery Research for Transportation (ABRT) program. However, this reduces the cell life and degrades performance at those high voltages. The cell electrolyte, typically made of carbonate-based solvents, significantly contributes to this performance loss as it tends to oxidize at higher voltages, generating species that degrade the positive electrode. The development of electrolyte systems and of stable interfaces to mitigate performance degradation is a priority. **Daikin America** is working on electrolytes with small fluorinated molecules to achieve stable high voltage (i.e.,

>4.3 V) battery operation. An ANL project on novel cathode materials and processing methods focuses on lithium- and manganese-rich, **'layered-layered' composite materials** and another on exploiting **Co and Ni spinels** in structurally-integrated composite electrodes. Of the remaining eight advanced cathode projects, three are being conducted at LBNL, one each at PNNL, ORNL and BNL, one at Binghamton University, and another at the University of Texas at Austin.

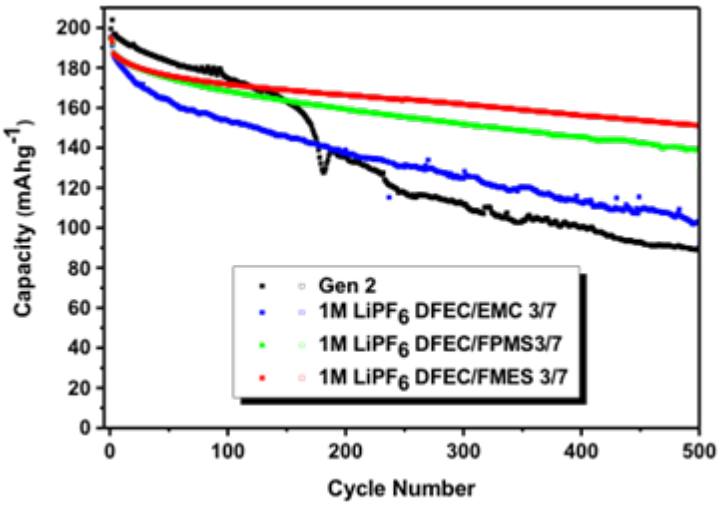

Figure ES- 4. Capacity retention of NMC532/graphite full cells cycled with Gen 2 (non-fluorinated) and various mixtures of fluorinated sulfone-based electrolytes. (C/3 for 100 for cycling between 3.0 and 4.6 V.)

- *Diagnostics* R&D includes nine projects, including two each by teams at ANL and LBNL. The teams at ANL are doing characterization studies of high-capacity composite electrode structures to address interfacial reactivity between electrode and electrolyte while the two LBNL teams are studying interfacial processes and doing *in operando* thermal diagnostics of cells. Also in this area of work, BNL is studying advanced *in situ* diagnostic techniques for battery materials, SLAC is conducting correlative microscopy characterization of oxide electrodes, and PNNL is conducting microscopy investigation on the fading mechanism of electrode materials. The remaining two diagnostics projects are based at universities (namely, the University of Cambridge, and the University of California at San Diego).

- Of the six *modeling* projects being funded, two are based at LBNL, including one on novel electrode materials from first principles and another on large-scale *ab initio* molecular dynamics simulation of liquid and solid electrolytes. A modeling project at ANL focuses on electrode materials design and failure prediction. The three remaining modeling projects are all based at universities (namely, the University of California at Berkeley, Texas A&M University, and the Brigham Young University).

- *Processing Science* R&D includes eight projects. Five of those are based at ANL – one on non-traditional approaches to synthesizing active cathode materials, one on active cathode materials with component concentration gradient structures, one on process R&D and scale-up of critical battery materials, and one on the cell analysis, modeling, and prototyping (CAMP) facility, as well as on materials benchmarking for CAMP. The University of Missouri, Columbia is working on an integrated flame spray process for low-cost production of battery materials, and Vanderbilt University on producing Li-ion battery anodes from electro-spun nanoparticle/conducting polymer nanofibers. A team project on the post-test analysis of lithium-ion battery materials includes three labs (ANL, ORNL, and SNL).

R&D on *beyond Li-ion battery technologies* includes solid-state technology, lithium metal systems, lithium sulfur, lithium air, and sodium-ion. The main areas of focus include new methods to understand/stabilize lithium metal anodes; Li polysulfides to enable the use of sulfur cathodes; and developing electrolytes for

lithium air and lithium sulfur cells. These systems offer further increases in energy and potentially reduced cost compared to the next-gen lithium-ion batteries. However, they also require additional breakthroughs in materials (often at a fundamental level) before commercial use. VTO is investigating the issues and potential solutions associated with cycling metal anodes. The main research topics include: coatings, novel oxide and sulfide-based glassy electrolytes, and *in situ* diagnostics approaches to characterize and understand Li metal behavior during electrochemical cycling.

- *Metallic lithium and solid electrolytes* R&D includes 11 projects, two of which are based at ORNL – one on mechanical properties at the protected lithium interface and another on composite electrolytes to stabilize metallic lithium anodes. A dendrite suppression project is ongoing at PNNL. The remaining eight projects are based at various universities – Stanford University, Texas A&M University (TAMU), University of Pittsburgh, West Virginia University, Pennsylvania State University, University of Michigan, and the University of Maryland. In one project at the University of Maryland, first principles calculations were applied to investigate the interface stability between garnet and formed Li-Al alloys (Figure ES- 5). It was found that the interface between Li-Al alloy and garnet may exhibit good chemical stability, which might facilitate Li ion transport through that interface.

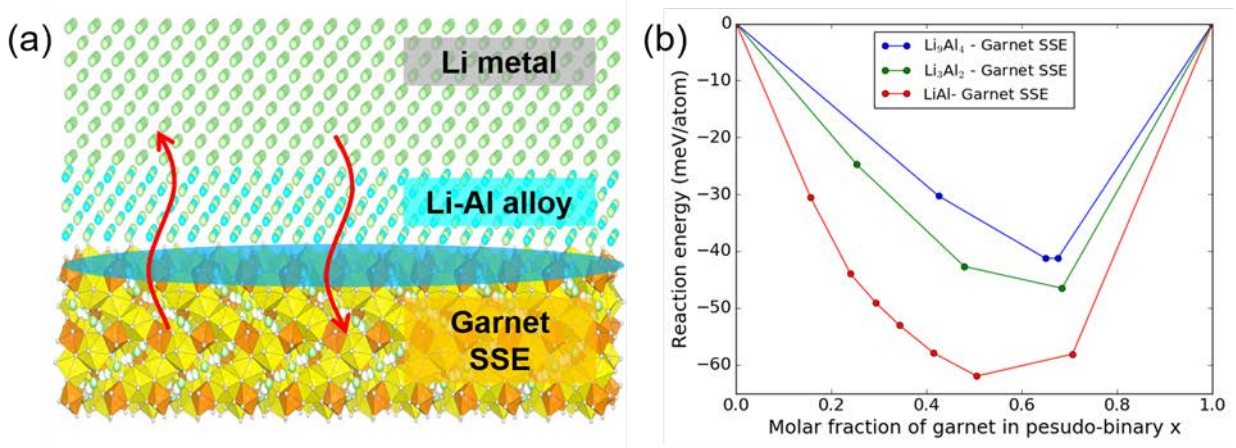

Figure ES- 5. Calculated mutual reaction energy, ΔED, of garnet and Li-Al alloy interfaces.

- *Lithium sulfur* R&D includes 13 projects – five of them at national laboratories and the remaining eight at various universities. The lab-based projects include one on lithium-selenium and selenium-sulfur couple (at ANL), advancing solid-solid interfaces (at ANL), multi-functional cathode additives (at BNL), simulations and X-ray spectroscopy of Li-S chemistry (at LBNL) and the development of high energy lithium sulfur batteries (at PNNL). The eight universities with lithium sulfur projects include Stanford University, TAMU, the University of Wisconsin at Madison, the University of Texas at Austin, Stony Brook University, University of Washington, Rutgers University, and the University of Pittsburgh.

- *Lithium-air batteries* R&D includes three projects – one at PNNL, another at ANL and one utilizing stable inorganic molten salt electrolytes at Liox Power.

- There are two *sodium-ion batteries* R&D projects ongoing – one at BNL and the other at SLAC.

The *Battery500 Innovation Center* is a combined effort by a team of four National Labs (PNNL, INL, BNL and SLAC) and five universities (University of Texas-Austin, Stanford University, Binghamton University, University of Washington, and University of California, San Diego). Its goal is to develop commercially viable Li battery technologies with a cell level specific energy of 500 Wh/kg while simultaneously achieving 1,000 deep-discharge cycles. The consortium keystone projects focus on innovative electrode and cell designs that enable maximizing the capacity from advanced electrode materials. The strategy is to take advantage of electrode materials that are commercially available (or are nearly so) and introduce least perturbation to the

cell configuration and manufacturing process of current technologies. Based on this approach, two battery chemistries, high nickel content lithium nickel-manganese-cobalt oxide (high-Ni NMC, Ni>60%), coupled with Li metal anode, and Li-S chemistry, indicate a potential to achieve an energy density of at least 500 Wh/kg. The Li anode combined with a compatible electrolyte system and two cathodes – one high NMC and another sulfur – is to be studied and developed to reach a high energy density. The consortium will work closely with the R&D community, battery/materials manufacturers and end-users/OEMs to ensure that these technologies align well with industry needs and can be transitioned to production.

Testing and Analysis

The *Battery Testing, Analysis, and Design* activity supports all other battery R&D activities. DOE works in close collaboration with USABC to develop requirements and test procedures. Other projects in this area include conducting testing (for performance, life and abuse) for contract deliverables, laboratory- and university-developed cells, and benchmark systems from industry; thermal analysis, thermal testing and modeling; cost modeling; other battery use and life studies; and the recycling of core materials. Battery technologies are evaluated according to USABC-stipulated battery test procedures. Benchmark testing of an emerging technology is performed to remain abreast of the latest industry developments. The current projects are in the following three areas:

- The *cost assessments and requirements analysis* activity includes an ANL project on developing the performance and cost model BatPaC. This ANL model, developed over time and rigorously peer-reviewed, is used to design automotive Li-ion batteries to meet the specifications for a given vehicle, and estimate the cost of manufacturing it. An analysis using BatPaC compared the estimated costs of cells and packs for different electrode chemistries (Figure ES- 6 shows the pack costs).

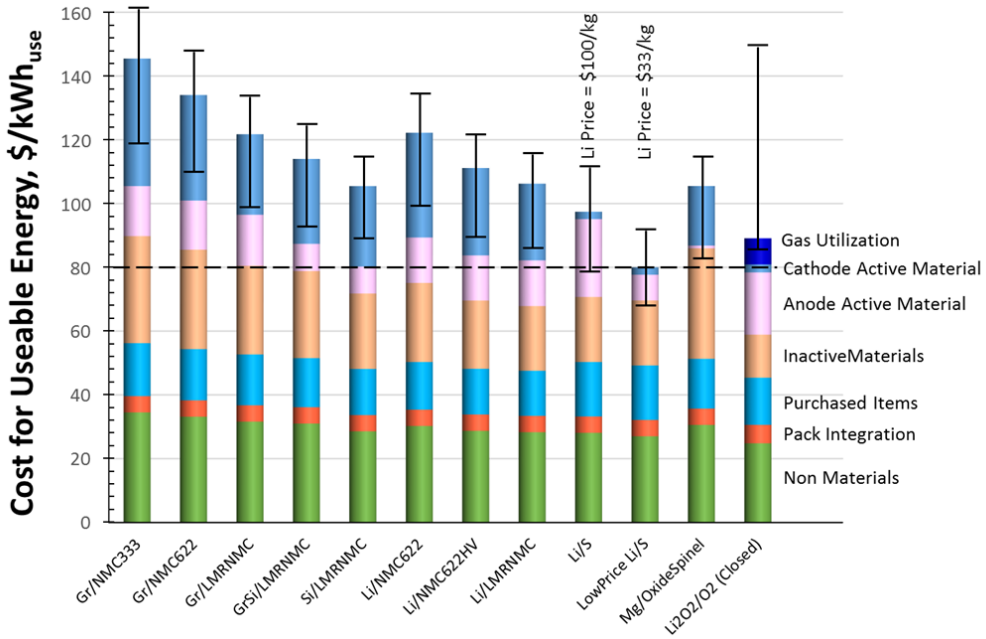

Figure ES- 6. Estimated costs of cells in automotive battery packs with different combination of electrodes. The packs are rated for 100 kWh_{Total} (85 $kWh_{Useable}$), 300 kW, 315 V, 168 cells, and produced at a plant volume of 100K packs/year.

- The *battery testing* activity includes performance, life and safety testing, and thermal analysis and characterization. It currently includes the following 4 projects:
  - Battery performance and life testing (ANL)
  - Electrochemical performance testing (INL, ANL)

  - Battery safety testing (SNL)
  - Battery thermal analysis and characterization activities (NREL)

- The *Recycling and Sustainability* activity involves studies of the full life-cycle impacts and costs of Li-ion battery production/use; cost assessments and impacts of various recycling technologies; and the available material and cost impacts of recycling and secondary use. It includes the following three projects:
  - Life cycle assessment of Li ion batteries (ANL)
  - Battery production and recycling materials issues (ANL)
  - Process and cost modeling of recycling activities (ANL)

Collaborative Activities

In addition to the above, VTO has established extensive and comprehensive ongoing coordination efforts in energy storage R&D across all of the DOE complex and with other government agencies. It coordinates efforts on energy storage R&D with both the Office of Science and the Office of Electricity. Coordination and collaboration efforts also include membership and participation in the Chemical Working Group of the Interagency Advanced Power Group (IAPG), in program reviews and technical meetings sponsored by other government agencies, and inviting participation of representatives from other government agencies in the contract and program reviews of DOE-sponsored efforts. DOE coordinates such activities with the Army's Advanced Vehicle Power Technology Alliance, the Department of Transportation/National Highway Traffic Safety Administration (DOT/NHTSA), the Environmental Protection Agency (EPA), and the United Nations Working Group on Battery Shipment Requirements. Additional international collaboration occurs through the International Energy Agency's (IEA's) Hybrid Electric Vehicles Technology Collaboration Program (HEV TCP); the G8 Energy Ministerial's Electric Vehicle Initiative (EVI); and bilateral agreements between the U.S. and China. The *U.S. China Clean Energy Research Center* conducts collaborative research both on rechargeable lithium-ion and beyond lithium-ion battery technologies to help develop the next generation of advanced batteries to help expand electrification of vehicles and enable smart grids internationally and its main objective is to understand and develop advanced battery chemistries based on lithium-ion and beyond lithium ion that meet 300Wh/kg energy density.

Organization of this Report

This report covers all the FY 2017 projects as part of the advanced battery R&D (i.e., energy storage R&D) effort in VTO. We are pleased with the progress made during the year and look forward to continued cooperation with our industrial, government, and scientific partners to overcome the remaining challenges to delivering advanced energy storage systems for vehicle applications.

David Howell

VTO Deputy Director

Vehicle Technologies Office

Steven Boyd

Manager, Batteries and Electrification Program

Vehicle Technologies Office

Tien Q. Duong

Manager, Advanced Battery Materials Research and VTO Battery500 Consortium

Vehicle Technologies Office

Peter W. Faguy

Manager, Applied Battery Research and Advanced Processing R&D

Vehicle Technologies Office

Brian Cunningham

Manager, Battery Development; and Battery Testing, Analysis and Design; and Small Business Innovation Research for Batteries

Vehicle Technologies Office

Samuel Gillard

Manager, Battery Testing, Analysis and Design

Vehicle Technologies Office

Table of Contents

List of Figures

List of Tables

(This page intentionally left blank)

Vehicle Technologies Office Overview

Vehicles move our nation. Vehicles transport more than $36 billion worth of goods each day[1] and move people more than 3 trillion vehicle-miles each year[2]. Growing our national economy requires transportation and transportation requires energy. The average U.S. household spends nearly one-fifth of its total family expenditures on transportation[3], making transportation the most expensive spending category after housing. The transportation sector accounts for 70% of U.S. petroleum use. The United States imports 25% of the petroleum consumed – sending more than $10 billon per month[4] overseas for crude oil.

To strengthen national security, enable future economic growth, and increase transportation energy efficiency, the Vehicle Technologies Office (VTO) funds early-stage, high-risk research on innovative vehicle and transportation technologies. VTO leverages the unique capabilities and world-class expertise of the national laboratory system to develop innovations in electrification, advanced combustion engines and fuels, advanced materials, and energy efficient mobility systems.

VTO is uniquely positioned to address early-stage challenges due to strategic public-private research partnerships with industry (e.g., U.S. DRIVE, 21st Century Truck Partnership). These partnerships leverage relevant expertise to prevent duplication of effort, focus DOE research on critical R&D barriers, and accelerate progress. VTO focuses on research that industry does not have the technical capability to undertake on its own, usually due to a high degree of scientific or technical uncertainty, or it is too far from market realization to merit industry resources. VTO's research generates knowledge that industry can advance to deploy innovative energy technologies to support affordable, secure, and efficient transportation systems across America.

Vehicle Technologies Office Organization Chart

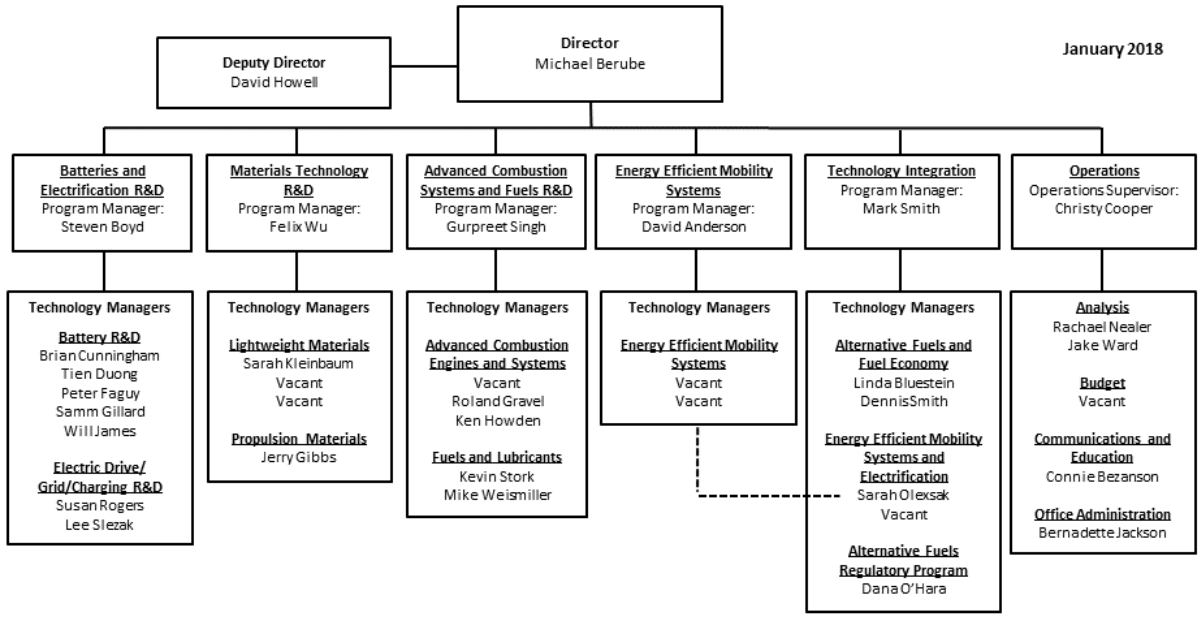

[1] https://ops.fhwa.dot.gov/publications/fhwahop16083/ch1.htm#t1

[2] https://www.fhwa.dot.gov/policyinformation/statistics/2015/vm1.cfm

[3] https://www.bls.gov/cex/2015/standard/multiyr.pdf

[4] Transportation Energy Data Book Edition 34, ORNL, Table 1.7 and Table 10.3; Overseas includes countries and territories outside the 50 States and the District of Columbia.

(This page intentionally left blank)

Batteries Program Overview

Introduction

During the fiscal year 2017 (FY 2017), the Vehicle Technologies Office (VTO) battery program continued research and development (R&D) support of technologies for plug-in electric vehicles (PEVs), e.g., plug-in hybrids, extended range electric vehicles, all-electric vehicles, and some hybrid electric vehicles (including those with 12 volt start/stop hybrid). One of the objectives of this support is to enable U.S. innovators to rapidly develop the next generation of technologies that achieve the cost, range, and charging infrastructure necessary for the widespread adoption of PEVs. Stakeholders involved in VTO R&D activities include universities, national laboratories, other government agencies and industry partners – including automakers, battery manufacturers, material suppliers, component developers, private research firms, and small businesses. VTO works with key U.S. automakers through the United States Council for Automotive Research (USCAR) – an umbrella organization for collaborative research consisting of Fiat Chrysler LLC, the Ford Motor Company, and the General Motors Company. Collaboration with automakers through the US DRIVE (Driving Research and Innovation for Vehicle Efficiency and Energy Sustainability) partnership enhances the relevance and the success potential of the research platform. An important prerequisite for the electrification of the nation's light duty transportation sector is the development of more cost-effective, longer lasting, and more abuse-tolerant PEV batteries and accordingly, VTO battery R&D is focused on the development of high-energy batteries for PEVs and very high-power devices for hybrid vehicles.

Goals

The goals of this research are to address barriers which hold back EVs from matching the full driving performance, convenience, and price of an internal combustion engine (ICE) vehicle. EVs have the advantage of a very high efficiency compared to other vehicle types, a simplified drive train, and a flexible primary energy source (i.e., the electricity needed to charge an EV can come from coal, natural gas, wind turbines, hydroelectric, solar energy, nuclear, or any other resource). Another current focus is the 12V start/stop (S/S) micro-hybrid architecture, in which the engine is shut down whenever a vehicle stops. Vehicles with the S/S functionality are being deployed worldwide. The 12V battery provides power for auxiliary equipment (e.g., the radio and air conditioning) and then restarts the engine when the vehicle moves. Current 12V S/S batteries, typically lead-acid batteries, have a poor life. Table 1 and Table 2 show a subset of the targets for EV and 12V start/stop micro hybrid batteries that have been set by U.S. DRIVE.

Table 1: Subset of EV requirements for batteries and cells.
(Cost and low temperature performance are critical requirements).

Energy Storage Goals (by characteristic)	System Level	Cell Level
Cost @ 100k units/year (kWh = useable energy)	$100/kWh*	$75/kWh*
Peak specific discharge power (30s)	470 W/kg	700 W/kg
Peak specific regen power (10s)	200 W/kg	300 W/kg
Useable specific energy (C/3)	235 Wh/kg*	350 Wh/kg*
Calendar life	15 years	15 years
Deep discharge cycle life	1000 cycles	1000 cycles
Low temperature performance	>70% useable energy @C/3 discharge at -20°C	>70% useable energy @C/3 discharge at -20°C
	*Current commercial cells do not meet this goal	

Table 2: Subset of targets for 12V start/stop micro-hybrid batteries (cost and cold cranking are critical requirements)

Energy Storage Goals (by characteristic)	Under the hood	Not under the hood
Maximum selling price	$220*	$180*
Discharge pulse (1s)	6 kW	
Cold cranking power, (-30°C)	6 kW for 0.5s followed by three 4 kW/4s pulses*	
Available energy	360 Wh	
Peak recharge rate (10s)	2.2 kW	
Sustained recharge rate	750 W	
Cycle life	450 k	
Calendar life	15 years at 45°C*	15 years at 30°C**
Maximum weight	10 kg	
Maximum volume	7 liters	
	*Current commercial cells do not meet this goal **Current cells almost meet this goal	

State of the Art

Battery R&D attempts to advance battery technology to help improve the market penetration of PEVs and hybrid vehicles by overcoming the current barriers. To accomplish this, it focuses on: (1) a significantly reduced battery cost, (2) increased battery performance, e.g., extreme fast charge (XFC) and low temperature performance for enhanced Li-ion), (3) improved life advanced chemistry cells, (4) increased tolerance to abusive conditions; and (5) more cost-effective recycling and sustainability.

The current status of the broad battery chemistry types (current Li-ion, next gen, and BLI) is summarized in Figure 1. Battery R&D spans mainly three areas:

- **Current Technology (enhanced) Li-ion:** Cells with today's materials (i.e., graphite anode/transition metal oxide cathode), but with features like XFC compatibility, low temperature performance and improved abuse tolerance.
- **Next-gen Li-ion:** Cells containing an alloy anode, usually Silicon-based, and/or a high voltage (>4.5 V) cathode.
- **Beyond Li-ion (BLI):** Cells containing Li metal anodes.

Over the past seven years, PEVs have become more commercially viable, with battery costs dropping almost 80% since 2010. Further cost reductions in high-energy batteries for PEVs are always desirable. In addition, although today's batteries approach very attractive cost numbers, they still need the ability to accept extreme fast charging (XFC) and to perform better in low-temperature operations, to favorably match ICEs in all-weather performance and "refueling" convenience. Research into "enhanced Li-ion" batteries (which would providing these functionalities) is one of the R&D focus areas.

For further gains in energy density and cost reduction, research is needed in both "next gen" chemistries (which employ an alloy anode and/or a high voltage cathode) and BLI chemistries. Cycle and calendar lives of next-gen and BLI chemistries are well short of EV goals. Most cells employing a significant amount of silicon provide (at most) 500 deep discharge cycles and less than two years of calendar life; BLI cells typically provide much less (a cycle life of 100 cycles or less). In addition, the requisite low temperature performance and extreme fast charge capability are lacking in all chemistries.

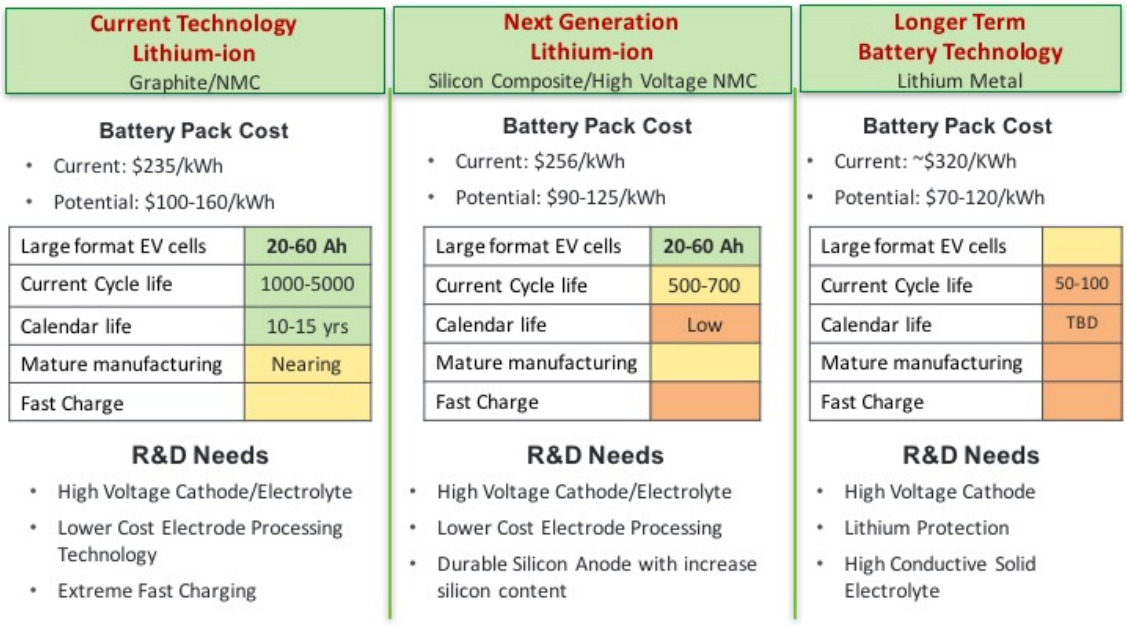

Figure 1. Chemistry classes, status, and R&D needs

An overview of the candidate battery technologies and their likely ability to meet the DOE cost goals are shown in Figure 2. Because of the large variation in different battery technologies, battery research also includes multiple activities focused to address remaining high cost areas within the entire battery supply chain.

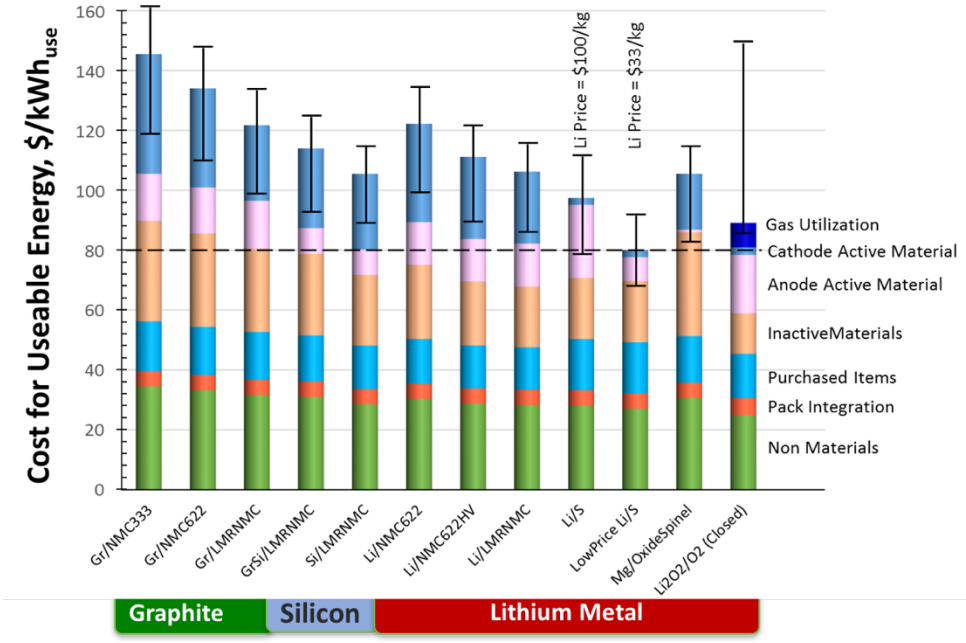

Figure 2. Potential for Future Battery Technology Cost Reductions

Battery Technology Barriers

The major remaining challenges to commercializing batteries for EVs and 12V SS micro-hybrid batteries are as follows:

A. Cost. The current cost of high-energy Li-ion batteries is approximately $200 - $300/kWh (on usable energy basis), a factor of two-three times too high from where it needs to be. The cost of Li-ion-based 12V micro-hybrid batteries (which offer significantly better life than conventional lead acid batteries) is approximately 50% too high compared to lead acid. The main cost drivers are the high cost of raw materials, costs associated with materials processing, the cell and module packaging, and manufacturing.

B. Performance. Historically, a higher energy density was needed to reduce the weight and volume of PEV batteries, but those weight and volume issues have been to a large degree been addressed. The use of higher energy materials is still an effective way to reduce costs further, but cell chemistries that provide higher energy have life and performance issues. Also, existing chemistries (e.g., graphite anodes paired with transition metal oxide cathodes) need improvement in XFC and low temperature performance to compete favorably with gas-powered vehicles in the areas of performance and customer convenience. The main performance issue with Li-ion 12V start/stop batteries is a challenging “cold start” requirement at -30°C coupled with high or room temperature life.

C. Life. The life issue for mature Li-ion technologies has mainly been mostly addressed. However, both next-gen and BLI cell technologies still suffer major cycle and calendar life issues. The life of Li-ion-based 12V start/stop micro-hybrid batteries is relatively good, however enhancing cold crank performance often shortens high temperature life.

D. Abuse Tolerance. Current Li-ion automotive batteries are generally used consistent with safe practices. Thus, although Li-ion is not intrinsically tolerant to abusive conditions (as is the case for gasoline as well), it can be engineered in a commercially acceptable product. The characteristics of next-gen and BLI chemistries to abusive conditions are not well understood. However, Li-metal-based batteries have a long history of problematic dendrite growth which can lead to internal shorts and thermal runaway.

E. Recycling and Sustainability. Currently, automotive OEMs pay a relatively large cost (5-15% of the battery cost) to recycle end of life PEV batteries. The various chemistries used in Li-ion cells results in variable backend value. Alternatively, unless they get recycled, Li-ion batteries could lead to a shortage of key materials (lithium, cobalt, and nickel) vital to the technology. Finding ways to decrease the cost of recycling could thus significantly reduce the life cycle cost of PEV batteries, avoid material shortages, lessen the environmental impact of new material production, and potentially provide low-cost active materials for new PEV battery manufacturing.

Program Organization Matrix

VTO’s energy storage effort includes multiple activities, ranging from focused fundamental materials research to prototype battery cell development and testing. The R&D activities can involve either shorter-term pre-competitive research by commercial developers or exploratory materials research generally spearheaded by national laboratories and universities. The program elements are organized as shown in Figure 3.

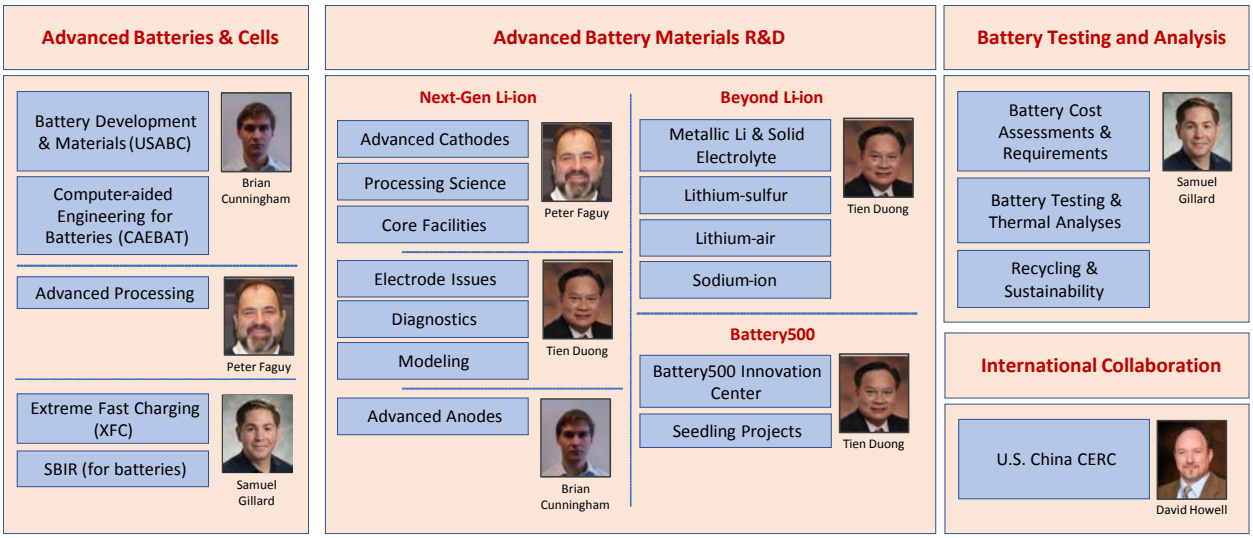

Figure 3. Battery R&D Program Structure

As a further resource, the Electrochemical Energy Storage Roadmap describes ongoing and planned efforts to develop electrochemical storage technologies for PEVs and can be found at the EERE Roadmap page http://energy.gov/eere/vehicles/downloads/us-drive-electrochemical-energy-storage-technical-team-roadmap. Battery R&D activities are organized into four program elements which are inter-related and complementary, namely:

- Advanced Batteries and Cells R&D
- Advanced Battery Materials R&D
- Battery Testing and Analysis
- International Collaboration

The *Advanced Cell and Battery Research and Development activity* focuses on the development of robust battery cells and modules to significantly reduce battery cost, increase life, and improve performance. Part of this effort takes place in close partnership with the automotive industry, through a cooperative agreement with the United States Advanced Battery Consortium (USABC). In this report, **Chapter I** focuses on the Advanced Cell and Battery R&D activity, including a short list of the energy storage SBIR project-starts. In FY 2017, the USABC supported thirteen cost-shared contracts with developers to further the development of batteries and battery components for PEVs and HEVs. In addition to the USABC projects, DOE supports battery and material suppliers via contracts administered by the National Energy Technology Laboratory (NETL) and development of tools for the computer aided engineering of batteries. Finally, a research project to understand and enable XFC in enhanced Li-ion systems was begun in 2017 and is described in that chapter of the report as well. Several Small Business Innovation Research (SBIR) projects, also supported by VTO, are focused on the development of new battery materials and components and are the source of new ideas and concepts and are covered in that chapter.

The *Advanced Materials Research activity* addresses fundamental issues of materials and electrochemical interactions associated with rechargeable automotive batteries. It develops new/promising materials and uses advanced material models to discover them and their failure modes, as well as scientific diagnostic tools and techniques to gain insight into why they fail. This work is carried out by researchers at several national labs, universities, and commercial entities. DOE recently focused research into the nature and stability of the solid-electrolyte interphase that forms on silicon anodes (a critical component of next-gen Li-ion cells). In this report, **Chapter II** focuses on the Advanced Materials Research activity. The silicon deep dive and SEISta programs are described in this chapter. Also, there is a high-energy high-voltage (HEHV) deep dive effort focused on understanding and mitigating the failure modes of transition metal oxide cathodes when operated at

high (>4.5V) voltages. This chapter also describes research into BLI technologies, such as solid-state battery technology, lithium metal, lithium sulfur, and lithium air systems. Some of the areas of focus include new methods to understand and stabilize lithium metal anodes; how to contain Li polysulfides to enable the use of sulfur cathodes; and developing electrolytes that support lithium air and lithium sulfur cells. The newly-started VTO Battery500 projects are managed in conjunction with this program element.

The *Battery Testing, Analysis, and Design activity* has a supporting role toward the other battery programs. It works in close collaboration with USABC to develop requirements and test procedures. Other projects in this area include performance, life and abuse testing of contract deliverables, laboratory- and university-developed cells, and benchmark systems from industry; thermal analysis, thermal testing and modeling; cost modeling; secondary usage and life studies; and recycling studies for core materials. It evaluates battery technologies according to USABC-stipulated battery test procedures and performs benchmark testing of emerging technologies to remain abreast of the latest industry developments. In this report, **Chapter III** focuses on the Battery Testing, Analysis, and Design activity. The *Recycling and Sustainability* element of this activity involves studies of full life-cycle impacts and costs of battery production and use; cost assessments and impacts of various battery recycling technologies; and the material availability for recycling and secondary usage and their cost impacts.

VTO has established extensive and comprehensive ongoing *collaboration* efforts in energy storage R&D across the DOE and with other government agencies, and this coordination is a key attribute of battery R&D efforts. It coordinates efforts on energy storage with the Office of Science, and the Office of Electricity. Coordination and collaboration efforts include membership and participation in the Chemical Working Group of the Interagency Advanced Power Group (IAPG), in program reviews and technical meetings by other government agencies, and the participation of representatives from other government agencies in the contract and program reviews of DOE-sponsored efforts. DOE also coordinates with the Department of Army's Advanced Vehicle Power Technology Alliance, the Department of Transportation/National Highway Traffic Safety Administration (DOT/NHTSA), the Environmental Protection Agency (EPA), and the United Nations Working Group on Battery Shipment Requirements. Additional international collaboration occurs through a variety of programs and initiatives. These include: the International Energy Agency's (IEA's) Hybrid Electric Vehicles Technology Collaboration Program (HEV TCP); the G8 Energy Ministerial's Electric Vehicle Initiative (EVI); and bilateral agreements between the U.S. and China. The collaborative activities with China under U.S. China CERC are described in **Chapter IV**.

Battery Highlights from FY 2017

The following are some highlights associated with battery R&D funded by VTO (including highlights related to market developments, R&D breakthroughs, and commercial applications).

- **EV market expanding globally.** The U.S. remains a leading market for EVs. It produces some of the most advanced PEVs available today. Recently, both the European Union and China experienced rapid growth in EV sales (the combined sales in those top three markets reaching almost 2 million in 2016). Consumer interest in PEVs is growing, despite occasional drops in gasoline prices. In 2017, U.S. PEV sales jumped 30% from 2016 levels as worldwide PEVs sales increased almost 50% (through September, for both years). There were 39 PEV models being offered for retail sale in the U.S. and nearly 750,000 PEVs on U.S. roads near the end of 2017.

- **Battery cost reduction.** The 2017 DOE PEV battery cost reduction milestone of $225/kWh was accomplished. DOE-funded research has helped reduce the current cost projection for an EV battery (for three DOE-funded battery developers) to an average $213/kWh of useable energy. This cost projection is calculated using ANL's public domain Battery Production and Cost model (BatPaC). It assumes a production volume of at least 100,000 batteries per year, the batteries meeting DOE/USABC system performance targets. DOE's goal is to continue to drive down battery cost to $100/kWh by 2022.

- **Technical assessment of extreme fast charge functionality.** Extreme fast charging (XFC), or charging an EV at power rates of up to 400 kW, stands to increase the utility of EVs. (For example, it has been found that utilizing 50kW fast charging for 1-5% of all annual charges leads to a nearly 25% increase in annual vehicle miles traveled.) ANL, INL, and NREL have collaborated together and with industry pertners to identify the technical challenges for XFC. R&D efforts for XFC could be focused on batteries, vehicles, infrastructure, and economic feasibility. The goal would be to explore technology solutions needed to achieve XFC. The key XFC challenges include:

    - more rapid and powerful charging generates higher temperatures, which can lead to battery degradation and safety issues (including the issue of lithium plating);
    - current power electronics are built for slower overnight charging and may be unable to withstand the stresses of higher-voltage battery systems for XFC; and
    - XFC's high, but intermittent demands for electricity could pose challenges to grid stability.

    The XFC research team is exploring solutions to these issues and examining factors related to vehicle technology, new demands on system design, and thermal management requirements.

- **Successful commercial applications.** VTO has a successful track record of planning and executing R&D on critical battery technologies which later move into commercial applications. Hybrid and electric vehicles on the market from all major car manufacturers use lithium-ion technologies developed under prior VTO-funded projects. Some lithium-ion chemistries developed with DOE support have also found their way into stationary applications. For example, the Saft Intensium system, which uses graphite/NCA chemistry developed with VTO support (Figure 4), has been installed at various locations in California, Hawaii, and Finland.

Figure 4. Saft Intensium Stationary Storage Battery

- **Fluorinated electrolyte to improve the performance of high voltage NMC532/graphite cells.** ANL discovered that an electrolyte-based on fluorinated sulfones improved the cycle life of NMC532/Graphite full cells. It evaluated performance of the electrolyte additive using a high energy high voltage (HEHV) protocol, which predicted the cycle number that will have 80% capacity retention under the protocol. This cycle number improved from 150 cycles with baseline electrolyte to 400 cycles in the presence of the new fluorinated electrolyte (Figure 5).

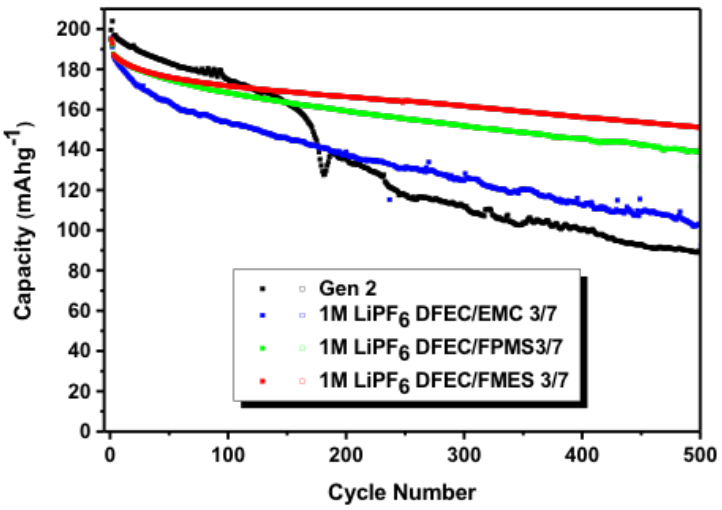

Figure 5. Capacity retention of NMC532/graphite full cells cycled with Gen 2 (non-fluorinated) and various mixtures of fluorinated sulfone-based electrolytes. (C/3 for 100 for cycling between 3.0 and 4.6 V.)

- **Morphology and stability of NMC materials.** The instability of NMC-based cathode surfaces is a major impediment to their use in high-energy, high-voltage Li-ion cells. Computational modeling at ANL revealed how NMC particles take shape under different synthesis conditions; and subsequent experimental synthesis at LBNL confirmed the predictions. Results of the study predict that the (012), (104), and (001) surfaces (Figure 6) are the dominant surfaces under normal synthesis conditions. However, only the (012) and (104) surfaces can pass lithium during cycling. In addition, the (104) surface is more stable than the (012). Thus, tailoring synthesis conditions to favor the formation of the (104) surface would enhance both the electrochemical performance and stability of NMC particles.

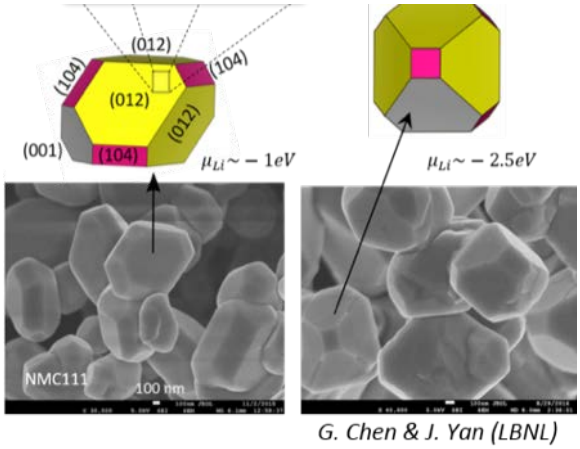

Figure 6. Simulated NMC particle shapes obtained under select synthesis conditions. (Bottom) images of NMC particles (LBNL) verifying the modeling results.

- **Understanding oxygen redox processes in high capacity Li-ion cathode materials.** Li- and Mn-rich layered oxides demonstrate an exceptionally high capacity (>250 mAh/g), well beyond the theoretical capacity solely from Ni and Co redox (i.e., 127 mAh/g for Ni redox in $Li_{1.2}Ni_{0.2}Mn_{0.6}O_2$). Lattice oxygen is typically believed to compensate for additional charge beyond transition metal (TM) redox. LBNL used cutting edge synthesis and characterization techniques, including resonant inelastic x-ray scattering (RIXS) and differential electrochemical mass spectrometry, to probe the activity of lattice oxygen in those cathodes. A striking feature appears at the charged state of $Li_{1.2}Ni_{0.2}Mn_{0.6}O_2$ which disappears after

2.0 V discharge. However, no such feature was observed for $Li_{1.2}Ni_{0.2}Ru_{0.6}O_2$. This unique feature, observed for the first time, is evidence of oxygen redox in the electrochemistry of $Li_{1.2}Ni_{0.2}Mn_{0.6}O_2$ and provides insight into oxygen redox to achieve high capacity cathode materials.

- **Surface dopants for oxygen retention in Li-excess cathode materials.** Li-excess materials show promise as high-energy cathodes except for certain barriers (e.g., a significant first-cycle oxygen release). High-throughput computational screening of multiple elements found suitable for surface doping and surface oxygen retention indicated Os, Sb, Ru, Ir, and Ta as best dopants for enhancing surface oxygen retention. LBNL measurement of 2% Ta-doped $Li_{1.3}Nb_{0.3}Mn_{0.4}O_2$ indicated that despite the low amount of Ta, the Ta-doped Li-excess cathode improved its electrochemical performance and significantly reduced oxygen evolution compared to the un-doped material.

- **A tool to map abuse response of Li-ion batteries**. The Energy Storage Team at NREL incorporated component level abuse models into a generic "safety-map" for Li-ion modules. The rate of heat generation from an abuse event is related to the short resistance. Additionally, the higher the thermal conductivity of the packaging material, the greater the rate of heat rejection from the cell to the surroundings. By plotting the rate of heat generation vs. heat rejection, NREL evaluated multiple module design parameters, e.g., the spacing between cells, flow rates for coolants, etc. Researchers from SNL then constructed battery modules consisting of 3 Ah $LiCoO_2$ COTS pouch cells in a 5-cell configuration. Aluminum and copper plates of 1/8, 1/16, and 1/32" thickness, were placed between cells as a passive thermal management barrier. Reduced propagation is achieved when a slight increase in material thickness from 1/16" to 1/8" was implemented, Figure 7. When plate thickness is decreased to 1/32", full propagation was observed. Mapping the rate of heat generation versus rejection, one can evaluate a variety of module design parameters.

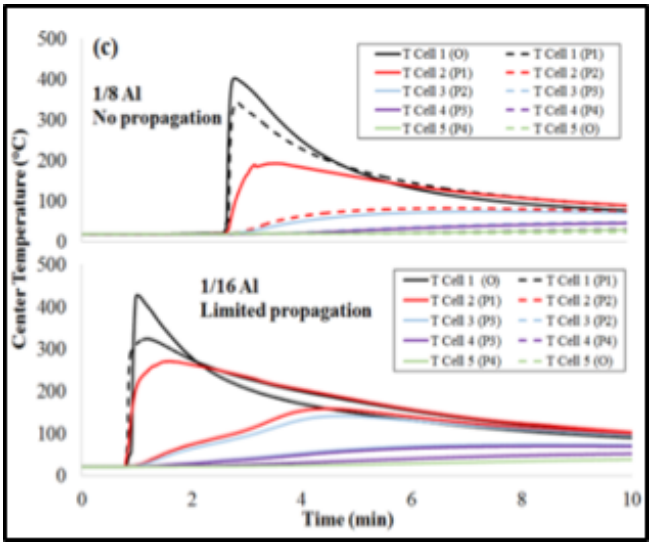

Figure 7. Experimental verification of propensity for propagation: the thicker aluminum plates offer higher rates of heat transfer away from the cell and as a result minimize the risk for propagation.

- **Low/Zero VOC processing of thick, crack-free electrodes.** The use of thick electrodes (>25mg/cm^2, >4mAh/cm^2) offers the opportunity to produce lower-cost, higher energy Li-ion batteries. In an effort to avoid cracking during electrode drying (often seen with aqueous binders) the influence of solvent surface tension on cracking was investigated. Small amounts of isopropanol (IPA) and/or Methyl Acetate (MeOAc) were tested, mixed in water as novel solvents, for electrode processing. Thick crack-free cathodes were produced with comparable performance to electrodes processed with conventional NMP solvent, Figure 8.

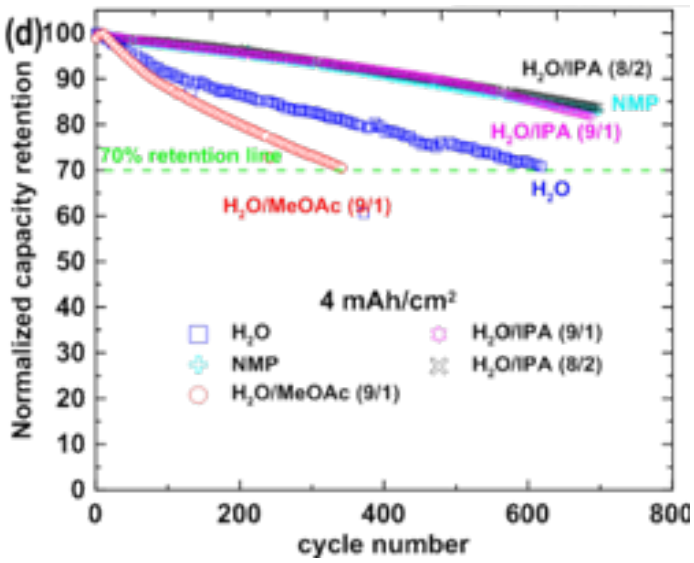

Figure 8. The aqueous processed cracked electrode reaches 70% capacity retention after 620 cycles due to its poor coating quality. With IPA addition to the aqueous binder, cycling performance is comparable to NMP solvent processed electrodes.

- **Porous Si electrodes enable long cycle life and controlled swelling.** One challenge to using Si-based anodes is the swelling it undergoes. A PNNL team designed a porous Si/C–graphite electrode to illustrate controlled swelling. Excellent agreement between the theoretical design and experimental data was demonstrated. The practical electrode (3 mAh/cm^2 loading) with a specific capacity of 650 mAh/g had an approximate 82% capacity retention over 450 cycles. The initial electrode swelling upon full lithiation was less than 20%. The calendered electrodes demonstrated less than 56% end-of-life swelling and approximately 90% capacity retention after 200 cycles. The NMC111 and the pre-lithiated anode full-cell achieved an approximately 84% capacity retention over 300 cycles**.**

- **High active material electrodes.** Physical Sciences Inc. (PSI) developed a technology for higher energy density Li-ion batteries by eliminating or reducing inactive, non-energy storing components, while extending the maximum voltage. PSI developed an active material coating that enables high active (HA) loading, greater than 98% by mass (Li-ion batteries typically have active material contents of 90-95%). It also provides a denser coating thus increasing the energy per unit volume. 3Ah cells constructed with HA electrodes cycled at 4.4V deliver 90% of their initial capacity after 1,000 cycles, see Figure 9.

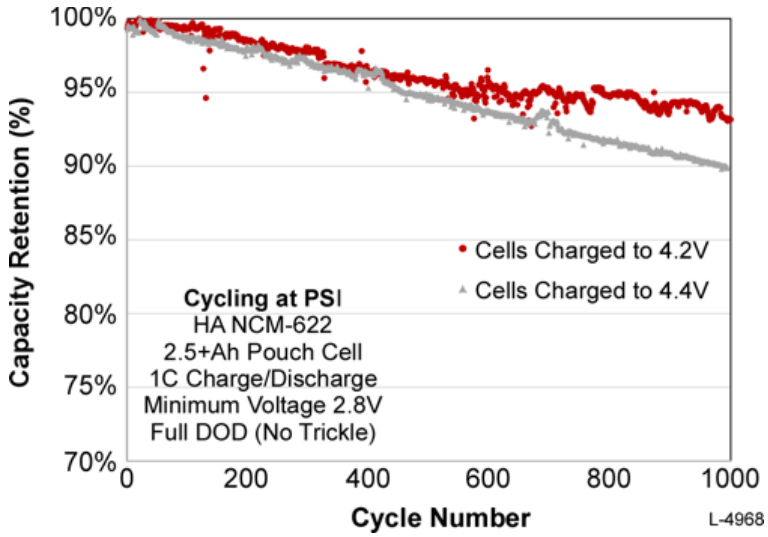

Figure 9. PSI HA cells cycled from 2.8 to 4.2 and 4.4V deliver ~90% of initial capacity after 1000 cycles.

- **Microporous silicon (µpSi) anode production.** Navitas Systems, in collaboration with ANL and NexTech Materials, demonstrated a novel, scalable approach to manufacture µpSi for next-gen Li-ion cells. The result is a manufacturing process for battery grade µpSi powder in high volume at a cost suitable for post-processing. The electrode is able to meet the 1300mAh/g and $25/kg target anode capacity and cost needed to reach DOE cost and performance goals, Figure 10.

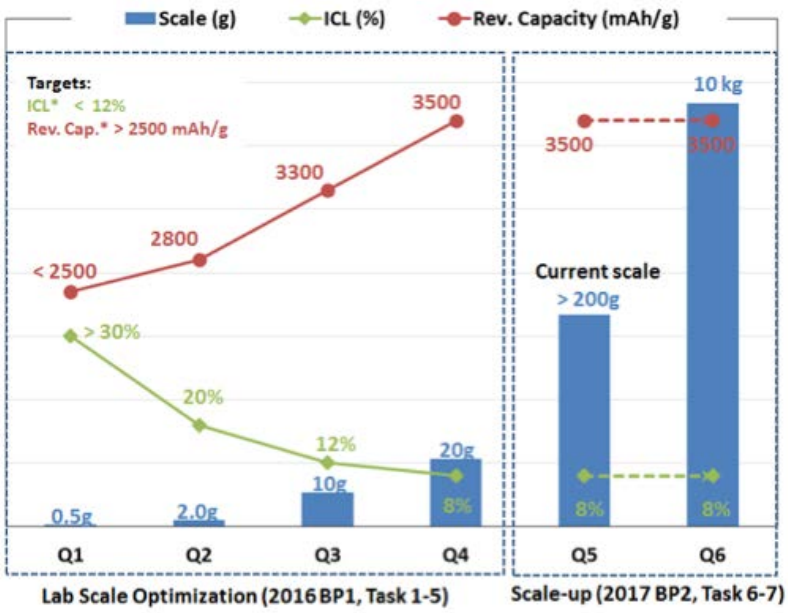

Figure 10. Capacity and ICL both improved during Navitas' material scale up procedures

- **Freon-mediated dense and conformal LiF protection layer on Li metal anodes.** Stanford University explored the possibility of gas phase reaction (using Freon R134a, 1,1,1,2-tetrafluoroethane, as the reagent) to produce high-quality, conformal, LiF passivation layers on 3D Li-metal anodes. This gas has several advantages: (1) gaseous Freon exhibits high permeability to coat the 3D surface conformally; (2) Freon 134a is low cost and commercially available; and (3) Freon 134a is non-toxic and environmentally friendly. By exposing lithium metal to Freon R134a gas, assisted with controlled gas

pressure, and reaction temperature, it was able to coat a dense and uniform LiF layer with tunable thickness directly onto metallic lithium. Symmetric-cell cycling corroborated the enhanced stability with LiF coating, with negligible voltage fluctuation observed for over 200 cycles.

- **Polysulfide trapping agent for improved Li/S batteries.** The University of Pittsburgh developed a directly-doped sulfur architecture (DDSA) electrode enabling high sulfur loadings of approximately 18 mg/cm^2 (18 mAh/cm^2) (approximately five times higher than typical slurry-coated electrodes). The DDSA electrodes are then coated with polysulfide trapping agent (PTA) that can bind polysulfides, preventing their entry into the electrolyte where they often migrate to the Li metal anode and cause capacity fade. Both the DDSA electrodes and PTA coated DDSA electrodes were tested in coin cells against lithium metal anode (Figure 11).

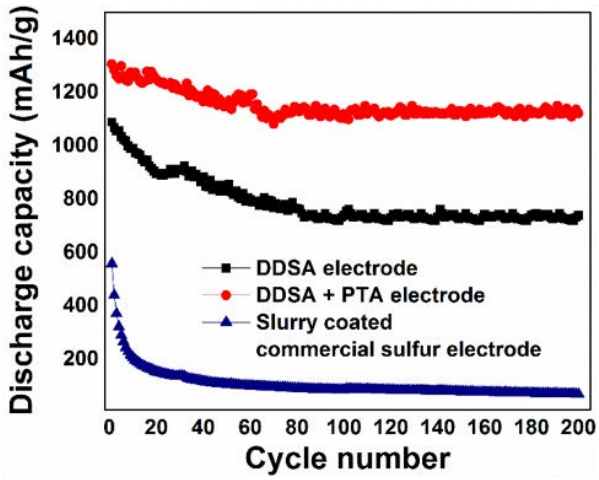

Figure 11. Cycling performance of DDSA electrode, PTA coated DDSA electrode, and standard slurry coated electrode.

- **Novel electrolyte enables fast charging and stable cycling of Li metal batteries.** PNNL discovered that an optimal amount (0.05 M) of $LiPF_6$ additive in LiTFSI–LiBOB dual-salt/carbonate-solvent-based electrolytes enhances the charging capability and cycling stability of Li metal batteries. In a Li metal battery using a 4-V Li-ion cathode at a loading of 1.75mAh/cm^2, 97.1% capacity retention after 500 cycles in attained (Figure 12) along with very limited increase in electrode overpotential at a current density up to 1.75mA/cm^2. The fast charging and stable cycling performances are ascribed to the generation of a robust SEI at the Li metal surface and the stabilization of aluminum current collector.

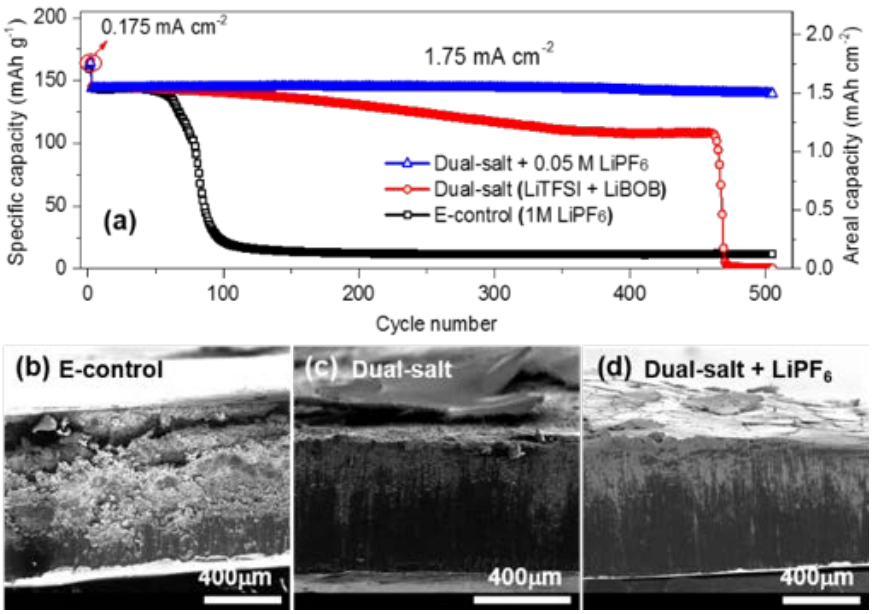

Figure 12. a) Capacity vs cycle number of Li/NMC cells with various electrolytes in EC-EMC solvent. (b-d) Cross-section of Li electrodes after 100 cycles using (b) conventional LiPF6 electrolyte, (c) LiTFSO-LiBOB dual-salt electrolyte, and (d) 0.05M LiPF6 added dual-salt electrolyte.

- **Self-forming artificial SEI for Li metal electrodes.** General Motors developed a simple physical vapor deposition process to coat Li metal electrodes with fluorinated nanocomposite coatings. The self-forming coating forms an SEI layer, conformal and dense, which effectively isolates Li metal from the electrolyte. The flexibility of the coating makes it easy to accommodate electrode volume changes. The high conductivity of the coating leads to more uniform current distribution to ensure homogenous Li plating and stripping. The protected Li metal electrodes, combining with high concentration salt electrolyte developed at PNNL, show significantly improved cycle stability in symmetrical cells under harsh testing conditions (Figure 13).

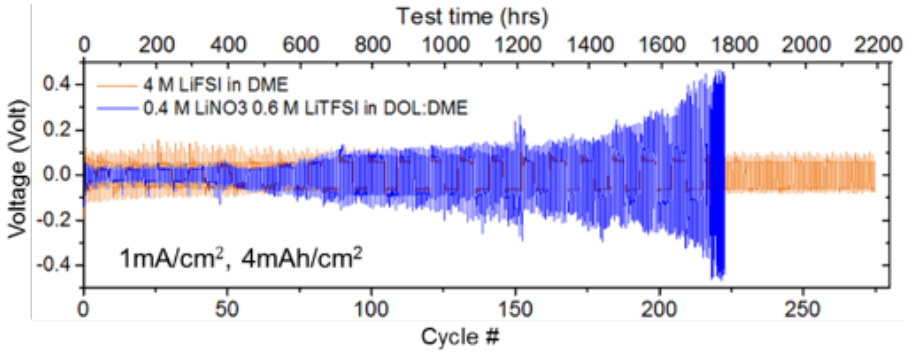

Figure 13. Fluorinated protective coating plus high concentration salt electrolyte enables improved Li/Li symmetric cell cycling compared to cells without the coating and in a low concentration salt electrolyte.

- **Improved interfacial contact between solid electrolyte and Li metal electrodes.** Over the last two decades, several solid electrolytes have been discovered. One class of ceramic solid, based on mineral garnet atomic structure, exhibits a good combination of rapid ion transport and stability. For the battery to function effectively, the garnet must bind tightly to the Li metal to reduce interfacial impedance; and metals typically do not bond to ceramics. Ideally, bonding between lithium and garnet electrolyte should be achieved with no coating. Recently, this was demonstrated at the University of Michigan that a simple

heat treatment to clean the surface, allows bonding between metallic lithium and the garnet, Figure 14. Without cleaning, the solid garnet electrolyte surface is passivated by a contamination layer consisting of lithium carbonate due to reaction with air. By removing the lithium carbonate layer through heat treatment, molten lithium bonds or wets the GSE as shown by the contact angle experiment. In addition, the effect of surface treatment is maintained upon cooling to ambient temperature. These findings could accelerate the development of advanced solid-state batteries that double the energy density of conventional Li-ion batteries.

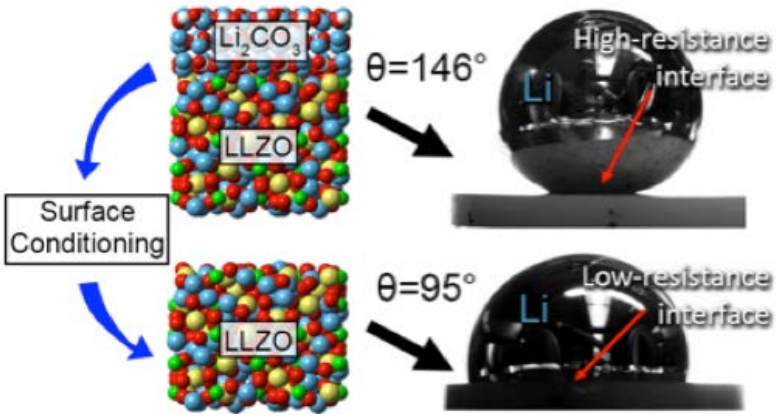

Figure 14. Evidence that Li metal can effectively bond to a solid ceramic as evidenced by theory (left), and lower wetting angle (right).

- **MERF– concentration gradient research.** Cathode materials with high energy materials in their cores and more stable materials on their surfaces promise both high energy, improved life, and enhanced abuse tolerance. The ANL MERF facility used scalable manufacturing processes to prepare two types of gradient materials in this class: 811 core-gradient and 811 core-shell, Figure 15a and Figure 15b. Figure 15c compares the electrochemical performance of the 811 core-gradient, core-shell and a commercial NMC811 cathode. The 811 core-gradient and core-shell cells show a 20% improved capacity retention compared to the commercial 811 non-core shell material. In addition, the core shell and concentration gradient cathodes show higher onset temperature and 35% reduced heat generation compared with the commercial NMC811, Figure 15d; thus showing enhanced abuse tolerance. These results demonstrate that the gradient particle structure is a practical and effective approach to stabilize high-energy and highly stable nickel-rich NMC cathode materials.

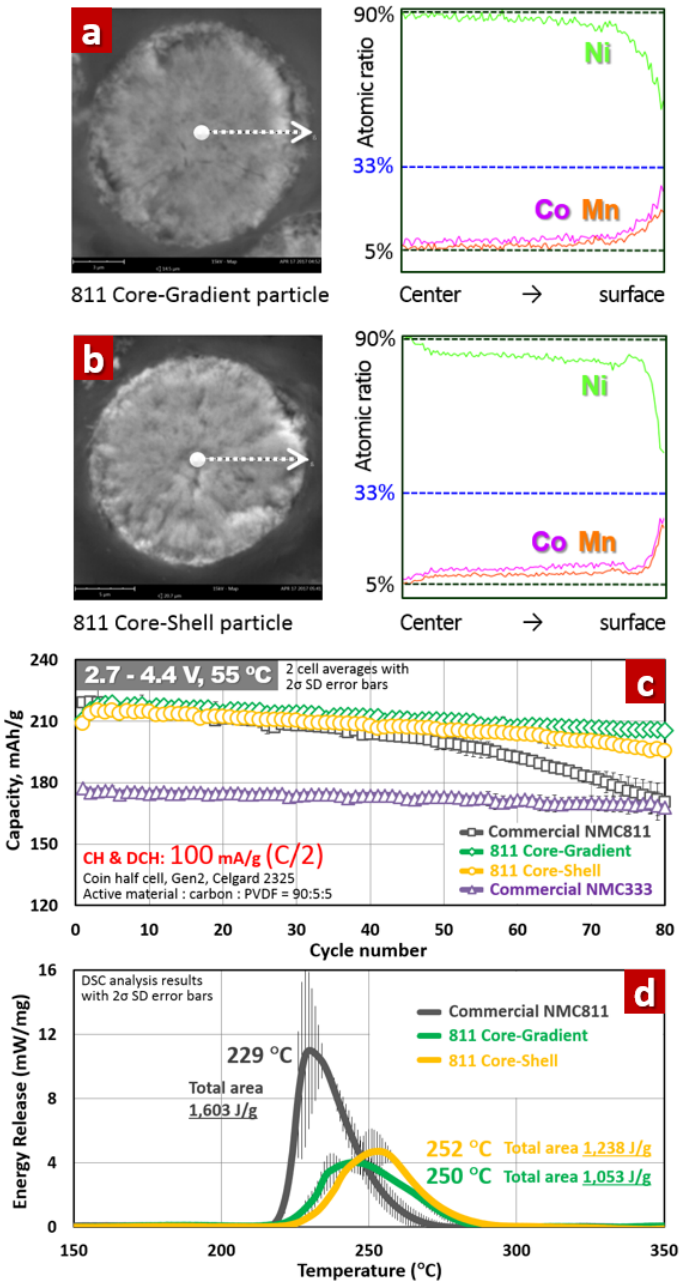

Figure 15. (a) Cross-sectional elemental mapping of the prepared 811 Core-Gradient cathode. (b) Cross-sectional elemental mapping of the prepared 811 Core-Shell cathode. (c) Comparison of electrochemical performance. (d) Thermal stability comparison.

- **BatPaC version 3.1 released.** BatPaC is a spreadsheet tool for the design of automotive Li-ion cells and batteries. Using user-supplied cell and pack design, it calculates the large volume manufacturing cost of cells and battery packs (50K-500K packs per year). New capabilities in the tool in v 3.1 include incorporating the cost of fast-charge and recycling cost recovery at the end of a battery's life.

- **Battery500 seedling projects.** DOE, in collaboration with the Battery500 team, awarded 15 "seedling projects" to supplement work within the Battery500 project. It is hoped that the seedling projects (Table 3) will bring additional ideas for solving difficult technical issues associated with lithium metal-based cells, and possible new ways of achieving the Battery500 goals.

Table 3: Battery500 Seedling Projects

Organization	Description	Funding
University of Maryland: College Park	Research innovative iron-based materials for high energy cathodes for high energy Li-ion battery technologies.	$400,000
Lawrence Berkeley National Laboratory	Research thick cathodes using freeze casting methods for solid-state lithium batteries.	$400,000
Penn State University Park	Research multifunctional Li-ion conducting interfacial materials that enable high- performance lithium metal anodes.	$399,194
Mercedes-Benz Research & Development North America, Inc.	Research a scalable synthesis to enable very thin coatings on solid state electrolyte membranes to enable high performance Li-Sulfur Battery.	$400,000
University of Maryland: College Park	Using 3D printed, low tortuosity frameworks, develop solid state Li-ion batteries.	$400,000
General Motors LLC	Design, engineer, develop, and integrate pouch-format cells for lithium-sulfur batteries to achieve high energy density and long cycle life.	$400,000
University of Pittsburgh	Research sulfur electrodes utilizing Li-ion conductor (LIC) coatings for high energy density advanced lithium-sulfur (Li-S) batteries.	$400,000
Cornell University	Research highly loaded sulfur cathodes and conductive carbon coated separators that enable high energy batteries.	$360,000
University of Maryland: College Park	Research advanced electrolytes to limit dendrite growth in lithium-metal cells.	$400,000
Texas A&M Engineering Experiment Station	Utilize an analytical and experimental approach to examine the interface between solid state electrolytes and lithium-metal anodes and identify potential methods for mitigating dendrite growth.	$400,000
Navitas Advanced Solutions Group, LLC	Research a solvent-free process to fabricate all-solid Li batteries.	$400,000
Wayne State University	Research novel full-cell, ultra high-energy Li- metal batteries based on 3-dimensional architectures.	$225,000
Oregon State University	Research and develop a new process to produce Li2S@graphene composite cathodes to inhibit polysulfides to enhance cycle life.	$353,500
SUNY University at Stony Brook	Research li-sulfur batteries using a novel sulfur rich nanosheet composite cathode.	$400,000
University of Houston	Research high-energy solid-state lithium batteries with organic cathode materials.	$400,000

I. Advanced Battery and Cell Research and Development

I.A USABC Battery Development & Materials R&D

I.A.1 High Energy Lithium Batteries for Electric Vehicles (Envia Systems)

Herman Lopez, Principal Investigator
Envia Systems Inc.
7979 Gateway Boulevard, Suite 101
Newark, CA 94560
Phone: 408-406-3210
E-mail: hlopez@enviasystems.com

Brian Cunningham, Technology Manager
U.S. Department of Energy
Phone: 202-287-5686
E-mail: Brian.Cunningham@ee.doe.gov

Start Date: June 1, 2014 End Date: December 31, 2017
Total Project Cost: $7,718,493 DOE share: $3,859,246 Non-DOE share: $3,859,247

Project Introduction

Electric vehicles (EVs) have received intense attention as a possible solution to reducing our dependence on fossil fuels and decreasing greenhouse gas emissions. One barrier preventing the widespread adoption of EVs relates to the lack of available high energy, low cost and safe energy storage solutions. Lithium-ion batteries (LIBs) are presently among the best energy storage solutions for current EVs. Further improving the performance of LIBs by integrating high capacity active materials, novel passive components and unique cell designs will be critical to the success and mass adoption of EVs.

This project is developing a new battery system based on novel high capacity Ni-Co-Mn (NCM) cathode blends and high capacity silicon-based anode composites that could meet the United States Advanced Battery Consortium (USABC) EV cell performance targets for 2020. In order to enable high Si-content anodes, a manufacturable and cost-effective pre-lithiation process will need to be developed to compensate for the high irreversible capacity loss (IRCL) of the anode. At the conclusion of the program, Envia aims to demonstrate LIBs with usable specific energy greater than 350 Wh/kg and a usable energy density greater than 750 Wh/l while meeting other performance requirements of EV cells (power, calendar life, cycle life, safety and cost). This will be achieved through collaboration among several organizations, each providing expertise on specific components of the material, processing and cell. Ultimately, large format cells meeting the USABC goals will be built and delivered to the national laboratories for testing.

Objectives

- Develop high capacity silicon-based anode composite electrodes capable of supporting long cycle life by controlling electrode pulverization, lithium consumption and conductivity loss.
- Develop high capacity cathode blend composites capable of supporting the energy, cycle life, calendar life, power, safety, and low/high temperature cell requirements.
- Develop a manufacturable cost effective pre-lithiation process that enables fabrication of large-format high-capacity pouch cells.

- Screen and down-select best electrolyte formulation and separator to support meeting USABC performance, cost and safety cell targets.
- Design and optimize active and passive cell materials with cell design meeting USABC EV cell goals.
- Build, test and deliver large format pouch cells integrating high capacity Si-based anode and cathode composites along with optimized electrolyte, separator and pre-lithiation processes that meet the USABC EV cell goals.

Approach

Envia is utilizing a system-level approach to screen, develop and optimize critical cell components (cathode, anode, electrolyte, separator), pre-lithiation processes (process and dose), cell design (N/P ratio, electrode design) and cell formation and testing protocols that will meet the USABC EV cell level goals for the year 2020. This consists of integrating high capacity Ni-Co-Mn cathode blends, pre-lithiated silicon-based high capacity anodes, high voltage electrolyte and coated separator into large capacity (~50 Ah) pouch cells. The developed cells will exhibit high energy density and power, good cycle life and calendar life and acceptable low temperature performance while meeting cell level cost and safety targets. Cells will be delivered and tested by three national laboratories: the Idaho National Laboratory (INL), the Sandia National Laboratories (SNL) and the National Renewable Energy Laboratory (NREL).

Envia is leveraging its material, process and cell development expertise to develop, modify and engineer material and cell-level solutions to meet cell specifications. In this project, Envia partnered with Daikin America (for electrolyte), Asahi Kasei (for separator), Nanoscale Components (for pre-lithiation processing), A123 Venture Technologies (for cell manufacturing), 3M (for Si alloys), and DuPont (for n-Si composites) to develop superior materials, processes and cells.

The program has been structured in a way that as it progresses, the cell targets increase in difficulty in specific energy, energy density, cycle life and cell cost. The program consists of five (5) cell-builds that include an initial baseline and a final program cell-build intended to integrate the lessons from the program and meet the final cell targets. The program has finished the first three cell-builds and is currently working on both cell-build #3 (CB#3) and cell-build #4 (CB#4) which are the final cell-builds and program deliverables. Cell-build #3 is an internal cell-build with the goal of developing 11 Ah capacity cells with specific energy >300 Wh/Kg and a cycle life of 1000 cycles. The internal cell development of cell-build #3 will serve to freeze the final cell design of the program (build #4). Figure I-1 shows the measured and projected specific energy, energy density, cycle life and cell cost for the various program cell-builds. As the figure shows, different cell-builds focused on different format and capacity cells. The baseline cell-build consisted of 21 Ah capacity cells, cell-build #1 consisted of smaller 1.2 Ah capacity cells, cell-build #2 consisted of 11 Ah capacity cells, while the remaining cell-build #3 and #4 will focus on 11 Ah and 50 Ah capacity cells, respectively.

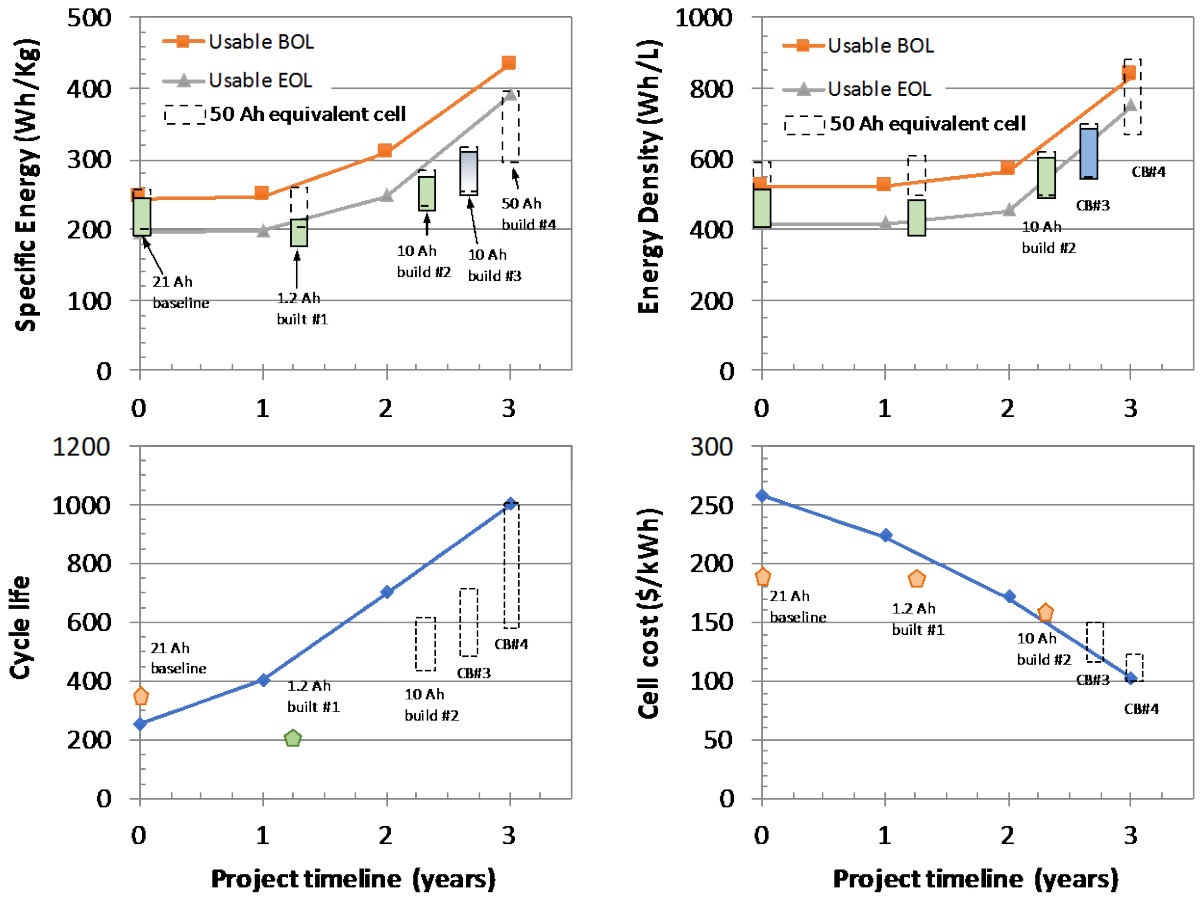

Figure I-1. Current and projected cell development progression throughout the USABC program

Results

Cell Development. Envia completed the assembly and validation of 11 Ah capacity (280 Wh/Kg specific energy) cells as part of the program's cell-build #2 (CB#2) deliverable. Envia delivered 28 pouch cells to the national laboratories (17 cells delivered to INL, 8 cells delivered to SNL & 3 cells delivered to NREL) in late May 2017. Build #2 cells improve upon the baseline by incorporating a higher efficiency 11 Ah cell design, as well as making use of a semi-automatic lithium powder pre-lithiation process enabled by Envia's recently acquired equipment. The pre-lithiation process using the new lithium metal powder equipment will continue to be used and improved for the remaining program cell-builds. Figure I-2 shows the reproducible cell capacity, specific energy, weight and thickness of the 28 cells delivered to the national labs as part of build #2 deliverable.

Cycle life continues to be one of the major challenges of working with silicon-based anodes. Due to the large volume expansion associated with silicon-based anode materials, pulverization and fragmentation are common failure modes that can greatly limit cycle life. Envia continues to optimize the cell design (loading, density, N/P, etc.) and material selection (anode, cathode, electrode additives, electrolyte, and separator) to enable high specific energy cells targeting >300 Wh/Kg and a cycle life of 1,000 cycles. Figure I-3 shows a normalized capacity plot of 21 Ah capacity pouch cells (245 Wh/kg) cycling at a C/3 rate in excess of 700 cycles before reaching 80% capacity retention, as well as 11 Ah capacity pouch-cells from a more weight- and volume-efficient cell form factor showing promising cycle life (> 500 cycles). The design of the 11 Ah capacity cells is similar to build #2 cells delivered to the national laboratories which show a specific energy of 280 Wh/Kg and a cycle life > 500 cycles before reaching 80% capacity retention.

It is encouraging to note that both cell designs integrate similar high SiO_x containing (>50%) anode electrodes and a high capacity cathode incorporating Ni-rich and Mn-rich NMC cathode blends. Cell design and material selection continue to be fine-tuned, as part of cell-build #3 (CB#3) development, to further improve the cycle life to > 1000 cycles and at the same time increase the specific energy > 300 Wh/Kg. Similar, yet higher capacity anode and cathode electrodes are being explored and integrated into new 11 Ah capacity cell designs as part of cell-build #3 development targeting the USABC cell specifications.

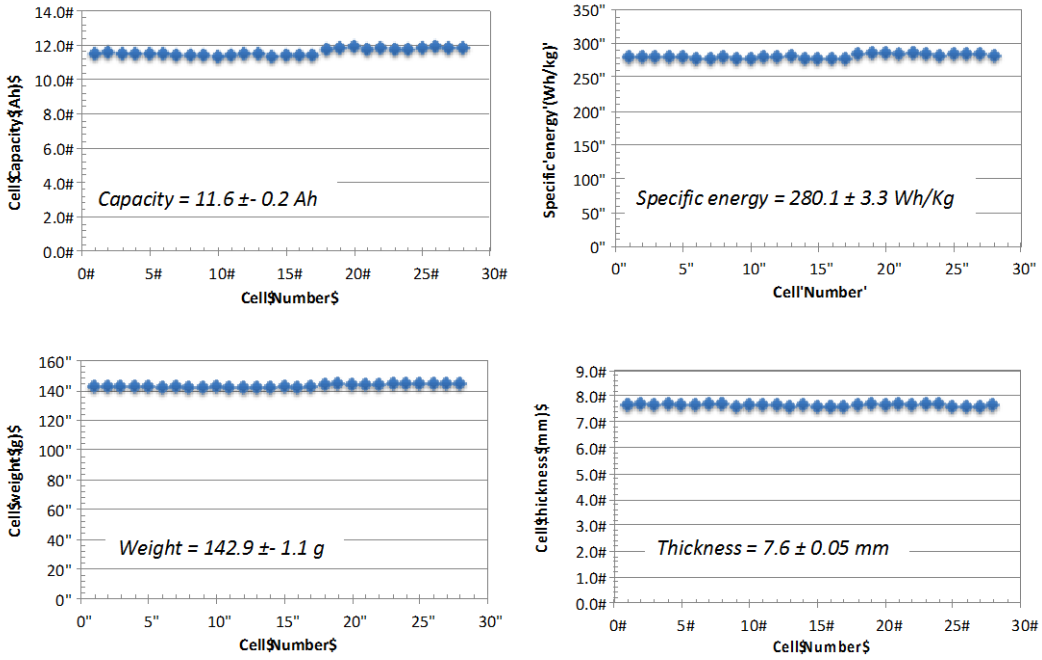

Figure I-2. Cell characteristics of the delivered build #2 cells

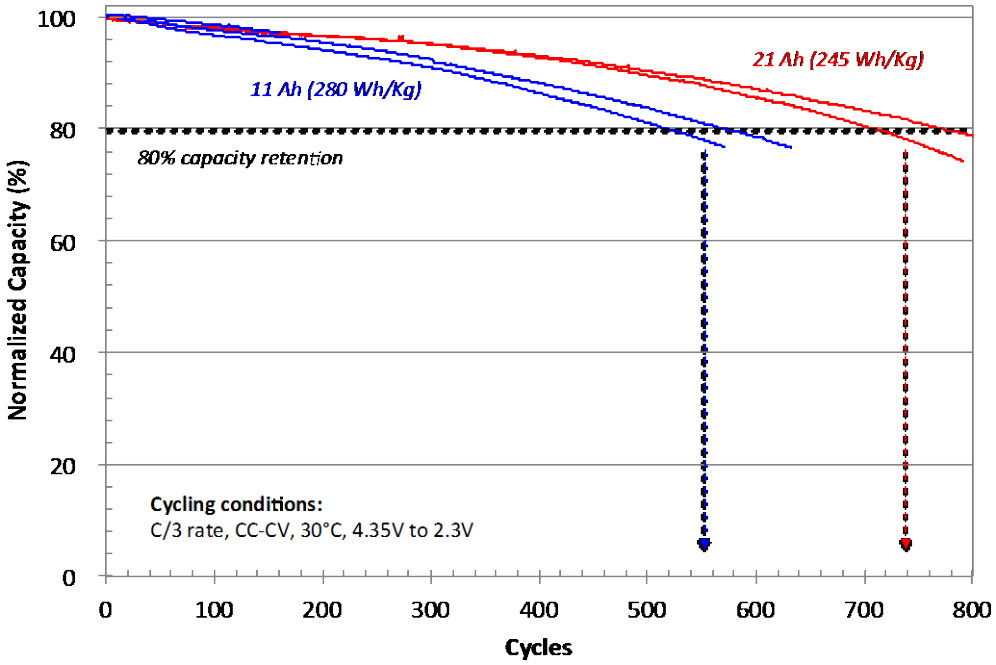

Figure I-3. Normalized capacity versus cycles for 11 Ah and 21 Ah capacity pouch cells

As part of the cell development, Envia continues to focus on failure analysis and cell teardown to understand and mitigate the failure modes of cycled cells. Extensive physical, chemical, structural and electrochemical analysis of cycled cells has shown that the electrochemical integrity of both SiO_x anode composites and NMC cathode blends remain intact even after 700 cycles. This suggests that the typical anode pulverization related failure is under control in our anode electrode systems. Moving forward, similar anode electrode systems are being integrated and optimized in current cell designs to meet USABC cell target specifications. Figure I-4 shows typical images of an open pouch cell undergoing the teardown and failure analysis.

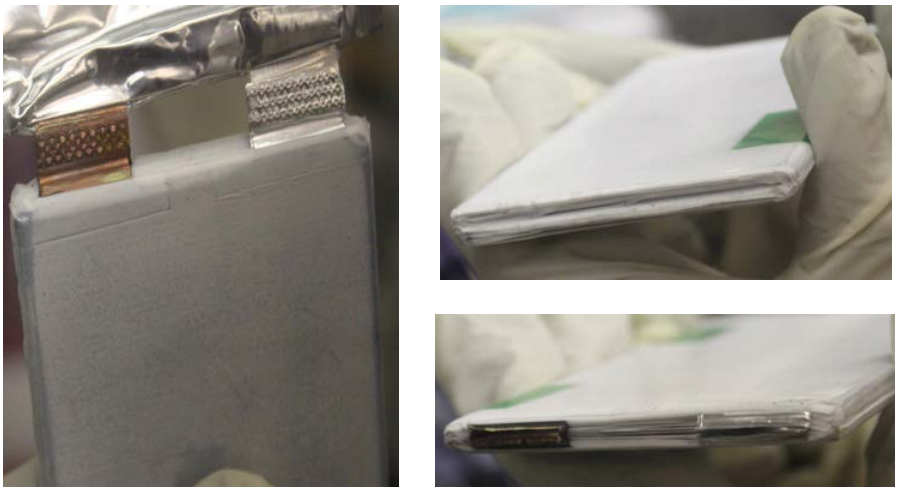

Figure I-4. Images of an 11 Ah capacity pouch cell undergoing teardown and failure analysis

For the final cell deliverable (cell-build #4) of the USABC program, Envia modified the Statement of Work to deliver large capacity cells to:

- Enable a fair comparison to other programs in the USABC portfolio that are also delivering large capacity cells
- Deliver a production representative cell
- Deliver cells which are closer to customer needs
- Gain experience in building and testing large capacity cells

The cell format for final large-capacity pouch cells has been finalized. The USABC technical team provided four options for the larger cell format, consisting of two sizes and two tab orientations. In order to maximize power and energy from the cells, the format with tabs on opposing sides was selected. To choose between the two suggested cell footprint options, the cell capacity as a function of specific energy, cell thickness, cell weight and number of anode layers was modeled. Based on the model results, a 50 Ah capacity pouch cell with a length of 320 mm and width of 102 mm was selected as the cell footprint to be developed and delivered at the conclusion of the USABC program. Envia will deliver 50 Ah capacity cells from the final cell-build #4 to the national laboratories for independent testing of cycle life, calendar life, energy, capacity, power, safety and thermal performance.

Pre-lithiation Development. A consequence of working with high capacity silicon-based anodes, and especially with SiO_x-based materials, is an inherent high irreversible capacity loss. To compensate for this loss, pre-lithiation is a requirement. Envia has partnered with Nanoscale Components, which pre-lithiates anodes via a scalable, manufacturable and cost-effective roll-to-roll electrochemical process. Early in the program, Nanoscale successfully pre-lithiated and delivered silicon-based anode electrode (A#7) to support 1 Ah

capacity build #1 cells. Other anode formulations and compositions were attempted and continue to be optimized during the program to develop a pre-lithiated anode capable of meeting the USABC EV cell targets.

Nanoscale completed its larger pilot scale pre-lithiation line, which can pre-lithiate electrodes up to 300 mm wide for large format pouch cells. Using the new pilot scale line, Nanoscale pre-lithiated Envia's high capacity A#14 anode formulation to the full target dosage. Excellent uniformity of pre-lithiation dosing was also demonstrated; sampled sections showed a standard deviation of dosage of less than 0.5% of anode capacity. Envia assembled 11 Ah capacity pouch cells with the pre-lithiated anode. Cell performance with the resulting cells is not yet optimized due to potential shipping and handling issues. Envia and Nanoscale continue to improve shipping and handling of pre-lithiated anodes so that resulting cells achieve optimal performance. (It should be made clear that, due to a number of technical hurdles, NS prelithiation won't be used in the final deliverable cells.)

Conclusions

Envia has shown >700 cycles before reaching 80% capacity retention from 21 Ah capacity pouch cells integrating a high SiO_x content anode composite, Ni-rich and Mn-rich NCM cathode blend, lithium powder-type pre-lithiation and optimized electrolyte, separator and cell design. Envia completed the assembly and delivery of 11 Ah capacity - 280 Wh/Kg specific energy cells as part of the program's cell-build #2 (CB#2) deliverable. 28 pouch cells were delivered to the national laboratories for independent testing. Envia continues to use a system-level approach to further develop and optimize critical material and cell components (cathode, anode, electrolyte, separator), pre-lithiation, cell design (N/P ratio, electrode design) and cell formation and testing protocols that will enable meeting the USABC EV cell targets. Development will continue as part of cell-build #3 with the goal of down-selecting the best materials, components and processes to integrate as part of cell-build #4 final program deliverable.

Key Publications

1. "High Energy Lithium Batteries for Electric Vehicles", ES247_Lopez_2017_p, US DOE Vehicle Technologies Program Annual Merit Review, AMR, 2017.

2. "High Energy Lithium Batteries for Electric Vehicles", ES247_Lopez_2016_p, US DOE Vehicle Technologies Program Annual Merit Review, AMR, 2016.

3. "High Energy Lithium Batteries for Electric Vehicles", ES247_Lopez_2015_p, US DOE Vehicle Technologies Program Annual Merit Review, AMR, 2015.

I.A.2 Development of a High Energy Density Cell and Module for EV Applications (LGCPI)

Mohamed Alamgir, Principal Investigator
LG Chem Power, Inc.
1875 Technology Drive
Troy, MI 48083
Phone: 248-291-2375
E-mail: alamgir@lgchem.com

Chulheung Bae, Principal Investigator
Ford Motor Company
Dearborn, MI 48121
Phone: 313-410-1398
E-mail: cbae@ford.com

Brian Cunningham, Technology Manager
U.S. Department of Energy
Phone: 202-287-5686
E-mail: Brian.Cunningham@ee.doe.gov

Start Date: February 1, 2015 End Date: January 31, 2018
Total Project Cost: $3,280,000 DOE share: $1,640,000 Non-DOE share: $1,640,000

Project Introduction

The development of a high energy density, low-cost EV battery fulfilling USABC requirements necessitates a very high capacity cathode as well as a high energy density anode. A survey of current cathode and anode materials having potential for meeting the performance, life and cost targets show that high energy density cathodes (such as Li-rich NCM or high Ni-content NCM) and Si-based anodes are the most attractive choices for this purpose. The current program is aimed at utilizing these electrode materials to achieve the objectives.

Objectives

- Development of a high energy density, low-cost cathode material to meet USABC targets for a long-range EV battery.
- Development of a high capacity Si-based anode capable of long cycle-life.
- Understanding/Optimizing high capacity electrode structures that will enable the manufacturing of low-cost, long-life EV batteries.
- Fabrication and testing of modules comprising high capacity cathodes and Si-based anodes using a suitable thermal management system. Since cells using Si anodes are expected to undergo a considerable volume change, the objective will be to develop a mechanical structure that will be effective in retaining the cells as well as thermally managing them to prolong life.

Approach

In order to achieve the program objectives, the following approach was pursued in partnership with LG Chem, South Korea.

- Use high capacity NCM cathodes (both Mn rich as well as high Ni content cathode materials).

- Use high capacity Si-based anode that has the best cycle-life at a high loading level.
- Develop high loading electrode to realize high energy density.

Results

A dual approach has been pursued to develop a high capacity and long-life cathode material: using Mn-rich NCM as well as Ni-rich NCM. Although the Mn-rich NCM has a very high capacity (~250 mAh/g), when charged to 4.6V, it has several well-known drawbacks such as inferior life, gassing, voltage fade as well as high resistance at low SOCs. We have pursued multiple avenues such as ALD coating, doping, chemical activation, as well as various electrolyte additives to solve these issues. While this let to improvement in data, it was not large enough to warrant continued studies with this material. For example, Figure I-5 shows the data for a cell built using our most optimum Mn-rich cathode and a high loading Si-based anode (prepared as the first baseline deliverable). The data show considerable impact on the delivered capacity as function of the upper voltage cutoff of 4.4 and 4.6V. The cycle-life of the cell was, however, poor as the capacity faded to less than 80% after 25 cycles at room temperature. A more dramatic fade was observed during storage at 60°C and SOC of 80%. Structural evolution, Mn dissolution and thick SEI formation are attributed to the rapid decay in cell performance. Given these poor life characteristics, studies with this cathode material were discontinued and Ni-rich NMC was selected as our primary path for the cathode chemistry. We selected ALD coating as one of the routes for improving cathode durability. Data showed that the capacity and the rate capability of the cathode are not adversely affected by the coating and even showed a slightly higher capacity and better capacity retention compared to its untreated counterpart.

In order to approach the usable energy density target of 750 Wh/l stipulated by USABC, one needs to significantly increase the loading level of Si-anode material. Since a high Si content adversely affects electrode properties such as adhesion, wettability etc. studies were carried out to optimize binder and conductive agents. Careful attention needs to be given to both the type and content of these components since they can impact various cell properties. For example, data show that the type and ratio of conductive agents within the electrode control the side reactions that can affect the first cycle Coulombic efficiency and discharge capacity.

To assess the impact of Si content on performance and durability, 10% and 30% loading levels were taken as case studies in our program. The cells contained a Ni-rich cathode.

Figure I-5 compares the voltage profiles of the cells using the 10% or 30% SiO-containing anodes. Data reveal that the OCV of the cell is reduced more by a higher SiO content (3.59V vs 3.51V). Further, the discharge resistance increases more in the lower SOC range for the 30% SiO cell.

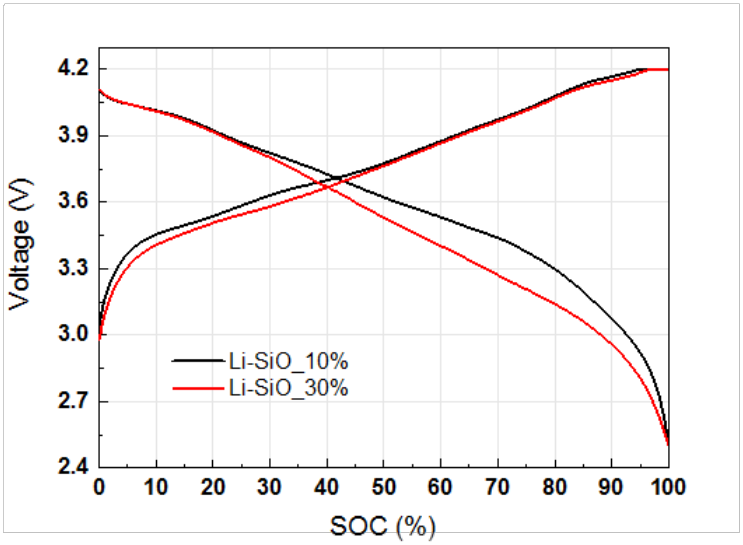

Figure I-5. Comparison of the charge/discharge profiles of cells containing 10 and 30% SiO anodes.

Figure I-6 compares the cycling performance of the 10% and 30% SiO-containing cells. For full depth-of-discharge cycling (100%-0%), there is a clear decrease in cycle-life when the SiO content is raised from 10% to 30%. However, when the cells are cycled within a narrower SOC window of 100%-20%, the cycle-life performances of SiO 10% and SiO 30% are not significantly different from each other in the first 100 cycles.

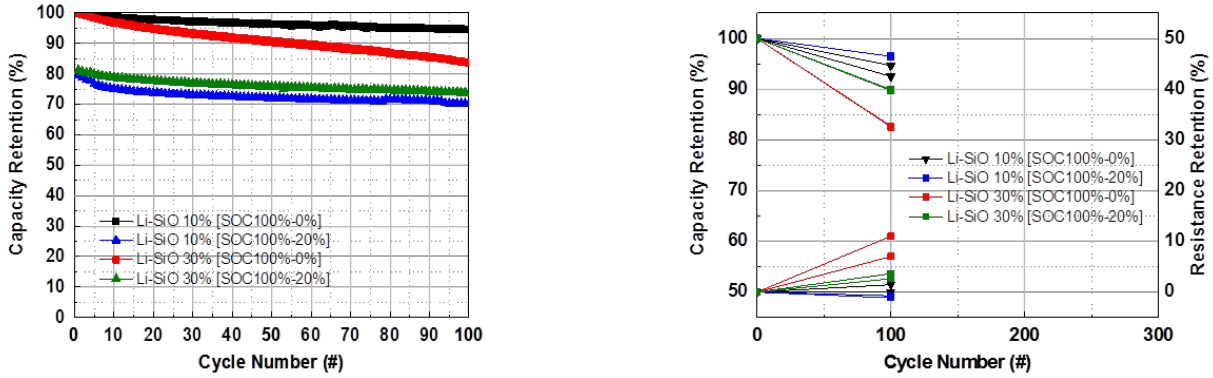

Figure I-6. Comparison of the cycling performance of cells containing 10 and 30% SiO anodes. Cycling carried out at 1/3ºC rate and 25ºC.

The storability of the two types of cells are shown in Figure I-7 during storage at 60ºC and SOC=100%. As the data indicate, there is a considerable decrease in the capacity retention, and a concomitant rise in resistance, for the cell having the higher amount of SiO.

It is well-known that a key challenge in working with Si-based anodes is to manage its swelling during cycling. To better understand this feature, we carried out cell thickness measurement during charge and discharge (Figure I-8). As the data show, increasing the SiO content leads to a significantly larger thickness increase in the first charge/discharge cycle. For example, the 10% cell showed an increase of ~2.4% during charging from 0 to 100%, while the 30% SiO cell showed an increase of 6%. The ratio of thickness increase, however, from 30% to 100% SOC was 1.3 and 4.4 for the 10% and 30% SiO cells, respectively. The change in thickness over life for these two types of cells remains to be evaluated.

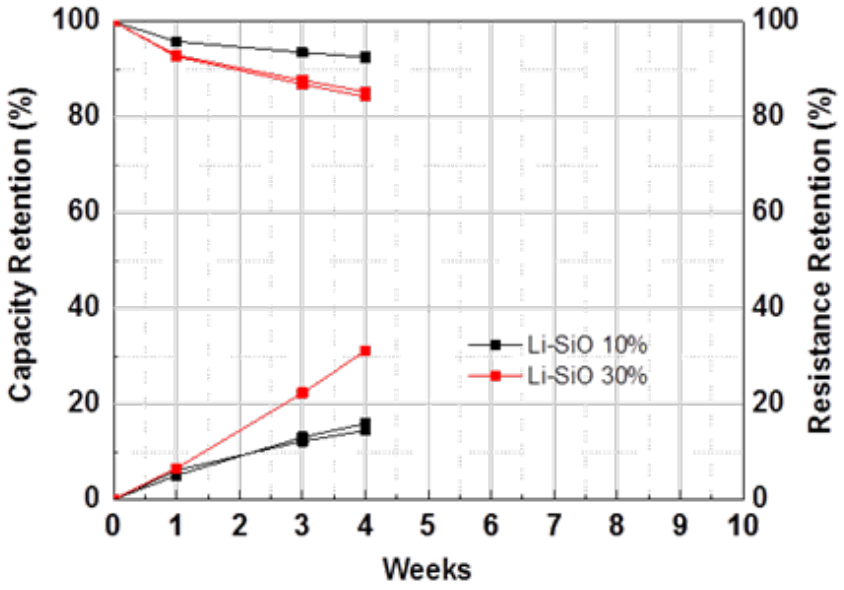

Figure I-7. Comparison of the storability of cells containing 10 and 30% SiO anodes. Storage was at 100% SOC and 60℃.

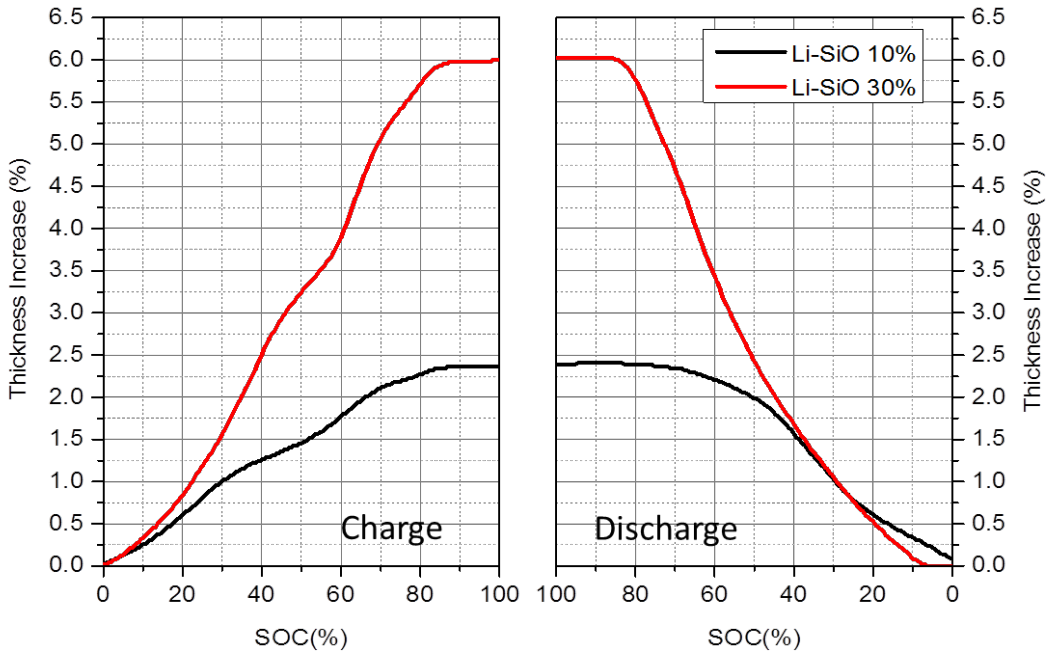

Figure I-8. Comparison of the thickness increase of cells containing 10 and 30% SiO anodes. The cycling was carried out at 1/3 C between 4.2 and 2.5V and 25℃.

Conclusions

Despite comprehensive studies involving doping, surface treatment and electrolyte optimization, among others, we did not find significant improvement in the durability of Mn-rich cathode containing cells; so work with this cathode was abandoned in favor of Ni-rich cathode. We showed that ALD coating improves the durability of the cells. Significant amount of studies were carried out to develop high performance Si-anodes by optimizing binder and conductive agents which are especially critical for high loading electrodes where adhesion issues become very pronounced. Preliminary studies with high loading Si-based anode showed reasonably good cycling at room temperature but the capacity fade and resistance rise at elevated temperature were still quite unsatisfactory.

However, work with Si-based anodes showed that we are unable to meet the USABC program targets and still be able to scale up and deliver large size EV cells (> 50 Ah) that are practical and have reasonable life targets.

I.A.3 High-Performance Semi-Solid Cell for EV Applications (24M Technologies)

Naoki Ota, Principal Investigator
24M Technologies, Inc.
130 Brookline Street
Cambridge, MA 02139
Phone: 617-553-1012 x132
E-mail: nota@24-m.com

Brian Cunningham, Technology Manager
U.S. Department of Energy
Phone: 202-287-5686
E-mail: Brian.Cunningham@ee.doe.gov

Start Date: June 15, 2016 End Date: June 14, 2019
Total Project Cost: $6,998,594 DOE share: $3,499,297 Non-DOE share: $3,499,297

Project Introduction

24M Technologies has developed a breakthrough manufacturing process that leverages proven and emerging chemistries to deliver lithium-ion batteries with a lower cost and containing less inactive materials than any current lithium-ion cell. In this program, 24M will develop large-format, automotive-scale cells leveraging high-energy advanced lithium-ion chemistries. 24M's unique electrode and cell architectures are capable of accommodating large volume-change active materials, and 24M's cells exhibit unprecedented levels of abuse tolerance. The manufacturing process requires less than one-half the number of unit operations of conventional lithium-ion technology; and, has been demonstrated in automated pilot production.

24M's proprietary semi-solid electrode technology enables unique cell architectures with several advantages over conventional Li-ion batteries. For automotive applications, the novel manufacturing method dramatically reduces manufacturing complexity and cost. Also, it is readily scalable per market demand. The small footprint for equipment and comparatively low capital equipment investment further reduce manufacturing risk.

24M's unique electrode and cell architectures significantly lower materials cost in each cell. 24M believes that its cell design has a lower material cost on energy basis ($/kWh) than any other Li-ion cell of comparable energy and power in the market or under development. Cells based on semi-solid electrodes have a higher active to inactive materials ratio than conventional Li-ion cells, providing an inherently sustainable advantage in the cell bill of materials.

Finally, unlike most other development approaches for advanced batteries, 24M's core technologies are platforms for electrode and cell design and manufacturing not limited to any particular set of active materials. Therefore, 24M's cells can leverage all of the active materials available today and those to be developed in the future. As a platform player, 24M maintains the flexibility to drop-in next generation active material as lithium-ion chemistries evolve and as alternative chemistries (such as Na-ion or Mg-ion) emerge.

Objectives

24M will demonstrate that its novel electrode, cell and manufacturing approach can be applied to high-energy density lithium-ion chemistries to enable mass production of automotive-capable prismatic Li-ion cells with a dramatically lower cost. The approach outlined below has been planned to develop high energy density semi-solid electrode formulations, and to demonstrate manufacturing of prototype cells based on those formulations that meet or exceed the USABC targets outlined in Table I-1 for each phase of the program.

Table I-1: Characteristics of the annual cell deliverables in the program

	Phase 1	Phase 2	Phase 3
Cell Footprint (cm^2)	80	80	80
Capacity (Ah)	6	10	10
Energy Density* (Wh/L)	400	640	800
Specific Energy** (Wh/kg)	200	290	350
Number of Cells	30	30	30

*Assuming 80% volumetric packing efficiency
**Assuming >95% gravimetric packing efficiency

Approach

24M has planned the following activities to achieve the objectives identified in the preceding section.

1. High Energy Materials Evaluation and Selection

Developing new semi-solid electrode formulations utilizing high energy active materials requires evaluation and selection of materials comprising a semi-solid suspension – containing active materials, additives, and electrolyte – as well as developing an appropriate mixing procedure that yields the semi-solid suspension with excellent electrochemical performance. Different combinations of active materials and additives will be formulated into semi-solid suspensions where the physical properties will be evaluated and ranked. The rheology of material suspension will also be tested in order to determine the consistency and repeatability of the electrode forming process. Candidate electrode formulations will then be used in cell fabrication to evaluate the electrochemical performance of the electrode. Ultimately, active materials and electrode formulations will be selected to optimally balance tradeoffs of power performance, safety, processiblity, and life (cycle and calendar) in a 24M automotive cell.

2. Processing Methods for Increased Active Solids Loading

Although increases in active solids loading may seem incremental, each time solids loading is increased, an entirely new formulation must be developed and processing method evaluated to ensure that ion and electron transport and rheological properties are optimized for manufacturing and cell performance. In this activity, 24M's current and alternative mixing methods will be evaluated and developed to obtain semi-solid electrodes with active materials loadings necessary for target high energy densities while achieving cycle life and safety performance target. This activity is complementary to, but distinct from, the active material evaluation and selection activity outlined above. New mixing methods and equipment are continually developed at 24M and these will be evaluated, and as necessary, developed to achieve the active materials loading levels required for a cell meeting USABC targets. 24M will create quality control metrics, and measure electrochemical performance to evaluate the performance of the semi-solid suspensions from the various processing methods.

3. Electrode Architecture Development

24M's current electrode forming process is based on automated dispensing and shaping of both anode and cathode semi-solid suspensions, using conventional foil current collectors. This activity will evaluate alternative electrode forming methods and cell architectures, including current collectors and investigations into cell formats with increased volumetric efficiency. As 24M continues to transition from pilot manufacturing to high-volume manufacturing methods, we anticipate continual improvements in the electrode and cell making operations. Additionally, the ideal processing methods for highly-loaded semi-solid suspensions based on high-energy active materials may differ from those developed for earlier electrode formations. Initially, this activity will evaluate current electrode structure and forming methods for compatibility with high energy active materials. Throughout the program, there will be continual evaluations to ensure that the developed cells are capable of meeting or exceeding the automotive power performance requirements. Finally, this area of activity will include a specific focus on safety and abuse testing of the developed 24M automotive cell.

4. Cost Modeling

24M's novel manufacturing approach is different from traditional Li-ion manufacturing methods and conventional cost models such as the USABC cost model cannot be directly applied for cost forecasting. Therefore, an additional activity is planned to develop and commission a cost model for 24M automotive cells to understand the cost at scale and the necessary level of capital investment. In Phase 1, the developed cost model for automotive cells will be developed and commissioned in consultation with USABC. Throughout the duration of the program, it will be applied to scrutinize the viability of the 24M automotive cell.

Results

We have achieved notable progress along numerous development pathways:

Successful screening of high energy density cathode candidate active materials for project Phase 2 and Phase 3 development.

Looking beyond Phase 1 development of NMC111, dozens of high energy cathode active materials from numerous suppliers were examined as candidates for Phase 2 and Phase 3 cell chemistries. Many of these materials were eliminated from consideration due to physical property of the powder and processing constraints. Of the materials tested electrochemically, three stood out as most promising for further development. One sample of engineered NCM 622 and two of NCM 811, each from different suppliers, showed a promising combination of reversible specific capacity (Figure I-9) HPPC performance. Therefore, these three materials were chosen for development in this program. In addition, the team continues to source promising candidate active materials from a network of suppliers, ensuring a strong pipeline of candidate material moving forward. Physical and electrochemical characterization procedures for these incoming materials have been streamlined and progress quickly upon samples being received.

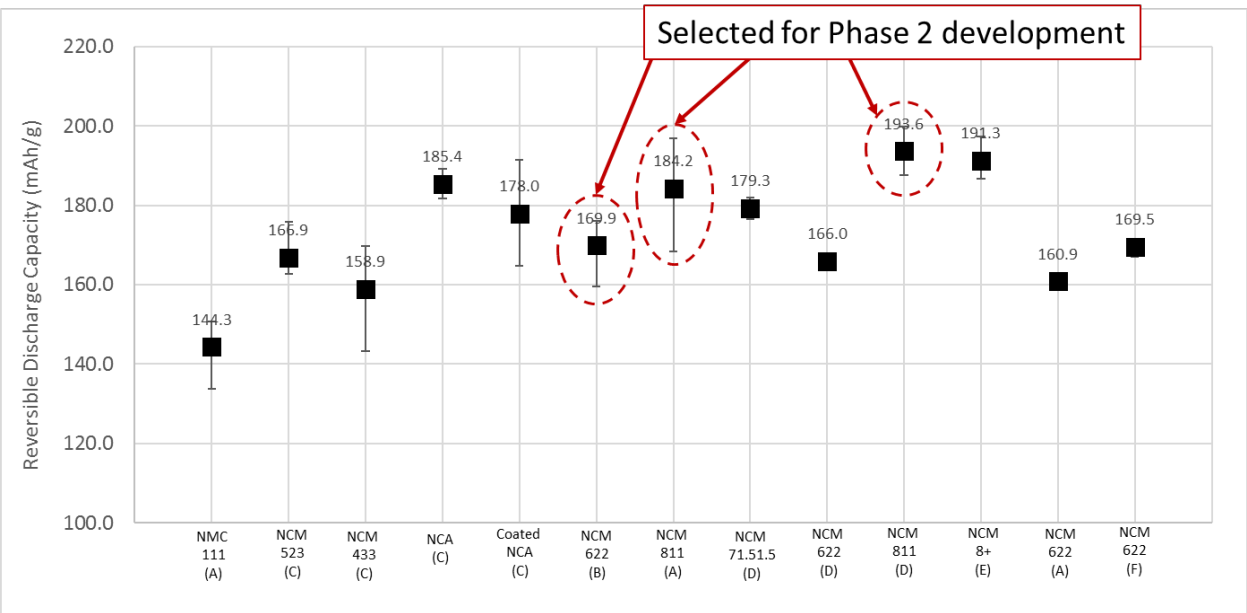

Figure I-9. Reversible specific discharge capacities measured during USABC screening for high energy density cathode active material candidates for program Phase 2 and Phase 3 development. Screening was performed using full pouch cells containing 24M's proprietary semi-solid electrode format for both the cathode and a control graphite anode.

Developed promising electrolyte with high low-temperature performance and a unique chemistry.

During Phase 1 of this project, the low temperature performance of 24M's cells fell below USABC targets. For the baseline electrolyte in use at the time, 80cm^2 active area pouch cells exhibited a retained energy of ~14% at -20ºC compared to room temperature performance, both tested galvanostatically at a rate of C/3. To improve this performance, work was conducted to find electrolytes or electrolyte additives that would help increase retained energy under low temperature testing conditions. Focus was paid to electrolyte components that did not drastically diminish electrolyte ionic conductivity, had a low freezing point, and maintained appropriate viscosities at low temperatures. A new electrolyte formulation was mixed using components fitting these criteria and tested in full pouch cells with NMC111 cathodes and graphite anodes. A voltage vs. discharge capacity curve for these cells during a galvanostatic discharge at a rate of C/3 in a -20ºC test chamber is plotted in Figure I-10, which also shows a curve for a cell with an identical architecture but using a baseline electrolyte rather than the low temperature electrolyte. The cell using the low temperature electrolyte retained >50% of the cell's room temperature discharge energy. This result is very promising in that it demonstrates that low temperature performance is not fundamentally limited by ionic transport across the thick, high areal capacity electrodes in 24M's cells.

Delivered Phase 1 deliverable cells of planned quantity and size on schedule.

Stacked cells with 24M's Phase 1 deliverable formulation were built using 24M's automated pilot manufacturing line and delivered on schedule. 30 test units with a median reversible discharge capacity of 6.17 Ah and a median C/3 useable energy of 22.3Wh were shipped to designated USABC testing partners. To satisfy internal development needs and external deliverables, 78 total stacked cells were built towards this milestone. The initial cells were used to validate process scale-up and the remainder for internal testing and/or were yielded out.

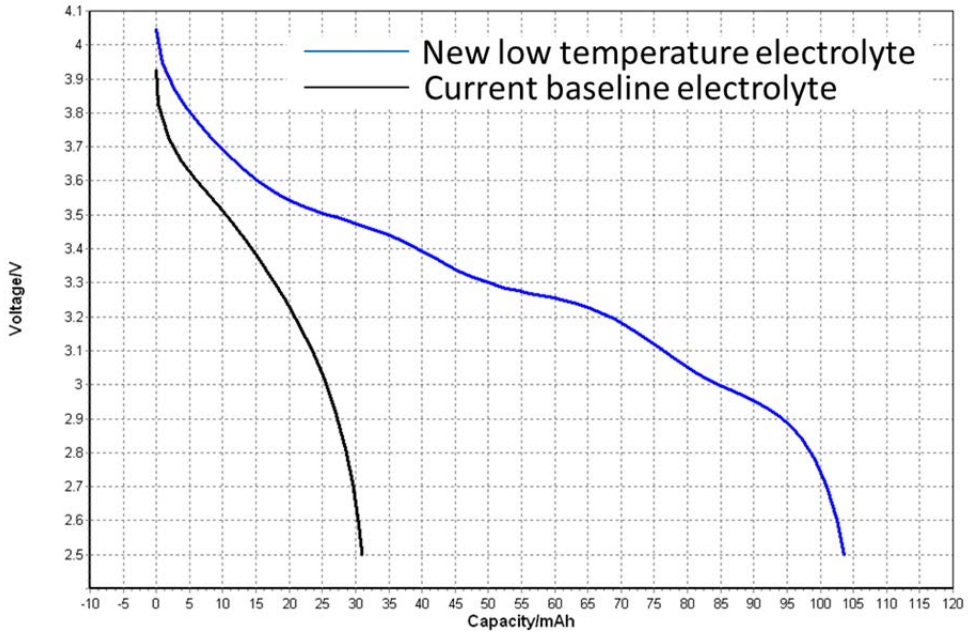

Figure I-10. Voltage vs. discharge capacity plots for pouch full cells using 24M's proprietary semi-solid electrodes measured at a rate of C/3 in a -20ºC testing environment for two different electrolytes. The cells using the current baseline electrolyte retained ~15% of their room temperature energy at the test temperature, while the newly developed low temperature electrolyte showed an energy retention of >50% at -20ºC.

Transitioned pilot manufacturing and processing procedures to NMC622 cathode active material.

Following completion of the deliverables for Phase 1 of this project in June 2017, the 24M USABC team began the process of transitioning the active material used in its semi-solid cathodes from NMC111 to NMC622 in order to improve cell energy density. The difference in physical properties for the NMC622 chosen for development during active material screening compared to the NMC111 previously employed necessitated process optimization to mix and form semi-solid electrodes of the desired quality and quantity for project Phase 2 development. At the conclusion of this optimization, the 24M build capability for NMC622 exceeds that achieved in Phase 1. Further, the relative ease of transition between NMC111 and NMC622 provides additional evidence that 24M's electrode and cell production method is chemistry agnostic and may be applied to a wide variety of cell chemistries.

Conclusions

In this program to date, 24M has successfully demonstrated a unique manufacturing method and electrode format for lithium-ion battery cells that can be applied to NMC111/graphite cells. Project Phase 1 deliverable cells were produced and delivered on schedule to USABC, and testing of these cells is ongoing. In addition, the 24M team has made significant progress in selecting active materials and improving processing capabilities for Phase 2 and Phase 3 development as cell energy densities requirements increase.

Key Publications

1. "Semi-solid Lithium-ion: A Breakthrough Battery and Manufacturing Platform," Naoki Ota (invited speaker), International Conference on Advanced Lithium Batteries for Automotive Applications, 2017.

I.A.4 Development of High Performance Li-ion Cell Technology for EV Applications (Farasis Energy)

Keith D. Kepler, Principal Investigator
Farasis Energy
21363 Cabot Boulevard
Hayward, CA 94545
Phone: 510-732-6600
E-mail: kkepler@farasis.com

Brian Cunningham, Technology Manager
U.S. Department of Energy
Phone: 202-287-5686
E-mail: Brian.Cunningham@ee.doe.gov

Start Date: February 1, 2017 End Date: September 30, 2019
Total Project Cost: $5,900,000 DOE share: $2,950,000 Non-DOE share: $2,950,000

Introduction

The goal of this project is to develop a high energy density, low-cost Li-ion cell technology that meets USABC goals for advanced batteries for EV's (for 2020 commercialization).

Objectives

- Develop an EV cell technology capable of providing 350 Wh/kg after 1,000 cycles at a cost target of $0.10/Wh.
- Develop improved cathode materials to meet USABC EV goals through collaborative development efforts with partner organizations.
- Develop Si-based anode electrodes to meet high energy cell design goals.
- Develop pre-lithiation technology.
- Develop and optimize electrolyte and conductive additives to stabilize high voltage cathode, achieve improved cycle life and abuse tolerancey of the cells.

Approach

- The key barriers for this project are achieving high energy density with stable chemistry to meet cycle life and calendar life goals as well as the manufacturing processes compatible of the new materials. To meet the USABC target of 350 Wh/kg, Farasis needs to use high-capacity anode (silicon) and cathode materials. To achieve desired energy density and cycle life, Farasis is screening critical cell components such as cathode, anode, electrolyte and separators. In addition, Farasis is pursuing Li source development for pre-lithiation, optimization of Li source, electrode design, cell design as well as the optimization of formation and test protocols. During this initial phase, the project focused on screening of the anode and cathode materials in coin cells. The capacity of the cathode should be higher than 200mAh/g and the anode must deliver between 500-1800mAh/g. The materials will be screened in single layer pouch cells and evaluated for impedance, rate and cycle life. 18650 cells were built using baseline anode and cathode electrodes to be used for electrolyte optimization and for relative safety of materials. Results from this initial screening were used to narrow the electrolyte compositions best suited for this chemistry and will be used for further optimization in the second round of small cell-builds. Farasis is continually working on the synthesis of lithium source materials and incorporating them as a pre-lithiation source. A

combination of device level testing and fundamental electrochemical measurements are used to guide the development of large form-factor cells for the Phase II of the project.

- Phase II of the project lats approximately 17 months and shifts to manufacturing and testing of larger format pouch cells using a refined subset of cell chemistries. Some ongoing chemistry development will continue in this phase to address specific issues identified in Phase I builds and to pursue further optimization of cell level performance. This will occur in two iterations starting with 10 -30 Ah Gen 1 cells and progressing to the final deliverable cells based on a larger pouch cell form factor, which will be 60 Ah using the optimized high-energy cell chemistry. Phase II will also include testing to guide system development in future applications; these tests will characterize cells in small groups to efficiently evaluate their behavior on a large scale where thermal management, cycling-induced gradients, and failure isolation become important.

Results

Collaborative Material Development

Cathode Active Materials Development.

Farasis has mapped the capacity of eight cathode materials targeting cathode capacity between 187-210 mAh/g and energy density of 297-325 Wh/kg (based on large form factor cells, 10Ah). For Gen1, we are targeting energy density of > 300 Wh/kg. (See Figure I-11.)

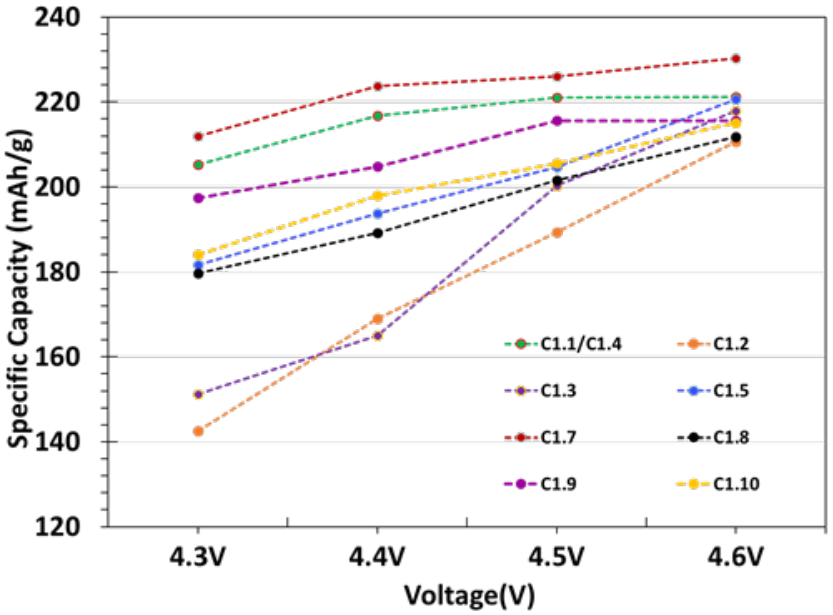

Figure I-11. Capacity for eight of the planned cathode material

Farasis then evaluated 12 cathode materials (high voltage NCM, LMR with NCM and Ni rich NCM) in a single layer pouch cells with a fixed capacity of Si anode with a target energy density of 290-310 Wh/kg in 10 Ah pouch cells. Based on the results for cycle life, DCR and rate capability Farasis down-selected the cathode materials with a target energy density of 300 Wh/kg. The down-selected cathode materials will go on to further optimization for the Gen 1 deliverable cells with a target cycle life of > 400 cycles and an energy density at the beginning of life of 300 Wh/kg. In parallel, Farasis is using the down-selected cathode material for optimization of the lithium source in single layer pouch cells to improve cycle life, and investigate the impact on impedance and safety of the cells. Figure I-12 shows the cycle life for the different cathode material with fixed anode capacity and targeted energy density of 300 Wh/kg in 10-30 Ah form factor cells.

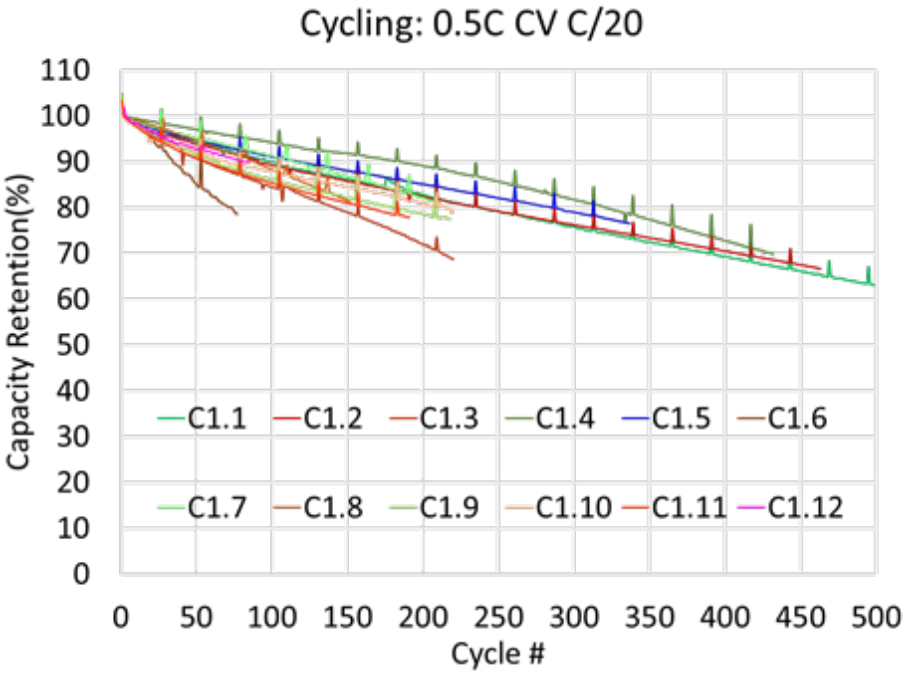

Figure I-12. Cycle life for the cathode materials

Negative Electrode Technology Development

Farasis has evaluated a range of Si materials (Si alloy, SiO, Si nanowires and Si nanoparticles) from suppliers in a single layer pouch cell format with target energy density of 290-310 Wh/kg. Farasis evaluated a range of Si materials with five (5) different cathode materials, and based on the cycle life, impedance and the rate capability of the materials the chemistry for the 300 Wh/kg cells, those materials were down-selected. To meet the USABC final goal of 400 Wh/kg,

Pre-lithiation Development

Farasis synthesized the lithium sources for pre-lithiation. During the 1st year it successfully synthesized large batches of lithium source material (for prelithiation) and tested those materials in full single layer pouch cells containing a Si-based anode. Farasis built small pouch cells incorporating the pre-lithiation source to determine its impact on cycle life. Figure I-13 shows comparisons of cycle life for the Si composite (> 1000mAh/kg) and cathode with and without a Li source.

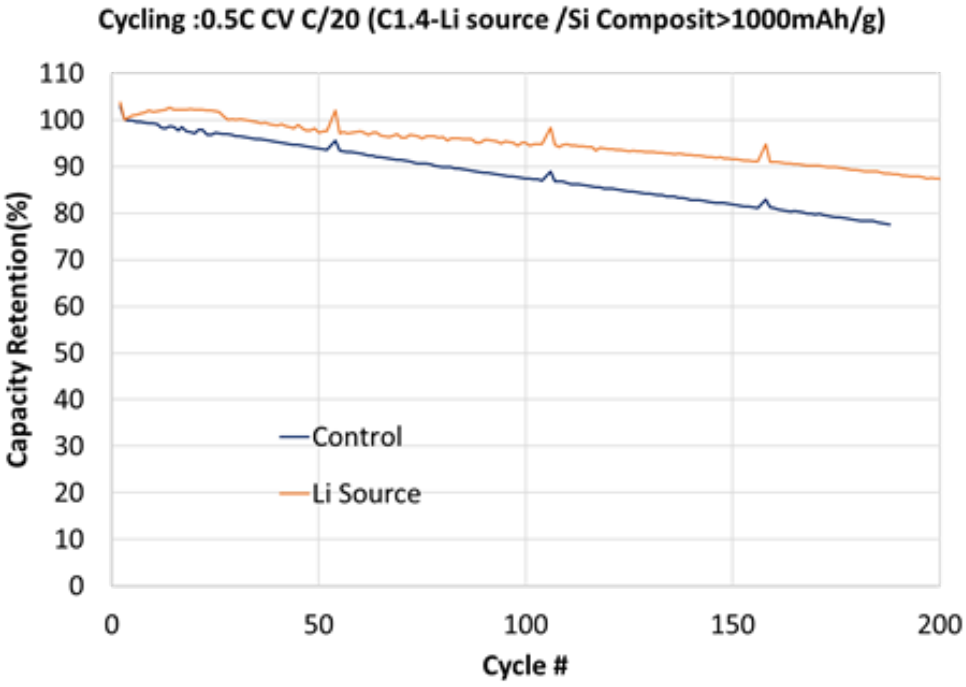

Figure I-13. Cycle life comparison of cathode (C1.4) with and without Li source and Si composite as an anode

Electrolyte Technology Development

Farasis is performing electrolyte exploration, evaluation and optimization in 3 Ah 18650 cells as well as on single layer pouch cells. Figure I-14 shows cycle life results for different electrolyte formulations paired with 300 Wh/kg chemistry without pre-lithiation in 10-30 Ah cells. The results show that the cycle life for EV12 is better (450 cycle @ 80% retention) as compared to other electrolytes. The cells with EV12 also exhibited lower impedance and better rate capability.

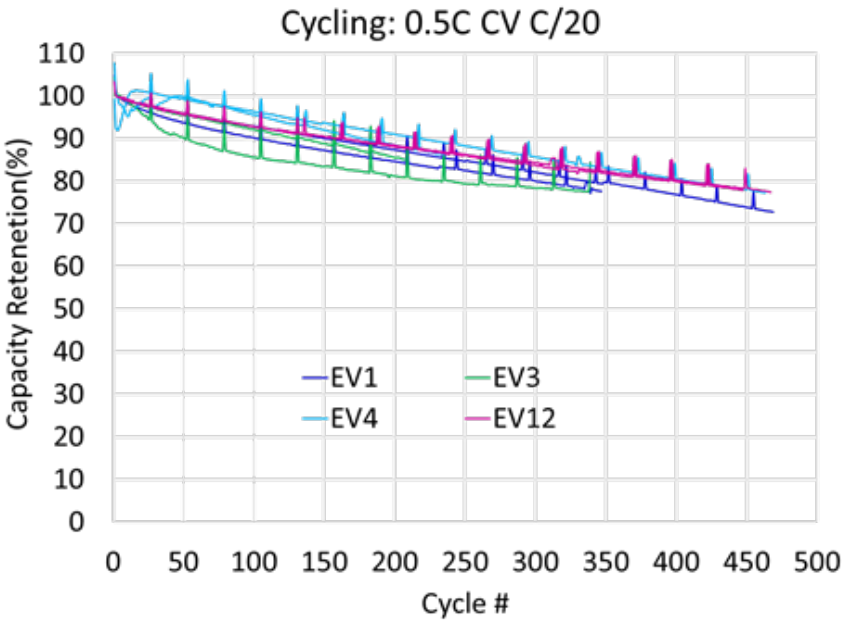

Figure I-14. Cycle life for the different electrolyte formulations

Cell Development

Farasis delivered baseline cells for testing during the first six months of the project. To meet the USABC target for Gen 1 (300 Wh/kg), Farasis built 200 3Ah 18650 cells with promising anode and cathode materials to be used in electrolyte optimization and to understand the relative safety of the materials. Based on the results of 18650 and single layer pouch cells with different anodes and cathodes, Farasis built 100 1.5Ah pouch cells for the down-selected chemistry targeting 300Wh/kg in 10-30 Ah cells design. The Gen1 chemistry during the 4th and 5th quarter will include further development for electrolyte optimization as well as the safety testing. In order to meet the USABC target, Farasis will continue to build multiple high capacity cells by implementing the improved chemistry from small cell results (cycle life, impedance, rate and safety) as well as the optimization of other cell components. Figure I-15 shows the cycle life for 1.5 Ah pouch cells. The predicted cycle life for these cells are in between 350-400 cycles.

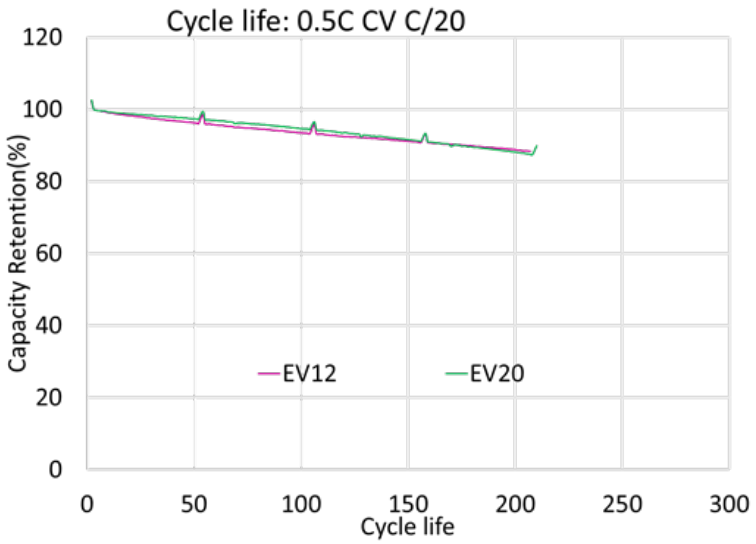

Figure I-15. Cycle life for the different electrolyte formulations

Conclusions

During the first eight months of the program, Farasis evaluated 12 possible high capacity cathode materials and four possible Si anodes. Farasis down-selected the chemistry for Gen1 deliverable (300 Wh/kg) cells with a cycle life of 450 while retaining 80% capacity in single layer pouch cells and without a prelithiation source. This chemistry can provide 300 Wh/kg in 10-30 Ah cells. Farasis had done the relative safety test on the different chemistries. Further optimization in Gen 1 chemistry is continuing for the different conductive additives and electrolytes. To meet the USABC goal, it will start working on high capacity Si (> 1000 mAh/g) with pre-lithiation. Farasis has incorporated a Li source in small layer pouch cells for high capacity anode materials to begin optimizing the impact on the capacity, cycle life, impedance as well as the safety of the cells.

I.A.5 Enabling Thicker Cathode Coatings for Lithium Ion EV Batteries (PPG)

Stuart Hellring, Principal Investigator
PPG Industries Inc.
4325 Rosanna Drive
Allison Park, PA 15101
Phone: 412-492-5526
E-mail: hellring@ppg.com

Brian Cunningham, Technology Manager
U.S. Department of Energy
Phone: 202-287-5686
E-mail: Brian.Cunningham@ee.doe.gov

Start Date: February 1, 2017 End Date: February 28, 2019
Total Project Cost: $1,200,000 DOE share: $600,000 Non-DOE share: $600,000

Project Introduction

To lower the overall cost of the electric vehicle (EV) lithium ion battery, PPG Industries, Inc. and partner LG Chem Power, Inc. will develop and demonstrate NMP-free cathode coatings with higher achievable thickness compared to conventional state-of-the-art coatings. These thicker coatings will permit fabrication of higher energy density batteries without decreasing electrochemical performance. Additional cost savings and reduced environmental impact will be realized through the elimination of NMP-based manufacturing.

Objectives

The objective of this program is to develop solvent-based binder systems for lithium ion cathode coatings that do not require the use of NMP and can be coated at a thickness of 150 micron (μ), and develop water-based binder systems that can be coated at a thickness of 110μ. Coatings and subsequent lithium ion cells will be manufacturable using existing standard industry equipment and demonstrate cell performance capability equivalent to current state of the art.

Approach

Reconfigure the electrode binder system into a novel formulated product in which polymer binder is dispersed, as opposed to dissolved, as nanoparticles in a solvent. This binder dispersion is stable chemically and possesses excellent shelf life. The unique design of PPG's NMP-free binders along with optimized processing parameters will mitigate film stress and enable the assembly of thicker, more flexible, homogeneous cathode coatings with higher active material loading per unit area. PPG's binders are fluoropolymer-based in combination with customized resins. The binder fluoropolymers and resins together form a composite that is designed to enhance dispersion stability and rheology to aid application, as well as final coating properties such as flexibility, cohesion, adhesion, etc., and electrochemical properties such as low resistance, and cycle and calendar life stability. Cell performance will be demonstrated in 1 Ah pouch cells built in partnership with LG, and tested in accordance with the USABC EV test manual.

Results

A successful binder scale-up enabled an application line trial to be conducted to prepare double-sided cathode foil for the baseline evaluation of current PPG solvent borne NMP-free coatings at an intermediate coating thickness before increasing to the very thick cathode coatings. The cathode formulations contained a Li-ion active material, Lithium Nickel Cobalt Manganese Oxide (NCM or NMC), conductive carbon, and PPG binder. Coating was applied on each side sequentially at a total coating weight per side of 22.7 mg/cm^2 comprising a weight ratio of 93/3/4 NMC/carbon/binder. This corresponds to an energy density of 3.17 mAh/cm^2 per side. These coated foils were calendar-pressed at our coating partner, to a porosity of 32% and

tested at PPG for peel strength and flexibility. Peel strength exceeded the 12.6 gf/15 mm target and passed the 25.4 mm mandrel-bend flexibility test. A roll of cathode-coated foil was shipped to LG Chem to be fabricated into 14 each of 1-Amp-hour pouch cells for battery performance evaluation. PPG also tested the binder shelf life stability.

The electrochemical performance testing indicates poor performance of the baseline cathode coating. The battery fails after 50 cycles. As shown in Figure I-16, from 50 cycles to 200 cycles, the resistance increased 4 times and the capacity retention dropped below 20%. After cycling, the pouch cell was disassembled for evaluation, and no electrolyte droplet was observed. Li metal plating was found on the anode and anode-facing side of the separator. This indicates potential electrolyte consumption by electrolyte side reaction.

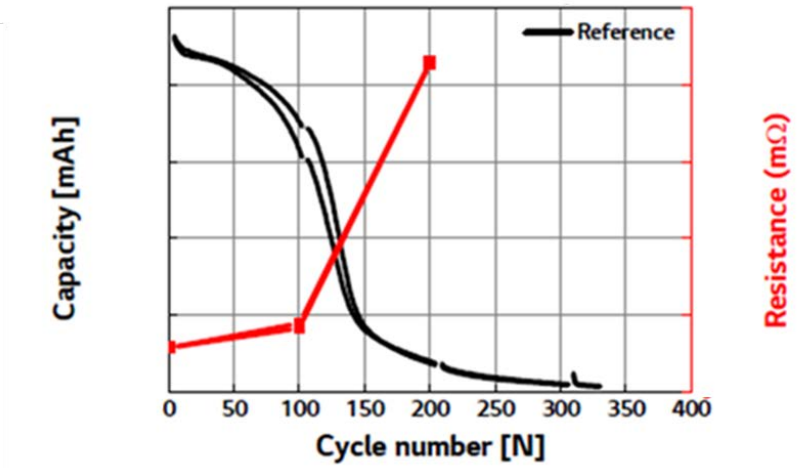

Figure I-16. USABC baseline battery performance after 300 cycles. (Data provided by LG Chem Power)

The project team identified the following possible root causes of the battery failure at LG Chem:

1. Binder side-reaction.
2. Cathode-anode mismatch.
3. Aged active material used for baseline.
4. Electrolyte side-reaction with additives.
5. Bad coatings made during line trials.
6. International shipping in uncontrolled condition.
7. Moisture exposure.

To identify the root cause of the battery failure, the PPG team is currently repeating the baseline cathode formulation with controlled variables. In the original baseline cathode coating sent to LG Chem, NMC 111 of unknown age was used as the active material. In a recent repeat, a fresh batch of NMC 111 from a different supplier is used to eliminate the problems related to aged active material and side-reaction with electrolyte. PPG also identified binder additives that can possibly cause side-reaction with electrolytes, and prepared an additive free binder formulation.

Scale-up line trials were conducted at PPG's coating partner to repeat the USABC baseline, and make an additive-free baseline repeat, and an NMP control. The coatings were assembled into 18650 cells for electrochemical performance testing at the coating partner's facility. The details of line trials coatings are listed in Table I-2. During initial high precision coulometry cycling, the cathode demonstrated good capacity

retention and the Coulombic inefficiency per hour performed better than the NMP control. The suspect additives also did not make a significant difference on cathode performance.

Table I-2: Scale up line trials for USABC baseline failure root cause analysis

Job Description	Active/Carbon/ Binder	Active Material	Carbon	Mass Loading	Cell Type
Baseline repeat	93/3/4	Shanshan NMC 111	LITX 200	25.4mg/cm^2	18650
Additive free baseline	93/3/4	Shanshan NMC 111	LITX 200	25.4mg/cm^2	18650
NMP control	93/3/4	Shanshan NMC 111	LITX 200	24.4mg/cm^2	18650

So long as the current testing passes 150 cycles, we will remake the baseline binder to have new baseline cells produced at LG Chem.

The goal of the second milestone is to formulate a thicker coating while maintaining adhesion, flexibility, and electrical conductivity. Toward the end of the third quarter, PPG prepared NMC 111 coatings with areal capacity of 4.5mAh/cm^2 and thickness of 129µm. The thicker cathode coating demonstrated high flexibility and passed ¼" Mandrel bend test. The 90° peel strength of pressed thicker coating is 106 gf/15mm, passing the requirement of 100 gf/15 mm. Figure I-17 demonstrated all the coatings developed for the first target and the areal capacity and adhesion (peel strength) are shown. Due to the extremely low binder content (3%), it is challenging to prepare a coating of thickness higher than 100µm while maintaining proper adhesion and flexibility.

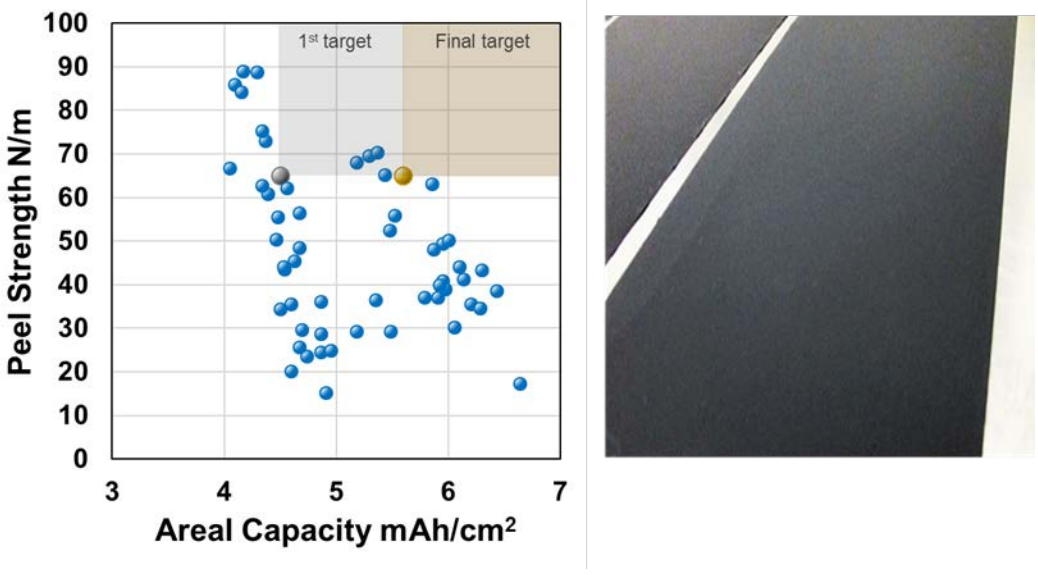

Figure I-17. Thicker coatings developed in third quarter. Left, Peel strength and areal capacity are shown and first target and final target regions are highlighted. Right, Coating appearance. (Data provided by PPG)

To meet the milestone target, PPG's effort focused on resin chemistry, formulation optimization, and process control. In a fully formulated slurry, properly dispersed carbon can form a percolated conductive pathway and decrease the resistivity. Another benefit of investing in carbon dispersion is better rheology control of final slurry, leading to better control on the film build after coating process. PPG improved the out-of-cell coating properties by optimizing carbon dispersions. By controlling the carbon dispersion, we can modify the viscosity of the fully formulated slurry and the final coating thickness. Another challenge is maintaining high adhesion

at high areal capacity. PPG explored the effect of resin chemistry, binder content, and carbon chemistry to optimize the peel strength of the final coating. The pouch cell testing for a thicker coating is on hold due to the baseline failure. A fresh repeat of the baseline coating will be sent to LG Chem in environmentally controlled packaging. A decision will be made once the battery testing results become available from LG Chem.

Conclusions

Problems were encountered with the first baseline cell-build. Another baseline test is underway, and preliminary results are encouraging. Once sufficient test cycles pass, PPG will remake the baseline cells at LG Chem and make the cells to test the coating for the second milestone.

I.A.6 Advanced High-Performance Batteries for Electric Vehicle Applications (Amprius)

Ionel Stefan, Principal Investigator
Amprius, Inc.
225 Humboldt Court
Sunnyvale, CA 94089
Phone: 800-425-8803
E-mail: ionel@amprius.com

Brian Cunningham, Technology Manager
U.S. Department of Energy
Phone: 202-287-5686
E-mail: Brian.Cunningham@ee.doe.gov

Start Date: January 1, 2015 End Date: October 31, 2018
Total Project Cost: $5,500,000 DOE share: $2,250,000 Non-DOE share: $2,250,000

Project Introduction

Silicon has significant potential as a new anode material because it offers nearly 10 times the theoretical energy capacity of graphite. However, when charged with lithium ions, silicon swells up to four times its volume, causing capacity fade and mechanical failure. Because of swelling, conventional approaches to silicon anodes have not produced cells with the long cycle life required for electric vehicle applications. Amprius' rooted silicon nanowire structure mitigates material and mechanical issues, and enables high energy density products with reasonable cycle life.

Objectives

- Amprius is engaged in a three-year, anode-focused USABC project to develop and deliver vehicle-size cells that meet technical requirements specified by USABC. Throughout the project, Amprius will improve its silicon nanowire anode material and cell performance in a baseline cell, and then transfer lessons learnt to larger cells. At the end of the project, Amprius will deliver ~40 Ah cells with end of life specific energies of 350 Wh/kg and energy densities of 750 Wh/L.
    - The project addresses the key performance and production challenges to the commercialization of high-capacity cells and batteries with silicon nanowire anodes. Barriers addressed:
        - Energy: Low Wh/kg & Wh/L
        - Cycle Life: <1,000 Cycles
        - Size: Small Anodes and Cells
        - Cost: High $/kWh
- Amprius' goal is to deliver cells that meet USABC's EV battery goals. Amprius' will deliver high-capacity pouch cells at the conclusion of the project's first, second and third years. Idaho National Laboratory will independently test the performance and safety of Amprius' cells according to USABC's test protocols.
    - Specific technical targets:
        - Available Energy Density @ C/3 Discharge Rate: 750 Wh/L
        - Available Specific Energy @ C/3 Discharge Rate: 350 Wh/kg

- DST Cycle Life: 1,000 Cycles
- Peak Discharge Power Density, 30 s Pulse: 1500 W/L
- Peak Specific Discharge Power, 30 s Pulse: 700 W/kg
- Peak Specific Regen Power, 10 s Pulse: 300 W/kg
- Calendar Life: 15 Years
- Selling Price @ 100K units: $100
- Operating Environment: -30°C to +52°C
- Normal Recharge Time: < 7 Hours
- High Rate Charge: 80% ΔSOC in 15 min
- Peak Current, 30 s: 400 A
- Unassisted Operating at Low Temperature: > 70% Useable Energy @ C/3 Discharge Rate at -20°C
- Survival Temperature Range, 24 Hr: -40°C to+ 66°C
- Maximum Self-discharge: < 1%/month

Approach

Amprius possesses an innovative silicon technology – an anode made of silicon nanowires attached to the current collector – that mitigates silicon swelling, unlocking silicon's potential, and can meet USABC's commercialization criteria.

Amprius' technology is unique in three respects: material, structure, and results. First, Amprius' anode material is made of silicon rather than graphite or a graphite-silicon composite. Second, Amprius' anode structure is composed of nanowires physically attached to the current collector, rather than particles. Third, Amprius has demonstrated both high energy and long cycle life in full cells with silicon nanowire anodes.

Amprius' unique, patent-protected material and structure – nanowires that are "growth-rooted" (i.e., grown directly on the current collector, without binders) – addresses swelling by enabling silicon to successfully expand and contract internally. Because the nanowires are attached to the current collector, Amprius does not rely on particle-to-particle contact and is able to achieve not only long cycle life, but also high electrical conductivity and power.

Before the USABC project, Amprius achieved >700 Wh/L at start of life and >400 cycles at C/2 rate and 100% depth of discharge (DOD). To meet the USABC goals during the project Amprius will:

- Increase specific energy and energy density by tuning anode structure and using advanced components (e.g., thinner substrates and separators). Amprius will also transition from LCO to NCM.
- Extend cycle life by optimizing anode structure and identifying and/or developing electrolyte formulations that improve Solid Electrolyte Interphase (SEI) stability and cell performance.
- Increase anode and cell size by developing methods for handling larger anodes; improving the uniformity of silicon growth and deposition technologies; reducing defect density; and utilizing manufacturing methods that inherently scale to larger dimensions.

Results

Amprius reduced the main gap in performance, cycle life, by identifying electrolyte additives that improve Solid Electrolyte Interphase (SEI) stability.

In FY2017, Amprius screened over 100 electrolyte formulations that included a variety of additives, solvents and salts. The main focus was on reducing reactions that produce gases at the cathode, especially at a high state-of-charge and high temperature. These reactions are particularly accelerated at high capacity NMC cathodes rich in nickel. The task is complicated by the fact that the electrolyte composition has to include additives that are beneficial to the cycle life of silicon anodes, not necessarily stable at high voltage, high temperature or on catalytically active cathodes. Thus, cathode additives were explored, as well as coatings on the cathode materials.

For screening, Amprius measured the relative capacity retention after either storing cells at full charge at 50°C or after cycling cells at 50°C for a number of cycles. For concentration optimization, it used a design of experiment methodology to reduce the number of combinations. In cycling, Amprius uses a typical test method: CC-CV at C/2 rate with 10% current taper and C/2 discharge rate, over the full voltage range (2.85-4.25V).

A sample set of results are shown in Figure I-18. Formulation ELY280 was developed in Year 1 for 10 Ah cells because it had very good room temperature and low temperature (not shown here) performance. However, a new formulation had to be developed in FY2017 (Year 2) to improve performance at high temperature (both Calendar and Cycle Life). Formulation ELY572 was selected for Year 2 deliverable cells. Electrolyte formulation development was done in Si/NCM cells with a 70% Ni-content cathode.

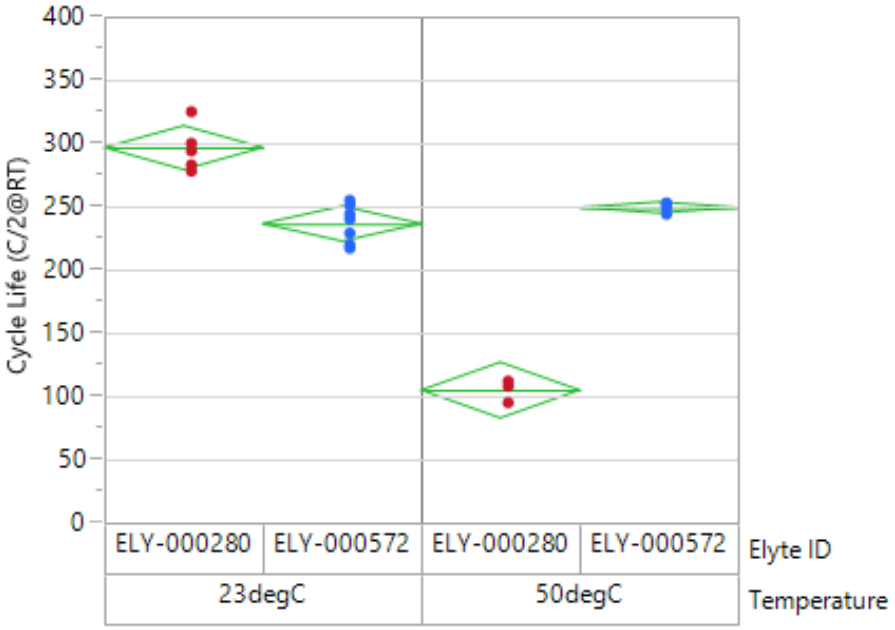

Figure I-18. Electrolyte formulation was optimized for better Calendar and Cycle Life in Si/NCM (70% Ni) cells

Amprius built and delivered to DOE for testing Silicon-NCM cells with average capacities of 10.6 Ah, specific energies of 345 Wh/kg, and energy densities of 860 Wh/L, an increase of 12% compared to previous year.

Amprius continued the cell design and development work started in Year 1 of the project by iterative design optimization of larger form factor. The Year 2 form factor, a 10 Ah cell, required a doubling in length and thickness of the cell tested in Year 1.

In parallel, more energy dense cathode materials were evaluated, including materials with high content of Ni (60 to 80% content). Amprius delivered a larger number of cells compared to that scheduled, to allow a comparison of the effects of Ni-content on cell performance and safety. *Amprius achieved an increase of about 12% in specific energy and energy density in Year 2 cells compared to Year 1 cells.*

The initial performance evaluation of Amprius' ≥ 10 Ah Silicon-NCM cells exceeded USABC's targets for Peak Discharge Power Density, Peak Specific Discharge Power, Peak Specific Regen Power, and Energy Density and is within 5% of the target in specific energy. Cycle Life and Calendar Life, as well as safety performance are under evaluation at Idaho National Laboratory and Sandia National Laboratory. A summary of the initial evaluation is shown in Table I-3.

Table I-3: Amprius' 10 Ah Silicon-NCM cells exceeded USABC performance goals

Characteristics at 30°C and End of Life	Units	USABC 2020 Goals Cell Level	Amprius 10 Ah Cells Si/NCM (70%Ni)
Peak Discharge Power Density, 30 s Pulse	W/L	1500	1900
Peak Specific Discharge Power, 30 s Pulse	W/kg	700	735
Peak Specific Regen Power, 10 s Pulse	W/kg	300	540
Available Energy Density @ C/3 Discharge Rate	Wh/L	750	860
Available Specific Energy @ C/3 Discharge Rate	Wh/kg	350	345

Amprius designed and started the project's final, Year 3 cells, to achieve a target capacity of ≥ 40 Ah.

Amprius selected the VIFB—/99/300 form factor for ≥ 40 Ah cells. This is a pouch cell with tabs on opposite sides (see Figure I-19). Amprius will use cell components (e.g., separator, pouch material and electrolyte) selected and/or optimized in the smaller, Year 1 and Year 2 form factors. The main effort of the task in FY2017 was to scale up the equipment and tooling for the 40 Ah form factor. In particular, Amprius started producing anode foils of larger size both in its batch, laboratory process, as well as in the newly developed roll-to-roll anode pilot line.

With the same components as the 10 Ah cells, Amprius achieved a small increase in specific energy (348 vs. 343 Wh/kg), and a much larger increase in energy density (921 vs. 862 Wh/L), due to a more favorable geometry. One of the first cells made in this form factor is shown in Figure I-19, next to its CAD model.

Figure I-19. CAD drawing and prototype 40 Ah cell with silicon nanowire anode

The 40Ah cells achieved the following specifications:

- Rated Capacity: 45.9 Ah at C/3 rate
- Vmax100 = 4.1V
- Vmin0 = 2.5V
- Cell weight = 450.7g
- Cell size = 6.0 x 96 x 288 mm (body only)
- **348 Wh/kg and 921 Wh/L**

Performance evaluation is ongoing and further design and assembly iterations are planned before delivery of the final cells.

Conclusions

During the project's second year, Amprius continued to make significant progress increasing cell energy, extending cell cycle life, and demonstrating that the silicon nanowire anode-based cells exceed USABC's goals. Amprius built and delivered 30 cells in the interim form factor, with a capacity of 10Ah. The initial evaluation at Idaho National Laboratory confirmed Amprius' results, including achievement of the initial power and energy targets.

Over the remaining year, Amprius will continue to increase cell energy by optimizing anode structure and exploring advanced components, extend cell cycle life by tuning anode structure and testing new electrolyte formulations, and finish the design and assembly of the final cells with capacities ≥ 40 Ah.

Key Publications

1. "Advanced High-Performance Batteries for Electric Vehicle (EV) Applications", ES41_Stefan_2017, US DOE Vehicle Technologies AMR, 2017.

I.A.7 Development of Active Materials to be used in Automotive Traction Applications: Rapid Commercialization of High Energy Anode Materials (SiNode Systems)

Cary Hayner, Principal Investigator
SiNode Systems
3440 S. Dearborn Street, #113N
Chicago, IL 60616
Phone: 612-220-3846
E-mail: caryhayner@sinode-systems.com

Brian Cunningham, Technology Manager
U.S. Department of Energy
Phone: 202-287-5686
E-mail: Brian.Cunningham@ee.doe.gov

Start Date: May 1, 2016 End Date: October 31, 2018
Total Project Cost: $3,995,245 DOE share: $1,997,622.50 Non-DOE share: $1,997,622.50

Project Introduction

As global usage of electric vehicles steadily increases, so does the power/energy requirement to meet mainstream needs. Performance trajectories of traditional lithium-ion technology, despite an annual 3-5% improvement in energy density since inception, suggest that long-term electric vehicle needs will not be met without an evolution beyond traditional energy storage materials (i.e., graphitic anodes). SiNode Systems has developed a novel Si-based, negative-electrode material which can enable a quantum leap in battery energy and power density, and significantly impact battery weight and run-times that burden today's electric vehicles.

Objectives

The project entitled "Rapid Commercialization of High Energy Anode Materials" has been established with the aim of extending, benchmarking and demonstrating the performance of SiNode System's advanced silicon-based anode materials in battery form factors and designs relevant for electric vehicle applications.

Approach

SiNode Systems has demonstrated a novel high energy density (>1,000mAh/g) Si-based negative-electrode materials technology with a long-term potential to replace graphitic-based anodes in lithium-ion batteries. SiNode's technology uses a proprietary silicon alloy-graphene material architecture to achieve: i) category-leading performance and ii) solutions to long-standing Si anode technical hurdles. The proprietary combination of silicon-based alloys and a flexible 3D graphene network helps to stabilize the active material during charge and discharge (see Figure I-20) by providing an interfacial barrier between the active material and the electrolyte which can accommodate large volumetric changes through a laminar graphene sliding mechanism. The 3D graphene-silicon architecture results in a minimization of capacity losses due to electrical disconnection, significantly improved active utilization (mAh/g) and partial stabilization of the SEI interface with a flexible physical barrier between electrolyte and active material.

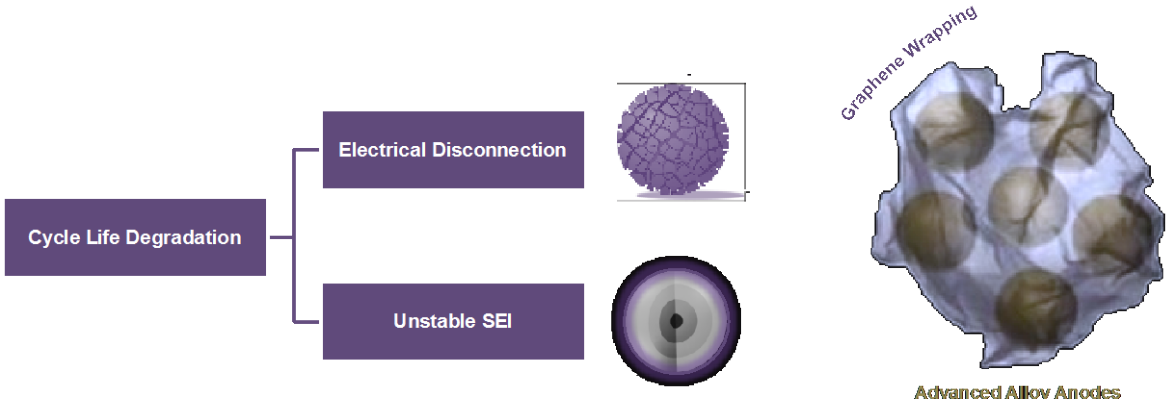

Figure I-20. Si-anode failure mechanisms (left), SiNode graphene-wrapped advanced silicon anode architecture (right)

SiNode has made continuous improvements against key USABC advanced electrode metrics over time, and demonstrated an attractive trajectory towards USABC advanced electrode goals. The goal of the program is the advancement and commercialization of advanced silicon-based active materials for high energy / high power EV batteries. Specifically, the program aims to demonstrate that SiNode technologies can cexceed USABC electric vehicle performance targets in USABC-recognized cell form factors, be produced at-scale by commercially viable methods and reach USABC cost targets at scale. To this end, a series of tasks have been developed to address the core technology gaps and their associated barriers: Task 1: Materials Stabilization and Analysis, 2. Manufacturing Scale-Up, 3. System Cost Reduction, 4. Cell Prototype Evaluation, 5. Downstream Cell Process Optimization and 6. Cell Characterization and Performance Evaluation.

SiNode has two strategic partners for this program. A123 systems will work with SiNode on Tasks 4 and 6, the pouch cell deliverables and PPG will work with SiNode on Tasks 2 and 3 to scale up the anode material.

Results

This year SiNode has developed a novel carbon-coating method for stabilizing the surface and SEI of its SiOx active particles, prior to graphene wrapping. (See Figure I-21.) Recently, this carbon coating process was refined and optimized. Experiments were undertaken with the goal of better understanding the impact of carbon coating amounts on the electrochemical cycling performance of the final composite, as well as improving the coating process to reduce the initial cycle loss and improve the first Coulombic efficiency (FCE).

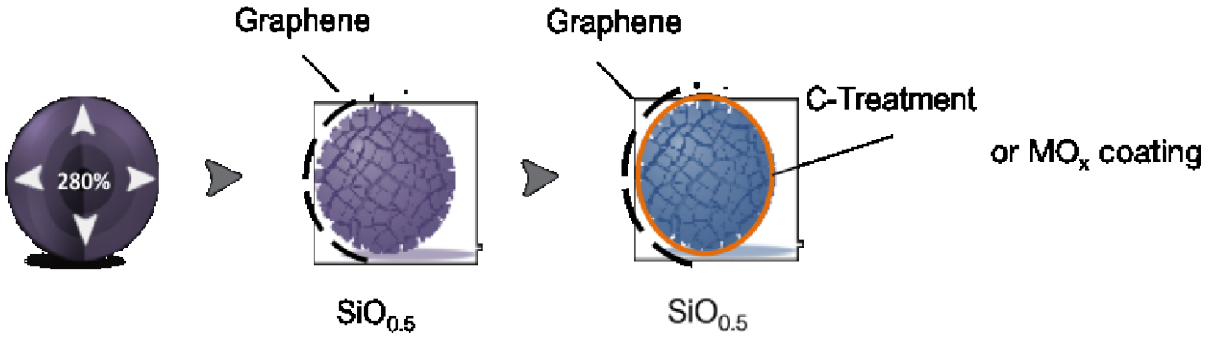

Figure I-21. Evolution of SiNode technology to meet USABC goals and specifications: (from left to right) pure silicon particle -> graphene wrapped silicon alloy (SiOx, x=0.5) -> C-coated (or MOx coated) and graphene wrapped silicon alloy (SiOx, x=0.5).

Through this work, SiNode was able to better understand and optimize our carbon coating procedure. Improvements to the surface morphology of the C-SiOx particle led to higher first cycle efficiency values (FCE), as shown in Figure I-22, and therefore higher energy. For our standard C-coating level, FCE improvements of 3% were observed by improving the carbon coating procedure, raising the pure material (i.e., >1500 mAh/g) FCE to over 79% - very close to the 80% target value cited by our customers.

Figure I-22. Improvements in FCE of our anode material seen by optimizing the surface morphology of the carbon coating.

Next, SiNode focused on both the scale-up and process refinement of an optimized C-coated graphene wrapped silicon alloy. A monthly production level of 2 kg has been achieved. In addition to improvements in production efficiency through increased solids-loading of our precursor, SiNode has also introduced process refinements and quality checks to ensure that the larger quantity of material produced remains up to par. The goal over the next quarter is to continuously improve SiNode's internal bandwidth to accommodate the needs of subsequent builds while maintaining consistent material performance.

This increased production has required improvements in the repeatability of the powderization process. By developing process controls, SiNode has been able to produce material that performs the same week-to-week. (See Figure I-23.)

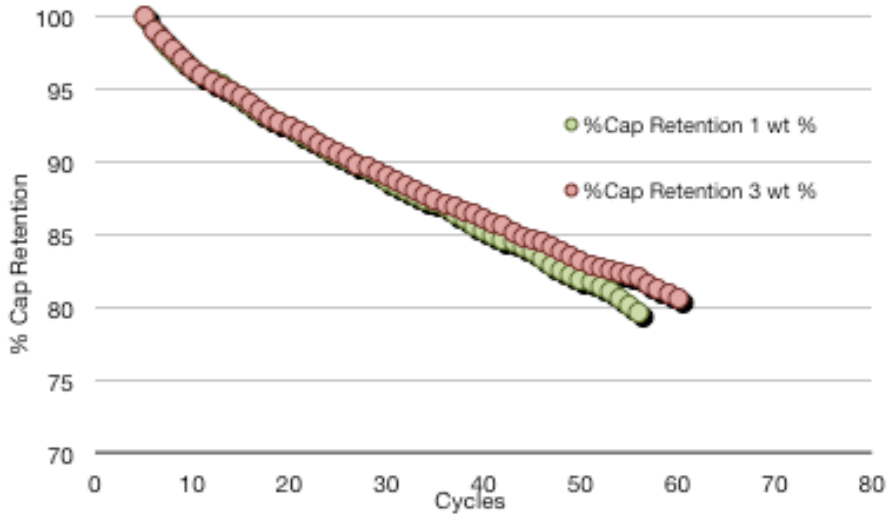

Figure I-23. Capacity retention as a function of cycles for 1 and 3 wt% precursor dispersions. The data is in full cell paired with an NCA cathode.

The production roadmap to the 1 Ahr cell deliverables was analyzed in Q6, and is shown in Figure I-24. There has been a gradual migration to higher graphene dispersions over time (from 1-3%), which has enabled additional bandwidth and higher production efficiency. In parallel, SiNode external production collaborations are expected to come online in the November-December timeframe which will provide additional production bandwidth as a result of larger pilot-scale equipment.

Figure I-24. 2017 production forecast and major technical milestones. Project needs and graphene dispersion levels are expected to increase throughout the course of 2017

For the 1 Ah cell deliverables, A123 was initially able to carry out a successful lab-based coating of the targeted 1000 mAh/g anode on a lab scale. The graph in Figure I-25 demonstrates updated cycling data from this cell, which completed its testing during this quarter.

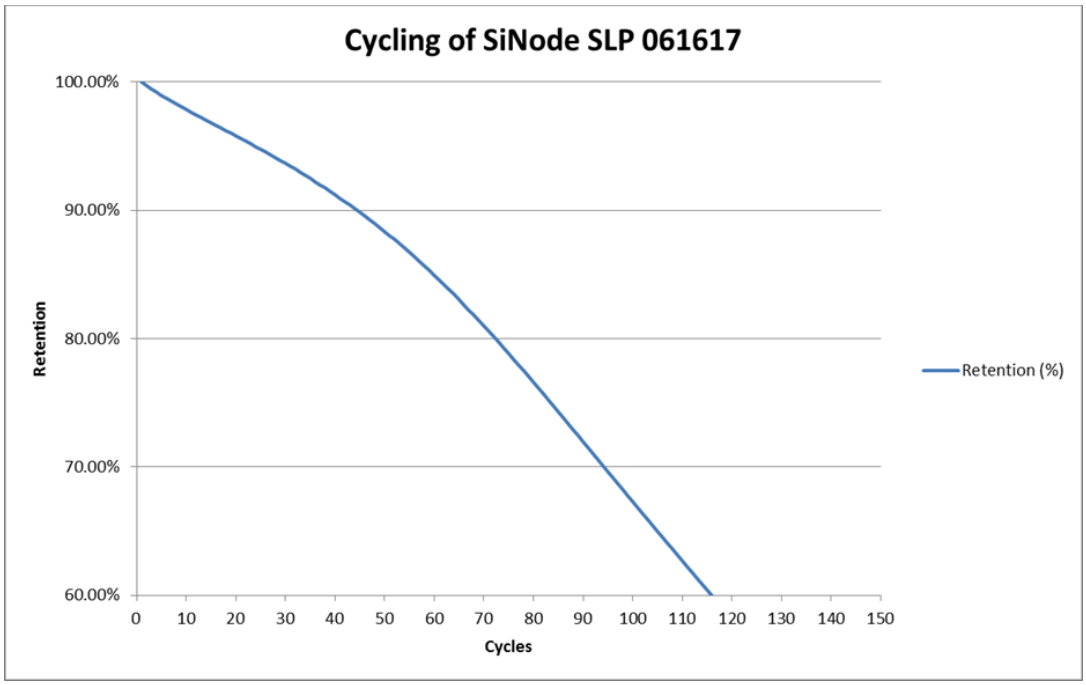

Figure I-25. Completed cycle life testing of full SLP cell manufactured with A123 hand coated anode

A123's goal was ultimately to be able to replicate this result using a large number of higher capacity deliverable cells, with anode successfully coated on full manufacturing equipment at its facility. During the latest quarter, A123 was able to complete the full manufacturing coated material (around 80 meters of double-sided electrode) required for the deliverable cells. The next step in the process is to move forward with the cell manufacturing process, with expected cell delivery during the final quarter of 2017.

Next, experiments were completed in which the amount of FEC used in SiNode's electrolyte formulations was reduced. Due to the addition of carbon coatings which stabilized the SiO_x surface, it is no longer necessary to add high quantities (20%) of FEC to stabilize the active silicon. Electrodes were constructed at the USABC-targeted 1000 mAh/g capacity and tested in a full cell format against an NCA cathode. As shown in Figure I-26, the cells were able to demonstrate the same cycling performance with 10% FEC as with the standard 20% FEC, enabling a decrease in the amount of FEC used by 50%. No other undesirable effects (i.e., low capacity, swelling) were observed when moving to 10% FEC. These improvements help align our cell design with industry practice and will help with cell manufacturing challenges such as gassing and swelling.

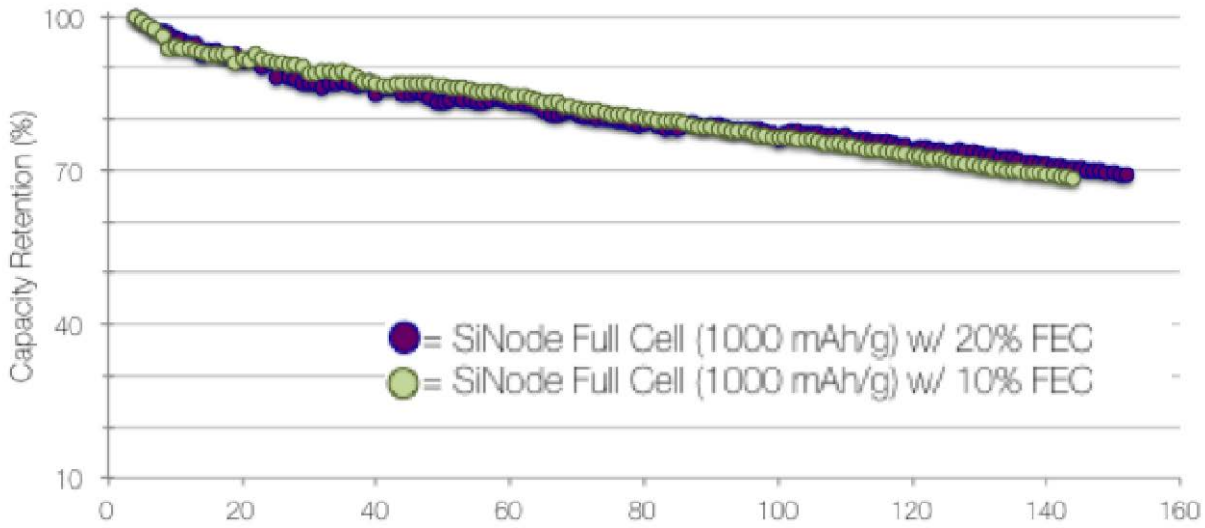

Figure I-26. Full cell capacity vs. cycle number plot for SiNode 1000 mAh/g anodes vs. NCA cathode with varying degrees of FEC electrolyte additive.

Conclusions

SiNode has entered the 18th month of the 30-month-long project. The 1 Ah cell deliverables will be delivered this quarter. A major milestone was achieved in the materials scale up with SiNode successfully completing the materials scale up for the 1 Ah cells.

Several challenges need to be surmounted over the coming year, including consistent improvements of the average coulombic efficiency, cycle life, electrode expansion, multi-kilogram production, successful battery electrode design and line-of-sight on materials cost reductions (i.e., graphene and silicon).

SiNode has demonstrated a cadence of innovation and product development over the past 18 months, and looks optimistically towards demonstration of viable performance in commercially relevant EV cells.

I.A.8 A 12V Start-Stop Li Polymer Battery Pack (LG Chem Power, Inc.)

Mohamed Alamgir (LG Chem Power - PI)
LG Chem Power, Inc.
1857- Technology Drive
Troy, MI 48083
Phone: 248-291-2375
Email: alamgir@lgchem.com

Brian Cunningham, Technology Manager
U.S. Department of Energy
Phone: 202-287-5686
E-mail: Brian.Cunningham@ee.doe.gov

Start Date: January 1, 2015 End Date: March 29, 2017
Total Project Cost: $1,820,000 DOE share: $910,000 Non-DOE share: $910,000

Project Introduction

12V Start-Stop batteries are gaining increasing attention as cost-efficient solution for global reduction of carbon emission. To achieve this goal, Li-ion batteries offer promising alternative to the incumbent lead acid (PbA) batteries because of their much higher specific energy and longer life. Key challenges for realization of this objective are cold-cranking power and cost, which were the focus of this program.

Objectives

The goal of this program was to develop a low-cost, abuse-tolerant 12V Start-Stop Li-ion battery that will be capable of meeting the life, cold-cranking and cost targets of USABC.

Approach

To achieve the above objectives, the following approaches were pursued.

- Develop a long-life, abuse-tolerant cell using LTO/LMO active materials.
- Tailor cathode and anode material properties such as morphologies/surface area to increase power.
- Optimize cathode and anode compositions, their porosities as well as electrolyte compositions, with respect to life and power.
- Develop a low-cost battery pack using a simplified BMS.

LG Chem, Seoul, South Korea, was the partner in this program.

Results

We present below a summary of the work carried out in this program.

Optimization of Cell

We developed three generations of cells in the course of this program. Different types of LMO cathode material were evaluated to develop a high power cell that meets the cold-cranking power goal. The materials varied in their particle sizes, surface areas, doping elements and doping levels as well as surface coatings. We also evaluated cathodes having different compositions by varying the type and amount of conductive agents and binder. These characteristics were optimized to lower electrode resistance to increase cell power. Approaches similar to these were also pursued to develop a high power LTO anode. A number of electrolyte compositions as well as separators of different thickness and porosities were also studied.

We also carried out studies to improve processing conditions such as electrode manufacturing and aging. For example, LTO is a nano-material and has the propensity to adsorb moisture that is deleterious to cell performance such as life and swelling. Thus, appropriate processing conditions needed to be developed to ensure a well-functioning LTO electrode.

Considerable improvement in cell life and power was achieved via the above studies. As an example, we show in Figure I-27 the continuous improvement in storage characteristics of the cells developed in this program. While the initial studies showed poor performance at 60ºC and 70% SOC, the A1 sample showed significant improvement in high temperature durability. Excellent cycle-life was also achieved even at the high temperature of 50ºC at the charge/discharge rate of 5C/5C (Figure I-28).

As mentioned earlier, a key challenge of Li-ion batteries for Start-Stop applications is to meet the cold-cranking power requirement. While the first generation cell delivered good performance and reasonable durability, its cold-cranking power capability was poor and the USABC target could be met only at 100% SOC. By tailoring the cathode, separator and electrolyte properties, the cell characteristics were improved and the final cell was able to deliver cold-cranking power at SOC = 70%. We do note here that to meet the USABC requirement the cold crank power needed to be met at SOC = 40%. These are Beginning-of-Life (BOL) data and cold-cranking power at End of Life (EOL) need to be verified. In addition, the durability of the cell was also significantly enhanced as evidenced by reduction in gassing at high temperatures. (See Figure I-29.)

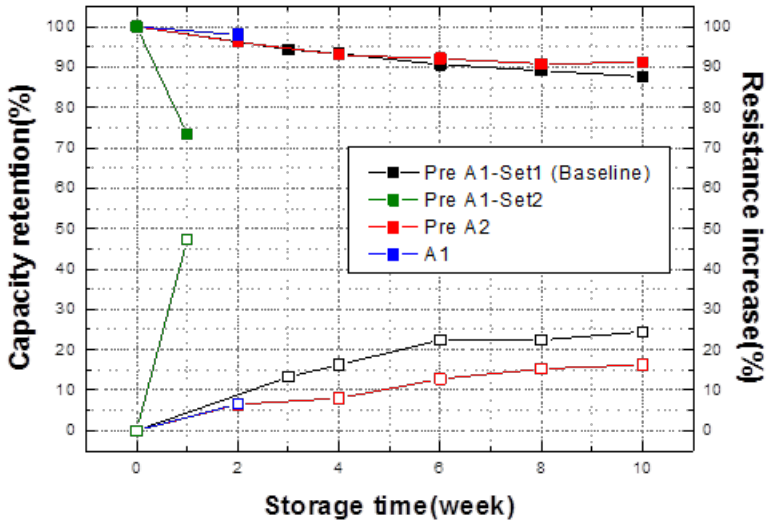

Figure I-27. Example of improvement achieved in the durability of the LTO/LMO cell in this program.

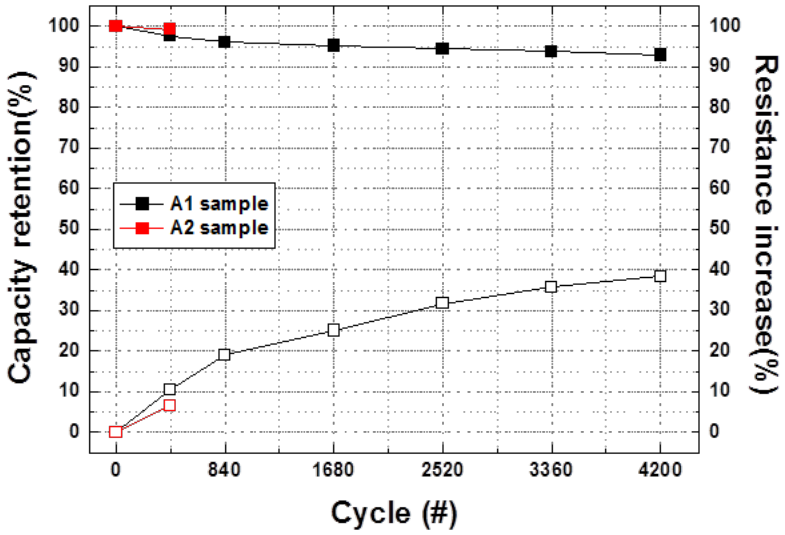

Figure I-28. Cycle-life data for LTO/LMO cells at 55oC and 5C charge and discharge rates.

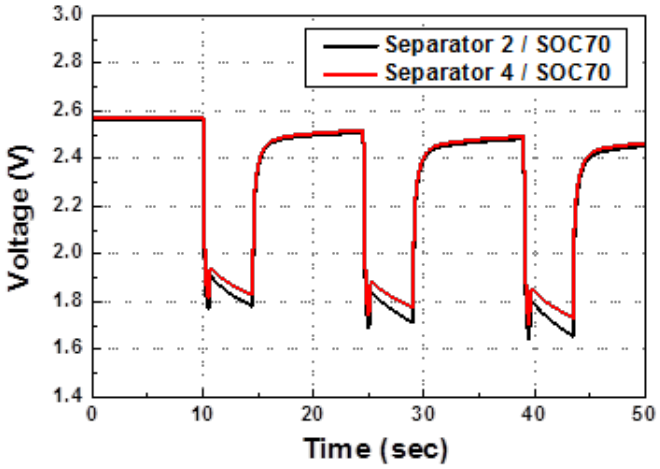

Figure I-29. Improvement of cold-cranking power as a function of separator properties.

Calorimetric studies were also carried out by NREL to thermally characterize the various generations of the cells. This involved heat generation, heat capacity and IR imaging measurements. The data showed that the efficiency of the cells improved through the cell generations (Figure I-30). For example, A1 cell showed a discharge efficiency at 0°C comparable to the preliminary cell version efficiency at 30°C. Additionally, for the A1 cell at a 2C full discharge, the efficiency of the cell dropped from 98.9% at 30°C to 96.9% at 0°C – a very attractive performance with regards to temperature. Under low rate discharges (< C/1), the cell chemistries' endothermic response dominates the Joule heating within the cell.

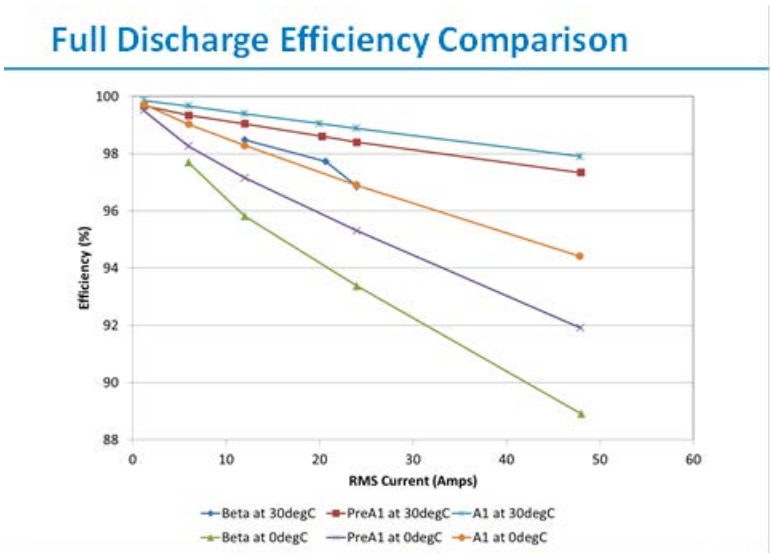

Figure I-30. Improvement in the discharge efficiency of the various generation of cells as a function of cell improvement.

The program cells showed outstanding abuse-tolerance. While the nail penetration and short-circuit tests yielded results with EUCAR ratings of 3 and lower, both the thermal stability and overcharge tests showed a EUCAR rating of 4 (venting with > 50% electrolyte loss).

Development of the 12V Start-Stop Battery Pack

A key objective of our pack development studies was to develop a long-life and low-cost battery pack using a simplified BMS system. A number of options to hold the cells in a mechanically robust manner were evaluated. Since the pack is under hood, a thermal management strategy was adopted to efficiently shield the cells from exterior heat while also allowing for heat rejection by the cells during operation. A low cost insulating foam was chosen which is also used as the cell retention frame. Illustrative simulations and tests demonstrated efficient cooling of the cells during operation and storage. For example, experimental data acquired from the pack at 75ºC for four (4) hours agreed quite well with these estimations indicating that the cells remain below 50ºC during this storage. A simple and low-cost battery management system was developed that is capable of cell balancing and state-of-charge estimation.

Two versions of packs were developed and delivered to the USABC for testing and evaluation. As the 2nd and final delivery, six battery packs were built and delivered to the National Labs for testing and validation according to USABC protocols. (See Figure I-31.)

Figure I-31. Picture of the 12V Li-ion Start-Stop battery pack delivered to USABC for testing.

Conclusions

Results we have acquired and presented above show that this two-year program was able to achieve significant progress towards the development of an LMO/LTO cell-based 12V Start-Stop battery that is technically and commercially competitive with its PbA counterpart. Considerable advances were made in the critical areas of cold-cranking power, life and abuse-tolerance. We also developed a simple thermal management and cell retention strategy that is low-cost but capable of meeting the thermal and mechanical requirements for automotive use. This approach in combination with a low-cost and potentially simplified BMS makes the LMO/LTO pack technology a next generation alternative to the 12V PbA battery.

To make it more competitive with a PbA battery, we need to further improve the cold-cranking capability. In addition, we need to address the gassing/cell swelling issues especially for higher temperatures application characteristic of under hood deployment. There is also a gap to the USABC cost target. Pack data obtained from the National Labs will aid in further establishing the gap to the USABC requirements and cycling data will enable us to determine whether one can use simplified BMS also.

Key Publications

1. “A 12V Start-Stop Li Polymer Battery Pack”, ES249_Alamgir_2017_p, US DOE Vehicle Technologies AMR, 2017.

I.A.9 USABC 12V Start-stop Module Development, Phase II (SAFT)

Thomas Greszler, Principal Investigator
SAFT SDD
107 Beaver Court
Cockeysville, MD 21030
Phone: 410-568-2590
E-mail: Thomas.Greszler@saftamerica.com

Alla Ohliger, Principal Investigator
SAFT SDD
107 Beaver Court
Cockeysville, MD 21030
Phone: 443-933-4944
E-mail: Alla.Ohliger@saftamerica.com

Brian Cunningham, Technology Manager
U.S. Department of Energy
Phone: 202-287-5686
E-mail: Brian.Cunningham@ee.doe.gov

Start Date: June 1, 2015 End Date: December 31, 2017
Total Project Cost: $6,100,000 DOE share: $3,064,700 Non-DOE share: $3,035,300

Project Introduction

Saft proposed to develop an advanced, high-performance battery module for 12V Start-Stop (12VSS) vehicle applications based on SAFT's proprietary LTO lithium-ion cell technology and continuation of development efforts undertaken in Phase I of the project.

Objectives

- Continue development of the cell electrochemistry based on SAFT's proprietary lithium titanate (LTO) lithium-ion battery technology and meet USABC technical targets listed in Table I-4.
- Design and develop 46 Ah cell and prototype module to meet USABC energy and cost targets.
- Develop module management and electronic controls.
- Deliver 46 Ah cells and 12V prototype modules to USABC.

Table I-4: USABC Cell & Module Performance Targets and SAFT Test Results

End of Life Characteristics (Capacity 1.5 Ah, Scaled-up 46 Ah)	Units	USABC Target	Note 1	Note 2
			1st Batch Cells	2nd Batch Cells
			45°C Calendar life	45°C Calendar life
		Under hood	Oct-17	Oct-17
Discharge Pulse, 1s	kW	6	24	Note 3
Max discharge current, 0.5s	A	900	901	Note 3
Cold cranking power at -30 °C (three 4.5-s pulses, 10s rests between pulses at min SOC)	kW	6 kW for 0.5s	6	7.3
	kW	4 kW for 4s	3.98	4.4
Min voltage under cold crank	Vdc	8	8	8
Available energy (750W accessory load power)	Wh	360	501	545.6, Note 3
Peak Recharge Rate, 10s	kW	2.2	2.2	Note 3
Sustained Recharge Rate	W	750	750	750
Cycle life, every 10% life RPT with cold crank at min SOC	Engine starts	450k	276.5K	Note 3
Calendar Life at 30°C, 45°C if under hood	Years	15 at 45°C	RPT12	Note 3
			6.7% complete	
Minimum round trip energy efficiency	%	95	99	99.5
Maximum allowable self-discharge rate	Wh/day	2	0.11	0.87
Peak Operating Voltage, 10s	Vdc	15	15	15
Sustained Operating Voltage – Max.	Vdc	14.6	14.5	14.5
Minimum Operating Voltage under Autostart	Vdc	10.5	10.5	10.5
Operating Temperature Range (available energy to allow 6 kW (1s) pulse)	°C	-30 to + 75	-1- to 75°C	-1- to 75°C
30 °C – 52 °C	Wh	360 (to 75°C)	502	Note 3
0 °C	Wh	180	437	Note 3
-10 °C	Wh	108	138.5	Note 3
-20 °C	Wh	54	Fail	Note 3
-30 °C	Wh	36	N/A	Note 3
Survival Temperature Range (24 hours)	°C	-46 to +100	N/A	Note 3

Notes:

1st batch 1.5 Ah pouch cells delivered in April 2016, 2nd batch 1.5 Ah pouch cells delivered in July 2017, Testing in progress

Approach

The cost of a Li-ion battery product is generally the most challenging requirement for deployment in the automotive industry. SAFT focused on optimization of the cell electrochemistry and cost-efficient design for cell and module suitable for mass production. SAFT's approach was to develop a low-cost lithium-ion cell electrochemistry meeting USABC technical performance requirements. SAFT analyzed technical gaps discovered during testing of the 1st batch C-size cells and continued to optimize cell electrochemistry to increase cycle-life/calendar life, limiting the impedance growth over time, and minimizing gassing. For electrode, SAFT focused on rational design of positive and negative electrodes including active materials, carbon network, binders and implementation of surface coatings; all have significant impact on cold crank and gassing. Samples of the LTO powder were delivered to Argonne National Laboratory, ForgeNano and ALD Nanosolutions for surface coating evaluation. For electrolyte, Saft focused on experiments to achieve good electrolyte conductivity at low temperatures.

To meet cost targets SAFT focused on industrialization plan for manufacturing of cells & modules. The approach was to develop cost-effective producible 46 Ah cell and module design (including electronics) and eliminate numerous design features that contribute to the overall cost while retaining performance and lifetime characteristics that are necessary for an automotive application.

Results

SAFT completed testing of the 1st batch C-size pouch cells and started testing 2nd batch cells with improved electrochemistry. The overall performance targets, outlined by USABC, are shown in Table I-4. Table I-4 also presents Saft's test results obtained from the 1st and 2nd batch cells. Batch 1 cells have impedance growth at high temperature 55°C and 65°C leading to decreased cold crank performance after initial control testing. Cells have no significant capacity fade after 1 year testing at 45°C cycle life, 45°C calendar life and 55°C calendar life. After one year of cycling testing at 45°C, batch 1 cells have minimal impedance growth. SAFT started testing cells from batch 2. Significant improvement can be seen in initial cold crank performance between batch 1 and batch 2.

Electrochemistry Development

LMO/LTO system has a higher gassing rate than LFP/LTO or NMC/LTO cells. In order to increase high temperature stability, SAFT reduced the Mn3+ content in active material. LCO was selected as an active material to be blended with LMO for its lack of Mn3+ content, OCV curve and high specific capacity. The trials concluded that the LMO:LCO (80:20) positive electrode combined with LTO decreased gassing rate, however degraded the cold crank performance. Therefore, LMO was selected as the final positive active material.

For negative electrode, it was found that LTO contributes to 70-80% of the cell total impedance. Therefore, SAFT focused to optimize LTO electrode formulation. Supplier 4 was selected as the final LTO supplier for 46 Ah cells. This LTO material improved cell cold crank performance while reducing gassing rate. Different electrode compositions were tested in order to reduce gassing. Two designs: design 2 with carbon black and graphite as conductive network, and carbon free design were down-selected as offering the best cold crank performance and minimizing cell gassing rate (Figure I-32). LTO carbon free was selected as optimal electrode design since this formulation allows increasing cell capacity while maintaining overall cell performance. Moreover LTO with high loading was selected and will be implemented in 46 Ah cells. This LTO design meets cold crank performance and gassing requirements along with a cell cost reduction.

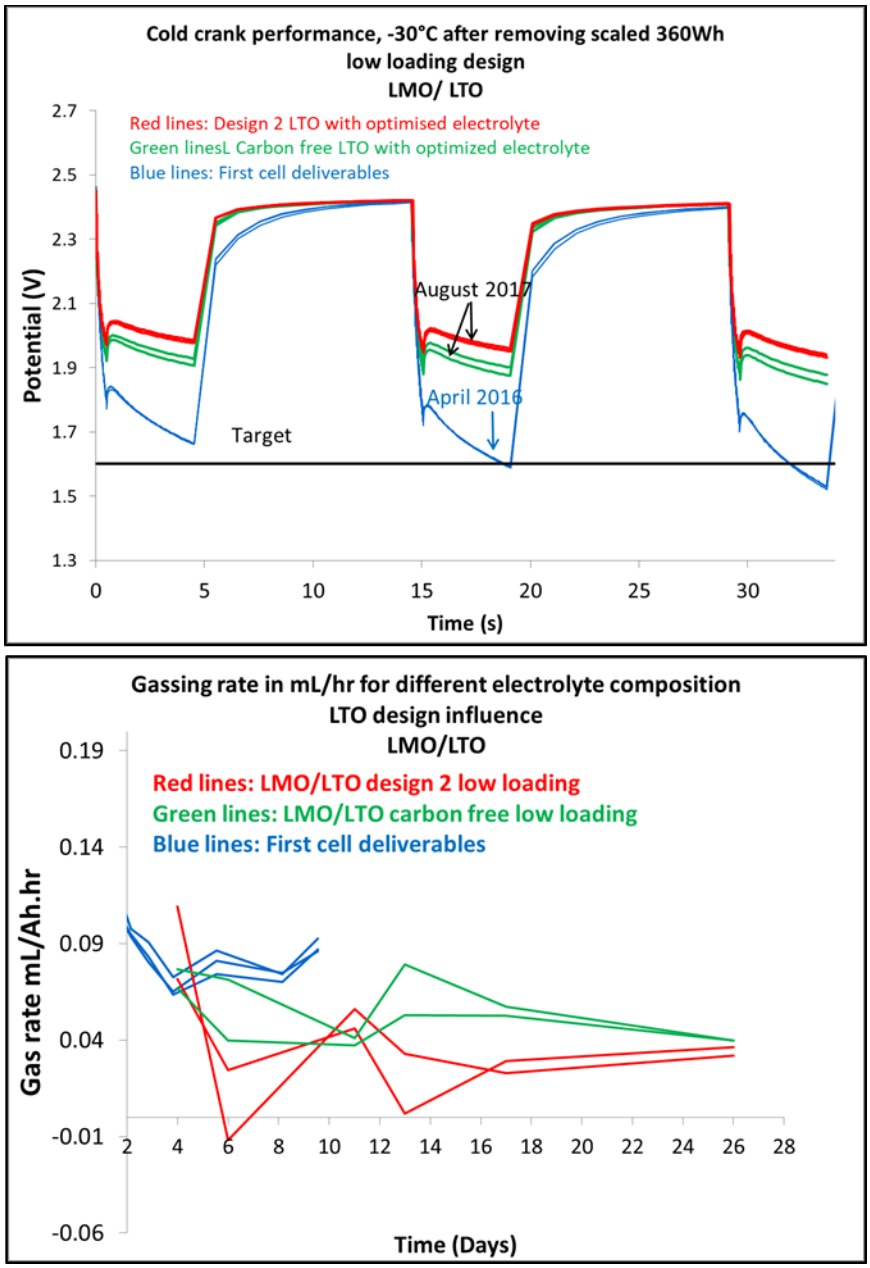

Figure I-32. (Top) Comparing cold crank performance of cells with Design 2 LTO and carbon free LTO versus the first cell deliverable baseline, (Bottom) Comparing gassing rate of cells with Design 2 LTO and carbon free LTO versus the first cell deliverable baseline

SAFT tested alumina coated separator and PP separator with different thicknesses and porosity. The goal was to improve cell wetting and cold crank performance. The separator 12 microns PP was selected as the best option to meet USABC requirements, specifically cold crank performance, and will be used for 46 Ah cells.

In conclusion SAFT selected LMO, LTO and separator suppliers for 46 Ah cells. LMO electrode formulation was finalized, while two LTO formulations are still being considered for 46 Ah cells. SAFT continues testing cold crank performance to finalize LTO formulation.

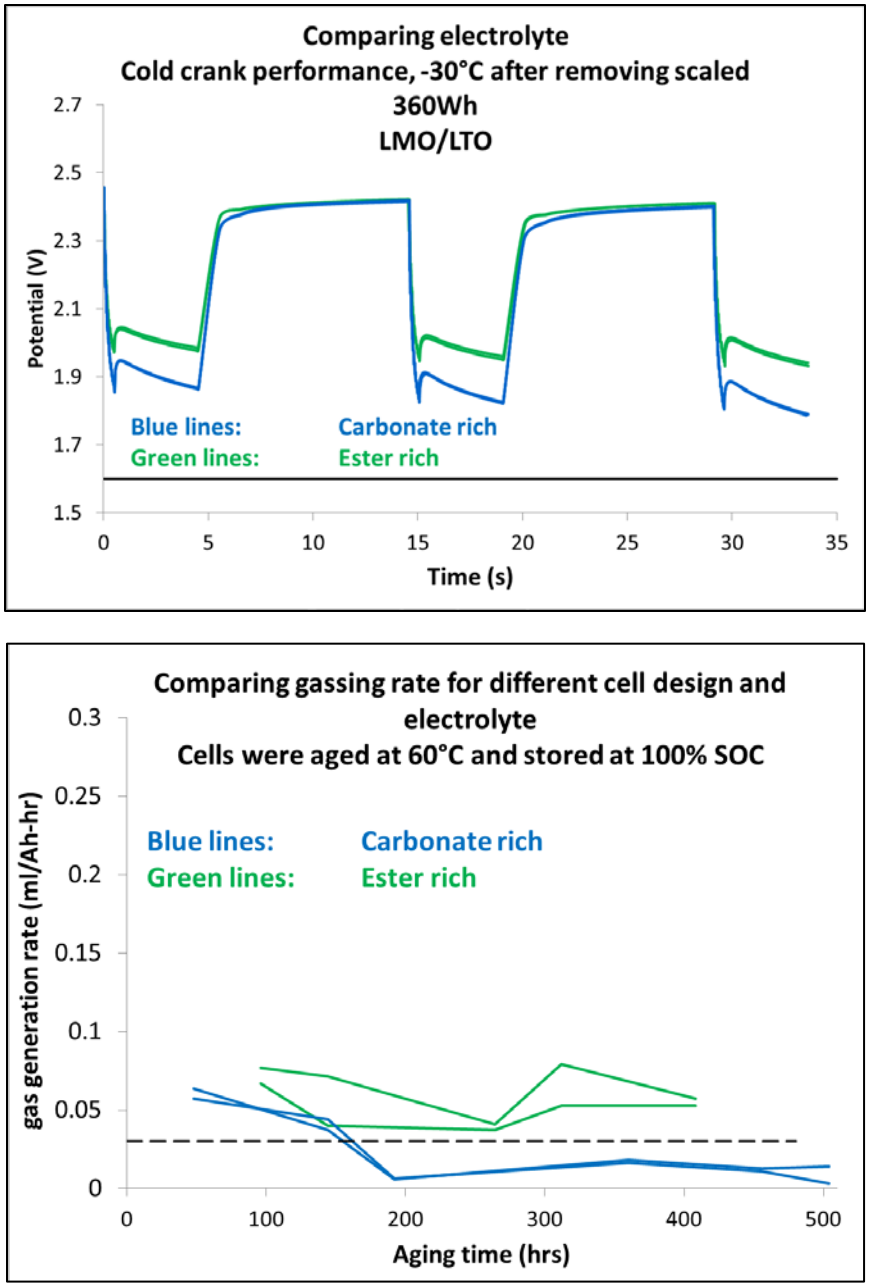

Figure I-33. (Top) Comparing cold crank performance of cells filled with ester rich electrolyte vs carbonate rich electrolyte, (Bottom) Comparing gassing rate of cells filled with ester rich electrolyte vs carbonate rich electrolyte.

To select electrolyte, SAFT tested electrolytes for conductivity at low temperature, boiling point, flash point, cell cold crank performance and cell gassing rate. Two electrolytes were down-selected and are being considered for 46 Ah cells fabrication: carbonate-rich electrolyte and ester-rich electrolyte. Both electrolytes offer good cold crank performance and gassing rate. The LMO/LTO cells with carbonate-rich electrolyte offer longer calendar/cycle life than ester-rich cells. Both cold crank results and gassing behavior for the two electrolytes are illustrated in Figure I-33.

Cell/Module Development

SAFT completed mechanical design of 46 Ah cell. The estimated finished cell size: 250 millimeters (W) x 216 millimeters (L) x 20.1 millimeters (T), and cell weight is ~1.99 kg, shown in Figure I-34.

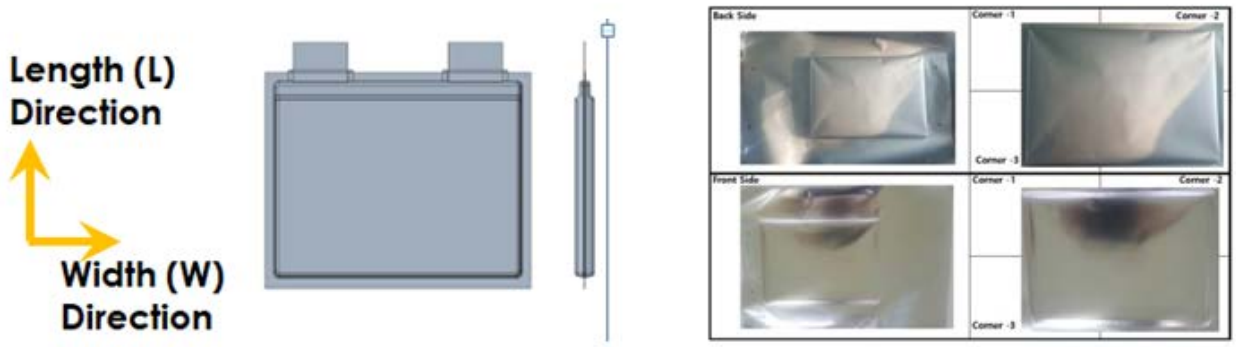

Figure I-34. Front and Side Views of the 46 Ah Pouch Cell (Left side); Photograph Showing Drawn Pouches (Right side). SAFT SDD

SAFT developed manufacturing process and ordered special tooling for manufacturing of 46 Ah cells. SAFT also completed design of the prototype battery module, shown in Figure I-35.

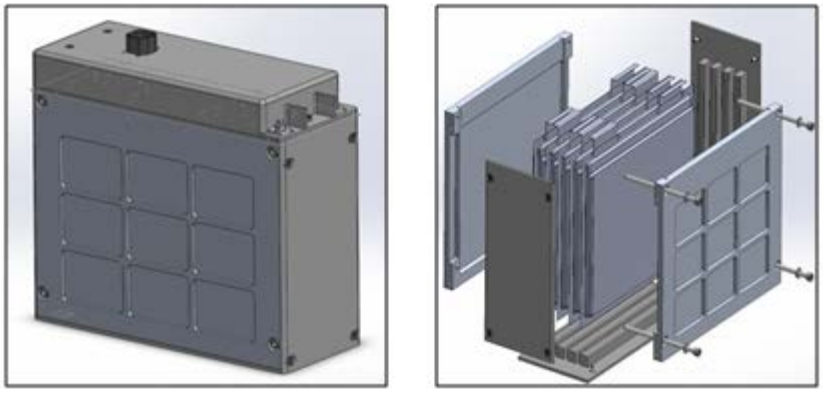

Figure I-35. 3D Model of USABC 12V S/S Prototype Model. SAFT SDD

Preliminary calculations on preliminary prototype module design (including electronics) resulted in overall volume of 9 liters (8 liters is USABC target). For mass production implementation additional design efforts are required to reduce module volume to meet USABC target. Weight of the module with cells and electronics was estimated to be 14.5 kg, meeting the USABC 15kg target.

For module electronics, SAFT has identified the overall structure of the system development and its integration into the module design. Battery module management will include: **cell voltage monitoring** (1.2 mV accuracy), **cell balancing circuitry** (60mA/cell capable), **temperature monitoring** (1 thermistor/cell) and **broadcast status** (state of charge/health, max current in/out and fault status). Figure I-36 shows block diagram detailing requirement for the electronic system.

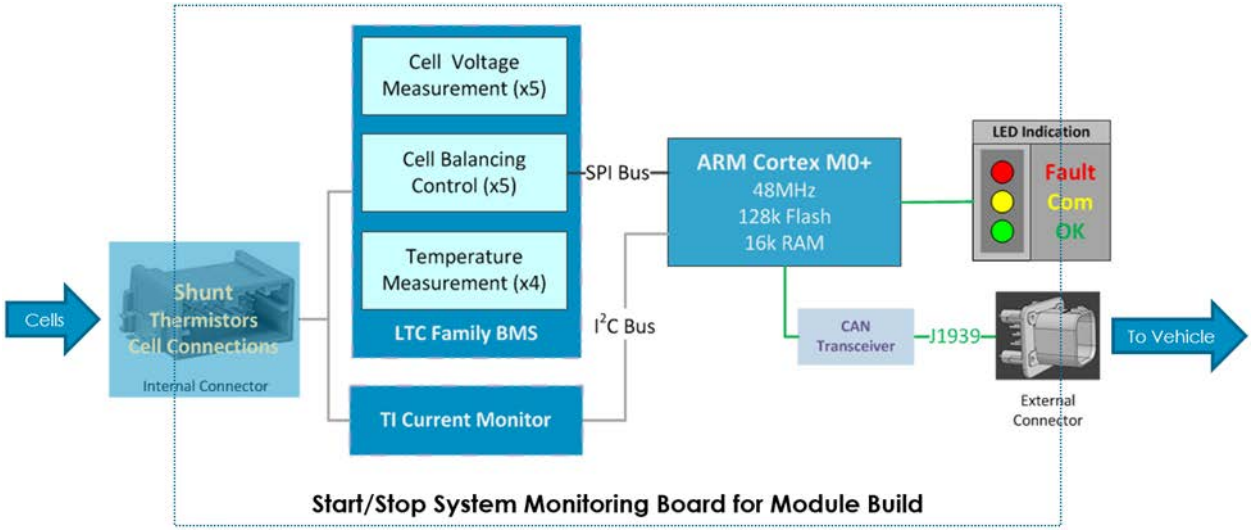

Figure I-36. Block Diagram Detailing the Requirements for the Electronic System. SAFT SDD

SAFT designed electrical control boards and manufactured proof-of-concept boards with test fixture, shown in Figure I-37. The proof-of-concept boards will be tested later this year.

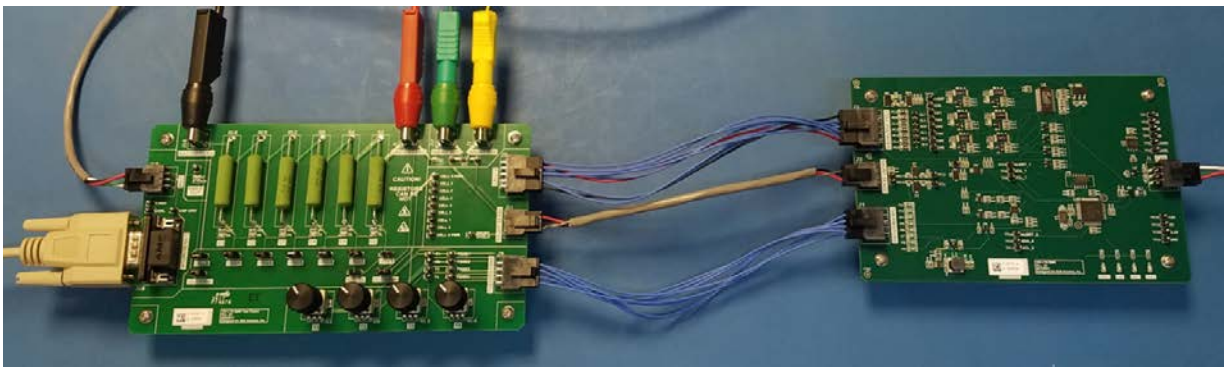

Figure I-37. Proof-of-Concept Electrical Control Board. SAFT SDD

Battery Module Cost Analysis

USABC cost target is $220 per unit. Preliminary cost analysis for cells, module hardware and electronics-based on 250k modules manufactured per year indicates meeting USABC target.

Deliverables

During reporting period Saft delivered 2nd batch of 1.5 Ah C-size pouch cells and 13 Ah prismatic cells to Idaho National Laboratory for testing.

Conclusions

SAFT delivered 2nd batch of 1.5 Ah C-size pouch cells with optimized electrochemistry to Idaho National Lab for testing. The 2nd batch cells with optimized chemistry were also tested at SAFT and met cold crank requirements. Testing is underway to complete calendar and cycle life for these cells.

SAFT continued to optimize electrochemistry formulations and suppliers to improve cell performance. For 46 Ah cells, SAFT finalized formulations and suppliers for LMO positive electrode, LTO negative electrode, separator and electrolyte.

SAFT completed mechanical design for 46 Ah pouch cell and prototype module, and moving forward with procurement of special tooling and development of manufacturing processes.

Key Publications

1. Thomas Greszler, “Li-Ion Technology for Space, Defense and Industrial Applications”, March 2017.

I.A.10 Advanced Polyolefin Separators for Li-Ion Batteries Used in Vehicle Applications (AMTEK)

Weston Wood, Principal Investigator
AMTEK Research LLC
250 N. Hansard Avenue
Lebanon, OR 97355
Phone: 541-259-3901
Email: wwood@entek.com

Robert Waterhouse, Principal Investigator
AMTEK Research LLC
250 N. Hansard Avenue
Lebanon, OR 97355
Phone: 541-259-3901
Email: rwaterhouse@entek.com

Brian Cunningham, Technology Manager
U.S. Department of Energy
Phone: 202-287-5686
E-mail: Brian.Cunningham@ee.doe.gov

Start Date: June 1, 2015 End Date: January 31, 2018
Total Project Cost: $2,085,490 DOE share: $1,042,745 Non-DOE share: $1,042,745

Introduction

One of the main barriers to mass adoption of electric vehicles is the cost of the battery pack for the given performance requirements (energy density, rate performance, safety, cycle life, calendar life). ENTEK will work towards helping move this technology forward by developing a separator for lithium ion batteries that will assist in enabling low cost, high voltage cells for EV applications. The overall goal of this project is to develop an advanced separator with high voltage oxidation resistance, improved safety features, and reduced cost to meet the electric vehicle requirements given by the USABC Program.

Objectives

The objectives for this work are to develop advanced separators with improved high voltage oxidation resistance, safety features (high temperature dimensional stability, shutdown temperature), and lower cost for lithium ion batteries in electric vehicle applications.

Approach

ENTEK's approach for this work is to incorporate nanoparticle filler into the microporous polyolefin base separator and apply a ceramic coating layer onto the surface of the separator for improved wettability, increased ionic conductivity, reduced thermal shrinkage, and improved oxidation resistance. In order to lower the cost of the separator using lower cost, in-line coating technologies will be evaluated that are compatible with our existing manufacturing process. In-line process capability, as opposed to an off-line secondary process, will be critical for achieving the lowest possible cost structure.

Results

The main tasks for November, 2016 through October, 2017 were 4.4V cell development for inorganic filled and ceramic coated separator. In addition, 4.9V cell development for ceramic coated separator has been initiated, and is currently under way.

Inorganic Filled Separator Development:

Various separators with silica filler loading levels ranging from 2.25 wt% to 20 wt% were previously investigated. The separator processing conditions were maintained constant throughout the trail and for all the filler compositions. Figure I-38 shows SEM images and pore size distribution of the inorganic filled separators compared to the control separator without filler (20 EPH). Despite the filled separator having higher porosity, the pore structure and pore size distribution between the filled and control separators appeared to be very similar. Table I-5 shows physical properties of selected trial samples. Increasing levels of filler resulted in higher porosity, higher air permeability (lower Gurley value) and lower electrical resistance (MacMullin Number). There was also a decrease in puncture strength with increasing filler level that was consistent with the decrease in polymer volume fraction in the separator. Puncture strength was still much higher than the limits set by USABC. The main benefits of such highly porous, filled separators are improved rate performance and wetting.

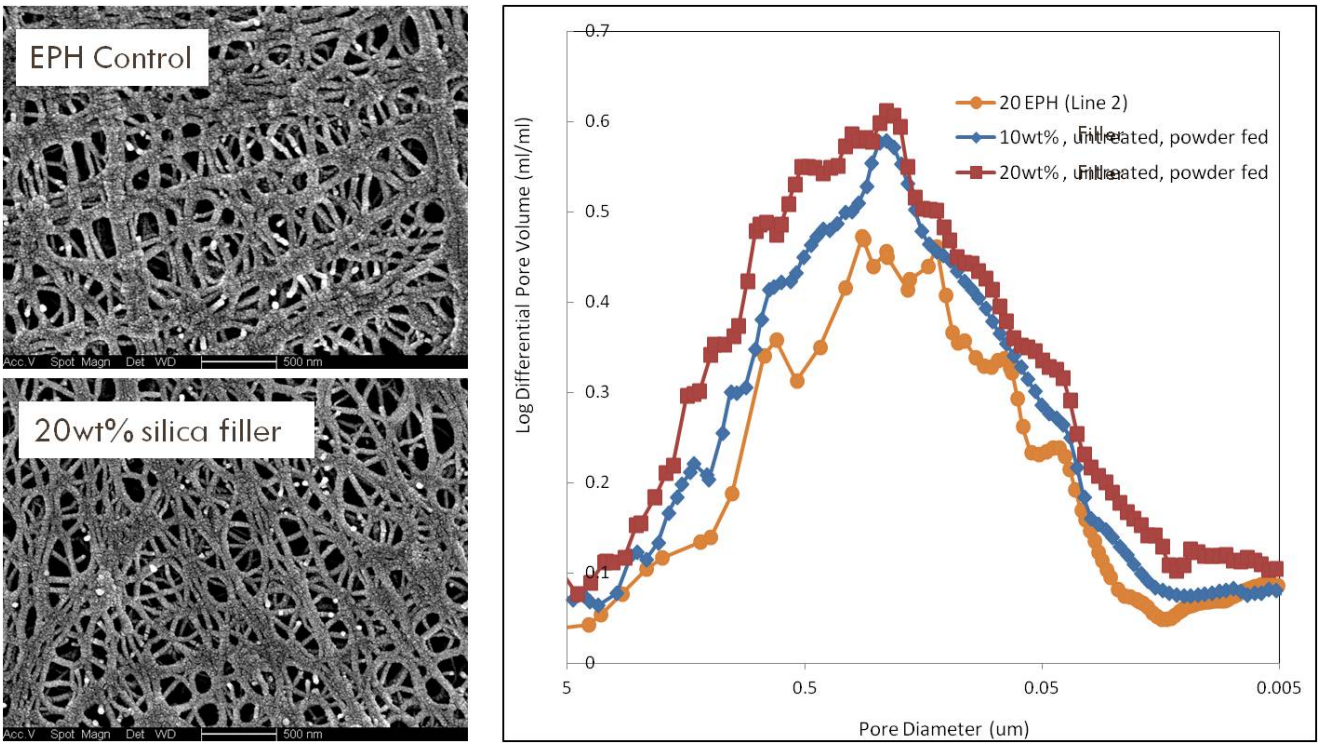

Figure I-38. SEM images (left) and pore size distribution (right) of inorganic filled separator for increased ionic conductivity.

Table I-5: Physical properties of samples optimized for increased ionic conductivity.

Sample Description	Porosity %	Thickness µm	Puncture gF	MacMullin# Dimensionless
20 EPH Control	48	20	463	7.5
Trial #5: 10 wt% Filler	59.0	20	440	4.3
Trial #5: 20 wt%Filler	65.3	20	393	3.3

Ceramic Coated Separator Development:

ENTEK's approach for ceramic coated separator development is to use nanoparticle coating formulations. Figure I-39 (top) shows a comparison between ENTEK's nanoparticle coated separator (primary particle size of about 20nm) and a more conventional coated separator with ceramic particle diameter of about 0.5 µm. SEM images in Figure I-39 (top) show a clear improvement in surface uniformity compared to conventional coated separator. Figure I-39 (bottom) also shows that less than half the coat weights required to reach high temperature dimensional stability when using the nanoparticle formulation compared to conventional coated separator. Reduced coating requirements may translate to reduced coated separator cost through raw materials reduction and faster coating speeds.

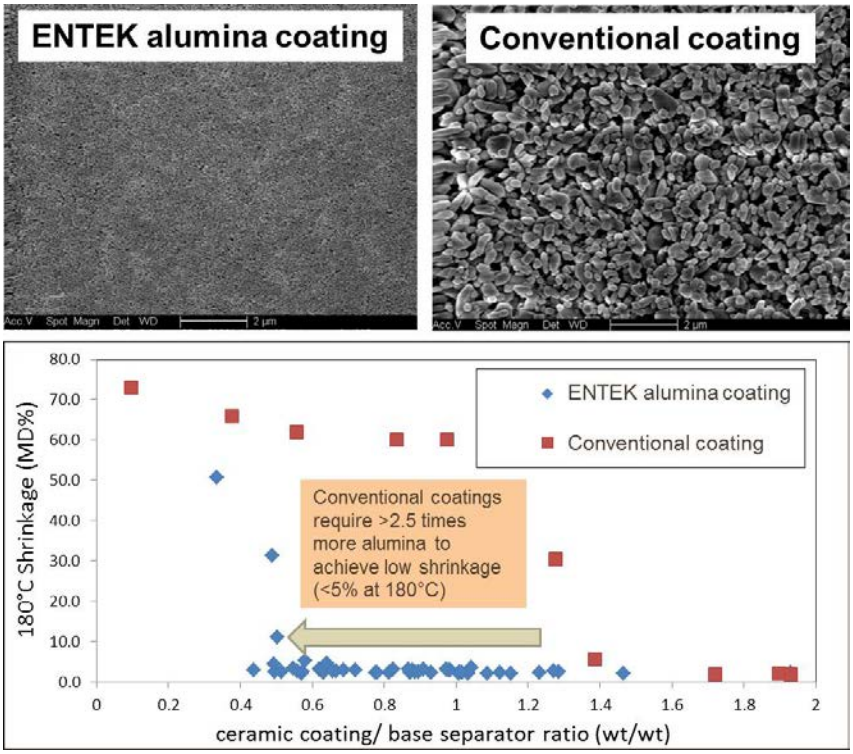

Figure I-39. Comparison between coat weight requirements for conventional and "nanoparticle" alumina coating onto separator. Conventional formulations require almost twice the coat weight to reach high temperature dimensional stability (<5% at 180°C).

4.4V Cell testing; NMC 622 positive electrode; coated separator evaluation.

Multiple sets of 18650 4.4V cells with 622 NMC positive electrodes were built at Farasis with ENTEK control (20 EPH), and ENTEK ceramic coated (HTDS 1604) separators. Cycle testing results (Figure I-40) show a considerable improvement in cycle life for the ceramic coated separator (HTDS) compared to the uncoated control (EPH). Furthermore when storing cells at 60°C, stability of open current voltage was improved (Figure I-41) and capacity fade was minimized (Figure I-42). We attribute these results in part due to an improvement in the voltage oxidation resistance of the ceramic coating on the separator.

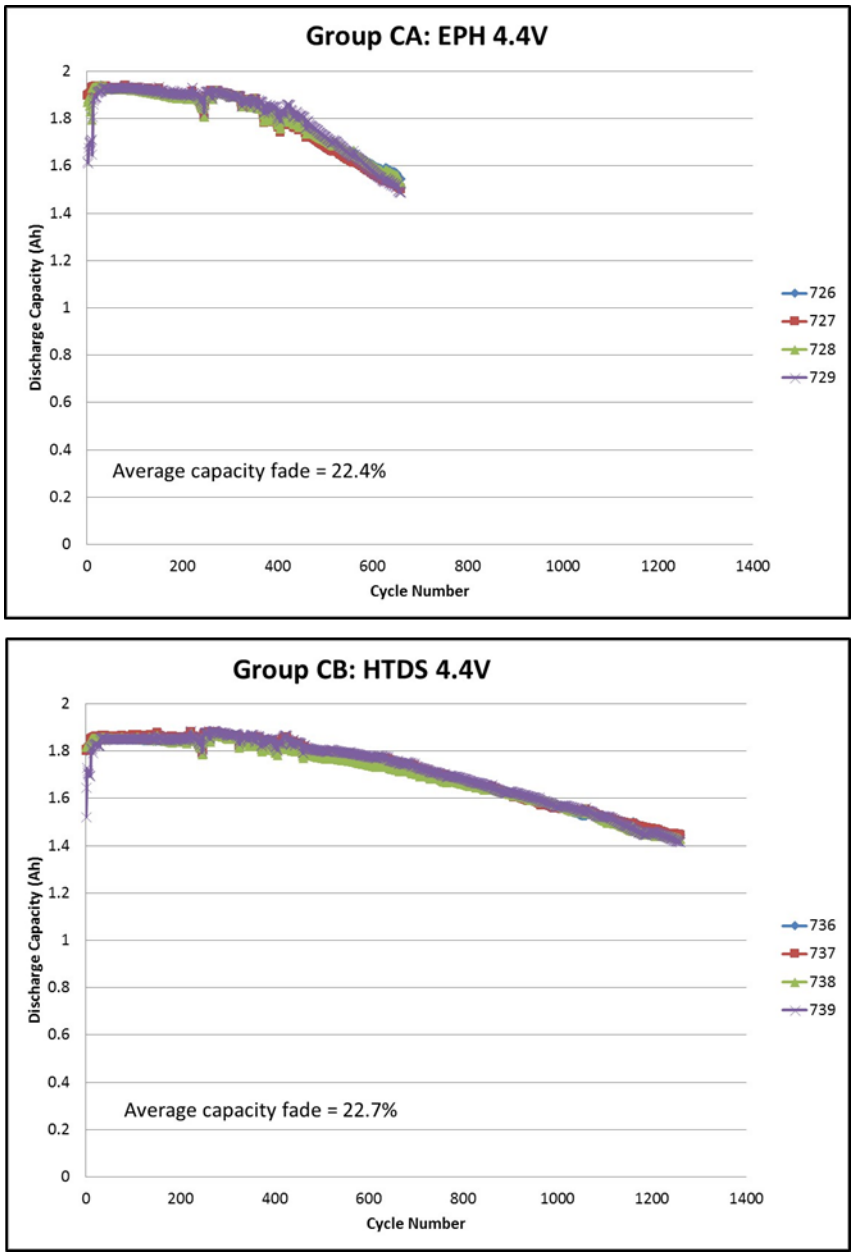

Figure I-40. Cycle life of 4.4V cells built with uncoated polyethylene separator (top) and alumina coated separator (bottom).

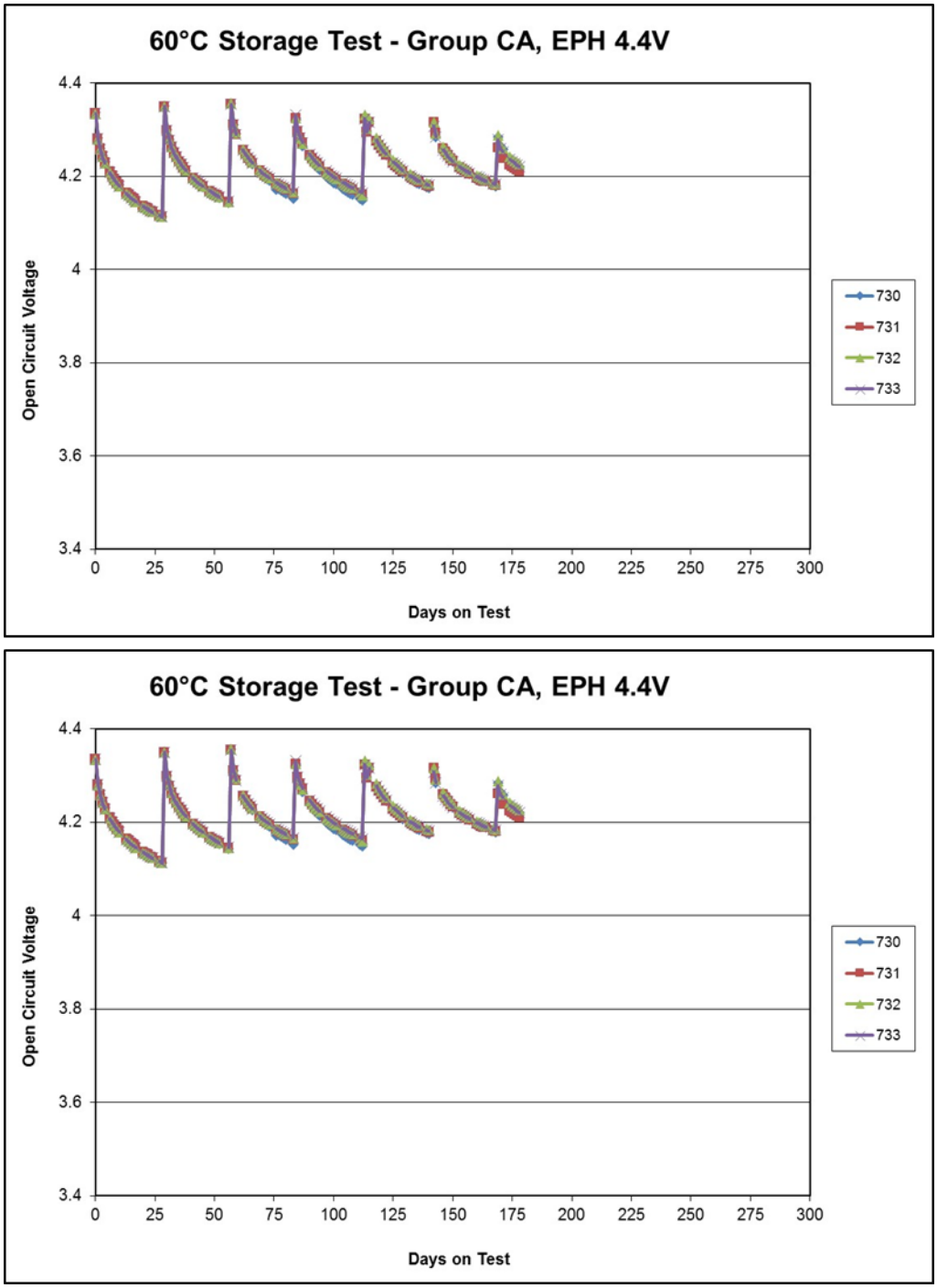

Figure I-41. Open circuit voltage of 4.4V cells stored at 60°C, built with uncoated polyethylene separator (top) and alumina coated separator (bottom). Cells were recharged to 4.4V every 30 days.

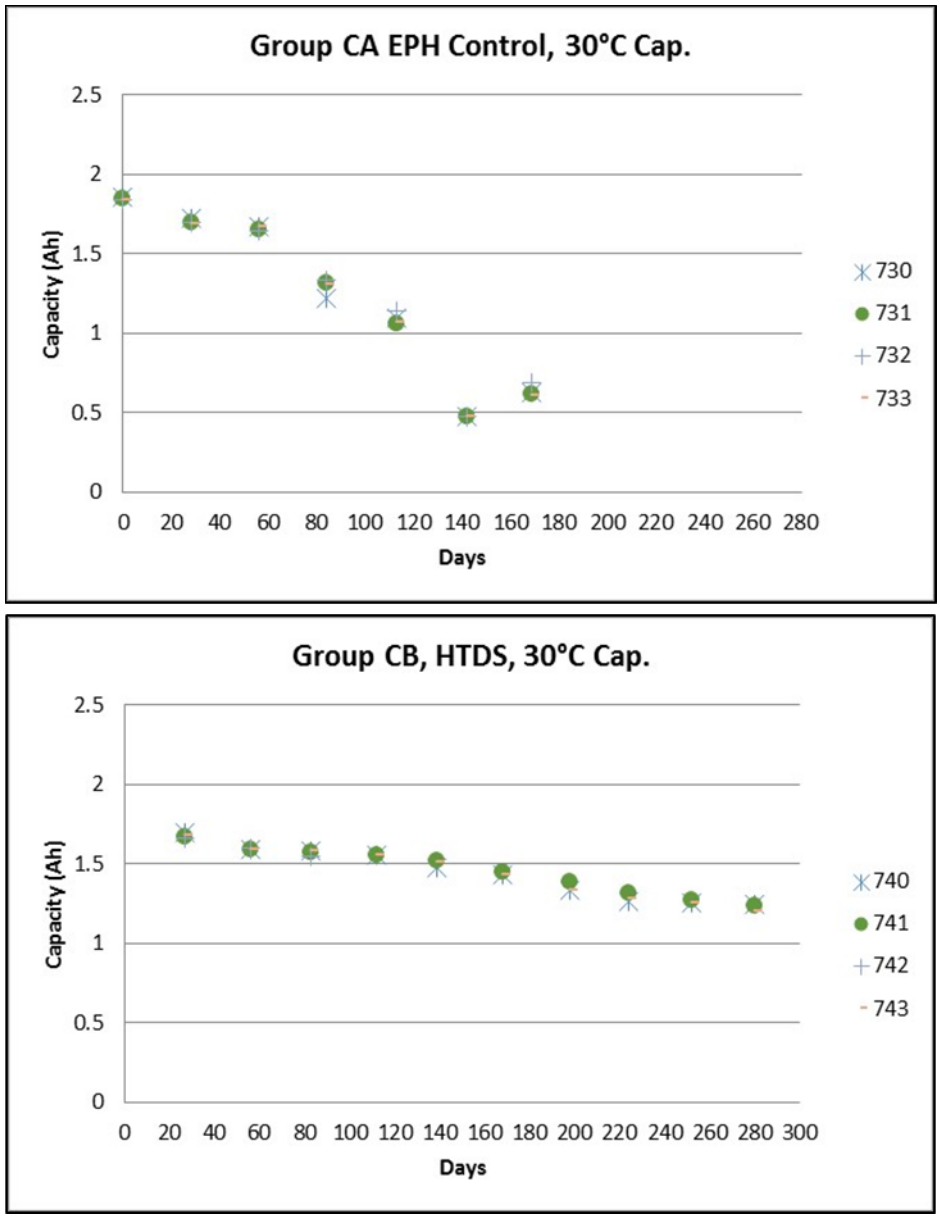

Figure I-42. Capacity of 4.4V cells stored at 60°C, built with uncoated polyethylene separator (top) and alumina coated separator (bottom). Capacity measurements were made at 30°C every 30 days.

4.4V Cell testing; NMC 622 positive electrode; inorganic filled separator evaluation.

Multiple sets of 18650 4.4V cells with 622 NMC positive electrodes were built at Farasis with inorganic filled separators having different filler contents. Applying a coating to the separator improved both cycle life (Figure I-43) and dramatically improved open current voltage stability (Figure I-44, Figure I-45).

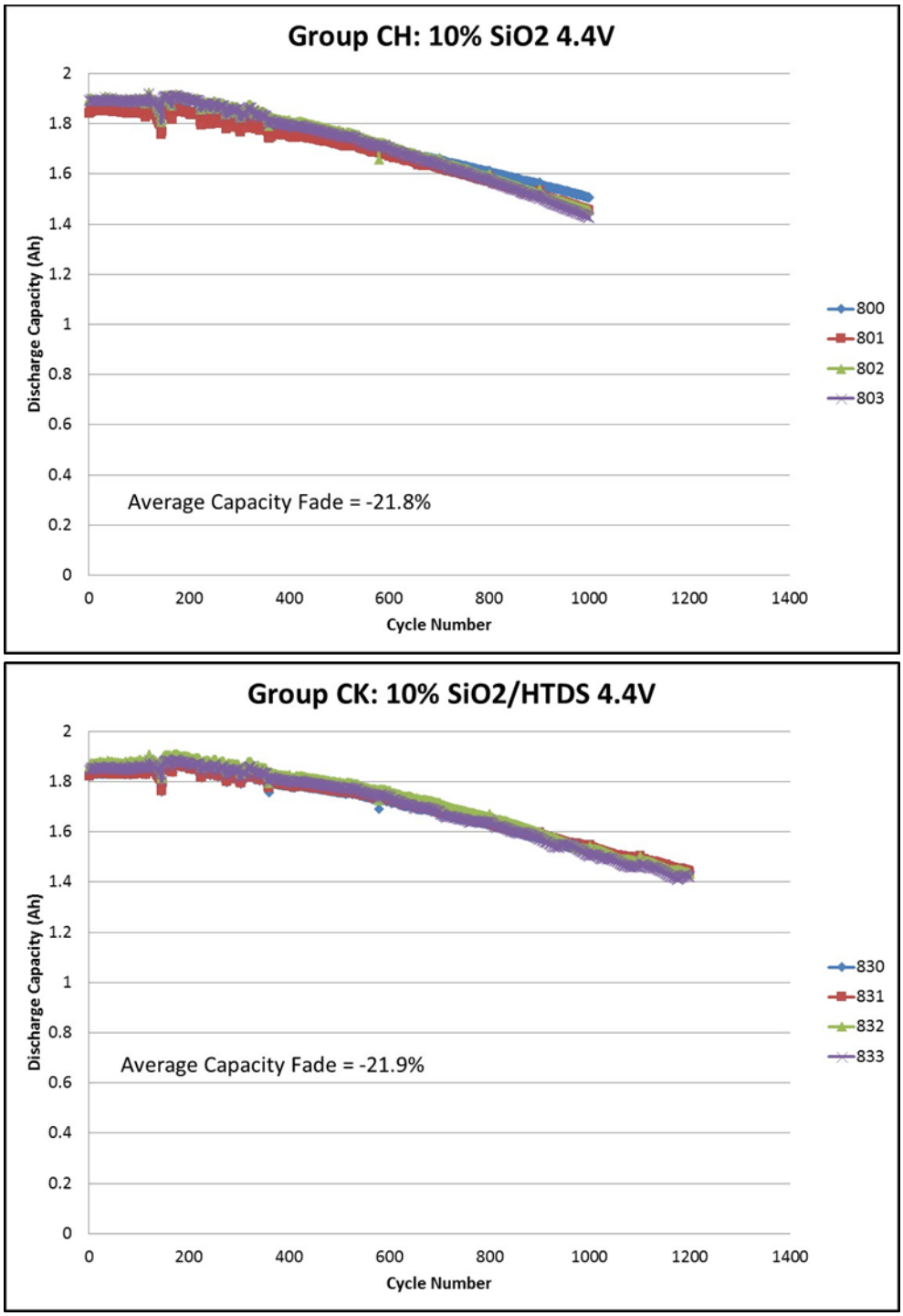

Figure I-43. Cycle life of 4.4V cells built with 10 wt% silica filled separator (top) 10 wt% silica filled separator, coated with alumina (bottom).

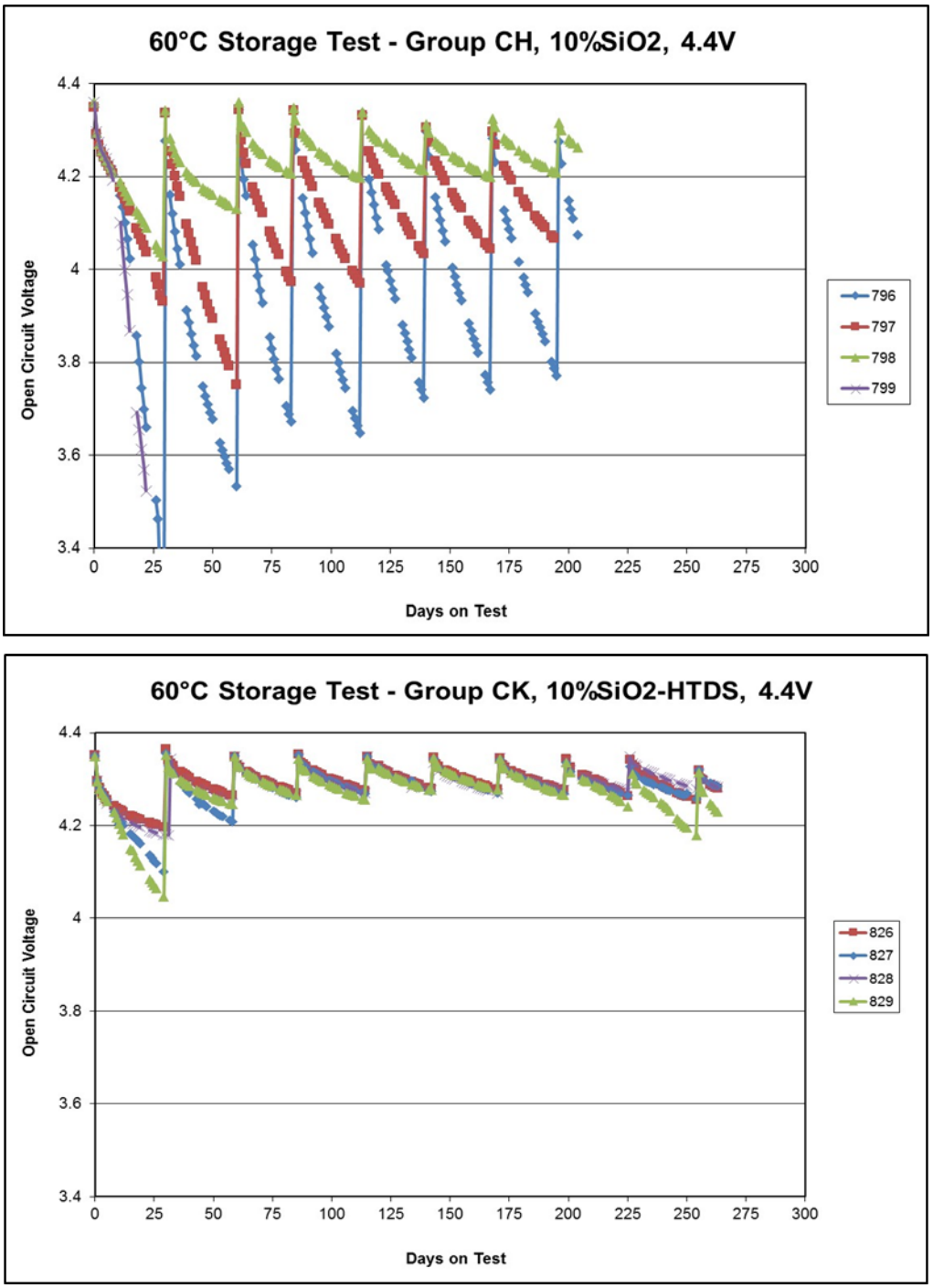

Figure I-44. Open circuit voltage of 4.4V cells stored at 60°C, built with 10 wt% silica filled separator (top) 10 wt% silica filled separator, coated with alumina (bottom). Cells were recharged to 4.4V every 30 days.

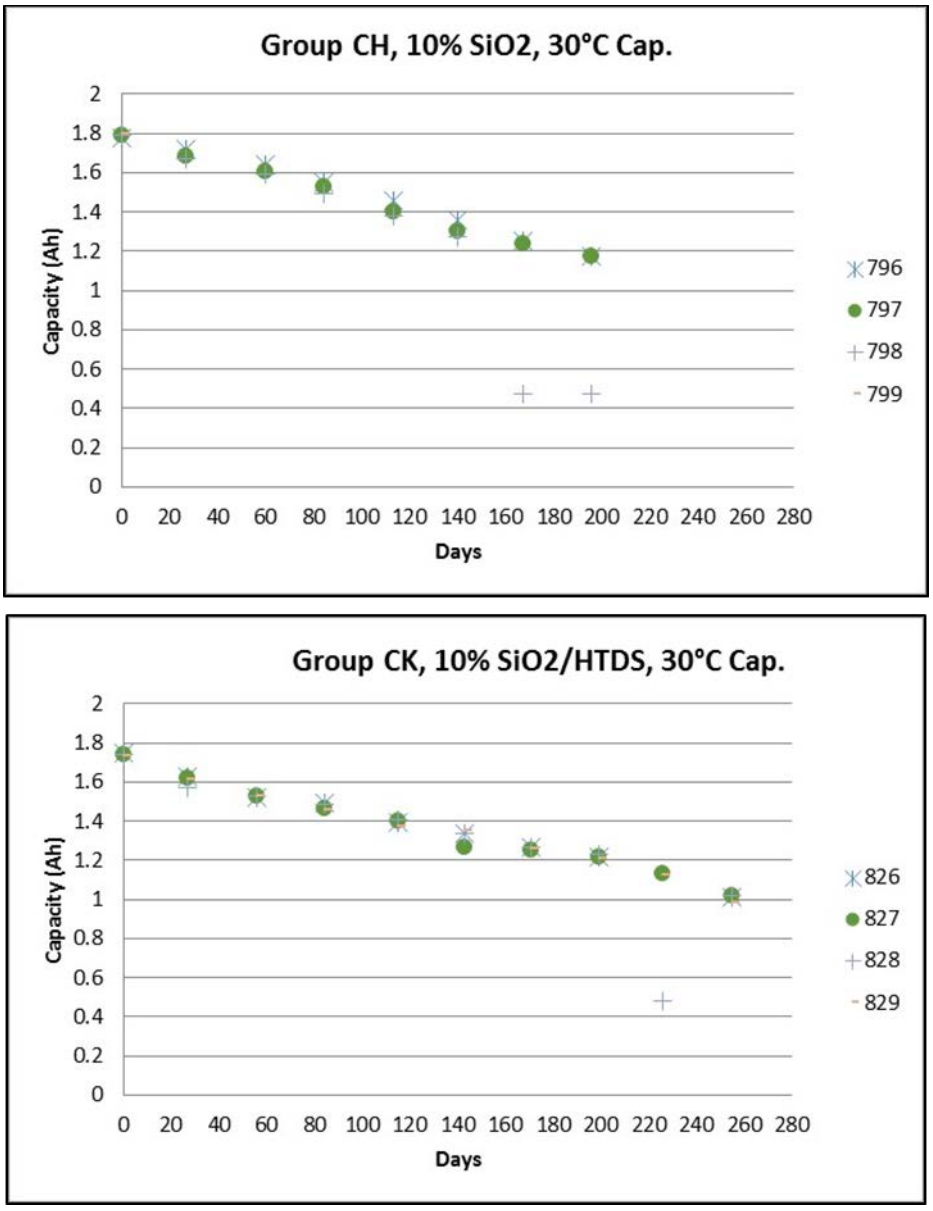

Figure I-45. Capacity of 4.4V cells stored at 60°C, built with uncoated polyethylene separator (top) and alumina coated separator (bottom). Capacity measurements were made at 30°C every 30 days

4.9V Cell testing, HV Spinel positive electrode:

Three sets of 4.9V pouch cells with HV Spinel positive were built at Farasis with uncoated control, nanoparticle ceramic coated separator (HTDS) and alumina coated separator with reduced moisture (LM). Figure I-46 shows cycle life (top) and storage testing (bottom) of the three sets of cells tested. Results showed 4.9V HV spinel cells built with ceramic coated separator outperformed uncoated microporous polyethylene control (EPH) with regard to cycle life and storage testing. Gas formation was more severe in cells built with the uncoated control separator. Severe degradation was observed on the uncoated control separator after tear down of the cells (brittle, black on cathode side). In contrast, the integretty and toughness of the ceramic coated separators were maintained. There appeared to be further improvement with the low moisture ceramic coated separator version (LM) though further work is required to varify this result. Further work will include ceramic and binder optimization to further improve cycle life and storage testing of the HV Spinel cells.

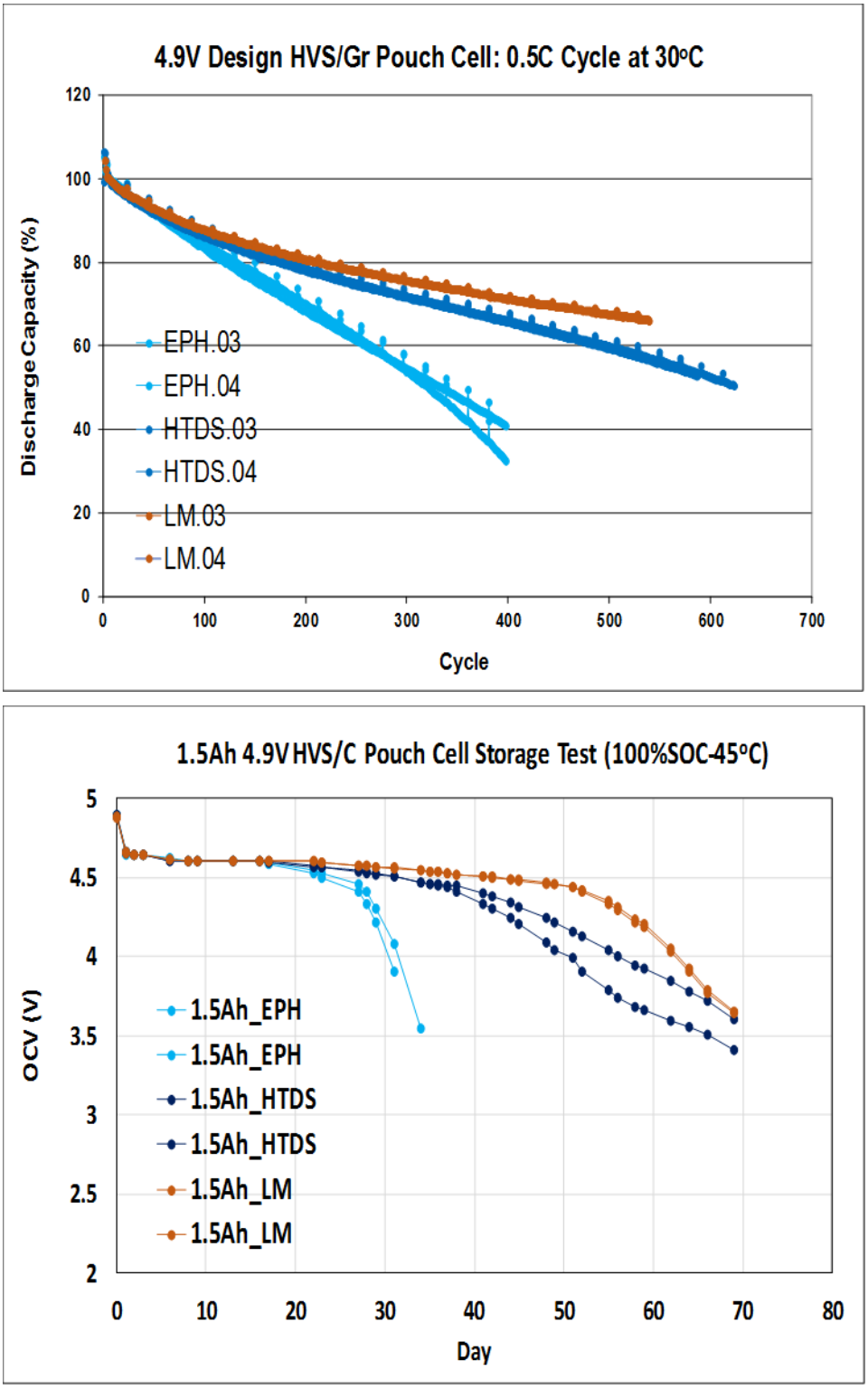

Figure I-46. Cycle life (top) and storage testing (bottom) for 4.9V HV Spinel cells built with uncoated and ceramic coated separators. Storage testing was performed at 45°C.

Conclusions

- The incorporation of moderate amounts of fumed silica into the base sheet yields large improvements in separator porosity and ionic conductivity. Mechanical strength is reduced, but is still acceptable.
- Ceramic coated separator with nanoparticle formulation (primary particles ~20nm) requires less than half the coat weight to reach high temperature dimensional stability (<5% shrinkage at 180°C) compared to conventional coated separator. This may translate to reduced coated separator cost (less raw materials required and thinner coating allows for faster coating speed).
- 4.4V cells built with NMC 622 cathode show considerable improvement in both cycle life and 60°C storage testing when incorporating ceramic coated separator compared to cells built with the uncoated control.
- Additionally, 4.9V HV spinel cells show considerable improvement in both cycle life and 60°C storage testing when incorporating ceramic coated separator. We attribute these results in part due to an improvement in the voltage oxidation resistance of the ceramic coating on the separator.
- Future work will include continuing the development of coatings for the improved voltage oxidation resistance for HV Spinel cells.

I.A.11 Advanced Separators for Vehicle Lithium Battery Applications (Celgard, LLC)

Junqing Ma, Ph.D., Principal Investigator
Celgard, LLC.
13800 South Lakes Drive
Charlotte, NC 28273
Phone: 704-588-5310
E-mail: Junqing.Ma@celgard.com

Brian Cunningham, Technology Manager
U.S. Department of Energy
Phone: 202-287-5686
E-mail: Brian.Cunningham@ee.doe.gov

Start Date: March 3, 2017 End Date: March 15, 2019
Total Project Cost: $2,500,000 DOE share: $1,130,000 Non-DOE share: $1,370,000

Project Introduction

Increasing the cell voltage and electrode capacity may be one of the most effective approaches to increasing the energy density of lithium ion batteries. Increasing cell voltage, however, would accelerate degradation of cell components including electrolyte, separator, and electrode binder to name a few. With recent advancements in electrolytes, the separator becomes a new limiting factor in advancing toward a high voltage (5 V class) battery system. When operated at high voltages, particularly at elevated temperatures, Li-ion cells may undergo degradation that is partially attributed to oxidation of the separator or to a deterioration in separator performance. During extended cycling at high voltages, especially at elevated temperatures, separators can suffer from intensified oxidizing electrochemical attacks on the surface facing the positive electrode, as well as degradation due to the strongly reducing environment on the surface facing the negative electrode.

Objectives

To enable the technical evolution towards 5.0 V lithium batteries, Celgard proposed to develop advanced separators that are cost effective and durable at high voltages, in collaboration with battery manufacturers. Two integrated approaches to the project are proposed in order to maximize success. The first is a unique coating technology capable of creating continuous, nanometer coatings on a base polyolefin separator. The second approach is a novel separator comprised of polymers that are stable in a 5.0 V Li-ion battery. A baseline of the present separator/coating technologies will be produced and compared against these advanced development concepts. Celgard will then work to select the most suitable material. Evaluation of the material will be conducted in conjunction with USABC and Farasis Energy, Inc. of Hayward, CA, USA. The battery maker subcontractor (Farasis) will provide a reproducible 5.0 V battery system to be used for testing during the program.

Approach

The work focuses on moving the current state of the art separator products from polyethylene (PE)or polypropylene (PP) plus binder and solvent-based ceramic coatings to an advanced product and process. Two basic approaches will be taken. The first approach includes a continuation of coatings but with an emphasis on moving to a novel advanced method to deposit continuous, nanometer coatings which will be used to protect the PP and/or PE from high voltage attack. The second approach includes the evaluation of novel polymers that are capable of withstanding the 5.0 V lithium battery environment.

Rationale for Novel Coatings

In this proposed research, Celgard will address such issues by developing several strategies to mitigate chemical and electrochemical attack on separators: (1) High efficiency blocking mechanism. Celgard will develop a nanometer-scale, ultra-dense coating on current polyolefin separators that will be highly efficient in protecting the polyolefin materials (such as PE and/or PP) from chemical attack without sacrificing porosity or the ionic conductivity of the electrolyte filled separator. (2) Chemical/free radical scavenging mechanism. The nanometer-scale coating will serve as a chemical/free radical scavenger that will quickly decrease the local concentration of free radicals before the oxidizing manganese ions and/or free radicals attack the separator material. The migration of side-reaction products from the high voltage spinel cathode to the graphite anode is responsible for much of the parasitic reactions damage at the graphite SEI and the consumption of active Li^+ in the cells. The proposed method for delivering the coating or layer is physical vapor deposition (PVD). This method is commonly used to produce very thin layers on plastic film materials and is proposed to be similarly deployed for the case of Celgard's battery separator films. The resulting coatings are extremely thin (nanometer-scale vs. micron-scale as obtained with the present slurry-based technologies), binder-free and homogeneous.

Rationale Novel Polymers

Besides polyolefin microporous membranes, a variety of new polymers have been used for preparing microporous membranes for lithium ion batteries in the past decade. The three most reported polymers are polyvinylidene fluoride (PVDF), polyacrylonitrile (PAN), and poly(methyl methacrylate) (PMMA). Many of them, such as microporous PVDF membranes, are chemically and electrochemically stable in lithium ion batteries using today's conventional technologies. In this proposed research, Celgard will investigate the application of two new materials to high voltage lithium ion batteries poly(4-methyl-1-pentene) (PMP) and PVDF. Celgard will develop two new separator materials (PMP and PVDF) and evaluate their stability in high voltage lithium ion battery applications.

For these candidate new separator materials, fabrication of novel separator and their performance in 5.0 V batteries will be demonstrated and evaluated in this project. It is challenging for any new polymers to be fabricated into battery separators since the resulting membranes must possess appropriate porosity and mechanical strength. Celgard has demonstrated that both PVDF and PMP can be integrated into Celgard's core separator manufacturing technology, however, the membrane properties need further improvements. An internal R&D effort is ongoing at Celgard to demonstrate PVDF-based separators. Despite their challenges, these new polymer separators have advantages when compared to PP and PE separators. For example, PVDF membranes are mechanically strong and have great wettability due to good affinity of PVDF to liquid electrolyte solutions.

Results

Celgard is working on the program tasks including separator design, cell demo and producing the required separator. The present status on this effort is displayed in Table I-6. Celgard completed a PVD coating trial at Bobst Manchester and successfully fabricated the planned separators. Celgard and Bobst fabricated several types of samples in this trial using the Celgard tri-layer H2013 separator as base material: (1) H2013 + 15 nm AlOx; (2) H2013 + 30 nm AlOx; and (3) H2013 + ~50 nm multi-layer coated separators. Samples #1 and #2 will be used to study the effect of coating thickness on cell performance. Sample #3 was prepared to evaluate the effectiveness of coating a combination material vs. AlOx coating alone.

For the new polymer separator approach, Celgard continued to evaluate: (1) PMP-PP composite separators using a solvent coating process and (2) PMP or similar high temperature polymer separators using Celgard dry separator manufacturing process. We are currently in the process of preparing the samples. Further testing in cells will be performed at Celgard and Farasis.

Table I-6: USABC Project Design Goals and Approaches

	Current State of the Art	Advanced Product and Process	Collaboration / Partner	Status Update
Design Goal	High Temperature Melt Integrity	Binder Free Nanometer-Coatings		
Design Approaches	Binder and Solvent Based Ceramic Coatings 2 to 4 µm coating thickness	Novel High Voltage Coatings to Protect PP and PE	Bobst Manchester, Dunmore, etc. PVD trial runs, fee-based	PVD coated separators prepared: H2013 base film with AlOx coatings 15 and 30 nm; ~50 nm multiple layer coatings
		Novel High Voltage Polymers to replace PP and PE as single Layer or Multilayer Constructions	Celgard test run; Specific Polymers, Such as PMP and/or PVDF	PMP/PP composite preparation in progress; PMP/polymer dry process planned;

All the fabricated PVD samples are currently being characterized by scanning electron microscope (SEM), Gurley number measurements, dielectric breakdown, and cycling test in NMC532 pouch cells (for evaluation of coating effectiveness only). All samples will be provided to Farasis for evaluation in LNMO-based 5 V cells. Figure I-47 shows some SEM micrographs of H2013 trilayer separator coated with 15 nm and 30 nm thick AlOx by PVD. The top-view and cross-section photos show that the coating is homogeneous and does not block the pores in the microporous structures. This uniformity of the coating is also confirmed by the Gurley number as summarized in Table I-7 (No significant change was observed.) The coated separators are not expected to decreased ionic conduction or rise the cell impedance, as the Gurley number decreased by only 10% over the original value for the base separator. Figure I-48 shows the shut-down performance of the PVD coated separators. All separators shut down at 127-130°C and a somewhat enhanced thermal stability was observed for the PVD samples at 170°C.

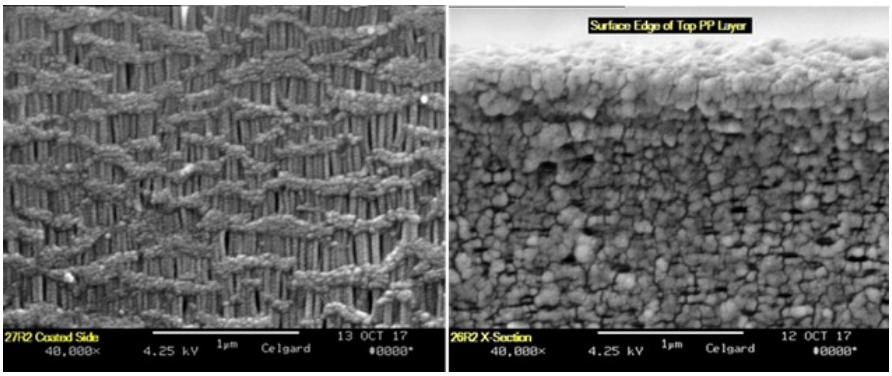

Figure I-47. SEM micrographs of the AlOx coated Celgard 2013 by PVD process: surface H2013_15nm AlOx (on left) and cross-section view of H2013_15nm AlOx (on right)

Table I-7: Gurley number of the PVD coated separators.

Sample	H2103	H2013_15nm AlOx	H2013_15nm AlOx	H2013_50nm Multilayer
AVG	372	328	339	335
STDEV	1.6	2.7	2.3	2.6
MAX	374	335	343	343
MIN	369	323	334	332
COUNT	15	15	15	15

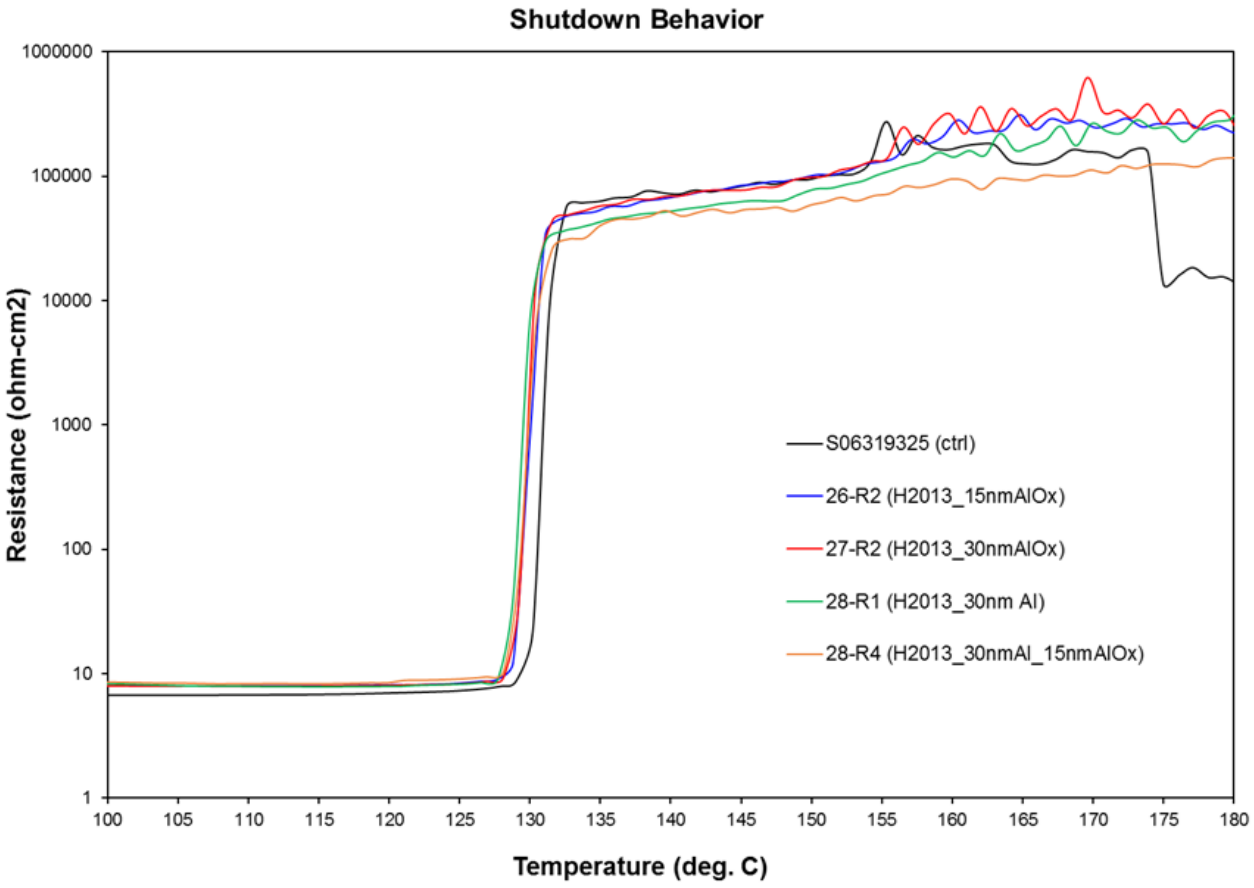

Figure I-48. Shut down performance for the PVD coated separators.

Farasis Energy has successfully fabricated and tested baseline 1.5 Ah LNMO/Graphite cells in the program. Farasis is currently working on improving the cycling performance by optimizing electrode formulations, electrolytes and cell design/configuration. Farasis fabricated the pouch cell by first initial sealing of cells and degassing after formation cycles. For 18650 cells, the cells header with current interrupt device (CID) were crimped after electrolyte was filled. Due to lack of a degassing mechanism, in-cell pressure slowly built up as a result of gassing therefore causing cell impedance to develop over testing and eventually, for some cells, CID was trigged and the cells were stopped. Figure I-49 and Figure I-50 show the cycling performance of H2013 control and ceramic coated baseline cells in 18650 and pouch cells respectively. Farasis continued this initial test and delivered six (6) pouch cells with the baseline separator to USABC in September 2017, according to the program's schedule.

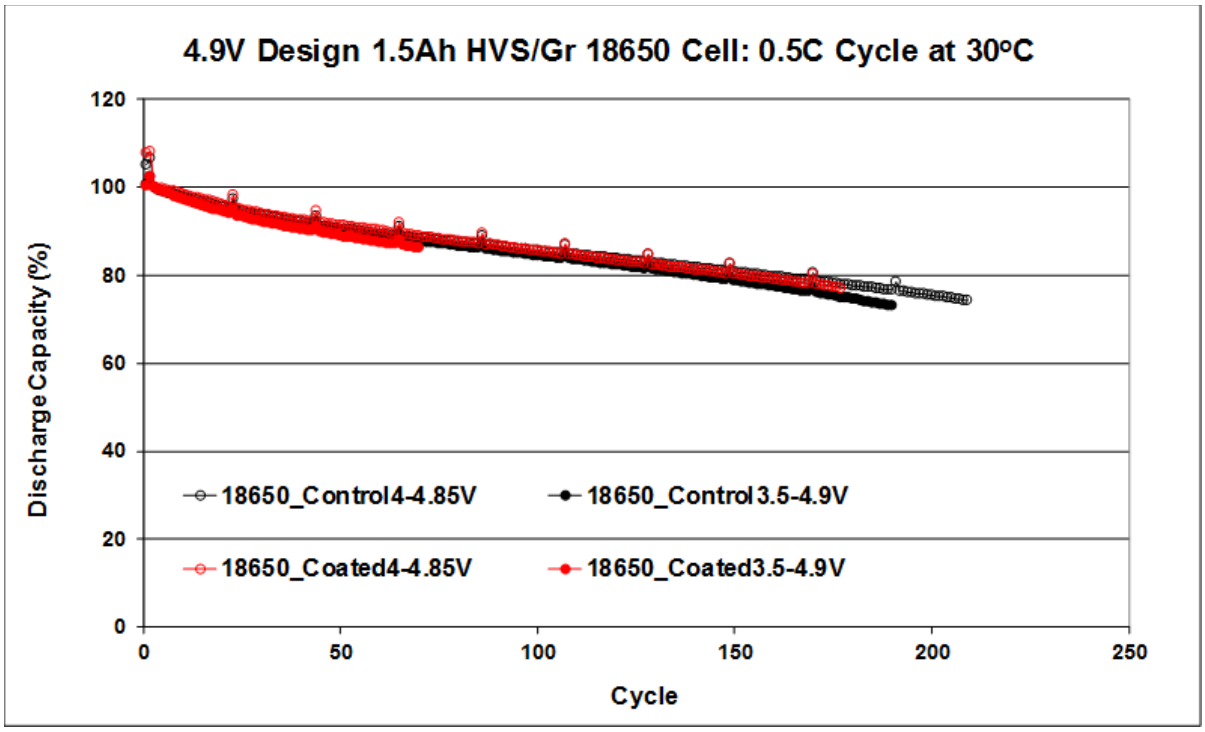

Figure I-49. Capacity retention of second batch of 18650 cells tested over the voltage ranges 4.0 -4.85 V and 3.5 - 4.9 V. No early failure but cycling is poor due to possible internal impedance increase.

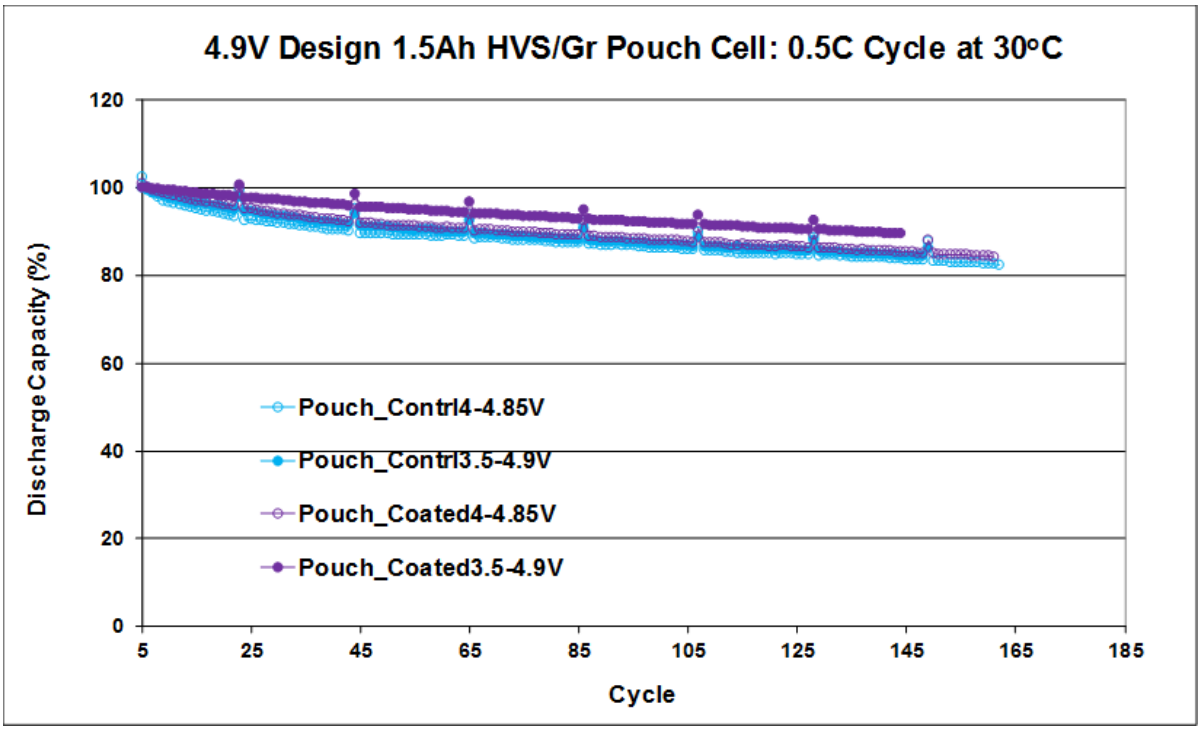

Figure I-50. Capacity retention of Farasis pouch cells tested over the voltage ranges 4.0 - 4.85 V and 3.5 - 4.9 V. Significantly improved cycling was observed over 18650 cells.

Some of the separators after cycling at Celgard and Farasis are currently being examined for damages/ degradation as a part of the failure mechanism study in this program. For the separators cycled in 5V cells, degradation was observed for all control separators. On the surface of Celgard PP film after the cycle test, thick electrolyte decomposition products was observed; however, the pores of the separator were not closed or collapsed. No decomposition products were observed for the PE separators after the cycle test. All PP and PE separators showed a decreased molecular weight after cycling in 5V cells. Wet PE separator in comparison, showed severe carbonization and complete pore collapse was observed (Figure I-51, on right).

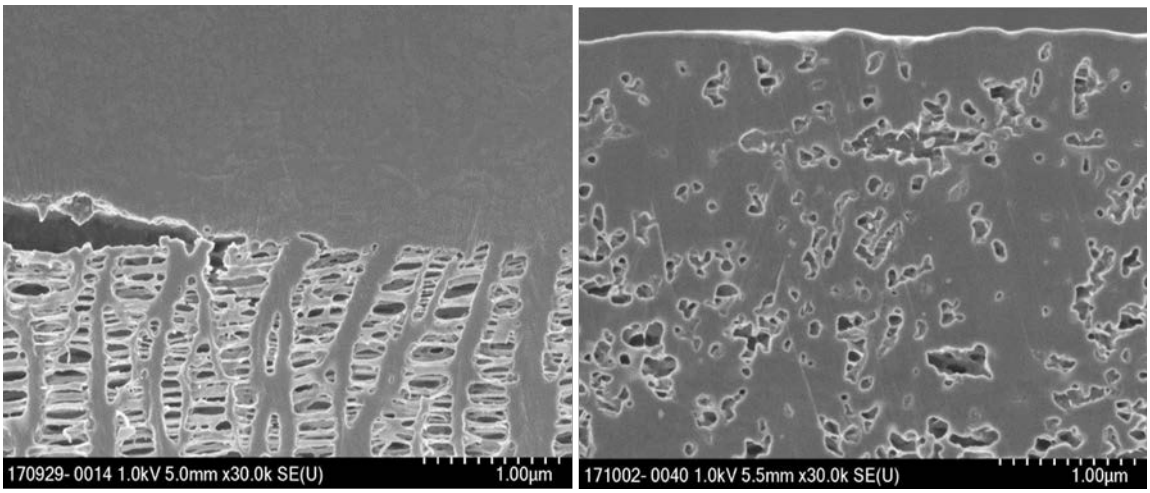

Figure I-51. SEM photographs of Celgard dry process PP (on left) and a commercial wet PE (on right) separator after cycling in 5V cells.

Farasis has delivered a set of six 1.5 Ah pouch cells to ANL as the 6-month deliverables. The six cells are 4.9 V HVS/C pouch cells with Celgard Q20S1HX ceramic coated separators. The electrolyte used is a developmental electrolyte formulation by Farasis. The cell capacity is around 1110 mAh at C/3 discharge (averaged static capacity measured from the six deliverable cells). Cell data shown in Table I-8 summarizes the Static Capacity (C/3, 3.5 - 4.9 V, no CV), open circuit voltage (OCV), AC impedance at 1kHz, and cell weight of the cells delivered.

Table I-8: A summary of the Static Capacity (C/3, 3.5 - 4.9 V, no CV), OCV, AC Impedance at 1 kHz, and Cell Weight of the cells delivered to ANL.

Cell I.D.	Static Capacity/mAh (C/3 to 3.5V @30ºC	AC imp. @1kHz/mΩ and 25ºC	OCV/V	Cell Wt/g (w/o Fixture)	Comment
Q20S.01	1076	64.4	4.602	36.17	Data collected prior to shipping
Q20S.02	1137	75.6	4.603	36.32	“
Q20S.03	1133	60.5	4.603	36.36	“
Q20S.04	1071	69.5	4.602	36.46	“
Q20S.05	1108	64.2	4.603	36.59	“
Q20S.06	1140	47.5	4.604	36.27	“

The six cells all went through formation steps at Farasis. The cycling conditions (at 0.5 C rate, between 3.5 – 4.9 V at 30ºC) developed by Farasis include the following conditions and specific requirements: Fixtures and static pressure required; regular cycle at 0.5 C; 0.5 C constant current (CC) charge to 4.9 V; Rest for 3min.; no constant voltage (CV) charging; 0.5 C CC discharge to 3.5 V; Rest for 3 min.; repeat for 20 cycles, and insert

one 0.2 C rate cycle for every 20 regular cycles and Repeat the above steps. Alternative voltage window for this test is between 4 and 4.85 V.

Conclusions

- The physical vapor deposition (PVD) process can effectively deposit an ultra-thin aluminum oxide layer on microporous separators, coating all micro-structures without blocking the pore or significantly decreasing the dielectric breakdown or increasing the Gurley Number.
- A 5 V chemistry has been demonstrated by Farasis using a proprietary stabilized electrolyte. Cycle life is decent for prototype cells and ANL will confirm cell performance using USABC testing protocols.
- Current commercially available polyolefin micro-porous separators suffer from structural degradation in high voltage cells, especially at elevated temperatures. An initial failure study suggests that the degradation of polyolefin separators and structural damages dependent on the separator material. The effectiveness of protection provided by the ceramic coating and PVD AlOx or by Al metal will be further evaluated to provide better understanding of separator degradation mechanism.
- Scalability of PVD coating process is promising. Low cost production appears highly achievable.

I.A.12 Hybrid Electrolytes for PHEV Applications (NOHMs Technologies)

Surya Moganty, Principal Investigator
NOHMs Technologies
1200 Ridgeway Avenue
Rochester, NY 14615
Phone: 607-379-5444
E-mail: surya@nohms.com

Brian Cunningham, Technology Manager
U.S. Department of Energy
Phone: 202-287-5686
E-mail: Brian.Cunningham@ee.doe.gov

Start Date: August 15, 2015 End Date: October 15, 2017
Total Project Cost: $1,639,044 DOE share: $819,522 Non-DOE share: $819,522

Project Introduction

Rechargeable lithium ion batteries (Li-ion) are promising energy storage options for plug-in-hybrid electric vehicles (PHEVs) and all electric vehicles (EVs). However, among other requirements for Li-ion batteries to be viable for transportation applications a high energy density cathode is required. High voltage cathodes have the potential to provide a solution for low cost, longer-range electric vehicles. This new class of electrode material can deliver capacity >250 mAh g^{-1}, that is ~65% higher than that delivered by current state-of-the-art cathodes. To access this high capacity, one has to operate the cell at a higher potential >4.5 V *vs* Li/Li^+. Conventional Li-ion battery electrolytes, however, are not stable above 4.2 Volts. Development of electrolytes that are stable at these higher voltages is critical to make use of this class of high voltage cathodes. An electrolyte innovation that enables temperature-stable 5V cell operation would transform the industry and enable rapid growth of new market segments.

Research and Development at NOHMs has resulted in a family of novel electrolyte formulations, which include ionic liquids to improve high voltage performance, safety, and high temperature durability of Plug in Hybrid Electric Vehicle ("PHEV") lithium ion batteries. NOHMs proprietary functional ionic liquids in-development for lithium ion battery electrolytes have displayed excellent electrochemical and thermal stability compared to state-of-art lithium ion battery electrolytes, and when compared with previously reported ionic liquid electrolytes demonstrate improved stability against graphite-containing anodes and high voltage cathodes, as well as improved rate capability and low temperature performance.

Objectives

The program objective centered on the development of functional ionic liquid-based electrolyte combinations with appropriate co-solvent combinations that exhibit high ionic conductivity, excellent cathodic & anodic stability and high thermal stability for applications in 5V Li-ion batteries. NOHMs objective was to create optimized electrolyte formulations that are stable above 4.5V, non-flammable, and which simultaneously overcome traditional barriers of effective SEI layer formation and cation co-intercalation in graphite associated with ionic liquids. The final project objective was to demonstrate the feasibility of these ionic liquid-based electrolyte systems in 2 Ah and 10 Ah Graphite//$LiMn_{1.5}Ni_{0.5}O_4$ and Graphite//$Li_{1.2}Mn_{0.55}Ni_{0.15}Co_{0.1}O_2$ full cells.

Approach

NOHMs has established partnerships with A123 Systems (A123) and Xerox to meet the USABC long term criteria for electrolytes - (1) cost, (2) high-voltage stability, (3) low-temperature performance, and (4) abuse tolerance. The A123 partnership for manufacturing and testing of cells, and a chemical company (Xerox)

partnership to scale a low-cost and high-purity synthesis process for NOHMs ionic liquid electrolytes. (See Figure I-52.) Research and development at NOHMs has resulted in a family of novel electrolyte formulations, containing functional ionic liquids projecting excellent high voltage stability. Effective component combinations were the result of carefully designed experiments, positioned to expose molecules with desirable physical characteristics, electrochemical competency, and thermal stability. Building on these results, NOHMs developed and evaluated novel electrolyte formulations suitable for NMC532 (4.5V) and LNMO (4.8V) cathode materials.

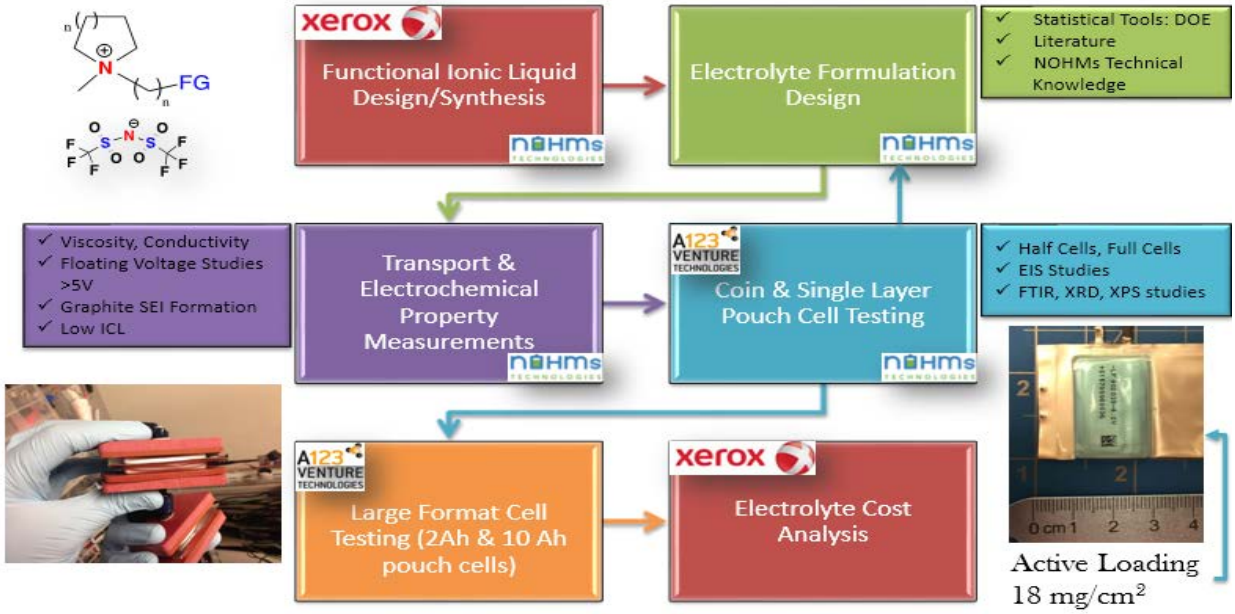

Figure I-52. Program approach from synthesis electrolyte and cell fabrication. The approach encompasses synthesis of novel functional ionic liquids, electrochemical testing, post autopsy analysis, 2 Ah & 10 Ah cell fabrication, and scale-up cost analysis.

Results

High Voltage Stability

Building on electrolyte screening protocols, NOHMs developed electrolytes and evaluated high voltage stability against NMC532 and LNMO using floating voltage measurements. Figure I-53 compares the measured leak current density of LNMO-Li half-cells, containing baseline and NOHMs electrolyte formulations. Two separate groups of cells were evaluated at 25ºC and 45ºC. Low leak current density is indicative of reduced oxidation at the specified voltage. NOHMs designed formulations showed excellent oxidative stability. NOHMs HVE135 electrolyte formulation showed excellent stability at the LNMO cathode. Even at elevated temperatures (i.e., 45ºC) the NOHMs formulation outperformed the baseline.

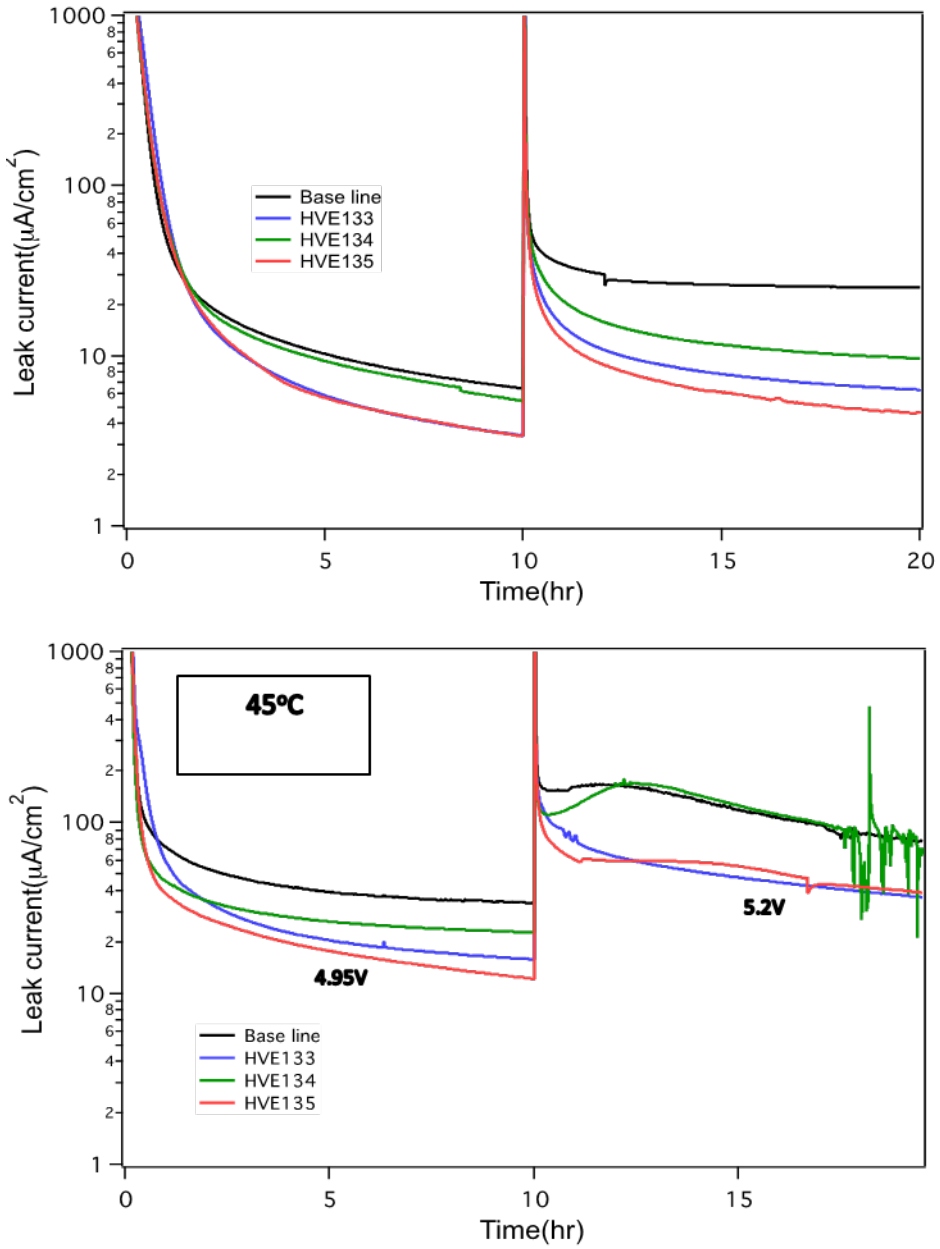

Figure I-53. Floating voltage profiles of LNMO|Li coin cells. The voltages are held for 10hrs at 4.95V & 5.2V. Leak current describes the severity of the oxidative reactions with the cathode surface.

Compounding desirable performance of graphite SEI formation with high voltage stability leads to well-rounded deliverable electrolytes. For instance, Figure I-54(A) reveals the superior voltage stability of the NOHMs 157 deliverable electrolyte when compared to baseline, and Figure I-54(B) portrays greater capacity retention from NOMHs 157 containing graphite/Li cells.

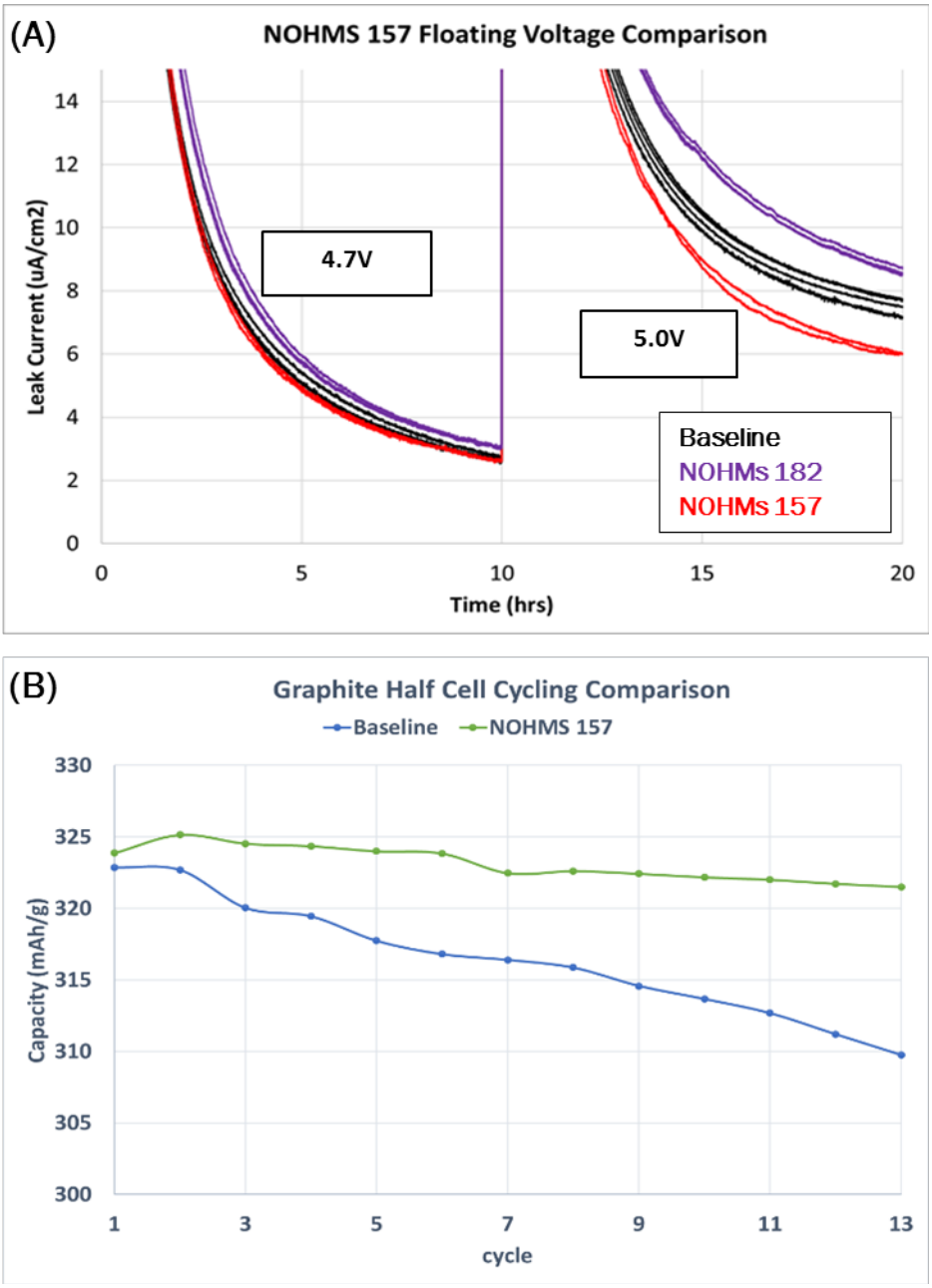

Figure I-54. (A) Floating Voltage in NMC532|Li coin cells at 23˚C using 10hr holds at 4.7V and 5.0V. (B) Graphite|Li half-cell galvanostatic cycling at C/10. Baseline electrolyte denoted as (30:70) EC:EMC + 1MLiPF$_6$

2) Full Cell Formulation Development

Thermal stability has been a focus for the high voltage formulations. Combining elevated temperature and high voltage cycling imposes additional stress on the cell, allowing decomposition reactions to become more severe and the SEI to degrade. Floating voltage and galvanostatic cycling at 45ºC has helped in pursuing formulations that remain stable when exposed to both elevated voltage and temperature. Figure I-55 shows that HVE157a, the 10 Ah NMC cell deliverable electrolyte, demonstrates no significant change in cycle-life when tested at room temperature (23ºC) and elevated temperature (45ºC). Figure I-56 shows the performance of 2 Ah NMO cells cycling at 1C/2C, 4.8V with NOHMs electrolyte HVE242.

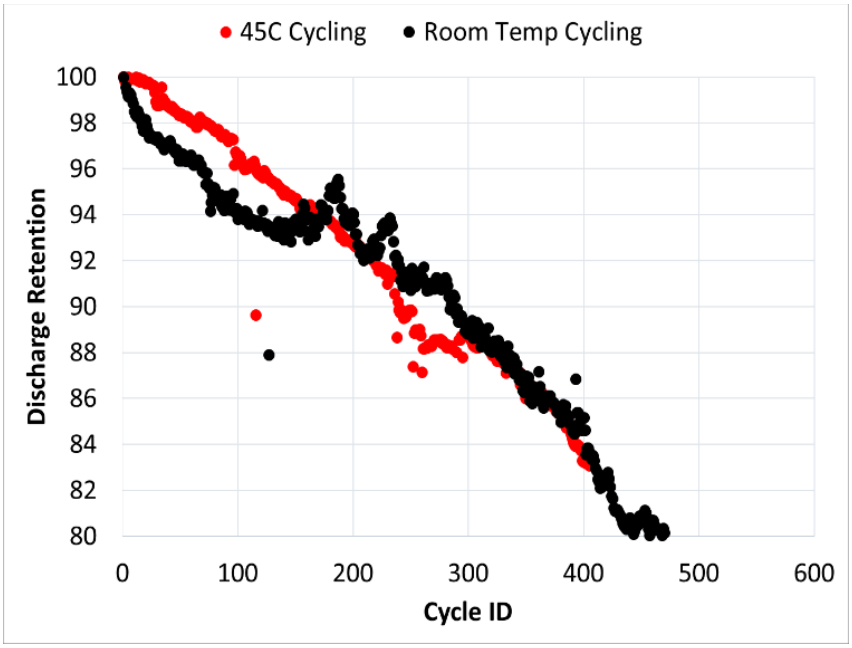

Figure I-55. 45°C vs room temperature comparison of HVE157a electrolyte in 155 mAh NMC442 cells; 3.0V-4.5V; C/2 rate. Cells project an average initial cycling capacity of 145 mAh and 150 mAh for room temperature and 45°C sample groups, respectively.

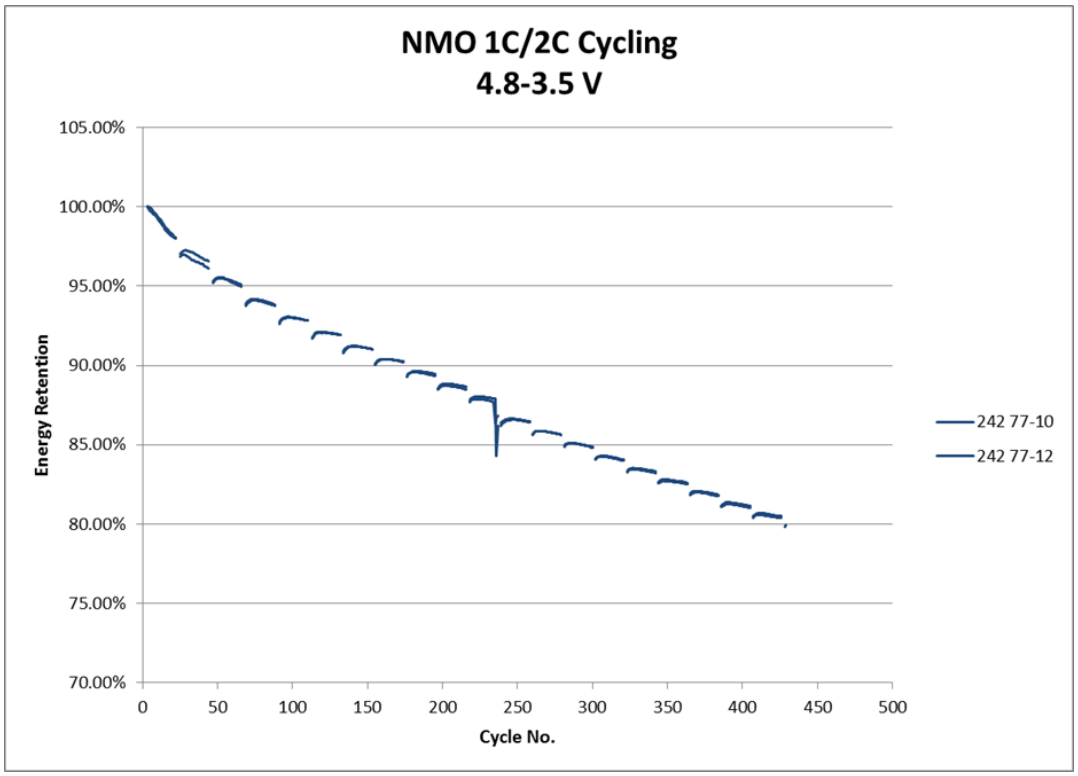

Figure I-56. Cycling Data for 2 Ah NMO cells with NOHMs electrolyte HV242, 1C/2C at 4.8V cutoff.

3) Elevated Temperature Storage and Operation

Elevated temperature storage tests revealed a weakness associated with the high voltage chemistries. Cells charged to 100% SOC and held at 60ºC for extended durations resulted in cell gas generation. NOHMs conducted storage tests on 155 mAh NMC442 and 5 Ah NMC532 cells to screen potential gas suppressing formulations. The formulation HVE302 shows great promise in reducing gas generation. The HVE302 formulation also demonstrated desirable performance characteristics, such as low impedance increases, little voltage change, and high capacity retention throughout the storage period. HVE302 having losses close to 15%, less than half the value of the baseline electrolyte (>30%). In addition, the HVE302 demonstrated promise in cycle-life and scalability when tested in 5 Ah cells. Figure I-57 demonstrated a 1.75x increase in cycle-life when compared to the baseline. These cells were cycled at 45ºC using 1C, demonstrating favorable thermal stability and rate capability respectively.

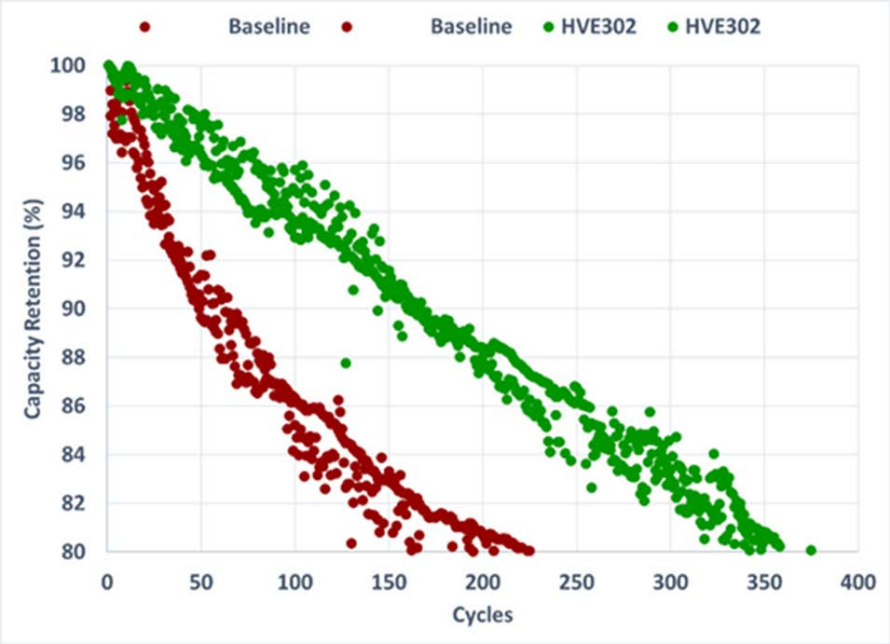

Figure I-57. Cycling performance of 5 Ah NMC532 cells cycled at 1C and 45ºC with a 4.5V cut-off.

4) Formulation Transport Characteristics

A significant attribute in ensuring favorable rate and low temperature performance, is the ionic transport properties of the electrolyte. Ionic liquids showing favorable performance have acceptable viscosities and do not require great electrolyte concentrations to perform, thus granting near baseline values in ionic conductivity. Figure I-58 compares the ionic conductivity of NOHMs HVE157 with baseline electrolyte. The conductivity values are comparable over a wide temperature range.

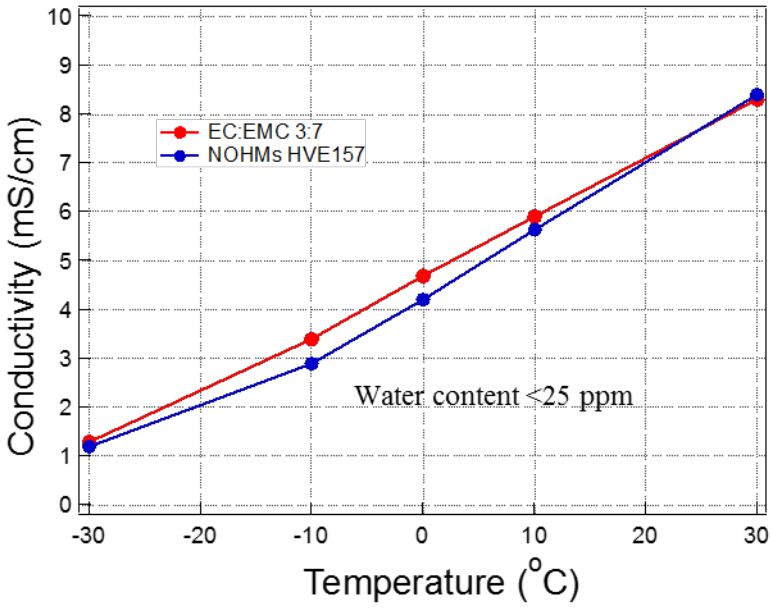

Figure I-58. Ionic conductivity of base line electrolyte and NOHMs HVE157 electrolyte over a wide temperature range.

5) NMC Deliverable Cell Performance

2 Ah NMC Cells tested at Idaho National Laboratory under-went calendar life testing, achieving greater than 4RPT segments. Cells show some decline in usable power at RPT4, but good retention of usable energy. Charge-sustaining (CS) and charge-depleting (CD) modes of operational power and energy were tested, in both modes of operation there is minimal loss in energy. Loss in power is a result of increased cell resistance. Decreasing resistance, increasing thermal stability, and gas reduction has shown promise in post deliverable electrolyte optimization, and is continuously pursued. Beginning of life (BOL) cold crank testing, using the battery size factor (BSF) of 379, revealed great voltage retention at -30ºC from all 3 completed cycles. The results were consistent across the two cells tested.

Abuse tolerance testing at Sandia National Laboratories consisted of overcharge, blunt force rod, short-circuit, and thermal ramp testing. The cells performed very well in short-circuit tests, and provided favorable results in the thermal ramp testing. The results from the accelerated rate calorimetry (ARC) further supported the thermal ramp results, demonstrating thermal runaway >210ºC. Given challenges with gassing at elevated temperatures and high voltage of the cathode at 100%SOC, it is no surprise the overcharge and blunt force rod test at 55ºC + 100% SOC, would be a focus point for future electrolyte optimizations.

Conclusions

A variety of functional ionic liquids were synthesized and screened against graphite anode and high voltage cathodes (NMC532, NMO) for both cathodic and anodic stability. Based on numerous screening tests (at NOHMs and A123 facility), NOHMs developed HVE157a deliverable electrolyte for thirty 10 Ah NMC532 pouch cells and HVE242 deliverable electrolyte for thirty 2 Ah LNMO pouch cells. Deliverable cells were submitted for testing at national labs.

Results from 2 Ah NMC & 10 Ah NMC cells show positive attributes highlighted in RPT4, and the 2 Ah NMO cells revealed great performance benefits, having >425 cycles to 80% capacity retention when cycled using 2C. National lab testing has also exposed areas of improvement, specifically in impedance reduction, thermal stability, and gas suppression. The HVE302 optimized electrolyte formulation has demonstrated great promise in tackling these areas of improvement, and may offer for future enhancements.

Fundamental understanding of the working mechanism of NOHMs designed electrolytes is ongoing to optimize the electrolyte composition.

In collaboration with A123, NOHMs will be delivering thirty 10 Ah LNMO (4.8V) cells for independent testing.

Key Publications

1. Hybrid electrolytes for PHEV applications, Surya Moganty et al., DOE Annual merit review meeting, June 2017.

I.A.13 Li-Ion Cell Manufacturing Using Directly Recycled Active Materials (Farasis Energy)

Michael Slater, PhD, Principal Investigator
Farasis Energy, Inc.
21363 Cabot Boulevard
Hayward, CA 94545
Phone: 510-262-6600
E-mail: mslater@farasis.com

Brian Cunningham, Technology Manager
U.S. Department of Energy
Phone: 202-287-5686
E-mail: Brian.Cunningham@ee.doe.gov

Start Date: February 1, 2017 End Date: February 28, 2019
Total Project Cost: $1,761,490 DOE share: $880,745 Non-DOE share: $880,745

Project Introduction

Rapid performance gains of Li-ion batteries in the past few decades have led to its adoption at an unprecedented scale. For this growth to be sustainable, the entire life cycle of the batteries must be accounted for, from raw material sourcing to end-of-life disposal and reuse. So far, the cost associated with end-of-life disposition of these batteries has not been included in the product price; coupled with a drive to use less costly materials in the batteries themselves we are arriving at a situation in which there is less intrinsic value in the elemental composition of the battery than it costs to recycle/dispose of them in a responsible manner. Thus there is a need for a recycling method that goes beyond treating the battery as an ore and can harvest some of the additional value that is invested in the product during complex raw material and cell manufacturing processes.

Objectives

There are four main objectives for this project:

1. Optimize direct recovery processes at larger scale (>8 kg cell/module input)
2. Optimize electrode formulations to make best use of refurbished active materials
3. Manufacture full-size LiBs on commercial production line using direct-recycled active materials
4. Quantify cost benefits of recovered material (economic analysis and include cost related metric in Gap Analysis)

Approach

Farasis Energy has been working on recycling technology for Li-ion batteries for a number of years. They have addressed the challenges of closing the loop of the Li-ion product life cycle by developing a method for recovery and reuse of valuable components in the batteries. The “Direct Recycling” approach refers to a technology for battery recycling in which material recovery is performed using physical separation processes and active materials are reused with minimal processing, ideally without the need for intermediate chemical transformation. In this way, some of the value invested in the materials (*e.g.*, synthesis process energy, particle size distribution and shape) can be recovered without the need to resynthesize these materials from their lowest value elemental form. Figure I-59 shows a flow chart for a straightforward direct recycling process used to recover the high value components of the Li-ion battery. In this approach, the entire cell or module is shredded after being fully discharged and deactivated. Safety is a key requirement for this step, and therefore measures

to prevent release of hazardous materials and fires are a primary consideration. The shredded material is subjected to a solvent extraction step, which removes the electrolyte while also stabilizing the cell chemistry by removing a source of hydrofluoric acid, which can damage the valuable active materials upon exposure to air and water during subsequent processing. The shredded mass is then screened/sieved to remove other battery components from the micron-sized active materials. This detritus is sent to the existing metals recycling industry leaving only the "Black Mass," a mixture of active anode and cathode particles with some binder, carbon, and small amounts of other components as contaminants. In this state, the recovered active materials are not immediately ready for use in new Li-ion cells for a number of reasons. The cathode material recovered is missing some lithium due to the inherent losses during the formation process and extended cycling and the graphite anode material contains some lithium and surface species generated during the formation and cycling processes. Finally, any contaminant species, including cathode material in the anode material, will render the materials unusable in new Li-ion cells.

Consequently, the next unit operations, while technically challenging, are critical to the success of the Direct Recycling approach. They involve the separation of the cathode and anode active materials from each other, the purification of these materials by removing contaminants, restoring the lithium content in the cathode material, and final regeneration in which the structural integrity of the materials is returned to its pristine state. Farasis has developed proprietary approaches to achieve these final steps that are chemistry independent, and have demonstrated the capability to achieve good separation yields, high purity and high performance materials using these methods.

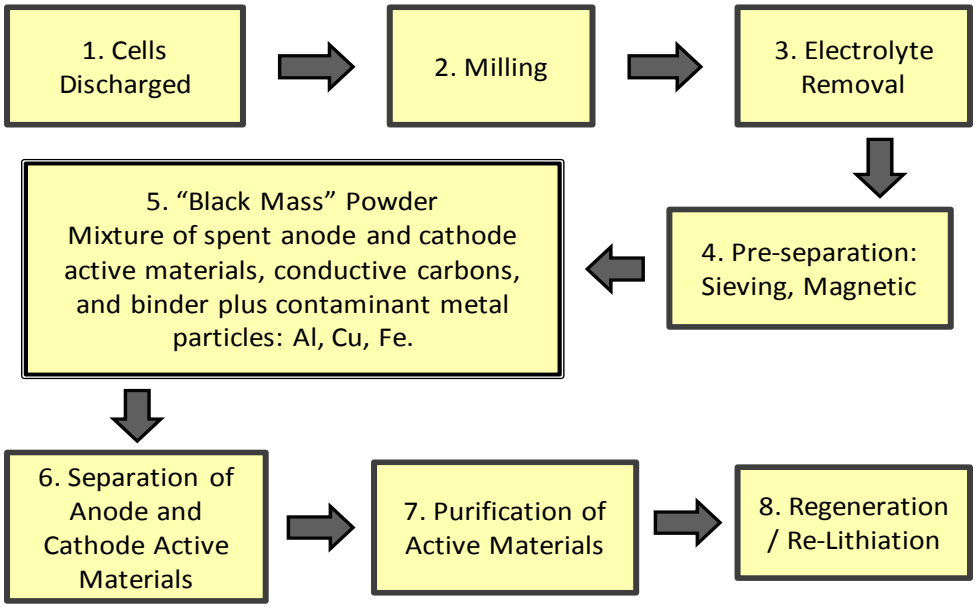

Figure I-59. Flow chart for direct recycling process for Li-ion batteries

Available evidence to-date suggests that modified surface chemistry of the isolated active materials is the primary challenge to address, which also provides an opportunity for improvements on the pristine materials' properties. Detailed structural investigations as to the nature of the changes are being explored in collaboration (via subcontract) with Robert Kostecki at Lawrence Berkeley National Laboratory in recognition of the team's leadership in battery materials characterization and research. The suite of analytical tools that will be used to inform the optimization of the recycling steps include:

- High resolution X-ray instrumentation at DOE's Synchrotron User Facilities, enabling detailed investigation of structural parameters such as microstrain and lattice defect

- SEM will be used for imaging particle morphology and surface chemical analysis by EDAX
- Electrochemical Impedance Spectroscopy will be used to determine intrinsic conductivity of materials and for electrode-level characterization during formulation research with recycled materials
- Particle size distribution measurements and gas adsorption analysis will be used to determine material physical characteristics such as particle size, surface area, and internal microporosity
- Raman spectroscopy will be used to study surface and near surface changes in material structure and chemistry which are difficult to characterize by other methods.
- Neutron diffraction will be employed in conjunction with XRD to more accurately characterize the structure of Li-containing materials. Due to the extremely weak scattering cross section of Li for X-rays, neutron diffraction is required to positively locate Li in the crystal structures (as opposed to inferring its presence from lattice spacing, which is not quantitative).

The direct recycled active materials will be used in iterative cell-builds of increasing feed complexity, through which insight will be gained on how to best incorporate recycling technologies in battery manufacturing resulting in more environmentally friendly, lower cost production of Li-ion batteries. A high-level summary of project deliverables (internal and external) may be found in Table I-9.

Table I-9: Overview of Program Hardware Deliverables and Build Strategy

Hardware Deliverable	Description	Source Material	Quantity ANL/FEI*	Delivery Date
Cell-build 1 (66 x ~ 2 Ah cells)	Control: pristine NMC/pristine Gr	commercial powders	9/12	Month 13
	recycled NMC/recycled Gr	manufacturing scraps	9/12	Month 13
	recycled NMC/pristine Gr	manufacturing scraps	0/12	Month 13
	pristine NMC/recycled Gr	manufacturing scraps	0/12	Month 13
Cell-build 2 (54 x ~2 Ah cells)	Control: pristine NMC/pristine Gr	commercial powders	9/12	Month 17
	100% recycled NMC/100% recycled Gr	BOL cells/QC rejects	9/12	Month 17
	blended: TBD % of recycled/TBD % new	BOL cells/QC rejects	0/12	Month 17
Final Build (54 x 25 Ah cells)	Control: 25 Ah FEI production cells	commercial powders	15/12	Month 22
	25 Ah cells with optimized (maximum) recycled content in each electrode	EOL cells and module parts	15/12	Month 22

* Each build will include cells for external (USABC/ANL) and internal (Farasis Energy) testing and evaluation

The measure of success of the program is being quantified by measuring the gap between recovered material and equivalent control test articles made using commercial grade active materials, which will be included with each build to allow comparative evaluation. While not included in the final deliverables, there will be development work addressing how best to handle mixed chemistry feed streams, which is an inherent challenge for direct recycling processes. Specifically, recovery of feed streams with NMC532 and mixed NMC/spinel compositions will be studied. Another important outcome of the program will be to refine current assumptions of a scaled production process (including milling, separation, purification, and regeneration operations) and evaluate revenue potential against capital and energy requirements and operating costs, thus ensuring that the technology is economically relevant.

Results

The initial phase of this project addressed increasing the scale of Farasis Energy's recycling process, moving to a scale relevant for commercial manufacturing equipment. This included qualification and installation of a 2 HP mill for shredding batteries, solvent extraction apparatus for electrolyte recovery, and vibratory screening gear for size-based separation as well as fume hoods and associated ventilation and power.

There are multiple potential feedstocks to address spanning manufacturing (scrap to end-of-life) systems. The first stage of the project has focused on the least complex feedstock: manufacturing residues, which eliminates some of the required processing steps; scaled-up processing for entire cells and systems will be optimized subsequently. A combination of thermal treatment and mechanical processing are used to isolate active materials (graphite or metal oxides) from current collector foils.

Composite electrodes are complicated metamaterials and complete de-mixing of the various components is not possible. Selective degradation of the minor components allows isolation of the desired active material. One approach to achieve this outcome is thermal decomposition; study of this process has revealed significant interaction between different components as evidenced by the thermogravimetric analysis results in Figure I-60, and these synergies will be strategically leveraged in the upcoming optimization work.

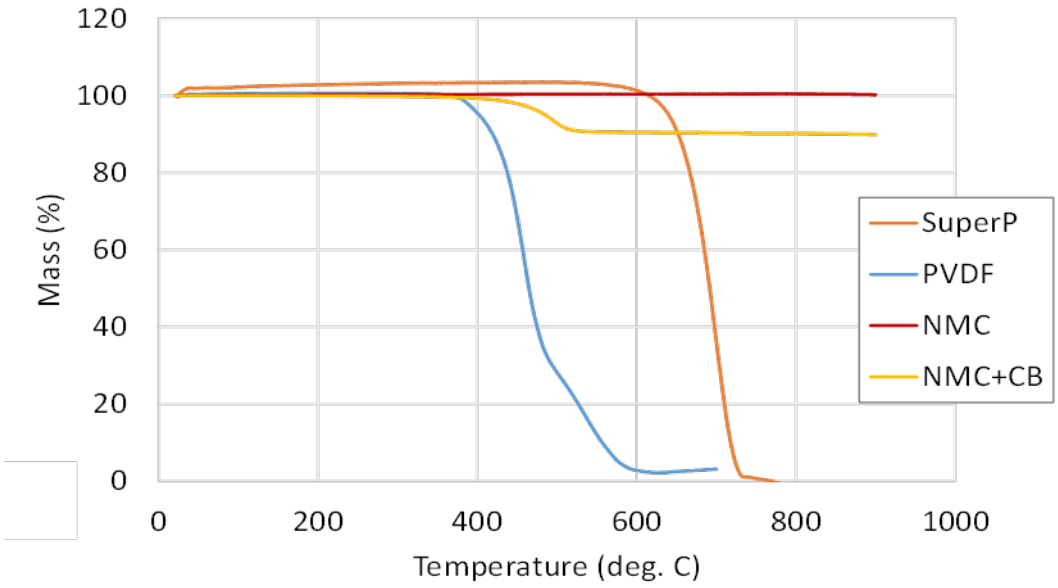

Figure I-60. Thermogravimetric analysis of composite positive electrode components at 10°C/minute

The shredding method and accompanying energy input can be tuned to increase the effectiveness of the process and subsequent processing steps. Tuning process parameters allows recovery of active materials with identical properties as the pristine versions of these materials as illustrated in Figure I-61.

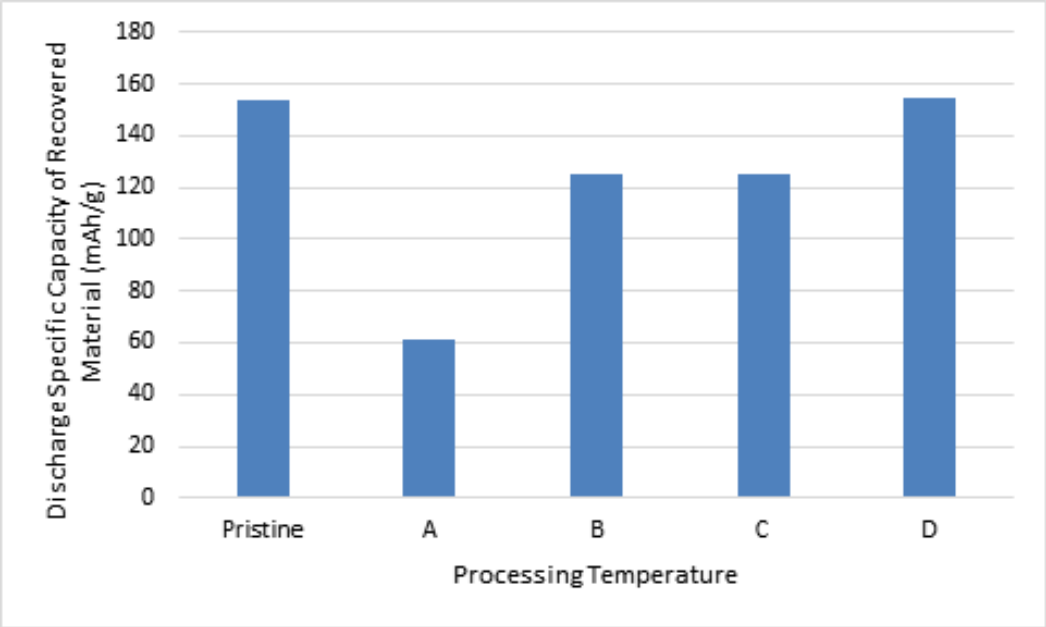

Figure I-61. Specific capacity of positive electrode active material recycled from scrap electrodes.

With feedstocks of cells that have been through the formation process, it is necessary to restore the lithium content of the cathode active material that is lost to the negative electrode for SEI formation. In advance of processing these input streams we have explored working with synthetically aged materials for reconditioning experiments. Multiple experiments into chemical delithiation using aqueous sodium persulfate and nonaqueous nitronium tetrafluoroborate were investigated for this purpose. Delithiation of NCM111 using sodium persulfate produced materials with voltage curves that have the expected shape, which indicates that delithiation has occurred, but the specific capacities were anomalously low as described in Figure I-62. It appears that it is difficult for chemical delithiation to produce materials with properties similar to electrochemically delithiated materials using commonly reported procedures, most likely due to stress gradients induced by rapid delithiation in the absence of electric fields present in a cell that facilitate lithium migration, although it may be possible to modify the reaction conditions to overcome this discrepancy.

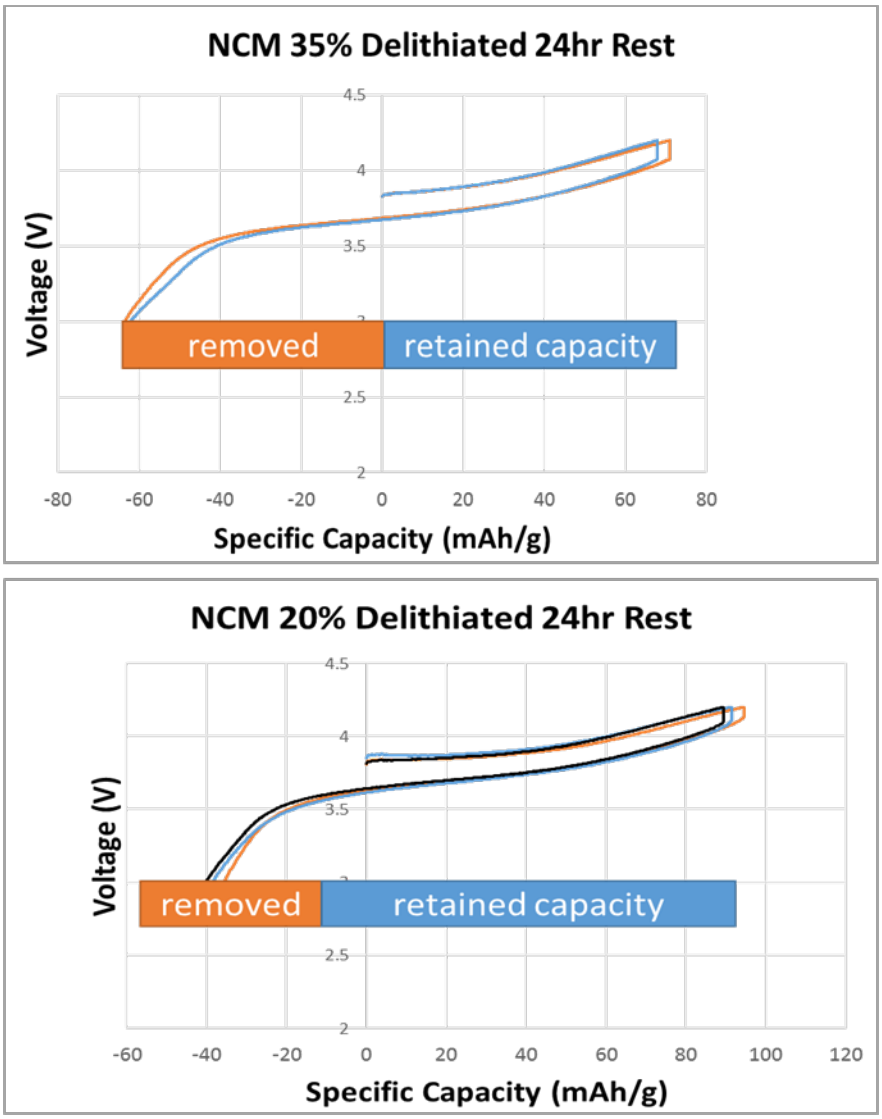

Figure I-62. Voltage curves of NCM111 (vs. Li/Li+, in 1.2 M LiPF6 in EC/EMC 3:7 w/w) which has been chemically delithiated with aqueous $Na_2S_2O_8$. The comparative specific discharge capacity of pristine reference material is 155 mAh/g.

Conclusions

Scaled up processing equipment for Li-ion battery recycling was evaluated and installed at Farasis Energy in Hayward. Initial processing of manufacturing residues has demonstrated that recovery of active materials with properties nearly identical to pristine materials is practical using commercially relevant Graphite//NMC cell chemistries. The next phase of the project will incorporate these recovered materials in deliverable test articles while process optimizations will begin on the more complex feedstocks comprised by aged cells and complete battery systems.

I.A.14 A Closed Loop Recycling Process for End-of-Life Electric Vehicle Li-ion Batteries (Worcester Polytechnic Institute)

Yan Wang, Principal Investigator
Worcester Polytechnic Institute
100 Institute Road
Worcester, MA 01609-2280
Phone: 508-831-5453
E-mail: yanwang@wpi.edu

Brian Cunningham, Technology Manager
U.S. Department of Energy
Phone: 202-287-5686
E-mail: Brian.Cunningham@ee.doe.gov

Start Date: February 2, 2016 End Date: January 15, 2018
Total Project Cost: $1,024,740 DOE share: $512,370 Non-DOE share: $512,370

Project Introduction

The purpose of this USABC project is to successfully recycle multiple 10 kg size batches of end of life EV batteries consisting of different incoming cathode chemistries via the patent pending recycling process developed at WPI, and produce PHEV format cells of a single chemistry using the recovered NMC111 cathode. Over the course of the two year development program, WPI/A123 systems/Battery Resourcers will improve the performance of the recovered cathode materials so that they exhibit performance equivalent to current commercial materials, as confirmed by A123 and National Lab testing using USABC PHEV test procedures. Other materials including steel, copper, aluminum, etc. will also be recycled.

Objectives

The objective of this program is to scale up and demonstrate the WPI-developed novel and efficient Li-ion battery recycling process, verify its claim of no or minimal sorting, and develop PHEV cell designs with a lower cost structure for improved industry sustainability. The USABC development program will advance the WPI recycling technology through the completion of three major tasks: 1) optimizing the synthesis parameters of the recovered $LiNi_{0.33}Mn_{0.33}Co_{0.3}3O_2$ (NMC111) cathode materials for improved particle density, particle size and electrochemical performance; 2) improving the recycling efficiency of cathode materials and lithium and 3) scaling the process from the existing 1 kg scale to the 10 kg scale or greater, as required.

Approach

In this project, WPI has been collaborating with A123 Systems and Battery Resourcers. Battery Resourcers is a start-up company that was co-founded by Yan Wang, Eric Gratz and Diran Apelian to commercialize WPI's recycling technology. WPI's primary focus is on developing and optimizing the recycling process and recovering NMC111 powder, A123's focus is on powder characterization and cell fabrication, and Battery Resourcers' focus is on scale up and cost analysis. The project goals are achieved through execution of the key tasks detailed below:

Improve the electrochemical performance of NMC111

One of the major tasks of the program is to increase the capacity and expected life of NMC111 that is recovered from a multi-chemistry mixture of PHEV/HEV/EV batteries to be equivalent to commercially available cathode material, or show no more than 5% difference in the metrics being tracked. WPI will further refine the ability to tailor the Ni, Mn and Co stoichiometry to consistently deliver the 1:1:1 product regardless of incoming chemistry variations. The project is structured to advance from beginning of program status involving coin cell testing through an intermediate 2 Ah cell to the final deliverable 25 Ah cells. WPI is

working with industrial partner A123 systems to evaluate and improve the properties and electrochemical performance of the recovered cathode material. By optimizing process parameters such as precipitation time and stirring rate, WPI can increase the particle density and specific capacity, which are key to successful commercialization of the recycling technology. The project is striving to increase the reversible capacity of the recycled cathode from 150 mAh/g to 155 mAh/g. However, project emphasis is ultimately aimed at the relative difference between cells made with recovered material and commercial NMC versus the absolute performance of both, as the latter can be affected by many factors unrelated to the recycling technology itself. For this reason, commercial control cells are generated at every stage for a meaningful benchmark and the difference is tracked using the recycling-adapted 3-tiered gap charts.

Improve the recovery efficiency

There are two facets to recovery efficiency: minimizing losses of desirable components in the various processing steps and minimizing the quantity of virgin materials required to supplement the incoming stream of spent batteries. Both aspects are being addressed in order to deliver the most favorable economics. To maximize the recovery efficiency of Ni, Mn, and Co as $Ni_{1/3}Mn_{1/3}Co_{1/3}(OH)_2$, the pH will be closely monitored and controlled. The most important step is the impurities removal operation in which Al, Cu and Fe impurities are removed as hydroxides. The amount of Ni, Mn and Co lost at this stage depends upon two primary factors: their concentration in solution and the pH. The lowest pH which can be obtained while maintaining impurity levels below targets must be determined, so as to allow for the maximum recovery efficiency. To maximize the recovery efficiency of lithium carbonate, the amount of water that is evaporated must be strategically tuned. By determining the concentration of the impurities ions present in solution (Na^+, SO_4^{2-}) from measured concentrations of sodium and sulfur, the exact volume point at which sodium sulfate becomes insoluble can be calculated using the K_{sp} of sodium sulfate at the temperature in question. This is be used to optimize the water added and subsequently evaporated, along with other purification and temperature related refinements to minimize unnecessary dilution and maximize yield.

Scale-up

The significant challenge of going from 1kg to 10kg experiments was approached by conducting the scale-up in stages. (The scale indicates the mass of shredded, spent battery feed entering the process). First, the work proceeded from 1kg experiments to 3kg (factor of 3), and then to 10kg (increase factor of 3.3). At each scale (1 kg, 3 kg, 10 kg), recovered material properties were compared against commercial cathode material using both powder and resultant cell attributes in clearly defined, measureable milestones. Ultimately, WPI exceeded the original targets of scaling the process to a 10 kg feed scale, and were able to successfully process multiple lots of 30-40 kg (each) of spent batteries.

Results

In order to generate NMC111 powder for 2 Ah cells, WPI conducted 5 large scale experiments, with each experiment using spent batteries from different and intentionally diverse recycling streams. A number of key process modifications were made as part of the optimization required in order to achieve the desired powder attributes, and the process was ultimately converted from a batch process to a semi-continuous one, and one capable of accommodating an incoming feed of 30 kg. of spent batteries. Each experiment produced over 3kg of NMC111 for evaluation and cell fabrication. The experimental information is the following.

Lot 03272017

Recycling stream: GM Volt batteries and LFP cells from A123

Cathode tap density: 2.30g/cc, D50: 20 µm

Lot 04212017

Recycling stream: FCA batteries

Cathode tap density: 2.51g/cc, D50: 11.6 µm

Lot 05152017

Recycling stream: GM Volt batteries, FCA batteries, electronics batteries and LFP cells from A123

Cathode tap density: 2.52g/cc, D50: 14.1 µm

Lot 06202017

Recycling stream: Ford Focus batteries

Cathode tap density: 2.60g/cc, D50: 10.2 µm

Figure I-63 shows the precursor and cathode material information for the 4 experiments used for the 2 Ah deliverables, and highlights the ability of the process to handle a diverse makeup of feed chemistries (see feed descriptions on the right). The slight variations in tap density and particle size reflect small differences in several process parameters between the lots, as the optimization effort was still underway as powder morphology was refined in approach of the target attributes. The 4 batches of powder represented below have been delivered to A123 for 2 Ah cell fabrication, and fulfillment of one of the project deliverables. Their electrochemical properties are shown in Table I-10 below, as tested by A123 Systems.

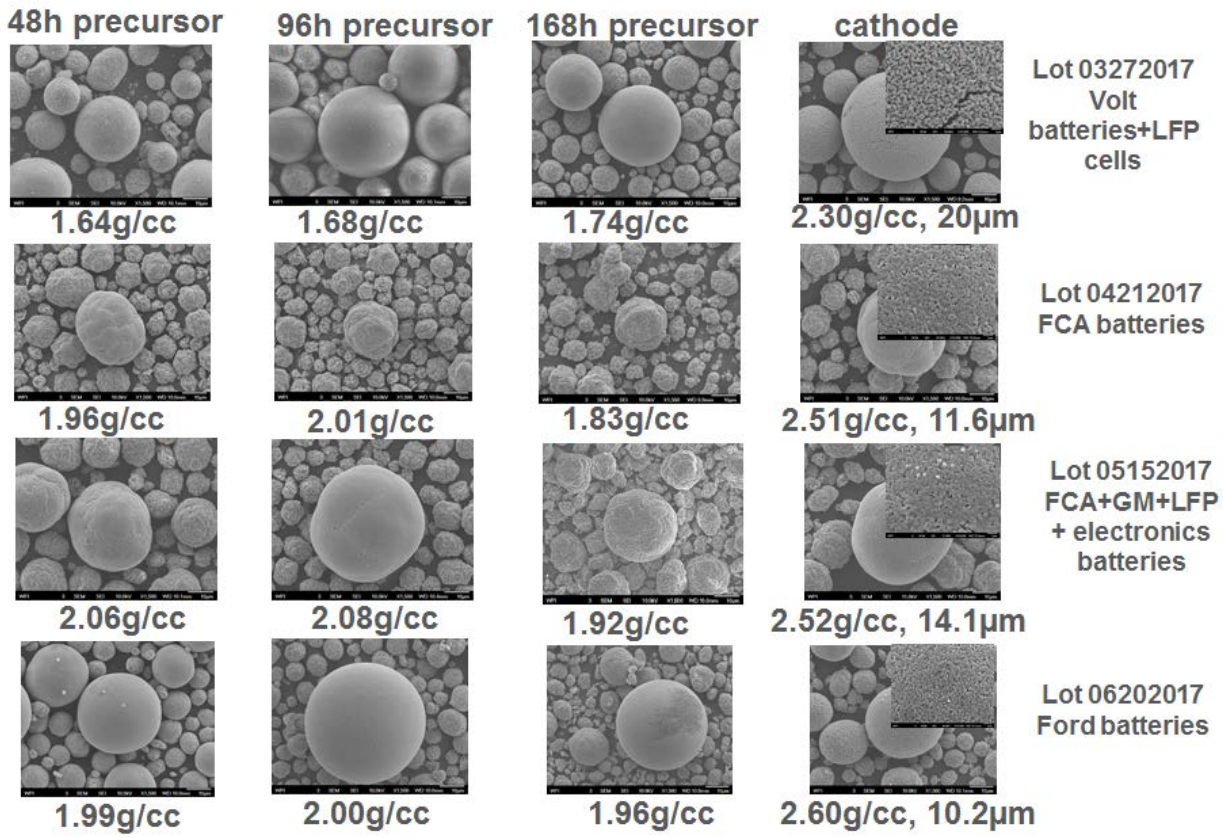

Figure I-63: Detailed precursor and cathode powder information from 4 different experiment for 2 Ah cells. Each 3 kg lot of powder was generated from approximately 30 kg of spent, shredded batteries of the provenance noted above.

In order to generate the required 8kg NMC111 powder for each of the two 25 Ah cells builds, WPI needed to conduct 2 experiments, with each experiment generating ~4kg NMC111 powder (and using a spent battery feed of >30 kg). One recycling stream consisted of Ford Focus batteries and LFP cells and the other recycling stream was comprised of FCA batteries. WPI completed the 4 final experiments and delivered 2 combined batches of 8kg powder to A123 for 25 Ah cell fabrication. Figure I-64 shows the precursor and cathode material information for the 4 experiments, with the details listed below.

Lot 08112017

Recycling stream: Ford Focus batteries and LFP cells

Cathode tap density: 2.56g/cc, D50: 13.9 µm

Lot 08302017

Recycling stream: Ford Focus batteries and LFP cells

Cathode tap density: 2.56g/cc, D50: 10.7 µm

Lot 09192017

Recycling stream: FCA batteries

Cathode tap density: 2.65g/cc, D50: 11.9 µm

Lot 10092017

Recycling stream: FCA batteries

Cathode tap density: 2.50g/cc, D50: 9.81 µm

The powder from the different recycling experiments shows similar morphology, tap density and particle size when compared to the previous 3kg powder lots for the 2 Ah cells. The first 8 kg batch of powder was obtained by mixing lots 08112017 and 08302017. Its tap density is 2.58g/cc and D50 is 11.7 µm. The second 8 kg batch of powder combined lots 09192017 and 10092017. At the time of writing of this report, the second batch was undergoing material characterization by A123 in advance of cell fabrication. Based upon the consistency of results with prior lots, it is expected that the powder will pass quality control evaluation and be used for the final deliverable 25 Ah cell-build. To date, A123 has tested numerous batches of WPI-recovered NMC111 and control powders with coin cells, and the most recent results are shown in Table I-10. A123's test results demonstrate that WPI synthesized material from different recycling streams exhibit similar electrochemical performance as the commercial material, and generally show better rate performance, which is quite unexpected. In addition to the coin cells, A123 has fabricated and tested single layer pouch cells with both control and WPI-recovered powder. The results again show that WPI recovered NMC111 has similar performance with control powder (The single layer pouch cells have been cycled more than 2,000 cycles.). Most of the 2 Ah pouch cells have now been built by A123 and will allow larger format comparative evaluation of WPI material performance versus control powders (commercial NMC111). Finally, the aforementioned 8 kg batches of WPI powder will be used by A123 to produce the 25 Ah final deliverables, which again will be evaluated against equivalent hardware control counterparts. Both 2 Ah and 25 Ah cells will be delivered to Argonne National Laboratory for independent assessment based on USABC PHEV testing protocol.

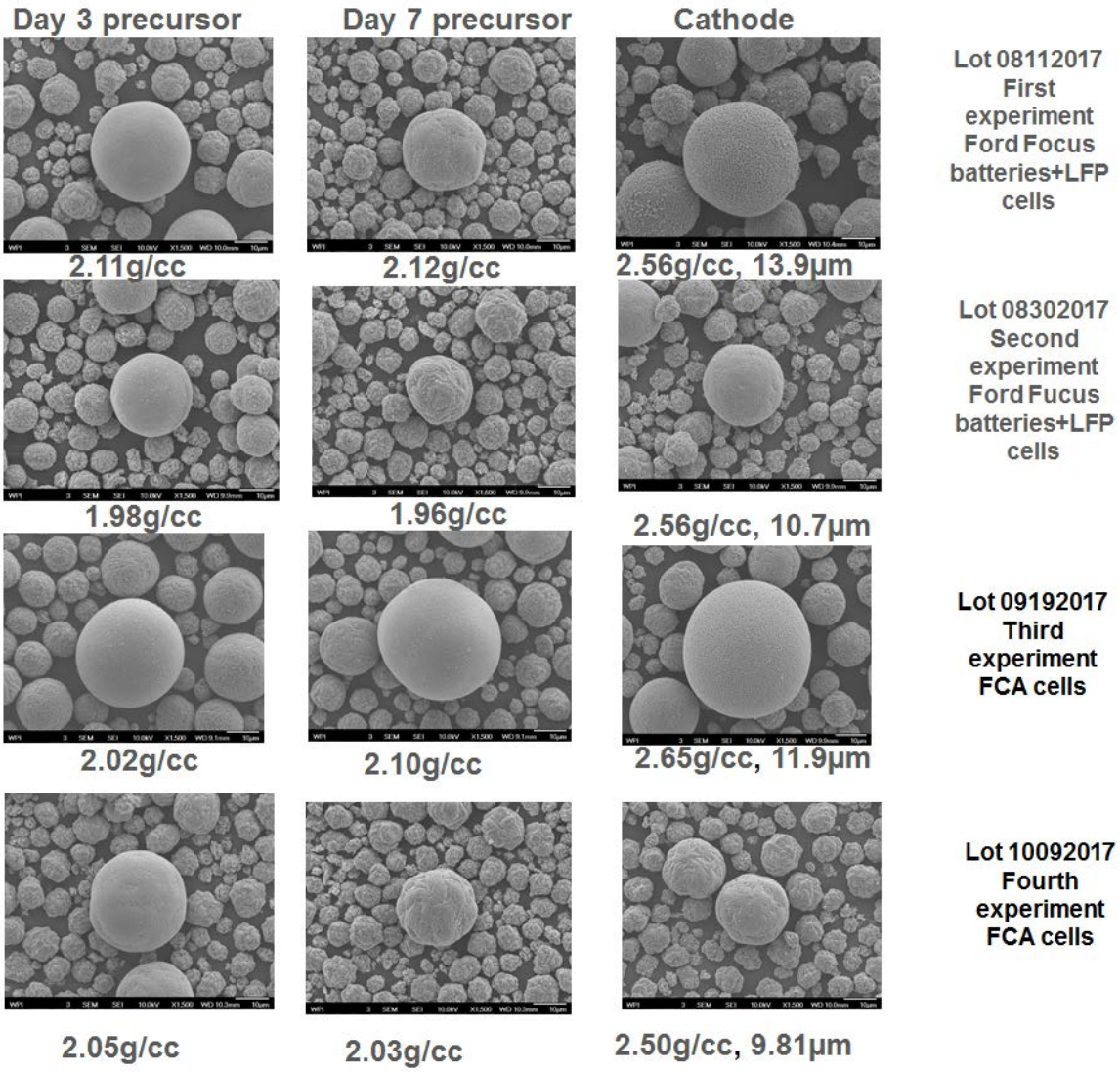

Figure I-64: Detailed precursor and cathode powder information from 4 different experiment for 25 Ah cells

Table I-10: Comparison between synthesized material and commercial material

Test	Metric	Control Powder (B)	03272017 3Kg Powder	04212017 3Kg Powder	05152017 3Kg Powder	06202017 3Kg Powder
Tap Density	g/cc	2.84	2.15	2.31	2.36	2.51
D50 PSD	um	9.2	20	11.6	14.1	10.2
BET	m^2/g	0.28	1.41	0.53	0.36	0.65
FCC/ FDC	mAh/g	174.7/ 157.2	177.3/ 163.5	178.1/ 152.3	170.1/ 149.2	177.3/ 157.0
Efficiency	%	90.0	92.2	85.5	87.7	88.6
1C	mAh/g	130.9	136.3	123.1	137.4	129.2
2C	mAh/g	119.4	128.6	113.0	128.4	120.8
5C	mAh/g	40.4	59.5	75.4	76.2	76.2
Full coating		Complete	Complete	Complete	Complete	Complete

Battery Resourcers officially joined the USABC project in February 2017 to further scale up the WPI process to a 50 kg (spent feed) scale, with the option of using their material for 25 Ah cells, if it was confirmed comparable or superior to the WPI powder. The validation of the process at the higher scale is expected to further inform commercialization potential of this technology and will allow a more meaningful economic model to be developed. Battery Resourcers adopted WPI parameters and conducted a few experiments with GM Volt batteries. Figure I-65 shows the precursor morphology progression over the course of the experiment. The particles become more spherical with increasing time, much like the WPI results. The tap density of the precursor is ~1.9g/cc, which is within the expected range. Battery Resourcers has synthesized cathode powder (tap density: 2.4g/cc) and delivered 200g cathode powder (Figure I-66) to A123 independent evaluation. The electrochemical results are increasingly similar to that of WPI recovered powder.

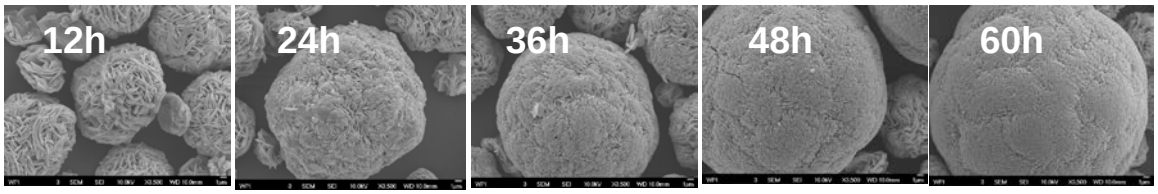

Figure I-65: The morphology of NMC111 precursor with reaction time at Battery Resourcers

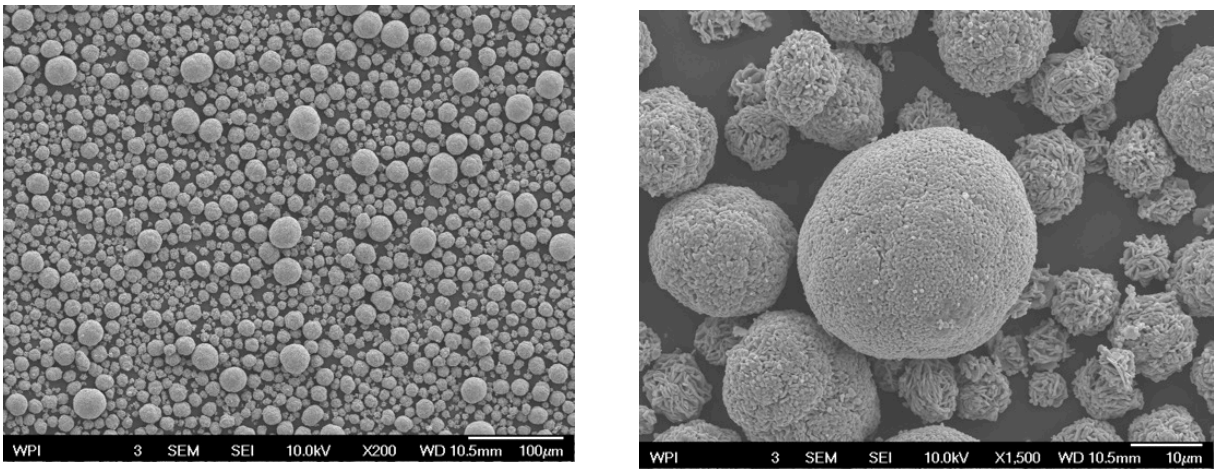

Figure I-66: NMC111 cathode powder synthesized by Battery Resourcers

Conclusions

In order to generate enough powder for 2 Ah and 25 Ah cells, significant process improvements were realized throughout the past year, and have allowed achieving and in some cases exceeding the powder and process targets established in the SOW. Furthermore, the process can now run with minimal supervision due to numerous improvements in system configuration and controls, as opposed to the constant oversight that was required at the beginning of the program. So far, WPI has recycled 1 GM Volt battery pack, 1 Ford Focus battery pack and 1 FCA 500e battery pack, significantly surpassing the quantities specified in the SOW.

During the recycling experiments, WPI has successfully demonstrated its capability of recovering NMC111 powder from different, chemically diverse recycling streams. The recovered powder shows high tap density, and good morphology. WPI has successfully delivered to A123 four 3kg lots of powder for the 2 Ah cells and two 8 kg lots of powder for 25 Ah cells. Based on initial coin cell and single layer pouch cell testing at A123, WPI recovered powder has similar performance with commercial cathode powder, with somewhat higher rate performance. These results clearly demonstrate the scalability and repeatability of WPI recycling technology.

In addition, Battery Resourcers has adopted and further scaled the WPI recycling technology, and has been able to generate promising, in-specification NMC111 powder, as recently confirmed by A123 Systems.

Key Publications

1. Yan Wang, Zhangfeng Zheng, Mengyuan Chen, A Closed Loop Process for the End-of-Life Electric Vehicle Li-ion Batteries, U.S. DOE 2017 Annual Merit Review and Peer Evaluation Meeting, Washington, D.C., June 5-9, 2017.

I.A.15 Perform USABC/USCAR Benchmarking Activities (FEV North America, Inc.)

Thomas D'Anna, Principal Investigator
FEV North America, Inc.
4554 Glenmeade Lane
Auburn Hills, MI 48326
Phone: 248-724-2861
E-mail: DAnna@fev.com

Greg Kolwich, Principal Investigator
FEV North America, Inc.
4554 Glenmeade Lane
Auburn Hills, MI 48326
Phone: 248-724-2924
E-mail: Kolwich@fev.com

Brian Cunningham, Technology Manager
U.S. Department of Energy
Phone: 202-287-5686
E-mail: Brian.Cunningham@ee.doe.gov

Start Date: June 1, 2015 End Date: October 31, 2017
Total Project Cost: $442,763 DOE share: $144,900 Non-DOE share: $297,863

Project Introduction

In the process of developing new powertrains for vehicles, benchmarking data (and subsequent analysis) is beneficial in the identification and characterization of similar products. Through this process, development targets can be established for the new products, relevant design features identified, and their influence on key attributes evaluated. A technical benchmark study is performed on the 2015 Volkswagen e-Golf as well as a detailed cost analysis performed on the 2016 Toyota Prius lithium-ion battery pack.

Objectives

- The 2015 VW e-Golf benchmark study consists of vehicle testing, key component (test stand) testing, and teardown analysis.
- The 2016 Toyota Prius lithium-ion battery pack cost analysis consists of a full battery pack tear-down for general part and manufacturing information gathering, process parameter model and database review, and cost modeling analysis.

Approach

For both programs, hardware tear-down, testing, and applicable analysis are performed at FEV's in-house facilities in Michigan. Technical reviews are collaboratively executed with feedback and guidance from OEM and DOE counterparts.

Results

- In 2017, battery pack tear-down (Figure I-67) and performance tests were completed. The e-Golf's battery pack was tested in an environmental chamber to understand its performance characteristics. The battery pack was connected to an AV-900 battery emulator to run the pack through multiple charge and discharge cycles at varying temperatures. Data including temperature and voltages were recorded while testing (Figure I-68).

- Upon disassembly of the Prius battery pack (Figure I-69) to the sub-component level, all parts were documented generating a manufacturing comparison bill of materials. This information feeds into the creation of process flows for manufacturing assumption-quote summary worksheets detailing rates and cost contributions (i.e., material, labor, manufacturing overhead and mark-up) for each operation involved in producing a component. Approximately 75% of the battery pack components are calculated using detailed cost models and the remaining 25% costed using benchmark/commodity pricing.

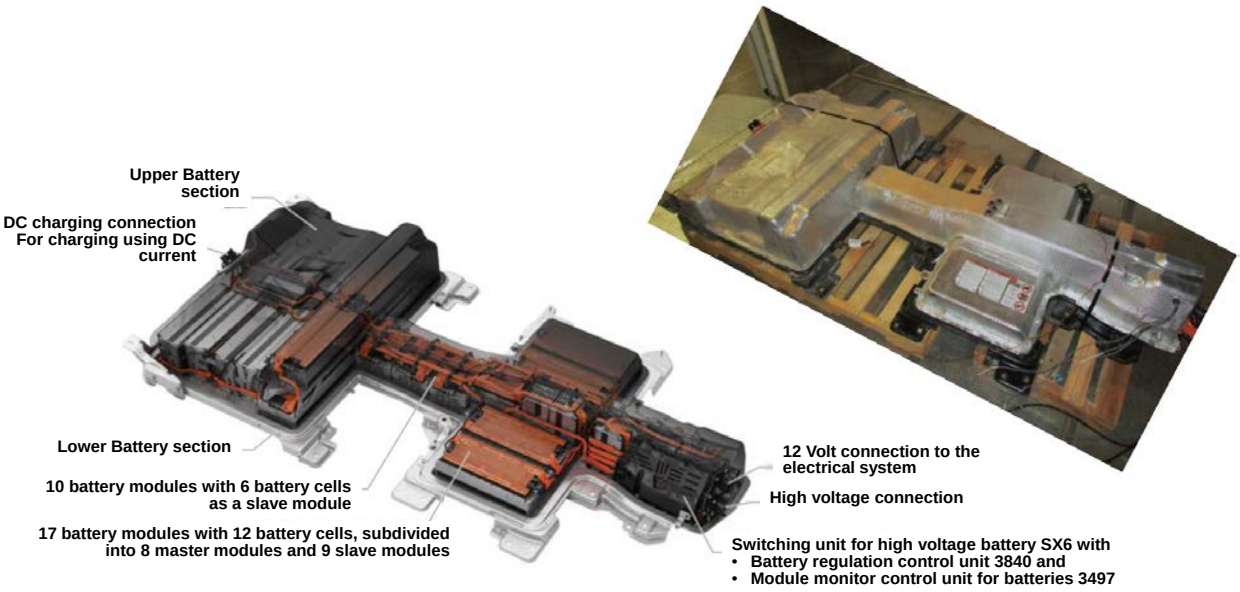

Figure I-67: 2015 VW e-Golf Battery Pack Physical Overview

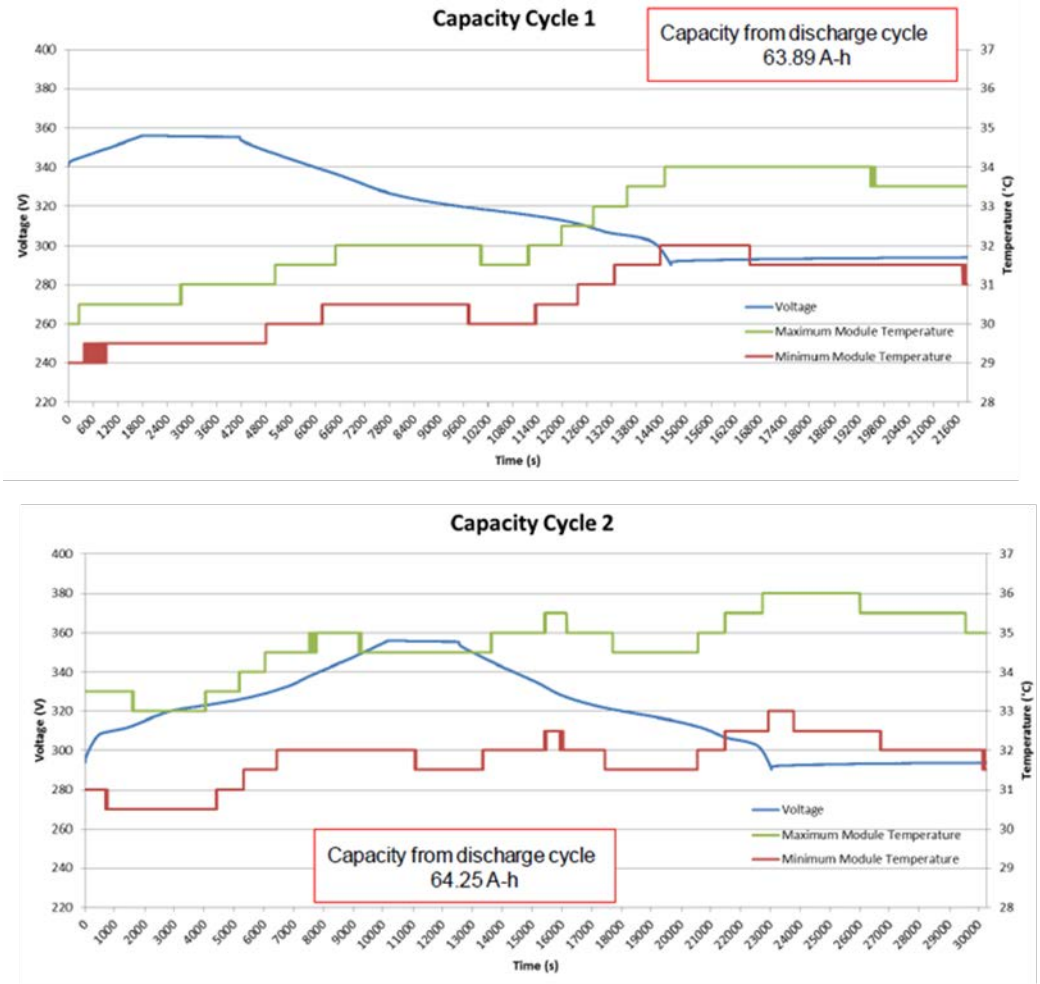

Figure I-68: Capacity Testing Cycles at C/3 Charge, 30min Rest, C/3 Discharge at 30°C

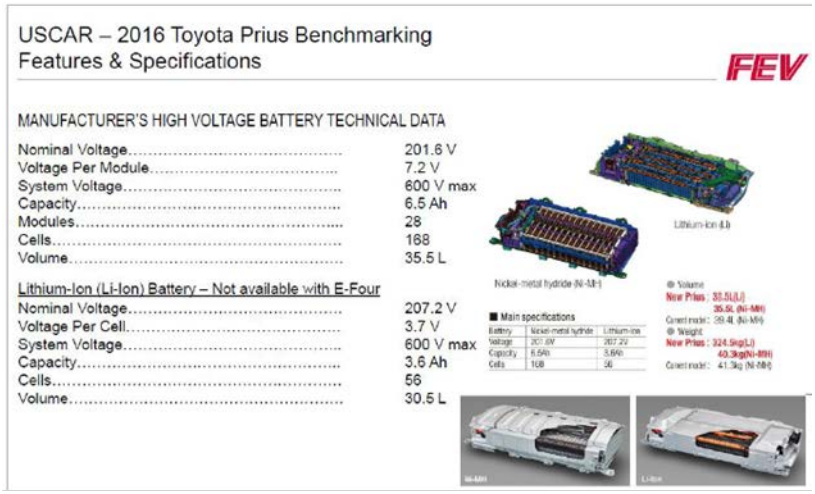

Subsystem	Information
Type	Li-ion HV Battery
Cells	56 Cells (26/row)
Nominal Voltage	DC207.2V
Capacity	3.6 ampere hour
Max System Voltage	600V
Cooling Specs	Air Cooled

Figure I-69: 2016 Toyota Prius Lithium-Ion Battery Pack Specification Summary

Conclusions

- The HV battery testing results showed that the battery pack performed nominally with capacity ranging from a low of 50.34 Ah during the -30°C test to a high of 65.03 Ah in the 45°C test. This compared favorable to the rated capacity of 66.1 Ah. The resistance of the battery pack varied from a low of ~0.09Ω during the 45°C test to a high ~0.52Ω during the -30°C test. The Pulse Power Capability of the battery pack varied from a low ~35 kW during the -30°C test to a high of ~180 kW during the 45°C test. Pack hardware and associated components are further detailed in the final report.

- FEV provided in-depth analysis of cost scenarios based on scaled volume (450k, 100k, and 50k units/year) assessments. A collaborative cell manufacturing assumption review with OEM and DOE counterparts motivated update recommendations to the USABC cost model templates.

I.B Advanced Processing

I.B.1 Low Cost Manufacturing of Advanced Silicon-Based Anode Materials (Group14 Technologies, Inc.)

Henry R. Costantino, Ph.D., Principal Investigator
Group14 Technologies, Inc.
100 NE Northlake Way, Suite 300
Seattle, WA 98105
Phone: 206-547-0445; Fax: 206-546-5304
E-mail: rcostantino@group14technologies.com

Peter Faguy, Technology Manager
U.S. Department of Energy
Phone: 202-586-1022
E-mail: Peter.Faguy@ee.doe.gov

Start Date: January 1, 2016 End Date: December 31, 2017
Total Project Cost: $4,040,000 DOE share: $2,810,000 Non-DOE share: $1,230,000

Project Introduction

Despite substantial investment in Lithium-Ion Battery (LIB) technology, most commercial cells still rely on graphite anodes – originally deployed in the '90's, because of their low cost and acceptable lithium capacity. A shift is underway to replace the graphite anode with a silicon containing material, but due to elaborate manufacturing techniques current costs exceed $100/kg. It is our vision to develop new anode materials that are high performance, and also easily scalable, employing low-cost materials and manufacturing processes. To this end, we have launched Group14 Technologies, spun out of EnerG2 Inc., a leader in carbon materials development, manufacturing, and commercialization. Group14's strategy is to develop low cost processes for manufacturing silicon-carbon (Si-C) composite materials that will enable a dramatic reduction in the cost structure of silicon-carbon anodes, i.e., by an order of magnitude, while maintaining the high performance that the LIB industry demands of these advanced anodes.

Objectives

The objective of this project is to develop a new low cost production process that is capable of mass-producing silicon-based lithium ion battery (LIB) anode material that can reach 1000 mAh/g after 1000 cycles and with a cell level cost target of < $125/kWh, validate performance in LIB full cells, and prove the cost basis at pilot scale.

Approach

Group14 is leveraging EnerG2's carbon technology to develop new approaches for low-cost manufacturing of high-performing Si-C composites. These Si-C composites comprise nano-sized and/or nano-featured silicon. The approach focuses on raw materials that are low cost and readily sourced. Likewise, the approach focuses on manufacturing processes that are low-cost and readily scalable. Specifically, both carbon and silicon components within the Si-C composite are based on low-cost precursors.

Group14 approach is to down-select Si-C composite materials and manufacturing processes at lab-scale, supported by robust characterization, including electrochemical characterization with a focus on electrochemical testing of the Si-C composite anode materials in full cell Li-ion batteries such as coin cells or pouch cells. Our philosophy for the electrochemical characterization is to employ relatively standard procedures and materials, i.e., industry-standard electrolyte, cathode, and battery cycling conditions. While we

are interested in potential synergies with our Si-C composite materials and the next generation of other battery materials (cathodes, electrolyte, etc.) our current intent is that our Si-C composite materials are a "drop-in" replacement for graphite powder as an anode material, compatible with current commercial anode and Li-ion battery manufacturing lines.

Consistent with our project plan, we have down-selected materials and processes, and have ordered manufacturing equipment for pilot scale (e.g., 1-10 kg) production. We are currently gearing up for pilot scale in terms of site readiness in preparation of equipment receipt, installation, and commissioning. Once all equipment has been commissioned, the purpose of the final stage of the project is to prove the cost basis at pilot scale, as well as validate the performance of the scaled-up Si-C composites in Li-ion battery full cells.

Results

The accomplishments during the first quarter of 2017 (Jan-Mar 2017) included further improvement of Si-C cycle stability at lab scale, progress towards scale up, and increased understanding of physicochemical characteristics relevant to electrochemical performance.

Down-selected path #2 (DSS #2) and down-selected path # 3 (DSS #3) – collectively, Process Path 2 - represent an internal path with respect to processing the Si-C composite. Regarding this path, the continued improvement in electrochemical performance at lab scale is presented in Figure I-70 (on a volumetric energy basis).

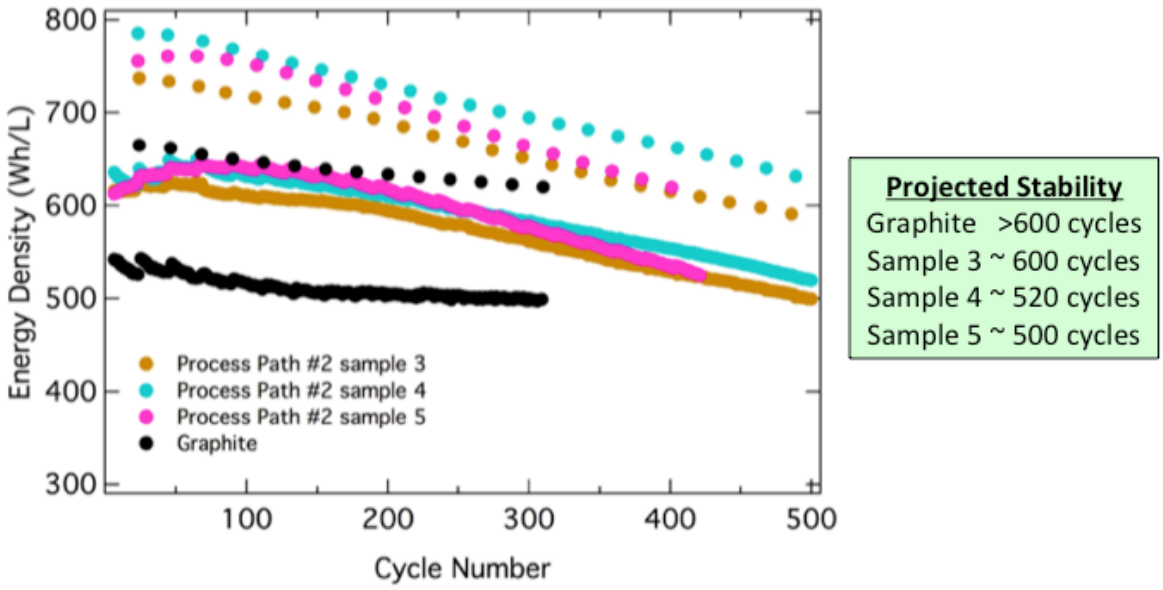

Figure I-70: Volumetric energy density (Wh/L) for Process Path 2 Si-C composites vs graphite, full cells cycled at C/2 rate with C/10 rate every 20 cycles, 2.5 – 4.2 V, with I/2 hold, 1 M LiPF6 in EC:DEC w/10% FEC, LiNiCoAlO cathode, excess anode=2-16%, anode=5% CMC-SBR, 5% Super-P, 59-63% graphite, 27-32% Si-C composite.

The data for volumetric energy density were calculated based on total volume (or mass) of anode and cathode materials, i.e., does not include other components of the battery system such as current collector, separator, or electrolyte. The anode comprised a blend of Si-C composite, conductive carbon, and graphite to achieve a capacity in the range of ~ 450 to 650 mAh/g, wherein the anode was paired with LiNiCoAlO (NCA) cathode. Details regarding the electrode and device preparation, as well as full cell testing parameters, are provided below Figure I-70. As can be seen, the performance of the Si-C composite lab scale is over 600 cycles.

Also during the first quarter of 2017, we made progress regarding our collaboration with Dr. Chongmin Wang and Dr. Langi Luo at Pacific Northwest National Laboratory (PNNL). Regarding this collaboration, we

analyzed numerous Si-C composite samples for not only their measured 2-dimensional and calculated 3-dimensional expansion by TEM during lithiation, but also their general structure, homogeneity, phase of silicon and/or carbon, primary particle size (Si-C composite size) and secondary particle size. Herein, we present the selected area electron diffraction (SAED) analysis of an exemplary Si-C composite corresponding to Process Path 2. The data are presented in Figure I-71. According to our collaborator's interpretation, there was no observable phase variation, in other words, the data were consistent with homogeneous distribution of nano silicon (~10 nm secondary particles) through the amorphous carbon matrix (~5 um primary particles).

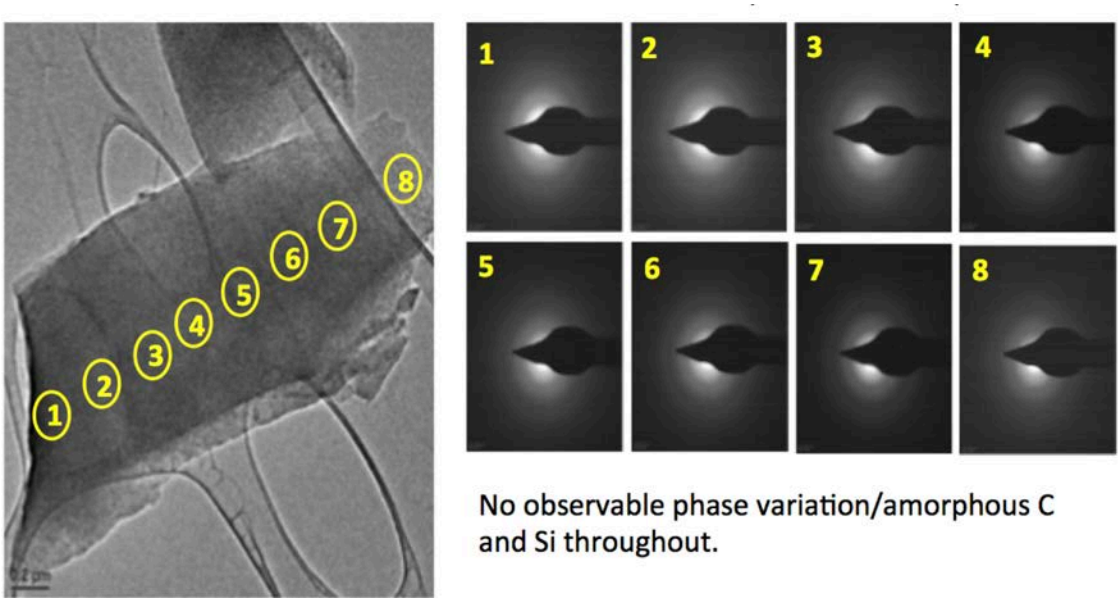

Figure I-71: SAED analysis of an exemplary Si-C composite corresponding to Process Path #2.

The second quarter of 2017 (Apr - Jun 2017) focused on achieving the project milestone to "Synthesize 1x10g Si-C with 1000 mAh/g; predicted 1000 cycles; < $125/kWh projected cost." To this end, we have presented to the DOE our achievement of 1000 cycle stability in a full cell coin cell as shown in Figure I-72 (on Wh/L basis) and Figure I-73 (on capacity retention basis), as presented to the DOE during a telecom held June 16, 2017. It was discussed that these data were generated for a electrochemical testing system wherein we employed an anode comprising a blend of Si-C composite (produced with Process Path 2, as discussed in previous reports) wherein said blend comprised typically ~30% Si-C, 60% graphite, 5% CMC-SBR, and 5% Super-P, and the anode excess in the full cell coin cell was typically 5-15%. It is noted that the 100 cycle stability achievement at this time involved cell optimization, specifically, pre-lithiation and voltage window of 2.5 – 4.12 V as noted in the legends to Figure I-72 and Figure I-73.

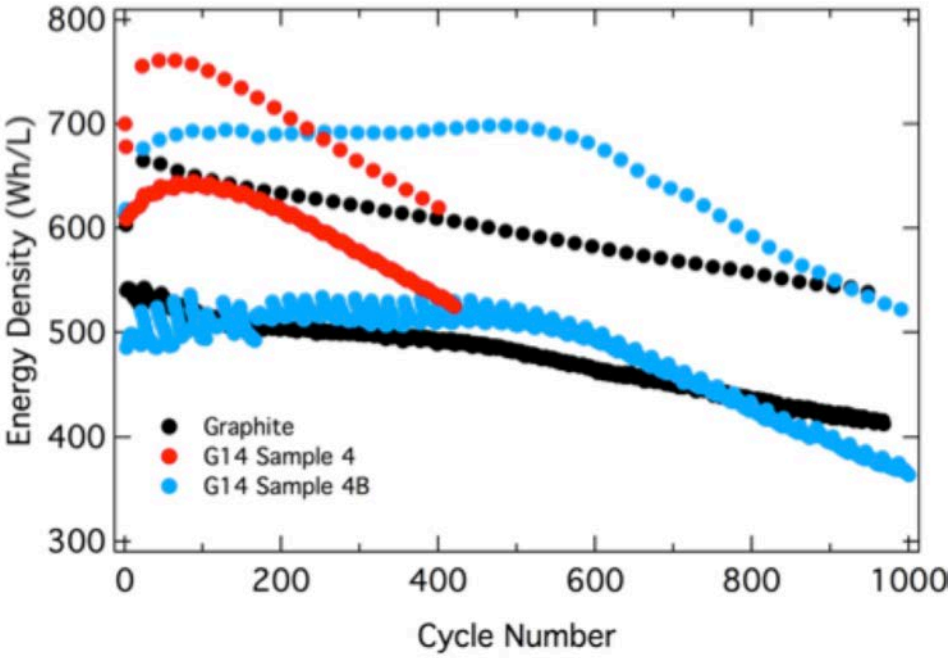

Figure I-72: Volumetric energy density (Wh/L) for Process Path 2 Si-C composites vs graphite, anode prelithiated by shorting with Li metal for 1 h prior to assembly, full cells cycled at C/2 rate with C/10 rate every 20 cycles, 2.5 – 4.12 V, with I/2 hold, 1 M $LiPF_6$ in EC:DEC w/10% FEC, LiNiCoAlO cathode.

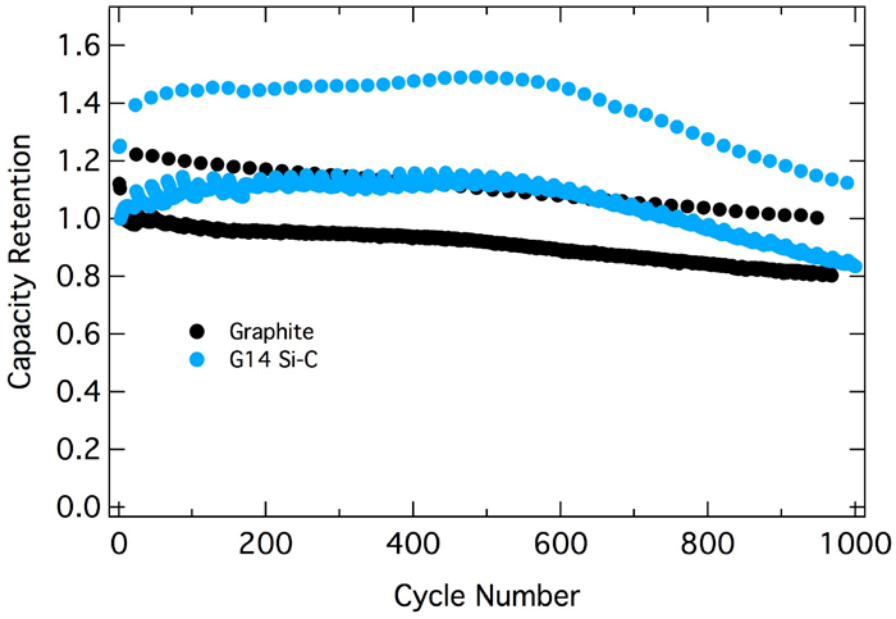

Figure I-73: Capacity retention (%) for Process Path 2 Si-C composites vs graphite, anode prelithiated by shorting with Li metal for 1hr prior to assembly, full cells cycled at C/2 rate with C/10 rate every 20 cycles, 2.5 – 4.12 V, with I/2 hold, 1 M $LiPF_6$ in EC:DEC w/10% FEC, LiNiCoAlO cathode.

We have made further progress regarding our collaboration with PNNL. Regarding this collaboration, numerous Si-C samples were analyzed for primary and secondary particle size, measured 2D expansion, phase of silicon and carbon, general structure and homogeneity. The data overview is presented in Table I-11.

Table I-11: Overview of Data Produced via the PNNL Collaboration.

#	Si wt %	Primary/Secondary Particle Size	Measured 2D Expansion	Phase of Silicon/ Carbon	General Structure	Homogeneity
1	40	5 um	20-47%	a-Si&L-Gr-C	Dense porous structure	Good
2	46	5 nm /2-5 um	20-36%	Poly-Si&a-C	Fine Si NPs in a-C matrix	Good
3	48	10-20 nm/2-5 um	55-76%	a-Si&L-Gr-C	Uniform dense particle of LGC with a-Si	Great
4	42	50-100 nm/2-5 um	20-42%	Poly-Si&a-C	c-Si NPs on porous C scaffold	Good
5	34	50-100 nm/2um	19-45%	Poly-Si&Gr-C	c-Si NPs on porous C scaffold with C coating	Good
6	41	30-40 nm/2 um	37%	Poly-Si&a-C	c-Si NPs aggregates on a-C	Great
7	39	20-30 nm/2-8 um	19-58%	Poly-Si&Gr-C	c-Si NPs aggregates covered with Gr-C	Great

Gr-C: Graphitic Carbon; L-Gr-C: Less Graphitic Carbon; Poly-Si: very fine poly Si NPs which shows on SAED pattern; a-C: amorphous carbon; c-Si: larger Si NPs which show scattered spots on SAED pattern; Homogeneity rate is based on the portion of the major phase.

It is important to note in Table I-11 that the interpretations and wordings are presented as provided by PNNL. As can be seen, the Si-C composites produced by Group14 can achieved 30-50% silicon loading in the carbon, wherein the reported silicon particle size can be as low as 5-100 nm for a primary carbon particle size in the range of 2-8 um. Various silicon and carbon phases can be achieved. Importantly, the reported 2-D particle expansion was as low as 19%, and the silicon distribution throughout the carbon particle was reportedly consistent with good or great homogeneity.

The primary focus during the third quarter 2017 (Jul – Sep 2017) – and our ongoing focus - concerns scale up towards pilot production (~1-10 kg). We have completed our down selection and equipment specification process. The deliverable for this activity was the ordering of the Si-C compounding reactor, and well as critical auxiliary equipment. The procurement of the Si-C compounding reactor and critical auxiliary equipment is underway. An important next step is the factory acceptance test, which is scheduled by the equipment vendor in mid-December 2017. Assuming a successful factory acceptance test, the equipment will be shipped and receipt is expected by end of December.

It was important to select a site for suitable and safe operation of the pilot equipment. To this end, we have considered various options, including installation of the equipment within the current EnerG2 facility in Seattle, WA. After careful consideration of the options, we decided to procure a new site for Group14. Specifically, Group14 has signed a lease for a ~4,000sf site in Woodinville, WA. Regarding this site, certain facility upgrades are underway in preparation of pilot plant installation. All such upgrades are planned for completion prior to receiving and installing the pilot equipment.

Conclusions

Group14 Technologies is developing low-cost, high-performing Si-C composite materials suitable as a drop-in for Li-ion battery anodes. We have successfully down-selected samples for scale up, and we have demonstrated ongoing performance improvements. We are also conducting mechanistic investigations into the stability afforded by our Si-C composites; in particular, our collaboration with PNNL has confirmed very low volume expansion for our materials. Regarding performance, we have demonstrated the potential to achieve 1000 cycle stability at lab scale. Our current focus is on the scale up towards pilot scale (1-10 kg), commensurate with the remaining project milestones.

Key Publications

1. US provisional patent application 62/469444, filed 09-Mar-2017.
2. USCAR talk entitled “Low Cost Manufacturing of Advanced Silicon-Based Anode Materials,” presented on May 16, 2017 at Detroit, MI.
3. Poster entitled “Low Cost Manufacturing of Advanced Silicon-Based Anode Materials,” presented on June 8, 2017 at the Annual Merit Review (AMR) meeting in Washington, DC.

I.B.2 Commercially Scalable Process to Fabricate Porous Silicon (Navitas Systems)

Pu Zhang, Principal Investigator
Navitas Systems
4880 Venture Drive
Ann Arbor, MI 48108
Phone: 734-205-1435
E-mail: pzhang@navitassys.com

Peter Faguy, Technology Manager
U.S. Department of Energy
Phone: 202-586-1022
E-mail: Peter.Faguy@ee.doe.gov

Start Date: November 17, 2015 End Date: June 30, 2016
Total Project Cost: $1,181,766 DOE share: $1,181,766 Non-DOE share: $0

Project Introduction

Navitas Advanced Solutions Group developed a novel, commercially scalable approach to supply microporous silicon (µpSi) to lithium ion battery manufacturers (Figure I-74) intended to reduce the cost and environmental impact of high capacity anodes needed to meet the EV battery goals.

Silicon nanocomposite materials have been identified as a viable anode technology for EV batteries. Presently, high capacity silicon-based anodes rely either on materials that are expensive (e. g., silane or nano-silicon powder) or on processes that are limited by low yield methods (e.g., chemical vapor deposition). Microporous silicon potentially avoids these limitations and is attracting increasing attention as a lower cost alternative for the manufacture of high capacity silicon-based anodes. Microporous silicon suitable for EV batteries is not currently available as a commodity material. Microporous silicon can be produced at lab scale through a metal catalyzed hydrofluoric acid etching process. However, this process is expensive and hazardous. Our proposed production route facilitates the availability of µpSi to lithium ion battery producers and developers at a scale and cost able to support EV battery production.

Objectives

The objectives for this program were:

1. Optimize at bench scale each of three process steps used to manufacture microporous silicon (µpSi) powder and identify associated critical to quality (CTQ) criteria
2. Qualify low-cost precursor materials for production of µpSi powder
3. Transfer technology to NexTech (scale-up partner) and establish pilot scale µpSi production (>1.0kg/batch).
4. Validate materials performance in an open-source baseline prototype cell design. (Irreversible capacity loss <25% and 4-week self-discharge < 15% at 60°C)
5. Establish the economic feasibility of µpSi manufacturing process (<25 $/kg at 1300 mAh/g).

The outcome of this program was a validated novel manufacturing process to provide a source of microporous silicon for EV battery production. The Navitas team transitioned this process from MRL 3 to MRL 6 (Manufacturing Readiness Level), providing the ability to deliver µpSi in adequate quantity to support pilot

scale electrode coating by EV battery OEM's at the scale needed to support cell design validation (typically 500 – 600 cells in the EV battery cell format)

Approach

To accomplish these goals Navitas teamed with Nexceris and Argonne National Lab (ANL) to establish a reliable domestic source of µpSi. Nexceris provided powder manufacturing scale up development and expertise. ANL performed material characterization and gives input to improve material design and process optimization. Navitas advanced this process from MRL 3 to MRL 6, providing the ability to deliver µpSi in adequate quantity to support pilot scale electrode coating by EV battery OEM's at the scale needed to support cell design validation (typically 500 – 600 cells in the EV battery cell format).

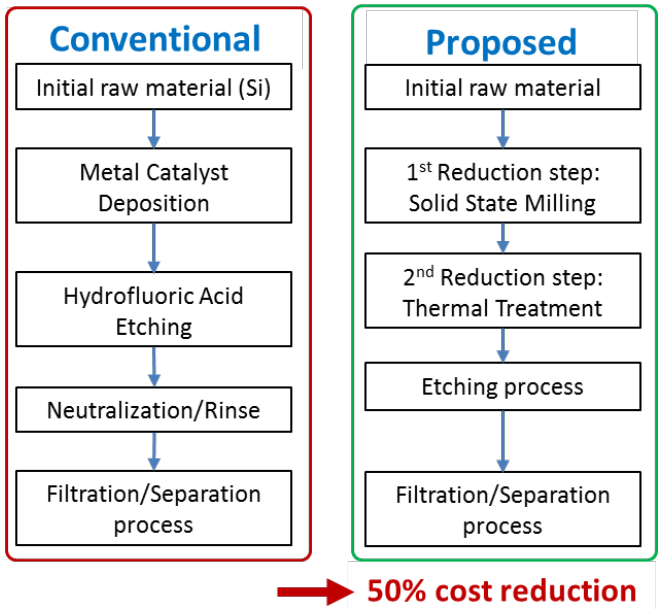

Figure I-74: Conventional production of porous silicon uses hazardous hydrofluoric (HF) acid and expensive metal catalyst. Navitas route reduces cost and impact, using SiO2 raw material and no HF.

The proposed µpSi production comprises a three-step process involving the usage of inexpensive commodity grade silicon oxide (refer to Figure I-74, Figure I-75, Figure I-76, and Figure I-77). Each step employs scalable industrial processing methods (i.e., mechanical mixing, thermal reduction, and etching). The combination of two steps reduces process temperature and times for the complete reduction silica, reducing operating cost compared to other methods. In addition, by avoiding usage of hydrofluoric acid, the proposed process also has environmental and non-hazardous advantages over the conventional route.

Results

In Budget Period (BP1), Navitas optimized µpSi powder fabrication process at lab scale and transferred thermal treatment and oxide removal process technology to Nexceris for scale-up. Navitas and ANL carried out detailed analytical characterization and electrochemical evaluation in a baseline nanocomposite anode design. The lab-scale µpSi powder met all the targeted properties (refer to Table I-12).

Table I-12: Physical properties of current µpSi powder

Property	Target	Actual
Particle size (µm)	5 - 50	10 - 30
BET surface area (m2/g)	< 200	28
Tap density (g/cm3)	> 0.6	0.63
True density (g/cm3)	2.0 – 2.4	2.2

Navitas and Nexceris developed a cost model for the µpSi manufacturing process. The cost model projected high volume (e.g., 1MT/month) manufacturing cost of µpSi at 50% lower cost than that of the conventional HF etching process. Further, a Si composite anode made with µpSi precursor will meet the EV Everywhere goal of $125/Wh for EV battery pack at anode cost < $25/kg (when combined with high Ni NCM cathode)

In Budget Period 2 (BP2), Navitas used Robust Engineering methods to optimize the mechanical milling process at an intermediate scale of 200g. The less influential parameters were relaxed to improve throughput and reduce milling time. Improved milling parameters were applied to large scale runs by an industrial milling partner who demonstrated results consistent with the lab scale powder. Navitas and the milling partner supplied enough milled precursor powder to Nexceris for the final demonstration.

Nexceris designed and built a thermal treatment furnace capable to process up to 10kg/batch. Calcination runs were conducted at 2kg scale. XRD diffraction analysis confirmed material composition and reproducibility. Additionally, Nexceris has designed and built the system for acid washing and powder filtration. The reactor can process > 4kg of calcined powder. Figure I-75 summarizes the progress under the program

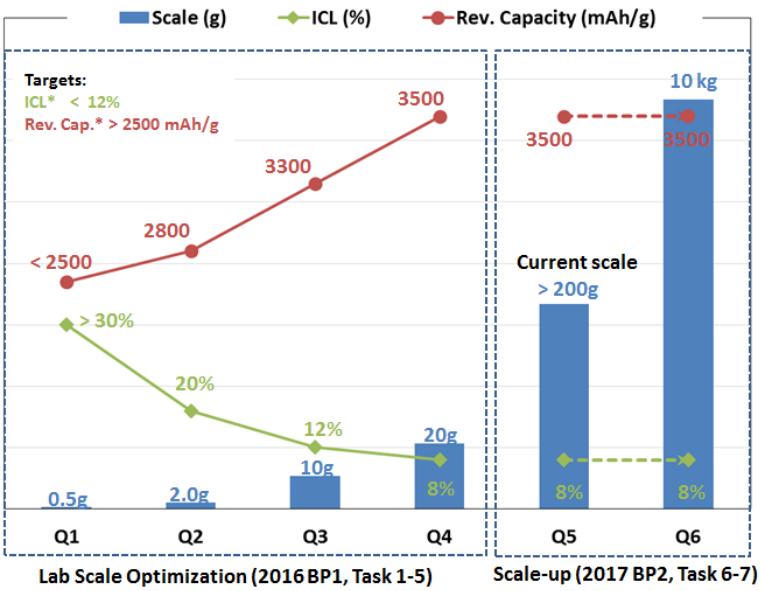

Figure I-75: Nearly theoretical capacity was reached as ICL was reduced to <10% as an indication that residual oxides were successfully removed. Batch size was scaled to multi-kg, adequate to support customer pilot scale electrode coating requests.

Navitas and ANL carried out analytical characterization, in addition to validation by electrochemical performance. The µpSi produced at 1kg/batch has shown a reversible capacity of ~3300mAh/g with an 8% ICL. The pilot scale µpSi powder met all the targeted properties (refer to Table I-12). The cost model

developed in BP1 was updated using data from the scale-up system. The model projects that the new processed µpSi powder costs 50% lower than the conventional HF etched powder.

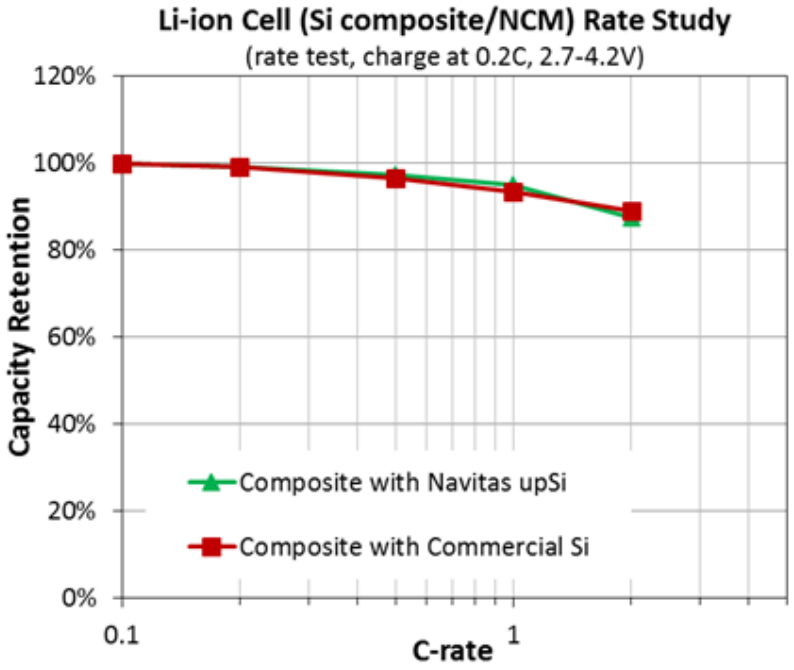

Figure I-76: Cells prepared using anodes incorporating Si composite anodes at EV battery loadings were able to meet cycle rate requirements and match commercial Si anode materials produced using higher cost materials and processes.

Full cells were assembled producing Si composite electrode using Navitas upSi. Rate and cycle life data are plotted in Figure I-76 and Figure I-77:

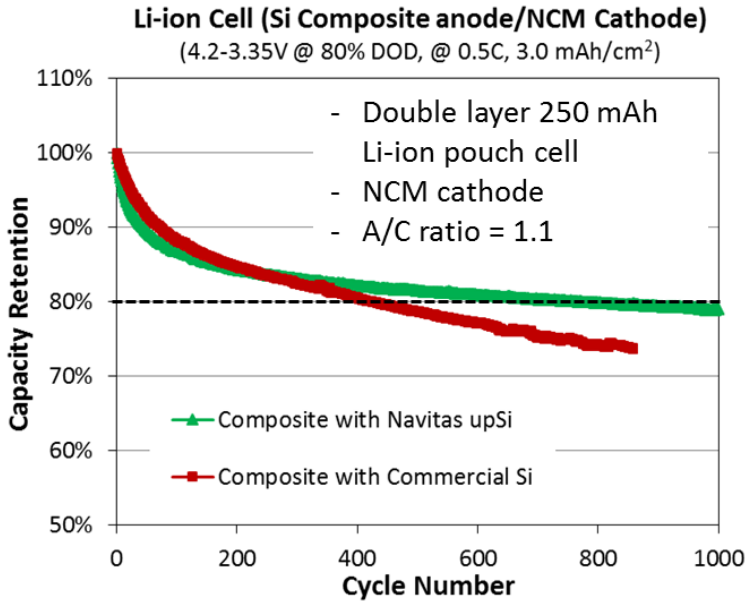

Figure I-77: In full cell testing at EV loading, Navitas showed 100% improvement in cycle life and was able to reach >900 cycles. The si anode was 92% active material having 650 mAh/g reversible capacity.

Conclusions

The Navitas μpSi fabrication process represents a novel approach to reduce the cost of silicon anode material manufacturing. This program met most of the MRL 6 criteria through a pilot scale demonstration for the manufacturing of porous silicon powder, while minimizing raw material added cost and limiting hazardous and environmental impact and using scalable industrial processing (i.e., mechanical milling, thermal reduction).

This process has been shown to be more efficient (higher yield) and economical on scaling up than conventional metal-assisted etching. The process significantly reduces the cost on $/mAh basis versus existing anode materials. The μpSi powders can be modified by customers to form nanocomposite structures through blending with graphite or coating with carbon or a metal oxide to decrease initial capacity loss (ICL) and improve cell cycle life, a key barrier to adoption of silicon anodes into EV batteries.

Key Publications

Processes to fabricate porous silicon and its use as feedstock for secondary battery electrodes
WO 2017008050 A1

Application number	PCT/US2016/041619
Publication date	Jan 12, 2017
Filing date	Jul 8, 2016
Priority date	Jul 8, 2015
Inventors	Peter Aurora, Pu Zhang, Michael Wixom

I.B.3 New Advanced Stable Electrolytes for High Voltage Electrochemical Energy Storage (Silatronix, Inc.)

Peng Du, Principal Investigator
Silatronix, Inc.
3587 Anderson Street Suite 104
Madison, WI 53704
Phone: 608-661-1964; Fax: 608-661-4630
E-mail: pdu@silatronix.com

Peter Faguy, Technology Manager
U.S. Department of Energy
Phone: 202-586-1022
E-mail: Peter.Faguy@ee.doe.gov

Start Date: October 1, 2015 End Date: February 28, 2018
Total Project Cost: $1,665,825 DOE share: $1,332,660 Non-DOE share: $333,165

Project Introduction

High-voltage mixed oxide cathode materials present several challenges due to their high chemical reactivity and electrochemical driving force at high cathode potentials. Uncontrolled surface reactions lead to significant decreases in capacity, increased cell resistance, and increased leakage current through the formation of SEI layers and leaching of metal ions from the oxides. In addition, carbonate electrolytes release CO_2 under oxidizing conditions, which leads to undesired surface film formation, as well as internal pressurization of the cell that can result in leakage or explosive release of the electrolyte. To date, no solvent system has been identified that meets all the requirements for compatibility with high-voltage cathodes including high electrochemical stability, low viscosity, wide temperature stability, and low cost.

Silatronix® is developing advanced, stable, high-voltage electrolytes to meet the DOE goals for electrochemical energy storage in transportation systems. Early generations of OS solvents have not been on Li-ion Road Maps, but recent Silatronix® innovations have created new OS3® solvents that exhibit exceptional electrochemical stability under the oxidizing conditions associated with high-voltage (HV) cathodes (exceeding 7V vs. Li/Li^+ before onset of significant parasitic breakdown current at Pt electrodes) and meet fundamental metrics (conductivity, viscosity) necessary for cell performance (i.e., rate capability, low temperature) in transportation applications and should therefore be considered for the roadmap.

Objectives

Silatronix® proposes to synthesize, characterize, and integrate novel solvents and additives into electrolytes to create the conditions necessary for reliable, long-lasting cells which operate at high-voltages (> 5V). This program will investigate the fundamental mechanisms of complex electrolyte behavior building upon advanced research by Silatronix® in new solvents and electrolyte formulations developed with these solvents. OS solvents have been shown to maintain synergy with existing electrolyte components, as well as advanced electrolyte salts and additives under development. Specific component materials developed by US Army Research Laboratory (ARL) for use in advanced electrolyte formulations will be evaluated for synergy with OS advanced solvents and used to demonstrate state-of-the-art voltage stability and commercially viable performance characteristics (e.g., rate). High voltage state-of-the-art electrodes from Argonne National Laboratory (ANL) and US Army Research Laboratory (ARL) will be evaluated with candidate formulations. The work plan includes the following specific targeted metrics to demonstrate electrolyte or electrolyte enabled performance:

- Synthesize, characterize, and integrate novel solvents and additives into electrolytes to create the conditions necessary for reliable, long-lasting cells which operate at high-voltages (> 5V).
    - Specific metric: oxidative stability in reference system (Pt electrode)
    - Prevent oxidative breakdown voltage above 6 V.
    - Provide parasitic current below 0.02 mA/cm^2 after 10 hours above 6 V at 50°C.
- Investigate the fundamental mechanisms of complex behavior of new solvent and additive materials within formulations containing commercial electrolyte components (solvents, salts, additives).
- Demonstrate commercially viable performance characteristics using state-of-the-art high voltage electrodes from Argonne National Laboratory (ANL) and US Army Research Laboratory (ARL).
    - Specific metric: cycling performance in 5V LNMO full cells
    - Full cell initial capacity ≥ carbonate control
    - Over 80% initial capacity after 300 cycles at ≥55°C

Approach

Silatronix® and ARL are synthesizing new materials based upon rational molecular design to achieve the superior oxidative stability required for HV applications. The fundamental electrochemical behavior of these materials is studied in reference cells to determine the oxidative breakdown voltage and mechanism of breakdown to produce a library of materials with superior fundamental oxidative stability for evaluation.

The performance and safety of the new HV solvents and additives in formulated electrolytes are evaluated with the HV cathodes provided by ANL (5V LNMO). Surface analysis is conducted after cycling to identify underlying mechanisms of degradation (i.e., surface film formation, metal dissolution, cathode morphology changes). Differential scanning calorimetry (DSC) is conducted on de-lithiated cathode material to understand the safety impact of the new HV materials. Solvation studies, using ESI-MS and NMR spectroscopy methods, is conducted to understand the Li^+ solvation behavior of the new OS solvents. These studies expand the understanding of the fundamental mechanistic behavior and include the relationship between the structure and properties of individual electrolyte components and the performance of a complete system. Top performing HV formulations identified are tested in 5V LNMO pouch cells (13 layers, 200-300 mAh) at ANL. The pouch cell analysis focuses on cycling stability and pouch swelling.

Results

Evaluation of New Solvents in Pt Reference Cells

In this program, Silatronix® synthesized more than 12 organosilicon (OS) solvents and characterized their physical properties and electrochemical behavior. These solvents include members of the high stability OS3® structural family and advanced OS4 family solvents which contain different functional groups than OS3®. Generally, these OS materials provided superior oxidative stability in Pt reference cells by linear scanning voltammetry (LSV) and constant voltage floating tests at 30°C and 50°C. As described in the 2016 report, four OS3® family solvents (OS3®, OS3a, OS3b and OS3c) with $LiPF_6$ salt satisfied the Go/No-Go Metric #1 (breakdown potentials > 6V at 30°C) and are good candidates for HV systems. Furthermore, the parasitic currents of these OS3® family electrolytes showed superior stability and satisfied Go/No-Go Metric #2 (50°C parasitic current <0.02 mAh/cm^2 at 6V). During this year, the oxidative stability of several more OS3® family solvents and two additional OS4 family solvents were evaluated in Pt reference cells using the same methods.

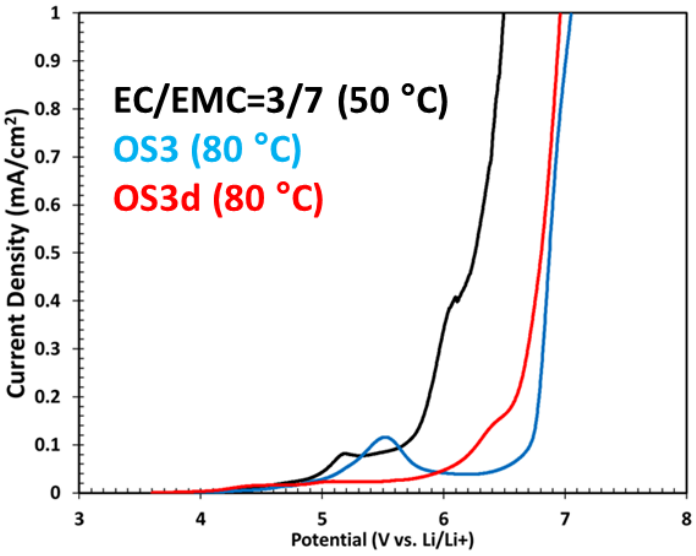

Figure I-78: Oxidative stability comparison at high temperature of OS3d vs OS3® vs carbonate control electrolyte.

Figure I-78 summarizes the oxidative stability (vs. Li/Li^+) measured at 80°C for OS3d (new OS3® family molecule made this year) and OS3®, and measured at 50°C for the carbonate control (EC/EMC, 3/7 %v). All electrolytes contain 1M $LiPF_6$. OS3d shows excellent oxidative stability between 5 and 6V. The measurement was conducted at elevated temperature as OS3d is a solid and does not dissolve $LiPF_6$ at room temperature. Figure I-79 shows the parasitic current behavior at 80°C for OS3d and OS3® with $LiPF_6$ in a 3-electrode cell (Pt: WE, Li/Li^+: CE, RE). Overall, the behavior at 5.0 and 5.5V is similar for OS3® and OS3d. Neither shows a significant current increase at these voltage levels. At 6.0V, OS3® does not show an increase in parasitic current while OS3d does (< 0.01 vs. 0.04 mA/cm^2). At 6.5V, both OS3® and OS3d show higher parasitic currents but OS3d has a significantly lower current density (0.06 vs. 0.16 mA/cm^2). Therefore, OS3d is a good candidate for the >5 V HV system.

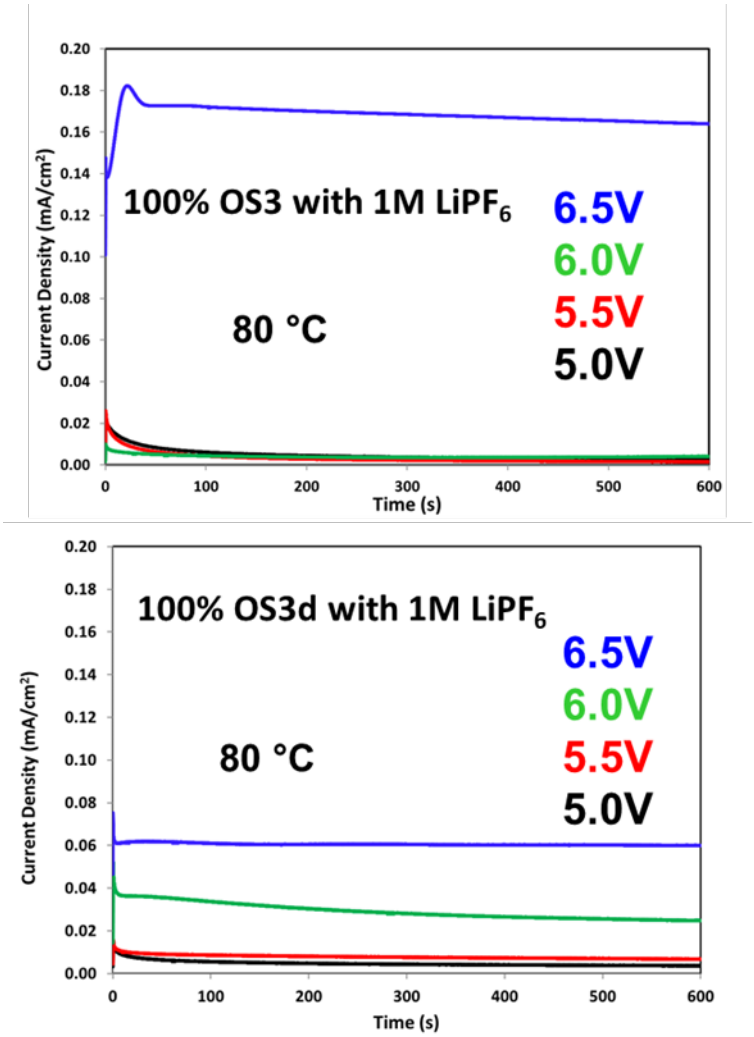

Figure I-79: Parasitic current results for LiPF6-based electrolytes in a 3-electrode cell (Pt: WE, Li/Li+: CE, RE).

In addition, OS4a and OS4b (OS4 family solvents) demonstrate a higher breakdown voltage than the EC/EMC carbonate control and OS3®, and will be evaluated in 5V LNMO full cell.

Full Cell Cycling and Stability Performance

ANL delivered single side coated 5V LNMO and MCMB electrodes to Silatronix® and ARL for the evaluation of advanced HV electrolyte materials. Initial screening of OS electrolytes was completed last year using a refined electrochemical method in both 5V LNMO half cells and full cells. Furthermore, cycling in LNMO half cells and full cells confirmed the importance of additives. The effect of OS3® concentration on full cell cycling performance was examined in coin cells previously in this program. Based upon the performance improvement observed for 2% OS3® and 5% OS3®, similar formulations were tested for OS3d, OS4a and OS4b. Figure I-80 summarizes the full cell cycling results for these new OS structures tested at the 2% concentration level. Both OS4 family molecules (OS4a – purple data, OS4b– green data) show improved capacity retention compared to the carbonate control. The enhanced stability OS3d (blue data) shows similar performance to the carbonate control blend. These OS formulations and the carbonate control have been selected for the first round of pouch cell testing at ANL. Each pouch cell undergoes formation (including de-gassing) followed by a rate test, HPPC test, and finally cycle life testing. All testing occurs at 30°C with a 3.5 to 4.9V voltage window.

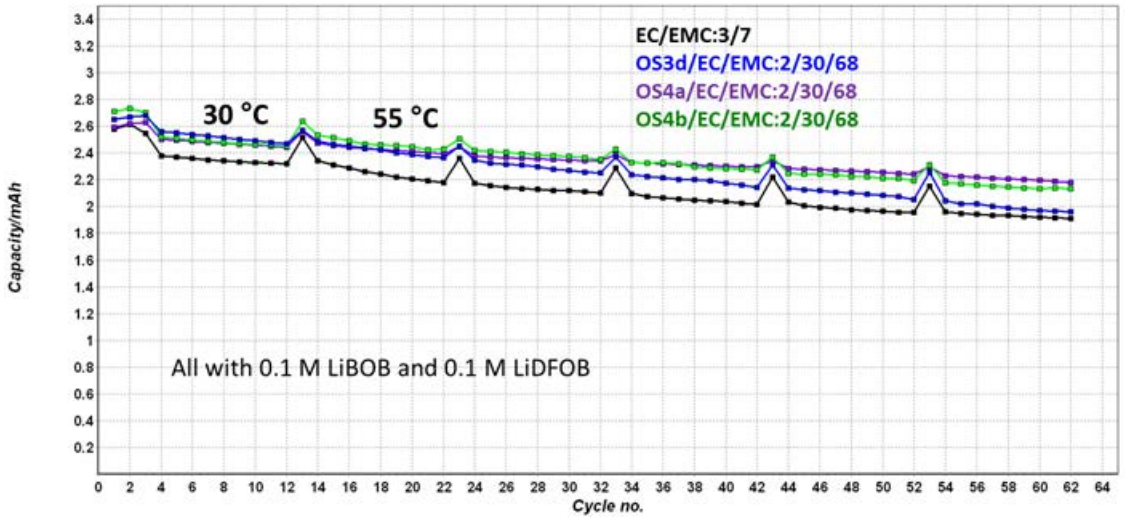

Figure I-80: Comparison of LNMO full cell performance with control carbonate electrolyte and 2% OS formulations (all with 1M $LiPF_6$). Cells are cycled at C/10 for 2 formation cycles and at C/2 for 10 cycles at 30°C, then continued 50 cycles at C/2 between 3.5 and 4.9 V at 55°C.

During the first round of testing, all pouch cells exhibited a large amount of gassing and the initial rate test could not be completed. After another de-gas step, the cells were transferred to the HPPC and cycle life tests. However, gassing continued and all cells failed quickly. Based on this result, this year Silatronix® continued the screening of HV electrolyte formulations in 5V LNMO cells focused on reducing gassing. In addition, Post-test degradation analysis was conducted, including XANES measurements at Argonne National Laboratory's Advanced Photon Source on beamline BM20 and SEM and XPS measurements at University of Wisconsin–Madison. The post-test degradation analysis serves to identify the composition of and evaluate the stability of the SEI layer and the bulk structure of the cathode active material after cycling.

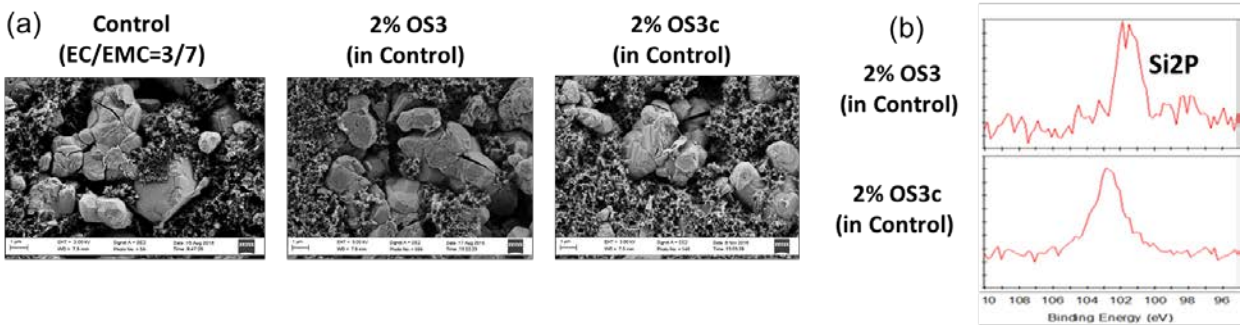

Figure I-81: (a) SEM images and (b) XPS surface composition data for the de-lithiated LNMO cathode after cycling (50 cycles at C/2 between 3.5 and 4.9 V at 55°C) with control carbonate and 2% OS3®, and 2% OS3c formulations. All electrolytes contain 1M $LiPF_6$.

Figure I-81 summarizes surface analysis data for 5V LNMO cathodes recovered from cells cycled with 2% OS3®, 2% OS3c and the carbonate control. The morphology of the electrode surfaces at 50% SOC was examined using scanning electron microscopy (SEM) to evaluate the SEI layer morphology and mechanical integrity. In Figure I-81a, the surface morphology of the cathodes is similar regardless of the specific electrolyte formulation. Therefore, the addition of 2% OS3® or 2% OS3c does not significantly affect the thickness and morphology of any surface layers formed on the LNMO cathode. Information regarding the composition of any surface layers formed on the LNMO cathode was obtained using X-ray photoelectron spectroscopy (XPS). Figure I-81b shows data from the Si(2p) regions for the cathode surface layers formed with 2% OS3® and 2% OS3c formulations. XPS surface analysis showed silicon present on cathode samples

after cycling with 2% OS3® and OS3c electrolytes, indicating that OS solvents are involved in cathode film formation. Similar results were obtained for anode samples after 50 cycles at 55°C, which means OS solvents also participate in anode SEI formation. Due to the gassing issues observed in the first pouch cell-build, post cell analysis using X-ray absorption spectroscopy (XANES) was performed to identify the stability of the bulk structure of the cathode active material. XANES spectra show more apparent shifts are present in the Ni K-edge data compared with Mn K-edge data, which indicates the oxidation of Ni(III) to Ni(IV) is the major contributor of this LNMO cathode, and the Li lost during cycling is more related to Ni-bonded Li rather than Mn-bonded Li. Among different electrolyte formulations, little to no change in the crystal structure is observed with or without OS molecules. This trend does not agree with the cycling performance differences observed and suggests the cathode/anode SEI layers lay a major role in cycling performance.

ESI-MS experiments were continued this year at ARL to investigate the Li^+ solvation behavior of OS3®/EC/EMC and OS3d/EC/EMC electrolytes. A summary of the results is shown in Figure I-82 and Figure I-83. Both OS3® and OS3d consistently coordinate with Li^+ more strongly than EC or EMC. Clusters of Li^+ with two solvents were the best represented in ESI-MS data. OS3d has a larger population of OS3d+EMC clusters than OS3d+EC, which is the most common OS3®/carbonate cluster. OS3d also shows lower populations of all non-OS3d clusters in general. Figure I-83 shows that OS3d appears to displace carbonate solvents from the Li^+ solvation sheath more than OS3® and is a stronger Li^+ solvator than OS3®.

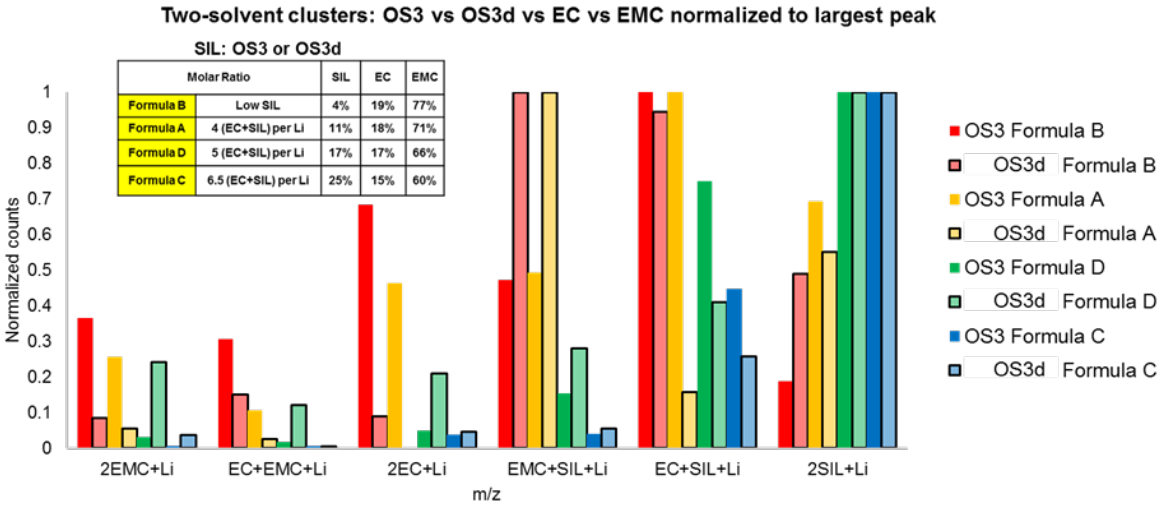

Figure I-82: Normalized ESI-MS counts as a function of cluster for OS/EC/EMC electrolyte formulations.

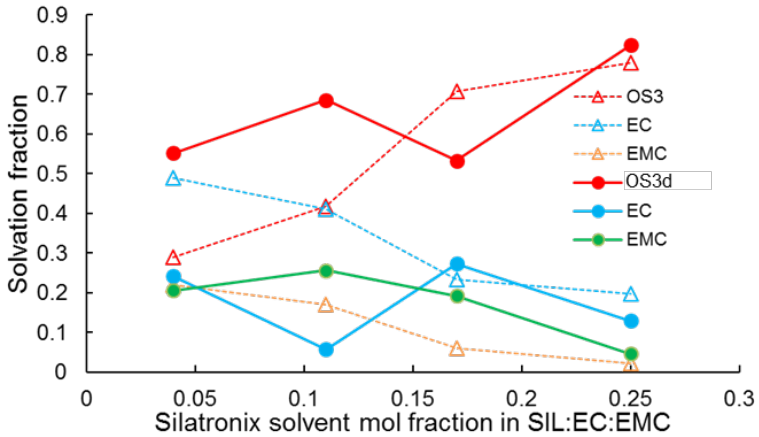

Figure I-83: Calculated fraction of bulk solvents participating in solvation based upon ESI-MS results in the previous figure.

Since the analysis of Li^+ solvation in HV electrolytes using an ESI-MS technique demonstrates that OS3® or OS3d compete well with EC for solvation of Li^+ and may contribute to the formation of SEI layers, Silatronix® performed Li^+ solvation studies using ^{13}C and ^{15}N NMR spectroscopy to evaluate Li^+ solvation behavior in the bulk solution. The competition between OS3® family solvents and commercial carbonate solvents (EMC, EC) was investigated in binary mixtures. Results show that OS molecules participate in Li^+ coordination in all electrolytes tested and certain modification of the functional group on the silicon can enhance or impede competition with EC and EMC.

Finally, due to the gassing issue observed in the 1st pouch cell-build, the 2nd pouch cell-build at ANL has focused on electrolytes with higher EMC content (lower EC content) and newer OS solvents (e.g, OS3d and OS4b). In addition, we revised our pouch cell testing plan to run the same test steps (Formation, Rate Study, HPPC and Cycle Life) with the new voltage window of 3.5-4.7 V to further reduce gassing. ARL also continued the electrolyte optimization in higher EMC content formulation using different HV additive packages. The results demonstrate that despite initial improvement in 30°C cycling capacity by all additives, only the HFIP additive exhibits high temperature stability and reliably improves high temperature cycling performance. Since the FEC containing electrolytes also showed gassing, additive optimization has focused on HFIP or borate additives (e.g., LiBOB, LiDFOB). Based on previous coin cell and pouch cell testing results, 8 high voltage (HV) electrolyte formulations were selected by Silatronix® and delivered to ANL for testing. Cells containing three HV electrolytes finished cycle life testing (422 cycles total) with ~70% capacity retention, which is superior to the carbonate control (~50% capacity retention after 222 cycles). Based on pouch cell cycling results from this round, six more electrolytes were optimized at Silatronix® and delivered to ANL in Q8. Cycle life testing and gas generation for these formulations are in progress and will be summarized in our final program report.

Conclusions

The focus of this program is the fundamental evaluation of high stability OS solvents and performance of OS-containing high voltage (HV) electrolyte formulations in 5V LNMO full cells. All OS molecules evaluated in this year demonstrate similar properties as previously tested OS molecules, including higher flash points than the carbonate control (EC/EMC, 3/7 %v). Superior oxidative stability (above 6V) is observed for new OS molecules in reference cells (Pt) by linear scanning voltammetry (LSV) and floating current testing. Full cell testing found that the addition of 2% OS3®, OS3d, OS4a and OS4b improves the 55°C cycling performance by reducing capacity degradation across 50 cycles compared to the EC/EMC control. ARL continued the analysis of Li^+ solvation in HV electrolytes using an ESI-MS technique, which demonstrates that both OS3® and OS3d consistently coordinate Li^+ more strongly than EC or EMC. Clusters of Li^+ with two OS are the best represented in ESI-MS data. Silatronix® continued the analysis of Li^+ solvation in HV electrolytes and results show all OS solvents participate in Li^+ solvation in EC and EMC binary mixtures at all tested carbonate concentrations. XANES spectra found little or no change in the crystal structure of the LNMO cathode based upon electrolyte formulations (with or without OS). This suggests the cathode and anode SEI layers are a key factor for cell performance. Due to the gassing issue observed in the first pouch cell-build, full cell testing has focused on electrolytes with higher EMC content, lower OS solvent concentration, and a reduced voltage window (4.7 vs 4.9V). To date, several electrolytes completed both the initial cycle life testing (222 cycles) and an additional 200 cycles. These formulations demonstrate much better cycling performance than the carbonate control. A final cycling testing and gas generation study are in progress to examine the behavior of the final six optimized HV electrolytes.

I.B.4 Improve the Safety Performance of Li-ion Battery Separators and Reduce the Manufacturing Cost using Ultraviolet Curing and High Precision Coating Technologies (Miltec UV International)

Dr. John Arnold, Principal Investigator
Miltec UV International
146 Log Canoe Circle
Stevensville, MD 21666
Phone: 410-604-2900; Fax: 410-604-2906
Email: gvoelker@miltec.com; jarnold@miltec.com

Peter Faguy, Technology Manager
U.S. Department of Energy
Phone: 202-586-1022
Email: Peter.Faguy@ee.doe.gov

Start Date: October 1, 2014 End Date: June 30, 2017
Total Project Cost: $2,354,000 DOE share: $1,955,000 Non-DOE share: $399,000

Project Introduction

This project was successfully completed this year. A commercial scale system (Miltec CX400) utilizing flexographic printing technology and UV curable binder was designed, built and operated to demonstrate the cost saving and performance enhancing potential of UV technology for the manufacture of ceramic coated separators. Polyethylene or polypropylene or layered polyolefins PP/PE/PP are the most common separators for Li-ion battery separators. These thermoplastic separators typically melt between 130-160ºC. While these temperatures are well above the normal operating temperature of lithium batteries, in the rare event something goes wrong, these temperatures can be reached. At such elevated temperatures, they can easily shrink to 60% of their original size—at that point they are not preventing the anode and cathode from touching, so the battery escalates from being too hot to being on an irreversible thermal runaway path until the battery dies or ignites. To prevent high temperature shrinkage and provide better structural strength and insulation, separator manufacturers are coating separators with a thin ceramic layer. (See Figure I-84.) Ceramic coated separators are considered an essential safety component of any large or high energy density battery, including EV or hybrid car batteries. The objective of this cost shared contract was to develop and demonstrate safer coatings and less expensive processes for ceramic coated separators. It is the intent of this project that the development of this technology will lead to safer vehicle batteries and faster incorporation and acceptance of hybrid and electric vehicles.

Objectives

The project had multiple objectives:

- To further develop and demonstrate the use of Ultraviolet (UV) curing technology to reduce the cost of applying ceramic coatings onto Li-ion battery separators by more than 50% while not decreasing the porosity of the separator by more than 10% and improving the safety attributes by reduced shrinkage and overall reduced risk of thermal runaway. Previously identified UV curable binders and associated curing technology will be shown to reduce the time required to cure separator ceramic coatings from tens of minutes to less than one second. This can result in increases in process speeds and significantly reduced capital cost, operating cost, and energy consumption.

- Develop and exercise a cost model to verify the cost savings.
- Investigate the use of patterns applied with high speed coating technology to improve the safety and performance of ceramic coated separators as well as reduce the cost of separators in a Li-ion battery.

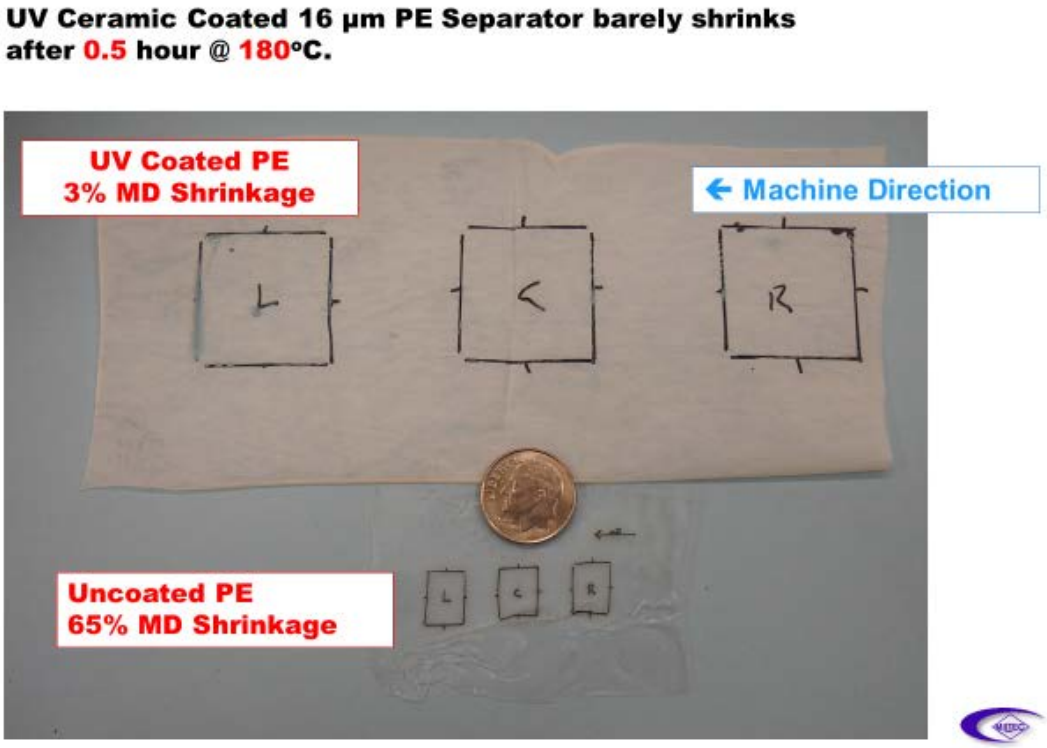

Figure I-84: PE Separator Shrinkage with and without UV Ceramic Coating

Approach

This project employed an iterative process of technology evaluation, implementation, testing, and resulting optimization. Multiple samples of ceramic coated separators were prepared using a combination of various UV curable binder chemistries and printing patterns. Multiple analytical tests were conducted to determine characteristics such as: porosity, tear strength, thermal transfer, puncture strength, thermal shrinkage, and permeability. At the end of this iterative development, printing patterns and optimum UV chemistries and base separator materials were coated using the Miltec UV CX400 and ceramic coated separators were prepared for extensive evaluation. Miltec received separator base material from various vendors; including Celgard, and applied either single or double sided ceramic coatings using the UV CX400 unit. After in-house testing, the coated samples were submitted to the vendors for extensive further evaluation. ANL conducted electrochemical and physical tests on the cells as well as the analytical tests. In addition to a UV curing process, we have developed a flexographic coating process specifically designed for separators to print and change patterns at a fraction of the cost. The ability to print patterns is another innovation of this project. By printing patterns, we should be able to maximize ionic flow through the separator while still providing the protection of a ceramic layer and reinforcing the separator against thermal shrinkage.

Results

The specific performance goals are shown in the tables below.

Table I-13: Performance Goals for Ceramic Coating Applied to 16 μm Trilayer, PP and PE

Parameter	Goal
Ceramic coating thickness and material	4 μm Aluminum Oxide (0.5-1 μm diameter.)
Gurley # (permeability) of coated separator	<10% increase over base uncoated separator
Shrinkage, Trilayer, and PP	MD <5% at 1 h, 150ºC TD <3% at 1 h, 150ºC
Ceramic coating cost	<$0.20 /m^2
Reduced thickness base separator	6-10 μm

Table I-14: Demonstrated Results

	Uncoated		Shrinkage			Coated		Shrinkage		
	Thickness, μm	Gurley's	130	150	180	Thickness, μm	Gurley's	130	150	180
PP	16	12	12.50%			6	21	1.10%		
trilayer	20	19	23.10%	29.30%		4	23		0.70%	
PE	14	6.7		40%		3+	9		1.60%	
Cellulose	25	1.4		0%		3+	2.5		0%	
UHMWPE	14	6		55%		4	11	(double sided coating of 2 μm)		4 %
PE	12	8.8	13.80%			1	11.1	2.20%		
PE	5	4.3	24.30%			1	5.9	7.50%		

As shown in Table I-14, the performance goals related to the use of a UV binder for shrinkage and permeability preservation for PP were all met or exceeded, with the exception of Gurley #. The interim goal of the project for PE was designated as 5% at 130ºC and that value was obtained with the exception of one PE separator of 5 μm thickness. The 5 μm thick separator with a 1 μm thick costing reduced the shrinkage from 24% to 7.5% at 130C.

As an additional process advancement we incorporated the flexographic process (Figure I-85) with our UV process. UV will work with roll and all forms of gravure, but there are advantages to the flexographic process. The accuracy of the flexographic process far exceeds that of the separator industry. Note the separator film does not go through a bath, when the press starts and stops the plate cylinder engages and disengages the film. This makes film and coating changeovers, cleaning, and many other processes quick and easy.

Besides introducing the concept of flexographic printing to the separator industry, we introduced the concept of printing ceramic patterns instead of the conventional solid coatings. The primary advantage of the patterned ceramic coating is that it allows more ion flow than the solid coating, while providing less shrinkage and more insulation than that of the uncoated separator. Many patterns were printed and tested for shrinkage. The pattern shown in Figure I-86 where the cross hatch is line with the MD and TD directions of the roll was most effective at reducing shrinkage.

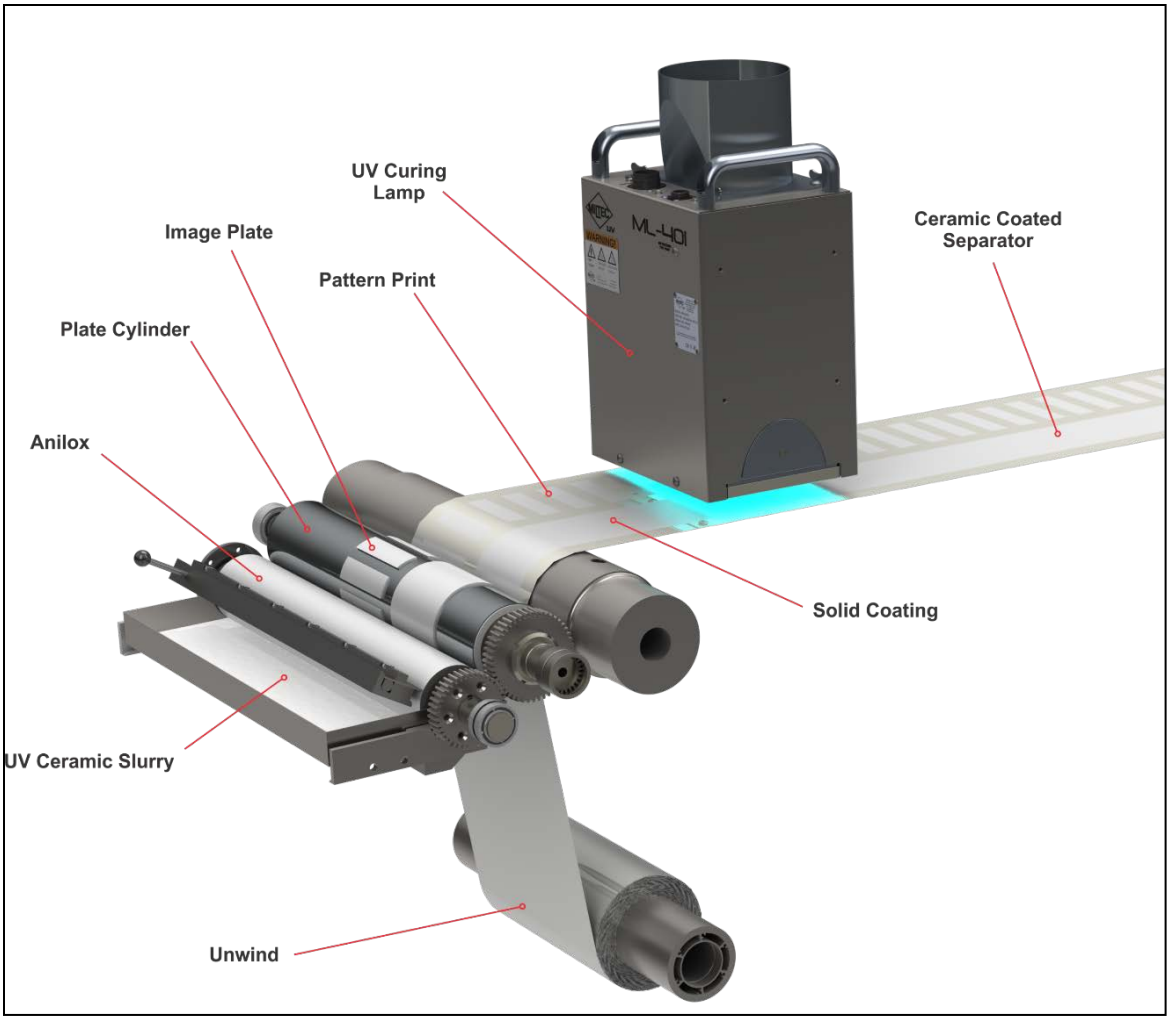

Figure I-85: In the flexographic process, the anilox meters the coating to the image plate which like a rubber stamp transfers the image to the separator. As shown, the left side is printing a pattern and the right side is printing a continuous coating.

Besides the advantage of ion flow and shrinkage reduction, there is 39% reduction in coating weight for the pattern shown in Figure I-86 versus that of a solid coating.

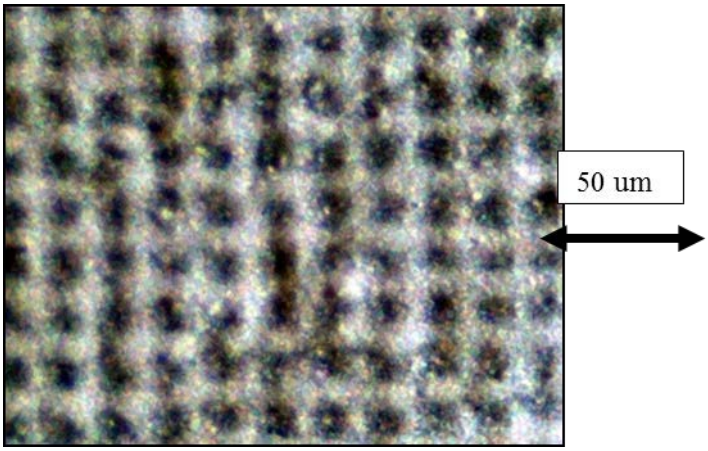

Figure I-86: Image of UV ceramic coated separator. The white ridges are the rigid coating that inhibits thermal shrinkage and holes allow more ion flow.

When we initially proposed the idea of pattern coatings, one objection raised by industry was that the differential ion flux through the separator might lead to dendrite growth.

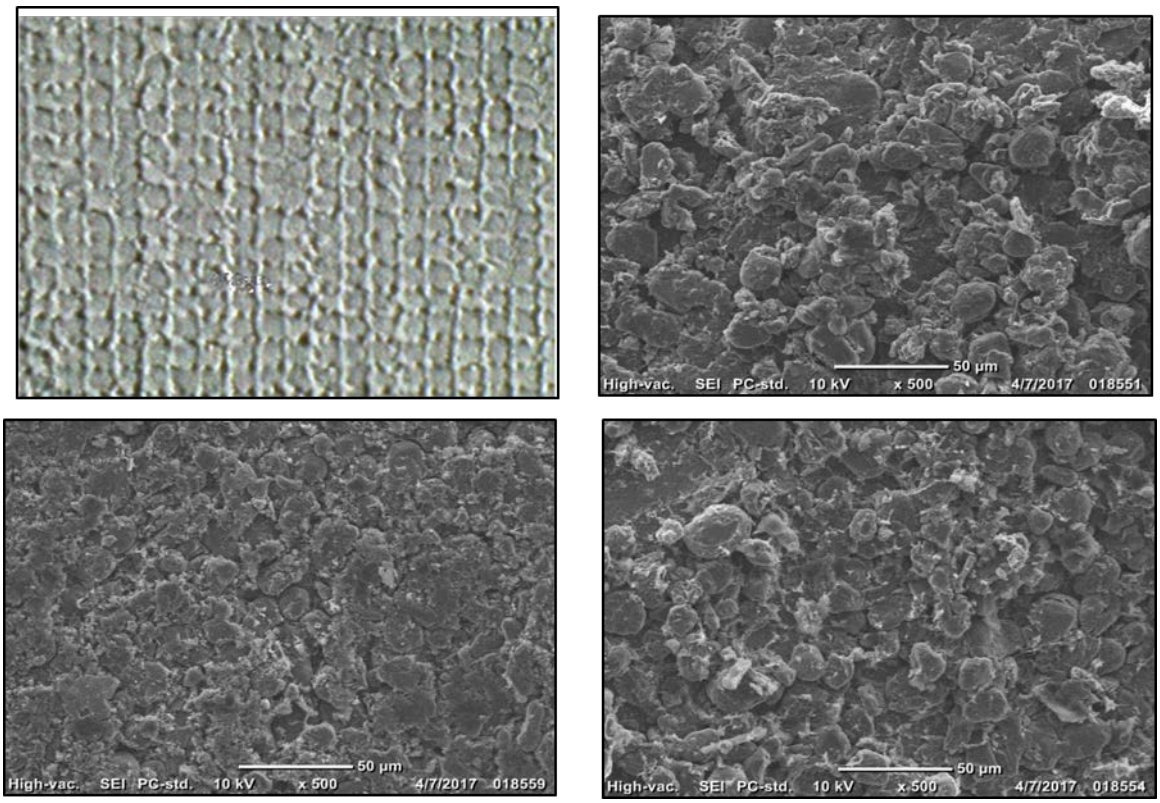

Figure I-87: Deeply lithiated graphite anode shows no mirror pattern of patterned coated separator. 10 x 10 Pattern Coated separator (upper left). Lithiated anodes with uncoated separator (upper right), solid coated separator (lower right), and pattern coated separator (lower left).

To evaluate this concern, we built coin ½ cells using a graphite anode. After 300 cycles, dendrites clearly grew. However, the dendrite growth showed no mirror pattern of the printed separator nor was there difference between the anodes for the uncoated and coated separators (Figure I-87). Therefore, we conclude that pattern

printed ceramic coatings on separators do not lead to significantly more dendrite growth than standard separators.

The initial coating experiments were conducted on a laboratory scale flexo coater and UV curing continuous line. From the successful operation of this unit, we developed design criteria for a commercial scale flexo coating and UV curing system capable of coating continuously up to 400 fpm.

The commercial scale coater/UV curing system called the CX400 (Figure I-88) was designed specifically to handle super thin polyolefin separator material with superior web handling, edge control, tension control and high-speed precision coating. The CX400 was designed to handle 440 mm wide separator material and operate at 400 fpm and 10 µm separator material. Miltec has successfully coated 5 µm thick separator material on the CX400. The CX400 has minimum unsupported web and a chill drum to achieve precise tension and separator temperature control. The separator is fully supported from nip to coating, drying, curing, and rewind to eliminate unsupported stress. It has a very small footprint and precise thickness control of <1 µm.

Figure I-88: Commercial Scale Coater, CX 400

Conclusions

By successfully completing this project Miltec UV has demonstrated:

- Precision single and double sided ceramic coatings (2-4 µm in thickness) on multiple base separator materials using a commercial scale machine (400 mm width and processing speeds to 130 m/min) that result in porosity decreases less than 10% and final shrinkage from 1-5% depending upon base material, temperature and time meeting USABC Li-ion battery separator requirements.
- Demonstrated the application of patterned ceramic coatings resulting in 39% material savings with no reduction in performance and demonstrated no additional dendrite growth as a result of the patterned ceramic coating.

- Developed and exercised a cost model to show a ceramic coating can be applied for less than $0.20/m2 and further reductions to $0.09/m2 are achievable with alternate ceramic materials.

Key Publications

1. Gary Voelker and Dr. John Arnold gave a presentation on the merits of UV binder for ceramic coated separators to the DOE USCAR representatives from Ford, Chrysler, GM and EPRI in Detroit May 17, 2017

2. Miltec UV had an exhibit with visuals and a video presenting the progress on UV binder for ceramic coated separators at the International Battery Conference, Fort Lauderdale, FL in March 2017 and the Battery Show, Novi, MI September 2017.

3. John Arnold presentation titled *UV Coating Processes to Enhance Li-ion Battery Performance and Reduce Costs* to the Electrochemical Society meeting at National Harbor Fall 2017.

4. Miltec UV website presenting details on the performance and potential for ceramic coated separators. http://www.miltec.com/technology/battery/uv-ceramic-coated-separators/

I.B.5 Co-Extrusion(CoEx) for Cost Reduction of Advanced High-Energy-and-Power Battery Electrode Manufacturing (PARC)

Ranjeet Rao, Principal Investigator
Palo Alto Research Center (PARC)
3333 Coyote Hill Road
Palo Alto, CA 94304
Phone: 650-812-4373
E-mail: ranjeet.rao@parc.com

Peter Faguy, Technology Manager
U.S. Department of Energy
Phone: 202-586-1022
E-mail: Peter.Faguy@ee.doe.gov

Start Date: December 1, 2015 End Date: August 31, 2019
Total Project Cost: $3,790,000 DOE share: $3,000,000 Non-DOE share: $790,000

Project Introduction

Most strategies for increasing the performance and reducing the cost of lithium-ion batteries have focused on novel battery chemistries, material loading modifications, and increasing electrode thickness. Increasing electrode thickness is a known approach to increase energy density and in turn overall cell capacity. However, practical thicknesses are constrained by ionic transport limitations that occur with increasing thickness, limiting cell power. We believe PARC's Co-Extrusion (CoEx) technology can overcome this limitation, enabling a substantial improvement in the performance of thick electrodes for most lithium-ion chemistries. CoEx has the potential to disrupt current manufacturing processes and enable the DOE 2022 goal of $125/kWh by enabling the simultaneous deposition of alternating regions of high ionic transport and high lithium density

Objectives

Our overall project objectives are to demonstrate Co-Extrusion (CoEx) printing technology at electric vehicle (EV) relevant scales by assembling large, 14 Ah pouch cells. These pouch cells will demonstrate an estimated ≥ 30% reduction in $/kWh costs through thick, structured high energy and high power electrodes, and a gravimetric energy density improvement of ≥ 20% relative to conventional electrodes of the same chemistry.

Approach

Co-Extrusion (CoEx) Cathode

Co-Extrusion (CoEx) is a deposition technology developed at PARC that uses engineered fluidic channels to cause multiple streams of dissimilar fluids to impart shape to one another [1]. The result is a high-speed, continuous deposition process that can create fine structures much smaller than the smallest physical feature within the printhead. By eliminating the small channels necessary for conventional extrusion and injection processes, CoEx is able to deposit highly loaded and viscous pastes at high process speeds under reasonable operating pressures. Depending on particle size, the CoEx process is capable of direct deposition of features as small as 25 µm with aspect ratios of 5 or greater, and print speeds > 400 mm/s (~80 ft./min). A CoEx printhead can serve the same function as the slot die printhead in modern battery manufacturing lines, depositing the electrode slurry onto the current collector web in a continuous roll-to-roll process. The thicknesses, widths, and lengths of the deposited CoEx features are dependent on the internal printhead geometry, slurry rheology, and process conditions. The precise flow paths are constructed out of a stack of replaceable printhead layers that can be easily exchanged, allowing for precise tailoring of the final deposited features within a single printhead design. PARC's scale-up of CoEx batteries for EVs builds on a solid base of experience in applying CoEx to solar cell manufacturing [2]. We have chosen a commercially relevant chemistry, $LiNi_{0.5}Co_{0.2}Mn_{0.3}O_2$ (NCM

523) and our strategy will be to scale the technology from coin cells (BP1) to 14 Ah pouch cells (BP3) by project completion. Our partner, Ford Motor Company, will provide PARC with baseline cell specifications in addition to EV-relevant cell characterization on the pouch cells developed during the course of the project.

High Capacity Graphite Anode

While PARC will use CoEx to develop thick, high performance cathode electrodes, ORNL will develop the thick, high capacity anode that will match the CoEx cathode. In addition, they will utilize ORNL's Battery Manufacturing Facility (BMF) to fabricate small scale pouch cells in BP2 and assist PARC with technology scale-up on ORNL's roll coater, in addition to running electrochemical rate and cycling tests. As part of the anode development, ORNL will refine graphite-based anode slurries for improved coating adhesion, agglomerate cohesion, and high ionic and electronic conductivity by modifying binder and conductive additive. Anodes will be prepared with an NMP/PVDF solvent/binder system and slot-die coated to a sufficient thickness to balance the CoEx cathodes. Beginning with baseline anode coatings with targets of 50-80 µm in thickness after calendering, 2.5-30 mAh/cm^2 in loading, and capacity > 350 mAh/g, ORNL will then work to demonstrate anodes that are thick (125 – 200 µm) to match the high capacity CoEx cathodes. These anodes will be shown to maintain their integrity after drying and calendering to 30-40% porosity.

Results

Co-Ex Cathode Modeling Results

CoEx modeling focused on three different CoEx models, cross-sections of which are outlined in Figure I-89a. Each structure is composed of the two alternating regions which would be created by CoEx inks that are co-deposited. For all of these structures, Region 1 is fixed to be a 90/5/5 composition of NCM/PVDF/Acetylene Carbon Black (ACB) by weight ratio, with volume fractions for the active material, inactives (PVDF and ACB), and electrolyte of 0.512, 0.152, and 0.336, respectively. The main difference between the structures is the nature of Region 2. For CoEx Structure Type 1, Region 2 is modeled as pure electrolyte, *i.e.*, 100% porosity. For CoEx Structure Type 2, Region 2 is modeled as a porous NMC electrode like Region 1, but with a higher porosity. CoEx Structure Type 3 is a hybrid design in which Region 2 is compositionally similar to Region 1, but is much thinner. A standard macrohomogeneous porous electrode model [1,3,4] was implemented in COMSOL [5] and extrapolated to two dimensions to capture the cross-section of the CoEx cathode geometry. The FY2016 report outlined our modeling results for the three types CoEx Types. These results are summarized in Figure I-89b, which shows gravimetric vs volumetric energy density for the highest performing structures (CoEx Type 1 and 3) as well as the baseline case. The thickness indicated in the legend is the thickness of Region 1, and for CoEx Type 3 structures the pad thickness is 50 and 70 µm for Region 1 thicknesses of 120 and 170 µm, respectively. Unless otherwise noted, the ratio of the width of Region 1 and Region 2 is 4. In general, modeling shows that CoEx Type 1 structures show higher gravimetric energy density but minimal gravimetric energy density benefit except for the case of extreme thickness (170 µm) or a high Region 1 / Region 2 ratio of 9. By contrast, the CoEx Type 3 structures are predicted to show an increase in both gravimetric and volumetric energy density even at moderate thicknesses and structure ratios.

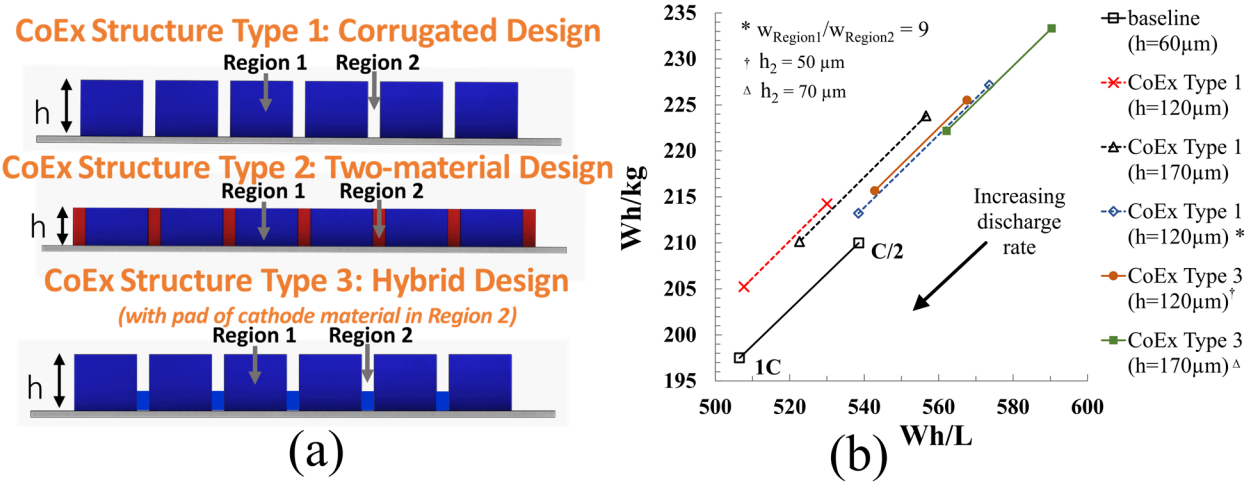

Figure I-89. (a) Schematic of different CoEx cathode geometries. (b) Summary of CoEx Type 1 and 3 modeling results, plotting gravimetric and volumetric energy densities as a function of discharge rate and CoEx geometry

Co-Ex Cathode Print & Electrochemical Results

Based on the modeling work above, cathode electrode structures were printed with the goal of replicating the CoEx Type 3 topology. The CoEx printhead takes two different battery ink formulations as input, which form Regions 1 and 2 when deposited. While the Region 1 formulation has the standard 90/5/5 (NMC / PVDF / Carbon Black) formulation as described in the modeling work in the previous section, the Region 2 ink formulation was modified with a higher solvent content such that upon drying, Region 2 would experience greater shrinkage, resulting in the "corrugated" structure seen in Figure I-90. Figure I-90 shows thickness profile measurements for CoEx cathode prints comparing three different Region 2 formulations. These thickness profile measurements were performed using a Stil chromatic confocal sensor on electrodes in the dried state, and a best effort was taken to overlay scans to align Region 1 and 2 between the different electrodes. The measurements shown are taken after calendering, showing that the CoEx structure is maintained after this standard electrode processing step. As can be seen, the main difference between these prints is the amount of material present in Region 2, with a minimum thickness ranging from approximately 5 µm (close to the CoEx Type 1 structure) to 80 µm. Region 1 thickness is similar for all three prints. Due to slumping during the drying process, the shape of Region 2 is more triangular rather than the rectangular shape that was modeled.

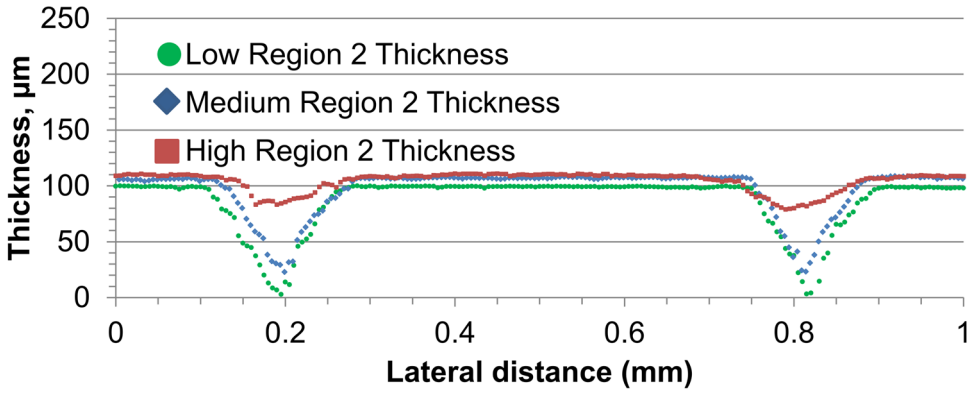

Figure I-90. Confocal profilometry scans of CoEx Type 3 structures, illustrating how electrode thickness varies orthogonal to print direction.

In order to test the effectiveness of CoEx electrode structuring, these cathodes were tested in half-cell configuration, the results of which are shown in Figure I-91 displaying (a) specific capacity vs. discharge rate and (b) specific capacity vs. discharge current. In these plots, we compare the three CoEx cathodes described above to the baseline electrode as well as a thicker, homogenous (unstructured) cathode that more closely matches the active material loading of the CoEx electrodes. Median values of the ~ 12 coin cells in each configuration are plotted, with a quadratic fit included to guide the eye. The legend below indicates the thickness of the electrode in Region 1 as well as the active material loading. A few conclusions can be drawn from these data. For one, all the CoEx cathodes perform similar to the baseline at discharge rates up to D/2, with performance dropping off at higher rates. Secondly, the CoEx cathodes perform much better than the unstructured electrode of similar loading, showing that the CoEx structuring is enabling greater utilization of the electrode. In fact, when plotted with respect to discharge current, which advantages thicker electrodes, the two CoEx electrodes with the thickest Region 2 pads outperform the baseline electrode. Based on this data, we can extrapolate the expected energy density improvement at the pouch cell level. If we consider a theoretical 1 Ah pouch cell, use of thicker CoEx cathodes results in fewer inactive layers (*i.e.*, current collectors and separators) compared to the baseline cathode. Using this simple geometric scaling argument, CoEx cathodes with a thick Region 2 are expected to show an improvement of approximately 10% in gravimetric and volumetric energy density at C/10 compared to the baseline condition. At C/5, the advantage is approximately 5%.

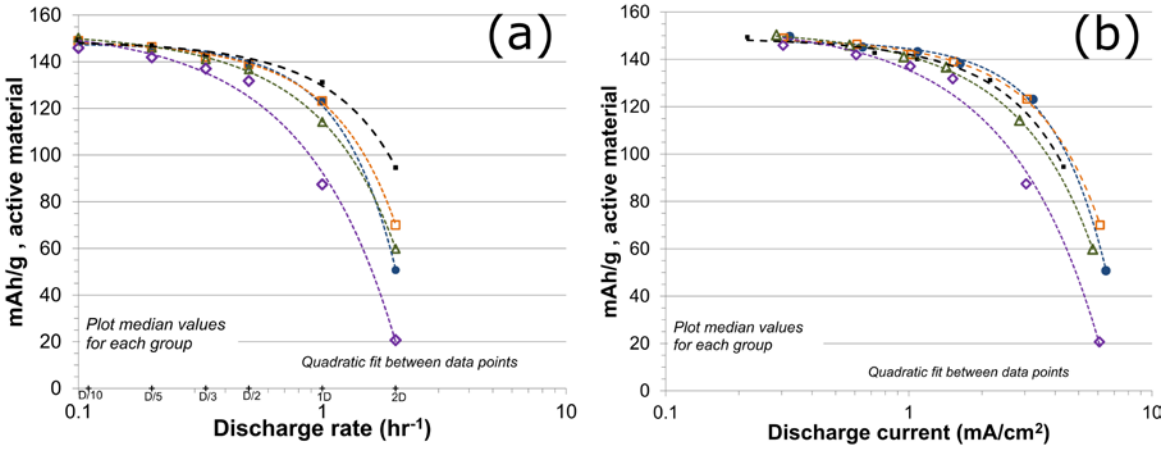

	Thickness (µm)	Active Material Loading (mg/cm²)
Baseline	69	15.8
Thick homogeneous	94	22.2
CoEx, Thin Region 2	102	21.6
CoEx, Intermediate Region 2	108	23.2
CoEx, Thick Region 2	113	24.7

Figure I-91. Specific capacity vs (a) discharge rate and (b) discharge current for a variety of CoEx Type 3 structures compared to baseline and thick homogeneous cathode electrodes.

Slot-Die Coated Anodes

In order to perform a more accurate rate performance comparison between a wider range of graphite materials, we made four additional slot-die coated anodes to compare with the Showa Denko and Hitachi MAGE 3 coatings made previously. These additional graphite materials were chosen based on their excellent electrochemical performance in our previous half coin cell tests carried out with doctor blade coatings. The rate performance of these four additional anodes was evaluated at two different areal capacities (~2.6 mAh/cm^2 and ~6 mAh/cm^2) in half coin cells using 1.2M $LiPF_6$ in 3:7 wt% EC/EMC electrolyte. Results for all six slot-die coated anodes (including the two coated previously) are plotted in Figure I-92.

While the performance of all six graphites was similar at 2.6 mAh/cm^2 below 1C discharge rates, Showa Denko and Superior SLC 1520T demonstrated slightly higher capacity retention at discharge rates ≥ 1C. While the, ConocoPhillips A12 and GrafTech APS19 showed slightly higher capacity retention at discharge rates ≥ 1C, these graphites along with the Hitachi MAGE exhibited significant delamination from the copper current collector after calendering**.** This delamination could be seen in many of the electrodes punched for coin cells, and in some cases, the electrodes separated from the copper foil entirely. We confirmed these observations more quantitatively by performing 180° peel tests on each different coating to determine the adhesion of the coating to the underlying copper current collector. Based on the observed delamination during processing and the peel test results, the ConocoPhillips A12, GrafTech APS19, and Hitachi MAGE graphites were eliminated as potential candidates. The three remaining graphite materials (Showa Denko, Hitachi MAGE 3, and Superior SLC 1520T) show similar electrochemical rate performance at 6 mAh/cm^2 (Figure I-92b). Therefore, we built single-layer pouch cells with each graphite to more reliably determine how they would perform in a full cell configuration and further narrow the graphite selection.

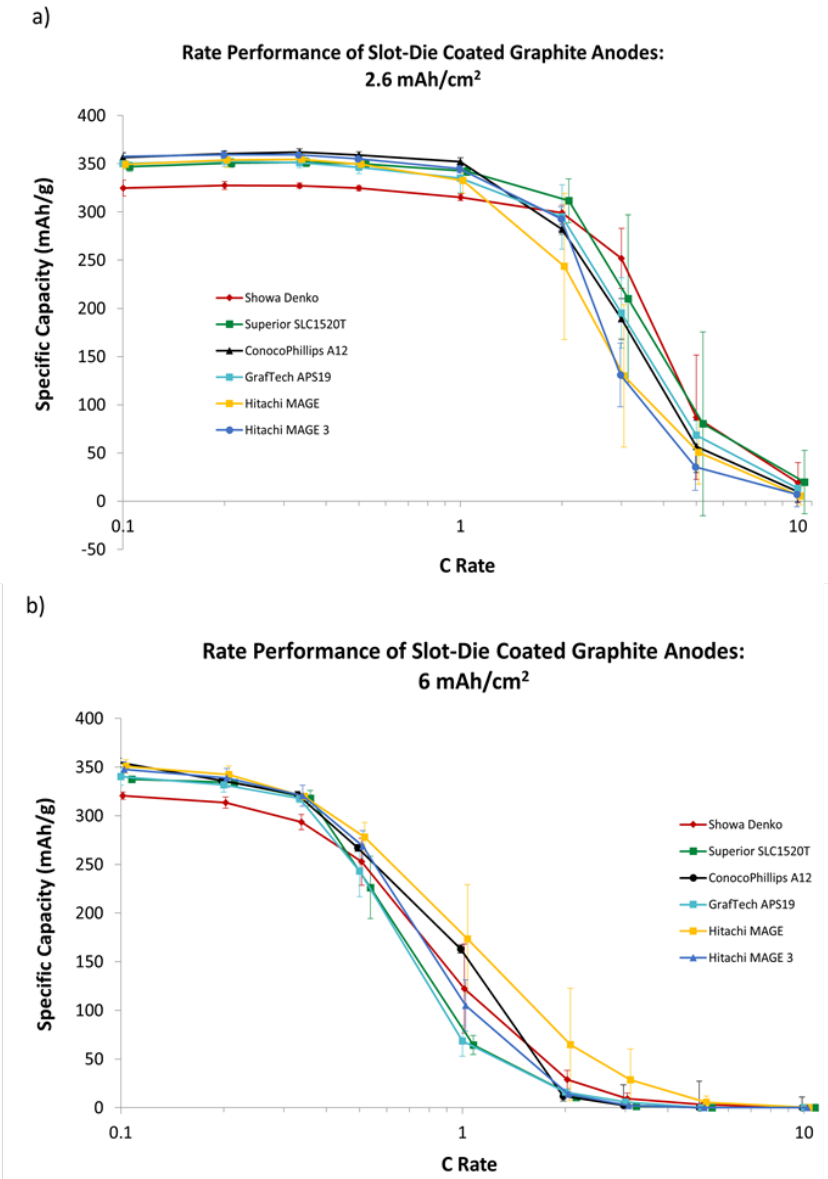

Figure I-92. Comparison of the performance of 6 different slot-die coated graphite anodes in half cells at a loading of (a) 2.6 mAh/cm^2 and (b) 6 mAh/cm^2.

Baseline Pouch Cells

Baseline pouch cells were made at two different capacities (1 Ah and 6 Ah) according to the specifications established previously. The recipes, areal loadings, and thicknesses for the anode and cathode coatings are listed below in Table I-15. Six pouch cells were made at each capacity. Half of the cells were used to evaluate the rate performance (C/5 Charge, Discharge at different C rates), while the other half were used to perform long-term cycle life testing (C/3 Charge, C/3 Discharge). Each 6 Ah cell contains two jelly rolls stacked on top of one another, each with its own set of tabs.

Table I-15: Composition and Processing Parameters for Baseline Anode Pouch Cells

	Anode	Cathode
Active Material	92 wt% Superior SLC 1520T Graphite	90 wt% Toda NMC 532
Conductive Additive	2 wt% Imerys C-Nergy Super C65 Carbon Black	5 wt% Denka Carbon Black
Binder	5 wt% Solvay 5130 PVDF	6 wt% Kureha 9300 PVDF
Areal Loading	7.5 mg/cm^2	14.7 mg/cm^2
Electrode Thickness	63 µm	55 µm
Calendering	45% Porosity	35% Porosity

Long-Term Cycle Life

Figure I-93 shows updated cycle life data for the 1 Ah and 6 Ah baseline pouch cells after 512-900 cycles One of the 6 Ah pouch cells experienced a power outage interruption, so the data shown only includes 512 cycles (even though the other two 6 Ah cells have completed 750 cycles). Although the 6 Ah cells continue to show marginally lower capacity fade than the 1 Ah cells, both sets of cells demonstrate slightly higher capacity fade than anticipated, with the 1 Ah cells decaying to 68% of their original capacity after 900 cycles. This may be a result of calendering the anode to 45% porosity rather than the typical 35%. This porosity value was originally chosen based on the results of our coin cell study with both calendered and uncalendered anodes, which showed that uncalendered anodes (~50-60% porosity) exhibited better rate performance than calendered anodes (~35% porosity). Conversely, calendering generally improves both the adhesion to the currentcollector and the electrical conductivity, which can influence long-term cycle life calendering. Therefore, 45% porosity was chosen for the baseline anodes in order to take advantage of the rate performance benefits of higher porosity and the adhesion and conductivity benefits of lower porosity. However, it appears that the capacity fade observed in the baseline cells made with higher porosity anodes may outweigh the rate performance benefits. Despite this capacity fade, the very similar performance of the 1 Ah and 6 Ah cells and the low cell-to-cell variation again demonstrate the ability to scale up pouch cell capacity without sacrificing performance.

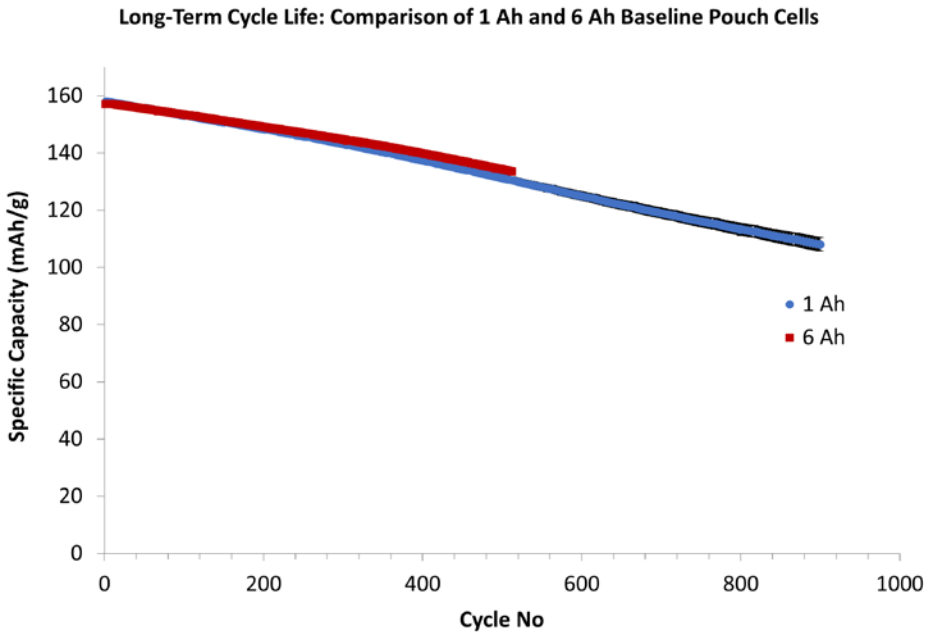

Figure I-93. Cycle life data for 1 Ah and 6 Ah baseline pouch cells. Cells are tested at C/3 charge and discharge with HPPC testing performed every 50 cycles.

Conclusions

PARC, ORNL, and Ford are collaborating to create a pilot scale demonstration of PARC's CoEx battery manufacturing technology for structured high energy and high power cathodes for cost-effective EVs. This year, we have completed the modeling of CoEx cathodes, identifying the most promising CoEx geometries for further study. Based on this modeling results, we have designed CoEx battery formulations that produce heterogeneous cathode structures with a variety of geometries. Our electrochemical testing shows that CoEx electrodes perform better than homogeneous electrodes of similar loading, supporting our hypothesis that interdigitating regions of high porosity within the cathode electrode improves lithium utilization in thick electrodes. We have also identified high performance anode materials and used them to create high capacity pouch cells which have been tested for performance and cycle life.

Key Publications

1. C.L. Cobb and S.E. Solberg, "Analysis of Thick Co-Extruded Cathodes for Higher-Energy-and- Power Lithium-Ion Batteries," *J. Electrochem. Soc.*, **164** (7), A1339-A1341, 2017

2. R.B. Rao, "Co-Extrusion of Electrodes for Both Energy and Power", U.S. Drive Electrochemical Energy Storage Technology Discussion, Southfield, MI, May 16 2017

3. C.L. Cobb, "Co-Extrusion: Advanced Manufacturing for Energy Devices," *2016 AIChE Annual Meeting, Battery and Energy Storage Technologies*, San Francisco, CA, November 14, 2016. (Session Keynote)

4. C.L. Cobb, "Modeling Co-extruded Cathodes for High Energy Lithium-ion Batteries," *229th ECS Meeting*, San Diego, CA, June 1, 2016.

References

1. C.L. Cobb *et al.*, "Modeling Mass and Density Distribution Effects on the Performance of Co-extruded Electrodes for High Energy Density Lithium-ion Batteries," *J. of Power Sources*, **249**, 357-366, 2014.

2. L.P. Richter *et al.*, "Progress in Fine Line Metallization by Co-extrusion Printing on Cast Mono Silicon PERC Solar Cells," *Solar Energy Materials and Solar Cells*, Vol. 142, pp. 18-23, 2015.

3. M. Doyle, T.F. Fuller, and J. Newman, "Modeling of Galvanostatic Charge and Discharge of the Lithium/Polymer/Insertion Cell," *J. Electrochem. Soc.* 140, 1526-1533, 1993.

4. T.F. Fuller, M. Doyle, and J. Newman, "Simulation and Optimization of the Dual Lithium Ion Insertion Cell," *J. Electrochem. Soc.*, 141, 1-10, 1994.

5. COMSOL v5.1: https://www.comsol.com/

I.B.6 Electrodeposition for Low-Cost, Water-Based Electrode Manufacturing (PPG Industries, ANL, Navitas, ORNL)

Stuart Hellring, Principal Investigator
Senior Scientist
PPG Industries
4325 Rosanna Drive
Allison Park, PA 15101
Phone: 412-492-5526
E-mail: hellring@ppg.com

Peter Faguy, Technology Manager
U.S. Department of Energy
Phone: 202-586-1022
E-mail: Peter.Faguy@ee.doe.gov

Start Date: October 1, 2016 End Date: December 31, 2018
Total Project Cost: $3,999,034 DOE share: $1,399,275 Non-DOE share: $999,759

Project Introduction

The state of the art for the manufacture of lithium ion cathodes is slot-die coating of a high-viscosity slurry of active battery materials, conductive additives, and a polymeric binder that is dissolved in N-methyl-2-pyrrolidone (NMP). NMP is an expensive consumable in electrode manufacturing with serious health concerns. It is on the candidate list of Substances of Very High Concern for authorization in the European Union. In the United States, NMP is on the EPA's Toxics Release Inventory and the California Department of Occupational Safety and Health has proposed a Threshold Limit Value of 1 ppm in air, similar to occupational exposure limit values established in Japan (1 ppm) and Germany (20 ppm). Alternative organic solvents have been insufficient to meet the needs of incumbent binder systems and present their own cost and exposure difficulties.

The current cost of high-energy Li-ion batteries (LIBs) is approximately $500-$800/kWh, while the EV Everywhere Blueprint 2022 goal is $125/kWh. Main cost drivers are the high cost of raw materials and materials processing, the cost of cell and module packaging, and manufacturing costs. Our proposed project addresses materials processing and manufacturing costs. To estimate the cost savings achievable by converting to an aqueous, electrocoat-based cathode coating system, PPG consulted with Argonne National Lab. Using BatPac, an estimated 17.1% savings on a per-cell basis was determined. Eliminating NMP from the process reduces cost by 8.9%. Further cost savings can be realized by eliminating the need to calender electrodes, and by an expected reduction in binder costs, for an estimated 17.1% savings over state of the art.

Solvent-based electrodeposition of pre-formed cathode active powders for producing electrodes for secondary lithium ion batteries has been evaluated by several groups. A variety of active materials have been electrodeposited onto various current collectors in solvents such as acetone and ethanol. Cathode active particle sizes used for these studies ranged from an average of 300 nm to 10.3 µm. Cathodes produced by solvent-based electrodeposition showed promising battery performance for metrics which include discharge capacity/rate capability, coulombic efficiency and cycle life retention.

However, the use of volatile organic solvents for manufacturing electrode coatings by electrodeposition has a number of serious drawbacks including VOC emissions, explosion risk, health risks from worker exposure, and cost. Using waterborne coatings significantly mitigates most of the concerns associated with organic solvent-based coating formulations. Benefits include lower voltage/current, better process temperature control and faster deposition rates due to a higher dielectric constant. Binder design, proprietary additives, and

electrochemical processing methods are used to ensure quality during manufacturing, to disperse pigment particles and stabilize the aqueous formulation bath against agglomeration and settling. Since charge-bearing functionality typically is hydrophilic, these functional groups are converted by crosslinking during the coating curing process to render the final film less hydrophilic.

Objectives

The objective of the project is to develop and demonstrate novel binders to enable a low-cost, water-based, electrodeposited lithium ion battery electrode coating system and manufacturing process capable of reducing cell costs by at least 20% while improving battery performance. In addition, the project will demonstrate a battery supply chain model that mirrors traditional automotive OEM supply chain models to reduce the risk of electric vehicles (EVs) and increase adoption. During this year, specific objectives for this project are as follows:

- Electrocoat an electrode with an energy density of 2.5 – 3.0 mAh/cm^2.
- Complete cell testing on 0.2 – 0.3 Ah pouch cells.
- Design and construct a pilot scale electrocoat roll-to-roll coater.
- Adjust estimate of cost savings using BatPac model.
- Demonstrate the ability to produce or commercially acquire kg quantities of active material suitable for the electrocoat process.

Approach

Electrocoat offers several manufacturing advantages over conventional slot-die or roll-coater application processes. One advantage is a greater coating density. Because electrophoretic deposition moves solid components to the substrate and dewaters a coating as it deposits, high density coatings with 90% by weight solids content are produced routinely from dilute formulation baths that have low viscosity. As an example, an aqueous wet film with 90% by weight solid content comprised of active, carbon, and binder will produce a dry cathode coating with less than 30 percent porosity. High density in electrodeposited coatings is achieved by controlling packing through particle size distribution where small particles embed in larger particle matrices through electrophoretic impregnation. Deposition of a dense wet film lowers stress in the dried film, a benefit for adhesion and cohesion. The self-insulating nature of the film build leads to high thickness uniformity. Unlike electroplating, electrocoat formulation are comprised of preformed and prequalified materials such as cathode-active powders, conductive carbon additives and binders that are deposited together to form the cathode coating.

The project will develop a viable electrodeposition process and will design and synthesize electrodepositable binders with flexibility and ionic mobility. The project will tailor and fabricate high-energy density active materials for compatibility and formulate stable water-based cathode coating systems. The project will establish electrodeposition process parameters and validate the performance and economics of the technology at a 1 Ah scale to ensure a path to commercialization. Argonne national labs will provide guidance and assistance developing active materials that are compatible with the waterborne electrocoat process through the synthesis of custom particles and particle coatings. Oak Ridge national lab will develop optimized drying conditions for electrocoat films through residual water analysis and pouch cell testing. Navitas Systems will provide testing of larger format cells.

Budget Period 1 includes development of the materials necessary for a successful e-coated electrode. Work will be split between concurrent active materials modification and e-coat system development. At the end of BP 1, targeted materials will be selected based on their performance characteristics.

Budget Period 2 will refine the coatings system to improve baseline performance. Cell validation scale will begin to increase, enabling refined quantification of the achievable cost reductions. The design and build of a bench scale coater for representative evaluation will support scale up in BP 3.

Budget Period 3 will optimize the coating system components to the point that large format cells will be built and evaluated. The budget period includes obtaining optimized, representative electrodes that will be tested for performance properties both independently and within cells.

Results

Battery performance improvements verified through pouch cell testing

Cathode electrodes for 60 mAh pouch cells were fabricated using electrocoat binders and the electrocoat deposition process. These cells were compared to cathode electrodes fabricated using a commercially available waterborne binder and drawdown application methods. Commercially available NCM 111 active materials were used in a formulation comprised of 92% active material, 4% conductive carbon, and 4% binder material. Double-sided, electrocoated electrodes with an average loading of 1.7 mAh/cm^2 per side (3.4 mAh/cm^2 per electrode) were fabricated into a 60 mAh full-cell pouch cell by Navitas Systems. Single-layer electrodes with an average loading of 1.5 mAh/cm^2 were fabricated into 60 mAh full-cell pouch cells by Navitas Systems using identical active materials and a commercially available waterborne binder. Pouch cells made from electrocoated cathodes demonstrated improved rate capability, cycle life, and internal resistance compared to the cathode electrodes fabricated using the commercially available waterborne binder (Figure I-94).

Additional testing is underway at Navitas Systems for 0.2 Ah pouch cells using commercially available LFP and NCM 111 materials. Pouch cells have been fabricated using double-sided electrocoated cathodes with an average loading of 2.5 mAh/cm^2 per side using NCM111 materials and an average loading of 1.0 mAh/cm^2 per side using LFP materials. Initial cycling data demonstrates similar battery performance as 60 mAh cells.

Electrocoat parameters optimized for film uniformity and adhesion

Electrocoat resins and formulations were engineered to produce uniform films with high film adhesion. An optimization of the resin composition and deposition parameters resulted in peel strength values comparable to those obtained using NMP-based application methods. The film adhesion of electrocoated and drawdown electrodes of identical composition and thickness were measured using a 90º peel test. Films were tested at a loading of 1.5 mAh/cm^2 using a composition of 92% NCM 111, 4% conductive carbon, and 4% binder material. The composition of the electrocoat binder played a significant role in the adhesion of both the drawdown and electrocoated films. The value of 81 N/m obtained using formulation 3 surpassed the value of 79 N/m obtained from the NMP-PVDF control sample at the same thickness (Figure I-95a). However, resin compositions with improved adhesion had reduced battery performance. Work is ongoing to realize high adhesion and energy storage capacity.

Electrocoat deposition parameters were designed to produce uniform films over large areas for a range of active material particle sizes. Active materials with a large particle size settle over time in low-viscosity electrocoat baths. Two approaches were considered to overcome the resulting film non-uniformity: (1) the formulation of a stable bath using small particle size and (2) the modification of deposition parameters to accommodate bath instability with large particle size. The first approach used NCM 111 cathode materials with an average particle size of 7 µm. These were easily stabilized in an electrocoat bath and did not settle overnight. The second approach used deposition conditions that accounted for non-uniformity in the bath solids concentration by locally modifying the deposition rate over the electrode surface. Optimized electrocoat parameters produced uniform films with a particle size of 11 µm enabling the use of commercially available powders (Figure I-95b).

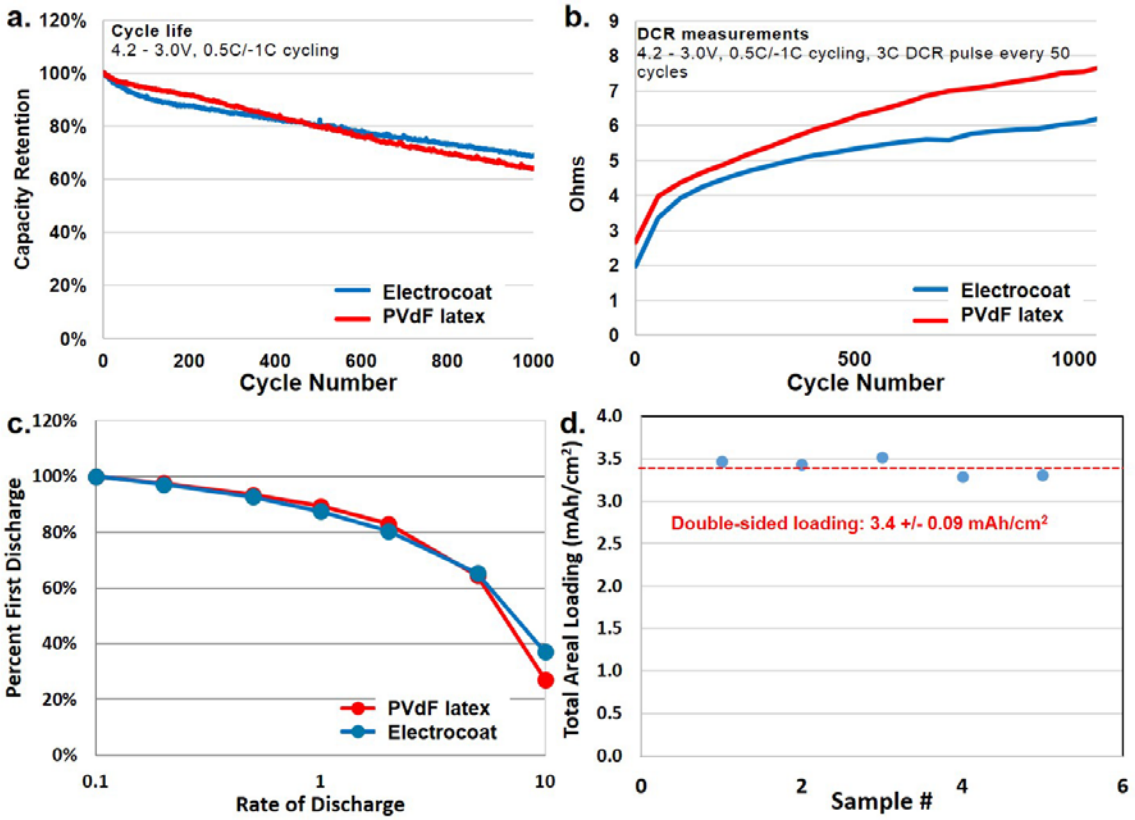

Figure I-94. (a) Cycle life testing demonstrating improved cycle life of electrocoated films after 500 cycles. (b) DCR measurements performed at 3.0 C. Electrocoated cathode materials demonstrate a lower internal resistance. (c) Rate performance of each electrode with electrocoated electrodes demonstrating an improved capacity retention at high rates. (d) Double-sided areal capacity measurements of five electrocoated films highlighting the reproducibility of targeted film thicknesses with this technique.

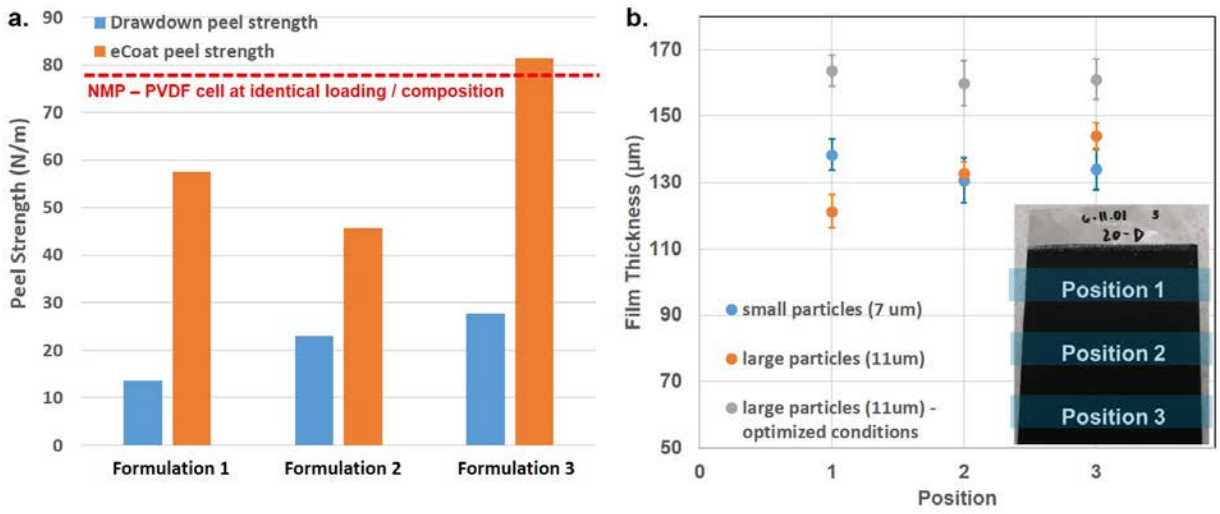

Figure I-95. (a) Peel strength measurements of electrocoat binders in cathode films fabricated using both drawdown and electrocoat fabrication processes. (b) Film uniformity measurements of electrocoated cathode films comprised of active materials of varying size and deposition conditions. Non-uniformities present from the use of large particle sizes may be overcome by the electrocoat deposition conditions.

Suitable active materials for electrodeposition were identified

Active materials that can be produced economically in kg quantities were investigated for compatibility with the electrocoat system. TVR synthesized NCM111 materials from Argonne National Lab and commercially available materials were screened for electrocoat deposition kinetics and battery performance. Two commercially available NCM111 materials, one commercially available LFP material, and one surface-treated commercially available NCM622 material demonstrated both high deposition rates and acceptable reversible capacities in a half-cell coin cell (Table I-16). Cells were cycled between 3.0 – 4.3V.

Table I-16 also shows the results from surface treatments were applied commercial material to increase the stability of a given active particle with the electrocoat system. Surface treatments on NCM622 resulted in significantly improved capacity, however, the electrocoat deposition kinetics suffered. ANL provided CO2 surface treatments to improve the capacity retention of NCM111 materials with minimal impact on the electrocoat deposition kinetics.

Roll-to-roll coating system under construction

A pilot scale minicoater is under construction by PPG Coating Services (MetoKote) to demonstrate roll-to-roll processing of electrocoated electrodes. Designs are completed for the mini-coater system and constructions has begun. Progress is on track to have a fully functional mini-coater delivered within the current budget period. A 5-inch wide foil will move through the coater at an adjustable speed designed to produce films with an areal capacity of 1.5 mAh/cm^2.

Table I-16: Active material screening in electrocoated electrodes. Suitable particles must demonstrate a coverage density of > 10 mg/cm^2 during electrocoat and battery performance characteristic of the active material used.

Material	Electrocoat Mass Deposited (mg/cm^2)	Initial Discharge Capacity at 0.1C (mAh/g)	Capacity at 1.0C Rate (mAh/g)
Preliminary NCM111-ANL material	8.76	81	0
Preliminary NCM111-ANL material	6.45	99	0
Preliminary NCM111-ANL material	12.75	121	0
NCM 111-Supplier 1	23	160	130
NCM 111-Supplier 2	4.83	142	101
NCM 111-Supplier 3	18	0	5
NCM111-Supplier 3 ANL surface treatment	15.09	131	62
NCM 111-Supplier 4, surface treated	15	132	60
NCM 523-Supplier 1	1	0	0
NCM 523-Supplier 2	3	0	0
NCM 523-Supplier 3	14.4	117	2
NCM 523-Supplier 3, ANL surface treatment	11.5	118	5
LFP-Supplier 1	17.1	130	3
LFP-Supplier 2	13.1	170	129
NCA-Supplier 1	13	0	0
NCA-Supplier 1, surface treated	9.03	0	0
NCM622 – Supplier 1	4.6	178	101
NMC622 – Supplier 2	13.4	0	0
NCM622 –Supplier 2, surface treatment A	2.46	163	19
NCM622 –Supplier 2, surface treatment B	5.76	178	49
NCM622 –Supplier 2, surface treatment C	5.22	183	144
NCM622 –Supplier 2, surface treatment D	4.92	165	102
NCM622 –Supplier 2, surface treatment E	4.92	168	102
NCM622 –Supplier 2, surface treatment F	5.99	174	96

Conclusions

Film adhesion and uniformity targets have been met using electrocoat fabrication of cathode electrodes. Sufficient film uniformity and adhesion, on par with solvent-based systems, has been demonstrated. In addition, the process of electrocoat improves film adhesion compared to conventional drawdown application methods.

Energy storage performance that meets the targets for this budget period were reached using materials produced on the kg scale. Commercially available active materials were identified that produce reliable energy storage properties with the chosen electrocoat formulation. Additionally, electrocoated cathode electrodes demonstrated improved battery performance compared to other commercially available waterborne binders in 60 mAh pouch cell testing at Navitas Systems.

A pilot scale roll-to-roll coater is under construction and the final design for the coater and oven system is completed. The operation of this system will demonstrate the commercial feasibility of this electrocoat process and electrodes will be tested on the 1 Ah scale.

Key Publications

1. Presentation at the 2017 U.S. Drive
2. Poster presentation at the 2017 Annual Merit Review

I.B.7 Development of UV Curable Binder Technology to Reduce Manufacturing Cost and Improve Performance of Lithium Ion Battery Electrodes (Miltec UV International)

Dr. John Arnold, Principal Investigator
Miltec UV International
146 Log Canoe Circle
Stevensville, MD 21666
Phone: 410-604-2900; Fax: 410-604-2906
E-mail: gvoelker@miltec.com, jarnold@miltec.com

Peter Faguy, Technology Manager
U.S. Department of Energy
Phone: 202-586-1022
Email: Peter.Faguy@ee.doe.gov

Start Date: December 1, 2015 End Date: September 30, 2018
Total Project Cost: $2,568,200 DOE share: $1,742,560 Non-DOE share: $513,640

Project Introduction

Previously identified UV curable binders and associated curing technology have been shown to significantly reduce the time required to cure electrode coatings. This revolutionary approach can result in dramatic increases in process speeds and significantly reduced capital costs and operating costs, reduced energy requirements and reduced environmental concerns and costs due to the virtual elimination of volatile organic solvents and associated solvent dryers and recovery systems.

The accumulated advantages of higher speed, lower capital cost, lower operating cost, reduced footprint, lack of VOC recovery, and reduced energy cost is a reduction in the manufacturing cost of electrodes. When commercialized, the resulting cost reduction in lithium-ion batteries will allow storage device manufacturers to expand their sales in the market and thereby accrue the energy savings of broader utilization of HEVs, PHEVs and EVs in the U.S., and a broad export market is also envisioned. In addition to equipment required to make and UV cure hand drawn cathode samples on high speed web conveyors with UV lamps; Miltec UV has a continuous coating and UV curing system (using three very high intensity UV lamps) to demonstrate the primary objectives of the project.

Objectives

The primary objective of this project is to provide performance data sufficient for lithium-ion battery manufacturers to commit to the first steps of making their own HEV, PHEV and/or EV lithium-ion electrodes with a UV drying process. This project involves an iterative R&D effort: making coin cells and pouch cells, followed by testing and analyses, then by adjustments in chemistry, mixing, coating, and UV curing to produce layered pouch cells at high processing speeds (200-300 feet per minute (fpm)) with performance equal or greater than that of a conventional cell with electrodes using PVdF and dried in a standard oven. This effort focuses on cathodes made with UV curable binders and is also investigating UV curable binders in the manufacturing of LTO-based anodes.

As a supplemental effort, Miltec and its team will investigate high speed coating techniques to demonstrate consistent thickness and edge control and will also conduct supplemental research on applying a UV cathode layer on top of an existing UV cathode layer to produce a thicker high energy cathode with sufficient porosity.

Approach

A major innovation of the use of UV curable binders in LIB electrode manufacturing is the potential for much higher processing speeds. Miltec UV and its partners have shown that once a condition for complete UV curing is determined (speed, thickness, number of lamps, etc.) then there is a linear correlation between process speed and number of UV lamps. For example, it has been shown that if UV curable coating completely cures at a cathode coating thickness of 20 µm with 1 lamp (600 W/in lamp) at a speed of 100 fpm, then that same 20 µm coating will completely cure at a speed of 300 fpm with 3 lamps.

Based on the difficulty of coating UV curable binder with slot die at higher speeds (>150 fpm), it is believed that coating technology other than slot die will most likely be required to achieve the very high process speeds made possible by UV curable binders (100 meters/minute). Miltec will evaluate and adapt the best from two coating processes used in the printing industry, flexography and letterpress printing.

Another important innovation being demonstrated in this project is the ability to make cathodes with multiple coating layers. This is made possible by the fact that, unlike a solvent-based system, the second and subsequent layers can be applied without the solvent in the second layer dissolving material in the layer below and the time between application and cure is so short that the second layer of liquid coating does not have time to flow into the pores of the first layer. Multilayered coating introduces the ability to make thicker, higher active material loading cathodes for EV applications. It also introduces the ability to change porosities and other characteristics such as material composition (active material and carbon) between layers. Miltec and ORNL will investigate and evaluate multilayered coatings and the potential advantages in this project.

The expected outcome of the project is to generate performance data from multilayer pouch cells (0.5–1.0 Ahr) fabricated using UV curable binder to demonstrate capacity, long term cycling, rate capacity, impedance, and repeatability equal to or better than a pouch cell with cathodes made using PVDF as a binder. Miltec is in contact with battery manufacturers and it is our belief that they will take the next steps once we demonstrate equivalent pouch cell performance. The most likely next step after the completion of this project would be the addition of a UV curing system to an existing cathode manufacturing line as a demonstration project; or possibly a stand-alone demonstration unit because of the relatively low capital and operating cost of a UV curing system.

Results

While the performance of the UV cathodes compares well with commercial batteries, there is always a technical drive to go to higher loadings. In an attempt to get ahead of the trend, we explored higher NMC loadings. Figure I-96 and Figure I-97 show a progression of higher NMC percentages, using different types of NMC and different loadings. By keeping the mass loading of the electrode at ~5 mg/cm2, we discovered that we could maintain relatively stable cycling.

So, in the realm of power cathodes, cathodes produced with a versatile, high speed, high capacity UV process can offer cost savings and some performance advantages.

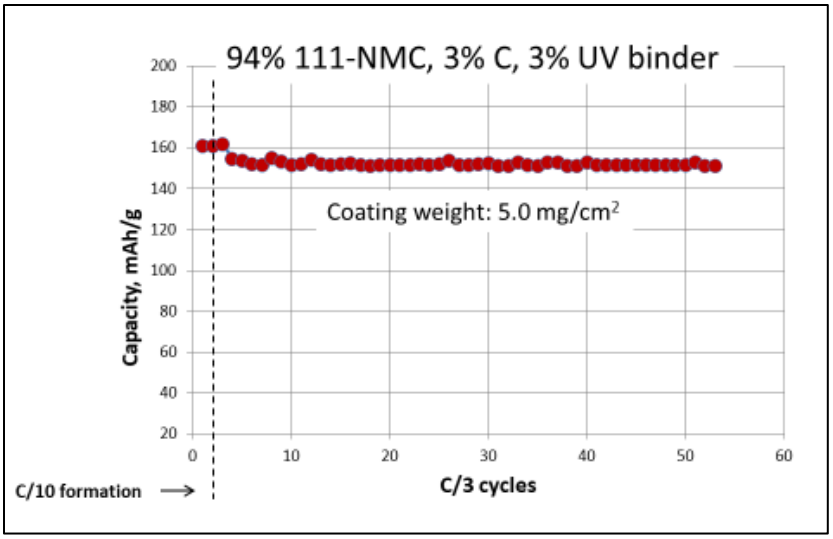

Figure I-96. Stable half-cell cycling of UV 94/3/3 power cathode.

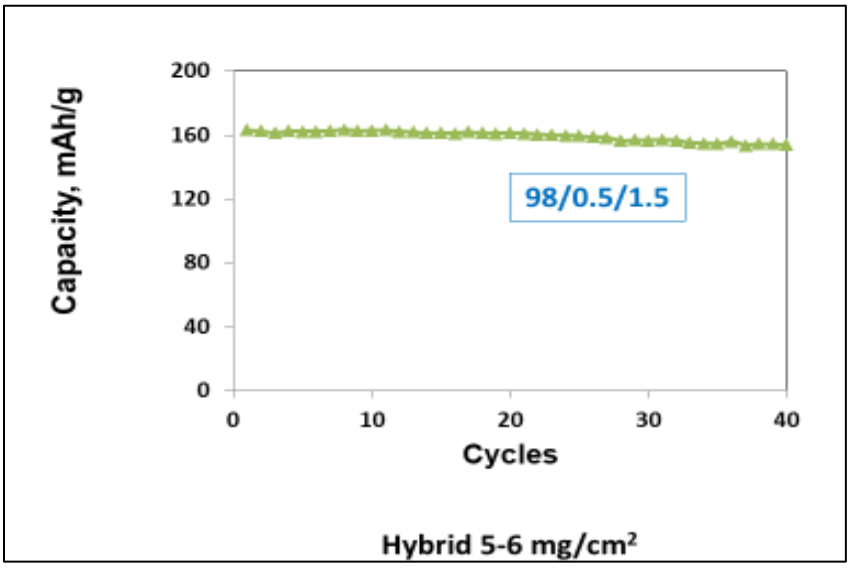

Figure I-97. Stable half-cell cycling of UV 98/0.5/1.5 power cathode.

Layered Cathode Coatings

For UV curing to work, light must penetrate through the coating. With various degrees of success, very thick coatings have been made. However, in real world production, the goal is to manufacture defect free product 100% of the time. Thicker coatings involve more risk. Instead of taking the risk path to make thicker coatings, we chose the path of layered coatings. Layered electrode coatings are an exciting possibility, offering flexible manufacturing and the potential for controlling electrode content at various depths. Many high-speed printing presses use layers of base coats, inks, and top coats to produce durable text and graphics. Multilayer UV printing is common in most print shops.

A major potential issue in manufacturing a LIB electrode is applying and curing a second layer without destroying or significantly altering the first layer. This issue becomes especially severe when using any solvated polymer (like PVdF) in an evaporative process. Because drying does not chemically change the

polymer, applying a second layer allows for solvent in the second layer to flow into the first layer and re-solvate it, thereby eliminating the advantage of a layered coating. In addition to the potential for changing the first layer, there is less reason to be interested in layered coatings when using PVdF and the traditional NMP solvent, as the evaporation speed for two separate layers will not be faster than evaporating a single layer at the same overall thickness. This eliminates a speed advantage for layered oven-dried binders.

UV overcomes both issues. UV irradiation eliminates the acrylate groups and forms a cross linked polymer that is not soluble in its original carrier. So, the wet applied top layer has no ability change the crosslinked first layer. Secondly, the process of application and curing in a UV process is significantly faster than oven-dried binders, meaning that there is not enough time for the second layer to flow into the first layer. To test these assumptions, we began by applying a single and double-layered electrode using a flexographic process. The goal was to produce two electrodes with the nearly the same thickness (~22-24 µm) and mass loadings (~5 mg/cm^2), yet one would be made in a single layer and the other in 2 layers. The double layered electrode was made by the method of application, cure, application, and a final cure, each using a single microwave UV lamp. Figure I-98 shows cycling results from this initial experiment.

As Figure I-98 demonstrates, the double-coated electrode performed even better than the single-layer electrode. This result shows there is no early signs of a barrier layer between the first and second layer.

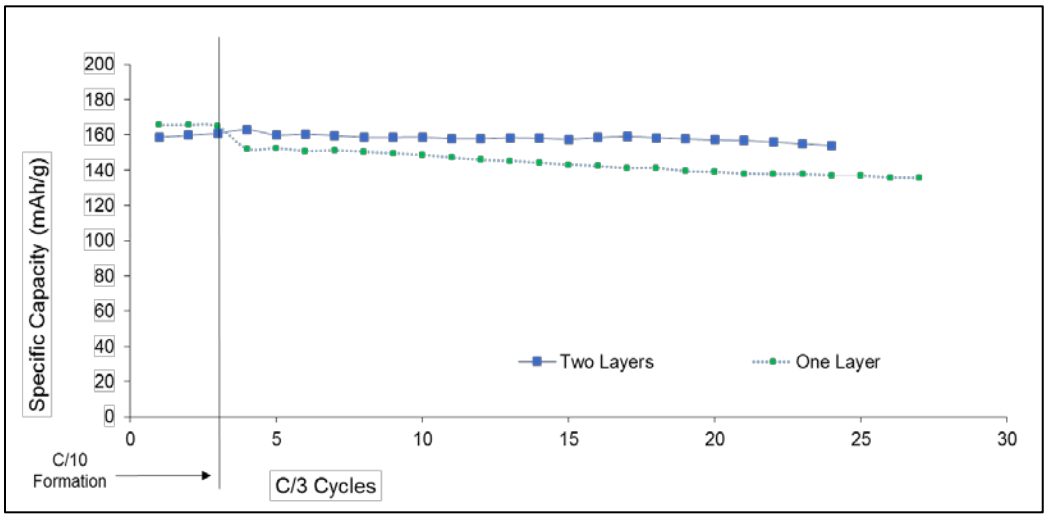

Figure I-98. Comparison of a NMC cathode utilizing a UV-curable cathode with a single and double layer, each electrode containing approximately the same amount of active material, at approximately the same thickness (~22-24 µm.) The double-layered electrode was made by application, cure, second application, and then a final cure. Each cure was performed with a single UV lamp, and the mass ratio of materials was 90:7:3 NMC: Carbon: UV Binder.

The layered coating in Figure I-98 establishes feasibility but does nothing toward producing a thicker electrode. Next, we used a slot die coater and made thicker electrodes. In this case we made a 90/5/5 NMC/Carbon/UV binder. The single coated electrode has an active material loading of ~3 mg/cm^2, and the double coated electrode has an active material loading of ~6 mg/cm^2. Cycling results from the half cells taken from this slot die run is shown in Figure I-99. The capacity retention of the double layer, double thick cathode is as good as that of the single layer cathode.

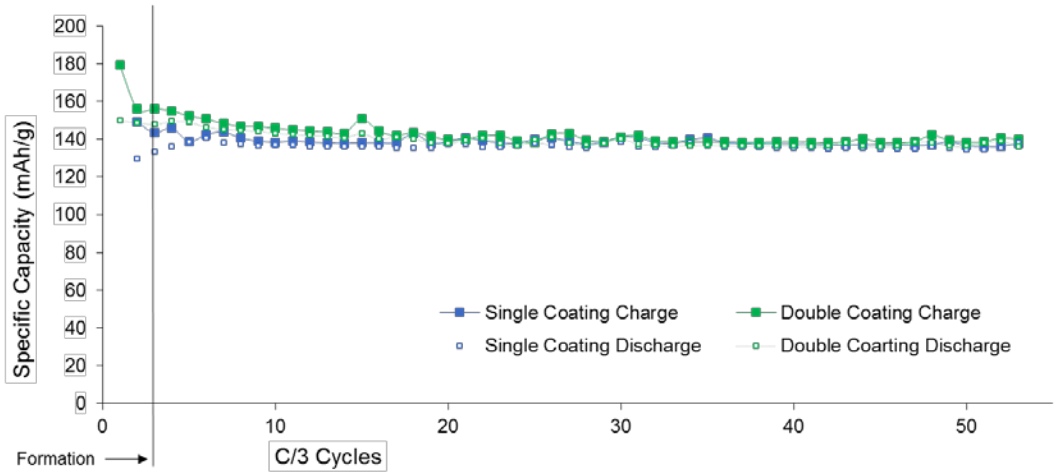

Figure I-99. Half-cell cycling data, comparing single and double cathode layers, each applied by slot die coating. The single coated electrode has a thickness of ~12 microns and an active material loading of ~3 mg/cm2, and the doubly coated electrode has a thickness of ~25 microns and an active material loading of ~6 mg/cm^2. The formulation of each slurry is the same, with a mass loading of 90/5/5 NMC.

Current work is developing thicker layers. At this point we have produced 12 mg/cm^2 of electrode material with one layer. The next experiment will aim to demonstrate that we can produce production reliable 24 mg/cm2 coatings with only two layers.

LTO Anode

Attempts to produce graphite anodes in the past were achieved but complicated by the high monomer absorbency of graphite and carbon and the UV absorbance of the carbon-based materials. Since most commercial graphite processes are water-based and not do not use NMP, the health advantages for UV graphite anodes are less than they would be for an NMP-PVdF process.

Discussions with industry partners led us to pursue the production of Lithium Titanate (LTO)-based anodes. That LTO is a white, light reflective material was serendipitous, and makes it an especially facile material to adapt into a UV process. We began by cycling half cells of a UV-cured LTO anode. Three C/10 cycles were followed by C/3 cycling, using a commercially-relevant active material loading of ~3.0 mg/cm^2. The results of this initial experiment are shown in Figure I-100.

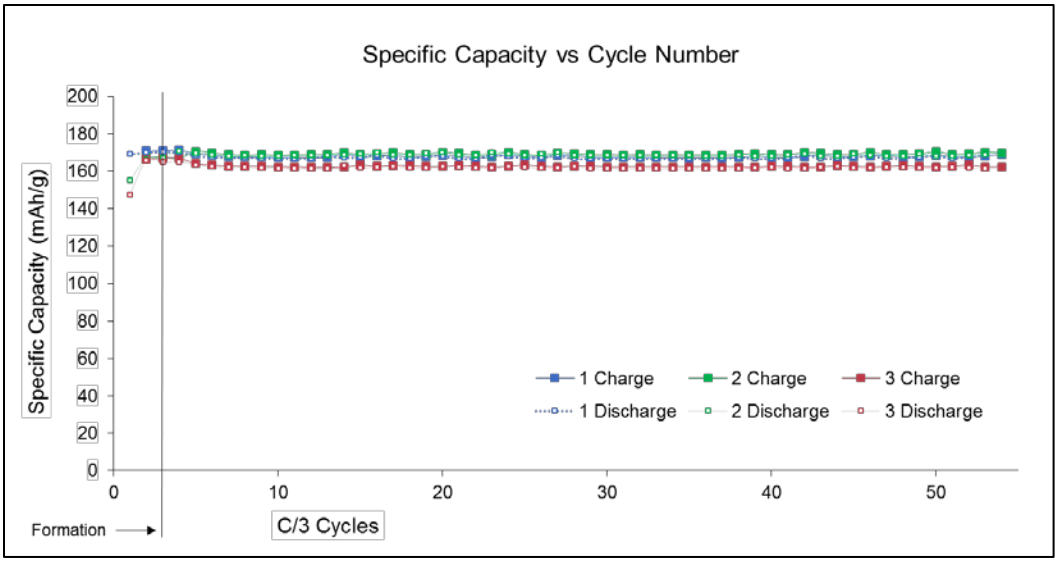

Figure I-100. Initial cycling tests on an LTO anode using a mass ratio of 93:4:3 LTO/CB/Binder, and electrode mass loading of ~3.0 mg/cm^2 of active material. These electrodes were cast by hand using a doctor blade, and cured at 60 fpm.

With stable cycling established, we moved on to test how the rate capability of LTO, which is a distinct advantage listed for this electrode material, would be preserved using our crosslinked UV-curable binders. The result of this experiment is shown in Figure I-101, where we used the same formulation and electrode mass loading, but ramped up the rate every three cycles, starting at C/10, then moving on to C/5, C/2, C, 2C,5C, and then 10C, and finally returning to C/5. Even at 10C, 60% of capacity was maintained.

With these recent successes with LTO, we intend to work with research and industry partners to produce LTO full cells using a UV-curable binder.

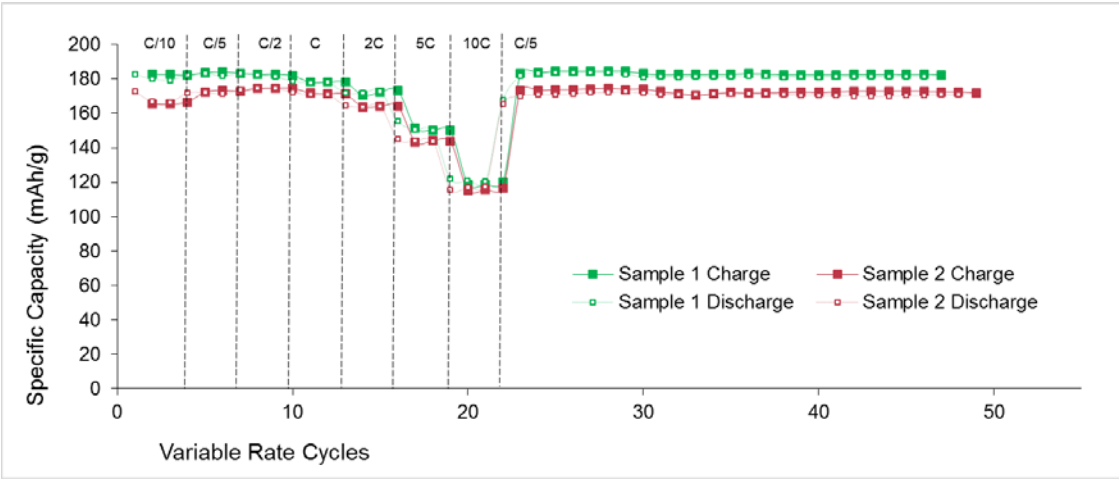

Figure I-101. UV LTO power anode (93/4/3 LTO/C/UV Binder), shows fast stable, high rate cycling. Electrode mass loading was 3.2 mg/cm^2 of LTO.

Conclusions

Miltec UV International and Argonne National Laboratory and Oak Ridge National Laboratory have made significant progress toward meeting the goals of this project. A three lamp UV curing system with a slot die coater and an interchangeable letterpress coater with a reel to reel control system is operational. Cathode coatings of 3%, 2% and 1% UV binder have been prepared, made into pouch cells and cycled with performance equal to PVdF reference cells. Double layered cathode coatings have been made with performance equal or greater than equivalent single-layer electrodes. This shows there is no impact on performance of this second layer, at least during the first 50 cycles. In addition, Miltec has demonstrated the ability to make LTO anodes using UV binder with performance equal to conventional LTO anodes. The coating and UV curing system in place will allow Miltec UV to complete the optimization and demonstrate the full potential of this technology. Miltec UV intends to vigorously pursue full development and commercialization of UV systems as applied to lithium-ion battery electrodes.

Key Publications

Miltec UV made various public releases of project results during the last year. These include:

1. Presentation at the DOE Annual Merit Review sponsored by the Vehicle Technology Office in June of 2017.

2. Gary Voelker and Dr. John Arnold gave a presentation on the merits of UV binder for LIB electrodes to the DOE USCAR representatives from Ford, Chrysler, GM and EPRI in Detroit, MI May 17, 2017.

3. Miltec UV had an exhibit with visuals and a video presenting the progress on UV binder for LIB electrodes at the International Battery Conference, Fort Lauderdale, FL March 2017 and the Battery Show, Novi, MI September, 2017.

4. Dr. John Arnold gave a presentation titled *UV Coating Processes to Enhance Li Ion Battery Performance and Reduce Costs* to the Electrochemical Society meeting at National Harbor Fall 2017.

5. Miltec UV has a fully operating website presenting details on the performance and potential for LIB electrodes made with UV curable binder. http://www.miltec.com/technology/battery/cathode-binders/

I.B.8 Towards Solventless Processing of Thick Electron-Beam (EB) Cured LIB Cathodes (ORNL)

David L. Wood, III, Principal Investigator
Oak Ridge National Laboratory
NTRC-2, 2370 Cherahala Boulevard, MS-6479
Knoxville, TN 37932
Phone: 865-574-1157
E-mail: wooddl@ornl.gov

Peter Faguy, Technology Manager
U.S. Department of Energy
Phone: 202-586-1022
E-mail: Peter.Faguy@ee.doe.gov

Start Date: October 1, 2014 End Date: September 30, 2019
Total Project Cost: $1,425,000 DOE share: $1,425,000 Non-DOE share: $0

Project Introduction

There are a variety of technical attributes to electron beam (EB) curing of lithium-ion battery (LIB) binders. EB curing uses solvent-free compositions that have low emissions (VOCs, etc.) and are recognized by federal, state and local governments as being a more desirable technology. Solvent or water-based processing requires high drying energy and results in significant CO_2 emissions. EB curing offers significant process energy savings, is ultra-high speed, and utilizes much more compact equipment than conventional drying ovens (much less plant floor space required). Furthermore, it is a relatively cool process and is compatible with heat-sensitive substrates. Conventional thermal drying of LIB electrodes is typically conducted using multiple temperature stages; however, EB can be conducted in a single step. Solvent-free electrode compositions are rated as non-flammable, which translates into lower insurance costs, less stringent storage requirements and, a reduction in handling hazards.

EB treatment is a fast, robust materials processing technology that commonly delivers low cost and excellent performance for high-volume materials production. Based on decades of development and commercial deployment, self-shielded machines routinely operate with high reliability and low maintenance in industrial roll-to-roll production environments. ORNL is developing, demonstrating, and transitioning technology for high-speed roll-to-roll EB processing of LIB electrodes (i.e., coating formation and binder curing) – in particular high-areal-loading (4 mAh/cm^2) NMC 532 cathodes for this project. Further specific advantages of this processing route for LIBs are:

- Unmatched throughput – We estimate ≥ 600 m^2/min throughput can be achieved based on ≥300 m/min line speed for roll widths up to 2 m ($1.5-2.0M installed with machine footprint ~10 m^2).
- Thicker electrodes – Up to 150 microns can be achieved at the throughput rate mentioned above. Coatings of several hundred microns could be processed at higher capital cost per unit throughput, modest reduction in energy efficiency, and larger equipment footprint.
- Excellent energy efficiency – Electrical efficiencies ≥60% are possible, including voltage transformer losses (i.e., ≥60% of electrical line energy is converted to productive EB energy).
- Environmentally friendly – EB processing requires no solvent or initiator and has low emissions.

Objectives

- Significant process energy savings demonstrated with NMC 532 cathodes.
- Ultra-high electrode processing speed.
- Utilization of significantly more compact processing equipment than conventional drying ovens.

Approach

ORNL is working on a multiphase approach to develop, demonstrate, and transition EB processing of roll-to-roll LIB materials:

- Phase 1 – Demonstrate the technology's key differentiating attributes of high throughput and thick layer processing (FY15-16) with ebeam Technologies.
- Phase 2 – Address the key challenges of EB curing parameters and resulting material performance; develop coating methods requiring little or no solvent. (FY17-18) with ebeam Technologies and Keyland Polymer.
- Phase 3 – Demonstrate an optimized curing system together with a high-speed coating line in partnership with a key equipment manufacturer and LIB producer (FY19).

Results

To successfully EB cure the resins into binders for thick electrodes (25 mg/cm^2) at high speed (500 ft/min), several strategies were used: (1) improvement of formulation to obtain crack-free, thick coatings (Z. Du, et al. J. Power Sources 354 (2017) 200); (2) Calendering before curing to lower the porosity and reduce trapped air in pores; (3) improvement of nitrogen purging in the curing chamber to reduce O_2 level; (4) increasing electron dose to generate more free radicals for offsetting the O_2 inhibition.

Table I-17 shows a summary of the trial runs at ebeam Technologies in Davenport, IA. Cathode coating samples were taped onto a paper leader material using clear packaging tape around the periphery of the sample. Prior to taping down the trailing edge of the packaging film over the coated electrodes, samples were purged several times with nitrogen. Then the film was pressed down to remove the majority of the nitrogen and quickly taped closed to minimize any air intrusion. The two packaging films implemented (biax nylon and Stretch-tite) were each about 15 μm thick, and the EB curing occurred at 500 ft/min (the upper limit of the ebeam Technologies pilot line) at 60 kGy and 250 kV.

Table I-17: Summary of the high speed curing trial runs at ebeam Technologies.

Run No.	Sample Name	Experimental details	EB conditions
1	1A 1B 1C	No packaging film; Covered and N_2 inerted using biax nylon film; Covered and N_2 inerted using Stretch-tite film.	275kV/60kGy 300 ft/min 300 ppm O_2
2	2A 2B 2resin	No packaging film; Covered and N_2 inerted using Stretch-tite film; Uncovered dry Ucecoat 7788 & 7689 resin.	250kV/50kGy 500 ft/min 560 ppm O_2
3	3A 3B 3C 3resin	No packaging film Covered and N_2 inerted using biax nylon film; Covered and N_2 inerted using Stretch-tite film. Uncovered dry Ucecoat 7788 & 7689 resin	250kV/60kGy 500 ft/min 300 ppm O_2

Figure I-102 shows the FTIR spectrum of pure resins in runs #2 and #3, with the "C=C" peak at ~810 cm^{-1}. The cross-linking at a high speed of 500 ft/min was confirmed by a decrease in the transmittance peak

intensity. A higher voltage used for run #3 yielded a higher extent of cross-linking compared to run #2 due to a higher electron dose for run # 3.

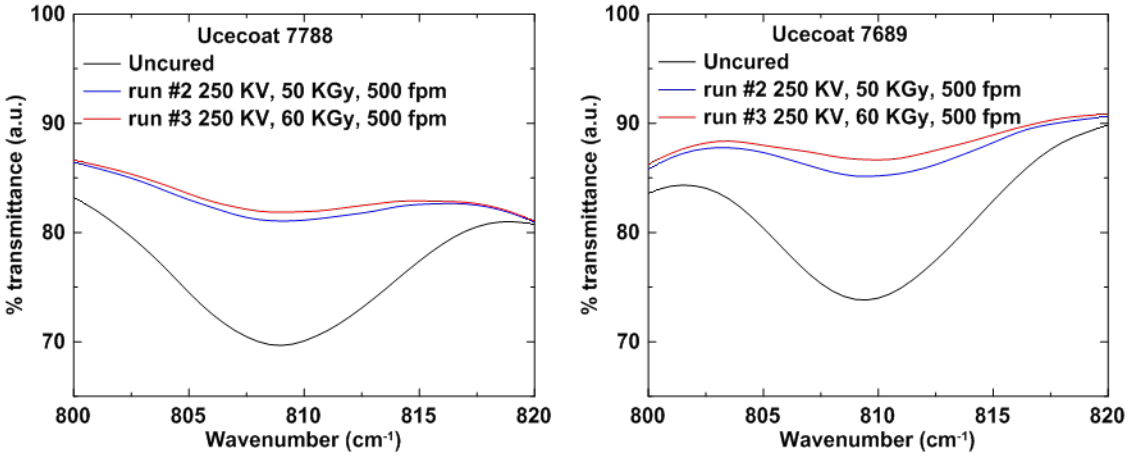

Figure I-102. FITR spectra of Ucecoat 7788 and 7689 resins used in runs #2 and #3.

Table I-18 shows a summary of the actual electron doses measured using dosimeters. A first dosimeter was placed under the packaging film directly on top of the coating (labeled as "Top"), and a second dosimeter was placed directly underneath the coated aluminum foil (labeled as "Bottom"). The values labeled "w/o Al foil" were calculated by eliminating dose reduction from the 15 µm Al foil. For 60 kGy curing, the samples with a line speed of 300 ft/min had the highest dose reading at the bottom, while a line speed of 500 ft/min slightly decreased the dose penetration into the samples. It was observed that the NMC 532 cathode coatings in the thickness direction received a dose range of 40-68 kGy, indicating the resins were fully cross-linked. Run #2 was carried out at dose of 50 kGy, and the overall coating dose range was within 30-53 kGy.

Table I-18: EB doses for different sample on the top and bottom of the samples.

Trial Number	Sample No	Conditions	Dose (kGy)		
			Top	Bottom	w/o Al foil
#1: 60 kGy, 275 keV, 300 ft/min, 300 ppm O_2	1A	No Film	61.1	34.7	43
	1B	Stretch-tite	61.4	36.7	46
	1C	Nylon	52.9	39.6	45
#2: 50 kGy, 250 keV, 500 ft/min, 560 ppm O_2	2A	No Film	50.3	22.9	30
	2B	Stretch-tite	52.3	23.9	31
#3: 60 kGy, 250 keV, 500 ft/min, 300 ppm O_2	3A	No Film	65.6	29.3	40
	3B	Stretch-tite	67	28.7	40
	3C	Nylon	66.5	29	40

The cured electrodes in Run #3 were assembled into 1.5 Ah pouch cells, and it was demonstrated that all cells had typical NMC 532 charge/discharge curves (Figure I-103a) and differential capacity curves (Figure I-103b). Good rate performance was achieved from C/10 to 2C (Figure I-103c), comparable to NMP processed electrodes with similar areal loadings. The retested cells retained about 91% capacity after 100 cycles, and 80.2% after 300 cycles (Figure I-103d), which achieved the stretch milestone specified for this project. Cell performance of the same coatings without any EB curing treatment were also included in Figure I-103d for comparison. As can be seen from the figure, the capacity drops rapidly for the first several cycles with only 60% capacity retention after 20 cycles.

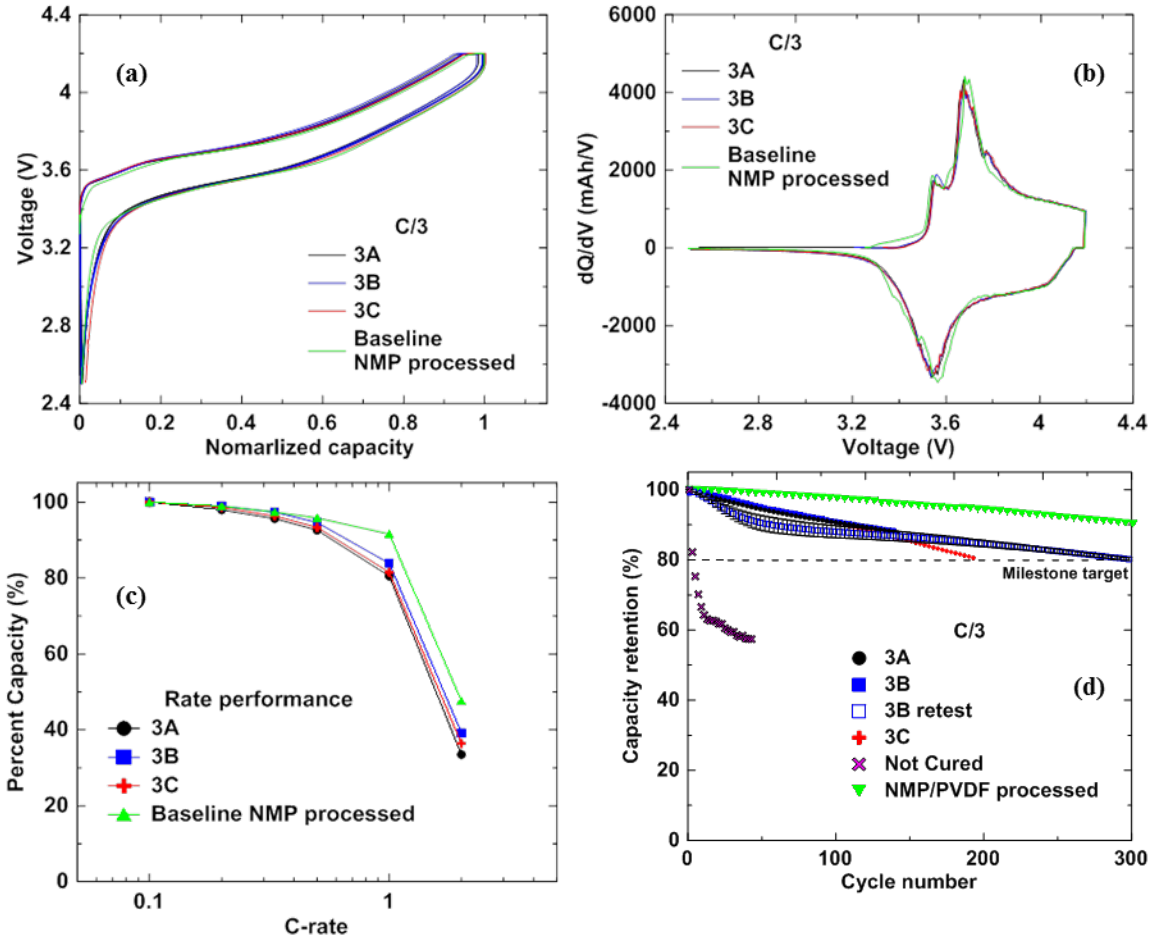

Figure I-103. (a) Charge/discharge voltage curves at C/3, (b) rate performance from C/10 to 2C, (c) differential capacity curves at C/3, and (d) cycling performance at C/3 charge/discharge rates for the 1.5 Ah pouch cells.

To develop an electrode coating method compatible with the ultra-high line speeds associated with EB curing, electrostatic spraying on aluminum foil was conducted at Keyland Polymer Ltd. using dry cathode powder that was composed of 8 wt% resin, 87 wt% NMC 532 and 5 wt% C65 carbon black. Prior to spraying, the dry cathode powder was prepared at ORNL as listed in Table I-19. Sample A was employed to demonstrate minimal water use for binder distribution in dry powder mixing. Samples B and D demonstrated the use of dry powders with the binder well dispersed over the powder surface. Samples C and E were equivalent formulations to samples B and D with the exception that a photoinitiator was added for UV curing.

Table I-19: Dry powder samples prepared for electrostatic spraying trial runs.

Sample	Resin	Photoinitiator (PI)	Solvent	Curing Method
A	Ucecoat 7689	None	No additional water	EB
B	Ucecoat 7689	None	DI water	EB
C	Ucecoat 7689	Omnirad 500	DI water	UV
D	PA50	None	Acetone	EB
E	PA50	Keyland Polymer	Acetone	UV

The morphology of the prepared dry powders is shown in Figure I-104. No difference was observed among samples A, B and D, indicating the binder was well dispersed in the NMC 532 and carbon black mixtures. After electrostatic spraying, samples were calendared (which significantly improved adhesion in all cases) followed by UV or EB curing. SEM images of the final electrode microstructures are shown in Figure I-105, and it was observed that sample A had good dispersion of carbon black among the NMC particles. Samples B and C exhibited typical morphology consistent with our standard aqueous processed NMC 532 cathodes. The carbon-black dispersion in NMC was excellent for samples D and E, which were processed with acetone, but it is not yet clear whether the addition of acetone promotes this improved dispersion.

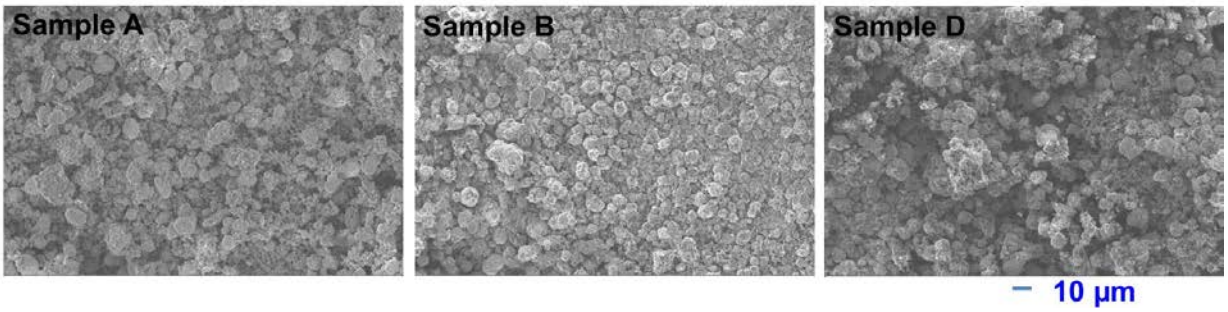

Figure I-104. SEM images of prepared sample A, B, and D dry powders.

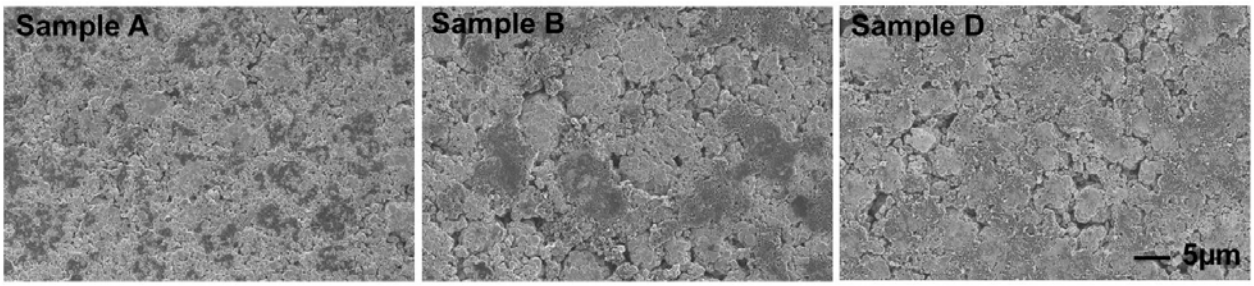

Figure I-105. SEM images of Sample A, B and D after calendaring and radiation curing.

The half-coin-cell charge and discharge profiles and rate performance for these formulations (samples A-E) are shown in Figure I-106, and they were tested using C/20 charging and discharging for the first three formation cycles followed by C/5 to 5C rate test with voltage cut-offs of 2.5 V and 4.2 V. All cells showed the typical charge/discharge features of an NMC cathode, indicating that the resin did not affect the lithiation/delithiation processes. Our baseline PVDF electrode performance is not shown in Figure I-106 since these electrodes had greater thickness, which affects the comparison. Sample E showed superior rate performance up to 3C discharging as compared to sample C, which could be ascribed to the better dispersion of carbon black in the cathode. Full coin cells were made for samples A and B to obtain short-term cycling performance when paired with graphite anodes (see Figure I-106c), and these cells were cycled at C/3 charge/discharge rates. Greater than 90% capacity retention was achieved after 100 cycles for both formulations, demonstrating that there is no benefit from adding additional water to the formulation (sample B vs. A).

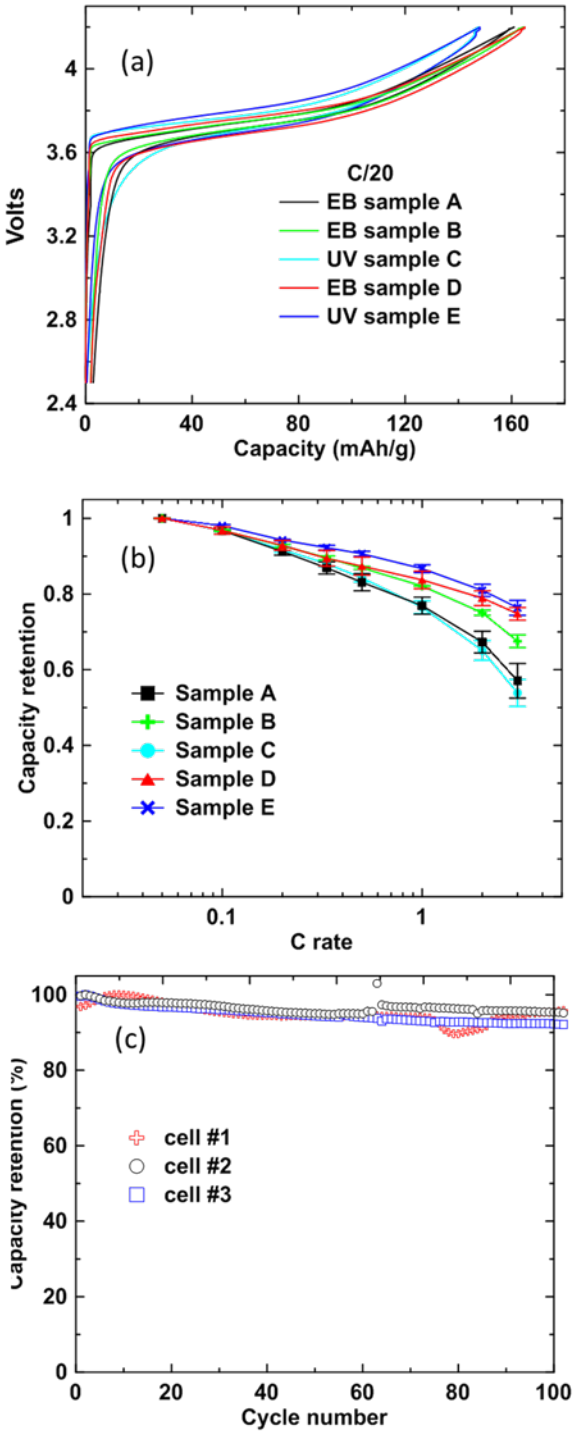

Figure I-106. (a) Voltage profiles in Li half cells, (b) rate performance in Li half cells, and (c) selected full-coin-cell cycling performance for samples A and B.

Conclusions

The project stretch milestone was successfully met by demonstrating no more than 20% capacity fade through 300 cycles at 0.33C/-0.33C in 1.5 Ah pouch cells with optimized cathode EB curing formulation and areal loading of 25 mg/cm^2 at a curing speed of 150-200 m/min, and completing pouch cell rate performance from C/20 to 1C. A "Go" decision was made by demonstrating 25 mg/cm^2 NMC 532 cathode coating areal weight with full EB cure and down-selected electrode formulation with selected industrial partner at 150-200 m/min.

Technical achievements include: (1) 150 m/min EB curing pilot line demonstration, (2) 1.5 Ah pouch cell performance evaluation, (3) dry powder mixing evaluation, and (4) electrostatic spraying of powder coating with good electrochemical performance.

Collaborative accomplishments include: (1) high speed curing trials are currently being scaled up at ebeam Technologies pilot line in Davenport, IA. (2) Electrostatic spraying powder coating is evaluated at Keyland Polymer in Cleveland, OH.

Commercial deployment is highly likely for this technology because of strong industrial collaboration, significant electrode production cost reduction, and impact on cell energy density (≥2× thicker cathodes).

Key Publications

1. U.S. Provisional Patent Application No. 62/492,370, "A Method of Solvent-Free Manufacturing of Composite Electrode Incorporating Radiation Curable Binders," 2017.

2. D. L. Wood, Z. Du, C. J Janke, J. Li, C. Daniel and C. Eberle, "Towards Solventless Processing of Thick Electron-Beam (EB) Cured Lithium-Ion Battery Cathodes," ES 207, DOE Annual Merit Review, June 8, 2017.

3. Z. Du, C. J Janke, J. Li, C. Daniel, D. L Wood, "Towards Solventless Processing of Thick Electron-Beam (EB) Cured Lithium-Ion Battery Electrodes," 232nd ECS meeting, National Harbor, MD, Oct 4, 2017.

4. Z. Du, K.M. Rollag, J. Li, S.J. An, M. Wood, Y. Sheng, P.P. Mukherjee, C. Daniel, D.L. Wood III, "Enabling Aqueous Processing for Crack-Free Thick Electrodes," *J. Power Sources*, **354**, 200 (2017).

5. J. Li, Z. Du, R. E. Ruther, S. J. An, L. A. David, K. Hays, M. Wood, N. D. Phillip, Y. Sheng, C. Mao, S. Kalnaus, C. Daniel, D. L Wood, "Toward Low-Cost, High-Energy Density, and High-Power Density Lithium-Ion Batteries," *JOM*, **69**, 1484 (2017).

6. Z. Du, D.L. Wood, C. Daniel, S. Kalnaus, and J. Li, "Understanding Limiting Factors in Thick Electrode Performance as Applied to High Energy Density Li-Ion Batteries," *Journal of Applied Electrochemistry*, **47**, 405 (2017).

I.B.9 Performance Effects of Electrode Processing for High-Energy Lithium-Ion Batteries (ORNL)

David L. Wood, III, Principal Investigator
Oak Ridge National Laboratory
NTRC-2, 2370 Cherahala Boulevard, MS-6479
Knoxville, TN 37932
Phone: 865-574-1157
E-mail: wooddl@ornl.gov

Peter Faguy, Technology Manager
U.S. Department of Energy
Phone: 202-586-1022
E-mail: Peter.Faguy@ee.doe.gov

Start Date: October 1, 2016 End Date: September 30, 2019
Total Project Cost: $1,015,000 DOE share: $1,015,000 Non-DOE share: $0

Project Introduction

This project at the DOE Battery Manufacturing R&D Facility (BMF) at ORNL builds on past research successes on battery electrode process development and optimization, cost reduction, and cell energy density and manufacturability improvements, which support the Vehicle Technologies Office (VTO) and Electrochemical Energy Storage Tech Team ultimate targets of $80-100/kWh-usable system cost, 500 Wh/kg cell energy density, and 800 W/kg cell power density. Our goal is to perform the science needed to reduce high-risk, high-payoff technologies to lower risk levels, such that U.S. industry will consider their integration in future products. Once a new material, process, or concept has demonstrated feasibility for integration and scaling, the BMF will work to make it a viable processing methodology (preferably with an industry partner) with validated performance in a full pouch cell design. While doing so, the BMF will leverage a large array of complimentary projects and sponsors that will provide additional experience and a fast, efficient methodology for solving problems faced by the domestic lithium-ion battery (LIB) industry.

Objectives

To generate a deep understanding of process-property-performance relationships that lead to lower cost and higher performing lithium-ion cells:

- Optimize electrode formulation chemistry and dispersion mixing and relate colloidal structure to electrode architecture.
- Develop understanding of relationship between coating deposition physics, electrode quality, and electrode performance.
- Optimize drying and calendering protocols for thick electrodes.
- Determine compatibility of Ni-rich cathodes (NMC and NCA) with water-based processing.
- Reduce cell formation and electrode wetting time and elucidate impact on SEI and CEI layer chemistry, morphology, and functionality.
- Develop materials and chemical characterization methods for high-speed electrode processing.

Approach

- Enable thick electrode coatings with next generation cell chemistries (NMC 811, NCA, Si/graphite, etc.) through thorough understanding of colloidal science and formulation chemistry.
- In-depth study of interrelationship of electrode processing steps.
- Generate processing science knowledge that can be used to strengthen U.S. domestic lithium-ion battery supply chain.
- Develop cohesive processing-property-performance database.
- Develop and utilize novel materials and chemical characterization techniques to shed light on active and inactive materials processibility.

Results

pH and ICP-MS analysis of NMC cathode active materials after exposure to water

We analyzed the stability of four different NMC compositions in water to evaluate the feasibility of using aqueous processing to prepare Ni-rich NMC electrodes for high energy density LIBs. The experimental procedure was designed to mimic actual electrode processing conditions. Samples of NMC 333, 532, 622, and 811 powders were each exposed to aqueous solutions at three different pH values (pH 2, pH 6.6 (DI Water), and pH 12) for three different time periods (4 h, 1 day, and 1 week). The powder was then filtered out of each solution, and the filtrate was analyzed by ICP-MS to determine the concentrations of Li and transition metal ions that leached out of the NMC material. The pH of the filtrate was also measured to provide additional information on changes occurring during water exposure. This first water exposure step is analogous to slurry preparation, where the active material is mixed with solvent (in addition to carbon black and binder) before being coated and dried.

Two sets of experiments were performed—one at high solids % (~63 wt%) to represent actual slurry conditions, and one at low solids % (~8 wt%) as a worst-case scenario to enhance the effect of water exposure. The pH results for both sets of samples at all three initial pH values are shown in Figure I-107a. Regardless of the starting pH, all of the high-solids samples become quite basic very quickly (> pH 11.5 within the first 4 hours). In general, the higher the nickel content, the higher the final pH, although the differences were small. The pH results for the low-solids samples (exposed to a greater volume of water) were similar, but NMC 333 showed a slightly greater time dependence at pH 2.

Figure I-107b shows the percentage of Li leached from the NMC samples during water exposure at all three initial pH values as measured by ICP-MS. In all cases, the higher the Ni content in the NMC, the higher the Li loss (NMC 811 had the highest leaching). As expected, the low-solids samples exposed to a greater volume of water showed more Li leaching and a greater time dependence than the high-solids samples. For instance, the amount of Li leached from NMC 811 after 1 week in DI water was ~9% for the *low*-solids case, compared to ~3% for the *high*-solids case. This difference was the greatest for NMC 811 and decreased with lower Ni content. In addition, the amount of Li leached from the *low*-solids samples increased over time, whereas it remained almost constant for the *high*-solids samples. Interestingly, the initial pH of the solution had little effect on the amount of Li leaching. However, it is important to note that if different acids or bases had been used to adjust the solution pH, the impact may have been greater. The corresponding ICP-MS transition metal results (not shown) indicate that Ni, Mn, and Co leaching from NMC is minimal (< 0.19%) at all concentrations and initial pH values.

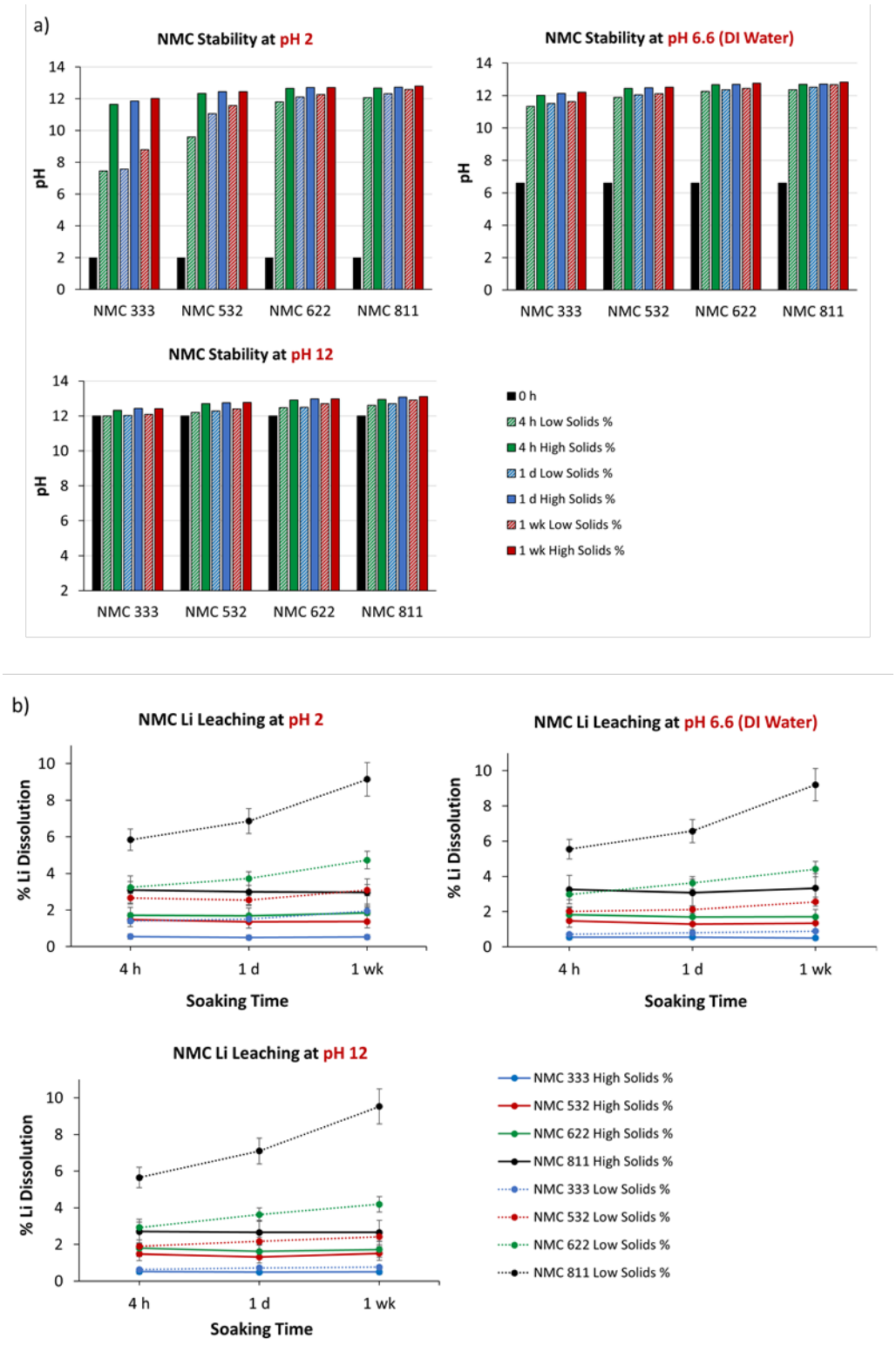

Figure I-107. Stability results after exposure of different NMC compositions to water, acid, and base solutions for different time periods. a) Measured filtrate pH values after soaking NMC in aqueous solutions with different pH values. Nitric acid was used to make the pH 2 solution, and ammonium hydroxide was used to make the pH 12 solution. b) % of Lithium leached from NMC (into the filtrate) after soaking in aqueous solutions with different pH values, as measured by ICP-MS.

A separate set of identical samples was made for characterization. These were prepared as described above, except instead of filtering out the powder particles after water exposure, the water was evaporated from the powder in a vacuum oven to simulate the typical two-step electrode drying process (in which the wet electrode coating is dried immediately, and a secondary drying step is performed in a vacuum oven before cell assembly). The dried powders were characterized by XPS, XRD, and Raman, which confirmed that there were no substantial changes to the NMC structure after water exposure.

Aqueous processing of NMC 811 single-layer pouch cells

Single-layer pouch cells (~100 mAh) were made using NMC 811 cathodes processed with either water or NMP (for comparison) and matching graphite anodes. The composition of the aqueous NMC 811 cathode slurry was 90 wt% Targray NMC 811, 5 wt% Denka carbon black,1 wt% Ashland carboxymethylcellulose (CMC), and 4 wt% Ashland acrylic emulsion, and the composition of the NMP-based NMC 811 cathode slurry was 90 wt% Targray NMC 811, 5 wt% Denka carbon black, and 5 wt% Solvay 5130 PVDF. Figure I-108 shows the capacity retention of aqueous- and NMP-processed NMC 811 cells after 200 cycles at 0.333C charge/discharge rates (charged to 4.2V). Although cells made with aqueous-processed NMC 811 cathodes show a slightly greater capacity fade (93% of original capacity after 200 cycles vs. 97% of original capacity for NMP-processed), the initial capacities of both sets of cells were the same, and both demonstrated good capacity retention after 200 cycles. Further optimization of the aqueous slurry rheology, by changing the order of addition or incorporating additives/dispersants, could help further improve performance. Binder supply chain delays have postponed our work in this area; nonetheless, these initial cycling results demonstrate that NMC 811 electrodes can be successfully made using aqueous processing, and cells made with these electrodes cycle nearly as well as cells made with the corresponding NMP-processed NMC 811 electrodes.

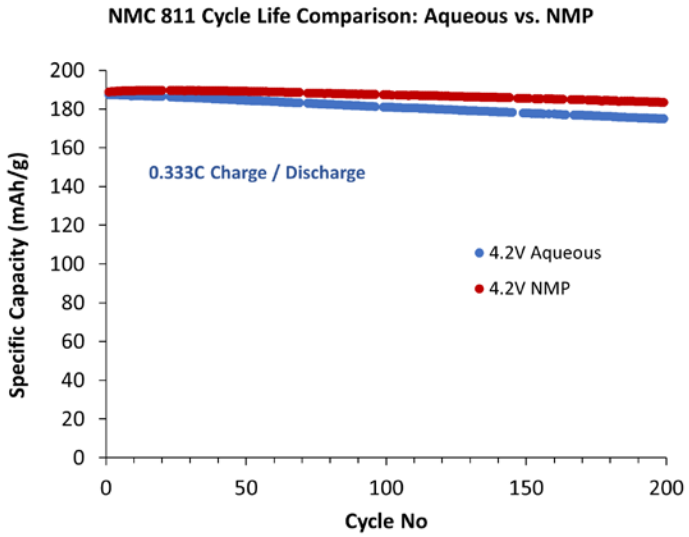

Figure I-108. Comparison of the capacity retention of single-layer pouch cells made with aqueous- and NMP-processed NMC 811 electrodes after 200 cycles at 0.333C charge/discharge rate. Data is an average of 3 cells, and the error bars represent the standard deviation of each cycle. The small breaks in the data are due to power outages. The active material loadings of the aqueous NMC cathode, NMP-based NMC cathode, and the Superior Graphite SLC 1520T anode were 11.3 mg/cm^2, 11.6 mg/cm^2, and 7.5 mg/cm^2, respectively. The cathode and anode thicknesses were 43 and 53 µm, respectively, and the porosity of all electrodes was 35%.

Aqueous processing of thick electrodes

Thick lithium-ion battery (LIB) electrodes promise to substantially increase energy density due to increased volume fraction of active materials and to reduce cost due to the elimination of the toxic organic N-methylpyrrolidone (NMP) solvent, but cracking of electrode coatings becomes a critical issue with aqueous processing of the cathode as active material loading increases above 20-25 mg/cm^2 (3.5-4.0 mAh/cm^2) as shown in Figure I-109a-d. The NMC 532 cathode with 15 mg/cm^2 loading was uniform and crack-free, but noticeable cracks with gap width of 50 µm and length of 300 µm were observed in the cathode with 17.5 mg/cm^2 loading. Further crack propagation is seen in Figure I-109c-d for increased loading in the manner of both crack quantity and crack dimension (width and length).

Figure I-109e is an illustration of cracking due to the build-up of capillary pressure during the drying process. Initially, all particles are suspended in the solvent after the slurry is cast onto Al foil. As the solvent evaporates, the air-solvent interface reaches the sediment surface. Menisci are formed between particles on the surface, and particles are subjected to a compressive force perpendicular to the air-liquid interface resulting from capillary pressure. As particles consolidate further, capillary pressure builds up and local gaps widen due to the increasing in-plane capillary forces. Eventually, the film cracks to release these stresses.

Since the capillary pressure during drying initiates film cracking, the reduction of surface tension is a straightforward method to alleviate or eliminate cracks. Isopropyl alcohol (IPA) is a widely used solvent in industry with a very low surface tension (23.00 mN/m, 20°C), and it is also miscible with water. The critical thickness or loading of the coating without cracking versus the solvent composition is shown in Figure I-109f. The crack-free loading increased gradually when more IPA was used during slurry preparation, which is attributed to reduced surface tension leading to decreased capillary forces during coating drying. A linear relationship was obtained between the critical loading and $(1/\gamma)^{1/2}$ where γ is the solvent mixture surface tension.

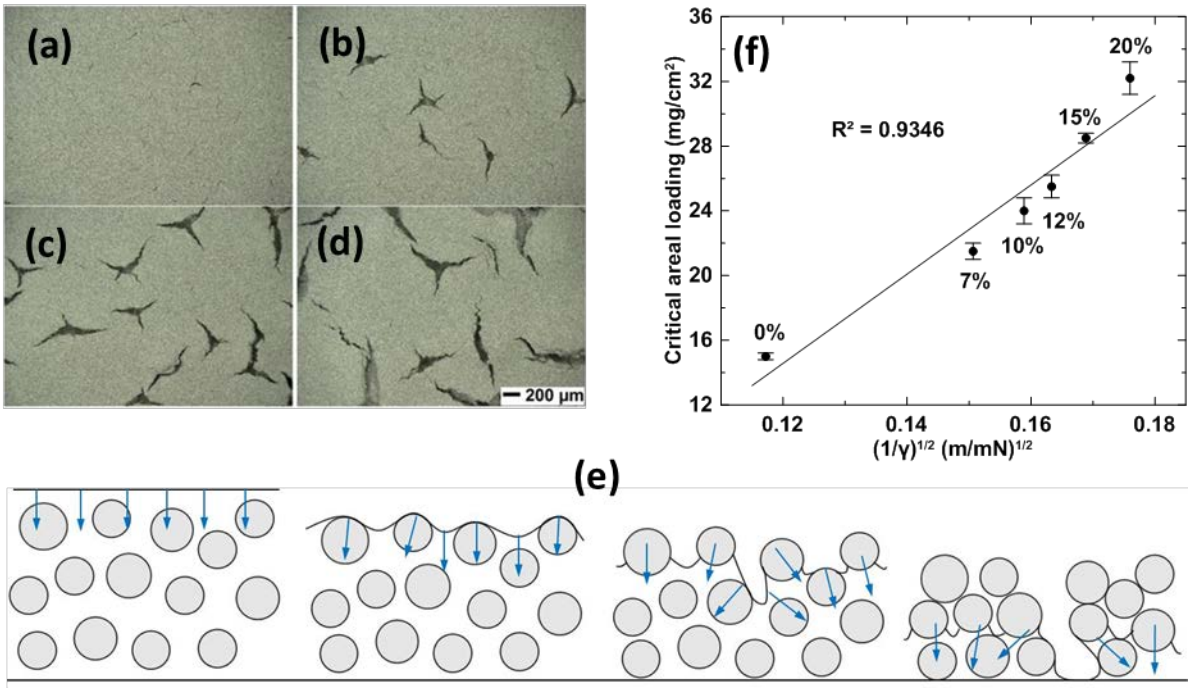

Figure I-109. Aqueous processed NMC 532 cathodes with different active material loadings: (a) 15 mg/cm^2, (b) 17.5 mg/cm^2, (c) 20 mg/cm^2 and (d) 25 mg/cm^2. (e) Illustration of the drying process. (f) Critical areal loading versus $(1/\gamma)^{1/2}$.

Compared to co-solvent optimized cathodes, the capacity of cracked electrodes deteriorated significantly when the discharge rate in 170-mAh pouch cells was higher than C/2 due to the poor quality of the coating. With the reduction of solvent surface tension during processing, coatings with good quality were formulated; thus, the rate performance capacity was improved with electrodes using IPA/water co-solvent processing. Long-term 170-mAh pouch cell cycling performance using different NMC 532 cathodes was evaluated, and with the addition of IPA during formulation, electrodes with IPA/water co-solvent processing exhibited greatly improved capacity and cycling performance compared to fully aqueous processed electrodes. Cathodes using IPA/water co-solvent processing had long-term cycling performance comparable to NMP processed electrodes, both achieving 83% capacity retention after 700 cycles.

Aqueous processing using carbon nanotubes (CNTs) as conductive additives

Aqueous processing of NMC 532 cathodes was investigated by incorporating CNTs as the conductive additive. Figure I-110a-f shows SEM images of these cathodes, and for the carbon black (CB) electrode (5% carbon black, 5% binder in the electrode), aggregates were formed in the interstitial space between NMC secondary particles. Being 0D in nature, the CB agglomerates do not connect with each other to form continuous and effective electronic paths. Higher resolution SEM in Figure I-110b shows some bare NMC primary particles without any coverage by carbon black. Therefore, the electrons associated with the local charge-transfer reaction have long transport pathways across several NMC primary particles to reach the CB conductive network. For the CNT-A electrodes (2.5% CNT, 5% binder), the CNTs were well dispersed across the electrode, and no obvious aggregates are seen in Figure I-110c. Figure I-110d shows that CNTs are uniformly spread over the entire surface of individual primary NMC particles. This 3D CNT network and intimate contact between CNT and primary NMC particles form a highly efficient electron conducting pathway. The CNT-B electrodes (1.5% CNT, 2.5% binder) in Figure I-110e-f show a similar morphology to CNT-A, even though the ratio of CNTs in the electrode is reduced to 1.5 wt%.

Figure I-110g and Figure I-110e show the normalized percentage capacity versus discharge rate for 85-mAh pouch cells. The cell capacity of the three different NMC 532 cathodes is nearly identical up to C/2 indicating the electrode conductivity is sufficient when discharged at C/2. However, there was significant deviation in performance at ≥1C between the CB baseline and the CNT substituted cells. The capacity of the CNT-B electrodes was also slightly better than that of the CNT-A electrodes from 1C to 3C, possibly due to better dispersion of CNTs in the electrode from the lower concentration of CNTs in the slurry. Long-term cycling performance of the three electrode types is shown in Figure I-110h for 85-mAh pouch cells. The CB baseline electrode showed relatively good performance with about 94.6% capacity retention after 200 cycles, but the cycling performance of the CNT-A and CNT-B cells was much higher with about 99.4% capacity retention remaining after 200 cycles.

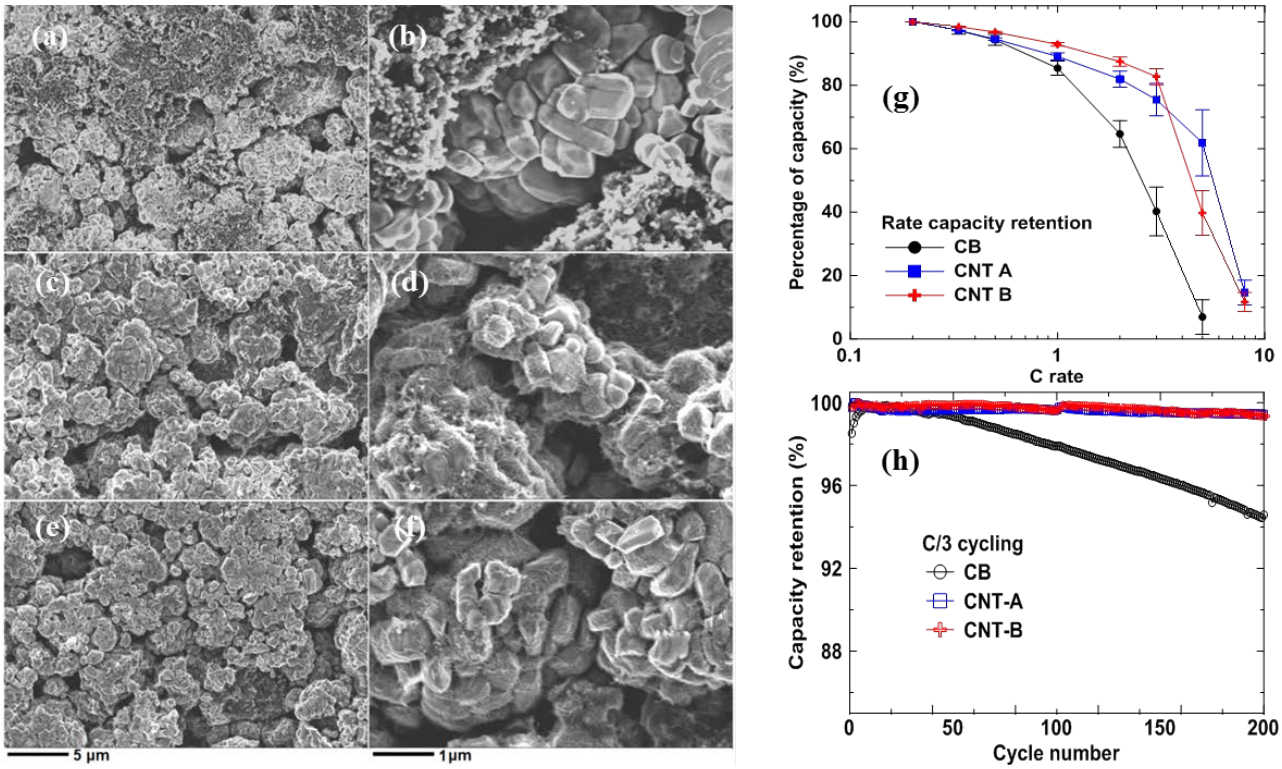

Figure I-110. SEM images of (a, b) CB electrode, (c, d) CNT-A electrode and (e,f) CNT-B electrode. (g) percentage of capacity (normalized to capacity at C/5) at different discharge C rates. (h) cycling performance at C/3.

Conclusions

The measured pH values of the NMC active materials exposed to water were comparable to the pH of an actual aqueous NMC 532 slurry (measured at 12.18), which confirms the relevance of our measurements. Overall, the Li ICP-MS results confirm that while Li leaching during water exposure is higher for Ni-rich NMC, it is minimal at actual slurry concentrations. Cathodes using IPA/water co-solvent processing had long-term cycling performance comparable to NMP processed electrodes, both achieving 83% capacity retention after 700 cycles. This finding was expected from the good morphology and physical integrity of electrodes using IPA/water co-solvent processing, which eliminates the detrimental interfacial resistances from the cracks in electrode. Besides better electrochemical performance of CNT-based cathodes, the total inactive components (binder and conductive additives) were also significantly reduced compared to CB electrode. It was calculated that the energy density of the cathode was increased by 11.7% at C/3 with a corresponding capacity loading and voltage increase of 6.67% and 4.77%, respectively. Therefore, this processing and electrode architecture modification is an extremely effective method for improving the energy and power density of Li-ion batteries.

Key Publications

1. Z. Du, K.M. Rollag, J. Li, S.J. An, M. Wood, Y. Sheng, P.P. Mukherjee, C. Daniel, D.L. Wood III, “Enabling Aqueous Processing for Crack-Free Thick Electrodes,” *J. Power Sources*, **354**, 200 (2017).

2. U.S. Provisional Patent Application No. 62/492,475, “Manufacturing of Thick Composite Electrode Using Solvent Mixtures,” 2017.

3. Z. Du, D.L. Wood, III, C. Daniel, S. Kalnaus, and J. Li, “Understanding Limiting Factors in Thick Electrode Performance as Applied to High-Energy-Density Li-Ion Batteries,” *Journal of Applied Electrochemistry*, **47**, 405–415 (2017).

I.C Computer-Aided Engineering for Batteries (CAEBAT)

I.C.1 Advanced Computer Aided Battery Engineering Consortium (NREL, ANL, SNL, Purdue U)

Dr. Kandler Smith, Principal Investigator
National Renewable Energy Laboratory
15013 Denver West Parkway
Golden, Colorado 80401
Phone: 303-275-4423
E-mail: kandler.smith@nrel.gov

Dr. Daniel Abraham, Principal Investigator
Argonne National Laboratory
9700 Cass Avenue
Lemont, IL 60439
E-mail: abraham@anl.gov

Dr. Joshua Lamb, Principal Investigator
Sandia National Laboratories
1611 Innovation Parkway, SE
Albuquerque, NM 87185
E-mail: jlamb@sandia.gov

Dr. Partha Mukherjee, Principal Investigator
Purdue University
585 Purdue Mall
West Lafayette, IN 47907
E-mail: mukher28@purdue.edu

Brian Cunningham, Technology Manager
U.S. Department of Energy
Phone: 202-287-5686
E-mail: Brian.Cunningham@ee.doe.gov

Start Date: October 1, 2016 End Date: September 30, 2018
Total Project Cost: $5,150,000 DOE share: $5,150,000 Non-DOE share: $0

Project Introduction

Building upon previous work under DOE's Computer Aided Engineering for Electric-Drive Vehicle Batteries (CAEBAT) Program, the current project seeks to (1) enhance and validate the predictive capability of computationally efficient electrochemical models for thick electrode designs as a path to lower battery cost and increase energy density; (2) develop and validate mechanical/electrochemical/thermal simulation models that describe the physiochemical processes encountered by batteries in the event of vehicle crash, possible internal short and thermal runaway, providing better understanding and enabling safer designs; (3) develop 3D models of electrochemical processes on the electrode microstructure length scale, providing better understanding of inhomogeneous electrode utilization that causes performance limitations and premature degradation. With NREL as lead, the Advanced Computer Aided Battery Engineering Consortium includes partner laboratories Argonne National Laboratory (ANL) and Sandia National Laboratories (SNL) conducting complementary experimental studies and Purdue University conducting complementary mesoscale modeling studies. ANL and SNL experimental studies are further described in separate chapters of this report.

Objectives

The Advanced Computer Aided Battery Engineering Consortium is working to develop modeling capabilities that help industry accelerate development of electric-drive vehicle (EDV) batteries, promote deeper and quantitative physical understanding and thereby improve battery performance, energy density, cost, safety and life. The project is divided into three tasks with the following objectives:

1. Computationally Efficient Electrochemical Modeling

Build upon recently published multiscale multidomain (MSMD) 3-D battery electrochemical-thermal simulation models with 100-1000 fold speedup to develop electrochemical parameter libraries for NMC523 and graphite electrodes from ANL Cell Analysis, Modeling and Prototyping (CAMP) facility. Demonstrate the accuracy of those models to capture the electrochemical performance of the CAMP electrode library with electrode loadings ranging from 1.6 to 7.5 mAh/cm^2. Identify tortuosity and other rate limitations inherent to these thick electrode designs to promote future lower cost, higher energy density batteries.

2. Mechanical/Electrochemical/Thermal Abuse

With SNL, build and experimentally validate simulation tools to predict the thermal-runaway behavior of lithium ion cells after a crash-induced crush. Include rate-dependent mechanical failure of individual cell components coupled with electrical, thermal and electrochemical reactions. Capture changes in cell behavior with aging. Implement battery crash abuse models in LS-DYNA coupling solid mechanics response with electrochemical/ thermal abuse user-defined functions. Partner with the USCAR Crash Safety Work Group (CSWG) to evaluate models, obtain feedback, and ensure they meet the needs of crash safety engineers.

3. Microstructure Modeling

Use microscopy and tomography experiments to characterize the microstructure of $Ni_{0.5}Co_{0.3}Mn_{0.2}$ (NMC523) and graphite porous electrodes with varying thickness, recipe and calendaring condition from the ANL CAMP library. With Purdue and ANL, identify and elucidate critical factors of electrode microstructure influencing rate limitations and inhomogeneous utilization using microstructural analysis, stochastic reconstruction, homogenization and direct numerical simulation of electrochemical physics on the complex 3-D geometry.

Approach

1. Computationally Efficient Electrochemical Modeling

Leveraging commercial materials and electrode designs from other DOE programs, the ANL CAMP facility produced high-quality electrodes of varying thickness and porosity. Negative electrodes using ConocoPhillips CGP-A12 graphite were produced with four different loadings ranging from 2.0 to 7.5mAh/cm^2 and in uncalendered and calendered variants with porosities of 51% and 37%, respectively. Positive electrodes utilized Toda $Li_{1.03}(Ni_{0.5}Co_{0.3}Mn_{0.2})_{0.97}O_2$ active material with loadings ranging from 1.6 to 5.8 mAh/cm2 and uncalendered/calendared variants of similar porosity. All cells used Gen II electrolyte, 1.2M $LiPF_6$ in EC:EMC (3:7,w/w). In addition to microstructure imaging experiments described later, all electrodes underwent electrochemical testing that consisted of galvanostatic intermittent titration (GITT) and constant current discharge rate tests. For modeling, the baseline thin electrode GITT and C/100 data were used to extract solid state thermodynamic, transport and reaction kinetic properties. Thick electrode data were used to validate macro-homogeneous electrochemical models and provide an estimate of tortuosity, a difficult to quantify parameter controlling effective electrolyte transport rate capability in the porous electrode.

2. Mechanical/Electrochemical/Thermal Abuse

We recently reported [1] a modeling approach to investigate propagation of mechanical failure across different layers within a cell. This approach enables us to identify the extent of damage across each component, when a lithium ion cell is subjected to mechanical impact and help us identify the limiting factor contributing to subsequent electrical and thermal events that follow a crash event. In FY17, the team gathered validation data by testing cells under a variety of different mechanical loading conditions – including variations to cell orientation, strain rates and ambient temperature. These results are summarized in section II.C.3 of this report.

In this section, we explore how thermal, mechanical and electrical properties of the cell components, which govern the failure response of the cell, evolve as the cell ages. All test samples were obtained from teardown of commercial NMC/graphite pouch cells. The cells were aged at 25ºC under 2C charge and 1C discharge rates across a voltage window of 4.1V to 3.0V for over 5000 cycles. All mechanical tests below were conducted using an Instron 5966 Dual Column Testing System. High strain-rate measurements using a modified dynamic tension fixture, are currently underway.

3. Microstructure Modeling

Figure I-111 shows the overall approach for microstructure characterization and modeling. Microstucture geometries are either experimentally or numerically generated. ANL and University College of London (Prof. Paul Shearing) generated FIB-SEM and X-ray computed tomography (CT) images of the ANL CAMP electrodes, resolving different length scales. CT imaging reasonably captures active material geometry (~0.5 to 100 µm) however is not capable of resolving carbon/binder additive (CBA) geometry due to inadequate resolution and phase contrast. To overcome this limitation, Purdue University has developed a set of algorithms to numerically generate the CBA and match its properties to FIB-SEM and electrochemical data. The microstucture geometry is used for several purposes: (1) for 3D electrochemical simulation on NREL's high performance computer (HPC), Peregrine, and (2) for calculation of effective properties that are applied in macro-homogeneous electrochemical models. Macro models are well suited to wide design space searches. The micro models inform the macro models and provide deeper physical understanding how electrode morphology influences performance and degradation. In FY17 the team initiated a study of tortuosity of the ANL CAMP electrodes that also included experimental measurements performed by Brigham Young University (Prof. Dean Wheeler).

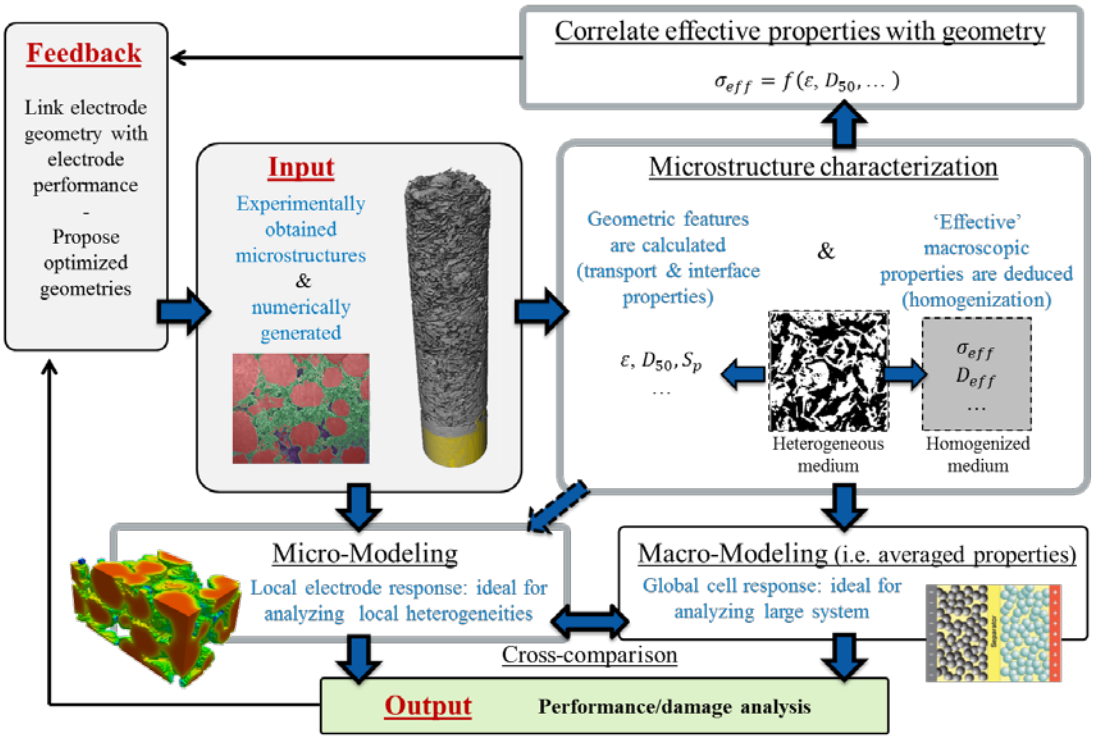

Figure I-111. Approach for microstructure characterization and modeling

Results

1. Computational Efficient Electrochemical Modeling

A parameter library was developed for ANL CAMP graphite and NMC532 electrodes using macro-homogeneous electrochemical models [2]. The team published its analysis of GITT and constant current data

for the ANL CAMP baseline 34 µm NMC532 electrode [3]. A similar article is under preparation for the baseline 44 µm graphite electrode. The kinetic and solid-state transport parameters were then applied in a modeling study of the twelve thicker electrodes from the ANL CAMP library. While most electrochemical model properties are measureable from unique experiments, electrode tortuosity – inhibiting Li+ ionic transport in the electrolyte phase – was treated as an adjustable parameter in the model. (Direct experimental measurements and microstructure modeling predictions of tortuosity are given in the microstructure section.)

Figure I-112 shows an example model voltage prediction compared to NMC532 half cell data for two different thickness electrodes. Figure I-112(a) shows excellent model agreement for the 88 µm calendered electrode. That electrode achieves 685 mWh/g-NMC energy density at the 1C rate. Figure I-112(b) compares model vs. data for the 129 µm calendared electrode. While thicker electrodes typically have higher energy density than thinner electrodes, the 129 µm electrode has less energy density, 635 mWh/g-NMC at 1C due to high tortuosity inducing electrolyte transport limitations. Tortuosity – the penalty for an ion to conduct and diffuse through a porous media of electrolyte as opposed to an open bath of electrolyte – can be expressed in terms of tortuosity, τ, or as a Bruggeman exponent, p,

$$D_{eff} = \frac{\varepsilon}{\tau} \times D_{bulk} = \varepsilon^{p} \times D_{bulk}$$

where ε is the volume fraction of pore space in the electrode, D_{bulk} is the diffusivity of ions in the open bath and D_{eff} is the effective diffusivity in the porous electrode medium. A Bruggeman exponent of 1.5 is typically used in the literature. The present study however found Bruggeman exponents in the range of 2-2.3 for ANL NMC electrodes and 2.7-3.3 for graphite electrodes. These values have implications when optimizing electrodes for high-rate capability and energy density. For the current electrochemical system, the NMC electrode cannot increase beyond 90 µm thickness without experiencing electrolyte transport limitations at the 1C rate, limiting 1C energy density to ≤250 Wh/kg.

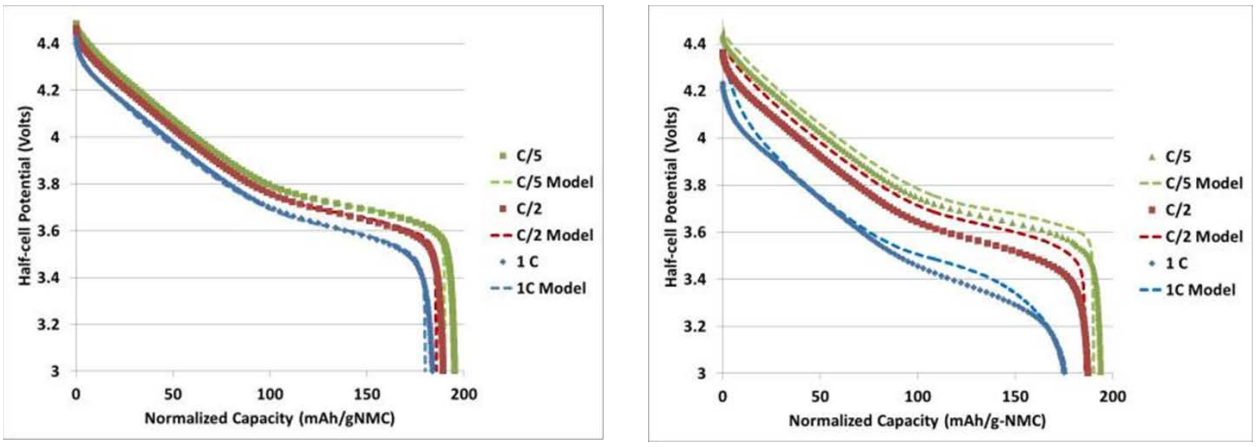

Figure I-112. Comparison of model to NMC532 half-cell data for (a) 88 µm and (b) 129 µm calendered electrodes.

2. Mechanical/Electrochemical/Thermal Abuse

Under the mechanical abuse modeling task, the team focused on characterizing properties of anodes, cathodes and separators from lithium-ion cells that were aged under different conditions and assessing the impact of cell aging on safety. Figure I-113 highlights some findings on the mechanical evaluation of cell components before and after aging. The tensile test results showed much more variability due to the large sample size requirement and non-uniform aging of the electrodes across the cell.

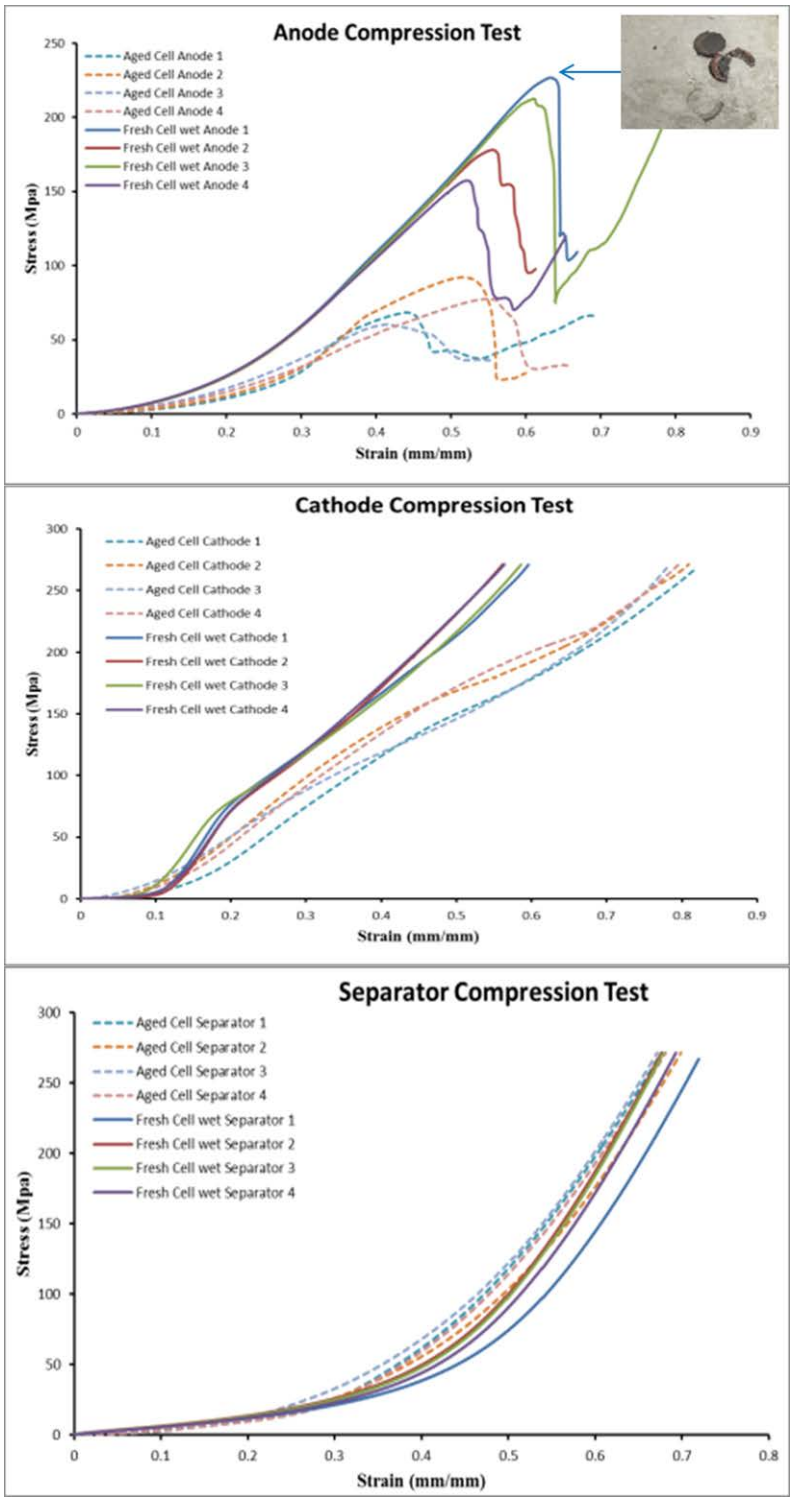

Figure I-113. Compression test results comparing stress- strain curves for fresh cell components against those collected from an aged cell: the anode samples typically show an earlier onset of failure, at lower ultimate strengths; the cathode samples show a very repeatable drop in the modulus – typically characteristic of the current collector. There is no statistical difference in the separator properties for the cell studied under this particular test condition.

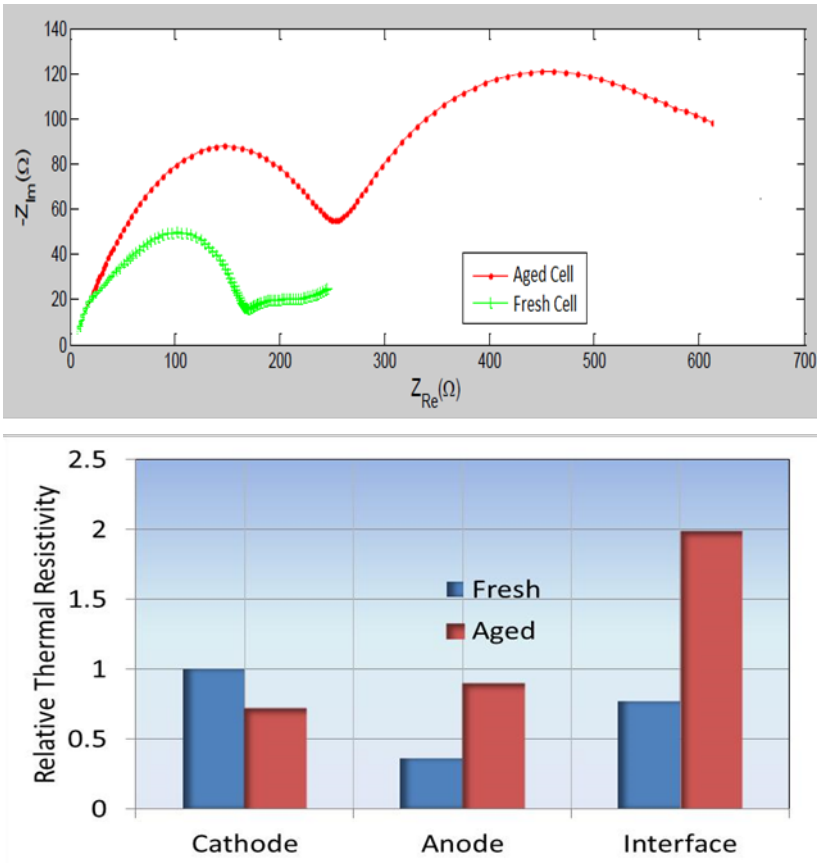

Figure I-114. Comparison of the electrical and thermal properties of cell components before and after aging

Similar analyses were performed to characterize the growth in the electrical resistance using electrochemical impedance spectroscopy (EIS) and thermal impedance using xenon flash reflectometry. Figure I-114 shows sample results. The cathode showed very little degradation compared to the anode in these tests as well. Careful measurement of thermal impedances in fact showed that the bulk thermal impedance of the cathode was no longer the dominant barrier for the heat generated within the cell to be transferred out of the cell. The interfacial contact between the anode and the separator accumulates more and more heat as the cell ages, signaling the onset point for thermal events within the cell.

3. Microstructure Modeling

A 3D electrochemical direct numerical simulation model was created in the FEniCS finite-element open-source environment to provide deeper insight into, for example, inhomogeneous utilization of the electrode not predicted by macro-homogeneous models. Such insight is needed for the community to continue to advance energy density and lifetime. The simulation domain size is chosen based on careful representative volume element (RVE) analysis in which larger and larger domain sizes are considered until results converge. Described in the article [4], electrode microstructure simulations must capture a volume as large as (60-90um^3) in order to fully represent volume fraction, particle size, connectivity, tortuosity and specific surface area of NMC. Graphite volumes can be slightly smaller. The model is being optimized to solve for several million degrees of freedom necessary to capture electrochemical transport/reaction physics on the full RVE domain using HPC. Initial numerical experiments demonstrate the model scales well to hundreds of parallel processors.

A present gap in predictive capability of electrochemical models is to predict the influence of inert components of carbon and binder – the so-called CBA domain – on electrode performance. CBA geometry is visible from small scale FIB-SEM images but not from the larger, electrode length scale CT imaging experiments. Purdue University developed mesoscale models and stochastic algorithms to virtually grow the CBA phase on active material from either virtual (Figure I-115b) or CT-imaged geometries (Figure I-115a). Described in the article [5], the amount and morphology of CBA has significant effect on electrochemical active surface area and electrode tortuosity. The team initiated a comparative study of tortuosity of the ANL CAMP electrodes as determined from (1) macro-homogeneous model fitting to electrochemical data, (2) microstructure homogenization, and (3) experimental measurement using symmetric cells and intercalation-blocking electrolyte (Dean Wheeler, BYU). Preliminary results show good agreement with the macro-homogeneous model results discussed previously. Additional findings on anisotropy of tortuosity include:

- NMC electrodes (quasi-spherical particles) are nearly isotropic, though small domains can be anisotropic
- Graphite electrodes (non-spherical platelets, sometimes agglomerated into potato-like particles) are highly isotropic. Transport is much slower in through-plane direction than in-plane
- Calendering increases anisotropy, slightly elongates NMC particles and reduces sphericity of both NMC and graphite particles.

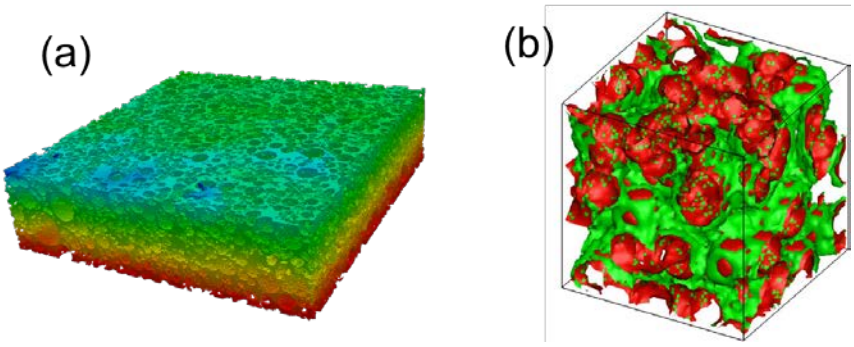

Figure I-115. (a) Homogenization simulation to determine effective electrolyte transport properties in porous electrode using geometry from CT imaging of an actual electrode. (b) Stochastic reconstruction of virtual geometry, showing CBA phase (green) on active material matrix (red).

Conclusions

The Advanced Computer Aided Battery Engineering Consortium – a partnership between NREL, ANL, SNL and Purdue University, with additional collaborators at UCL and BYU – continues to develop and validate simulation models that promote deeper understanding of battery physics and enable acceleration of next generation designs. In this second year of the three year project, mechanical abuse models were enhanced to capture the abuse response of aged cells. In the final year, those models will be validated versus off-axis and high speed crush tests at SNL. This year, the team further published electrochemical properties of ANL CAMP electrodes, validated electrochemical models and carried out a comparative study quantifying electrode tortuosity using different modeling and experimental methods. In the final project year, the 3D electrochemical microstructure model will be applied in validation studies versus ANL CAMP electrodes and the combined model toolset will be applied in studies to promote deeper physical understanding of electrode inhomogeneity and enable higher energy density and higher rate designs.

Key Publications

1. Z. Wu, L. Cao, J. Hartig, S. Santhanagopalan, “Effect of Aging on Mechanical Properties of Lithium-Ion Battery Components," ECS Trans., 77 (11) 199-208 (2017).

2. C. Zhang, S. Santhanagopalan, and A. Pesaran, “Simultaneously Coupled Mechanical-Electrochemical-Thermal Simulation of Lithium-Ion Cells," ECS Trans., 72 (24) 9-19 (2016).

3. S. Santhanagopalan, C. Zhang, M.A. Sprague, and A. Pesaran, “A Representative-Sandwich Model for Simultaneously Coupled Mechanical-Electrical-Thermal Simulation of Lithium-ion Battery Cell under Quasi-Static Indentation Tests.” J. Power Sources, 298, p. 102-113 (2016).

References

1. C. Zhang, J. Xu, L. Cao, Z. Wu and S. Santhanagopalan, “Constitutive Behavior and Progressive Mechanical Failure of Electrodes in Lithium-ion Batteries," J. Power Sources, 2017.

2. G-H. Kim, K. Smith, J. Lawrence-Simon, and C. Yang, “Efficient and Extensible Quasi-Explicit Modular Nonlinear Multiscale Battery Model: GH-MSMD," J. Electrochem. Soc., A1076-1088, 2017.

3. Verma, K. Smith, S. Santhanagopalan, D. Abraham, K.P. Yao, P.P. Mukherjee, “Galvanostatic Intermittent Titration and Performance Based Analysis of LiNi0.5Co0.2Mn0.3O2 Cathode,” J. Echem. Soc., accepted.

4. F. Usseglio-Viretta, K. Smith, “Quantitative Microstructure Characterization of a NMC Electrode,” ECS Transactions, 77 (11) 1095-1118 (2017).

5. A. Mistry, D. Juarez-Robles, M. Stein IV, K. Smith, P.P. Mukherjee, “Analysis of Long-Range Interaction in Lithium-Ion Battery Electrodes,” J. Echem. Energy Conversion & Storage, 13 (3) 2016.

I.C.2 Advanced Tool for Computer Aided Battery Engineering (ANL)

Dr. Daniel Abraham, Principal Investigator
Argonne National Laboratory
9700 Cass Avenue
Argonne, IL 60439
Phone: 630-252-4332
E-mail: abraham@anl.gov

Brian Cunningham, Technology Manager
U.S. Department of Energy
Phone: 202-287-5686
E-mail: Brian.Cunningham@ee.doe.gov

Start Date: October 1, 2016 End Date: September 30, 2018
Total Project Cost: $200,000 DOE share: $200,000 Non-DOE share: $0

Project Introduction

The main goals of DOE's Computer Aided Engineering for Electric-Drive Vehicle Batteries (CAEBAT) Program were introduced in a prior section. In this section, we describe the experimental studies conducted at Argonne National Laboratory (ANL) to support the development of 3D models of electrochemical processes on the electrode microstructure length scale and to provide an understanding of factors that limit electrode performance and cause premature degradation. These studies are intended to complement and enhance the experimental and computational work being conducted at the partner national laboratories and universities.

Objectives

The key objectives of our work can be summarized as follows:

1. To provide the positive and negative electrodes needed to accomplish the various tasks listed in an earlier section.
2. To characterize the electrodes using conventional electrochemical techniques, both in half-cell and full-cell configurations, and to provide the data for the development of 3D electrochemistry models.
3. To develop advanced tools, including spectroscopy and diffraction techniques, which can provide deeper insights on the correlations between electrode microstructure and electrochemical performance.

Approach

1. FIB-SEM imaging of positive and negative electrodes.

Positive and negative electrodes, of varying thickness and porosities, were fabricated at the Cell Analysis, Modeling, and Prototyping (CAMP) facility located at ANL. These electrodes were used to generate electrochemistry and microstructure data to support the computational efforts at the National Energy Renewable Laboratory (NREL) and Purdue University (Purdue). Focused Ion Beam (FIB)-Scanning Electron Microscopy (SEM) images of representative electrodes were obtained at the Frederick Seitz Materials Research Laboratory, University of Illinois at Urbana-Champaign. Images of electrode cross-sections were then used to generate 3D images of the electrode microstructure. X-ray tomography data were also obtained at the Advanced Photon Source (APS) located at ANL. These FIB-SEM and X-ray images are used to complement the computed X-ray tomography (CT) data obtained by our partners at University College London. Electrode microstructure information obtained from these various data are used as input for the 3D models that relate electrochemistry to electrode architecture.

2. Electrochemistry data in a Full cell configuration

In the previous year (FY 2016), we reported the *half-cell* performance of positive and negative electrodes of varying thicknesses and porosities. This year we obtained *full-cell* data, using a fixed porous graphite-based negative electrode and NCM523-based positive electrode of various thicknesses and porosities to elucidate the effect of the latter variables. Our cells contained the Gen2 electrolyte, which comprises 1.2 M $LiPF_6$ salt in ethylene carbonate (EC): ethyl methyl carbonate (EMC) (3:7, w/w) solvent and Celgard 2325 separator. The electrochemistry tests were conducted under galvanostatic conditions, with currents that ranged from 0.1C to 1C. The resulting data were provided to partner laboratories for electrochemistry model development.

3. Lithium-ion diffusion coefficients and their relationships to changes in oxide crystallography

We obtained the lithium-ion diffusion coefficient in the NCM523 layered oxide, using the galvanostatic intermittent titration technique [1]. In order to explain and elucidate the trends obtain in the diffusion coefficient vs. oxide lithium content profile, we conducted in operando X-ray diffraction measurements at beamline 6-BM of the APS. We noted strong correlations between the lithium-ion diffusion coefficients and crystallographic parameters of the NCM523 oxide, which increased our confidence in the lithium-ion diffusion data provided to NREL for battery modeling.

Results

1. FIB-SEM imaging of the positive electrodes (cathodes)

Resolving the carbon-binder distribution around active particles in electrodes is a challenge using X-ray tomography. Therefore, the X-ray data were supplemented by FIB-SEM imaging with nanometer scale resolution. The calendered standard ANL electrode (AC015, porosity = 34%, thickness = 34 µm) and a thick electrode in its uncalendered (LN2487-113-13, porosity = 49%, thickness = 160 µm) and calendered (porosity = 37%, thickness = 129 µm) states were imaged. As shown in Figure I-116, the low porosity calendered electrodes show tighter active particle packing compared to the uncalendered electrode.

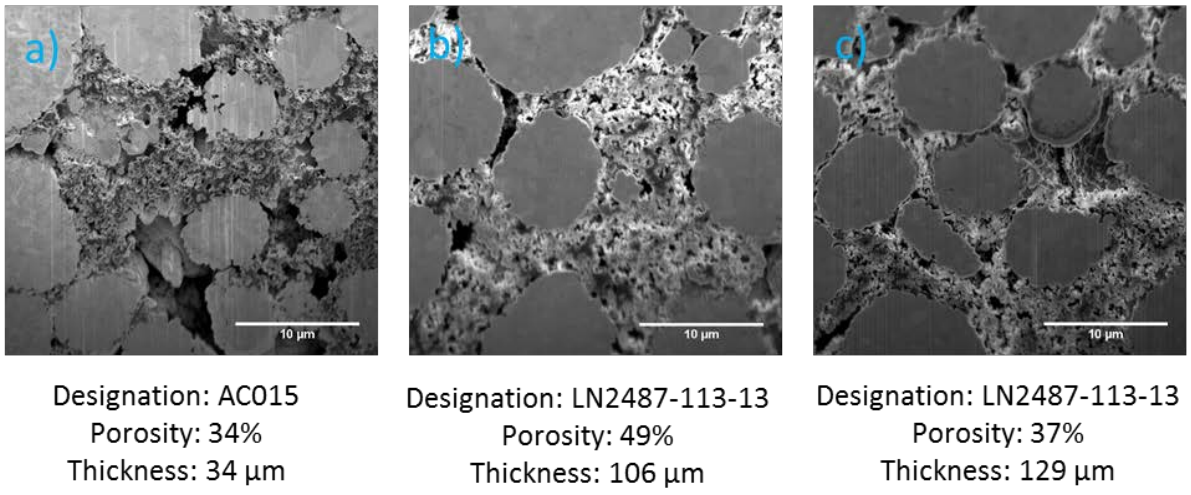

Figure I-116. FIB-SEM images of (a) calendered baseline, (b) uncalendered, (c) calendered NCM523 electrodes

The carbon-binder structure displays both nanometer and micrometer scale pores which are expected to be the channels for electrolyte transport through the electrode. The nanopores are distributed within the carbon structure while micropores are seen around the NCM523 active particles. The micropore openings near the active particles are likely regions of increased lithium insertion/extraction from the electrolyte while area covered with carbon-binder are electron hotspots. As is shown in the CAEBAT report by our partner at NREL, the presence of these additional fillings increase the effective tortuosity from a Bruggeman exponent of 1.5, when modeling the electrode as packed spherical particles, to 2-2.3. It is unclear from these images whether the packing of the nanoporous carbon-binder structure increases after calendering. Interestingly, the sphericity

of active particles appears to decrease upon calendering (compare Figure I-116b and Figure I-116a, Figure I-116c). Additional FIB-SEM images are being obtained, and image quantification is being performed, to elucidate the contribution of the carbon-binder structure to the increase of the tortuosity and Bruggeman factor.

One specific issue with the FIB-SEM images shown in Figure I-116 is the visibility of structures behind the imaging plane which complicates quantification of the amount of material within the image plane. In an effort to address this issue, epoxy (KwikWeld steel reinforced epoxy glue) was used to fill the micropores so as to confine imaging to the imaging plane. Filling of the macropores was achieved; however, because of contrast similarity between the carbon-binder structure and the epoxy filler in the SEM images we were unable to obtain accurate quantification of the pore volume and the carbon-binder matrix (see Figure I-117). A filler that can provide sufficient contrast difference composite is still being sought for accurate quantification of various features in the electrode microstructure.

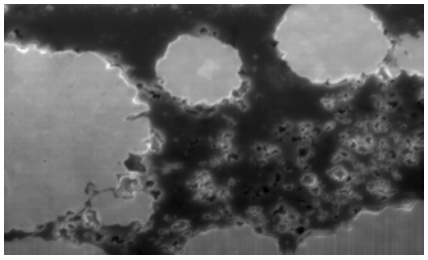

Figure I-117. FIB-SEM of AC015 electrode using an epoxy filler to confine imaging to the image plane.

2. Electrochemistry data in Full cell configuration

The performance of NCM523 cathodes against a fixed graphite anode (LN3024-126-5, uncalendered) was quantified. Results of these electrochemical characterization are presented in Figure I-118 and Figure I-119.

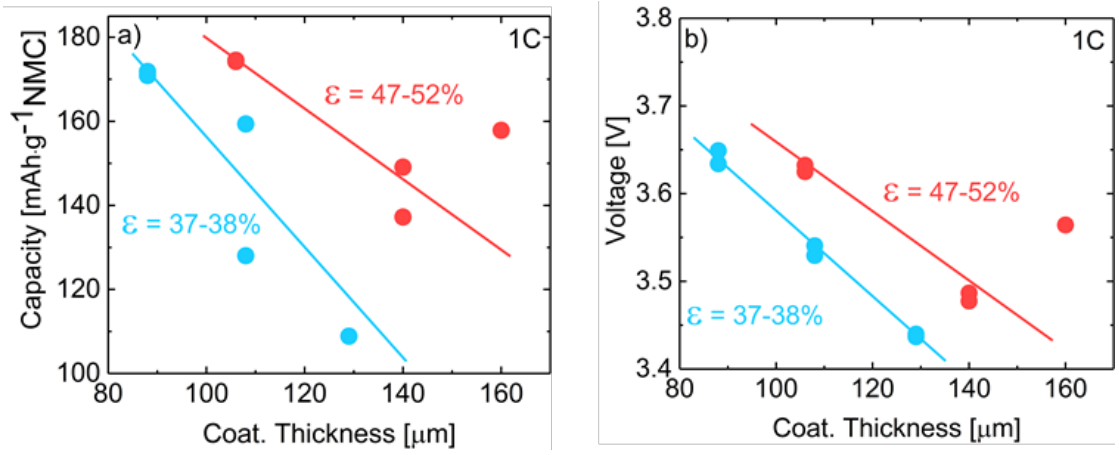

Figure I-118. Full cell electrochemical performance data during 1C discharge after the formation cycles (a) average capacity, and (b) average cell voltage versus electrode coating thickness and porosity (ε). The anode (uncalendered graphite, Coating thickness = 173 μm, Porosity = 51.8%) was kept the same for all these measurements.

Generally, as the cathode porosity is decreased via calendering, capacity output (Figure I-118a) and average cell voltage (Figure I-118b) decreases during cell discharge. Figure I-119 shows details of the influence of cathode thickness and porosity on discharge capacity and voltage at a 1C cell discharge rate. Discharge capacity and average cell voltage increase with decreasing thickness for a given porosity (Figure I-119a); also, capacity and average cell voltage increase with increasing porosity for a given thickness (Figure I-119b). These findings hold for rates ranging from 0.1C to 1C.

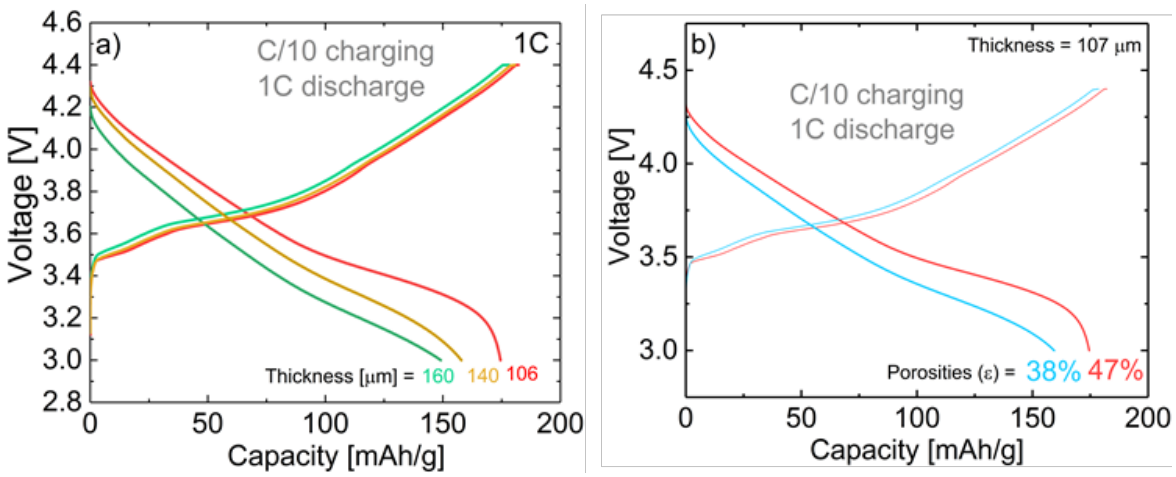

Figure I-119. Performance comparison during 1C discharge in full-cells as a function of (a) electrode coating thickness with porosities fixed at ~47-52% and (b) electrode porosity at fixed thickness of ~107 μm.

3. Lithium-ion diffusion coefficients and their relationships to changes in oxide crystallography

Measurements of lithium-ion diffusion coefficient in the NCM523 oxide electrode by the GITT technique were reported in reference [1]. The validity of the extracted values, and trends versus lithium content of the oxide, was systematically examined in the framework of crystallography. We explain modulations of the diffusion coefficient as a function of charge in Figure I-120.

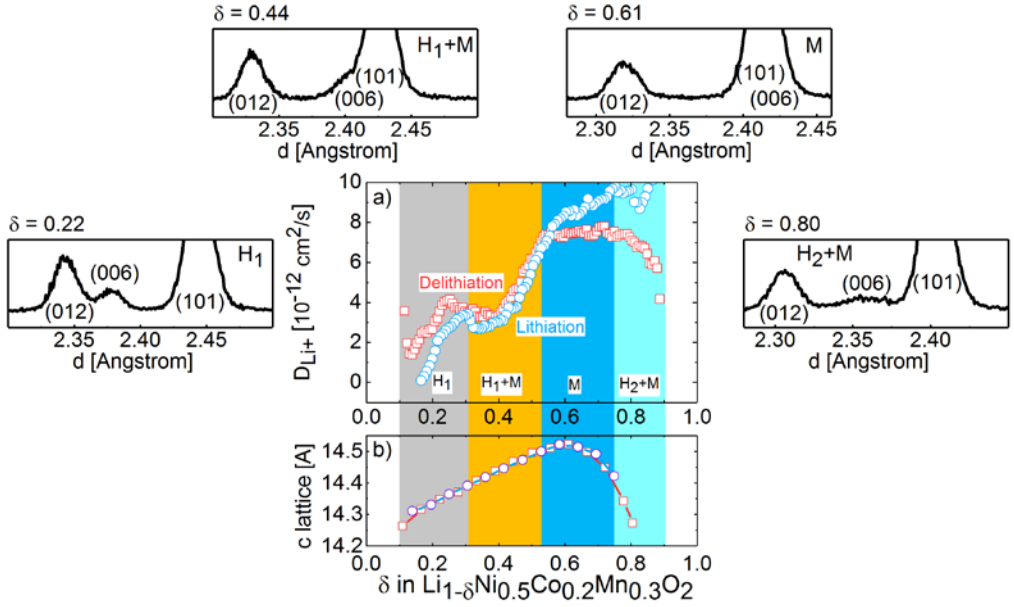

Figure I-120. (a) Chemical diffusion coefficient of lithium-ions in NCM523 oxide particles and (b) c-lattice parameter of the oxide crystal structure NCM523 during charge (delithiation) and discharge (lithiation).

Some noteworthy findings from our study are as follows: (i) mobility of lithium-ions in NCM523 increases fivefold (Figure I-120a) after roughly half the lithium-ions in the oxide are removed because of the large expansion of the crystal lattice along the *c*-direction (Figure I-120b); (ii) four crystal symmetry changes occur in NCM523 during discharge and charge (see sample XRD spectrum provided for each highlighted region in Figure I-120); (iii) these crystal symmetry changes are responsible for major inflections in the mobility of lithium in the active materials and (iv) the diffusion coefficient profile is correlated to overpotentials (voltage increase) during fast charging. This work is complementary to the work reported in reference [1], and a manuscript is currently being prepared for publication [2].

Conclusions

In support of the various tasks listed in section II.C.1 we have conducted electrochemical characterization of twelve different cathodes and anodes fabricated to attain various porosities and thicknesses. These data have been provided to our partner organizations (NREL and Purdue) for the development of 3D computational models of electrochemical behavior.

We have demonstrated through high resolution FIB-SEM imaging that the carbon-binder matrix in the NCM523 electrodes display both micropores and nanopores, which can significantly affect the measured electrode tortuosity and ancillary Bruggeman factor.

Calendering of electrodes results in compaction and deformation of the active NCM523 particles in battery electrodes, which increases tortuosity. The microstructural changes caused by calendaring has been shown to impact the electrochemical performance both in half-cells and full cells; in summary, the performance decreases with increasing electrode thickness and decreasing porosity.

With the goal of increasing confidence in the lithium-ion diffusion coefficient values obtained on the NCM523 oxide using a galvanostatic intermittent titration technique, operando energy dispersive X-ray diffraction data were obtained at the Argonne Advanced Photon Source. We show that the lithium-ion diffusion coefficients increases because of the c-lattice parameter increase observed during oxide delithiation. Other changes in the diffusion coefficients were related to the crystal symmetry changes that occur in the oxide lattice. We also showed that the diffusion coefficient values have a strong effect on the lithium-ion transport during high-current charging, and needs to be considered during the design of electrodes for fast-charge scenarios.

References

1. Verma, K. Smith, S. Santhanagopalan, D. Abraham, K.P. Yao, P.P. Mukherjee, “Galvanostatic Intermittent Titration and Performance Based Analysis of $LiNi_{0.5}Co_{0.2}Mn_{0.3}O_2$ Cathode,” J. Electrochem. Soc., 2017, 164, A3380−A3392.

2. Koffi P.C. Yao, John S. Okasinski, Jonathan D. Almer, Daniel P. Abraham, “Phase Modulation of Lithium-Ion Diffusion in $Li(Ni_{0.6}Co_{0.2}Mn_{0.2})O_2$: Implications for Fast Charging”, manuscript in preparation (2017).

I.C.3 Battery Abuse Testing (SNL)

Joshua Lamb, Principal Investigator
Sandia National Laboratories
1515 Eubank SE
Albuquerque, NM 87185
Phone: 505-284-9709
E-mail: jlamb@sandia.gov

Brian Cunningham, Technology Manager
U.S. Department of Energy
Phone: 202-287-5686
E-mail: Brian.Cunningham@ee.doe.gov

Start Date: October 1, 2016 End Date: September 30, 2018
Total Project Cost: $400,000 DOE share: $400,000 Non-DOE share: $0

Project Introduction

This project aims to provide experimental support, including support for validation and parameterization, for mechanical failure modeling work as part of DOE's Computer Aided Engineering for Electric-Drive Vehicle Batteries (CAEBAT) program. This work involves mechanical deformation testing on both charged and discharged cells, including abusive mechanical testing leading to battery failure. The mechanical data generated is provided to the modeling teams to provide empirical parameterization as well as validation for newly developed models. Testing fully charged cells and packs (abusive battery testing) also allows for a better understanding of what conditions are most likely to lead to a potentially hazardous thermal runaway event.

Objectives

Experimental determination of mechanical properties of lithium ion batteries and materials

- Experimentally validating simulation tools used to predict thermal runaway events caused by crash induced crush. This includes rate-dependent mechanical failure and properties of individual cells as well battery packs.
- Provide collected data to the consortium to aid in model development.
- Partner with the USCAR Crash Safety Work Group to obtain feedback on experimental methods as well as develop new tests that may be of relevance to crash safety engineers.

Approach

Sandia's Battery Abuse Test Laboratory was used to perform mechanical testing on full cells and packs for this project. This facility can contain and withstand thermal runaway of lithium ion cells and packs of up to 1 kWh of total energy. Mechanical test capabilities include a 100 klb_f large crush fixture and a 10 klb_f nail penetration and small-scale crush fixture. Recording capabilities include force, displacement, temperature and voltage measurements at rates of up to 1 kHz. Data recording rates varied depending on duration of testing.

Mechanical deformation results collected at Sandia have been provided to NREL and the technical working groups. This has also included collaboration and information sharing with the USCAR Crash Safety Working Group, with the ultimate goal of understanding what hazards lithium ion batteries may pose during extreme mechanical deformation events, such as an auto collision. Quarterly meetings also provide information sharing and collaboration with the broader consortium, including NREL, ANL, SNL and Purdue University, as well as members of the ORNL consortium.

Results

Testing at Sandia in FY17 focused on determining the mechanical behavior of single cells both in charged and discharged states. This builds upon work performed in FY16 looking at the overall mechanical behavior of packs and preliminary work looking at single cells. Three point bend tests were performed on 5 amp hour commercial off the shelf (COTS) lithium ion cells. The first tests performed were on fully charged cells to determine at what point catastrophic failure is likely to occur when subjecting these cells to extreme mechanical deformation. Selected results from testing on fully charged cells are shown in Figure I-121 and Figure I-122.

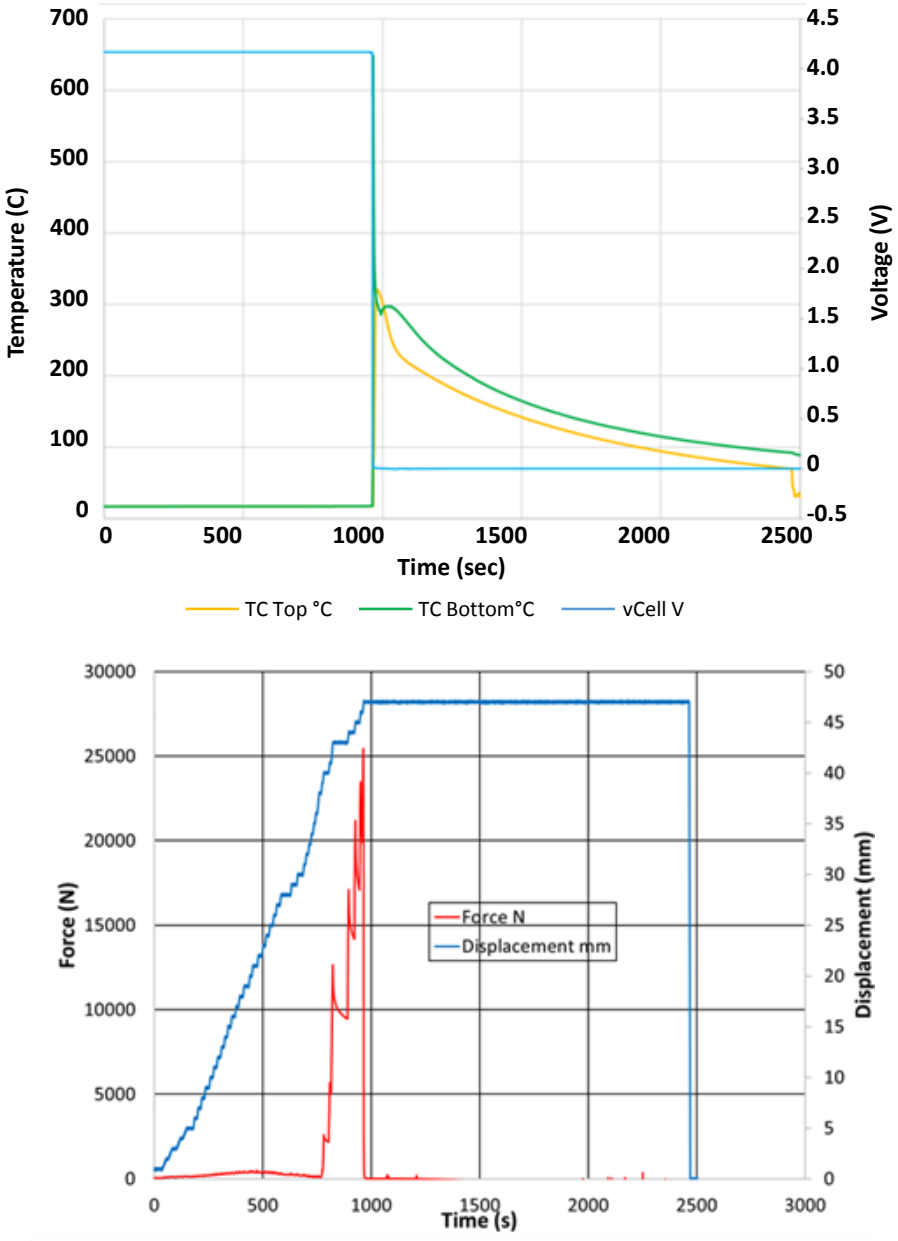

Figure I-121. Three point bend testing of fully charged cell. No runaway was observed due to the bending of the cell. Runaway occurred when enough displacement occurred to begin compressing the cell with significant force.

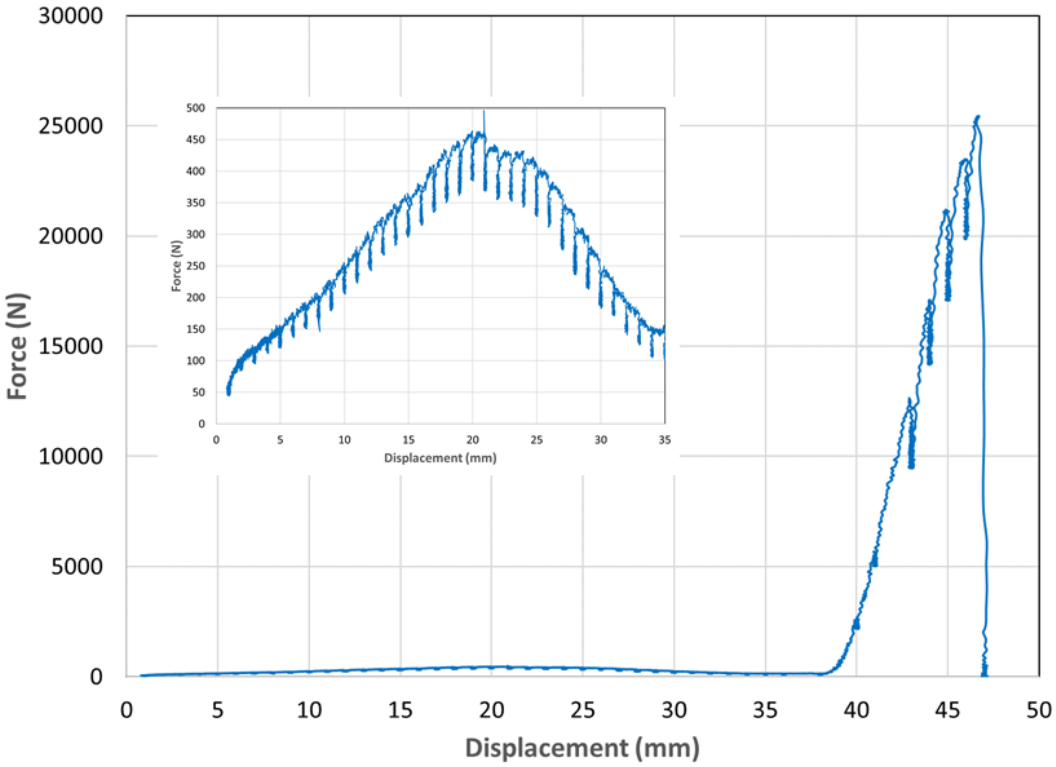

Figure I-122. Force vs displacement curve for test performed in the previous figure.

In Figure I-121 and Figure I-122, deformation was applied in 1 mm increments with voltage and temperature monitoring to determine at what level of displacement thermal runaway occurred. Figure I-121 shows the voltage, temperature, force and displacement results versus time, while Figure I-122 shows the Force vs. Displacement curve for the test. No runaway was observed during the initial bending. The observed thermal runaway occurred when enough deformation occurred to begin compressing the cell against the base of the fixture, with cell failure occurring due to compression of electrode layers rather than breakage from the bending force.

The next step of this work was to determine the mechanical behavior of these cells under these conditions. The bend test was applied at strain rates from 0.01 mm/sec to 10 mm/sec to observe how the deformation was impacted under increasing rates of deformation. This data is shown in Figure I-123. This shows that there is little apparent strain rate impact at low levels of deformation, however some changes were seen in the yield points of the cells where a maximum force was reached and the cells exhibited irreversible plastic deformation. The data shows yield stresses that shift towards lower deformation levels and a higher overall force observed before the yield occurred as the deformation rate was increased.

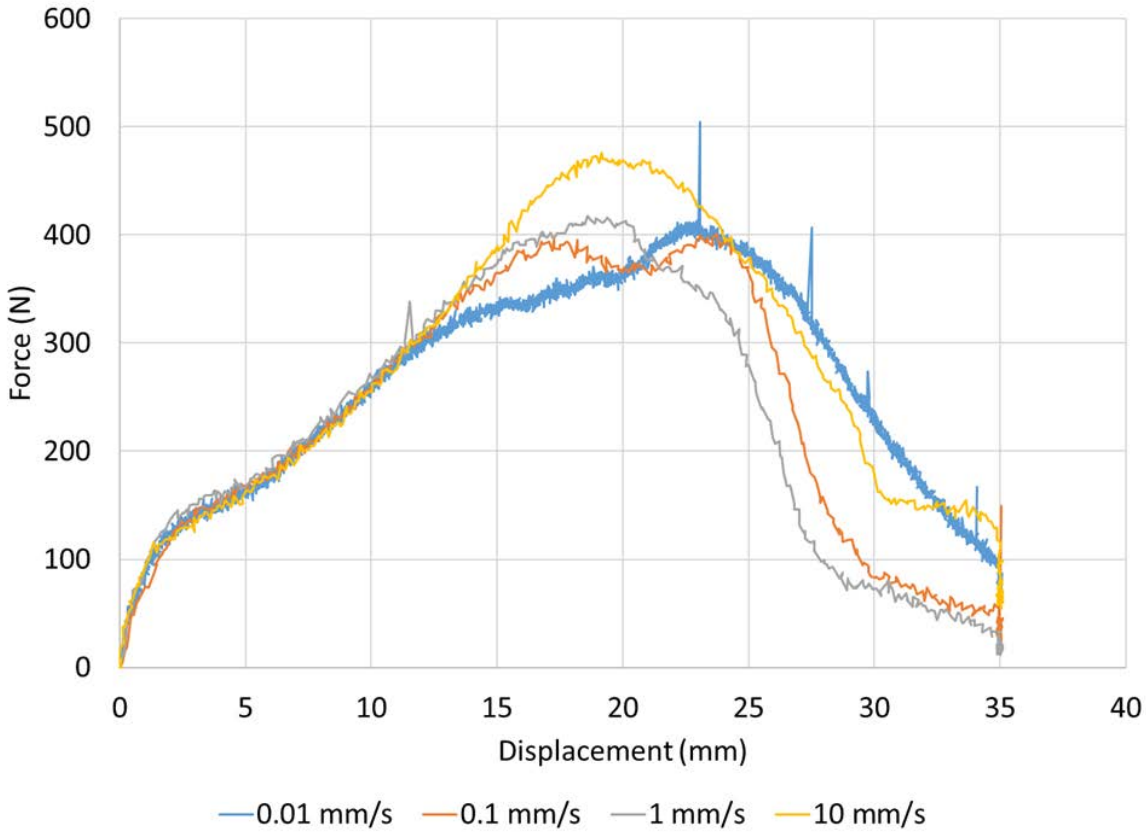

Figure I-123. Results of three point bend tests on cells at increasing displacement rates.

Building on work presented in the previous year, alternate orientations of compressive force were applied to cells. These results are shown in Figure I-124. This shows compression along an axis parallel to the tabs (Figure I-124, top) and diagonally through the cell (Figure I-124, bottom). Both orientations show little effective change at the lowest rates, with little change from 0.01 to 0.1 mm/sec in either orientation. The compression parallel to the tabs saw a more significant shift in the force at higher rates, with the force dropping at equivalent displacements when rates of 1 and 10 mm/sec were applied. Changes were observed in the diagonal orientation as well, however these changes were less systematic than other observed results. The diagonal direction also saw some evidence of fracturing failure within the cell at higher levels of force, with sudden drops in the force as the electrode stack likely fractured.

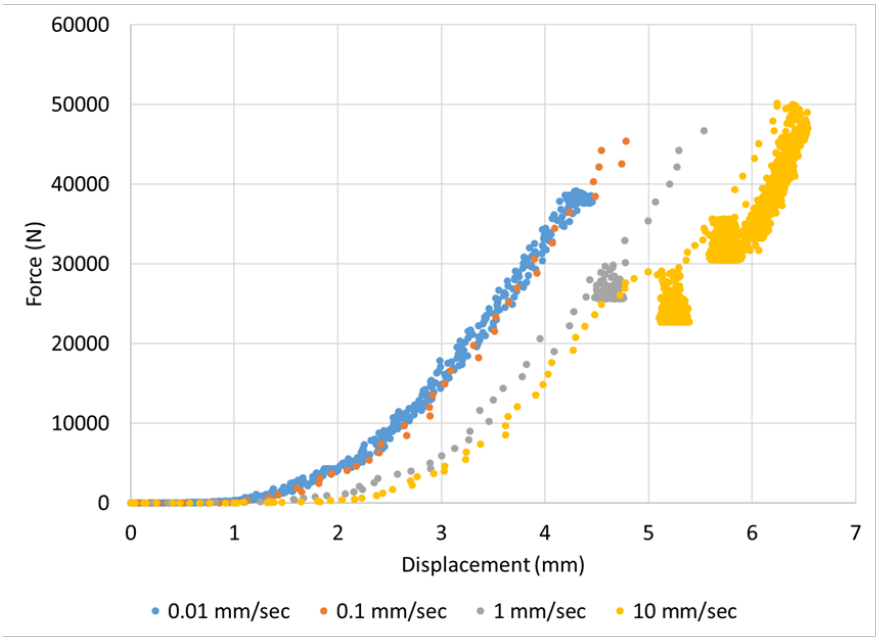

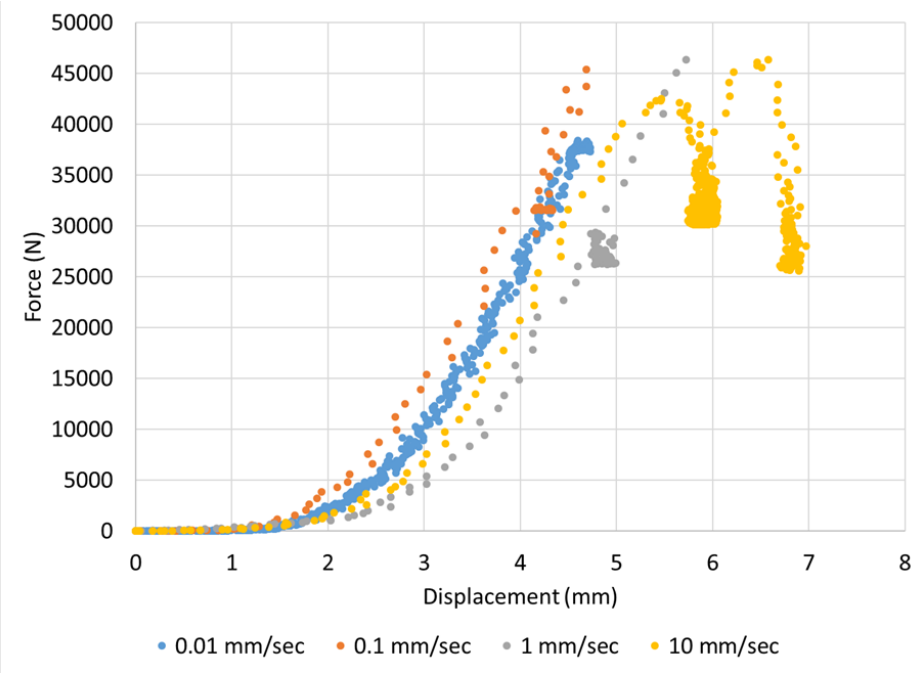

Figure I-124. Impact of strain rate at cell orientations parallel to cell tabs (top) and diagonal to cell tabs (bottom).

Work performed to date has focused on deformation rates that are predominantly quasi-static. These tests are useful for determining materials properties and establishing parameters for fundamental materials modeling. However, understanding how batteries fail during the types of impacts observed during auto collisions requires the use of elevated strain rates. A drop tower apparatus is under construction at SNL. (See Figure I-125.) Final fabrication is underway with initial testing planned for early CY 18.

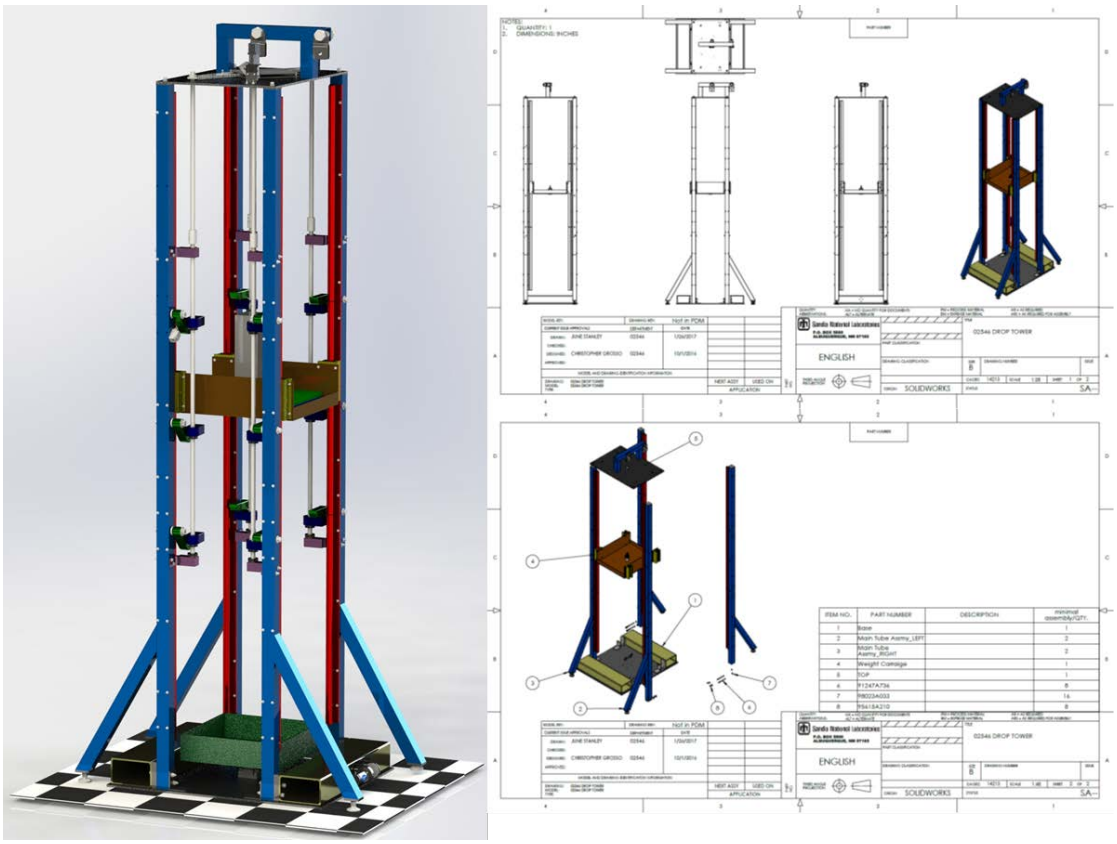

Figure I-125. Design drawings of SNL impact tester.

Conclusions

Sandia continues to provide experimental validation results to the NREL consortium as well as providing a broader understanding of the conditions likely to cause a potentially dangerous thermal runaway event in lithium ion batteries. The current work shows that mechanical compression events continue to be the most likely to cause a thermal runaway event. A single bend introduced to the cell was not able to create a thermal runaway in and of itself. Further testing will be providing experimental support to determine the mechanical failure response of aged cells, as well as the response of cells and packs to high rate mechanical deformation.

I.C.4 Consortium for Advanced Battery Simulation (ORNL)

John Turner, Principal Investigator
Oak Ridge National Laboratory
1 Bethel Valley Road
Oak Ridge, TN 37831-6164
Phone: 505-412-1945
E-mail: turnerja@ornl.gov

Brian Cunningham, Technology Manager
U.S. Department of Energy
Phone: 202-287-5686
E-mail: Brian.Cunningham@ee.doe.gov

Start Date: October 1, 2015 End Date: September 30, 2018
Total Project Cost: $1,000,000 DOE share: $1,000,000 Non-DOE share: $0

Project Introduction

CABS is an integrated partnership between Oak Ridge National Laboratory (ORNL), Lawrence Berkeley National Laboratory (LBNL), and Sandia National Laboratories (SNL). The project report is divided into three sections (I.C.4, I.C.5, and I.C.6) that include contributions from individual Laboratories. Sections I.C.5 and I.C.6 also report updates from industry-led projects. Mechanically induced internal short-circuit is believed to be the main cause of battery failure and thermal runaway in crashes involving electric vehicles. To accurately predict the internal-short we need to capture the deformed material variations and its influence on the transport properties. In this report, we highlight new experiments conducted to develop constitutive relations for mechanical response of constituent materials, effective transport properties for electrochemical behavior of electrodes under deformation, coupled simulations at layer resolved scale to predict the behavior of the damaged batteries.

Objectives

The objective of this project is to characterize failure of the cell components under mechanical crush, develop coupled simulation tools to predict electrochemical behavior, and develop constitutive relations and failure criterion for mechanical response. The progress towards these objectives is achieved by delivering the following milestones for FY17:

1. E4: Data from mechanical deformation tests
2. C2: Validated constitutive models and failure criteria for electrode materials and spirally wound, wound prismatic, and stacked electrodes under indentation
3. I4: Demonstrated ability of VIBE to simulate onset of short-circuit due to mechanical abuse informed by microstructure

Approach

To address some of the critical impediments in understanding the battery failure, we first developed new experimental protocols to measure mechanical properties of electrode materials and cell components. This ensures that we have gathered all the necessary material parameters for the constitutive relations used in the models. Simultaneously we have developed new experimental protocols to study failure leading to internal short circuit. The diagnosis from this experimental evidence is used to develop formulation of new models for mechanical behavior of battery components. Also, we had to understand the influence of mechanical impact on transport properties and how it acts as a precursor to the internal short of the cell. To this end, we have developed electrochemical models at the continuum scale informed from the mesoscale simulations on NMC

microstructures. These various efforts allowed us to investigate some of the challenging internal short simulations under extreme mechanical deformations and predict the behavior of the batteries.

Results

Milestone E4: Data from mechanical deformation tests:

Mechanical properties of battery components have been experimentally measured under different loading conditions in order to aid development of constitutive models for mechanics of battery cell and couple to thermal models. (See Figure I-126.) Significant effort was dedicated to mechanics and failure of battery separators, as these are critical safety components in the cell. Overall the following are the highlights of the results (detailed description can be found in the Milestone E4 "Data from mechanical tests" report submitted to EERE):

- Complete study of temperature and strain rate effect in battery separators
- Data from biaxial tests and critical failure strain
- Coupling between electrode parameters (thickness, porosity) and electro-chemical behavior
- Mechanical behavior of battery electrodes and pouch material

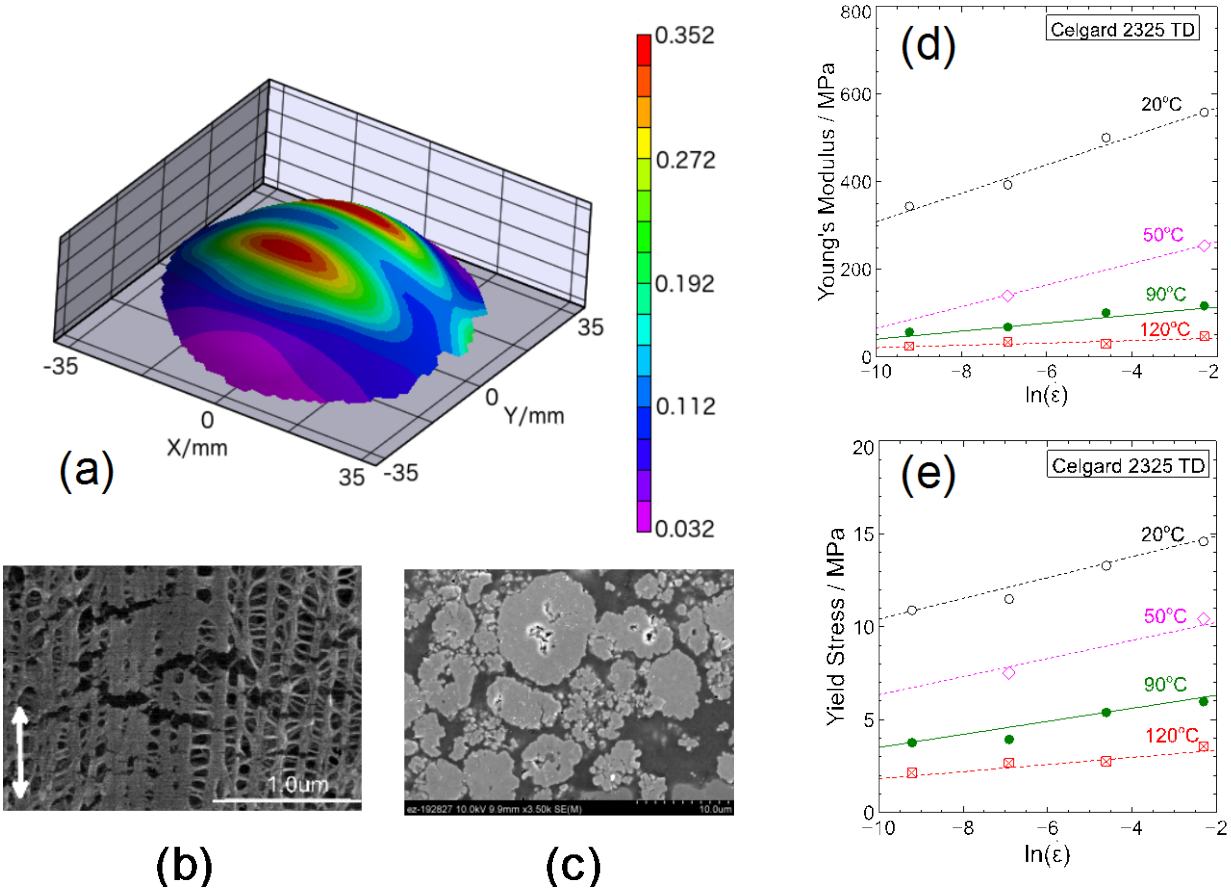

Figure I-126. Examples of the results from mechanical testing: a) first principal strain distribution in polymer separator under biaxial loading; (b) tensile cracks in separator lamellae; (c) microstructure of electrode compressed by calendering; (d,e) Young's modulus and yield strength of Celgard separator under different temperatures and strain rates.

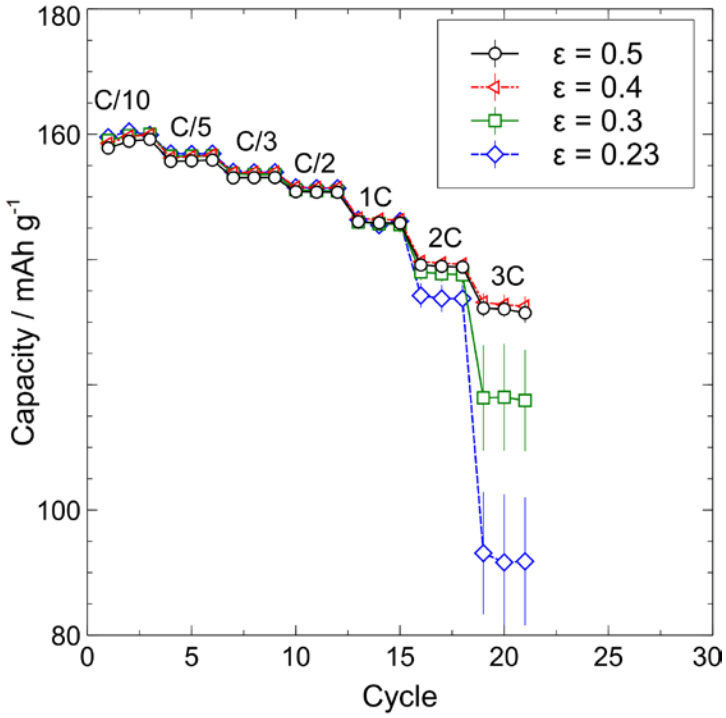

Figure I-127. Rate performance of NMC(532) electrodes depending on porosity after calendering

In addition to investigation of mechanical behavior of battery components, effect of electrode microstructure on cell performance was studied. (See Figure I-127.) For this purpose, positive (NMC532 (Toda America); wt% NMC/PVdF/carbon black 90/5/5) electrodes were made at the ORNL Battery Manufacturing Facility and calendared to create a set of samples with six different porosities (0.53, 0.5, 0.4, 0.3, 0.23, 0.18). Fracture of electrode particles and fragmentation can be noticed (Figure I-126(c)) as the result of calendering. The electrodes were tested in coin cell hardware vs Li metal electrodes. The porosity of 30% appears to be a demarcation line after which the performance of positive electrode decreases, especially at high applied current densities.

Milestone C2: Validated constitutive models and failure criteria for electrode materials and spirally wound, wound prismatic, and stacked electrodes under indentation:

Experimental Characterization of Deformation and Failure

In order to understand the response to the materials inside the cells, we carried out incremental indentations of the cells in aluminum cans, established FEA model to simulate the deformation. Post-mortem analysis using cross-section imaging and x-ray computed tomography (XCT) were performed on indented cells. The on-set of internal short-circuit and various failure modes of anode, cathode and separator have been analyzed. An unexpected fragmentation of anode current collectors was first observed by XCT and later confirmed by examination of single components using x-ray radiography and scanning electron microscopy (SEM). The origin of short-circuit under spherical indentation has been attributed to the cathode current collector failure. Finite element analysis model was modified to simulate the spherical indentation and cell response. The simulated load vs. displacement curves were validated by experimental results. The simulation model is also used to validate results obtained from 3-point bending tests.

Li-ion cells in aluminum cans for small electronic appliances were used in the single-side indentation tests with 650-670 mAh in capacity. A half inch diameter indenter was used at a loading speed of 0.05”/min. A series of cells were indented with increments of 0.01” and 0.02” followed by several cells indented until internal short circuit was detected from open circuit voltage drop. The FEA simulation was based on a

previously developed model. One set of the indented cells were cut in half, back filled with epoxy and polished for cross-section imaging. Other cells were scanned with a 3D X-ray computed tomography (XCT) at ORNL before cross-sectioning. 3-point bend tests were also performed.

XCT images, Figure I-128, were taken across the indented area from X and Y directions. The layers were stretched and started to fold symmetrically away from the indenter. At the very last image(s), which were at the center of the indentation, 2-3 cathode layers collapsed and electrode-to-electrode contacts were visible. In XCT we also observed mud-cracks in the current collectors. When the indented cell components were taken out for examinations, there was no visible cracking in the area surrounding the failure point. The anode was scanned by x-ray, which penetrated carbon but not the copper. The radiographs clearly showed extensive cracking of the copper current collector. On the other hand, the anode did not show any cracking under SEM. At a closer look, a crack was observed in the exposed copper layer near the center hole. The remaining area was covered by graphite without any sign of cracking. This was the first experimental proof that hidden fragmentations were induced by the spherical indentation in the anodes. The graphite, in the presence of electrolyte, was able to move and fill the cracked area without showing any cracks on the surface. The fragmented current collectors play important roles in the safety and continuous operation of the cells. It also provided additional details of the cell components behavior under mechanical compression. Out of the three layers in a jellyroll, the separator can be stretched very thin and the anode can also take large deformation due to the fragmentation of the current collectors. The final failure was induced when the aluminum current collector reached its strain limit. When the first Al layer cracks, it propagates to more than one layer creating a shear which can propagate through the bonded active anode material and rip the separator along the same crack lines. The initial contact was created between the anode and cathode. We were able to experimentally confirm the behavior of all the layers and identify which layer is responsible to the failure that leads to short-circuit:

1. Anode with Cu current collectors: Graphite is more compressible and the fragmentation of Cu helps the anode to take more deformation

2. Separator: The separators can be stretched far beyond the thickness of the cell without failure. It is unlikely to be the first failure layer

3. Cathode with Al current collectors: When the other two layers could take more compressive loading, Al layer would eventually crack and trigger internal short-circuit. Therefore, it had been identified as the origin of failure.

We also performed 3-point bending tests on a series of cells, with 3.81 mm to 1.91 mm displacement. The load vs. Time plots of four cells with incremental displacements all followed the same loading curves and showed very repeatable mechanical responses.

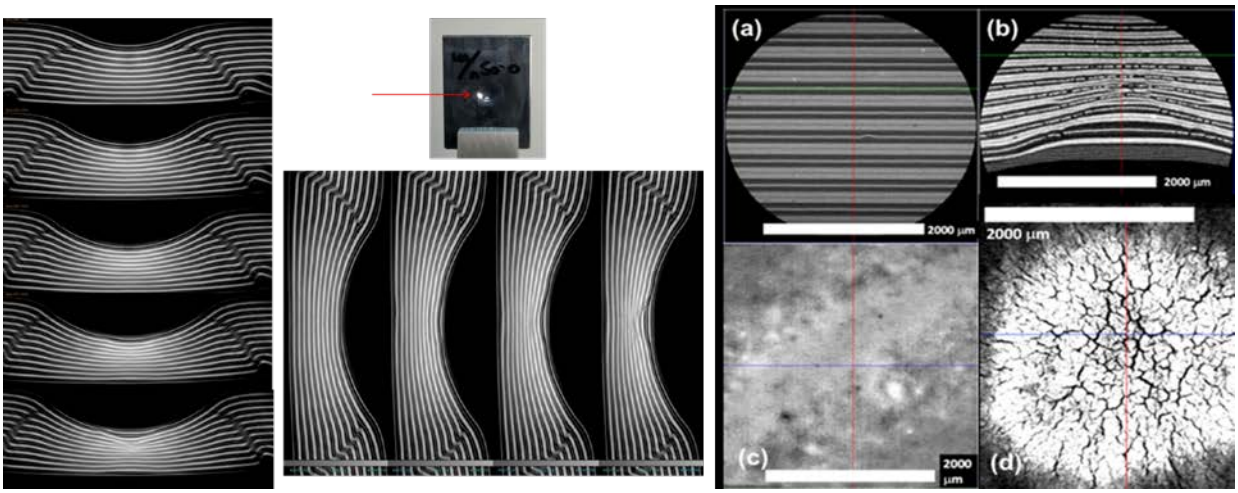

Figure I-128. X-ray tomography images of an indentation that led to short circuit and XCT images of the copper current collectors showing cracking and mud-cracks

Upscaling of mechanical behavior from geometric features of mesoscale structures

The electrodes can be considered as granular media, where the mechanical connectivity, force networks, and transport could be described using Fabric Tensor formulations. Fabric Tensors are well-established, non-local directional measures of internal connectivity and structure of granular media and solids. They are also extensively used in the field of damage mechanics [1] to describe the deterioration of material due to cracks and the reduction in the connectivity and force transport pathways. Using these tensors descriptions granular and damage mechanics can be constituted with a physical interpretation of microstructure effects and correlate to macroscopic properties such as skeleton stress tensors and stiffness tensors. In our previous work [1] we have explored the use of Fabric Tensor as a method of modeling the inter-particle contacts and connectivity of the active particle network in the battery electrode microstructure. Based on Ebner's experimental data we have calculated the Fabric Tensor for different calendaring pressure and concentration of Lithium ion in the battery. Building on this work, a second order deviatoric Fabric Tensor is used to characterize the fabric anisotropy in electrode material. To describe anisotropic elasticity in a porous medium, we use Cowin's [1] expression of stiffness tensor as a function of second-order fabric tensor, F_{ij}, representing the anisotropic geometry of internal structure in electrode material. Based on spherical approximation, the Fabric Tensor (F) is calculated using model described in [1] for the experimental data at concentration of 90, 92 and 96 percentage and the pressure value of 0, 200, 600 and 2000 bar. The value for bulk modulus (k) and shear modulus (g) is taken as 0.5 and 0.2 GPa respectively. The variation of Young Modulus in 3 different directions for various loading of NMC 90, 92 and 96% is shown in Figure I-129. The ratio of modulus in 3rd direction and 1st direction had decreased with increase in pressure. With this formulation, we have successfully demonstrated that given the mechanical properties in isotropic case we can predict the evolutions of properties due to reorganization of microstructure under deformation.

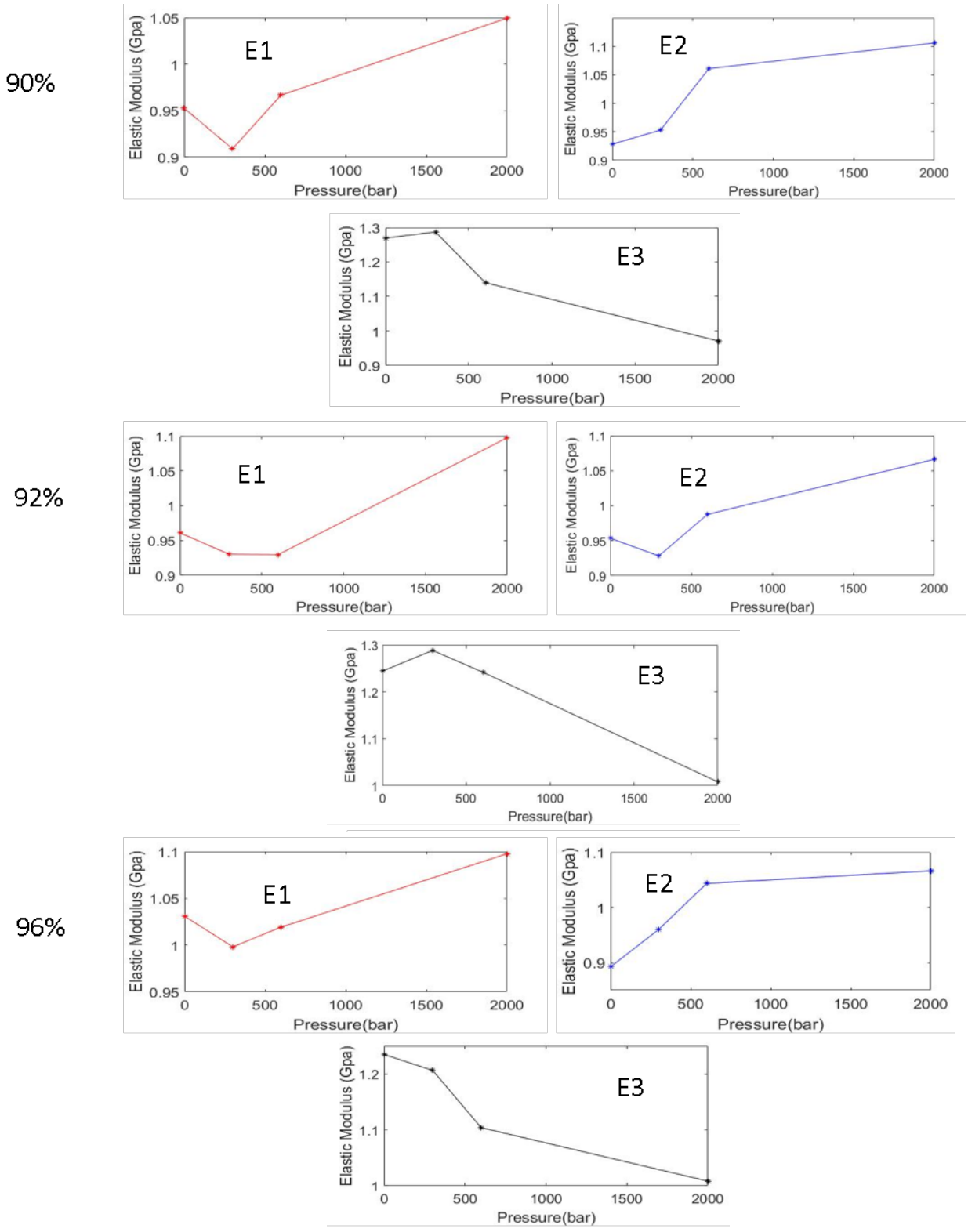

Figure I-129. Variation of Young Modulus in 3 different direction as a function of pressure and concentration

Milestone I4: Demonstration of VIBE/OAS to simulate onset of short-circuit due to mechanical abuse informed by microstructure simulations

For this milestone, we developed a computational framework to investigate the cycling behavior of the damaged cells. Towards this effort a constant loading of electrodes calendared at different pressures are constructed for estimation of total thickness of the NMC reconstructions from the mesoscale imaging data ETH-Zurich. Using these multiple thickness values corresponding to different porosities, homogenized meshes with resolved components for cell sandwich are generated. The effective electronic conductivities are calculated by Sandia team for different porosities with assumed binder distribution from the meso-structure simulations on the NMC cathode described in section I.C.5. Using these properties on the continuum scale meshes we were able to simulate constant current discharge behavior that was able to predict reduced capacity, as seen in Figure I-130(b).

This clearly shows influence of calendared pressures on the material reorganization at the meso-scale and the effect on transport at the electrode scale and the ability of the framework to capture these effects. In the next study, we want to show the coupling of mechanical and electro-chemical simulations to reproduce the capacity loss in the damaged cell due to deformation. Once the cell undergoes permanent damage, the performance evaluation of the cell shows ~5.0% reduction in extracted capacity, as seen in Figure I-130(a). We saw the evidence from X-ray tomography imaging from previous section on the fragmentation of copper current collectors prior to the internal short. Thus, we rezoned the areas where the copper is fragmented as electrically isolated regions. As we go deep into cell thickness away from the point of contact the area of fragmentation is reduced. Then we performed a constant current discharge on the full cell to compare against the un-deformed cell. In the Figure I-131 we show the solid phase potential and concentration on the first three layers starting from the point of contact. The contour plots show gradients developed across the in-plane direction between electrically damaged copper collector and the undamaged regions. The electrically isolated regions do not contribute to the extracted capacity during the discharge of the cell and hence a reduced capacity of the cell.

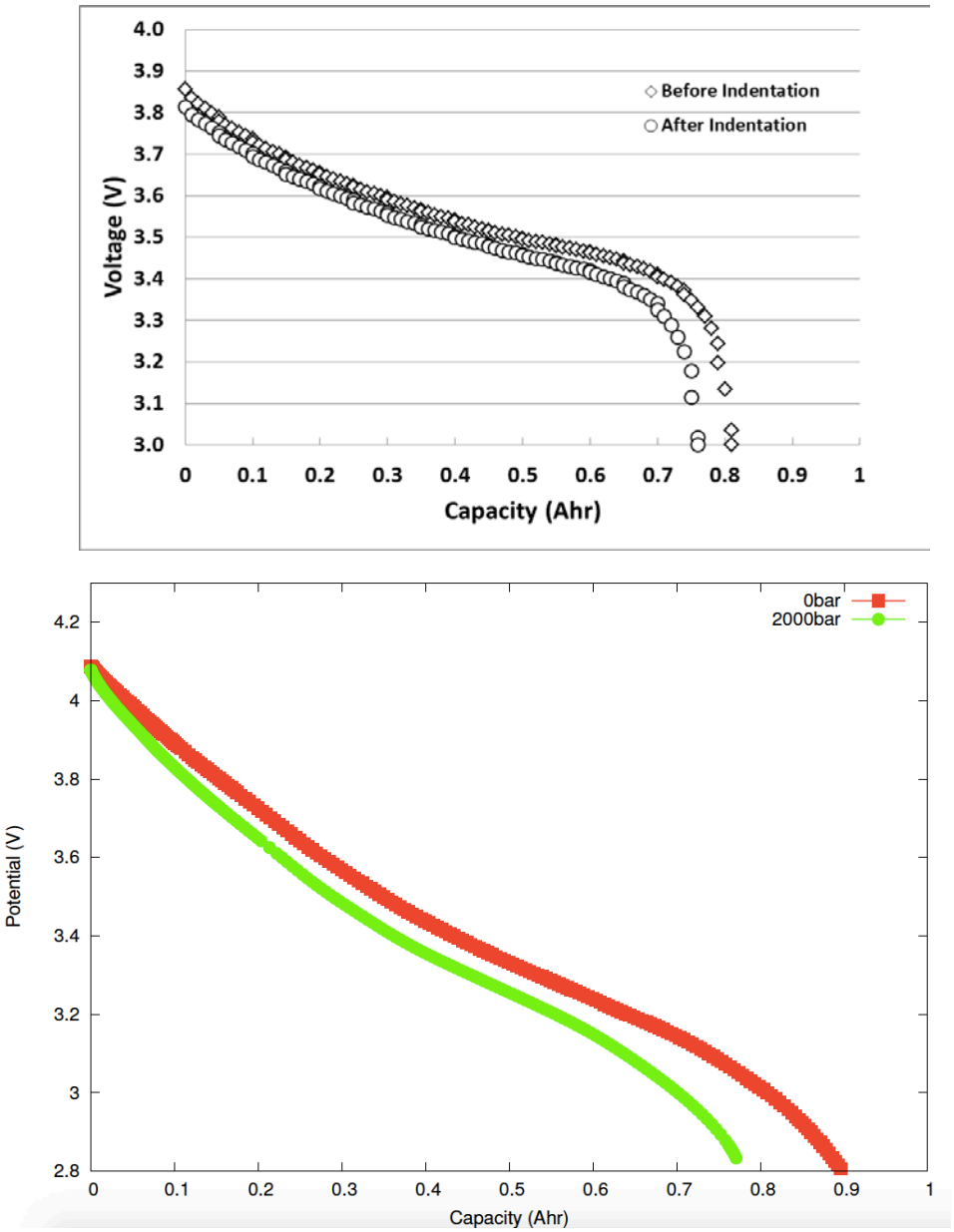

Figure I-130. (a)Reduced extracted capacity of cells damaged under 80% indentation (b) Reduced extracted capacity of electrodes calendered under various pressures

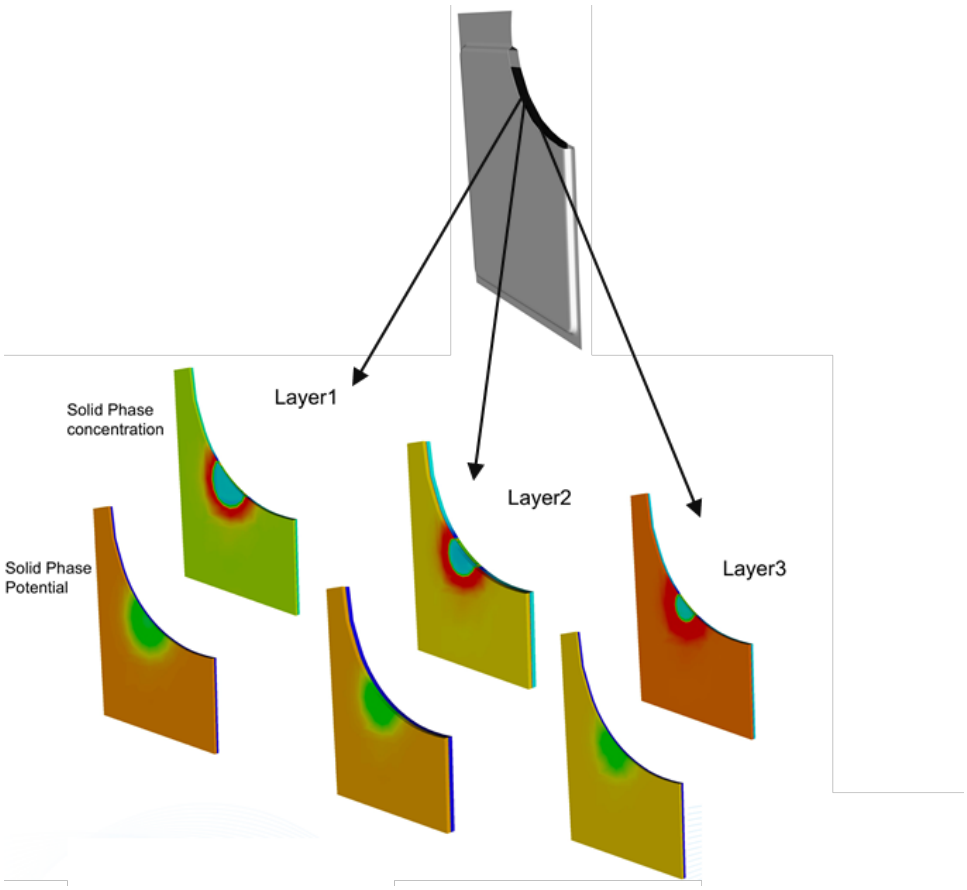

Figure I-131. Full cell coupled electrochemical simulation with electrically isolated regions

Conclusions

Understanding the failure of battery components under extreme mechanical deformations has been the prime motivation for this project. Several experiments have been conducted on individual constituent materials to characterize the mechanical and transport behavior and evaluate parameters for the material models. Using these material models in the VIBE computational framework developed under CAEBAT program, the cumulative response of the battery under crush is simulated. A prior to short, the damage to the copper current collectors caused permanent loss of the cycling capacity of the batteries. Robust numerical algorithms were developed to predict the material failure and capacity loss of the batteries.

Key Publications

1. Kalnaus, S., Wang, Y., Turner, J.A. Mechanical behavior and failure mechanisms of Li-ion battery separators. Journal of Power Sources 2017, 348, 255-263
2. Wang, H., Kumar, A., Simunovic, S., Allu, S., Kalnaus, S., Turner, J.A., Helmers, J.C., Rules, E.T., Winchester, C.S., Gorney, P. Progressive mechanical indentation of large-format Li-ion cells. Journal of Power Sources 2017, 341, 156-164
3. Wang, H., Watkins, T. R., Simunovic, S., Bingham, P. R., Allu, S., Turner, J. A. Fragmentation of copper current collectors in Li-ion batteries during spherical indentation. Journal of Power Sources 2017, 364, 432–436.

References

1. Stershic A.J., Simunovic S. and Nanda J., Modeling the evolution of lithium-ion particle contact distributions using a fabric tensor approach, Journal of Power Sources 2015, 297, 540-550.

I.C.5 Consortium for Advanced Battery Simulation (SNL)

Scott A. Roberts, Principal Investigator
Sandia National Laboratories
1515 Eubank SE
Albuquerque, NM 87123-0836
Phone: 505-844-7957
E-mail: sarober@sandia.gov

Brian Cunningham, Technology Manager
U.S. Department of Energy
Phone: 202-287-5686
E-mail: Brian.Cunningham@ee.doe.gov

Start Date: October 1, 2015 End Date: September 30, 2018
Total Project Cost: $1,350,000 DOE share: $1,350,000 Non-DOE share: $0

Project Introduction

Multi-physics simulations of battery performance are typically performed at the macroscale, including entire cells, cells stacks, batteries, packs, and modules. These types of simulations typically model the electrodes using homogenized equations and properties, often utilizing effective medium theory. These electrodes, however, are comprised of packs of active material particles, polymeric binders, and conductive additives. These materials are combined to form a complex mesostructure that is influenced by material choices and processing conditions. This mesostructure strongly influences the macroscopic performance of the electrode and is of particular importance in abuse scenarios, where it is difficult to experimentally determine mesostructure evolution and properties.

Study of the influence of these mesoscale effects on the macroscale behavior of electrodes is the focus of this project. We are utilizing microtomography of NMC cathodes to create detailed simulation domains within Sandia's Sierra/Aria code suite using the Conformal Decomposition Finite Element Method (CDFEM). These imaging-derived particle networks are augmented with a conductive binder morphology that we designed. Physics simulations are then performed on these mesostructures, including the calculation of effective properties (e.g., electrical conductivity, ionic tortuosity, Young's modulus) and fully coupled electrochemical-mechanical (dis)charge simulations. The results of these simulations are upscaled to feed into macroscale models developed by our ORNL teammates.

Objectives

The objective of this project is to improve the fidelity of battery-scale simulations of abuse scenarios through the creation and application of microscale (particle-scale) electrode simulations. Our specific FY2017 objectives are twofold:

1. Accurately represent NMC microstructure, including the active binder phase, within the simulation framework
2. Begin to feed information from the microscale to the battery scale

Successfully accomplishing these objectives will impact the VTO by improving the ability to assess battery response to abuse scenarios (e.g., crush) computationally, enabling many parametric computer tests rather than expensive and dangerous experiments.

These objectives have been formalized into three FY2017 milestones that have been completed and were contributed to by this project:

1. I3: Demonstration of ability to construct 3D meshes of electrodes using reconstructions from micro-tomography
2. I4: Demonstration of VIBE/OAS to simulate onset of short-circuit due to mechanical abuse informed by microstructure simulations (ORNL lead, SNL contributor)
3. CDa/1.8: Investigate the role of polymeric binders for mitigating stress

Approach

Our approach centers around simulations performed using Sandia's Sierra Mechanics suite of codes. In particular, physics simulations are performed using the Sierra/Aria multi-physics code and the mesoscale geometric representation is performed using CDFEM implemented within Sierra/Krino.

Experimentally gathered electrode tomography data forms the foundation of our mesostructure representation. We are in the process of utilizing data gathered within the scope of this project by our CABS teammates and collaborators at Lawrence Berkeley National Laboratory (LBNL) and Argonne National Laboratory (ANL) (Higa, et al., 2017). For the work shown here, however, we have utilized microtomography from Vanessa Wood's group from ETH-Zurich. Specifically, Ebner *et al. (Ebner, Geldmacher, Marone, Stampanoni, & Wood, 2013),* published and made publicly available a high-quality data set of NMC electrodes. Material properties were gathered from a variety of sources detailed in our FY2016 report.

Computational representations of the NMC particle mesostructures are created using the CDFEM algorithm. This workflow has been discussed in detail in two journal publications (Roberts, Brunini, Long, & Grillet, 2014) (Roberts, et al., Insights Into Lithium-Ion Battery Degradation and Safety Mechanisms From Mesoscale Simulations Using Experimentally Reconstructed Mesostructures, 2016), but will be summarized here for completeness. The commercial software Avizo (Thermo Fisher Scientific) is used to binarize images, label individual particles, and create a smooth surface mesh for each particle which can then be exported as a faceted STL file. The faceted STL representation of each particle is then superimposed on top of a regular tetrahedral background mesh. CDFEM is used to decompose the background mesh to be conformal to the particles. A new addition to this workflow/approach this year is the subsequent addition of a conductive binder phase to create a "binder bridge" morphology. The details on this level-set-based algorithm was published by Trembacki et al. (Trembacki, Noble, Brunini, Ferraro, & Roberts, 2017) and will be discussed in more detail in the results section. A visualization of the resulting geometry is shown in Figure I-132.

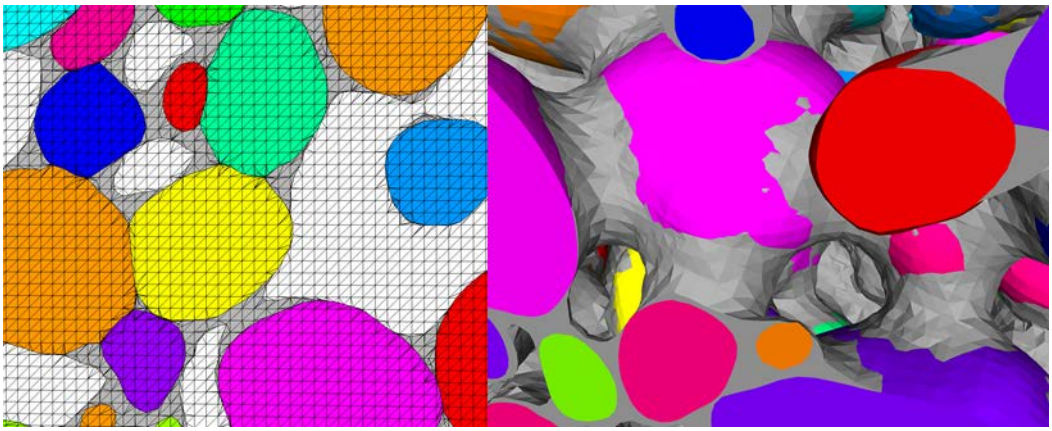

Figure I-132. 2D (left) and 3D (right) representations of a small NMC cathode domain illustrating the microtomography-derived particle microstructures combined with the "binder bridge" conductive binder representation.

Results

The key technical results arising from our three FY2017 milestones are derived in this section.

Milestone I3: Demonstration of ability to construct 3D meshes of electrodes using reconstructions from micro-tomography

One of our overarching goals is to understand how the manufacturing process (primarily calendaring pressure, in this case) affects the cathode microstructure, and therefore battery performance. Additionally, mechanical abuse can change the porosity in similar ways to calendaring pressure, and understanding these changes on the microscale will help to predict cell performance under mechanical insult.

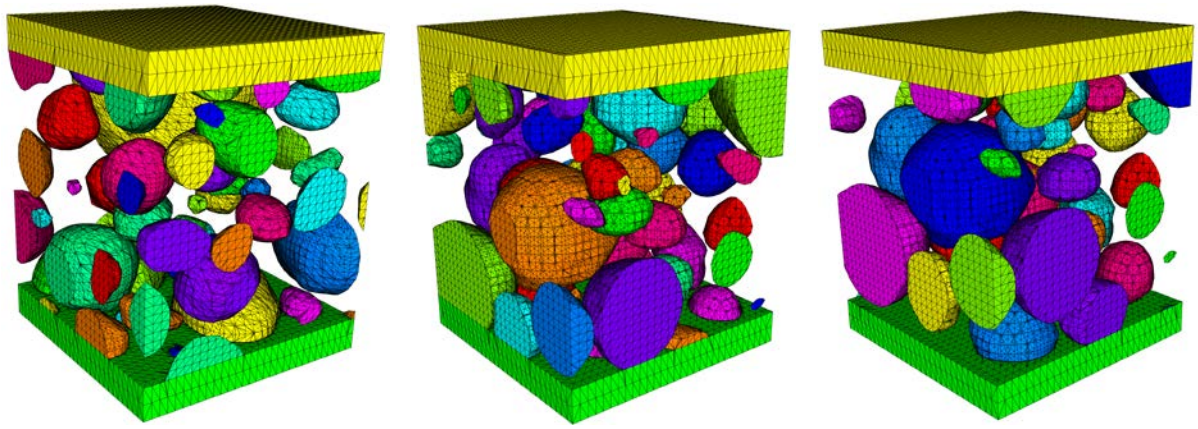

Figure I-133. Computational meshes generated for three calendaring pressures (0 bar, left; 300bar, center; 600 bar, right)

To begin to address these issues, we have created meshes for three calendaring pressures (0, 300, and 600 bar) from the ETH-Zurich data set, and the resulting meshes are found in Figure I-133. These data are for a subset of the domain (30 µm x 30 µm x 30 µm) for ease of rapid processing and for visualization. These images clearly show that at higher calendaring pressures, the particles are more consolidated (closer together). This should impact performance characteristics such as the effective electrical conductivity, simulations that are currently underway.

It is worth noting that the mesh resolution for this reconstruction is relatively coarse, with just a few (5-10) elements across the width of most particles. Solution verification work is underway that suggests target mesh resolutions for desired solution error levels. This will likely require more refined meshes than are currently used, and the meshes will be appropriately updated upon the conclusion of that work.

Milestone I4: Demonstration of VIBE/OAS to simulate onset of short-circuit due to mechanical abuse informed by microstructure simulations

While this milestone was primarily owned by ORNL partners, we performed a number of mesoscale simulations to support the mechanical abuse simulations. The effective properties of NMC cathodes were computed from the electrodes images using X-ray computed microtomography described in the previous section.

As mentioned in the previous section, requisite data for full 3D mesostructure reconstruction of a crushed cathode is not readily available. Thus, we must utilize alternate sources to visualize the mesostructure evolution over the course of a crush test. Data made publicly available by Ebner et al. (Ebner, Geldmacher, Marone, Stampanoni, & Wood, 2013) provides tomography data at multiple values of binder composition and calendering pressures. This allows us to approximate the early stages of cathode compression by surveying effective property dependence on the porosities obtained from different calendering pressures. Primary properties of interest will include effective electrical conductivity of the NMC particle network and the tortuosity of the cathode electrolyte phase.

Effective conductivity and tortuosity values can be obtained by solving charge conservation equations on the full mesostructure reconstructions. For the values presented here, we use data for 92 wt% NMC333 cathodes calendered at 0 bar, 300 bar, 600 bar, and 2000 bar. The full domains in each case spanned a significantly large area, so simulations were performed on smaller subdomains taken at random locations throughout the full sample. These domains measured 100μmx100μmx60μm, which was determined to be a significantly large subdomain size by a recent Sandia verification study (Roberts, Mendoza, Brunini, & Noble, A Verified Conformal Decomposition Finite Element Method for Implicit Geometries). Material properties for NMC333 were detailed in a previous report (Ferraro & Roberts, 2016). Effective property results are shown in Figure I-134.

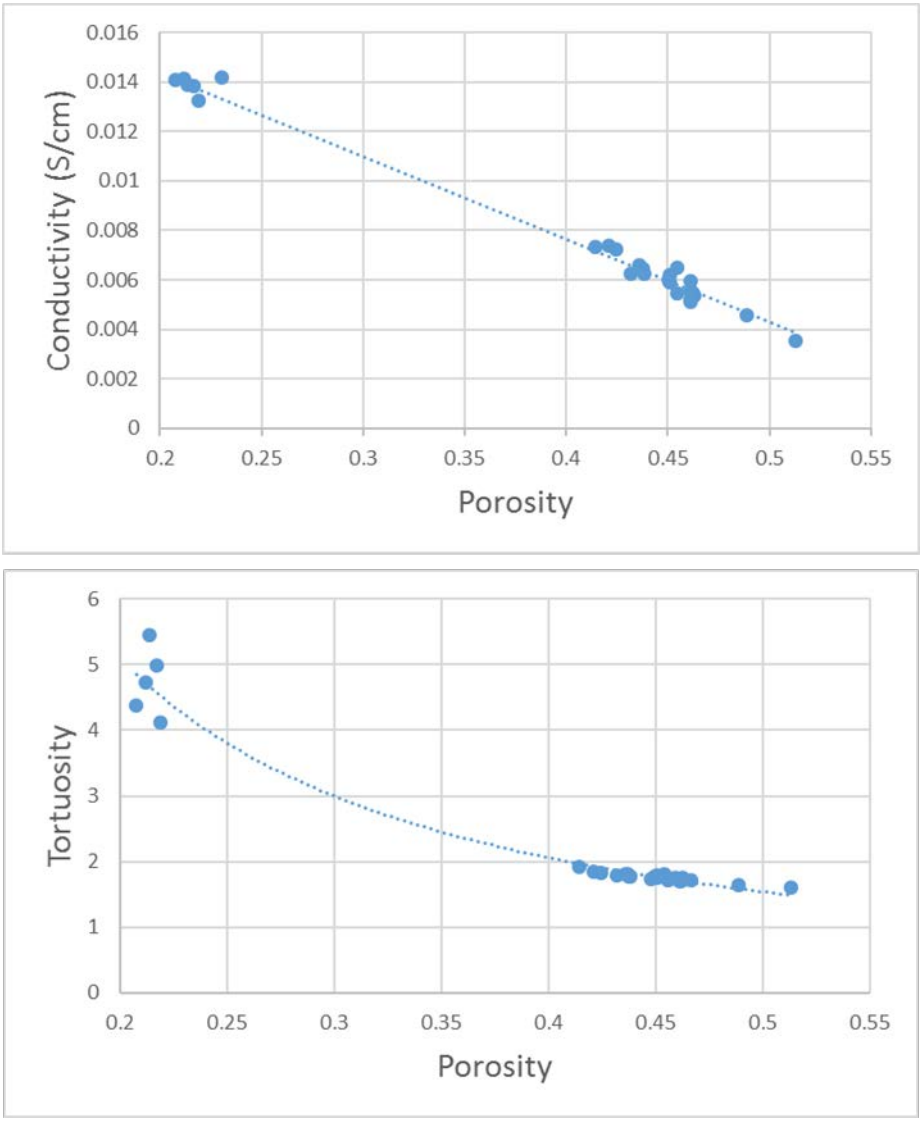

Figure I-134. Effective electrical conductivity and electrolyte-phase tortuosity measured from sampled subdomains with varying porosity. Effective conductivity exhibits linear behavior with a trendline of $k_{eff} = -0.0334\ \varepsilon + 0.021$. Power-law behavior was assumed for tortuosity, with a trendline $\tau = 0.623\varepsilon^{-1.31}$.

Charge conservation over a fixed voltage drop allowed us to calculate both effective conductivity and tortuosity of the NMC cathodes. Results are reported for individual subdomains sampled from the four reported calendering pressures. Subdomain porosities varied slightly throughout each cathode, but remain close to the reported values in each case. Overall, we can obtain a linear trend of effective conductivity vs.

porosity which demonstrates an increase in conductivity as the particles are compressed closer together, thus decreasing porosity. Additionally, we see that tortuosity increases as the cathode becomes compressed. Typically, tortuosity is estimated from a Bruggeman approximation $\tau = \varepsilon^{-0.5}$. However, this approximation is known to underestimate tortuosity for porosities under 0.5. Thus, we have shown a trend demonstrating the same power-law behavior $\tau = a\varepsilon^{-b}$ which is able to represent the higher tortuosity values calculated for these subdomains.

Milestone CDa/1.8: Investigate the role of polymeric binders for mitigating stress

Sandia's FY17 goal as part of the CD-adapco FOA project is to investigate the role of polymeric binder within NMC cathode particle-bed mesostructures. We investigated the binder's role in effective electrode properties and behavior through advanced methods development and accompanying simulations. Our investigation of stresses generated within the mesostructure both with and without considering the presence of binder is of relevance to this milestone. The work was published in the *Mathematical Modeling of Electrochemical Systems at Multiple Scales Focus Issue* of the *Journal of the Electrochemical Society (Trembacki, Noble, Brunini, Ferraro, & Roberts, 2017).*

In this publication, we demonstrated that even a thin layer of binder separating adjacent NMC particles can reduce swelling-induced stress predictions by a factor of 4.5 versus a case where NMC particles are in contact (Figure I-135). This indicates that incorporating sufficient binder when manufacturing electrodes may be necessary to reduce or mitigate swelling-induced stresses experienced by NMC particles and therefore reduce the likelihood of mechanical degradation and fracture.

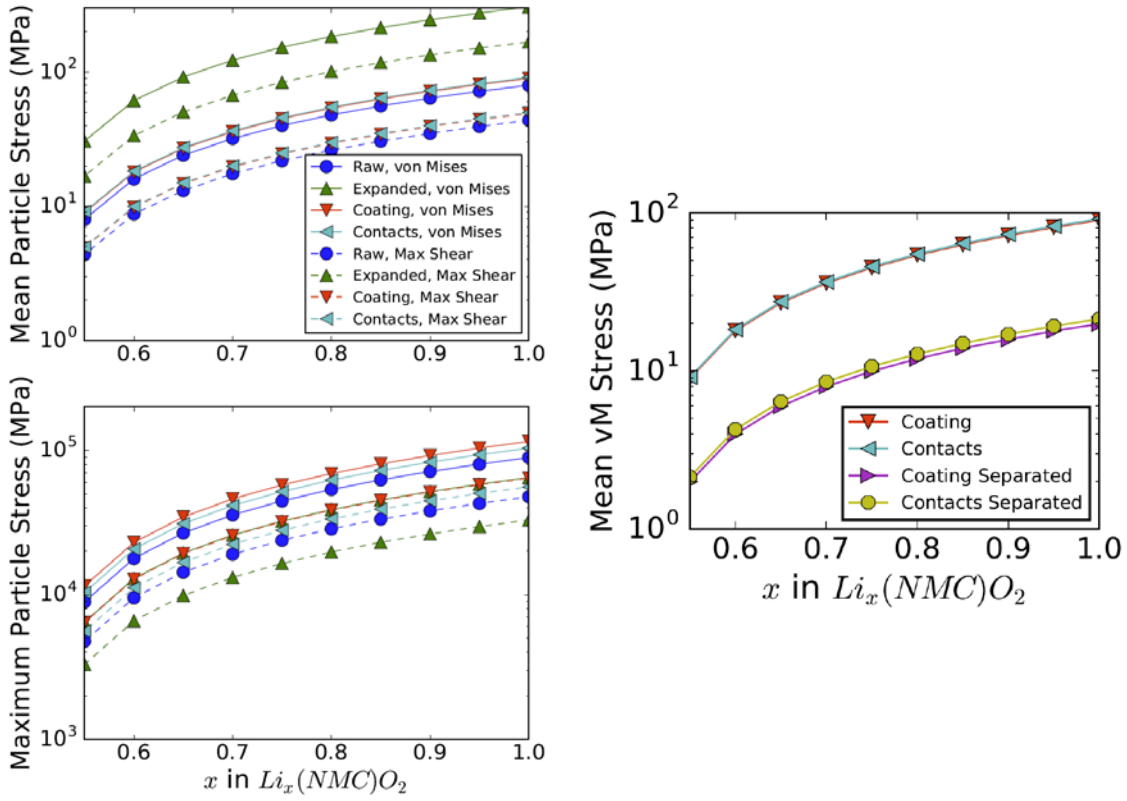

Figure I-135. Left: Maximum and mean stresses experienced by the NMC particles for all mesostructure representations. Both von Mises stress and maximum shear stress are displayed. Right: Mean von Mises stress for the two binder representations, including cases where particles are separated by a composite binder layer.

Conclusions

We have demonstrated an approach for representing experimentally derived battery electrode mesostrutures in a computational framework suitable for performing coupled multi-physics battery performance simulations. In pursuit of this we have created a new algorithm for analytically representing the secondary conductive binder phase morphology in these mesoscale representations and demonstrated the importance of accurately capturing this morphology. We have used this model to calculate many effective properties that are relevant for mesoscale modeling efforts. These effective properties have been upscaled and implemented within the VIBE code and used to analyze battery abuse scenarios.

Key Publications

1. Ebner, M., Geldmacher, F., Marone, F., Stampanoni, M., & Wood, V. (2013). X-Ray Tomography of Porous, Transition Metal Oxide Based Lithium Ion Battery Electrodes. *Advanced Energy Materials*, 3, 845--850.

2. Ferraro, M., & Roberts, S. (2016). *Collect Constitutive Models for NMC Materials and Report on Use of Mesoscale Data to Project Lead: CABS Milestone C1.1 Report*.

3. Higa, K., Wu, S.-L., Parkinson, D., Fu, Y., Ferreira, S., Battaglia, V., & Srinivasan, V. (2017). Comparing Macroscale and Microscale Simulations of Porous Battery Electrodes. *Journal of The Electrochemical Society*, 164, E3473-E3488.

4. Roberts, S., Brunini, V., Long, K., & Grillet, A. (2014). A Framework for Three-Dimensional Mesoscale Modeling of Anisotropic Swelling and Mechanical Deformation in Lithium-Ion Electrodes. *Journal of The Electrochemical Society*, 161, F3052-F3059.

5. Roberts, S., Mendoza, H., Brunini, V., & Noble, D. (n.d.). A Verified Conformal Decomposition Finite Element Method for Implicit Geometries. *Journal of Computational Physics*.

6. Roberts, S., Mendoza, H., Brunini, V., Trembacki, B., Noble, D., & Grillet, A. (2016). Insights Into Lithium-Ion Battery Degradation and Safety Mechanisms From Mesoscale Simulations Using Experimentally Reconstructed Mesostructures. *Journal of Electrochemical Energy Conversion and Storage*, 13, 031005--031005.

7. Trembacki, B., Noble, D., Brunini, V., Ferraro, M., & Roberts, S. (2017). Mesoscale Effective Property Simulations Incorporating Conductive Binder. Journal of The Electrochemical Society, 164, E3613-E3626.

I.C.6 Consortium for Advanced Battery Simulation (ANL, LBNL)

Venkat Srinivasan, Principal Investigator
Argonne National Laboratory
9700 S. Cass Avenue
Lemont, IL 60439
Phone: 630-252-6003
E-mail: vsrinivasan@anl.gov

Brian Cunningham, Technology Manager
U.S. Department of Energy
Phone: 202-287-5686
E-mail: Brian.Cunningham@ee.doe.gov

Start Date: October 1, 2015 End Date: September 20, 2018
Total Project Cost: $588,004 DOE share: $588,004 Non-DOE share: $0

Project Introduction

Our CABS teammates are developing simulations of battery operation at both the microscale and macroscale. This project focuses on obtaining experimental data required for simulation development. For microscale simulations, electrode microstructure information is needed to construct simulation domains, and information about microstructure evolution is needed to understand electrode degradation. At both the microscale and macroscale, electrolyte solution transport properties for concentrated solution theory are needed to accurately describe battery operation under realistic, high-rate conditions.

Our "CD-adapco" subproject complements the main CABS project by focusing on the development of techniques and tools for obtaining reliable electrochemical cycling data and for rapidly process large quantities of electrode tomography data. This subproject aims to combine these approaches to obtain qualitative insight into electrode performance, allowing rapid screening of candidates for simulation studies.

Objectives

1. Provide microstructural information about battery electrodes by using X-ray microtomography
   A. For both pristine electrodes and electrodes soaked in electrolyte solution
   B. For cycled electrodes
2. Provide electrolyte solution transport properties that are compatible with concentrated solution theory
3. Provide tools to analyze tomography data and apply these for the imaged electrodes to construct surface meshes for use in simulation and further analysis to understand connections between electrode structure and performance.
4. Collect cycling data and provide insight into the influence of cell construction on observed performance.

Approach

Pulsed field gradient nuclear magnetic resonance (PFG-NMR) experiments performed by Kee Sung Han of EMSL at PNNL were used to determine concentration dependence of the tracer diffusion coefficients of lithium ions (Li^+), hexafluorophosphate ions (PF_6^-), EC, and DEC. Binary diffusivities were obtained by applying the generalized Darken relation, in which the binary diffusivities are related to the tracer diffusivities and mole fractions of each species. Concentrated solution theory was then applied to calculate the conductivity, transference number and diffusivity of the salt. These were then corrected for the degree of ion

pairing, which was obtained by fitting the conductivity calculated through concentrated solution theory to the experimental conductivity measured by a conductivity meter.

For the “CD-adapco” subproject, composite electrodes containing 4% (by mass) PVDF, 3.2% conductive additive, and 92.8% NMC532 particles obtained from our ORNL teammates were fabricated in an argon-filled glovebox in LBNL’s battery fabrication laboratory (collaboration with Yanbao Fu and Vince Battaglia, LBNL). Three doctor blade heights were used. After the laminates were left to dry overnight in the glovebox, their dry thicknesses were measured by a micrometer as approximately 40 microns, 76 microns, and 122 microns, corresponding to cells designed for higher power density or higher energy density. This fulfilled our Q1 milestone under the “CD-adapco” subproject.

A no-go decision was taken for the Q2 “CD-adapco” milestone, for which it was determined through discussions at both ANL and LBNL that obtaining electrochemical data using pouch cells containing reference electrodes would not be cost-effective, given the time and cost to construct these cells and concerns about proper interpretation of the resulting data. Instead, coin cells were constructed in the LBNL battery fabrication laboratory from the laminates produced for the Q1 milestone, with the help of tools designed and fabricated for this project that ensured precise placement of cell components. Future work will use these tools to probe the effect of variations in cell construction on cell performance. The cells were placed in temperature chambers and attached to galvanostats. They underwent the same formation procedure used by our teammates at ORNL for cells using the same NMC active material (four cycles at C/20 rate), followed by a sequence of charging at C/10 rate and discharging at a range of increasingly fast rates (to the extent that this was possible), ranging from C/10 to 10C (with rates based on capacities estimated from laminate masses).

Small (5/64” diameter) disks were punched from the laminates produced for the Q1 milestone using a hammer-driven punch and interleaved with polyimide disks in custom sample holders designed under the CABS project in FY16. These holders maintain light pressure on the samples, holding the samples relatively flat for imaging, and also allow for optional injection of electrolyte solution for investigating binder swelling due to solution uptake. These samples were assembled at LBNL and transported to ANL for microtomography imaging at APS beamline 2 with the assistance of beamline scientist Xianghui Xiao. These were imaged with a 10x optical lens, and reconstructions were performed with the TomoPy package from ANL, fulfilling our Q3 milestone.

In order to meet the Q4 milestone efficiently, it was necessary to automate the tomography data postprocessing pipeline developed under the “CD-adapco” subproject in FY16. Fully automating this process already required substantial restructuring and rewriting of existing computer programs, so it was determined that only a moderate amount of additional effort would be needed in order to package the software for release as open-source software. The software is designed so that users can adjust our usual pipeline to their needs by modifying the sample processing scripts. The key steps in this processing pipeline are described in the following paragraphs.

Tomography reconstructions produced by both TomoPy and by the ImageJ and Octopus-based ALS reconstruction software come in the form of a sequence of TIFF-format image files representing successive horizontal “slices” of voxels through the cylindrical reconstruction volumes. The sample holders and punch diameter selected for extracting samples from laminates were chosen to be only slightly larger than the reconstructed volumes. This was done to minimize the amount of material through which X-rays are transmitted but which are not inside the reconstructed volume; this excess material reduces the quality of the reconstructed data. As the sample holder diameters are slightly larger than the punch size, samples can shift slightly during assembly, and as multiple samples are stacked into each holder to improve imaging throughput, the samples rarely have perfect vertical alignment, so compromises are made during sample positioning in order to maximize the amount of usable data. Invariably, the edges of some samples, showing some damage from the punch, will appear in some reconstructions. In addition, the reconstruction algorithms frequently show numerical artifacts near the axis of the reconstructed cylinders. At the same time, manual extraction of

usable data tends to be time-consuming and inconsistent, particularly when one wants to examine enough image data in order to ensure good representations of the extracted samples. The first task is to extract a ring of non-overlapping cuboid columns that extend through the length of the reconstructed cylinder and which are located away from both the axis as well as the outer edge. These blocks are then used in further processing.

The postprocessing software then examines each block, computing average voxel intensities across each horizontal slice and making use of statistical clustering in order to distinguish slices that contain electrode regions from the surrounding foil and plastic material. By doing this, the software may be able to distinguish multiple electrode samples stacked into a single sample holder. The success of this clustering approach is dependent on good contrast in the reconstructions and suitable guesses of cluster means.

The individual electrode samples are typically slightly tilted relative to the camera horizontal, which complicates their use in analysis. In order to calculate the degree to which these samples are tilted, several small columns are extracted from each electrode region, and the clustering method is again employed to estimate the height of one of the electrode surfaces in each column. A linear least-squares fit is used to fit a plane to these interface locations, and rotations along the two axes in the horizontal plane are then calculated from the fitting plane. Each electrode block is rotated virtually. To remove directional bias, the corners of the rotated region are tracked so that a final cuboid can be extracted from the rotated region without including any filler voxels that were originally outside of the electrode.

Histograms are then computed for each finished electrode block. A heuristic for detecting unusable samples (such as those with cracks or those that might have been improperly processed) based on histogram shape is then employed, leaving a final set of usable samples. The histograms of these remaining blocks are compared with experimental data to obtain intensity thresholds that can be used to segment the electrode blocks according to expected component volume fractions. Electrode porosity was determined based on wet electrode thicknesses measured from tomography reconstructions, which differ from dry electrode thicknesses as we reported in our first 2017 publication.

It is at this point that one can optionally produce Avizo (FEI) TCL script files that direct Avizo to load the voxel data files, segment voxels by material type, and produce particle surface meshes. This procedure was adopted from one provided by our teammates at SNL and makes use of Avizo's particle separation capabilities, which can create interfaces between neighboring voxelized particles that cannot be clearly distinguished in the X-ray microtomography data due to imaging limitations or artifacts. Separate surface meshes are created to envelop each particle, as required by our teammates at SNL. Our implementation of this procedure has reduced the computer memory requirements for processing, allowing data sets that originally could not be processed within 32 GB of RAM to run on computers with as little as 4 GB of RAM.

While the construction of particle surface meshes was needed to fulfill part of our role within the CABS team, that is, generating surface meshes suitable for use in microscale simulations, the construction of individual particle meshes also has the advantage of providing detailed information about each particle. To fulfill the Q4 "CD-adapco" milestone, computer programs using the VTK library were written to examine the arrangement of surface meshes, providing quantitative information about electrode microstructure.

Finally, in preparation for the FY18 milestone involving tomography imaging of cycled electrodes, a trial pouch cell with a 1 cm^2 NMC532 cathode was constructed at the CAMP facility by Andrew Jansen (ANL) and again imaged at APS beamline 2 with the help of beamline scientist Xianghui Xiao.

Results

The degree of dissociation as a function of concentration of $LiPF_6$ in EC/DEC, determined by using concentrated solution theory to analyze both conductivity and self-diffusivity measurements, is shown in Figure I-136. Only 61% of salt molecules are dissociated at 0.1M. This decreases to 37% at 1.25M and then appears to increase to 39% at 1.5M. This limited salt dissociation has implications for solution-phase transport.

It is standard practice to assume complete salt dissociation. Applying concentrated solution theory and instead accounting for the limited degree of dissociation results in corrections to the solution transport properties. The salt diffusivity correction (not shown) is relatively small, but the corrected transference number values show stronger concentration dependence and are generally significantly smaller than the uncorrected values (see Figure I-137).

The microtomography postprocessing pipeline software package was approved for release as open-source software by LBNL and DOE, and was released on August 4, 2017 as the "TomPost" package. This Python 2 package should be compatible with a range of platforms. It requires the installation of the ImageJ image processing package from NIH, and optionally, a license for the Avizo meshing package, along with the "sed" stream editor, which is commonly found on Linux, BSD, and Mac OS X systems, and which is available on Windows systems through Cygwin. More information is available on the TomPost website at https://sites.google.com/a/lbl.gov/tompost/, which contains a link to the download site on Bitbucket.org, which tracks download counts for this package as required by DOE rules. This automated approach to postprocessing provides several benefits. The postprocessing script provides a precise record of the lengthy postprocessing procedure used to transform the raw reconstructed data into data suitable for analysis and use in simulation domains. The automated system also saves time and reduces errors by minimizing the need for user involvement. It is now only necessary to provide straightforward configuration and hints to the program (such as sample orientation, which is readily visible from the reconstructed data) before running the pipeline. An examination of records from FY16 suggests that the full automation of this process has reduced postprocessing time from days to hours, enabling the processing of large quantities of tomography data. Finally, automation minimizes human visual bias in analyzing the tomography data; for example, determining the boundary between an electrode sample region and a plastic spacer or current collector can be done visually, but this is time consuming and introduces the possibility of use of inconsistent visual criteria by a single researcher over time or among multiple researchers. In FY18, the TomPost package and electrode data, including tomography reconstructions of electrodes fabricated by our ORNL teammates in FY16, will be made available from a centralized repository alongside other software and data released by the CABS team.

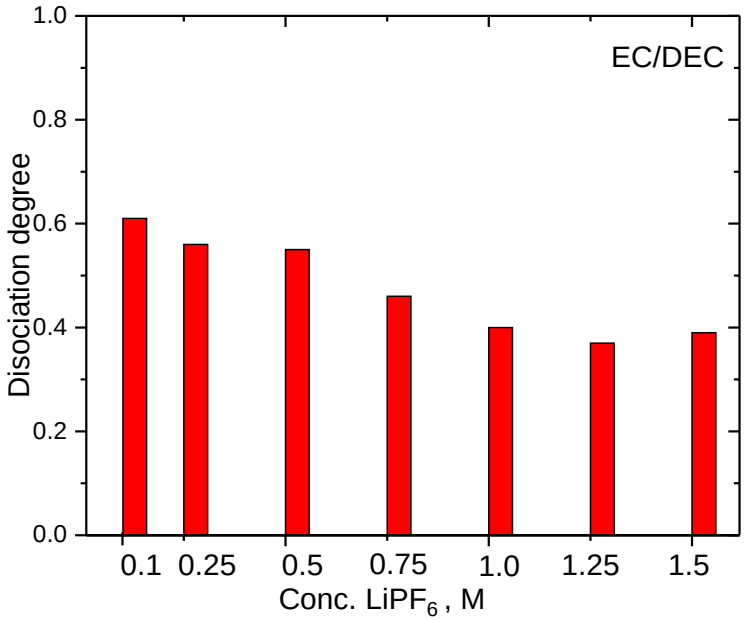

Figure I-136. $LiPF_6$ dissociation degree in EC/DEC (1:1 by weight).

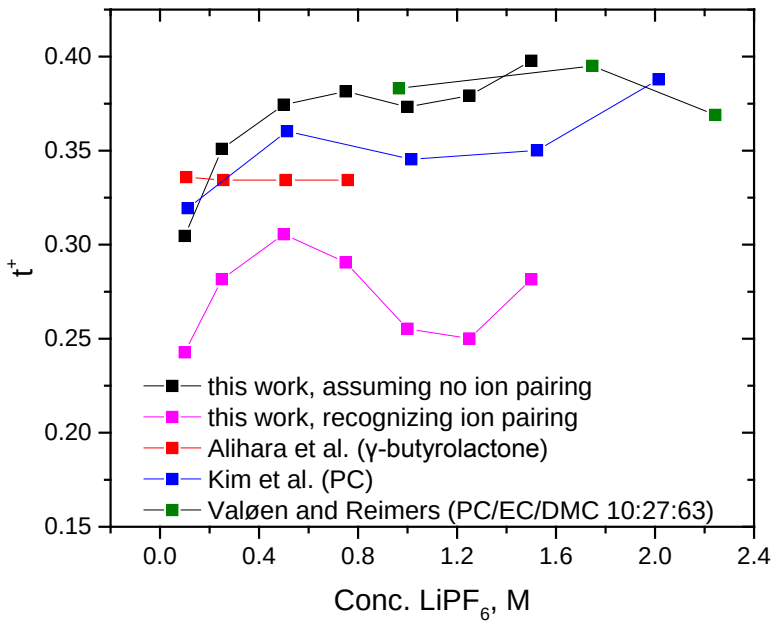

Figure I-137. Li^+ transference numbers as functions of concentration, showing correction due to recognition of ion pairing. Published results for other solvents are shown for comparison.

Figure I-138 shows capacity data from the cycling experiments with coin cells constructed from the electrodes fabricated with three distinct thicknesses. All discharge capacities have been normalized to capacities at C/10. All three cells show sharply decreased capacity at with increasing C-rate, although at lower C-rates this is consistent among the electrodes of different thickness and so likely to be due to solid-phase transport limitations rather than resulting from electrode structure. At higher C-rates, increasing electrode thickness has a significant effect on relative capacity reductions. Previous modeling work by our group and others has suggested that such decreases result from transport limitations in the solution phase within the electrode pores, with thicker electrodes requiring ions to travel farther, on average.

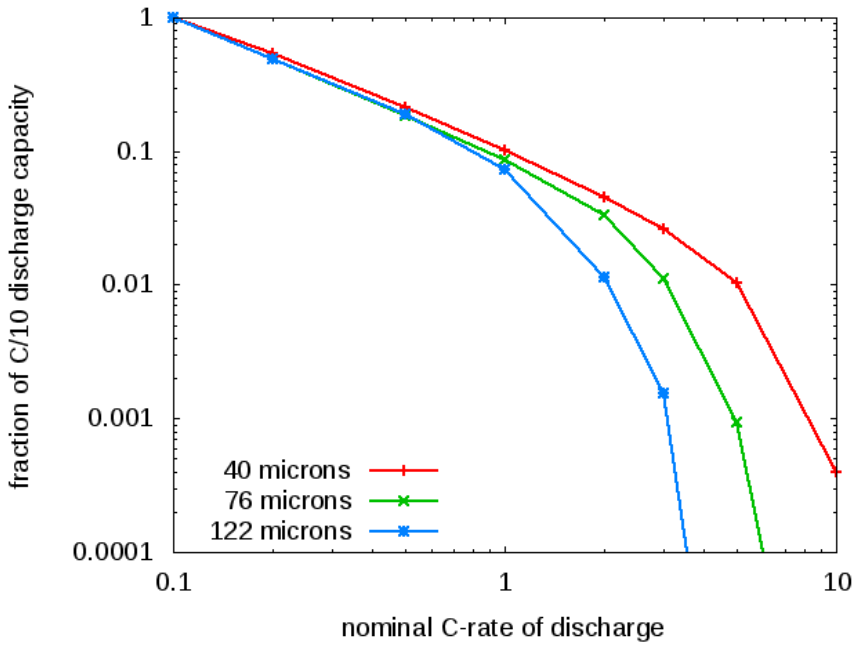

Figure I-138. Discharge capacities relative to C/10 capacities for representative cells with cathodes of three thicknesses

Our postprocessing pipeline generates a separate surface mesh for each particle, allowing a closer look at particle arrangements. Custom VTK-based programs were used to calculate particle location distributions and radial distribution functions from the particle mesh data sets, with approximate particle centroids determined by averaging surface mesh vertices. Particle volume distributions were computed directly from voxel intensities in the fully-processed voxel blocks. However, we were unable to detect any clear correlations between electrode thickness and internal structure. It is therefore likely that varying only doctor blade height has little effect on NMC particle arrangement in the resulting laminates beyond changing electrode thickness.

In preparation for the FY18 cycled electrode microtomography milestone, a trial pouch cell was imaged at APS beamline 2. A reconstructed slice through this cell is shown in Figure I-139. The cathode and surrounding pouch are readily visible, and single particles within the electrode can be seen. Similar reconstructions of these pouch cells, taken before and after cycling, will be used with the TomPost package and custom analysis tools in order to detect subtle changes in electrode structure.

Some of the text in this report, describing the transport property measurements, along with the accompanying figures, was taken from our second publication of 2017. (Reproduced with permission from *J. Electrochem. Soc.*, 164, A2434 (2017). Copyright 2017, The Electrochemical Society)

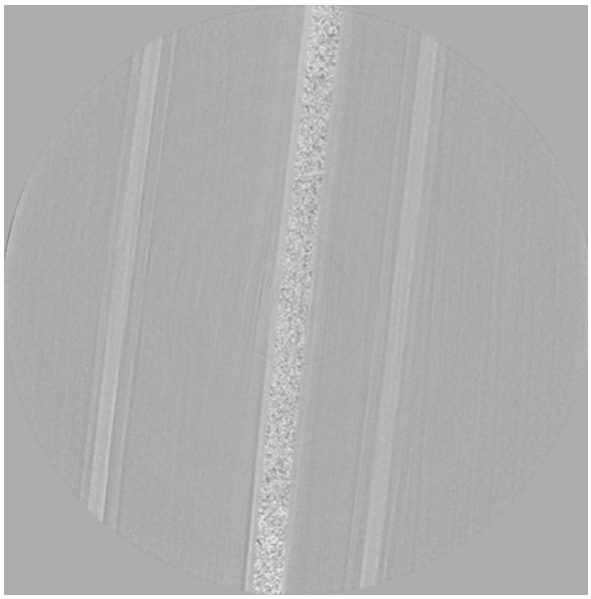

Figure I-139. Reconstructed slice of pouch cell from micro-tomography trial

Conclusions

Pulsed field gradient NMR and conductivity data was used to determine degree of dissociation of $LiPF_6$ in EC/DEC (1:1 by weight), using on the generalized Darken relation and concentrated solution theory. The degree of dissociation was found to decrease from 0.61 to 0.37 as concentration was increased from 0.1M to 1.25M. Analysis of our previous published data for $LiPF_6$ in PC, showed that the dissociation degree decreased from 0.675 to 0.51 over a concentration range of 0.5M to 2.0M. This ion pairing information was then used to correct transport property values computed for concentrated solution theory, with the transference number values showing particularly large changes.

Under the "CD-adapco" subproject, we have packaged and released our tomography postprocessing pipeline as open-source software. It performs fully-automated postprocessing of TIFF image stacks into particle surface meshes, reducing processing times from days to hours. This has been used to process microtomography data that we obtained for electrodes fabricated with three different thicknesses. As expected, electrode thickness appears to affect cell capacity at high C-rates. However, detailed analysis of particle surface meshes does not suggest a correlation between electrode thickness and particle arrangement within porous electrodes when electrode thickness is varied only by adjusting doctor blade height.

A trial test of pouch cell imaging for the FY18 cycled electrode tomography milestone showed promising results. Further imaging work is scheduled at APS for December 2017.

Key Publications

1. K. Higa, S.-L. Wu, D. Y. Parkinson, Y. Fu, S. Ferreira, V. Battaglia, and V. Srinivasan, "Comparing Macroscale and Microscale Simulations of Porous Battery Electrodes," *J. Electrochem. Soc.*, 2017, 164, 11, E3473-E3488, doi: 10.1149/2.0501711jes
2. Z. Feng, K. Higa, K. S. Han, and V. Srinivasan, "Evaluating Transport Properties and Ionic Dissociation of $LiPF_6$ in Concentrated Electrolyte," *J. Electrochem. Soc.*, 2017, 164, 12, A2434-A2440, doi: 10.1149/2.0941712jes
3. Open-source software: K. Higa, "Tomography Postprocessor for Battery Electrodes (TomPost)", https://sites.google.com/a/lbl.gov/tompost/, released on August 4, 2017.

I.C.7 Development and Validation of a Simulation Tool to Predict the Combined Structural, Electrical, Electrochemical and Thermal Responses of Automotive Batteries (Ford Motor Company)

Dr. Chulheung Bae, Principal Investigator
Ford Motor Company
Energy Storage Research
2101 Village Road
Dearborn, MI 48121
Phone: 313-410-1398
E-mail: cbae@ford.com

Brian Cunningham, Technology Manager
U.S. Department of Energy
Phone: 202-287-5686
E-mail: Brian.Cunningham@ee.doe.gov

Start Date: January 1, 2016 End Date: December 31, 2018
Total Project Cost: $4,375,000 DOE share: $3,500,000 Non-DOE share: $875,000

Project Introduction

This is the second year of a three-year project to develop a practical simulation tool for predicting battery abuse response. The project plan including major constituents and progression based on case studies is shown in Figure I-140.

The first half of the project is focused on developing an Alpha version of the model. This includes developing new, battery-specific keywords within LS-DYNA, identifying electrical, thermal, and mechanical input parameters, validating the model for performance situations where the cells are cycling in their intended operating mode, demonstrating preliminary abuse simulations for external short and crush, and enhancing the composite element formulations within LS-DYNA to provide accurate representations of battery material mechanics. Importantly, one-way coupling mechanisms linking the structural response to the electrical and thermal response have been implemented, and initial simulation predictions have been compared to test results from previous studies to confirm that the solvers are directionally accurate. Physical testing of full cells has recently begun to for model validation, and additional testing of cell components has been conducted to better determine critical physical parameters for the model.

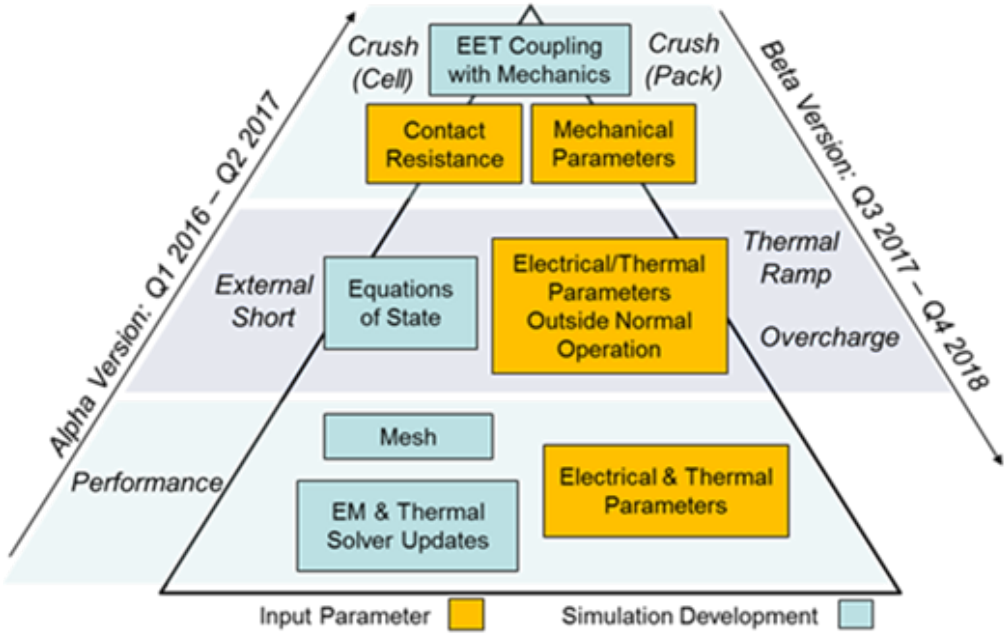

Figure I-140. Project schematic showing major constituents and progression of Alpha and Beta versions.

Objectives

Develop and validate a simulation tool to predict the combined structural, electrical, electrochemical and thermal (SEET) response of automotive batteries to crash-induced crush and short circuit, overcharge, and thermal ramp, and validate it for conditions relevant to automotive crash.

Approach

Develop material constitutive models and finite element method (FEM) element formulations that capture the mechanical response of cell components, including the case material, electrodes, separator, and their interactions with electrolyte.

Clearly identify the required input parameters for the material constitutive models, FEM element formulations, and exothermic, electrochemical reaction state equations governing multiphysics phenomena during crush-induced electrical short, thermal ramp, and overcharge conditions.

Design and execute a test matrix encompassing automotive crash strain rates, at a number of kinetic energy levels and physical orientations likely to occur in vehicle impacts.

Develop integrated modeling tools which demonstrate high-fidelity predictions of the onset of thermal runaway from the experimental test matrix using commercially available cells, module, and packs, spanning multiple chemistries relevant to automotive applications.

Maintain high-fidelity predictions while exploring methods to reduce the computational complexity of the model, and deliver a practical tool that is integrated with ORNL's OAS, for a broad customer base within automotive product development.

Results

The second year saw significant progress in many areas leading to a workable, validated model. Work continued in refining the mechanical, EM and thermal solvers with composite t-shell elements, all of which are now essentially complete and in use. It was shown that using composite t-shell elements in the mechanical solver can save computational time significantly while achieving almost the same result as using standard solid elements. Since in impact events the mechanical solver takes the majority of the simulation time, using composite t-shell elements has a potential to reduce the total simulation time considerably, which is critical in large-scale simulations such as module or pack level simulations. It was also shown that simulation results using composite t-shell elements are almost identical to results using solid elements in the EM and thermal solvers (see Figure I-141). Because of that, composite t-shell elements can currently be applied to all the solvers that are needed in the proposed battery safety model. It allows us to use one mesh for the entire model and saves time in the model development process. (Note that in previous reports and presentations we used both composite t-shell and layered solid elements in reference to the same mesh. In this report, we use only the term composite t-shell.)

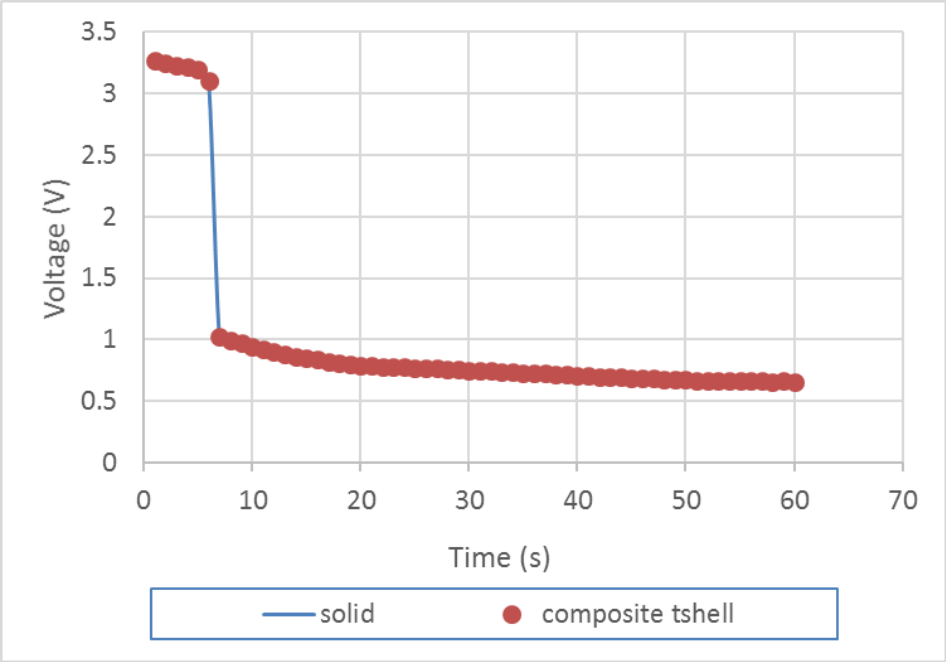

Figure I-141. Comparison of voltage evolution in two models.

The electrochemical properties of type D and E cells have been obtained from the cycling tests data via optimization processes. With these properties, the model prediction of the cell voltage profile during discharging and charging matches measurements very well. We built models for type D and E cells, applying the same boundary conditions as experiments in order to check if experimental results can be captured by simulations. The comparison of cell voltage profile during charge and discharge at different temperatures with different initial SOC is shown in Figure I-142, where it can be seen that the model results match experimental measurements well. This indicates that the parameters used in Randle circuit models for both types of cells may capture the battery behaviors over a wide range of conditions.

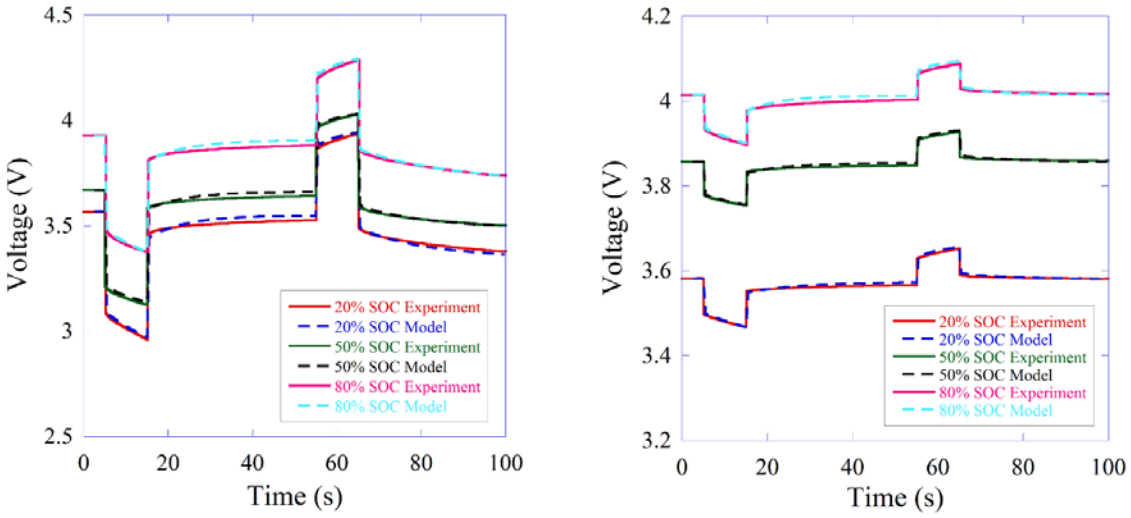

Figure I-142. Compare model predictions and measurements of the voltage profile of a type D (left) and type E (right) cell when it is discharged and charged with different initial SOCs.

Additional simulations for shear and crush were run on Type D cells using composite t-shell elements (Figure I-143) with very good agreement with experimental data for load/displacement (Figure I-144). We have performed the simulation for the shear test using the composite t-shell element as shown in the right hand side of Figure I-143. The dimension for the cell is 164 mm X 220 mm X 5.58 mm. Due to symmetric boundary condition we modelled only the half of the cell in x direction and a portion of the cell(10 mm in length) in y-direction. Nodes on the left hand side is fixed while the right hand has symmetric boundary condition. Top node are moved with a fixed velocity till displacement of 1.5 mm. We have used 9 elements across the thickness and each element has 16 integration points comprising 4 integration points for positive electrode (cathode), negative electrode (anode) and separator, 2 integration points is used to represent current collectors. All the components are modelled using MAT-24 material model, parameters for all the components are given in Table I-20. The number of composite t-shell elements is 1188 and it took 554 second to complete the simulation on 16 processors. These simulations worked better – had better agreement, fewer elements, less computation time – than simulations with standard solid elements.

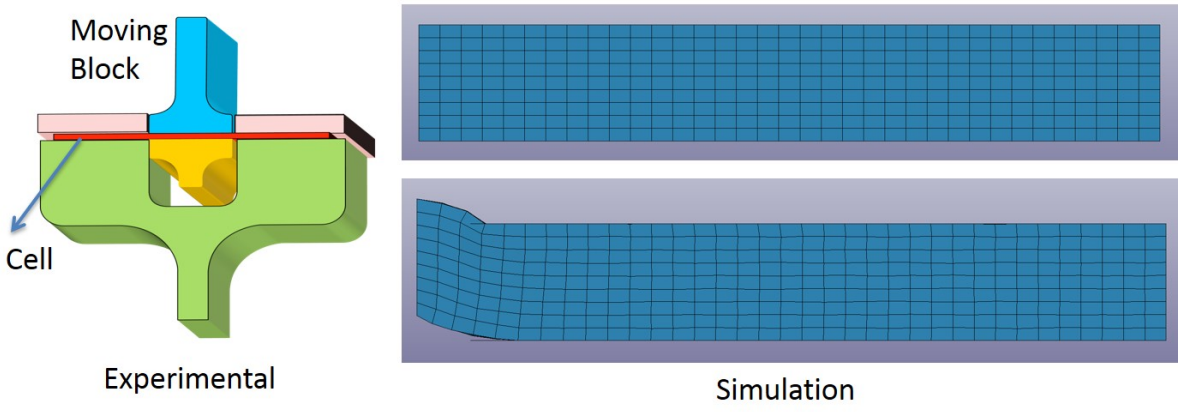

Figure I-143. Experimental and Simulation setup for Type D Cell

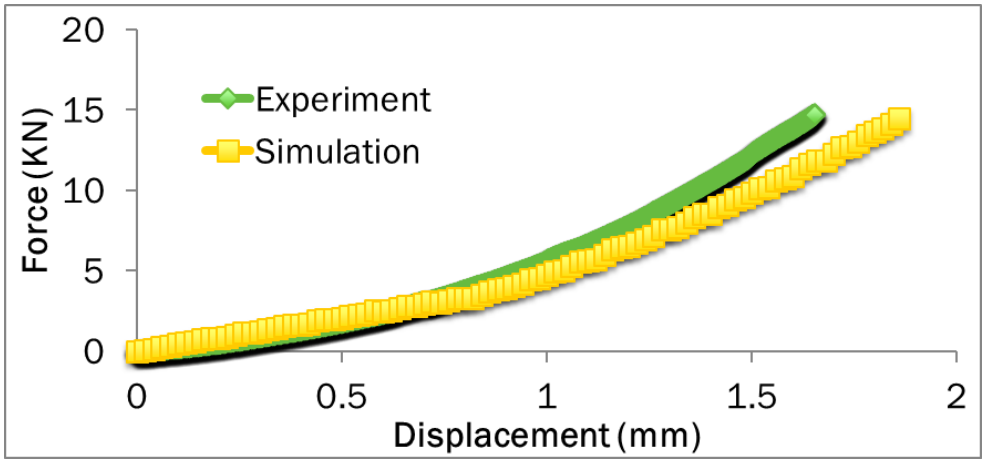

Figure I-144. Load displacement curve obtained by experiment and simulation

Table I-20: Parameter for component of the cell.

Component	Thickness (mm)	Elastic Modulus (Gpa)	Yield Strength (Gpa)	Tangent Modulus (Gpa)
Anode	0.064	0.45	0.04	0.01
Separator	0.023	0.50	0.045	0.01
Cathode	0.053	0.55	0.04	0.01
Aluminum Current Collector	0.015	70	0.24	0.1
Copper Current Collector	0.009	110	0.24	0.1

Both Type D&E cells were tested under shear conditions at Ford, and then shipped to ORNL for x-ray computed tomography analyses. Type D cell analysis results indicated that excessive damage was observed in the shear-stressed area and 2 – 3 step shearing might provide details on the progress of the cell component deformation. Additional shear tests were then run again to detectable short circuit, and also stopped at displacements less than creating a short.

Work continued using microphotographs of cell separators to determine statistics of the void fractions, which were then used to create 3D reconstructions. During this year, new models were created and refined and fibrils were added to better simulate type D & E separators. Simulations based on the new models compared well with experimental results.

Required platens and indenters were constructed at Intertek, and quasi-static crush testing started. Several Type D and E cells were tested but there were no shorts induced at the highest loading with the current equipment. New load cells, platens, and indenters were designed, purchased or constructed, and testing will resume in the fourth quarter. Fabrication of fixtures for the high-speed impact tests should also be completed and testing started in the fourth quarter.

A test matrix was developed for the cells, and a test site is selected. A preliminary version of the software has been developed and demonstrated for external short circuit and crush leading to internal short circuit scenarios. Techniques such as the use of composite t-shell elements and macro scale meshes were developed to reduce simulation complexity, and demonstrated significant reductions in calculation times. In the coming year,

validation experiments will be performed and simulations will be carried out to confirm the model predictions align with physical experiments.

Conclusions

The second year has been successful, with the project essentially on track and nearly all milestones accomplished. Cell characterization experiments were completed, as were the multi-physics solvers. Model integration was completed and the Beta version assumptions developed. Validation testing was started, but is behind schedule. Spending continues to be below estimated. It is expected that the final year will result in a validated, practical simulation tool that can be used to predict battery response to abuse.

Key Publications

1. The PI made a presentation on this project at the Department of Energy Annual Merit Review on Publications June 6, 2017.

2. Jie Deng gave a presentation at *the 232th ECS Meeting* in National Harbor, MD, on October 4, 2017.

3. Modeling of Battery Cells Using New Composite t-shell Element Formulation, in preparation, *Journal of Power Sources*.

I.C.8 High Fidelity Fast Running Multi-scale Multi-physics Battery Pack Software (General Motors, NREL, ANSYS and ESim)

Dr. Shailendra Kaushik, Principal Investigator
General Motors LLC (Prime)
30500 Mound Road
Warren, MI 48092-2031
Phone: 248-807-4156
E-mail: Shailendra.Kaushik@gm.com

Dr. Kandler Smith, Principal Investigator
National Renewable Energy Laboratory (Sub)
15013 Denver West Parkway
Golden, CO 80401
Phone: 303-275-4423
E-mail: Kandler.Smith@nrel.gov

Erik Ferguson, Principal Investigator
ANSYS, Inc. (Sub)
10 Cavendish Court
Lebanon, NH 03766
Phone: 603-727-5631
E-mail: Erik.Ferguson@ansys.com

Dr. Ralph White, Principal Investigator
ESim, LLC (Sub)
5 Brandywine Lane
Columbia, SC 29206
Phone: 803-240-7132
E-mail: White@cec.sc.edu

Brian Cunningham, Technology Manager
U.S. Department of Energy
Phone: 202-287-5686
E-mail: Brian.Cunningham@ee.doe.gov

Start Date: March 22, 2017 End Date: December 31, 2019
Total Project Cost: $2,477,808 DOE share: $1,738,968 Non-DOE share: $738,840

Project Overview

Building upon previous projects under DOE's Computer Aided Engineering for Electric-Drive Vehicle Batteries (CAEBAT) Program, the current project seeks to significantly enhance the computational efficiency and usability of simulation software to optimize and accelerate the design of automotive battery cells and packs. The project consists of the following five tasks: (1) To implement the new computationally efficient multiscale multidomain (GH-MSMD) electrochemical simulation method in ANSYS FLUENT, (2) Extend development of a holistic multiphysics reduced-order model (ROM) builder based on ANSYS FLUENT simulation results and the existing infrastructure of ANSYS DesignXplorer (DX) using deep-learning methods including neural networks, (3) Research the discrete empirical interpolation method (DEIM) as an option for improving the efficiency and accuracy of a nonlinear ROM for the electrode domain or cell domain, (4) Develop and implement an interactive system interface for MSMD and GH-MSMD in ANSYS and (5) Develop and implement physics-based life models of Li-ion batteries in ANSYS.

Objectives

The overarching objective of this project is to develop multiscale multiphysics battery pack engineering software that significantly surpasses the most advanced software in computational speed by a factor of 100 while resolving complex interplays of physics across length scales ranging from materials (~micrometers) to large automotive battery pack systems (~meters). Specific objectives include enhancing computation speed and stability while still resolving nonlinearities of the battery's dynamics and enhancing multiphysics integrity of the pack-level model, and enabling model-based diagnostics and prognostics for battery life and safety. To meet these needs, the project team will perform collaborative research, development, and demonstration in multiple synergistic directions, including cell/module/pack scale-coupling methods, ROM modeling techniques, battery life models, and user interface (UI) enhancements. The project will enhance the ANSYS Battery Design Tool (ABDT) that was originally developed in previous CAEBAT projects. For clarity in what follows, the ABDT is the software layer that provides a battery-specific UI, automates battery-simulation workflow, and calls proprietary ANSYS products as services.

Approach

Physicochemical processes in lithium ion batteries occur in intricate geometries over a wide range of time and length scales. As the size of the battery increases, macroscopic design factors in combination with highly dynamic environmental conditions significantly influence the electrical, thermal, electrochemical, and mechanical responses of a battery system. NREL pioneered the multiscale multidomain (MSMD) model, overcoming challenges in modeling the highly nonlinear multi-scale response of battery systems. The MSMD model as shown in Figure I-145 provides flexibility and multi-physics expandability through its modularized architecture. The project team previously collaborated on combining new and existing battery models into engineering simulation software that provides 3-D battery pack simulation modeling capability. Because of increasing complexities when configuring additional electrical and thermal connections between the cells, the computational cost of simulating a battery pack response is still high: results take weeks, unless low-fidelity sub-models are used to represent the battery's current/voltage response. Therefore, substantial improvement of computational efficiency is needed. Software tools also need improved usability and flexibility to reduce both the computational time and the engineering labor required to keep pace with battery design changes, including geometry and configuration. These improvements would enable the use of models in design and management tradeoff studies of performance/life in large vehicle battery pack systems, which are typically composed of several hundred large-format individual cells.

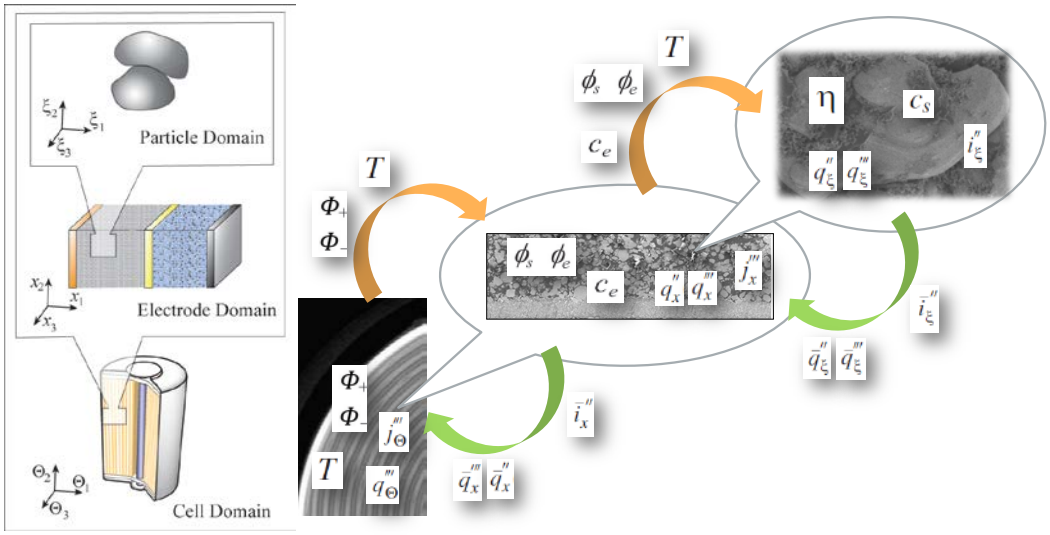

Figure I-145. A diagram of intra- and inter-domain coupling protocols used in NREL's MSMD framework, integrating widely varied scale battery physics in a computationally efficient manner with hierarchical modular architecture

For large automotive battery pack design and development, the current state-of-the-art battery pack engineering software lacks the combination of sufficient computational speed, physics-based predictive capability and solution accuracy. Led by General Motors (GM), the team comprised of GM, ANSYS, NREL and ESim proposed to develop and implement an innovative nonlinear multi-scale battery model framework in the commercial software package, ANSYS FLUENT. The proposed software offers greater computational efficiency while retaining expandability and modularity. In a previous project supported by DOE, NREL developed a new innovative quasi-explicit nonlinear multi-scale multi-physics framework, GH-MSMD. The new framework uses time-scale separation and variable decomposition to eliminate several layers of nested iteration but keeps the modular framework architecture that is critical to battery behavior simulations. Fast electronic charge balance is differentiated from processes related to slow ionic movements. During the preliminary benchmark test carried out at the electrode domain model (EDM) level, the GH-MSMD implementation demonstrates significant computational speed improvement compared to the original MSMD. Figure I-146 presents the comparison of electrical and thermal response predicted by 4 different model combinations, simulating a battery for a mid-size PHEV10 sedan driving a US06 cycle for 20 minutes. The model outputs from different models are nearly identical. The most efficient GH-MSMD model option runs the 1200 second simulation in only 0.74 seconds, while the original MSMD runs the same case in 654 seconds. Based on the encouraging preliminary benchmark result at the EDM level, we propose to improve computational speed of the pack-level simulation by a factor of 100 from the state-of-the-art models.

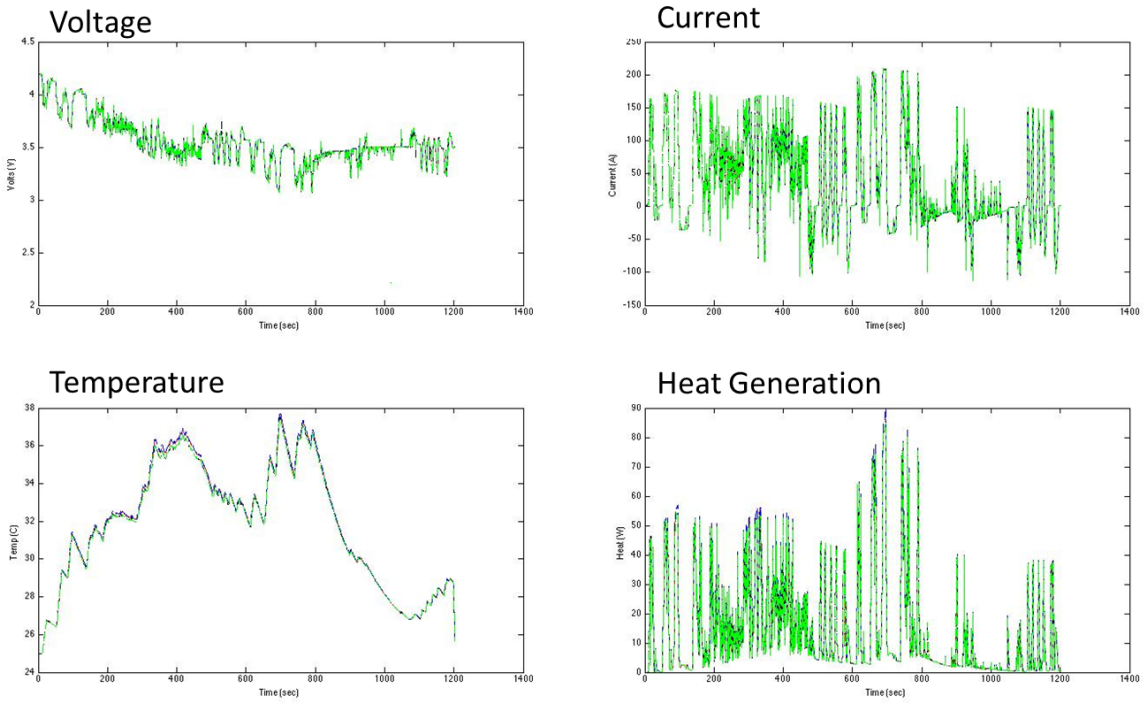

Figure I-146. Comparison of electrical and thermal response of a battery for mid-size sedan PHEV10 US06 20 minutes driving power profile from the 4 different model combinations

Due to the pace of battery design change, the physical complexity of packs, and the number of user application scenarios that need to be studied, system-simulation with ROM remains an essential research need. Addressing ROM limitations will complement the expected progress from GH-MSMD, in a multi-pronged attack on the computational-efficiency challenge. It is increasingly evident that more advanced ROM techniques – available from the general literature – need to be integrated into the CAEBAT software tools to have the maximum impact on battery innovation. One particular area of importance is macro-modeling approaches for designs in

which parameters other than battery state of charge and coolant flow rate vary. The designer needs to approximate the electrical and thermal performance of the pack while varying design parameters such as the geometry and physical properties. Extending the system modeling with parameterized ROM techniques will allow manufacturers to look at many "what-if" scenarios, and perform optimization and sensitivity analysis, after a single ROM-building process. Effective parallelization and intelligent sampling of the parameter space are the key elements that need to be investigated and developed. This ROM can be built from a FLUENT analysis, driven by the ANSYS DesignXplorer software tool with its design of experiments and response surface processes. It will be exposed both as a generator of fast approximate predictions in ANSYS Workbench, and as a reusable model for use in systems-engineering analysis tools, vehicle simulators, or even real-time battery management systems with hardware in the loop. In addition, state-of-the-art ROMs typically lose validity when severe nonlinearities arise in the system. Because vehicle batteries are often used in a regime where nonlinearity becomes significant (e.g., continuous high-rate charge/discharge or low-temperature cycling), a nonlinear ROM, which is fast enough while coupling kinetic, thermodynamic, and transport equations over complex component geometries, has been desired. The team is exploring a new ROM that retains acceptable accuracy under severe nonlinear conditions at a computational cost comparable to existing ROMs. The project team will further investigate partial orthogonal decomposition (POD) and DEIM ROMs where the battery electrochemical behavior is coupled with the thermal behavior. We have implemented DEIM for one- and two-cell batteries. Applying it to larger batteries will require either a method for connecting such small DEIM models together, or obtaining the connectivity information from FLUENT and applying DEIM directly to the full geometry of a multi-cell battery.

Finally, new modeling approaches developed in CAEBAT I are being investigated for application at the electrode domain level to enhance computational efficiency and track changes in battery cell performance during lifetime of the cell. Developed by ESim, a new nonlinear state variable implementation of the Newman P2D electrochemical model will help accelerate studies of non-uniform usage of a battery for temperature gradient or non-optimized electrical design. The merit of this novel application of ROM will be researched and evaluated. During CAEBAT I, ESim further extended an existing equivalent circuit model (ECM) to include capacity fade due to cycling of cells by adding a branch for the capacity loss on charge due to the solid electrolyte interface (SEI) formation reaction at the anode. Figure I-147 presents this ECM, where an SEI formation branch has been added in parallel with the anode branch.

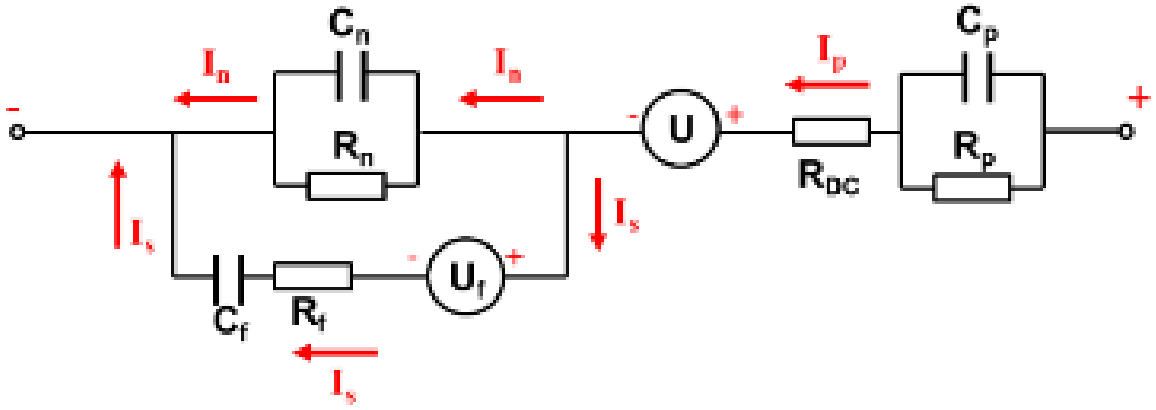

Figure I-147. Equivalent circuit model with an SEI formation branch

Results

Earlier this year, NREL documented and published the GH-MSMD modeling approach in The Journal of the Electrochemical Society [1]. Figure I-148 shows an example EDM simulation. NREL is supporting GH-MSMD implementation in ANSYS FLUENT and has introduced the GH-MSMD method to project team members. NREL has also performed preliminary evaluation of the ANSYS interactive system interface.

MATLAB is selected to run ANSYS FLUENT as a server for interactive simulation demonstration to accomplish a model feasibility study on fast, high-fidelity model-based diagnostics and prognostics of pack-level life and safety.

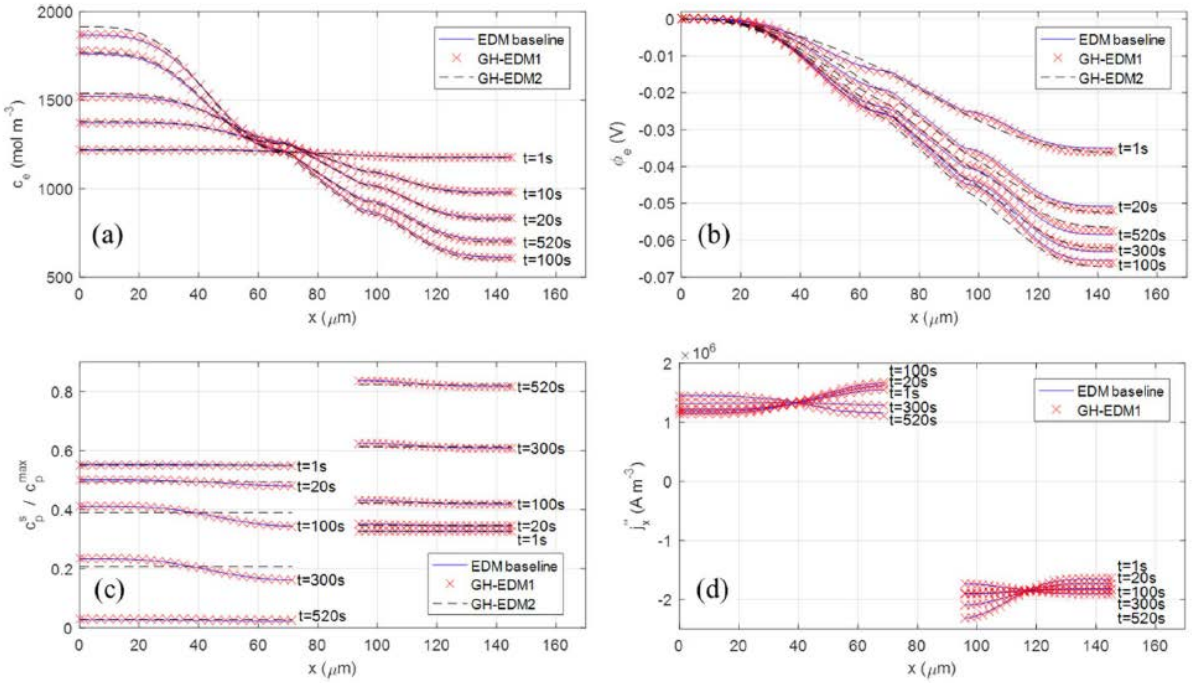

Figure I-148. GH-MSMD electrode-domain model (EDM) simulations from Kim, J. Echem. Soc., 2017. (a) Electrolyte salt concentration, (b) electrolyte phase potential, (c) solid surface concentration, and (d) volumetric current density during 5C discharge at 25°C.

ANSYS has begun implementation of the GH-MSMD method in FLUENT. The essential idea of the GH-MSMD method is similar to the circuit model used in FLUENT. It assumes that at each level (pack domain, electrode domain, cell domain), the potential change can be written as $\Phi = G + Hi$. G and H at the higher level can be constructed from the G and H at the lower level. As a result, a battery pack's electric load condition can be quickly distributed to the lower hierarchical level and avoid the need for inner iterations. In NREL's GH-MSMD paper [1], this method was applied to the Newman P2D model. Focusing on the cell-level during the first year, the team identified several opportunities to implement GH concepts. When solving electrochemical physics at the 3-D cell level, the GH method allows transfer current to be distributed non-uniformly throughout the cell and still maintain good computational efficiency. The need to repeatedly solve cell potential distribution is eliminated. Thanks to algebraic relationships, the Newman P2D electrochemical sub-model is solved only once per time step, instead of once per iteration in the direct method. Figure I-149 shows the updated FLUENT user interface, where the GH-MSMD model will be available by enabling cell clustering as an enhancement to the FLUENT reduced-order method. It is compatible with all the electrochemical sub-models including the NTGK, ECM, Newman's P2D and the user-defined electrochemistry model. These enhancements are planned to be released in FLUENT R19.0 in January 2018.

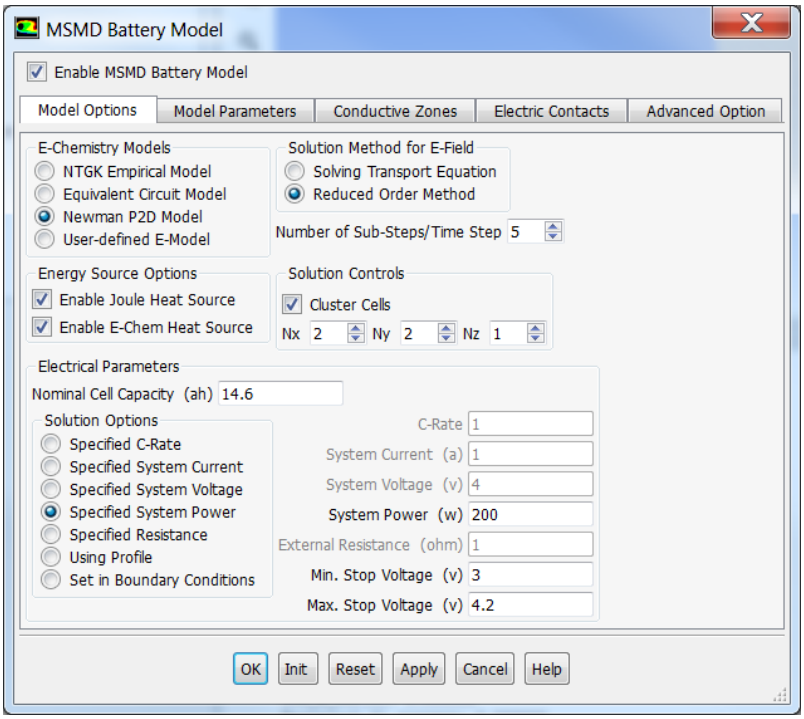

Figure I-149. Updated FLUENT MSMD Battery Model panel

ESim extracted the values for the circuit components (C_p, R_p, C_n, R_n, R_{DC}, and U) from the HPPC data obtained at 25°C and different cycling stages (BOL, 500 cycles, and 1000 cycles). In fitting the model to the HPPC data, the SEI branch is ignored. In the HPPC tests, the transient responses of a cell at different depths-of-discharge (DODs) were measured. During a specific high power pulse, the change in DOD is very small, so all the parameters can be regarded as constants. By fitting the model to the transient response data during a pulse, the parameter values at a specific DOD can be obtained. Through a pulse-to-pulse fitting procedure, the circuit parameters as functions of DOD can be obtained. This procedure is illustrated in Figure I-150.

Conclusions

The project is on track to finish by the end of 2019. GH-MSMD implementation in FLUENT is ongoing. Initial implementation has shown up to 20x computational speedup capturing 3-D electrochemical physics. Non-linear, dynamic ROM for fast simulation of battery packs using deep neural networks has begun and preliminary results show promise for additional computational speedup of 3-D thermal/flow physics. Novel approaches including an additional branch in the equivalent circuit model to represent SEI layer growth show promise to efficiently model battery life and extract relevant model parameters from aging test data.

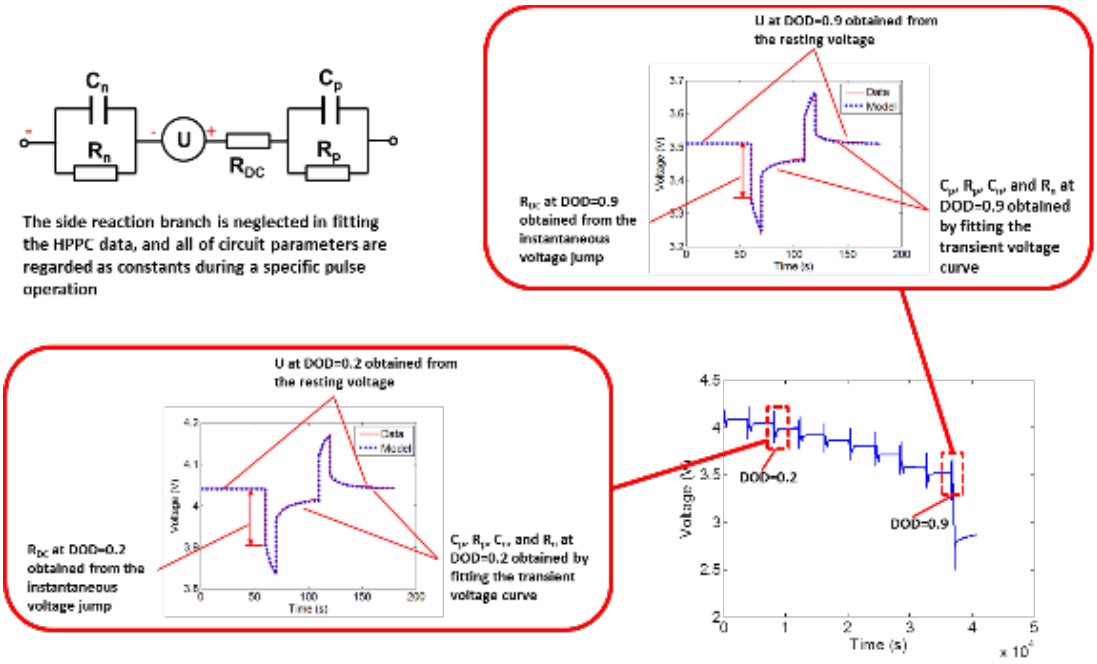

Figure I-150. Illustration for circuit component extraction

Key Publications

1. M Guo, X Jin, and R E White. "Nonlinear State-Variable Method (NSVM) for Li-Ion Batteries: Finite-Element Method and Control Mode." J. Electrochem. Soc. 164.11 (2017): E3200-E3214.

2. M Guo, X Jin, and R E White. "Nonlinear State-Variable Method for Solving Physics-Based Li-Ion Cell Model with High-Frequency Inputs." J. Electrochem. Soc. 164.11 (2017): E3001-E3015.

References

1. G.-H. Kim, K. Smith, J. Lawrence-Simon, C. Yang, “Efficient and Extensible Quasi-Explicit Modular Nonlinear Multiscale Battery Model: GH-MSMD”, J. Electrochem.Soc., 164(6), A1076-A1088 (2017)

I.D High Energy, Long Life Lithium-Ion Battery (NREL)

Kandler Smith, Principal Investigator
National Renewable Energy Lab
15013 Denver West Parkway
Golden, CO 80401
Phone: 303-275-4423
E-mail: Kandler.Smith@nrel.gov

Brian Cunningham, Technology Manager
U.S. Department of Energy
Phone: 202-287-5686
E-mail: Brian.Cunningham@ee.doe.gov

Start Date: October 1, 2016 End Date: March 31, 2018
Total Project Cost: $600,000 DOE share: $600,000 Non-DOE share: $0

Project Introduction

Energy-dense, long-life energy storage is needed to improve market readiness and enable higher penetration of electric vehicles. Today's state-of-the-art lithium-ion EV battery lasts around 10 years and provides just 100-250 miles range, both inferior to conventional vehicles. Across virtually all of today's Li-ion chemistries, Li loss capacity fade is the dominant mechanism that limits lifespan. High-energy Li-ion electrode materials presently under research and development (e.g., silicon) suffer even shorter life than today's materials because of large volume change during cycling that fractures electrode surface films and accelerates Li loss. In addition to lifetime challenges, large irreversible Li loss on the first cycle limits the beginning-of-life performance of these high-energy electrodes. To boost initial capacity, these materials presently require pre-lithiation as an extra manufacturing step, adding unwanted cost to the cell. This project seeks to overcome the barrier presented by limited useable Li inventory in order to enable higher energy, longer life batteries.

Objectives

The objective of the project is to increase cycle lifetime of both graphite and silicon (Si)-based Li-ion cells. For cells employing Si, the proposed technology will also increase initial capacity. The device will be low cost, passively controlled, and occupy minimal weight and volume. Sspecific objectives include:

- Extend calendar and cycle life by 50% for Li-ion graphite/NMC (nickel-manganese-cobalt) and Si-X/NMC systems
- Re-lithiate the Si anode following the formation cycle to increase Si-anode Li-ion system energy density by 20%
- Design the system such that it adds less than 5% to the cost, weight, and volume of Li-ion cells, and is compatible with cell manufacturing and safety
- Pending resources, work with commercialization partner in year 3 to transition the technology to the marketplace

Approach

The proposed objectives will be met by introducing an excess Li reservoir into Li-ion cells that can be released to boost capacity upon demand, increasing initial performance and extending lifetime. Different from previous concepts, the proposed technology is controlled passively and can deliver a slow, continuous release of Li ions throughout the cell lifetime and/or a fast, triggered release of Li ions on demand. The device is projected to add less than 1% to the cost, weight, and volume of today's cells. In addition to extending lifetime, the device is a practical way to pre-lithiate Li-starved systems to boost their initial capacity, addressing a present roadblock hindering commercialization of high-energy anode materials such as silicon. The successful project will design and demonstrate the proposed device on cells using both today's graphite-based and tomorrow's high-energy Si-based negative electrode material presently under investigation by the DOE Applied Battery Research for Transportation (ABRT) program.

The team leverages unique expertise at NREL and ANL. NREL is a recognized expert in the electrochemical characterization and model-based design of electrochemical couples and large-format cells under DOE's CAEBAT program, including diagnosis and modeling of degradation mechanisms in automotive systems and environments. ANL's Cell Analysis, Modeling, and Prototyping (CAMP) laboratory is the leading DOE facility for producing high-quality electrochemical couples in partnership with DOE's Si Deep-Dive project. (See Section IV.B.1 of this report for additional description of the CAMP facility.) ANL's high energy density Si anodes when demonstrated together with NREL's supplemental Li technology may represent the best progress to date amongst labs, universities, and industry to reach DOE's VTO Battery500 Strategic Goal for EV batteries of 500Wh/kg and 1000 cycles.

Results

During FY 2017, NREL demonstrated significant capacity recovery and life extension for three different graphite-based cells. Recently, the excess Li device was used to recover capacity in high energy density silicon anodes cells fabricated by ANL at their CAMP facility. Major accomplishments include:

- 20-33% capacity recovery demonstrated for graphite/lithium manganese oxide (LMO) pouch cells
- 5.5% capacity recovery demonstrated for commercial graphite/lithium iron phosphate (LFP) 18650 cell
- 4% capacity recovery for graphite/NMC commercial 18650 cell after 400 cycles
- 7-8% capacity recovery for ANL Si anode pouch cells after 50 cycles

The excess Li reservoir device was inserted into several low capacity LMO/graphite pouch cells to demonstrated capacity recovery and life extension. LMO is a good demonstration candidate because Mn dissolution catalyzes SEI growth which irreversibly consumes Li at the graphite anode surface resulting in rapid capacity fade. The cells were cycled approximately 120 times with different charge cutoff voltages at room temperature resulting in 34-50% capacity fade (Figure I-151). Next, the cycling was suspended and lithium-ions were inserted into the active cell from the excess Li reservoir. Due to the location of the device the re-lithiation was done at a very rapid rate and only required two days to complete. Figure I-151 shows the resulting capacity restored was between 20-33% for all three cells.

Similar cycle aging and re-lithiation has also done for higher capacity commercial cells with graphite anodes. Results are summarized in Table I-21. Capacity recovery and life extension has been demonstrated for 18650 A123 cells with graphite/LFP chemistry having an initial name plate capacity of 1.1 Ah. A123 cells were cycled at their operational limit of 55° C to accelerate capacity fade from loss of available lithium ions. Commercial graphite/NMC cells with a nameplate capacity of 2.2 Ah were cycled at their operation limit of 45°C. Both cell types were cycled at C/2. For the A123 cell, life was extended by approximately 50% using the excess lithium reservoir once. The device is designed to be able to use multiple times or continuously which would further extend life.

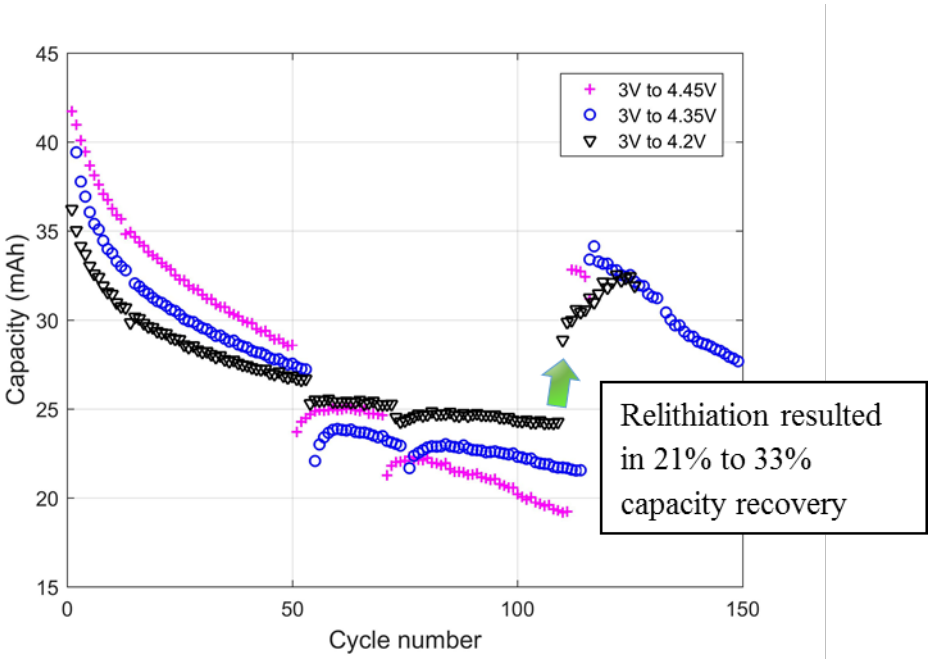

Figure I-151. Excess Li reservoir used to restore capacity of LMO/graphite pouch cells after ~120 cycles. The graphite/LMO pouch cells were cycled at room temperature with different charge cutoff voltages.

Table I-21: Summary of capacity recovered using excess Li reservoir for commercial graphite cells

Cell	Graphite/LFP	Graphite/NMC
Number of Cycles	150 at 55°C	400 at 45°C
Capacity Fade	120 mAh (-11%)	400 mAh (-18%)
Capacity Recovered	60 mAh (+6%)	90 mAh (+4%)

Capacity recovery from the proposed excess lithium reservoir is an ideal technique to restore capacity for next generation Si-based anodes that suffer from high rate of lithium consumption due to rapid SEI growth. To support demonstration of the device, the ANL CAMP facility supplied NREL with 400 mAh Si- graphite/ NMC pouch cells. These cells consist of 14 electrode pairs with each having an active area of 14.1 cm^2. The anode consists of 15 wt% Si and has an initial capacity of 520-590 mAh/g-electrode and 600-670 mAh/cm2 compared to 350 mAh/g and 400 mAh/cm^2 for a standard graphite-only electrode. Initial cycling of 6 cells at room temperature is shown in Figure I-152. Cycling protocol consists of 8 initial cycles at C/10, then 8 cycles at C/5, and continuous cycling at C/3 all with a voltage range of 3.0V to 4.1V. Cycling shown for cells 1-4 are standard pouch cells, while cells 5 and 6 have the NREL device inserted prior to cycling and sitting in an idle state. These results show the device has been successfully inserted and, as-desired, the non-triggered device has no negative impact to cycle life.

After 50 cycles, the excess Li reservoir device was added to cells 2 and 3 and used to recover capacity. Cycle capacity before and after adding the idle device remained the same. A capacity boost of 27 mAh (8% of C/3 capacity) was achieved for cell 3 after triggering the excess Li reservoir to recover usable Li ions as shown in Figure I-153. The measured capacity fade rate before and after re-lithiation was approximately 1.4 mAh/cycle. The fade rate not accelerating indicates that lithium-ions have been inserted back into the active cell in a uniform fashion. Similar recovery and fade results were also achieved for cell 2.

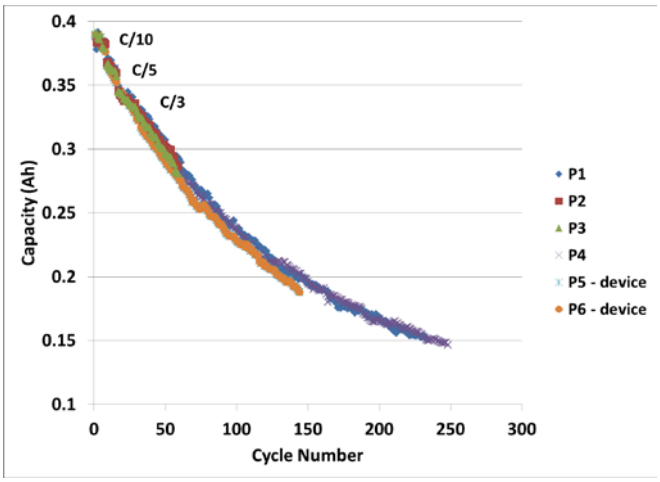

Figure I-152. Cycling of 400 mAh ANL silicon-graphite/NMC pouch cells at room temperature without (cells 1-4) and with device inserted but not triggered (cells 5 and 6). These results demonstrate that the device has no unintended negative impact to cycle life when integrated in a cell and left in the idle state.

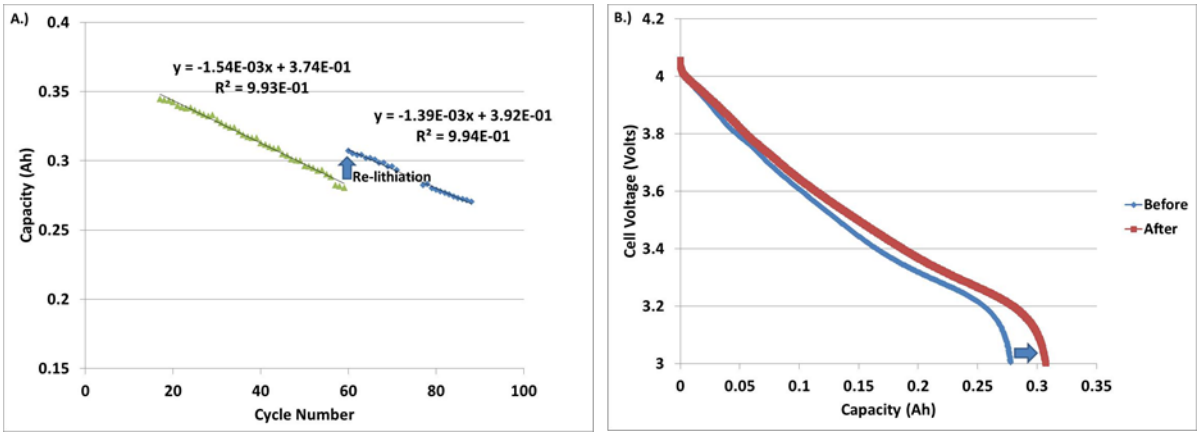

Figure I-153. Cycling of 400 mAh ANL Si pouch cell #3 before and after triggering device showing 8% capacity restored. A.) The measured capacity fade rate before and after triggering the device is relatively constant indicating Li-ions have recovered relatively uniformly. B.) Discharge voltage curve before and after re-lithiation.

Conclusions

NREL has demonstrated that the proposed excess Li reservoir device can be used to recover capacity and extend lifetime for both state of the art graphite and silicon-based cells. Significant capacity recovery of 20% to 33% has been shown for LMO/graphite pouch cells at relatively high re-lithiation rates. A life extension of 50% has also been demonstrated for A123 commercial cells. Further, the device has been shown to also enable capacity recovery and life extension for high energy density silicon-based cells. Next steps include exploring the best location for device, working with commercial vendor(s) to develop device that is manufacturing ready, determining the rate at which the device can be used, and using the device continuously while the cell is cycling.

Key Publications

1. “LONG-LIFE RECHARGEABLE ION BATTERIES” U.S. Patent Application # 15/685,485 filed on 08/24/2017

I.E Material and cell studies to enable extreme fast charge (XFC) (INL)

Christopher J. Michelbacher, Principal Investigator
Idaho National Laboratory
2525 Fremont Avenue
Idaho Falls, ID 83402
Phone: 202-586-3384
E-mail: christopher.michelbacher@inl.gov

Samuel Gillard, Technology Manager
U.S. Department of Energy
Phone: 202-287-5849
E-mail: Samuel.Gillard@ee.doe.gov

Start Date: July 1, 2016 End Date: May 31, 2017
Total Project Cost: $775,000 DOE share: $775,000 Non-DOE share: $0

Project Introduction

Decreasing energy consumption across the U. S. transportation sector, especially in commercial light-duty vehicles, is essential for the United States to gain energy independence. Recently, powertrain electrification with plug-in electric vehicles (PEVs) have gained traction as an alternative due to their inherent efficiency advantages compared to the traditional internal combustion engine vehicle (ICEV). To be truly completive to the ICEV refueling experience, battery electric vehicle (BEV) charging times must dramatically decrease. Extreme fast charging (XFC), or charging an EV at up to 400-kW stands to decrease vehicle charging time as well as increase the utility of a BEV. As such, Figure I- 154 shows how utilizing fast charging at 50-kW for 1-5% of all annual charges nets the vehicle owner a nearly 25% increase in annual vehicle miles traveled (from [1, 2]). Automotive companies, battery manufacturers, codes and standards bodies, charger manufacturers and

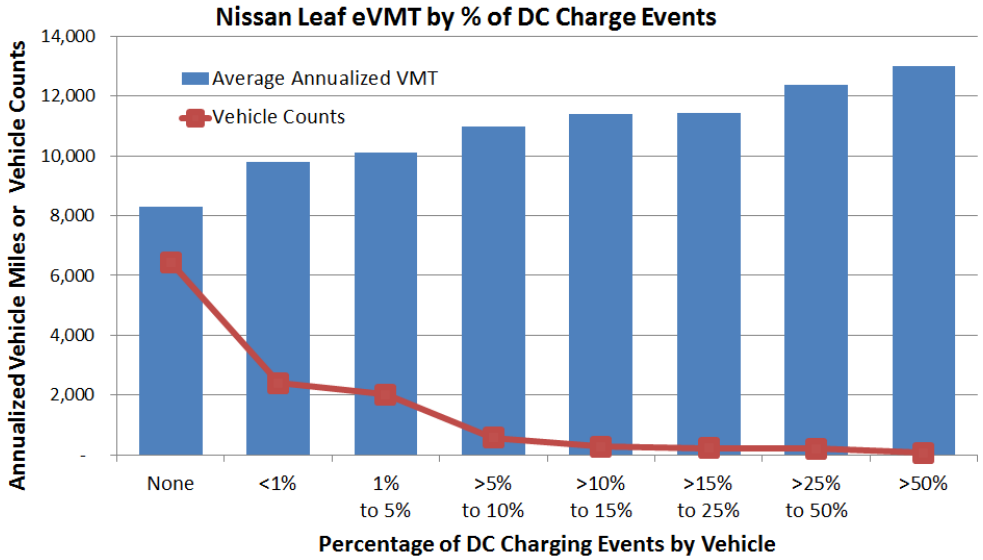

Figure I- 154. Analysis by California Air Resource Board (CARB) shows increased yearly vehicle miles traveled when using 50 kW fast charging. When compared with a vehicle that never fast charged, nearly a 25% increase in annual miles traveled was realized when 1% to 5% of total charging events were fast charges.

network operators, and utility suppliers can all be impacted with the introduction of XFC technologies. For successful XFC implementation, collaborations across technology intersections and overlaps need to be fostered. To accelerate these interactions, the project team engaged with industry to identify technical challenges and develop a report outlining the limiting factors for XFC implementation in BEVs. A combined analysis found in the report includes impacts to and R&D recommendations for battery performance, battery thermal management, vehicle design, and infrastructure with economic considerations.

Objectives

For XFC to be successful, stations should be able to recharge a BEV in less than 10 minutes and provide approximately 200 additional miles of driving. However, this introduces a host of new challenges that need to be addressed. As a result, it is expected that packs designed to meet XFC will initially be significantly more expensive than BEVs optimized for current charging technology. From the battery cell to the power grid these 400-kW chargers are connected to, this research outlined in the report discusses issues that need to be addressed at each level in order to implement a 400-kW charging network. Although the report is U.S.-focused, the findings should be applicable to other countries with mature automotive infrastructures. Technical gaps and challenges posed by XFC are investigated and divided into primary focus areas: batteries, vehicles, and infrastructure with economic considerations. Outcomes from this research could be used to inform the development of technical targets and research and development plans for stakeholders.

Approach

A multi-national laboratory team consisting of Argonne National Laboratory (ANL), Idaho National Laboratory (INL), and National Renewable Energy Laboratory (NREL) engaged with industry stakeholders to identify barriers and opportunities for technology R&D solutions needed to achieve 400 kW charging power levels and combine the findings into a single document for governments and private industries to reference. Industry perspectives on the direction of fast charging were used to guide and bound the technology gap assessment report, inform the team on areas needing an extensive literature review, and develop use-cases to assess the economic feasibility of XFC. The report was been broken into three sections: (1) an executive summary, (2) a summary report, and (3) appendices complete with four technical manuscripts. The executive summary is intended to introduce XFC and convey the high-level technical challenges/gaps and introduce potential R&D solutions with minimal technical discussion. In the summary report, these gaps and R&D solutions are addressed with more technical detail. The reader should be able to understand the bulk issues and linking technicalities associated with XFC by reading the summary report; however, the reader does not need to be an expert in the field. The manuscripts contained in the appendices are intended for persons with technical backgrounds or those looking to learn more about XFC technologies though a technical lens. The appendices were written with the intent to be published in technical peer-reviewed journals for which citations are listed in the Key Publications section.

Results

Battery

The U.S. Department of Energy (DOE) has a goal of reducing the production cost of a BEV battery to ultimately $80/kWh, increase the range of EVs to 300 miles, and decrease charge time to 15 minutes or less. In order to achieve this goal, a major effort within the battery research community has focused on increasing the energy density of the cell, which refers to the amount of energy stored in a specified weight or volume. Increasing electrode thickness is an effective way of improving the energy density of a cell. However, thicker electrodes present several barriers to fast charging. As electrode thickness increases, charge times must also increase in order to avoid lithium plating. Lithium plating occurs when the charge rate exceeds the rate the lithium ions can intercalate into the crystal structure of the anode, which causes metallic lithium to form on the surface as shown in Figure I- 155 (from [3]). Lithium plating can negatively affect performance of the electrode and lead to accelerated degradation of the battery, as well as impact cell safety. Therefore, it is thought that thinner electrodes are better suited for XFC applications, but this occurs with a tradeoff in increased battery cost. Referencing Table I- 22 (from [4]), the analysis indicates that fast charge nearly

doubles cell cost from $103/kWh to $196/kWh. The increase in cell cost is largely based on decreasing the anode thickness. Using thinner electrodes requires more cells to achieve the same energy density.

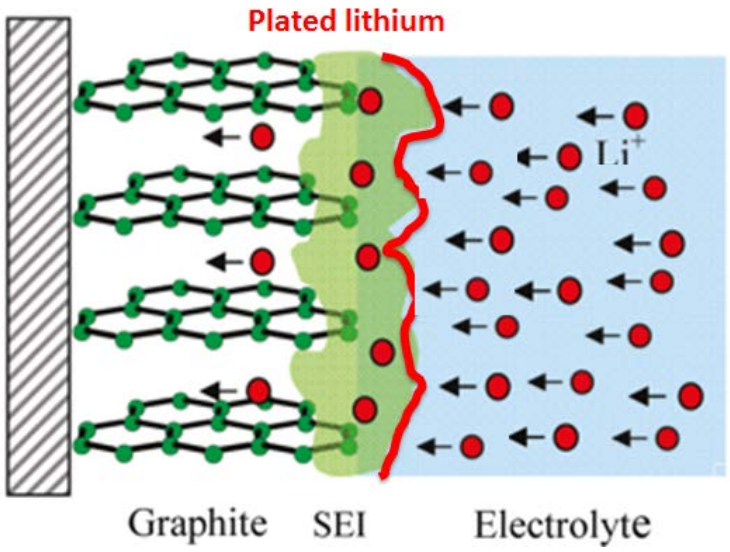

Figure I- 155. At high charge rates, a much larger number of lithium ions move to intercalate into graphite as represented by the red dots. However, there is not enough time or space for intercalations; therefore, lithium ions may start plating as metal onto the surface of the graphite electrode, shown as a thick red line).

Managing the heat generated in the battery during a charging event is also a potential barrier to XFC because temperatures in excess of 45°C will rapidly degrade battery lifetime. Higher temperatures can also introduce safety concerns as materials contained within the battery can begin to chemically and mechanically degrade.

The report cites the need for materials R&D in order to minimize or mitigate localized heating and lithium plating with thicker electrodes. Research in electrode design can help with implementation of advances made through materials' innovations. A study of the impact of XFC on the existing current-state-of-the-art can inform material, electrode, and cell design research. These studies may also reveal differences in the safety of cells subjected to XFC protocols, which is an area also in need of more research to fully understand the impacts and to develop mitigations. Research toward development of new charging protocols that may extend battery life should also be considered.

Development of new technologies for XFC battery pack thermal management is needed in order to preserve battery life. More complex battery management systems may be needed to cope with higher pack voltages, more complex thermal management systems, and cell balancing during charging. Higher voltage packs also bring additional electrical safety concerns that need to be understood.

Table I- 22: BatPaC simulation comparing the effects of charging time on the required anode thickness, heat generation in the pack, and the resulting temperature rise, pack cost, and incremental cost of charging faster than 1-C (60 minutes) rate. Cell Chemistry: NMC 622-Graphite, Pack Energy: 85 kWh; Rated Power (10-second burst): 300 kW; Maximum Allowable Current Density (MACD): 4 mA/cm^2; Number of Cells per Pack: 240

Charging Time, ΔSOC=80%, minute	**8**	**10**	**23**	**47**	**53**	**61**
Charging Time, ΔSOC=60%, minute	5	7	15	30	34	39
Charger Power Needed, kW	601	461	199	100	88	77
Anode Thickness, µm	**14**	**19**	**43**	**87**	**98**	**103**
Heat Generated during Charge, kWh per pack	2.35	2.20	1.89	1.77	1.75	1.45
Post-Charge Cell Temperature (ΔSOC=80%), degrees C	22.4	24.4	25.9	26.4	26.4	19.5
Cell Mass, kg	2.75	2.40	1.74	1.49	1.46	1.45
Cell Cost to Original Equipment Manufacturer, $ per kWh	**$229**	**$196**	**$132**	**$107**	**$104**	**$103**
Cost Difference, $ per kWh	$126	$93	$30	$4	$1	$0

Vehicles

Similarly as with the battery, the vehicle is constrained by cost, weight, and volume. For XFC-capable vehicles, these parameters are greatly influenced by the current delivered to the vehicle during a 400-kW charge, where all parameters rise with increased current. By increasing the BEV battery pack voltage from the current industry standard of 400 V to more than 800 V, the current needed for XFC drops by at least half. However, increasing the pack voltage impacts components such as the electric drive motor and the power electronics onboard the vehicle, including the power inverters. Higher voltages also bring new challenges associated with interoperability because legacy and XFC-enabled vehicles could interface with the same charging infrastructure. Developing an XFC-capable vehicle may introduce challenges with the high-voltage system architecture, power electronics and electric machines, the charging system, thermal management, cyber and physical security, and BEV/EVSE interoperability. The trade-off between driving range and recharge time has historically been a barrier to BEV adoption. XFC seeks to balance these parameters, along with vehicle cost.

BEV owners require consistent charging experiences; therefore, interoperability of XFC charging systems with vehicles of different models and charging capabilities could be studied. Cybersecurity research of the vehicle and charger communications is needed to ensure BEVs can provide reliable transportation. Furthermore, standardization to ensure interoperability between new and legacy vehicles accessing XFC and existing networks is needed. Testing and evaluation of existing vehicles to XFC charger connectors to determine safe, reliable, and robust operating limits could be considered. Researching the impact higher pack voltage has on the overall volume, weight, and cost for power electronics may be needed for XFC-enabled vehicles. Increased system bus voltages will require reevaluation of semiconductor materials used in vehicle power electronics, in addition to improved insulation materials needed to maintain electrical safety and durability.

Infrastructure

Successful installation of nationwide, 400-kW capable, public infrastructure requires many barriers to be addressed. A key challenge is to coordinate across the many stakeholders such as vehicle manufacturers, utility suppliers, XFC charger manufacturers and network operators, battery developers, codes and standards

bodies, and policy makers. Specific topics such as power requirements for XFC charger installations, utility rate structures, and the connector type for vehicle-to-charger connections can impact the effectiveness of XFC and should be considered by stakeholders as a group. XFC infrastructure should be able to accommodate all vehicle types, even if the vehicle is not XFC capable.

Optimization of XFC charging station location is needed within cities and across highway corridors to account for user convenience and availability of power from the utility. Co-located distributed energy resources as seen in Figure I- 156 (from [5]), may be needed to minimize station operation costs, limit grid impacts, supplement power provided by electric grid, and accommodate ideal XFC station placement.

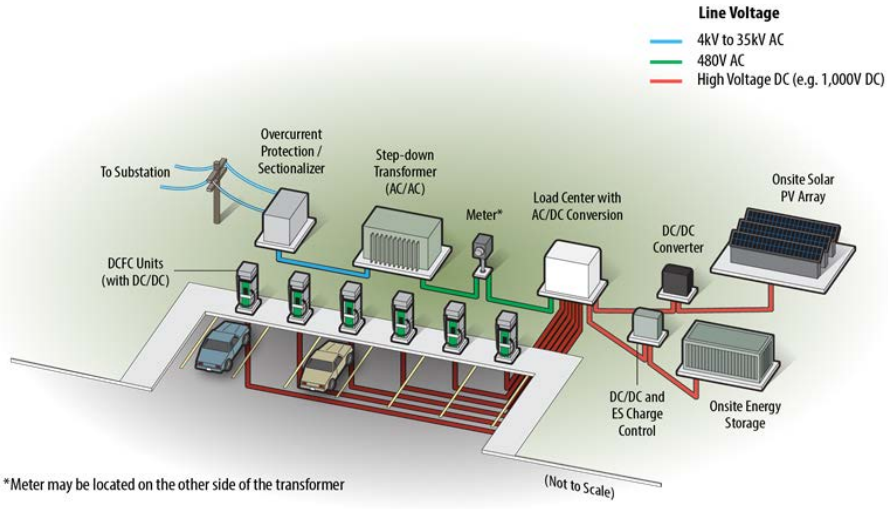

Figure I- 156. XFC station showing different design options such as co-located energy generation and storage which may be used to reduce station operating costs, minimize grid impacts, supplement power provided by the electric grid and accommodate ideal XFC station placement.

Researching advanced materials to reduce and manage thermal loads within the charger and the cable connecting the vehicle-to-charger is needed for XFC applications. Automation for XFC should be considered; however, this may increase overall system cost. Stakeholder engagement to harmonize XFC station permitting and siting requirements, along with codes and standards related to liquid-cooled cables and vehicle-to-charger connector design, should be a focus. Best conducted by industry, understanding where XFC stations need to be sited to serve demand, both commercial and private, and where appropriate grid resources exist to initially serve the greatest number of consumers should be investigated. The tradeoffs and operational benefits realized by using co-located distributed energy resources integrated with utility generation could be considered and studied.

Conclusions

Many technical gaps and challenges for XFC have been identified in this research which impact several key technology sectors such as automotive OEMs, battery manufacturers, codes and standards bodies, EVSE manufacturers and network operators, and utility suppliers. For XFC to be successfully implemented, these technology sectors need to foster new levels of collaboration and communication regarding technology intersections and overlaps.

Battery cost is often cited as a barrier to EV adoption. XFC could increase the cost of a cell by more than 90%, with anode thickness the primary cost driver. Within the battery cells, a bulk of the research identified centers around the anode and mitigating the onset of lithium plating and minimizing heat generation, which can lead to dramatic cell degradation and pose safety concerns. Heat generation in general is a known mechanism for electrochemical and mechanical battery material degradation. As such, thermal management of

batteries when subjected to XFC protocols require R&D. Thermal management research coupled with robust battery management controls and charging protocols R&D will help achieve XFC while prolonging life.

For vehicles, higher voltage battery packs, up to 1000V from conventional EV's 400V systems, can drive much research in the electrical architecture of the vehicle and power electronics which support the electric drive system. Cybersecurity and interoperability of vehicle and EVSE communications is needed to ensure XFC capable vehicles, and legacy vehicles alike, can provide reliable transportation and not be disrupted by cybersecurity events or differences in charging equipment.

In infrastructure, conductive EV charging using a cord and plug require research in thermal management of the charger power electronics and charge cable. For wireless charging technologies, electromagnetic field shaping and shielding have the bulk of the R&D investment. XFC's intermittent demand for electricity could pose challenges to the electric grid's stability which raises concerns from utilities as a potential for cybersecurity vulnerabilities. Infrastructure sees the introduction of the largest and most broad base of stakeholders ranging from EVSE manufacturers and network operators to utility suppliers and regulators. Coordination and cooperation within this group of stakeholders is recommended in order for XFC to make it to market.

The gaps identified within this research could serve as a useful guide for research programs spanning varying degrees of technology maturity across a broad industry landscape. Identification and dissemination of XFC technical issues will help the stakeholder community focus and advance each technology area at a quicker pace than may otherwise be possible if each organization were to undertake a similar effort on its own.

Key Publications

1. Bloom, I. et al. "Enabling Fast Charging – A Battery Technology Gap Assessment." *Journal of Power Sources*, vol. 367, 1 Nov. 2017, pp. 250–262., doi:10.1016/j.jpowsour.2017.06.055.
2. Keyser, M. et al. "Enabling Fast Charging – A Battery Thermal Technology Gap Assessment." *Journal of Power Sources*, vol. 367, 1 Nov. 2017, pp. 228–236., doi:10.1016/j.jpowsour.2017.07.009.
3. Meintz, A. et al. "Enabling Fast Charging – Vehicle Considerations." *Journal of Power Sources*, vol. 367, 1 Nov. 2017, pp. 216–227., doi:10.1016/j.jpowsour.2017.07.093.
4. Dufek, E. et al. "Enabling Fast Charging – Infrastructure and Economic Considerations." *Journal of Power Sources*, vol. 367, 1 Nov. 2017, pp. 237–249., doi:10.1016/j.jpowsour.2017.06.079.

References

1. Lutsey, N., S. Searle, S. Chambliss, and A. Bandivadekar, 2015, "Assessment of Leading Electric Vehicle Promotion activities in United States Cities," *International Council for Clean Transportation*, July 2015.
2. McCarthy, Michael, 2017, "California ZEV Policy Update," *SAE 2017 Government/Industry Meeting*, Society of Automotive Engineers, January 25, 2017, Walter E. Washington Convention Center, Washington, DC, conference presentation.
3. Challenges for Rechargeable Li Batteries, John B. Goodenough and Youngsik Kim, Chemistry of Materials 2010 22 (3), 587-603, DOI: 10.1021/cm901452z.
4. Howell, David, et al. "Enabling Extreme Fast Charging: A Technology Gap Assessment." *Department of Energy*, Office of Energy Efficiency Renewable Energy, 23 Oct. 2017, https://energy.gov/eere/vehicles/downloads/enabling-extreme-fast-charging-technology-gap-assessment.
5. Francfort, J. et al. "Considerations for Corridor and Community DC Fast Charging Complex System Design." INL/EXT-17-40829, Idaho National Laboratory, May 2017.

I.F Small Business Innovation Research (SBIR)

Samuel Gillard, Technology Manager
U.S. Department of Energy
Phone: 202-287-5849
E-mail: Samuel.Gillard@ee.doe.gov

Objectives

Use the resources available through the Small Business Innovation Research (SBIR) and Small Business Technology Transfer (STTR) programs to conduct research and development of benefit to the advanced batteries effort within the Vehicle Technologies Office.

Introduction and Approach

The advanced batteries effort of the Vehicle Technologies Office supports small businesses through two focused programs: Small Business Innovation Research (SBIR) and Small Business Technology Transfer (STTR). Both programs are established by law and administered by the Small Business Administration. Grants under these programs are funded by set aside resources from all Extramural R&D budgets; 3.0% of these budgets are allocated for SBIR programs while 0.45% for STTR grants. These programs are administered for all of DOE by the SBIR Office within the Office of Science. Grants under these programs are awarded in two phases: a 6-9 month Phase I with a maximum award of $150K and a 2 year Phase II with a maximum award of $1M. Both Phase I and Phase II awards are made through a competitive solicitation and review process.

The advanced batteries team participates in this process by writing a topic which is released as part of the general DOE solicitation. Starting in FY12, the advanced batteries team decided to broaden its applicant pool by removing specific subtopics and allowing businesses to apply if their technology could help advance the state of the art by improving specific electric drive vehicle platform goals developed by the DOE with close collaboration with the United States Advanced Battery Consortium.

Phase II Awards Made in FY 2017

Under the SBIR/STTR process, companies with Phase I awards made in FY 2016 are eligible to apply for a Phase II award in FY 2017. The following two Phase II grants were awarded in FY 2017 (from among the four Phase I grants that were conducted in FY 2016):

Coulometrics (Chattanooga, TN 37404-2812)

This project will develop state-of-the-art processes for the conversion of natural flake graphite and other graphitic materials into high quality lithium-ion battery (LIB) grade anode materials. This will enable a $1B industry to develop and create a supply chain for graphite that does not exist in the United States today. This project will complete 4 years of work by Coulometrics to develop new environmentally friendly and low cost processes for the conversion of graphitic materials into a high quality LIB anode material that exhibits: Lower cost; improved purification through an environmentally friendly process, and; A high quality and consistent material suitable for demanding electric vehicle applications. Currently, all natural graphite for lithium ion batteries originates in China. This represents the most profitable value-added market for graphite with no current beneficiaries in the US. This is true even though vast high-quality flake graphite deposits exist in the US and Canada and the US also boasts some of the highest quality petroleum coke that can be used to produce synthetic graphite. Many junior graphite and petroleum companies are eager to see their materials used for LIB anode material. However, new state-of-the-art process technologies are required that will: spheronize the graphite with higher yield than what is currently used in China; purify the spheronized and synthetic graphite, and; CVD coating of the spheronized graphite to provide high efficiency and long life in LIBs. Coulometrics has increased spheronization yield from 30 to 70%, demonstrated new thermal purification technologies that achieve record graphite purity, and developed a new CVD coating process that has allowed us to achieve

unprecedented LIB life even when compared to world class cells used in Tesla vehicles today. Coulometrics graphite anode materials meet all automotive specifications including high capacity (>355 mAh/g) and high first cycle efficiency (92-95%). Coulometrics is already working with leading US battery manufacturers and has support for this effort from Tesla Motors and K2 Energy. It considers each a beachhead customer for both automotive and military markets that are the focus of our commercialization plan. The goal of the Phase II effort is to continue the development of graphite products that focus on longer life, higher charge rate and resistance lithium plating, and cost reductions through process innovation. Coulometrics is currently able to build and test 2.4 to 3.0 Ah 18650 cylindrical lithium ion batteries and performance state-of-the-art high precision coulometry testing to determine life and charge rate capabilities. This work also involves commercial partners and sending full 18650 cylindrical cells for verification. Full qualification and a current target price of $4-5/kg could make this material attractive to LIB manufacturers currently paying more than $14/kg in high volume. Coulometrics has established a new joint venture called PUREgraphite with Graphitecorp funding the commercialization effort with $10M. Coulometrics owns 50% of PUREgraphite and will continue to develop the material.

Saratoga Energy (Berkeley, CA, 94710-2737)

A breakthrough electrolysis process to manufacture graphite from carbon dioxide has been developed. Graphite is the primary active anode component used in lithium-ion batteries for electric vehicles and constitutes 10-14% of the total cell cost. The graphite produced could offer a 70% cost saving compared to commercial incumbents. In addition, the company's graphite features another very important characteristic: it enables fast-charging of lithium-ion batteries – up to three times faster than standard anodes. Thus, upon success of the project, it will contribute to: reducing the cost of batteries for electric vehicles and dramatically improving charging performance. During Phase I, the company improved the performance of its graphite anode material by optimizing synthesis conditions and demonstrated long-term cycling stability on small full-cells. In Phase II of this SBIR project, three objectives will be met. The first objective is to further refine the graphite production process to maximize material performance. The second objective is to demonstrate fast charging capabilities and long-term cycling stability on larger, 2 Ah lithium-ion full cells. The third objective is to demonstrate the feasibility of this process at a small pilot scale, paving the way for further customer sampling and qualification, as well as providing necessary process data for a demonstration-scale plant design. Lower cost and improved battery charging will contribute to greater customer acceptance of electric vehicles, helping the deployment of clean energy technologies. As an added benefit, this graphite could be made from waste carbon dioxide and, if produced from renewable electricity, would have a negligible carbon footprint.

Phase I Awards Made in FY 2017

Nine Phase I grants were awarded in the Summer of FY 2017.

Amasatan Technologies (Andover, MA)

The fundamental functional components within lithium ion batteries are the anode, cathode, and electrolyte. Currently, cathode material dictates battery performance and is the most expensive of the three, accounting for up to 25% of the battery pack cost. Reducing the cost of the cathode material represents a significant decrease in the cost of the battery. Cathode cost is determined mostly by raw material and production costs. The goal of this project is to reduce (i) the production cost of cathode materials and (ii) the environmental footprint associated with cathode material production while maintaining high- performance. For this, the company will focus on NMC 532, which is the current industry standard for state of the art automotive batteries. The company expects the underlying technology to be developed in this program to be broadly applicable to all transition metal oxide cathodes, and maybe also resulting in more viable pathways to the next generation cathode materials – the so-called ni- rich NMC's. It will use Amastan's UniMelt™ single-step continuous microwave- generated plasma materials processing technology. Unlike conventional incumbent cathode material manufacturing techniques requiring many processing steps and producing environmentally unfriendly chemical byproducts, adding to cost, the proposed process is carried out in a continuous single step without process byproduct. The UniMelt process uses solution precursor mixed at the molecular level as feedstock. The solution precursor is used to produce uniform diameter droplets that are injected into a uniform temperature

electrodeless plasma column of up to 4" in diameter, where they undergo chemical reactions. This offers each precursor droplet the same thermal path and thermal history, leading to tight control of phase purity, size and size distribution of the product. The preliminary technical results of this phase will enable comprehensive cost analysis of the final cathode material production at commercial scale.

Ge Solartech, LLC (Troy, MI)

Ge Solartech, LLC will develop and demonstrate a novel synthesis process that can efficiently produce nickel-rich NMC materials. This proprietary process uses pure metals as precursors, avoiding time and energy consuming steps in the conventional hydroxide co-precipitation process because the cost of pure metals is much lower than that of their corresponding compounds and can directly be used as the starting materials without requiring any further treatment. This process can reduce process cost by 70% compared with that of the current hydroxide co-precipitation process. The success of this synthesis process will help in achieving objectives for novel low-cost materials and improvements in manufacturing processes. In Ni-rich materials, a replacement of a small amount of Li by Ni gives larger reversible capacity because NiO_2 slabs bonded together by the Ni allow much more Li ion de-intercalation. However, Ni atoms in the Li layer can block the passage of Li+ transport, leading to poor performance in rate capacity. Therefore, Ni2+ cations in lithium layers should be controlled within a certain range in order to obtain higher performance. In order to tailor the degree of cation mixing, there is a need for a new synthetic protocol. The proposed solid-state synthesis method enables the control of the amount of cation mixing by programming reaction conditions. The conditions, such as precursors, duration of ball milling, reaction temperatures and oxygen environments, are crucial in determining crystal structure and cation mixing that influence the electrochemical performance of the NMC electrodes. Working with the Chemical and Materials Engineering Department at the University of Kentucky, Ge Solartech will, during Phase I, develop and test new nickel-rich NMC cathodes and will characterize and optimize material formulations, as well as improve synthesis methods. Based on its PI Dr. Huang's previous experience as a Senior Scientist in the Battery Materials Division of BASF, it expects that materials capable of 250-270 mAh/g could be developed in Phase I. Ge Solartech plans to use high capacity Si and graphite composites as anodes to build full cells. By using thick, high performance nickel-rich cathodes and Si-graphite composite anodes, Ge Solartech expects full cells to reach a capacity close to 200 mAh/g. At the completion of Phase I, Ge Solartech will submit a proposal to the DOE for a Phase II project that will scale up production of nickel-rich NMC materials to a prototype level. In Phase II, a full cell capable of 2 Ah will be built to validate the findings of Phase I.

Giner Inc. (Newton, MA)

Conventional lithium-ion batteries demonstrate great potential for applications in electrical vehicles, but they face some major challenges such as low energy density and high cost. It is worthwhile to pursue alternative strategies to address the barriers of cost and energy density. This company proposes to develop advanced rechargeable lithium-sulfur (Li-S) batteries that have much higher theoretical energy density and lower cost. It will improve the practicality and cycle life of Li-S batteries to make them more commercially viable. In the Phase I project, it will improve the energy density and cycle life of Li-S batteries via two approaches. First, highly conductive lithium-ion exchange membranes will be used as battery separators. Second, concentrated Li electrolytes will be used in electrodes. These efforts will prevent cathode sulfur loss due to the polysulfide shuttle mechanism, thus significantly enhancing the cycle life of Li-S batteries. The proposed lithium-sulfur technology will address two major barriers for electrical vehicles, cost and energy density; therefore directly facilitating the deployment and commercialization of electrical vehicles. It may also be applicable in the consumer market to portable electronics and communication devices.

NextGen Battery Technologies, LLC (Arlington, VA)

Cathode materials with significantly higher specific capacities than what is currently available are critical to meeting the DOE's specific energy and energy density goals of 350 Wh/kg and 750 Wh/L at the cell-level, respectively. New materials capable of accommodating more than one lithium ion per transition metal can have a transformational impact on the energy density. Manganese-based cathode compositions, while low-cost and environmentally friendly, are also capable of multi-electron transfer. The proposed Phase I effort aims to

advance the state the art by demonstrating manganese-based cathode materials with ultrahigh capacity and cycling stability. The objective of the Phase I program is to develop and demonstrate at the pouch cell level, a new high energy density cathode material that is capable of meeting DOE's target of 350 Wh/kg cell-level energy density. Building on previous work, the Phase I feasibility effort will show that novel ionic substitutions in the crystal structure of manganese-based cathode materials can lead to a high capacity cathode material that is stable to long term cycling. Stabilized manganese-based cathode materials will be synthesized in gram quantities and characterized for composition, phase purity, particle size, surface area and thermal stability. Select batches with the desired particle characteristics will then be tested for electrochemical properties (e.g., specific capacity, rate capability and cycle life) in a coin cell format. A large batch of the most promising candidate material will be produced to demonstrate scalability, and the powder will be used to fabricate and test pouch cells with a capacity of at least 200 mAh. The market for lithium ion batteries is growing rapidly driven by the growth in electric vehicles and grid-based storage. The availability of low-cost and high performance battery materials, particularly cathode powder, is key to enabling battery manufacturing infrastructure in our country. The proposed program, when successfully implemented, will lead to rechargeable lithium-ion batteries with significantly higher energy density than what is currently possible today.

CAMX Power (Lexington, MA)

Successful commercialization and market adoption of electric drive vehicles (EVs) requires development of Li-ion storage technologies that can deliver >350Wh/kg, well above what can be achieved with current battery materials. Implementation of next generation cathode and anode materials is needed to further increase specific energy of Li-ion cells. However, without pre-lithiation, some of the most promising anode materials having high capacity (but low efficiency) cannot be used. CAMX Power would develop a safe and scalable pre-lithiation technology that will enable the use of very high capacity, long life, but low first cycle efficiency Si-based anodes to demonstrate lithium-ion cells capable of meeting specific energy, power, and life targets for EV batteries. It will leverage its CAM-7® cathode material and its work on Si-based anodes to demonstrate lithium-ion cells that utilize pre-lithiation and are able to meet the 350Wh/kg target. During the Phase I effort it will explore the impact of active materials on the extent of pre-lithiation achieved and test different pre-lithiation process parameters and environmental stability of pre-lithiated electrodes. It will also demonstrate that optimally pre-lithiated cells with a Si-based anode can meet the scaled energy targets. Moreover, process scalability will be demonstrated in 200+mAh pouch cells. Proposed technology will enable production of batteries with >350Wh/kg specific energy making it extremely attractive for implementation in both portable power and EV batteries. By increasing the energy density of EV batteries, and thus increasing the driving range of vehicles between recharges, it is anticipated that this technology will further lead to increased market adoption of electric vehicles.

CAMX Power (Lexington, MA)

For use in congested traffic, the start-stop vehicle technology (micro-hybrid) offers the promise of significant increases in fuel economy and reduction of pollutant emissions, without a large increase in the vehicle sales price. A key enabling component of the start-stop system is the battery. Present start-stop systems employ lead acid batteries because of their low initial cost and excellent low-temperature performance, but these batteries suffer from life limitations especially when subjected to repeated deep-cycling and high charge rates. Consequently, alternate battery systems with improved life characteristics are the key to enabling widespread adoption of start-stop vehicles. Li-ion technology is the leading candidate to replace lead-acid batteries in start-stop systems and several battery companies have announced Li-ion batteries for start- stop applications. However, most Li-ion battery systems offered today suffer from one or more disadvantages such as poor low-temperature performance, poor high-rate charge acceptance, or high cost relative to lead acid batteries. This is at least in part because the materials in these batteries are not optimized for the specific requirements of start-stop applications. CAMX Power is developing Li-ion technology for start-stop applications that overcomes the limitations of the current Li-ion systems by tailoring its proprietary CAM-7 cathode material for use opposite lithium titanate anode (LTO) anode in pouch cells that provide excellent cold-cranking capability, elevated-temperature stability, cycle life and safety for 12V start-stop batteries. CAMX Power has already shown that CAM-7 cathode/LTO anode pouch cell technology provides excellent (-30ºC) cold cranking capability and

elevated-temperature stability (without pouch cell gassing/swelling). In the proposed program, CAMX will optimize the CAM-7 material for the start-stop battery application, and will develop a scheduled maintenance procedure for CAM-7/LTO start-stop vehicle batteries that further extends performance and life. The CAMX POWER start-stop battery technology will facilitate widespread commercialization of start- stop micro-HEVs by enhancing the available energy, dynamic charge acceptance, and life of Li-ion batteries used in micro-HEVs. Rapid, widespread adoption of affordable micro-HEVs in traffic- congested areas of the country can yield benefits including reduced adverse health impacts from pollution in urban and other high traffic areas, and reduced economic impacts of fluctuations in global petroleum supply and price.

Saratoga Energy Research Partners, LLC (Berkeley, CA)

Saratoga Energy, a start-up company located in Berkeley, California, is developing a breakthrough electrolysis process to manufacture low-cost carbon nanotubes (CNTs) from carbon dioxide. CNTs provide an exceptional array of properties that enable the fabrication low-cost, high-energy lithium-ion batteries thus addressing the driving range limitations of electric vehicles. The global market size for CNTs was estimated to be $2.26 billion in 2015 making this an attractive opportunity. In the work conducted thus far, Saratoga Energy has established that its synthesis process could potentially be 90 times less energy intensive than the state-of-the-art (CCVD) and it has the potential to manufacture CNTs for under $5/kg - 100X cheaper than the current market price for CNTs. Lithium-ion batteries using Saratoga Energy CNTs have up to 20% higher volumetric and specific energy which translates to extended driving range of electric vehicles, or smaller, less expensive battery packs. Thus, upon the success of the project, it will provide two essential contributions fully aligned with the mission of the DOE Vehicle Technologies Office: reducing the cost of electric vehicles and dramatically improving driving range. In Phase I of this SBIR project, two tasks will be addressed. The first objective is to produce a masterbatch of CNT material and optimize its dispersion properties. The second objective is to fabricate high areal capacity anodes with the aid of the companies CNTs and demonstrate high performance on 250 mAh lithium-ion full cells paired with NMC cathodes. In Phase II, the project will attempt demonstrating the feasibility of the synthesis process at a small pilot scale, paving the way for further customer sampling and qualification, as well as providing necessary process data for a semi-works plant design. In parallel, the long-term cycling stability, cycling efficiency, and abuse resistance of lithium-ion batteries (constructed with Saratoga Energy's CNTs will be demonstrated on larger 2 Ah cells. The societal and public benefits directly derived from the features of Saratoga Energy CNTs – lower cost, improved energy density, and rate capability will contribute to greater customer acceptance of electric vehicles - helping the deployment of such technologies. As an added benefit, the company's CNTs are made from carbon dioxide, and if produced from renewable electricity, would have a negligible carbon footprint.

Hazen Research, Inc. (Golden, CO)

Development of superior Li-ion batteries (LIBs) is a critical part of the DOE mission to improve the economic, social, and environmental sustainability of electric vehicles (EV). DOE seeks to reduce the cost of the EV batteries from the current more than $250/kWh to less than $125/kWh by 2022. To achieve this goal, the materials and manufacturing costs of the battery components must be reduced significantly. This is especially true for the cathode materials and their manufacturing methods, which account for approximately 30% of the total cost of the state-of-the-art LIB. A large percentage of the total cost is due to the high cost of the components of the cathode materials and their complex manufacturing methods. Layered Ni-rich oxides of the type $Li(Ni_{1-x-y}Mn_xCo_y)O_2$ with Ni greater than 0.6 (Ni-rich NMC) have recently gained prominence because of their high capacities (200 to 225 mAh/g), high-voltage cyclability (2.0 to 4.5 V), and low cost. Significantly improved performance of hierarchically structured (compositionally gradient) Ni-rich NMC (Ni equals 0.4) cathode powders exhibiting local elemental segregation have been reported through spray pyrolysis. It is believed that both the chemistry (all-nitrate precursors) and the method (horizontal spray pyrolysis) can be further improved and developed into a scalable manufacturing method for the new generation of low-cost, high-capacity, high-voltage Ni-rich NMC cathode materials, such as $Li(Ni_{1-x-y}Mn_xCo_y)O_2$ (Ni greater than 0.6). These cathode materials will contain the desired compositional gradient and surface chemistry that will enable superior long-term performance. Hazen Research, Inc., in collaboration with the National Renewable Energy Laboratory (NREL), will develop and demonstrate a high-throughput and scalable manufacturing

method for the production of Ni-rich NMC cathode materials of the type $Li(Ni_{1-x-y}Mn_xCo_y)O_2$ (Ni greater than 0.6) by combining a vertically fed spray pyrolysis with a fluidized-bed reaction in a single reactor. This approach will mitigate the possibility of agglomeration, and uniform Ni-rich NMC cathode particles can be produced in a single reactor, making it a continuous production process. The $Li(Ni_{1-x-y}Mn_xCo_y)O_2$ (Ni greater than 0.6) particles having a Ni-rich core, but a Mn-rich surface, will be produced through rationally developed precursors for spray pyrolysis. The proposed single solution precursors will use Li, Ni, Mn, and Co starting materials with similar decomposition temperatures (nitrates) along with minor components of Ni and Mn materials with increasing decomposition temperatures (carboxylates and fluorinated carboxylates) maintaining the overall stoichiometry. This novel inorganic–metalorganic composite precursor is expected to form particles with the targeted Ni-poor and Mn-rich surfaces upon spray pyrolysis. Amorphous powders formed during spray pyrolysis can be reacted further and crystallized to uniform particles with increased tap density through fluidized-bed reactor processing. The approach, combining spray pyrolysis and fluidized-bed reaction in a single reactor, using an inorganic–organic precursor, is novel and is expected to lead to a low-cost manufacturing method for the production of these next-generation cathode materials. Along with its high capacity, the Ni-rich NMC cathode particles of $Li(Ni_{1-x-y}Mn_xCo_y)O_2$ (Ni greater than 0.6) produced by this combined method are expected to retain the compositional gradient favorable for the high voltage (2.0 to 4.5 V) and stable cycling performance. During this Phase 1 effort, the Hazen–NREL team will perform the following tasks: develop inorganic–metalorganic precursors for the spray pyrolysis to produce compositionally gradient Ni-rich NMC, $Li(Ni_{1-x-y}Mn_xCo_y)O_2$ (Ni greater than 0.6) cathode powders; design, build, and demonstrate a combined spray pyrolysis and fluidized-bed reactor for the manufacturing of Ni-rich NMC cathode powders with capacity more than 200 mAh/g and cycling between 2.0 and 4.5 V; validate greater than 200 mAh full cells (with more than 95% capacity retention over 250 cycles) using the cathode powders produced under the recommended USABC testing protocols. The EV market is estimated to be $12.8 billion in 2017, with an annual growth close to 60% from 2008–2017; the North American portion of the market alone is expected to reach $5.8 billion in revenue. Through an improved and scalable manufacturing of the low-cost high-performance Ni-rich NMC cathode powders, our approach will directly influence this market and significantly reduce the cost of state-of-the-art EV batteries. The demand for layered $LiMO_2$ (M=Co/Mn/Ni/Al) type cathode powders was approximately 75,000 t in 2014 and is projected to be approximately 225,000 t in 2025, representing an approximate 200% increase in demand in less than 10 years. The technology developed under this proposal is directly applicable to manufacturing of materials with a huge market demand. The project will further advance EV battery technology and assist in accomplishing the following: improve the competitive position of United States industry in the field of advanced materials and manufacturing to create jobs; enhance energy security by reducing dependence on foreign oil; save money by cutting fuel costs for American families and businesses; and protect health, environment, and safety by mitigating the effect of energy production on climate change.

II. Advanced Materials R&D

II.A Next-gen Lithium-ion: Advanced Electrodes R&D

II.A.1 Higher Energy Density *via* Inactive Components and Processing Conditions (LBNL)

Vincent Battaglia, Principal Investigator
Lawrence Berkeley National Laboratory
1 Cyclotron Road
Berkeley, CA 94720
Phone: 510-486-7172
E-mail: vsbattaglia@lbl.gov

Peter Faguy, Technology Manager
U.S. Department of Energy
Phone: 202-586-1022
E-mail: Peter.Faguy@ee.doe.gov

Start Date: October 1, 2015 End Date: September 30, 2018
Total Project Cost: $3,600,000 DOE share: $3,600,000 Non-DOE share: $0

Project Introduction

The vast majority of automobiles purchased in the US use internal combustion engines. This is because the alternative, renewable option, the plug-in electric vehicle (PEV), is considered to be too expensive and lacks the accustomed range one gets from filling a vehicle with a petroleum-based fuel. It is generally believed that if a battery could be produced with higher energy density, electric vehicles could meet a 300-mile range and approach a cost payback period of 5 years, making them much more attractive to the average consumer. Many researchers are attempting to increase energy density by extracting more capacity from today's Li-ion battery chemistries or developing new anode and cathode materials altogether. The goal of this project is to increase the energy density by reducing the fraction of inactive components by determining how to produce thicker electrodes.

As it turns out this is not as simple as increasing the gap in the slot-die coater. Thicker electrodes tend to delaminate more easily, especially during the slitting process. Thicker electrodes also require more time to dry which changes the balance of the physics during drying. More drying time allows more time for the denser active materials to settle through the polymer rich slurry resulting in a non-uniform distribution of components. Thicker electrodes also experience greater hoop stress on the outer surface during winding. It is possible that these phenomena can be effectively addressed by changing the molecular weight of the binder and the morphology of the conductive carbon additive. This project seeks to investigate this approach using tools at our disposal at the Lawrence Berkeley National Laboratory.

Objectives

By investigating different binder sources, slurry viscosities, binder molecular weights, binder fractions, conductive additive morphologies, calendering temperatures, and drying rates, we hope to identify the physics that dictates the conditions for a smooth laminate that adheres well to the current collector has a high loading and is windable to a ½ cm mandrel. A basic understanding of the interplay of these parameters should help electrode manufacturers to specify the properties required of the individual components and for the suppliers of those components to develop the next generation materials sooner.

Approach

Over the last decade our group has developed the techniques and skills necessary to fabricate high quality electrodes with small quantities of materials: by small, we mean as little as 10 grams of active material. These electrodes, when cycled in 12 cm^2 pouch cells or 1.6 cm^2 coin cells perform as well as laminates produced on pilot and large production coaters with regard to power density and cycleability. This allows us to do a multitude of experiments in a short amount of time with minimal effort and waste. Two years ago we established a means of cross sectioning electrodes and performing EDS measurements to establish the average composition as one moves from the current collector up to the surface. We have established excellent relationships with Tier 1 battery suppliers that are willing to send us their highest-grade materials and are also willing to send us experimental material and discuss with us some work they have performed in the area.

This combination of resources allows us to produce non-ambiguous results. Thus, through a combination of investigating a host of processing conditions, materials, using relevant diagnostic techniques, we expect to determine the properties of electrodes required for high functionality and to be able to relate those properties to processing conditions and individual materials' characteristics.

Results

What follows is a compilation of results for fiscal year 2017 in roughly chronological order. One of our earliest investigations was the impact of calendering temperature on electrode workability. A single laminate of NCM of approximately 4 mAh/cm^2 was fabricated and allowed to dry by natural convection in the glovebox. Once dry, the calendering machine was turned on and the temperature of the rollers adjusted and allowed to come to equilibrium at several different temperatures (27, 50, 75, 100, and 125ºC). A section of the laminate was calendered to 30% porosity at each of the different temperatures. An SEM was taken of each of the compressed electrodes. The SEM revealed that for all of the electrodes, the secondary particles of NCM were flattened and, for most particles, cracked. An example is provided in Figure II-1 of the laminate calendered at 100ºC.

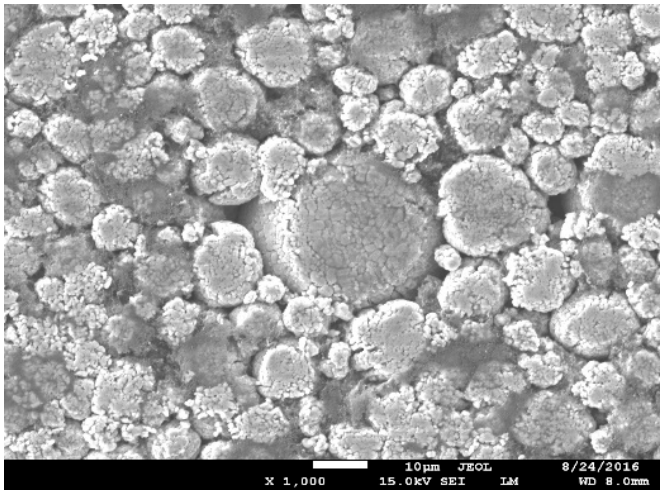

Figure II-1. SEM of surface of a laminate calendered at 100ºC to 30% porosity. Notice flattened and cracked particles.

Once the electrodes were calendered, they were assembled in coin cells for electrochemical testing. The electrodes were put through a rate performance test and long-term cycling. The rate tests revealed that all of the laminates performed relatively the same (Figure II-2), indicating that the calendering temperature had little impact on power performance. Once the rate performance test was completed, the cells were put on full charge and discharge cycle tests at C/3. As it turned out, the electrodes calendered at 100ºC cycled the best (Figure II-3). At 350 cycles, these electrodes only displayed a 12.5% capacity fade. The others were very near to or greater than 20% capacity fade, which is considered end-of-life. These results still need to be confirmed with additional cell testing.

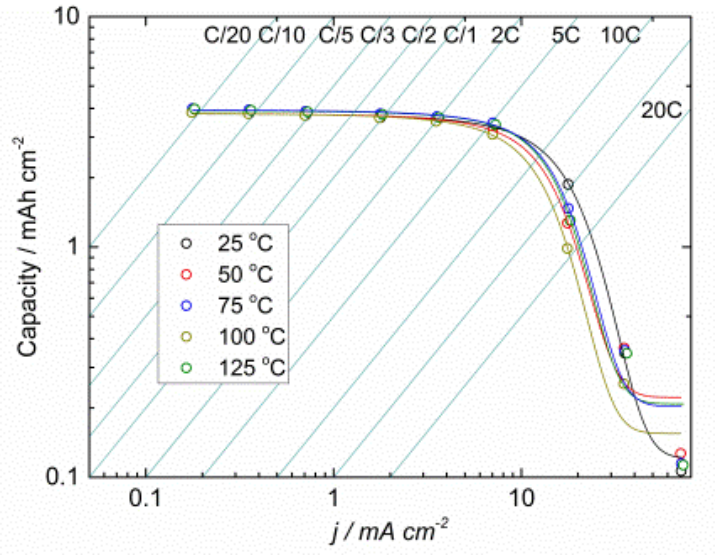

Figure II-2. Rate performance of a laminate calendered at different temperatures.

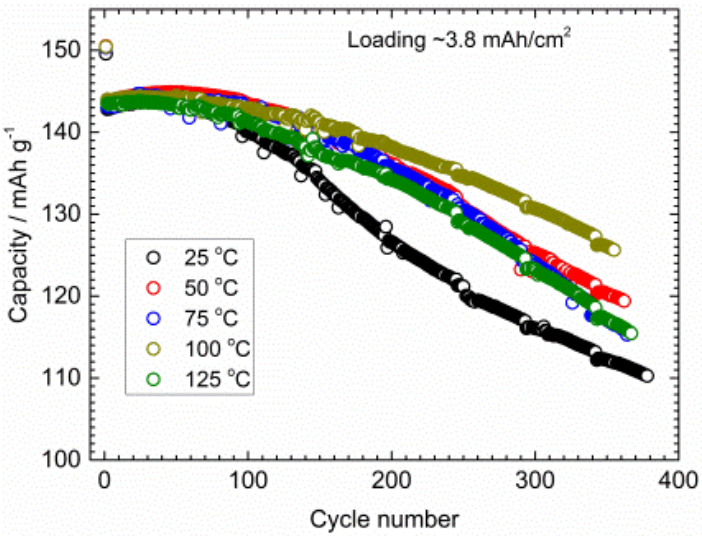

Figure II-3. Cycling performance of laminates in coin cells calendered at different temperatures.

Figure II-4 is a plot of cell resistance of the cathode *versus* depth of discharge for three cells with reference electrodes. The data shows that the area specific resistance drops with electrode thickness. If the resistance is normalized for cathode particle area, the order of resistance reverses but are more closely bunched together. This strongly suggests that the resistance of the electrodes is dominated by the charge transfer resistance of the active material. We intend to use similar cells to quantify cell failure modes of cycled, thick electrodes.

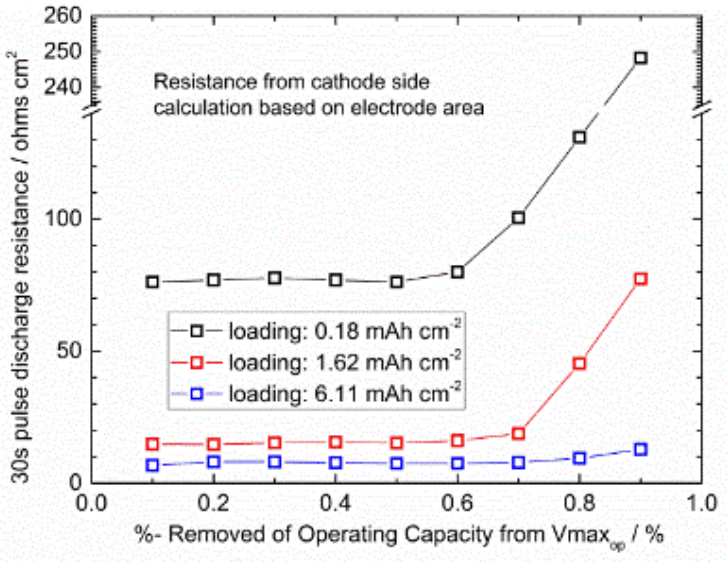

Figure II-4. Resistance for three loadings.

As described in one of our first reports in 2016 on the fabrication of thick electrodes, if we follow our typical procedures for making thick electrodes as we do low- and mid-loading electrodes, which includes drying in a glovebox *via* natural convection, a film of carbon and binder forms on the surface of the electrode. We investigated the impact this film has on cell performance.

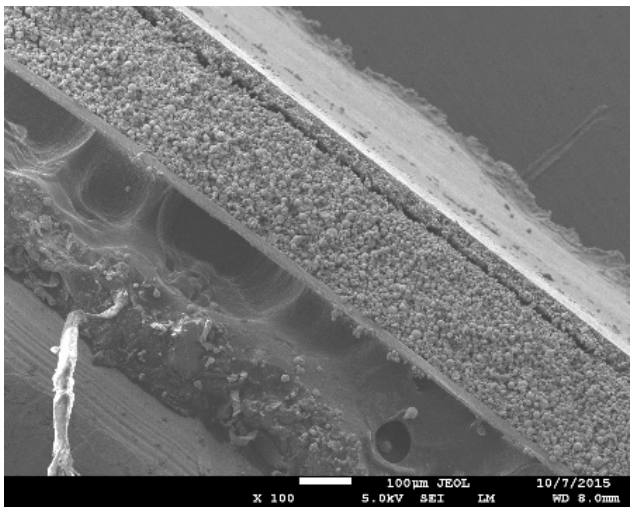

Figure II-5. Cross section of a dry electrode. Note layer on top of the electrode that appears to slightly detach.

Figure II-5 shows an SEM of a cross sectioned electrode made using our typical electrode fabrication procedures. A film can clearly be seen on the electrode surface. EDX indicates that this film consists almost entirely of carbon black and PVDF binder. This laminate was tested in a coin cell in three ways: 1) as is, 2) with the film removed from half of the surface, and 3) with the entire film removed. A fourth electrode of

similar loading was also produced using the same electrode formulation but modifying the processing conditions to prevent film formation. Figure II-6 shows the 30-second pulse discharge resistance for the four different cells *versus* depth of discharge. The electrode with the surface film shows twice as much resistance as the electrode where the film was removed. The electrode with half of the film removed, shows a resistance that is halfway between the two. The electrode prepared to have no surface film to begin with has nearly as low a resistance as the cell with the film removed. It is possible that this film consists of excess binder and carbon black that is not needed to make a high power electrode. We shall attempt to measure the fraction of carbon black and polymer in the surface film and fabricate a laminate without this excess. It will be interesting to see if electrodes can be produced that perform as well without the excess and that this might prove to be a method for determining the minimum amount of binder and conductive carbon one requires for producing a think electrode with high power performance.

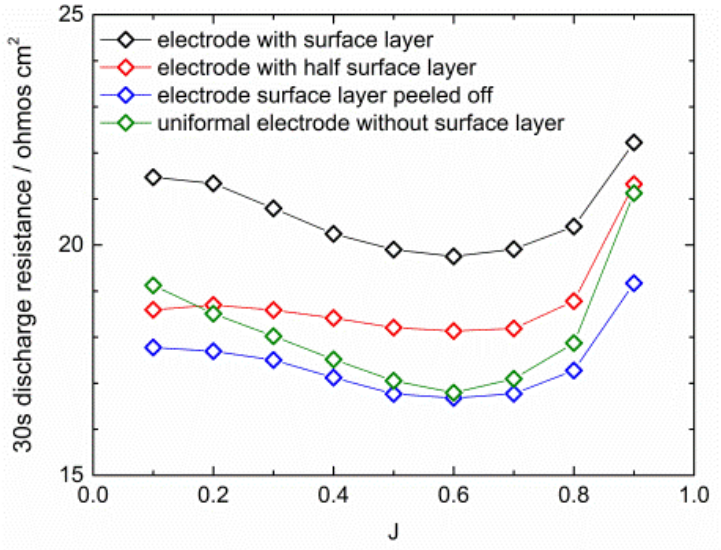

Figure II-6. 30-sec resistance of four cells: with the surface film, with half the surface film, surface film removed, no film to start with.

To date, we have been investigating changes to electrode homogeneity and performance as a result of changes to the inactive components and to the processing conditions. This includes changes to the binder molecular weight, the slurry viscosity, the addition of carbon nanotubes, and impacts of calendaring at different temperatures. Because binder molecular weight appears to have the greatest impact, we dove deeper into the effect of this parameter by assessing five binders of different molecular weights, see Table II-1.

Table II-1: Molecular weights for five commercial binders.

PVDF Commercial Name	KF1100	Kynar 761	HSV500	HSV800	HSV900
Molecular Weight	280 k	400 k	>400 k	<1 M	> 1 M

With our experience over the past few years in fabricating thick laminates, it is clear that the viscosity of the laminate is critical to its final homogeneity, especially when allowed to dry *via* natural convection in a glovebox. As the molecular weight of the binder goes up, the viscosity of the laminate goes up. In order to cast electrodes through a doctor blade, more NMP is required of slurries consisting of higher molecular binders. Once the laminates are cast and allowed to dry, they are cross sectioned and evaluated for their compositional uniformity using techniques developed here at LBNL. Other parts of the laminates are put through a bend test of rollers of ever reducing diameters while still other portions of the laminate are cut into circular electrodes

for coin cell testing. This assessment was not completed in time for this report; there are, however, some preliminary results.

As stated, when electrodes are allowed to dry overnight, the laminate with the lowest molecular weight binder ends up with a thin layer of binder and conductive carbon on the surface of the laminate. We believe that when provided a long time to dry (hours), the dense, large, active material particles can settle down to the current collector and the lighter, conductive agent and binder float to the top. A higher molecular weight binder appears to inhibit this separation.

We also find that laminates with higher molecular weight binders can be bent around smaller mandrels. Thus, higher molecular weight binders are beneficial to making thick electrodes that are to be wound to form cylindrical cells.

Since electrodes in industry are typically dried in approximately three minutes (this is based on a coating speed of 30 m/min and a drying length of *ca*. 100 m), we think it is imperative to perform studies on electrode uniformity and performance based on electrodes dried on the order of minutes, not hours. Efforts to dry laminates freshly cast in a glovebox are now underway. Preliminary results indicate that thick electrodes with low molecular weight binders dry uniformly, but those of high molecular weight display large crevices (mud cracking) where the current collector is clearly visible when looking down at the electrode. Unfortunately, thick laminates of low molecular weight binders do not possess the required properties to prevent delamination or adequate electrode bending. Mud cracking often occurs when a solvent leaves the pores of a slurry resulting in a layer of solvent around a portion of the solids with surface tension that pulls the solids together. If the solids cannot move easily, stress builds in the laminate until a defect occurs and a crack is generated that relieves the stress. These results suggest that an optimization of the binder content and molecular weight may result in both uniform laminates that bind well and do not crack under bend tests. We shall also assess electrodes made from a combination of binders of different molecular weights. Preliminary results in this area were very encouraging.

Conclusions

From the effort in 2017, we have been able to conclude the following.

Calendering

Electrodes of NCM that consist of 10 micron secondary particles and a binder and carbon content of less than 8% should not be calendered below 40% porosity, no matter the temperature, otherwise the risk of breaking the active material particles escalates. Calendered electrodes do not “bounce back” after the addition of electrolyte even after a week of soaking but do expand to their original thickness after cycling. Calendering improves the mechanical properties of the laminates but this may strictly be a geometric factor where thinner electrodes have less hoop stress than thicker electrodes when wound around the same mandrel diameter.

Natural convection drying

Slow drying allows more time for active material particles to settle and separate from the conductive carbon and polymer leading to a film of carbon and binder on the surface of the electrode. This film increases the areal resistance of the electrode when measured in a pouch cell. If the film is gently removed, the resistance of the electrode is decreased to that of an electrode that is prepared in such a way as to avoid forming a film. At this point, we know we can make thick electrodes without a film if we either increase the molecular weight of the binder or reduce the amount of solvent in the slurry – both result in a higher viscosity slurry. Thus, we don’t know if viscosity is solely responsible for the improvement or if chemistry plays a role. Thick electrodes with high molecular weight binder can be wrapped around a smaller mandrel than those with low molecular weight binder. Thick electrodes with high molecular weight binder have a more uniform composition and adhere more strongly to the current collector than electrodes with low molecular weight binder.

Fast drying

*W*hen attempting to fabricate thick electrodes at today's industrial rates (*ca*. 3 minutes), we find that electrodes with low-molecular weight binder dry more evenly than those with high molecular weight binder. Those with high-molecular weight binder display "mud cracking." This phenomena can be attenuated if the drying temperature is sufficiently lowered to extend the time to drying by a factor of three (this would effectively reduce production rates by a factor of three, hence, increasing cost.)

These findings suggest that to produce laminates at a rate of 30 m/min may require a binder of a molecular weight between 300,000 and 1,000,000. Our goal for the rest of the project continues to follow the original proposal trajectory of investigating methods to fabricate thick electrodes at drying rates commensurate with today's manufacturing rates.

Key Publications

1. Manuscript on the effect of binder content on electrode fabrication in preparation.

2. "Nature of the Impedance at Low States of Charge for High-Capacity, Lithium and Manganese-Rich Cathode Material Batteries and Energy Storage," Wenfeng Mao, Guo Ai, Yiling Dai, Yanbao Fu, Xingyun Song, Herman Lopez, and Vincent Battaglia, *J. Electrochem. Soc*. **163**(14): A3091-A3098, 2016

3. "Improving the over-all performance of Li-S batteries *via* electrolyte optimization with consideration of loading condition," Guo Ai, Zhihui Wang, Yiling Dai, Wenfeng Mao, Hui Zhao, Yanbao Fu, Yunfei En, Vincent Battaglia, Gao Liu, *Electrochimica Acta*, Volume **218**, 10, Pages 1–7, 2016

II.A.2 Electrode Architecture-Assembly of Battery Materials and Electrodes (Hydro-Quebec)

Karim Zaghib, Principal Investigator
Hydro-Québec (IREQ)
1806 Lionel Boulet
Varennes, QC J4X 1S1
Phone: 450-652-8019
E-mail: Zaghib.Karim@ireq.ca

Tien Duong, Technology Manager
U.S. Department of Energy
Phone: 202-586-7836
E-mail: Tien.Duong@ee.doe.gov

Start Date: October 1, 2012 End Date: December 31, 2017
Total Project Cost: $340,666 DOE share: $170,333 Non-DOE share: $170,333

Project Introduction

The target of the DOE Program is to identify the next generation of high-energy batteries. Achieving this target will require materials of higher capacity and improved coulombic efficiency or cells with higher voltage. High-capacity anode materials such as Si or Sn alloys have the potential to fulfill the energy density requirements for EV/PHEV applications. However, large volume expansion during the lithiation process of these materials usually leads to fast capacity fade that hinders its practical applications. Real-time SEM observations during charge/discharge of Si-anodes demonstrated that decreasing the particle size to nanometer scale is an effective means of accommodating the volume change, and thus delaying its degradation.

HQ proposed a strategy to design the architecture of the Si-anode material that tolerates the volumetric expansion and provides acceptable cycle life with low capacity fade. The particle size, binder type and electrode composition are the main parameters that define the formulation of the Si-anode. The porosity of the electrode has a direct impact on the performance, and therefore was optimized by investigating various mixing methods.

Objectives

The goal of this project is to develop an electrode architecture based on nano-Si powders. To achieve the objective, this project investigates the structure of nano-Si powders that provide acceptable volume change and long cycle life, while still maintaining the high capacity performance of Si. In our previous work, we successfully produced low-cost metallurgical nano-Si powders that yielded nano-Si/C composites which showed better processability during mixing and coating. However, designing full cells with high energy density and long cycle life is still a big challenge. Anodes with high loading are a prerequisite for high energy density. A long cycle life of > 900 cycles with low loading electrodes was achieved, but it was very difficult to achieve >100 cycles with the appropriate loading level.

The project scope will include the control of the particle size distribution of the Si nano-powder, crystallinity, Si composition and surface chemistry of the nano-particles. At this stage of the project, a significant effort will be allocated to failure mode analysis of nano-Si anodes before and after cycling. We expect that this analysis will help to understand the failure modes of the anode and help guide the effort to improve the particle morphology and electrode architecture.

Approach

1. Explore a variety of synthesis methods to produce low-cost nano-Si materials with controlled purity and particle morphology.
2. Develop an appropriate silicon-anode architecture that tolerates volumetric expansion and provides an acceptable cycle life with low capacity fade.
3. Identify a binder and electrode composition by investigating parameters that define the electrode structure such as porosity, loading and electrode density. The optimized Si-anode will be matched with a high-voltage NMC cathode to fabricate large format Li-ion cells.
4. Use *in-situ* techniques such as SEM and impedance spectroscopy to monitor the particle and electrode environment changes during cycling.
5. Achieve cost reduction by moving from the more costly Si (>$50/kg) to metallurgical Si which is projected to be $3~$5/kg.

Results

1. 1.5Ah Full Cell Test Result

Li-ion pouch laminated cells based on NMC//nano-Si/C composite with a capacity of 1.5Ah were assembled (Figure II-7a). The loadings are 2.2 and 10.3 mg/cm^2, respectively, for the anode and cathode. The anode/cathode ratio was 1.15 based on the capacities of the half cells with these cathode and anode materials. The electrochemical performance (formation capacity, rate capability and cycle stability) were evaluated. The capacity of the cell at 0.2C rate revealed a discharge capacity around 1400 mAh between 2.75 V and 4.4 V, which is 95% of the designed cell capacity (Figure II-7b).

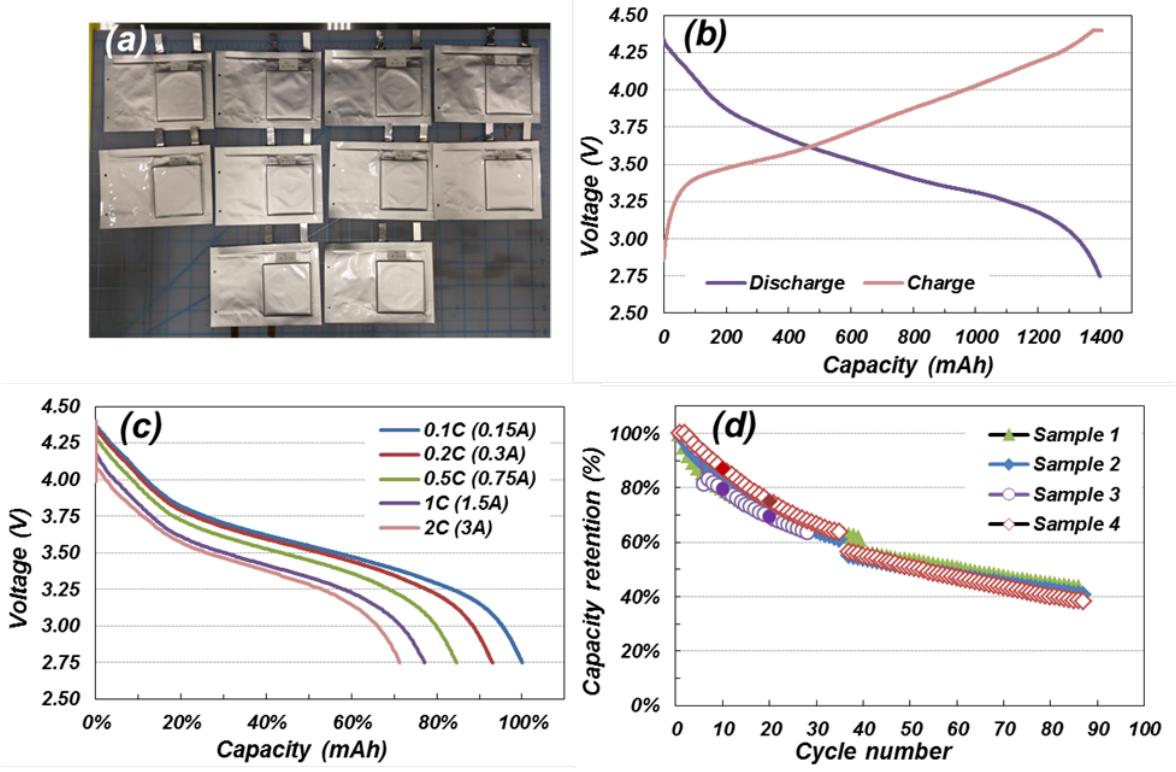

Figure II-7. Full cell performance of 1.5 Ah pouch-type cell (a) assembled cell (b) voltage profile during charge-discharge between 2.75 V and 4.4 V at 0.2C rate (c) rate capability at different current rates and (d) cycle life at room temperature.

The rate capability of the cells was evaluated at different currents (0.1-2C). At 2C rate, the cell delivered 70% of the capacity obtained at 0.1C (Figure II-7c). The voltage profiles showed similar behavior at the different rates, and the cells have low IR drop. However, the cycling stability of these cells shows high capacity fade (Figure II-7d). The capacity decreases continuously with cycles, and the capacity retention was only 40% during the experiment lasting 90 cycles. We attribute this capacity fade to the instability of the anode material. The loss of contact between Si anode particles and the mechanical disintegration of the anode film are the main cause of this capacity fade.

2. nano-SiO_x

As part of an effort to mitigate the volume expansion of Si particles during charge/discharge, Hydro-Quebec synthesized SiO_x with a mixed morphology of nano-fibers and nano-particles. Figure II-8 shows that the material is composed of randomly mixed nano-fibers with a diameter 10-100 nm and nano-particles < 100 nm. The material is synthesized in the one-step plasma process without post treatment. The process parameters, such as precursor feeding rate, gas flow rate, and carrier gas concentration, were controlled to obtain the morphology with different fiber-to-particle ratio. Figure II-8 shows the results obtained by using 2 different process conditions. For condition A, a mixture of Ar and He was used as a plasma sheath gas, while a mixture of Ar and H_2 was used for condition B.

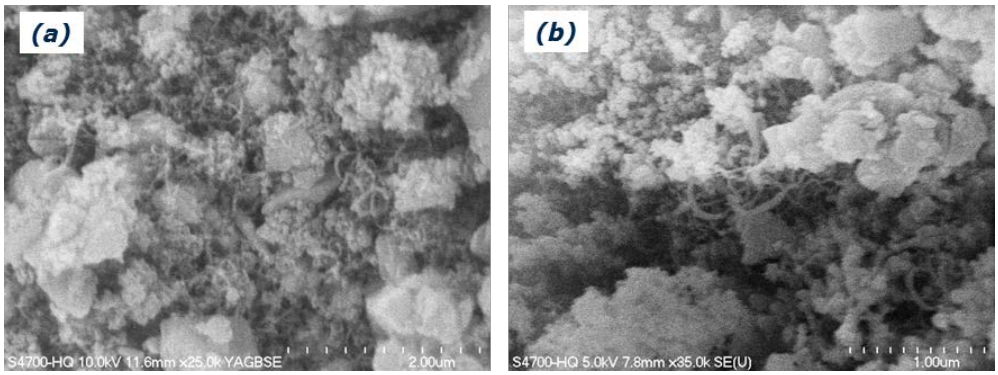

Figure II-8. SEM images of nano-SiO_x fibers (a) condition A and (b) condition B.

The electrochemical performance was tested with a coin-type half-cell containing 1M$LiPF_6$-EC-DEC-10%FEC, and the result is shown in Figure II-9. The loading of active material (SiO_x) was around 0.5 mg/cm^2 and the electrode density was 0.7g/cc. The composition of nano-SiO_x was 50% and a water-based binder was used in the electrode. The capacity was about 1050 mAh/g for condition A and 1150 mAh/g for condition B at C/24. After the first charging reaction, where the irreversible capacity is obtained due to the conversion reaction of SiO_x with Li^+, the coulombic efficiency was > 95% in the following cycles. The capacity retention was quite stable without capacity loss after 90 cycles at C/6 rate (Figure II-9b).

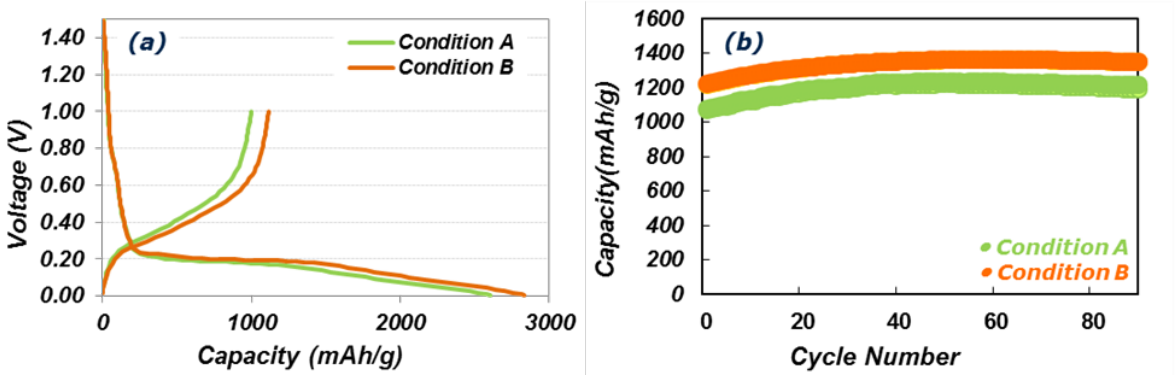

Figure II-9. Electrochemical performance of (a) 1st charge/discharge voltage profile with C/24 rate between 1.0 V and 0.005 V and (b) cycle life with C/6 rate at room temperature.

The results show that SiO_x is a promising material in high-capacity anodes. However, further effort is needed to improve the morphology and enhance the coulombic efficiency in the first cycle.

3. Electrospray Process

During this project year, Hydro-Quebec focused on improving the electrochemical performance with different synthesis routes to produce nano-Si/C composites by exploring the electrospray process. In our previous efforts, the capacity and cyclability was improved with heat treatment of the electrode with polyimide binder. Based on this result, we synthesized nano-Si/C composite secondary powders with polyimide-binder solutions.

The syringe was charged with slurry at a high electric potential of 20kV, and the distance from the ground electrode plate was 10 cm. The powder samples are obtained with a water bath filled to 5 mm with deionized water, and the injection speed was 50 µl/min. The samples are filtered and heat treated at 600°C for 3 hours in a N_2 flow furnace. As it can be seen in Figure II-10a, the powder is composed of two different shapes; small-size flakes (< 100µm) and large-size spheres (< 400µm). The electrochemical performance was tested with a coin type half-cell, and the results are shown in Figure II-10b. The anode loading was approximately 1.05 mg/cm^2, and the electrode density was about 1.0g/cc. A water-base acrylic resin was used as a binder without any problem with gas generation. The capacity was about 3500 mAh/g at C/24, and the 1st cycle efficiency was 76%.

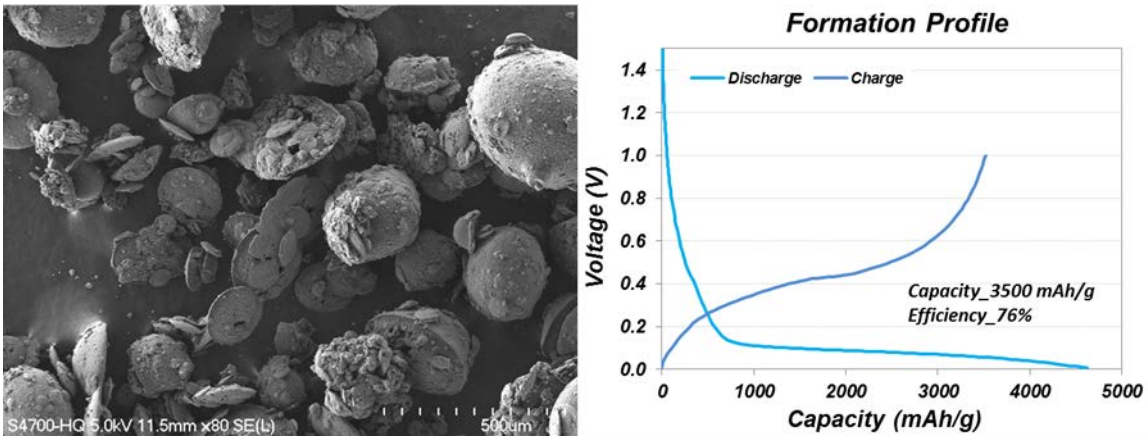

Figure II-10. (a) SEM image of nano-Si/C composite made by electrospray process and (b) 1st cycle discharge/charge voltage profile.

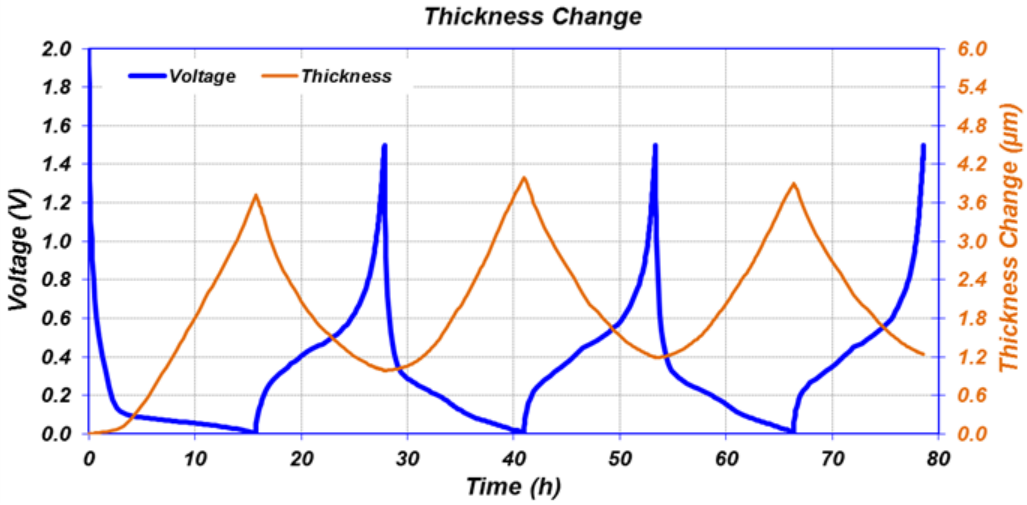

Figure II-11. Cell thickness monitoring during cycling with C/24 rate between 1.5 V and 0.005 V at room temperature.

The anode thickness change was monitored by an electrochemical dilatometer, see in Figure II-11. The thickness increases after SEI formation and reached 3.7 µm at the end of the 1st discharge. The thickness increase is equivalent to 12% of the fresh electrode. In the following charge step, the thickness decreases by about 2.7 µm, and the electrode is 1 µm thicker than that of the fresh electrode due to SEI formation during the first cycle. Further effort will focus on understanding the variation in thickness during cycling by modifying the binder and the electrolyte.

4. Optimization of Electrospray Process

In the previous electrospray trials, a composite of secondary micro-size nano-Si/C with polyimide binder solution was produced. Based on this result, we evaluated different stable nano-Si/C composites with various types of carbons to optimize the electrospray process.

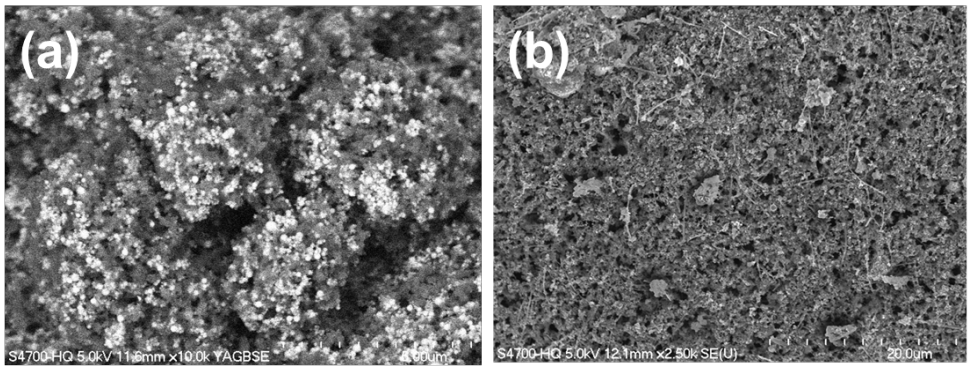

Figure II-12. SEM image of (a) version 1 nano-Si/C composite made by electrospray process and (b) version 2.

The powder was produced by the same procedure in a water bath. The composite version 1 is composed of nano-Si, acetylene black and polyimide binder. In composite version 2, carbon fibers are added in the formulation. Figure II-12a shows an SEM image of composite version 1; the powder is well mixed with carbon but looks less dense. On the other hand, in Figure II-12b with composite version 2, the structure of the composite with carbon fibers appears stronger and textured.

The electrochemical performance was tested with a coin type half-cell, and the results are shown in Figure II-13. The total loading of the anode was around 1mg/cm^2 (1 mAh/cm^2), and the cells were cycled at C/6 rate for charge and discharge. The composite version 2 that contains carbon fiber showed more stable

capacity than that with composite version 1 after more than 100 cycles. In addition, the coulombic efficiency of the cell containing composite version 2 was higher. After ~50 cycles, the cell with composite version 1 showed decreasing efficiency, whereas the efficiency of the cell with composite version 2 continued improving. This behavior is attributed to the presence of the carbon fiber network, which helps to maintain the electronic contact between particles in spite of the volume changes.

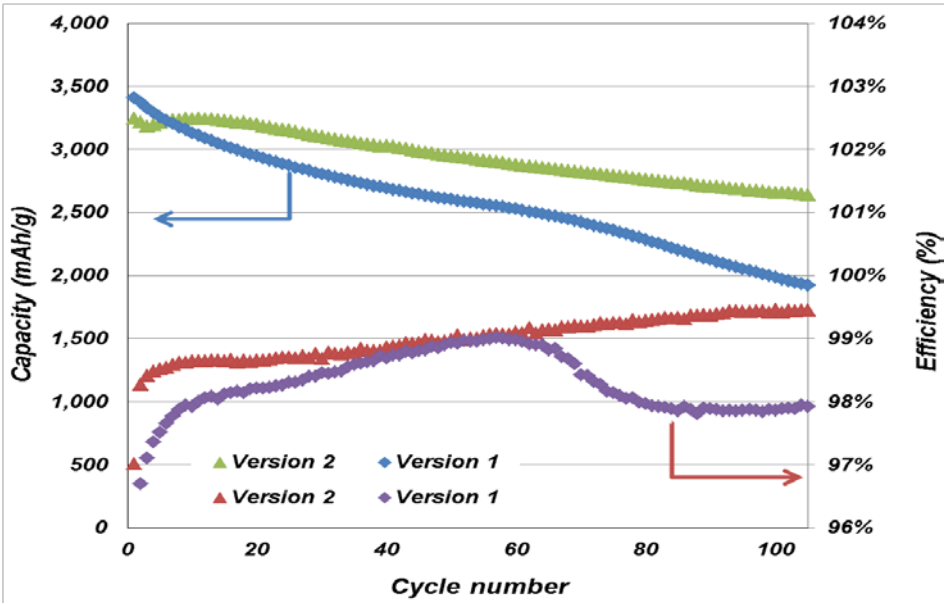

Figure II-13. Cell performance during cycling at C/6 rate between 1.5 V and 0.005 V at room temperature.

Conclusions

During this year, Hydro-Quebec synthesized nano-SiO_x fibers by a plasma process. This material has showed a stable cycle life, but effort is still needed to improve the 1st cycle coulombic efficiency. The electrospray method was explored to produce nano-Si/C composites with polyimide binder. With this method, we obtained mechanically stronger powder than with other binders, PVDF,CMC and Alginic acid. The carbon in the electrospray composition has an effect on performance of the final product. Adding VGCF carbon fiber showed a net improvement in the cycle life and coulombic efficiency by maintaining the electronic contact between particles in spite of the volume changes.

As deliverables of project year 2017, Hydro-Quebec delivered SBR/CMC binder materials and 1.5 m of anode electrode with water-based CMC/SBR binder in the 3rd Quarter, and 20 g nano-Si/C composite powders produced by the electrospray process in the 4th Quarter.

Key Publications

1. BMR 2017 1st Quarterly Report, January, 2017
2. BMR 2016 2nd Quarterly Report, April, 2017
3. BMR 2016 3rd Quarterly Report, July, 2017
4. BMR 2016 4th Quarterly Report, October, 2017

II.A.3 Design and Scalable Assembly of High-Density, Low-Tortuosity Electrodes (MIT)

Yet-Ming Chiang, Principal Investigator
Department of Materials Science and Engineering
School of Engineering
Massachusetts Institute of Technology
77 Massachusetts Avenue
Cambridge, MA 02139-4307
Phone: 617-253-6471
E-mail: ychiang@mit.edu

Tien Duong, Technology Manager
U.S. Department of Energy
Phone: 202-586-7836
E-mail: Tien.Duong@ee.doe.gov

Start Date: May 22, 2013 End Date: April 3, 2017
Total Project Cost: $1,075,344 DOE share: $1,075,344 Non-DOE share: $0

Project Introduction

The high cost ($/kWh) and low energy density of current automotive lithium-ion technology is in part due to the need for thin electrodes and associated high inactive materials content. If successful this project will enable use of electrodes based on known families of cathode and anode actives but with at least 3 times the areal capacity (mAh/cm2) of current technology while satisfying the duty cycles of vehicle applications. This will be accomplished via new electrode architectures fabricated by scalable methods with higher active materials density and reduced inactive content, and will in turn enable higher energy density and lower-cost EV cells and packs.

Objectives

The objective of this project is to develop scalable high density low-tortuosity electrode designs and fabrication processes enabling increased cell-level energy density compared to conventional Li-ion technology and characterize and optimize the electronic and ionic transport properties of controlled porosity and tortuosity cathodes as well as densely-sintered reference samples. Success is measured by the area capacity (mAh/cm^2) that is realized at defined C-rates or current densities.

Approach

Two techniques are used to fabricate thick, high density electrodes with low tortuosity porosity oriented normal to the electrode plane: 1) Directional freezing of aqueous suspensions; and 2) Magnetic alignment. Characterization includes measurement of single-phase material electronic and ionic transport using blocking and non-blocking electrodes with ac and dc techniques, electrokinetic measurements, and drive-cycle tests of electrodes using appropriate battery scaling factors for EVs.

Within ABMR, this project collaborates with Antoni P. Tomsia (LBNL) in fabrication of low-tortuosity, high-density electrodes by directional freeze-casting, and with Gao Liu (LBNL) in evaluating Si anodes. Outside of ABMR, the project collaborates with Randall Erb (Northeastern Univ.) on magnetic alignment fabrication methods for low tortuosity electrodes.

Results

This project was completed during the second quarter of FY 2017. The following two milestones were completed:

1. Go/No-Go Milestone: Fabricate and test half-cells and full lithium-ion cell in which both cathode and anode are prepared by magnetic alignment, and in which at least one electrode is prepared by non-sintering process. Go/No-Go Criteria: Measured area capacity of a half-cell is at least 10 mAh/cm^2 and of a full cell is at least 8 mAh/cm^2. (12/31/16). (Completed)

2. All milestones have already been completed. For this report, additional results are reported for preparation of low-tortuosity thick electrodes from other materials beyond what were previously demonstrated, using the non-sintering magnetic alignment method. (03/31/17). (Completed)

In the second quarter of FY 2017, additional results were reported for preparation of low-tortuosity thick electrodes from materials beyond $LiCoO_2$ (Umicore, average particle size 2–4 μm) and MCMB 6-28 (Osaka Gas, average particle size 6 μm), which were reported in the previous quarterly reports for this project. The goal is to investigate whether the non-sintering magnetic alignment method can be generally applied to various electrode materials.

Commercially available electrode materials were chosen for this study: $LiFePO_4$ (LFP, MTI Corporation, D50 ~3.5 μm), OMAC-carbon (Osaka Gas), $LiNi_{1/3}Mn_{1/3}Co_{1/3}O_2$ (NMC333, Toda, average particle size~10 μm), $LiNi_{0.8}Co_{0.15}Al_{0.05}O_2$ (NCA, Toda, average particle size 2-5 μm), and MCMB (MTI Corporation, D50 ~18 μm). These materials were mixed with acetylene black, polyvinyl alcohol, water, and a small amount of ferrofluid (~5 vol%) and sonicated using an ultrasonic probe to make the emulsion-based slurries, whose formulations are similar to those used for $LiCoO_2$ (Umicore) and MCMB 6-28 (Osaka Gas) reported in our previous quarter reports. The slurries were then dried in silicone molds on top of magnets to make the electrodes. After initial drying, the electrodes were rinsed thoroughly using kerosene and acetone and further dried at 100ºC under vacuum.

The electrodes were cross-sectioned and examined using scanning electron microscopy (Figure II-14). Figure II-14A and Figure II-14B show that vertically aligned pore channels are successfully introduced into LFP and OMAC-carbon electrodes. The result with NMC333 electrode was less satisfactory (Figure II-14C).

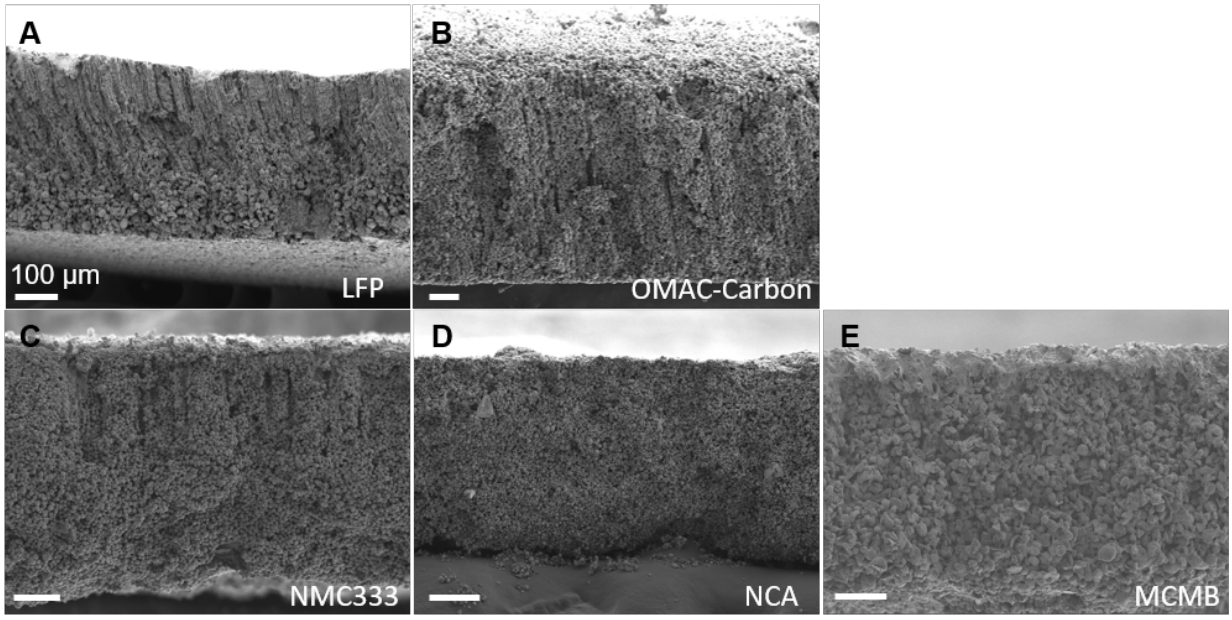

Figure II-14. Electrodes of different materials prepared by the non-sintering magnetic alignment method. A, LFP (MTI Corporation). B, OMAC-carbon (Osaka Gas). C, NMC333 (Toda). D, NCA (Toda). E, MCMB (MTI Corporation).

Conclusions

The results demonstrate that the non-sintering magnetic alignment method can indeed work with electrode materials beyond the previously tested $LiCoO_2$ (Umicore) and MCMB 6-28 (Osaka Gas). The result with NMC333 electrode was less satisfactory. Vertically aligned pore channels were observed but they did not completely span the thickness of the electrode. For NCA and MCMB (MTI) electrodes, vertically aligned pore channels were not observed. The specific reasons are not yet clear, but particle size and surface chemistry may play important roles; these factors may be further investigated.

II.A.4 Advanced Lithium Ion Battery Technology – High Voltage Electrolyte (Daikin America, Inc.)

Ron Hendershot, Principal Investigator
Daikin America, Inc.
2749 Highway 20 West
Decatur, AL 35601
Phone: 256-260-6302
E-mail: hendershot@daikin-america.com

Joseph Sunstrom, Principal Investigator
Daikin America, Inc.
2749 Highway 20 West
Decatur, AL 35601
Phone: 256-260-6314
E-mail: sunstrom@daikin-america.com

Alec Falzone, Principal Investigator
Daikin America, Inc.
2749 Highway 20 West
Decatur, AL 35601
Phone: 256-260-6342
E-mail: afalzone@daikin-america.com

Tien Duong, Technology Manager
U.S. Department of Energy
Phone: 202-586-7836
E-mail: Tien.Duong@ee.doe.gov

Start Date: October 1, 2016 End Date: December 31, 2019
Total Project Cost: $1,826,895 DOE share: $1,250,000 Non-DOE share: $576,895

Project Introduction

The use of electrolytes containing small fluorinated molecules to enable stable high voltage (> 4.3 V) battery operation is the focus of this project. Previously, Daikin has shown that it is possible to operate lithium ion batteries utilizing several different cathode chemistries up to 4.5 V. This is accomplished by reducing the gas generation originating from electrolyte decomposition at high voltage. The primary mechanism for this is not completely understood, but the hypothesis is that the fluorinated molecules form a film on the highly oxidizing cathode. It is known that battery cycle performance above 4.5 V drops significantly, however the source of the observed performance loss is not yet understood. The target for this project is to achieve 300 cycles above 80% capacity retention at 4.6 V. A better understanding of gas evolution, which happens above 4.3 V and the failure mode above 4.5 V, is sought in order to propose mitigation strategies which will facilitate better high voltage performance in lithium ion batteries.

The battery industry trend for cathode materials is toward reducing the overall cobalt content (i.e., higher nickel) for a variety of reasons. Some of which include: increasing cost, loss of supply, and human rights issues. The experiments proposed for this project will encompass a range of cathode materials with successfully higher nickel content. This will be performed in order to comprehend how fluorinated electrolyte interacts with various cathode surfaces. This is with the anticipation that the lithium ion battery industry will

move towards nickel-rich cathodes, which can operate at higher voltage in order to achieve more energy-dense batteries.

Objectives

This three-year project can be divided into three main milestone topics, each spanning one fiscal year: 1) understanding of gassing mechanisms and kinetics, 2) examining physical and chemical aspects of film formation, and 3) observation of chemical and structural evolution of electrode surfaces at various operating conditions. The FY 2017 budget period involves the analysis of electrolyte gassing mechanisms as a function of cathode chemistry, voltage, temperature and fluoroethylene carbonate (FEC) concentration. The Daikin formulations often contain at least two fluorinated compounds, one of which is FEC. It has been established in a previous Daikin project that while FEC appears to enhance cycling performance, it gasses at high voltage. Sampling of gas generated during cycling is to be accomplished by gas chromatography/mass spectrometry (GC/MS). It is hoped by identifying individual gases both qualitatively and quantitatively that a better knowledge of the factors which contribute to gas formation can be attained. We then aim to select mitigation strategies to avoid decomposition pathways due to gas generation.

Approach

The baseline of current best-practice fluorinated electrolyte was determined by reviewing already obtained data from high-voltage lithium ion batteries from a previously funded project (DOE EE0006437). In parallel, an up-to date literature and patent review has also been performed to explore other cutting edge developments in 2017. Three electrolytes were selected as standards for this project: 1.2 M $LiPF_6$ ethylene carbonate (EC)/ethyl methyl carbonate (EMC) 80:20 (v/v %), 1.2 M $LiPF_6$ EC/EMC/fluoroether (FE) 20:60:20 (v/v %) and 1.2 M $LiPF_6$ FEC/EMC/FE 20:60:20 (v/v %). These represent electrolytes with zero, one and two fluorinated solvents added, respectively. All electrolytes also contain propane sultone (PS) (1% w/w) as an additional anti-gassing additive. 200 mAh dry wound cells have been purchased as test vehicles. The cathode chemistries studied (with increasing mole fractions of nickel are: $LiCoO_2$ (LCO), $LiNi_xMn_yCo_zO_2$ (NMC xyz = 111, 532, 622) and $LiNi_{0.8}Co_{0.15}Al_{0.05}O_2$ (NCA) all paired with artificial graphite anodes. Analysis of the gases produced at high voltage (> 4.3 V) will be completed and compared to cells cycled at a baseline voltage of 4.2 V, which is the current battery industry standard. A post mortem analysis of the gas sampled cells will be conducted for qualitative and quantitative gas analysis. In addition, the cathodes and anodes will be removed for surface analysis to observe SEI film formation and changes in material properties. A mass balance approach to the cells will be used in order to propose performance limiting factors and strategies to overcome them.

Results

Setup of Experimental Tools, Review State of the Art and Establish Study Baselines – Milestone 1

Work in the first year (FY 2017) has been divided into two tasks which progress against the first four milestones: 1) establishing a baseline based on knowledge learned from first DOE funding opportunity and 2) initiating setup of instruments and samples for gas analysis.

Final cell test results from Argonne National Laboratory were received at the end of March. The cycle testing results are shown in Figure II-15 for three groups:

a. Group 1 hydrocarbon electrolyte cycled to 4.5 V, (black trace)

b. Group 2 fluorocarbon best practice electrolyte cycled to 4.5 V, (red trace)

c. Group 3 fluorocarbon best practice electrolyte cycled to 4.6 V, (blue trace)

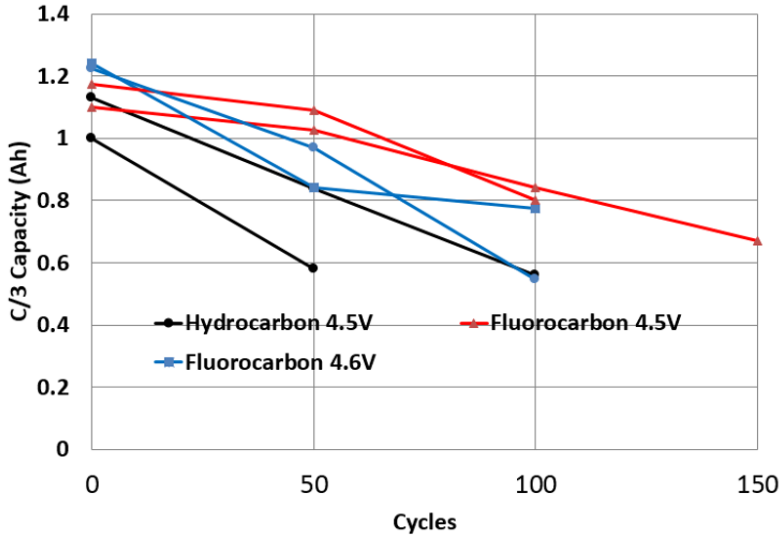

Figure II-15: Cycle life (C/3) discharge for a) Hydrocarbon electrolyte charged to 4.5 V (black), 2) fluorocarbon electrolyte charged to 4.5 V (red), and fluorocarbon electrolyte charged to 4.6 volt (blue)

The results confirm previous Daikin internals results which indicate that fluorocarbon electrolyte performs better than hydrocarbon up to 4.5 V but there is a performance decrease when the upper voltage is extended to 4.6 V. This result fixed the study voltages to 4.2 (both electrolytes work), 4.5 (only fluorinated electrolyte works) and 4.6 V (neither electrolyte works) as initially proposed.

Additional baseline experiments were performed in order to adjust experimental parameters to generate gas in a reasonable timeframe for analysis. Figure II-16 displays the volume change in pouches containing NMC111 charged cathodes with graphite anodes stored with electrolyte at 60°C. The targeted temperature settings were established at 35, 45 and 50°C.

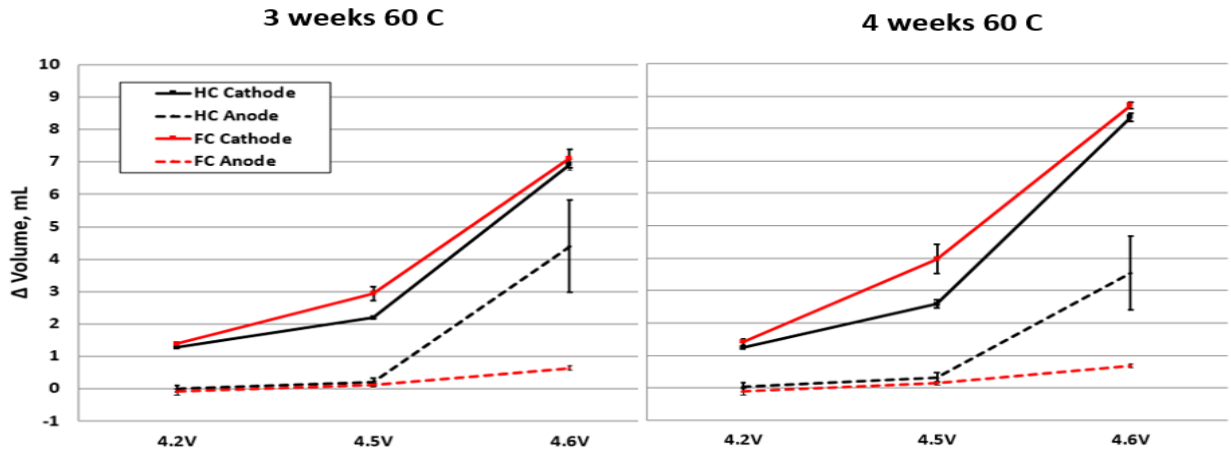

Figure II-16: Gas volume change at 3 weeks (left) and 4 weeks (right) for NMC111 cathodes with graphite anodes when exposed to electrolyte at 60°C

Gas Composition as a Function of Voltage and Cathode – Milestone 2

In order to determine the gas composition as a function of various operating conditions (FEC, voltage, cathode material, etc.), we constructed ninety (LCO, NMC622) 200 mAh cells for an extended open circuit voltage (OCV) test to be carried out at various temperatures for analysis. These cells underwent initial formation then were charged to constant voltage to the desired voltage (4.2, 4.5, and 4.6 V) and placed into ovens at 35, 45, and 55°C. Following this extended aging period with intermittent volume measurements, the cells were discharged and punctured with a gas tight syringe for headspace analysis.

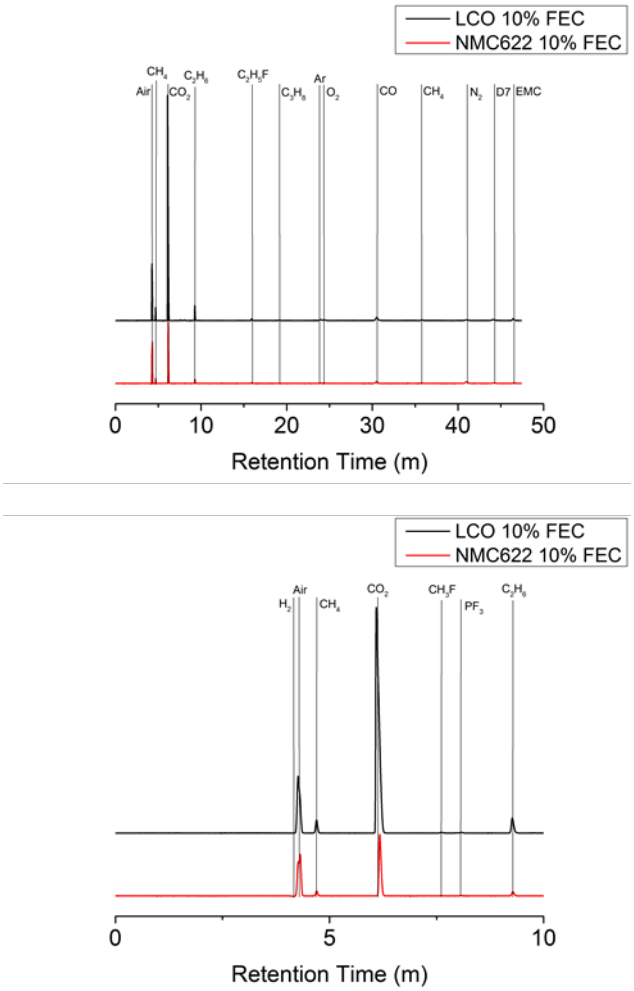

Figure II-17: TCD chromatogram overlays of 4.6 V LCO and NMC622 cells with 10% FEC concentration in the electrolyte. On the top is the full spectrum, whereas the bottom focuses on 0-10 minutes. H_2 is seen in the NMC622 cell and PF_3 in the LCO cell.

Gas analysis and the determination of components was performed using GC-MS/TCD (thermal conductivity) instrument. Figure II-17 depicts the full TCD chromatograms (left) and 0-10 minutes (right) of both LCO and NMC622 cells with 10% FEC. The peaks in the TCD chromatograms were confirmed through integration with mass spectrometric detection (MS). It was necessary to compare the retention times of detected species in different cells in order to confirm their assignment and reproducibility.

Table II-2 summarizes GC-MS/TCD qualitative results from a calendar (4.6 V, 55ºC) life test. The cells underwent formation (2 cycles), were charged to constant test voltage of 4.6 V, and then placed in a 55ºC oven. The cell volume and OCV were monitored over a period of 3-4 weeks.

Table II-2: Gas Composition of LCO and NMC622 Cells as a Function of FEC Concentration Determined by GC-MS/TCD

[FEC]	CH_4	C_2H_2	C_2H_4	C_2H_6	C_3H_6	C_4H_{10}	CH_3F	C_2H_5F	CO	CO_2	O_2	H_2	PF_3
LCO 10%	X		X	X	X	X	X	X	X	X	X		X
LCO 20%	X	X		X		X	X	X	X	X	X		
NMC622 10%	X		X	X			X	X	X	X	X	X	
NMC622 20%	X	X		X			X	X	X	X	X	X	

Two different concentrations of FEC (v/v %) were tested during the extended aging experiment. The LCO cathode cells with 10% FEC exhibited the largest amount of gas produced, in addition to the only battery evolving the larger hydrocarbon gases. In all batteries, CO_2 and CO are the largest components of the analyzed gas. Also present are quantifiable amounts of methane, ethane, and O_2. The additional gases (PF_3, etc.) are present in trace, but measureable quantities. Although the NMC 622 cells produce quantifiable amounts of H_2, we cannot rule out the presence in LCO cells due to detection limits (> 8.5 v/v %) while using helium as the carrier gas in a GC-MS/TCD instrumental setup.

Although the molar quantification of detected gases is ongoing, the integrated TCD intensities can be compared to determine the ratio of gas generation. Of the cells investigated to date, the cells with the highest nickel % (NMC622) generate larger amounts of both fluorinated gases (CH_3F and CH_5F), however did not generate flammable hydrocarbons such as butane, propane, and propene. Further investigation into the origin of higher hydrocarbons in LCO cells is underway.

The presence of PF_3 in the LCO cell at 4.6 V with 10% FEC was an unexpected development, and can be attributed to decomposition of the $LiPF_6$ salt. The mechanism for the formation of PF_3 in not currently understood.

Gassing Kinetics of FEC – Milestone 3

Cycle life testing with intermittent gas measurement experiments were performed on cells containing either LCO or NMC622 cathodes to understand the effect of FEC on battery cycling and gassing. The baseline electrolyte was 1.2 M $LiPF_6$ EC/EMC/FE (20:60:20) + 1% PS. A series of test electrolytes were made by replacing EC with FEC in 5% increments with the final end member electrolyte being 1.2 M $LiPF_6$ FEC/EMC/FE (20:60:20) + 1% PS. Figure II-18 depicts the discharge capacity versus cycle number of both NMC622 and LCO cells at 4.6 V and 4.2 V. As expected, discharge capacity at 4.2 V was retained throughout 200 cycles, with all cells ranging from 93-95% after cycling at 0.7C. In addition, there was no noticeable effect on the capacity of batteries with the addition of FEC for 4.2 V cycling (Figure II-18).

Addition of FEC into the electrolyte resulted in better cycle performance in both chemistries. However, LCO cells cycled at 4.6 V hit the 80% cutoff at < 50 cycles regardless of the FEC content of the electrolyte and ceased operation after 100 cycles (Figure II-18 top). However, the NMC622 cells when cycled at 4.6 V showed remarkable improvement with added FEC. Only three electrolytes (0, 5, 15% FEC) are shown for clarity. The noticeable cycling improvement is first evident with 10% FEC, with marginal improvements up to 20%. The NMC622/graphite cell (blue trace, Figure II-4 top) cycled at 4.6 V is trending toward project target of 300 cycles. This data along with the gassing and OCV data above suggest that the performance drop in the LCO system at high voltage is due to degradation of the cathode but additional experiments to examine the cathode structure/chemistry need to be completed for confirmation.

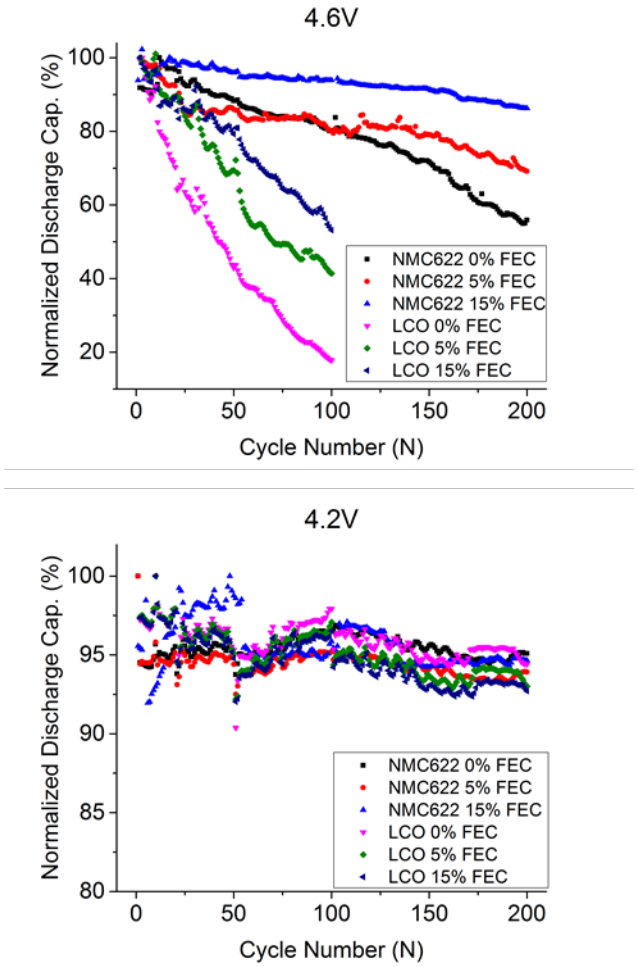

Figure II-18: Normalized discharge capacity (%) versus cycle number (N) of NMC622 and LCO cells cycled at 4.6 V (top) and 4.2 V (bottom). LCO cells ceased operation after 100 cycles at 4.6 V, whereas NMC622 cells completed the desired 200 charge/discharge cycles. Electrolyte is 1.2 M $LiPF_6$ [EC/FEC]/EMC/FE (20:60:20) + 1% PS.

Gassing Kinetics Based on Cathode Composition – Milestone 4

Gassing kinetics of two cathode chemistries (LCO and NMC622) have been determined through volume change measurements over a period of 3-4 weeks, with cells stored at 45°C after formation and final charge to 4.6 V. The data shown in Figure II-19 (top) shows the volume change versus time (days) of both LCO and NMC622 cells with two different electrolytes: 1.2 M $LiPF_6$ EC/EMC/FE (20:60:20) + 1% PS and 1.2 M $LiPF_6$ EC/FEC/EMC/FE (10:10:60:20) + 1% PS. The measured OCV versus time of these cells is also depicted in Figure II-19 (bottom).

As seen in Figure II-19, there is more gas generated in the LCO cells at 4.6 V (left), which is consistent with the OCV drop (right). A decrease in measured OCV indicates that the cathode is being reduced. The cathode can be reduced through multiple mechanisms, one of which includes the oxidation of the graphite anode. One other mechanism includes oxygen defect formation in the cathode material due to crystal structure instability. While additional FEC seems to delay OCV loss, it does not impact gas generation to the same degree.

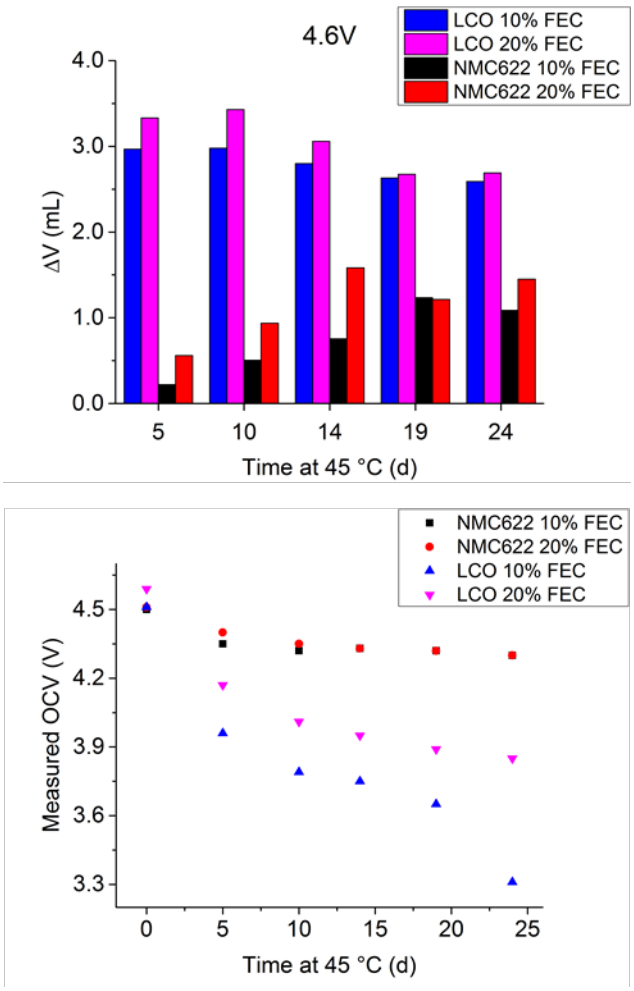

Figure II-19: Volume measurements versus time in 4.6 V NMC622 cells during an OCV calendar life test at 45°C as a function of FEC concentration (top). Measured OCV versus time in 4.6 V NMC622 and LCO cells during the same calendar life test also as a function of FEC (bottom)

Conclusions

Significant work at Daikin in the first year involved setup and validation and training for equipment needed to complete this project. This included expanding our cell cycling capability from 20 to 104 channels and commissioning of several new pieces of equipment (e.g., GC/MS).

An examination of both the existing data and current literature was completed to set baselines for this study. Third party data from final cells of previous Daikin project confirm the there are two battery performance failure points. The first occurs above 4.3 V, which is attributed to electrolyte decomposition resulting in gas generation. It has been shown that the use of fluorinated electrolyte greatly diminishes the decomposition reaction, resulting in enhanced performance. The second failure point occurs above 4.5 V. The baseline experimental voltages for this project have been set at 4.2, 4.5 and 4.6 V in order to study chemical and physical changes which occur when at or near these failure points.

Gas composition has been established for both the LCO and NMC622 cathode materials. Both contain significant amounts of CO, CO_2, CH_4 and O_2 along with select fluorinated hydrocarbons attributed to the decomposition of FEC in the electrolyte.

For both chemistries studied, the addition of FEC to electrolyte results in increased cycle life and capacity retention. However, that benefit for LCO cells is not sufficient to permit viable high voltage operation. The full cycling performance benefit of FEC in the electrolyte is realized at a 10% (v/v %), and can be marginally increased with additional FEC. The data obtained thus far for LCO cells (OCV loss, gas evolution, etc.) suggests that decreased performance is due a non-electrolyte component failure, but rather the result of an inherent property of the cathode material.

II.B Next Generation Lithium-Ion: Advanced Anodes R&D

II.B.1 Next Generation Anodes for Lithium-Ion Batteries: Research Facilities Support

Dennis Dees, Principal Investigator
Argonne National Laboratory
9700 South Cass Avenue
Argonne, IL 60439
Phone: 630-252-7349
E-mail: dees@anl.gov

Peter Faguy, Technology Manager
U.S. Department of Energy
Phone: 202-586-1022
E-mail: Peter.Faguy@ee.doe.gov

Start Date: October 1, 2015 End Date: September 30, 2019
Total FY17 Project Cost: $3,600,000 DOE FY17 share: $3,600,000 Non-DOE share: $0

Project Introduction

Silicon has received significant attention as a viable alternative to graphitic carbon as the negative electrode in lithium-ion batteries due to its high capacity and availability [1]. Elemental silicon can theoretically store >3500 mAh/g, nearly an order of magnitude higher than graphite (372 mAh/g and 818 mAh/mL, respectively). However, several problems have been identified that limit its utility including large crystallographic expansion (~320%) upon lithiation which translates to particle cracking, particle isolation, and electrode delamination issues. Further, there are fundamental and volume change related SEI stability issues, which affect cycling efficiency. The wealth of previous studies in this area is both a testament to its potential and the size of the challenge that must be overcome, requiring a great amount of innovation on multiple fronts.

BatPaC [2], a techno-economic program designed to model lithium-ion battery performance and cost, was utilized to establish program relevance by connecting DOE/USABC pack performance targets to anode targets. Generally, research with silicon containing anodes is focused on improving the specific capacity of graphite. However, this simple metric requires a more detailed analysis with factors such as the impact on average cell voltage, and volumetric capacity. It is notoriously difficult to select appropriate metrics that will enable an accurate calculation of the energy of a single electrode. Most methods estimate the volumetric energy density of active materials with the simplistic assumption that bulk density of the electrode does not undergo change in volume during cycling. While this serves well for most cathodes where the voltage can be fixed against lithium it is inappropriate for electrodes such as silicon.

As shown in Figure II-20 (left frame), BatPaC calculations indicate anode volumetric capacities greater than 1000 mAh/cm^3 (= $\rho \cdot \varepsilon \cdot Q$ [g/cm$^3_{act}$ · cm$^3_{act}$/cm$^3_{elect}$ · mAh/g]) generally minimizes battery cost with an advanced NMC cathode. Note that higher capacities result in diminishing savings in cost. The analysis (right frame) also predicts that silicon-graphite electrodes with less than 75 wt% graphite can achieve the target. Finally, alloys of inactive metals (not shown) with silicon (or tin) can meet the volumetric capacity target as long as the metal choice is inexpensive (e.g., iron rather than nickel or cobalt).

Next Generation Anodes for Lithium-Ion Batteries, also referred to as the Silicon Deep Dive Program, is a five National Laboratory consortium assembled to tackle the barriers associated with development of an advanced lithium-ion negative electrode based upon silicon as the active material. This research program baselines

promising silicon materials that can be developed or obtained in quantities sufficient for electrode preparation within the consortium facilities. Composite electrode and full cell development leverages recent investments made by DOE-EERE-VTO in electrode materials and characterization. The primary objective of this program is to understand and eliminate the barriers to implementation of a silicon-based anode in lithium-ion cells. The Labs are focused on a single program with continuous interaction, clear protocols for analysis, and targets for developing both the understanding and cell chemistry associated with advance negative electrodes for lithium-ion cells. First and foremost, this undertaking is a full electrode/full cell chemistry project leveraging baseline electrodes prepared at the consortium facilities. All efforts are directed to understanding and developing the chemistry needed for advancing silicon-based anodes operating in full cells. Materials development efforts include active material development, binder synthesis, coatings, safety, and electrolyte additives. Efforts include diagnostic research from all partners, which span a wide range of electrochemical, chemical and structural characterization of the system across length- and time-scales. Specialized characterization techniques developed with DOE-EERE-VTO funding, include neutrons, NMR, optical, and X-ray techniques being employed to understand operation and failure mechanisms in silicon-based anodes. In addition, several strategies to mitigate lithium loss are being assessed. The project is managed as a single team effort spanning the Labs, with consensus decisions driving research directions and toward development of high-energy density lithium-ion batteries. A detailed list of participants is given in Figure II-21.

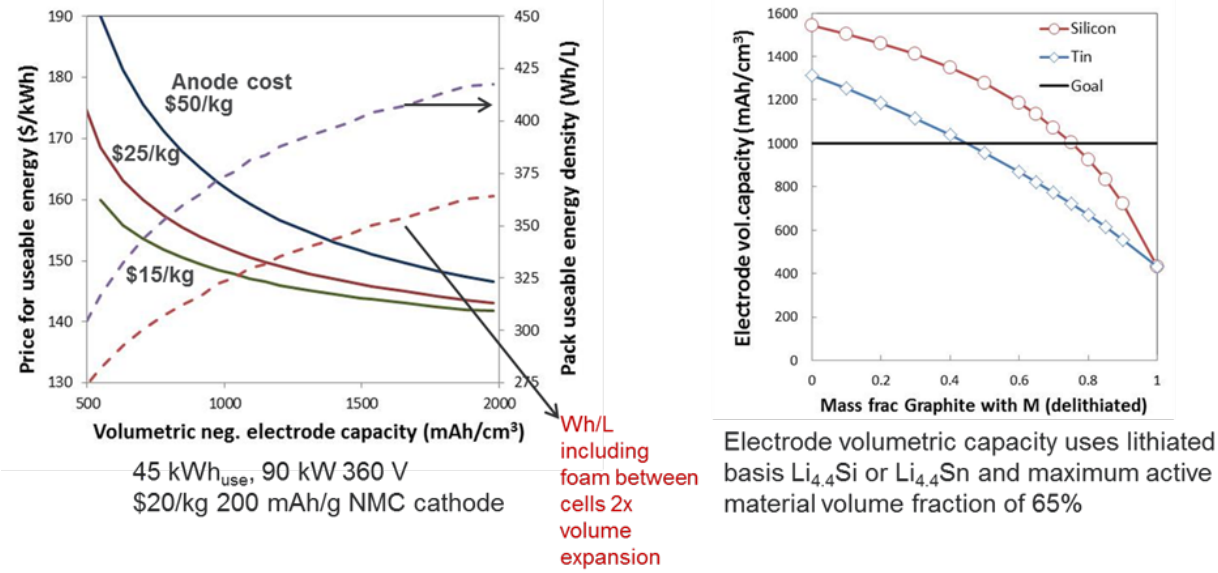

Figure II-20. Battery Performance and Cost (BatPaC) model utilized to establish program relevance

Figure II-21. Program participants including Laboratories, research facilities, and individual contributors.

Objectives

- Understand and overcome the science and technology barriers to the use of silicon-based anodes in high-energy density lithium-ion batteries for transportation applications.
  - Stabilize the SEI
  - Stabilize the electrode
- Demonstrate functional prototype lithium-ion cell chemistries which meet the DOE/USABC performance targets.

Approach

Sandia National Laboratories (SNL), Oak Ridge National Laboratory (ORNL), National Renewable Energy laboratory (NREL), Lawrence Berkeley National Laboratory (LBNL), and Argonne National Laboratory (ANL) have teamed together to form an integrated program. Technical targets have been developed and regular communications have been established. Throughout the program, there is a planned focus on understanding, insights into, and advancement of silicon-based materials, electrodes, and cells. All anode advancements will be verified based on life and performance of full cells. Toward that end, baseline silicon-based materials, electrodes, and cells have been adopted, along with full cell testing protocols.

In examining improvements, changes to the baseline cell technology will be minimized. As an example, silicon active material coating improvements will be verified on baseline silicon materials in electrodes fabricated by the battery research facilities. All other components in the prototype cells (i.e., positive electrode, separator, electrolyte, etc.) will be from the baseline technology. There are many testing protocols that can be utilized to benchmark the baseline technology. This program has adopted a testing protocol from the literature [3] that has worked well for lithium-ion cells with silicon containing anodes. Shown pictorially in Figure II-22 the test starts with three slow (C/20) formation cycles, an HPPC cycle, and then the C/3 aging cycles. The test ends with another HPPC cycle and threes more slow (C/20) cycles. All constant current cycling is symmetric between charge and discharge rates. The tests are run at 30°C. If there is little or no aging in the first 100 cycles, the protocol can be repeated. This protocol effectively examines capacity, impedance, and aging effects in about a month's worth of testing.

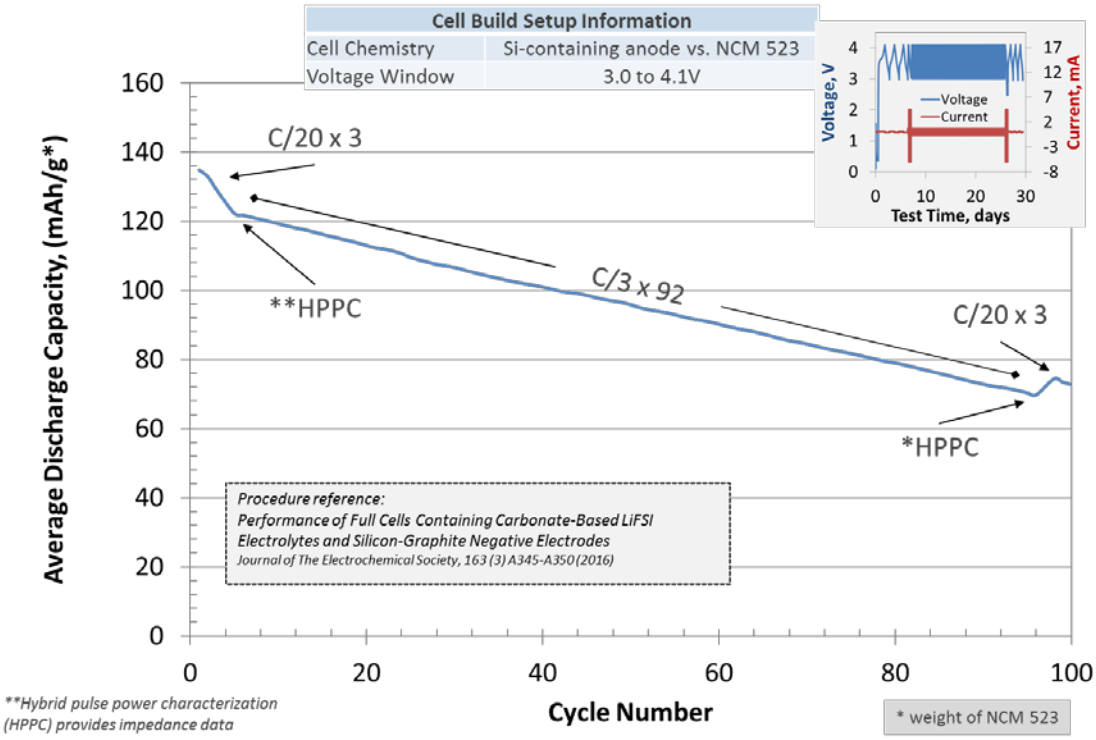

Figure II-22. Full cell testing protocol.

As the program matures, materials developments will be incorporated into baseline silicon-based materials, electrodes, and cells. Scale-up of materials, incorporation of materials advancements into electrodes and prototype cells, and characterization and testing of cells, as well as evaluation of safety and abuse tolerance are part of a wide range of integrated studies supported by battery research facilities at the National Labs working closely with the program. These research facilities include the Battery Abuse Testing Laboratory (BATLab), the Battery Manufacturing Facility (BMF), the Cell Analysis, Modeling, and Prototyping (CAMP), the Materials Engineering Research Facility (MERF), and the Post-Test Facility (PTF).

Communication of programmatic progress to battery community is critical. This will generally be accomplished through publications, presentations, reports, and reviews. Further, the program is open to industrial participation and/or collaboration that does not limit program innovation or the free flow of information. Finally, this program is highly integrated with our sister program on SEI-Stabilization, called SEI-Sta for short. In general, SEI-Sta is focused on the development and characterization of model systems,

thin-film well-defined active area electrodes on which it is easier to extract fundamental information on lithium-silicon phase formation, lithium transport, and interfacial phenomena (e.g., SEI formation and growth).

Results

Development of New Baseline Electrodes (ANL)

Silicon Supplier: Nanostructured and Amorphous Materials

The Silicon Deep Dive program acquired 6 kg of 70-130 nm average particle size (APS) silicon from Nanostructured and Amorphous Materials (NanoAmor, Prod:0143KE) and MagE3 graphite from Hitachi. Early in FY17, these materials were designated to become a new baseline silicon electrode due to data suggesting ~150 nm particle size for silicon being a good target to receive capacity (mAh/g) benefits by having a lower ratio of inactive surface components to active components. In addition, the previous baseline silicon material (50-70 nm APS from NanoAmor) had been discontinued by the supplier.

The 70-130 nm silicon from NanoAmor was put through the same process of slurry preparation and electrode fabrication as the previous baseline material. From these processes we observed several differences including: powder color and handling, particle morphology, range of particle distribution sizes outside of the product spec, slurry gas generation, poor coating quality, and material capacity compared to the 50-70nm from NanoAmor. These differences highlight potential challenges presented in slurry preparation and electrode fabrication for various silicon products even when being provided from the same source.

While the NanoAmor materials have served as a valuable source of silicon powders in early developments of slurry design and electrode coating strategies, ultimately, due to the change in product selection, unexpected powder properties, and the difficulty to coat a 15 wt.% 70-130 nm silicon electrode at >3 mAh/cm², the program looked for alternative sources and products to become the next baseline material for the Silicon Deep Dive.

New Silicon Supplier: Paraclete Energy (PE) based in Chelsea, MI

A promising U.S. silicon supplier, Paraclete Energy (PE), provided multiple samples for evaluation. The received powders were described as SiO or Si core with a SiO_2 shell with an average particle size of 150nm. The particle size analysis (MERF at ANL) and SEM images (Linghong Zhang at ANL) were collected and demonstrate Paraclete's improved control of particle size (Table II-3). Initial electrochemical performance evaluations also showed expected capabilities from previous silicon powders and warranted further evaluation. A scaled-up 500 gram (Initial Scale-up) sample of the original (initial 100g) sample was received and evaluated via NMR (Baris Key at ANL). The NMR results of the "Initial Scale-up" showed a large amount of organic carbon with concern over the possible negative impact on the electrochemical performance. Thus, Samples A, B, C, and D were processed with different variables at PE and sent to Argonne for analysis. The collaboration gives ANL the ability to have the product tailored to the Silicon Deep Dive needs.

Multiple experimental electrodes were fabricated using the aqueous slurry processing and coating strategies described earlier in this section by the CAMP Facility. The high quality 15 wt.% silicon electrodes were fabricated using the powders found in Table II-3 at the ~2 mAh/cm² to match to the Electrode Library that the CAMP Facility maintains. Additional electrode optimization was not needed to coat these electrodes and the initial 15 wt.% silicon coatings show promise in coating high quality >3 mAh/cm² electrodes with minimal to no slurry preparation or coating adjustments necessary.

Table II-3: (Top) Experimental silicon samples from Paraclete Energy with particle size and SEM image information. (Bottom) Brief sample descriptions.

Sample	Description	D50 (um)	SEM Images of powder at various level of magnification
K16-013-MC	Initial 100g	0.96	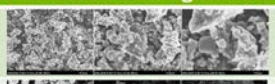
C17-301-LS	"Initial Scale up"	0.12	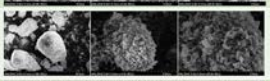
C17-001-LS	Sample A	0.1	
C17-016-LS	Sample B	0.09	
C17-022-LS	Sample C	0.1	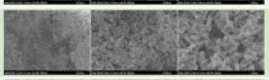
C17-021-LS	Sample D	0.11	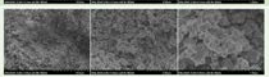

ID	Description
Initial sample	Initial Scoping Sample
Initial Scale-up	Scale-up of initial sample
Sample A	Scale-up of initial sample with improved drying
Sample B	Different silicon feed stock with improved drying
Sample C	Initial sample silicon feed stock manufactured using alternative method
Sample D	Initial sample silicon feed stock, but oxidized in a different manner

Half-cell coin-cell data of 15 wt.% silicon experimental electrodes are shown in Table II-4. The formation data shows the 1st discharge (lithiation) capacity, irreversible capacity loss, reversible charge (delithiation) capacity at a C/10 rate, and 1st cycle coulombic efficiency. Silicon-containing electrodes generally have lower cycling coulombic efficiencies throughout cycling compared to graphite-only electrodes, so determining a true reversible cycle capacity can be arbitrary. All of the testing was performed using 4 coin cells (CR2032) for each electrode using electrolyte with the composition 90 wt.% (1.2 M $LiPF_6$ in EC:EMC 3:7 by wt.%) + 10 wt.% (FEC) using the cycling window of 0.05 to 1.5 V vs. Li metal. The results suggest comparable initial capacities between the samples.

Table II-4: Half-cell coin-cell formation testing results of experimental silicon samples from Paraclete Energy. The capacity values are normalized to the total weight of the silicon, graphite, and carbon black present in the electrode.

Sample	1st Cycle Discharge Capacity (mAh/g)	Irreversible Loss (mAh/g)	Reversible Cycle Charge Capacity (mAh/g)	1st Cycle Efficiency (%)
Original Sample	831	151	679	92.4
Sample A	750	61	684	90.6
Sample B	618	108	592	88.3
Sample C	743	87	656	89.3
Sample D	747	93	653	90.9

Voltage Window: 0.05–1.5 (V)

Full-cell coin-cells were then fabricated using the various ~2 mAh/cm² (0.05 to 1.5 V vs. Li metal) silicon-containing (PE) electrodes versus a standard 90 wt.% NMC532, 5 wt.% Timcal C45 carbon black, and 5 wt.% PVDF made for the Electrode Library at the CAMP Facility [A-C013A]. The approximate n:p capacity ratios for the electrode couples are between 1.1 and 1.3 for a voltage window of 3.0 to 4.1 V in a full cell. The Silicon Deep Dive cycling protocol was used to evaluate these materials and for comparison purposes.

Figure II-23 shows the resulting full cell testing on the Paraclete Energy silicon samples. Samples A and D showed the best performance of the 4 samples provided by PE and are similar to the previous baseline electrode performance (50-70 nm Si NanoAmor, [A-A006A]). Sample D performed slightly better than Sample A in the final 3 cycles, thus “Sample D” was selected to be scaled-up to a 500 g sample “Scale-up of Sample D” for purposes of becoming the new silicon material for the future baseline electrodes. Early indications from initial coatings show improved coating quality and integrity with the “Scale-up Sample D” for both low and high (>3.0 mAh/cm²) coating loadings after calendering. Henceforth, in this section the “Scale-up Sample D” powder was used as the silicon components of the electrodes fabricated. The initial baseline electrodes [A-A012] using the new silicon source (PE) for this project was coated at a loading of 3.63 mg/cm² with an expected mAh/cm² of ~2 in half-cell testing (Table II-5).

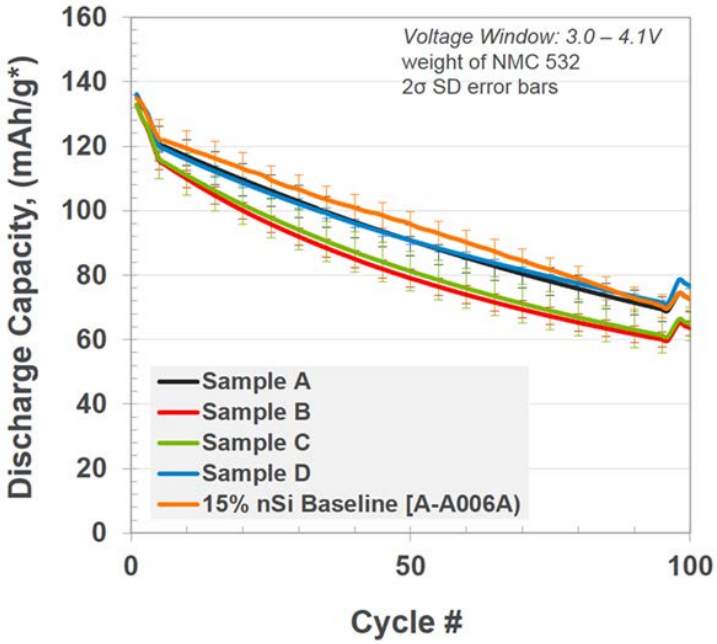

Figure II-23. Full-cell coin-cell results showing average discharge capacity vs. cycle number. The Silicon Deep Dive full cell cycling protocol was used for evaluating the experimental silicon electrodes compared to the original silicon-containing baseline electrode [A-A006A]. The cycling protocol consists of three slow (C/20) formation cycles, an HPPC cycle, and then C/3 aging cycles, followed by a 2nd HPPC cycle, and finally three more slow (C/20) cycles. The capacity values are normalized to the weight of NMC532.

Table II-5: Half-cell coin cell formation testing results of new baseline 15wt.% silicon-containing electrodes. The silicon powders used are "Sample D" and "Scaled-up Sample D" from Paraclete Energy. The capacity values are normalized to the total weight of the silicon, graphite, and carbon black present in the electrode.

Sample	Total Coating Loading (mg/cm²)	1st Cycle Discharge Capacity (mAh/g)	1st Cycle Efficiency (%)	Reversible Cycle Charge Capacity (mAh/g)	Reversible Cycle Charge Areal Capacity (mAh/cm²)
Sample D	3.88	747	90.9	653	2.39
A-A012	3.63	803	91.0	723	2.56
A-A013	3.00	842	89.3	716	2.07

Voltage Window: 0.05–1.5 (V), 30°C

A 2nd baseline electrode [A-A013] with the same materials and composition but at a lower coating loading of 3.00 mg/cm² was made to lower the n:p ratio closer to 1.1. Full cells were then made using these new baseline materials paired against the same cathode [A-C013A] using the Silicon Deep Dive Protocol to evaluate the cycling performance. Figure II-24 shows the full cell cycling performance comparison of the original baseline material [A-A006A], Sample D, and the new baseline electrodes [A-A012] and [A-A013] being tested under the Silicon Deep Dive full cell cycling protocol. The protocol reveals that similarities of the performance for the 4 electrodes suggesting that the "Scale-up Sample D" powder is adequate to replace the previous baseline electrode and the two n:p ratios chosen retain a similar capacity retention (Figure II-24).

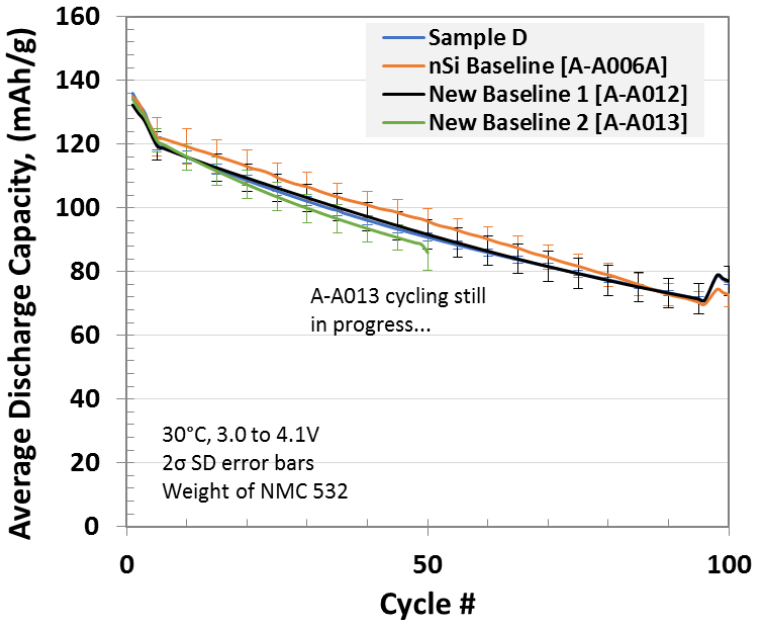

Figure II-24. Full-cell coin-cell results showing average discharge capacity vs. cycle number for the Silicon Deep Dive baseline electrodes vs. NMC532 [A-C013A]. Data shows the average values based on 4 coin cells for each electrode pair. The capacity values are normalized to the weight of NMC532.

Encouraging aspects of working with Paraclete Energy are that they have demonstrated their ability to control particle size and customize processing steps to target surface chemistries. The electrochemical data is also comparable to the previous baseline electrode performance and the silicon source provides a dependable and repeatable silicon powder from batch to batch. Lastly, Paraclete Energy has been eager to engage in collaborations with the CAMP Facility and the Silicon Deep Dive Program to further develop their processing techniques of silicon products for improved lithium-ion battery performance.

Processing Science of Silicon Containing Anodes (ORNL)

The transition from n-methyl-2-pyrrolidone (NMP) to aqueous processing has proven important for graphite anodes. These aqueous-based electrodes function as effectively as their NMP counterparts, but without the environmental concerns of NMP. The addition of Si into graphite electrodes has made for a more difficult transition to aqueous-based slurries. Unlike graphite, Si has increased reactivity with water, the consequents of which are not yet fully understood. Furthermore, minimizing the water in Li ion batteries is crucial to avoid unwanted parasitic side reactions that can cause the production of gasses through reduction to H_2 and additional HF build through the hydrolysis of $LiPF_6$. Here we study both NMP and aqueous systems for Si-graphite electrode fabrication. During this work we identified severe gassing reactions that occur during electrode formulation mixing. The effects of solvent selection were examined by gas analysis of Si-graphite composite slurries. Si powders from these slurries were further examined with FTIR and NMR.

A custom stainless steel sealed vessel was manufactured to measure changes in pressure of Si slurries, Figure II-25. The 0.5 L vessel was designed to replicate the mixing of Si slurries for large scale preparation of Si-graphite electrodes. This vessel mixed the slurry using a roller mill and ZrO_2 media. Though this does not match the energy of a planetary ball mill commonly used in our slurry preparation, it gives a relative indication of any reaction that may occur over a reasonable time scale. Si powder (Nanoamor 70-130 nm), carbon black (Imerys C45), and the slurry solvent were mixed for up to 100 hours, (Figure II-26-Left). Between 0 and 1 hours, both water and NMP-based slurries decreased in pressure, likely due to the consumption of O_2 from the air, after that the water-based slurry slowly increased in pressure for the first 24 hours before rapidly

increasing after additionally mixing. The NMP-based slurry did not change significantly after the initial pressure lost. In addition to the Nanoamor Si, Alfa Aesar 325 mesh Si was tested in water-based slurry and produced a similar pressure build. This shows that the reaction occurs independent of Si particle size. Gas was collected from the head space and tested by mass spectrometry, (Figure II-26-Right). The water-based Si slurry showed a large H_2 signal, which is not present for the NMP-based slurry. This accounts for the large increase in pressure for the water-based slurry, following reaction 1.

$$(1) \qquad Si\ (s) + H_2O\ (l) \rightarrow SiO_2\ (s) + H_2\ (g)$$

Figure II-25. Image of reactor vessel on roller mill. Note the pressure gauge pointing to the right.

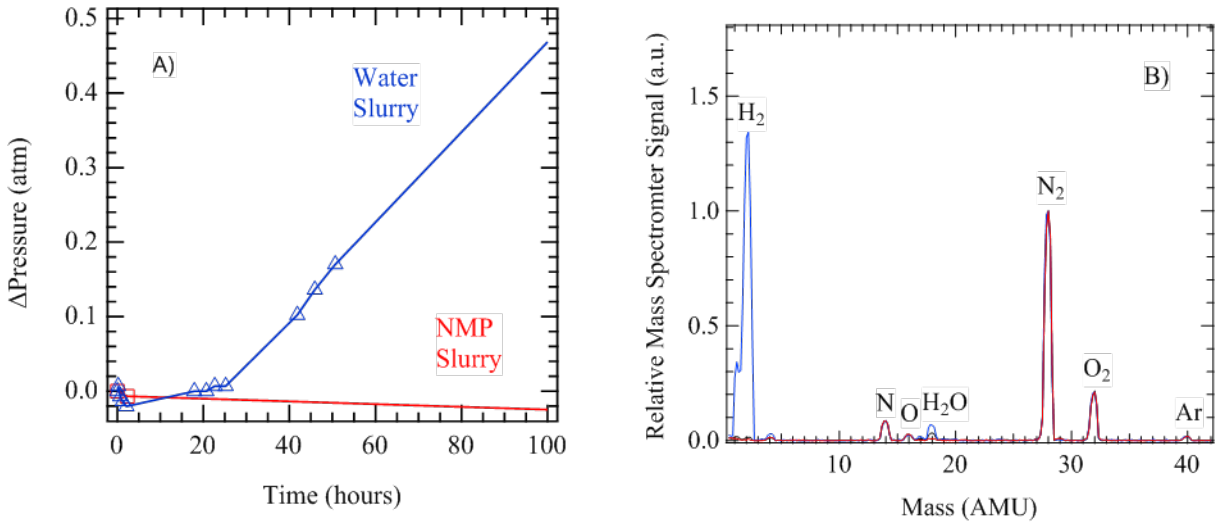

Figure II-26. (Left) Pressure vs time plot showing changes to NMP and water-based Si slurries in sealed pressure vessel. (Right) Mass spectrum of head space collected from water-based Si slurry (blue trace), NMP-based Si slurry (red trace), and ambient air (black trace).

In addition to hydrogen all samples showed various decreases in oxygen content (relative to atmospheric N_2 in the cell) which we attribute to oxidation from O_2 in the air which reacts during milling according to reaction 2. In both cases the oxidation proceeds but the extent of oxidation varies pointing to a role of the solvent in the reactivity of the silicon. Additional studies showed evidence for the formation of CO_2 from the decomposition of binders and/or reactions with graphite and carbon black. Together these results indicate a quite complex reaction environment that is actively changing the electrode chemistry and its resulting cycleability and reproducibility.

$$(2) \qquad Si\ (s) + O_2\ (g) \rightarrow SiO_2\ (s)$$

Role of Drying Temperature in Reproducible and Reliable Si Anodes (ORNL)

Water is a major impurity in silicon electrodes. [4] In addition to the Si, polyacrylic acid (PAA) is a well-known "superabsorber" of water. [5] To evaluate its effect and ways to mitigate it a drying study was completed. To determine if residual water is problematic in Si-graphite electrodes when utilized in full cells, coatings were tested using LiPAA binder in a water slurry and PAA binder in an NMP-based slurry. Secondary drying of each was completed at temperatures ranging from 100°C to 200°C.

Thermogravimetric analysis (TGA) of PAA and LiPAA binders

Water was analyzed in PAA and LiPAA by Karl-Fisher titration. As received PAA was 1.14% water by weight, compared to LiOH titrated LiPAA (dried at 80°C), which was only 0.03%. TGA was used to investigate optimal temperatures to remove water from these binders (Figure II-27 Left). The TGA of PAA displays four distinct regions of weight loss, which are more easily identified by its first derivative (DTGA), (Figure II-27 Right). Though not immediately recognizable, LiPAA shares these same regions of weight loss, but with a much more gradual sloping profile. The DTGA is expanded 10X for LiPAA to identify the peaks of interest. In both binders, the first two regions of weight loss can be assigned to free water (40°C) and adsorbed water (75°C for LiPAA and 125°C for PAA). In PAA, this is followed by another region of weight loss, beginning at 140°C and reaching a maximum at 208°C. This feature is much broader in DTGA of LiPAA, starting at 85° C and reaching a maximum at 190°C. This weight loss is related to the dehydration of carboxylic acid group. [6] These neighboring carboxylic acid group will react to form an anhydride, subsequently releasing water as a byproduct. This extent of this reaction is considerably less for LiPAA since 80% of the carboxylic acid groups are already substituted for carboxyl groups paired with Li^+ counter ions. This decomposition continues at 250°C for PAA with breakdown of the anhydride and releasing of CO_2, but this occurs at temperature beyond normal electrode drying conditions. To our knowledge, a detailed study of the thermal degradation of LiPAA has not been completed, but other alkaline earth polyacrylates are known. NaPAA undergoes main chain and side group scission above 400° C, meaning it is stable in normal electrode drying conditions. [7]

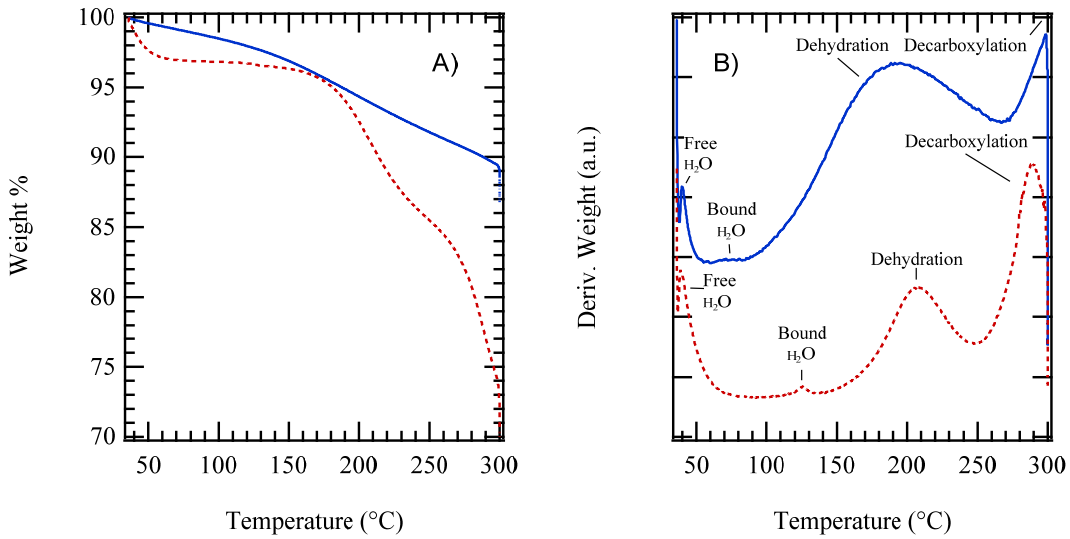

Figure II-27. TGA (Left) and DTGA (Right) of "as received" PAA (dashed red line) and LiPAA (solid blue line). The DTGA of LiPAA was expanded 10X to more easily identify features.

KF titration of electrode materials

Given the cross-linking reaction indirect KF titration of the electrodes in chloroform was used to get an accurate water content without heating the material to drive water off. Each slurry was dried at room temperature, the solid components were ground, and each were dried under vacuum overnight at the designated temperature. Both LiPAA and PAA-based Si-graphite electrodes had a similar water content of ~2100 ppm when dried at 120°C. Upon increasing the drying temperature to 150°C, PAA-based electrodes increased to roughly 4 times (i.e., 7927 ppm) the water content of the LiPAA-based electrode. TGA shows that PAA begins to decompose around this temperature, releasing water as a byproduct. It is well known that Si strongly binds water at temperatures up to 250°C. [4] The water content of PAA-based electrodes increase at this temperature, because any water released during the decomposition of the binder is adsorbed by the Si, which cannot be driven off at this temperature. Though the value of 7927 ppm seems high, it is still below the theoretical value of 12,500 ppm, which is the max amount of water released during the decomposition of PAA, where the binder accounts for 10% of the total mass of the electrode.

Influence of Drying on Full Cell Performance.

The water results presented above were used to direct the investigation of a Si-graphite:532 NMC cathode full cell. The Si-graphite composite electrodes were produced with 15% (by mass) Si nanoparticles (Nanoamor, 70-130 nm), 73% graphite (Hitachi, MagE 3), 2% carbon black (Imerys, C45), and 10% binder (LiPAA or PAA). LiPAA-based electrodes utilized a water-based slurry while PAA-based electrodes used n-methyl-2-pyrrolidone (NMP, Sigma-Aldrich, ≥99%). Slurries were then prepared by first dry mixing dried Si, carbon black, and either NMP or water in a planetary ball mill. This Si/carbon black slurry was added to a graphite/binder slurry and mixed in a planetary mixer. The solid content was ~36% by mass. The slurries were coated on Cu foil by custom slot die (Frontier Industrial Technology) and coated to loadings 3.4 mg cm^{-2} and 3.3 mg cm^{-2} for PAA and LiPAA-based anodes, respectively.

Electrodes underwent secondary drying in a vacuum oven at a desired temperature for 18 hours under static vacuum at 25 mm Hg. Full cells were matched against 12.9 mg cm^{-2} $LiNi_{0.5}Mn_{0.3}Co_{0.2}O_2$ (NMC-532, Toda) cathodes. Based on initial capacities of each anode, the LiPAA-based Si-graphite composite had an anode to cathode capacity ratio of 1.30, while the PAA composite was 1.13. Pouch cells were filled to 3X the total pore volume of the pouch cells with Gen 2 electrolyte. Cells were cycled following the ANL protocol.

Full cell cycling data for both composites at various secondary drying temperatures is displayed in Figure II-28. LiPAA-based Si-graphite cells had no detectable variation based on secondary drying temperature. The initial discharge capacity of 137 mAh g^{-1} (per mass cathode) aligns well with first cycle Coulombic losses. There was a slight degradation in capacity upon increasing rate to C/3 127 mAh g^{-1} and continued to decrease during aging to 91 mAh g^{-1}. Returning to C/20 after 97 cycles saw 8 mAh g^{-1} increase, comparable to the initial capacity drop in line with the rate change.

PAA-based Si-graphite cells displayed a trend along with secondary drying temperature. 140°C PAA Si-graphite cells and below performed better than those above this drying temperature. First cycle discharge capacity ranged between 130 and 116 mAh g^{-1}, with electrodes dried at 160°C being the highest and 120°C being the lowest, though all within the error bars of each other. 160° C PAA Si-graphite cells and above declined rapidly in capacity to ~75 mAh g^{-1}, before settling at 62 mAh g^{-1} after 96 cycles, while 140°C PAA Si-graphite cells and below showed a more gradual decline in capacity to 71 mAh g^{-1}. Similar to those constructed with LiPAA Si-graphite cells, all PAA cells increased in capacity by 9 mAh g^{-1} upon return to C/20.

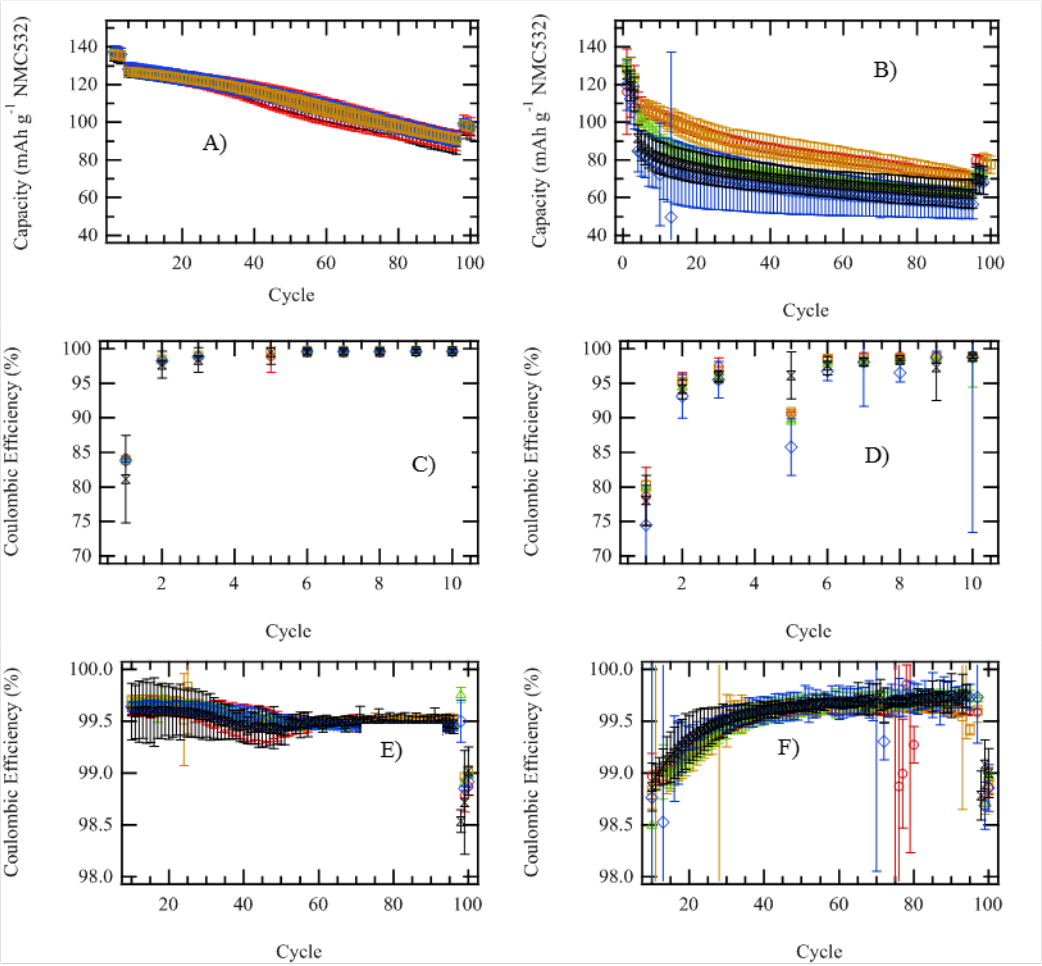

Figure II-28. Cycle life of A) LiPAA-based full cells and B) PAA-based full cells. The first 10 cycle Coulombic efficiency of C) LiPAA-based full cells and D) PAA-based full cells. The long term Coulombic efficiency of E) LiPAA-based full cells and F) PAA-based full cells. The secondary drying temperature on the Si-graphite composite anodes are 120°C (red circle), 140°C (gold square), 160°C (green triangle), 180°C (blue diamond), and 200°C (black hour glass). Each point is an average of 3 cells.

LiPAA Si-graphite cells obtained first cycle Coulombic efficiencies of 84%, except for the 200°C LiPAA Si-graphite cells, which were slightly lower at 82%. These cells rapidly increased to 99.6% within the first 5 cycles and maintained this for 30 cycles for degrading slowly to 99.5%. Upon returning the LiPAA Si-graphite cells to C/20, they dropped to a Coulombic efficiency of 98.9%. PAA Si-graphite cells had a first Coulombic efficiency of 80%, except for 180°C PAA Si-graphite cells, which were 75%. Opposed to the LiPAA Si-graphite cells, the PAA Si-graphite cells slowly increased in Coulombic efficiency over 40 cycles to 99.6%. PAA Si-graphite cells cycled at 140°C and below leveled off at 99.6%, while cells at 160 and above continued to slowly increase to 99.7%. All the cells dropped to a Coulombic efficiency of 98.8 - 99.0% after returning to C/20 which is clearly not ideal for a commercial application

In summary, this data shows that the electrodes cast in water (LiPAA binder) with lower residual water content cycle better than the NMP cast PAA electrodes (with higher water content). Interestingly, the PAA performance is dramatically influenced by drying temperature. This is consistent with the previous TGA data which showed significant water loss above 140°C due to dehydration. At higher temperatures, the decomposition of the PAA produces a far worse binder.

Cell Optimization, Impact of Electrolyte Volume Addition (ORNL)

This study aims to explore the correlations between electrolyte volume, electrochemical performance, and properties of the solid electrolyte interphase in pouch cells with Si-graphite composite anodes and NMC532 cathodes. [8] We conclude that a minimum electrolyte volume factor of 3.1 times the total pore volume of cell components (cathode, anode, and separator) is needed for better cycling stability. Less electrolyte causes increases in ohmic and charge transfer resistances. Lithium dendrites are observed when the electrolyte volume factor is low. The resistances from the anodes become significant as the cells are discharged. Solid electrolyte interphase thickness grows as the electrolyte volume factor increases and is non-uniform after cycling.

For this study the electrolyte was 90 wt.% "Gen 2" and 10 wt.% fluoroethylene carbonate (FEC). Gen 2 is the electrolyte formulation adopted by Argonne National Laboratory (ANL) and Oak Ridge National Laboratory (ORNL) and is 1.2 M $LiPF_6$ in ethylene carbonate:ethylmethyl carbonate (EC:EMC) (3:7 by weight). FEC was included as an additive in Gen 2 because of improvement in cycle life of Si anode with it. Electrolyte volume factor, F, was defined as the supplied electrolyte volume divided by the total cell pore volume (the sum of pore volumes in anode, cathode, and separator). The contribution of electrode separation and edge effects to the total void volume depends on the cell geometry and configuration. Thus, the optimum factor, F, would be expected to be different for other cell designs such as 18650's. The electrolyte volume would also vary with the surface roughness of the electrodes. Five volume factors from 1.6 to 3.5 were investigated at 25ºC with four cells in each volume factor group. Each cell had 100 mAh capacity at C/20 with a single-side coated anode and cathode. Details of the processes and conditions for the cell assembly, test equipment, and test set-up are elaborated elsewhere. [8] All cell assembly was completed in the DOE Battery Manufacturing R&D Facility (BMF) dry room (dew point ≤ -55ºC) at ORNL. The electrodes were fabricated at, and provided by, the Cell Analysis, Modeling, and Prototyping (CAMP) Facility at ANL. The anode contained 73 wt.% graphite, 15 wt.% 50-70 nm silicon, 10 wt.% lithium polyacrylate (LiPAA), and 2 wt.% carbon. [9] The LiPAA binder was prepared by titration of polyacrylic acid with LiOH to neutral pH.

Testing included 3 formation cycles at C/20 charge and discharge rates, an initial DC resistance test (1 cycle), 92 aging cycles, a final DC resistance test (1 cycle), and 3 final cycles. [9] Cells were cycled with cut-off voltages of 4.1 V and 3.0 V for all tests. The voltages were held at 4.1 V during charging until the current dropped to C/20. AC electrochemical impedance spectroscopy (EIS) tests were included after the final cycles to analyze resistances in detail. The hybrid pulse power characterization (HPPC) test was used to investigate the DC resistance of full cells at different depths of discharge (DOD). Discharge C-rate for the HPPC pulses was 3C (1C rate is based on 130 mAh g^{-1} of NMC). XPS depth profiles were used to estimate the SEI layer thicknesses and insoluble components. All cells were discharged to 3 V at C/20 before disassembly, and the anodes were harvested in an argon atmosphere glove box. The harvested electrodes were lightly rinsed with EMC solvent, dried in the glove box, and loaded in a vacuum transfer module to avoid air and moisture contact. The transfer module was directly inserted into the XPS chamber with a base pressure 10^{-9} Torr. Hence, the electrode samples analyzed by XPS were never exposed to ambient air and moisture. The analysis depth is expected to be 5−10 nm. [10]

Correlation of Electrolyte Volume and Capacity Fade

During the first three cycles, cell-to-cell variations in discharge capacity were large for all factor groups. Figure II-29 shows average discharge capacities and irreversible capacity losses (ICLs) during first three (1^{st} – 3rd cycle) at C/20, aging cycles (4th – 97th cycle) at C/3, and last three cycles (98th – 100th cycle) at C/20 charge and discharge rates with 95% confidence intervals as error bars. During the first three cycles (Figure II-29a - b), F1.6 showed the lowest average discharge capacities (87 - 97 mAh g^{-1}) with the largest error bars (44 - 43 mAh g^{-1}, one-side) while F2.1 showed the smallest error bars (9 - 3 mAh g^{-1}, one-side) and the highest average discharge capacities (134 mAh g^{-1}). ICLs at F1.6 were also the highest (30.4 mAh g^{-1}, 3.6%) while those at F2.6 were the lowest (21.3 mAh g^{-1}, 1.5%). After 100 cycles (Figure II-29e - f), F3.5 group showed the highest discharge capacity (65 mAh g^{-1}) which was slightly higher than F3.1 group (63 mAh g^{-1}) but the difference was insignificant considering the error range. Their ICLs were also the lowest (2.7%). Capacities of F1.6 at C/20 during the final cycles seem closer to those of F3.1 and higher than those of

F2.1 and F2.6. However, the capacities of F1.6 remained far below the other groups during the aging cycles at higher rate (C/3) (Figure II-29c). While the error bars for the F1.6 group were large, clear trends in the capacity and ICL were observed for the other groups after the aging cycles (Figure II-29e and 10f). During the aging cycles, both F3.1 and F3.5 showed the highest capacity retentions (about 52% from the maximum capacity to the final capacity) and the lowest ICLs (Figure II-29c and Figure II-29d). In general, capacity and capacity retention increased with increasing volume factor up to F3.1.

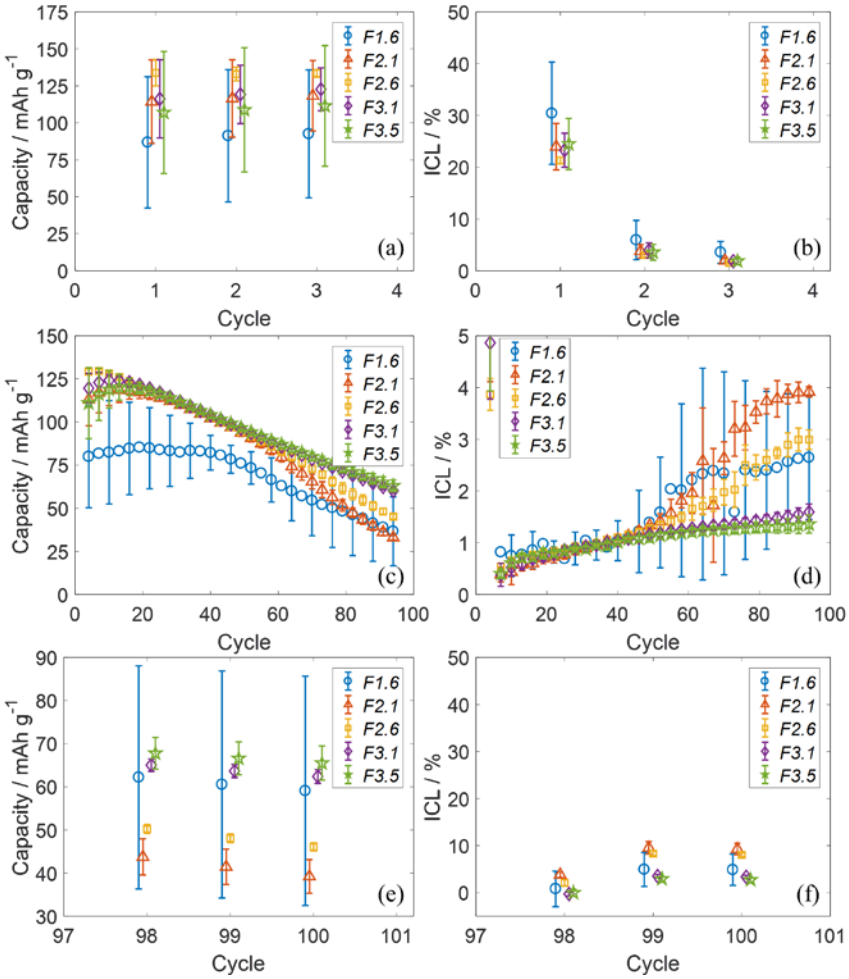

Figure II-29. Correlation of electrolyte volume and cell cyclability. Discharge capacities during (a) first three cycles at 0.05C/-0.05C, (c) aging cycles at 0.333C/-0.333C, and (e) last three cycles at 0.05C/-0.05C for different electrolyte volume factor groups, F; corresponding irreversible capacity losses (ICLs) during (b) the first three cycles, (d) aging cycles and (f) the last three cycles. Cut-off voltages were 3 and 4.1 V. Voltage for the aging cycle was held at 4.1 V until current reached 0.05C. Error bars correspond to 95% confidence intervals.

The Si particles experienced changes not only in volume but also in shape, which further destabilized the SEI layer. Figure II-30 shows top-down SEM images of (a) the pristine Si-graphite anode and (b) F1.6 and (c) F3.5 anodes cycled for 100 times and discharged. Unlike the pristine anode, which showed spherical Si and conductive carbon particles (not distinguishable in the image), the shape of particles covered by SEI became irregular after cycling. The change in particle shape agreed well with an earlier TEM study. [11] SEI covering the particles was bulkier for F3.5 compared to F1.6, which implies that electrolyte decomposed more on Si particles at F3.5 due to the more abundant electrolyte (reactant). SEI thickness analysis also showed thicker SEI at F3.5 than at F1.6 and is elaborated later.

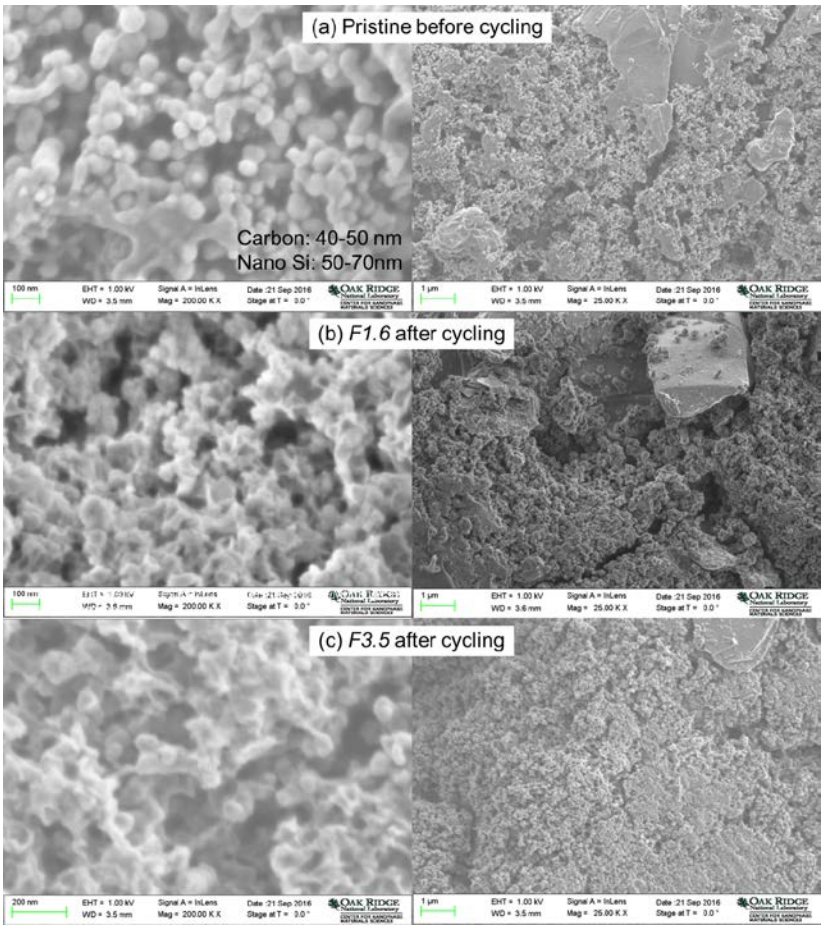

Figure II-30. SEM images of (a) pristine 15 wt.% Si-graphite anode and (b) F1.5 and (c) F3.5 anode cycled 100 times. Magnification of the images on left and right are 200,000 X and 25,000 X, respectively.

The SEM images also show the presence of some relatively bare graphite particles that were not covered with silicon and carbon. This is consistent with the Raman mapping data reported in this report. EDS results from F1.6 and F3.5 showed that the silicon-carbon rich areas had more oxygen and fluorine elements than the graphite-rich areas. This indicates that SEI was formed preferentially on the silicon-carbon areas, since oxygen and fluorine are key elements of SEI components such as lithium carbonate and LiF. EDS analysis showed 3.5-4.8 atomic percentage of Si at the graphite rich zone because effective analysis depth is large at 20 kV (e.g., 1-2 µm in Si). Because of the same reason, silicon atomic percentage was not significantly high at the silicon-carbon rich zone.

Low electrolyte volume, F1.6, led to lithium dendrite formation on an anode. After 100 cycles, the separator for F1.6 was also dry. Visual inspection of the F1.6 anode revealed that some regions of the electrode did not contribute to charge-discharge processes properly due to lack of electrolyte. These areas were relatively bright and light green in color similar to the pristine anode. Darker areas indicated where the electrode did cycle. The color change is due to the conversion of crystalline Si to amorphous Si during lithiation. The dendrites formed on dark areas surrounded or near by the relatively-bright areas due to the locally low negative-to-positive capacity ratio. Unlike F1.6, there was plenty of electrolyte on the separator for F2.6 and F3.5 groups and no lithium dendrites were observed.

Resistance Analysis of Full Cells

Resistances were characterized before and after aging cycles using HPPC. Figure II-31 shows the individual cell resistances during discharge for different factor groups. F1.6 showed the highest resistance on average with large cell-to-cell variations. In general, the resistances of all cells increased as voltage decreased. The initial resistances (4th cycle) of F2.1 and above were almost identical (32 – 35 Ohm-cm^2 near 3.6 V) while those of F1.6 were much higher (57 – 66 Ohm-cm^2 near 3.6 V). After the 97th cycle, cells in the F3.1 and F3.5 groups demonstrated the lowest resistance (about 50 Ohm-cm^2 near 3.6 V), followed by F2.6 (average 73 Ohm-cm^2), F2.1 (over 90 Ohm-cm^2), and F1.6 (average 127 Ohm-cm^2). Hence, F3.1 represented the minimum electrolyte amount to minimize resistance increase during cycling. This was also consistent with the long-term cycling data (Figure II-32), which showed the least capacity fade for the F3.1 and F3.5 groups. The resistances were also measured using EIS at different voltages after 100 cycles. Figure II-32 shows selected impedance data of different factor groups between 3.7 V and 3.8 V and areal resistances at different voltages. The EIS results were in agreement with the HPPC results with the lowest resistance at F3.1 and F3.5 groups (26 – 30 Ohm-cm^2 near 3.6 V), which was just a few Ohm-cm^2 lower than the HPPC results. Similar to the HPPC results, there was no significant difference in resistances from F3.1 and above.

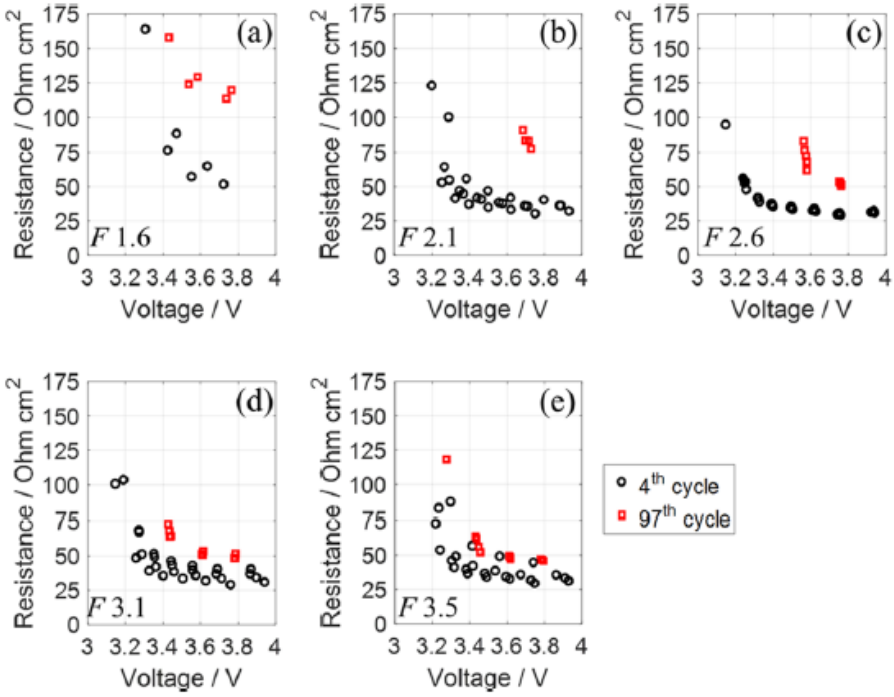

Figure II-31. Resistances of 15 wt.% Si-graphite/NMC532 cells from HPPC tests at different voltages during discharge at 4th and 97th cycles for electrolyte volume factor group F1.6 (a), F2.1 (b), F2.6 (c), F3.1 (d), and F3.5 (e).

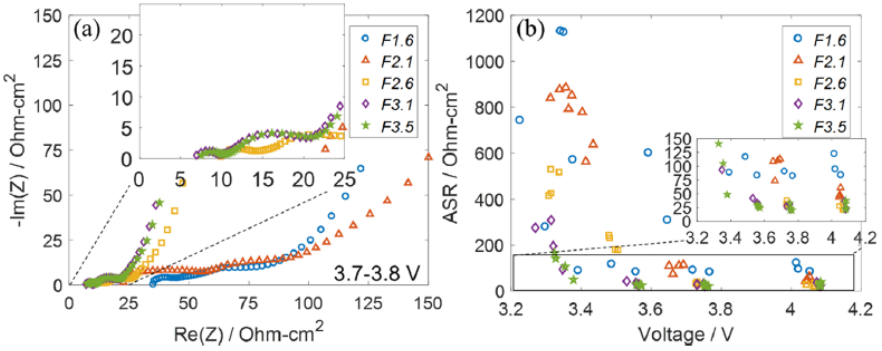

Figure II-32. (a) Impedance spectra of 15 wt.% Si-graphite/NMC532 cells near 3.75 V after 100 cycles with different electrolyte volume factor groups. (b) Total resistances from EIS at different voltages. (Equivalent circuit model for the EIS data fitting is shown in the next figure.)

Figure II-33a shows the equivalent circuit model used to fit the EIS data along with definitions of the circuit elements and their frequency domains. As examples, Figure II-33b and Figure II-33c illustrate EIS data ranges and the corresponding frequency domains of F3.5 for the fits at 4.1 V and 3 V. The resistance elements obtained in this study were ohmic resistance (Rohmic), surface film resistance (Rsf, or SEI resistance), charge transfer resistance I (Rct1, or anode charge transfer resistance), and charge transfer resistance II (Rct2, or cathode charge transfer resistance). For full cells with graphite anodes, the frequency domain II that belongs to anode charge transfer resistance, Rct1, does not generally appear as a distinct semi-circle. [12,13] However, the Rct1 was a significant component for full cells with Si-containing anodes, especially at low voltages.

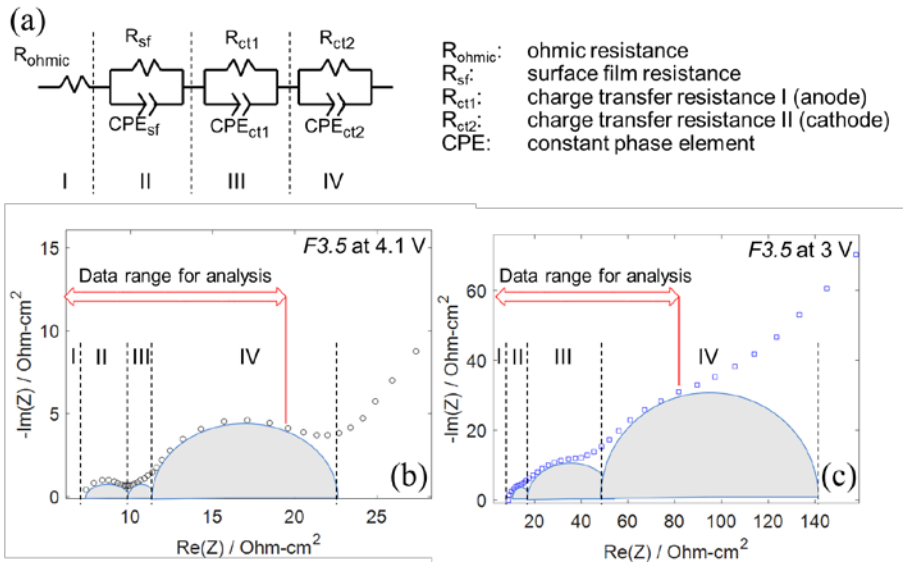

Figure II-33. (a) Equivalent circuit model for EIS data fitting and definitions and four frequency domains of elements. As examples, EIS data of F3.5 at (b) 4.1 V and (c) 3 V after 100 cycles and their data ranges for the fittings.

Each resistance derived from the EIS after 100 cycles is shown in Figure II-34. The electrolyte resistances indicated as Rohmic were affected by low electrolyte volumes. The highest Rohmic was measured for F1.6 (about 35 Ohm-cm^2) followed by F2.1 (about 20 Ohm-cm^2). F2.6 and above showed similar electrolyte resistance (about 10 Ohm-cm^2). Rohmic was independent of voltage, as expected. In contrast, all other resistances increased at lower voltages. Surface film resistance, Rsf, is related to the SEI layer and was the lowest at F3.1 and F3.5 (2 - 3 Ohm-cm^2 near 3.6 V). While the SEI layer for the higher factor group (F3.5) was thicker than the lower factor group (F1.6 and F2.6), this SEI layer was likely porous. Anode surface analysis

section explains SEI thicknesses and porosities in detail. F3.1 and F3.5 also showed the lowest anode (Rct1, 2 - 3 Ohm-cm^2 near 3.6 V) and cathode charge transfer resistance (Rct2,12 - 13 Ohm-cm^2 near 3.6 V). The charge transfer resistances for volume factors of F2.6 and below were higher than those of F3.1 and F3.5 especially at voltages below 3.6 V. The charge-transfer resistance also became more voltage-dependent as the electrolyte volume decreased. This is reasonable because energy requirement resulting in voltage loss becomes higher as the electrolyte volume decreases.

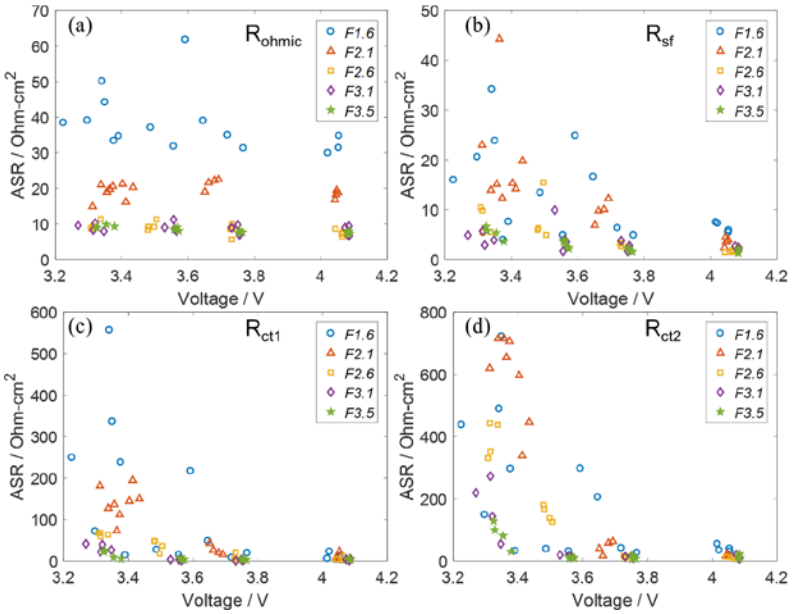

Figure II-34. (Areal specific resistances (ASR) from EIS at different voltages in different electrolyte volume factor groups, (a) ohmic resistance (Rohmic), (b) surface film resistance (Rsf), (c) anode charge transfer resistance (Rct1), and (d) cathode charge transfer resistance (Rct2).

Anode Surface Analysis

Three factor groups (F1.6, F2.6, and F3.5) were selected for anode surface analysis since the electrochemical performance of F3.1 is similar to F3.5. The thicknesses of the surface film (SEI) were estimated using XPS depth profiles and were consistent with FTIR data. Figure II-35 shows surface film element profiles of the three groups along the depth direction from the surfaces. All specimens were taken from the same location at each anode to avoid a geometric effect. The depth was calculated based on the assumption that the film has the same etching rate as SiO_2. The counts per second (CPS) data from element peaks were smoothed using the LOESS model (locally weighted polynomial regression). The thicknesses were estimated based on the CPS of elements corresponding to SEI or silicon active components along the thickness direction. [12] Four elements were chosen for the estimation: Li from LiF (55.6 eV), Si from bulk Si0 (99.6 eV) and Li_xSiO_y (102.8eV), C from carbonates (292.6 eV), and O from carbonates (532 eV for C = O and 533.5 eV for C - O). LiF and carbonates form SEI components from electrolyte decomposition. Li_xSiO_y forms from the conversion of surface silicon oxides and is one of dominant species on cycled silicon surfaces. [10, 14, 15] In Figure II-35, each CPS of elements was normalized by its own maximum because the CPS varied with different elements.

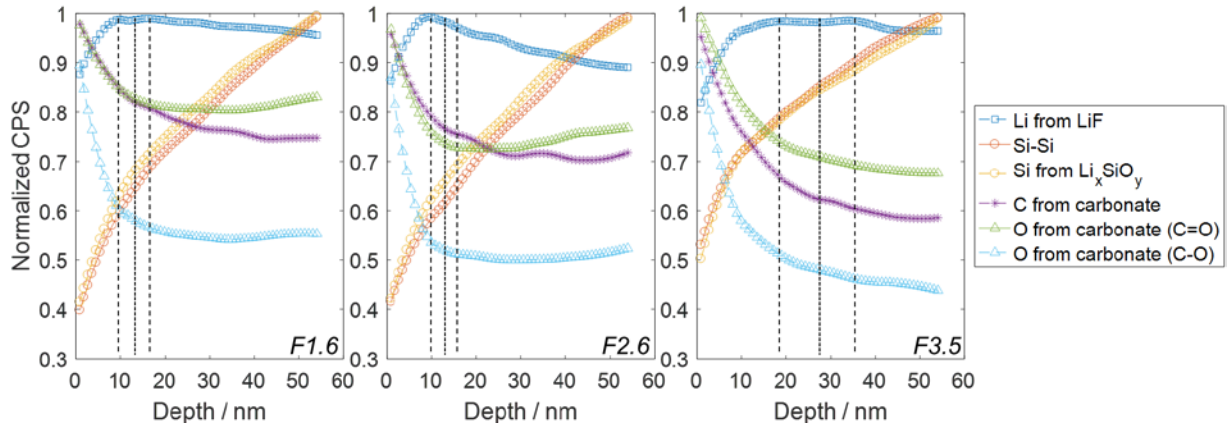

Figure II-35. Depth profiles of SEI (LiF and carbonates) and active material (Si-Si and Li_xSiO_y) elements. Black dashed and dotted lines are possible ranges of SEI/Si interface and averages of the ranges, respectively. The depth on x-axis was based on the assumption that the film has the same etching rate as SiO2. CPS of each element was normalized by its own maximum value.

The ranges of estimated SEI thicknesses were 9-16 nm for both F1.6 and F2.6, and 17-34 nm for F3.5. The estimated thickness of SEI at F3.5 is near the radius of the original Si particle (50-70 nm). The thick SEI layer is ascribed to Si because the SEI layers on pure graphite anodes without Si are only about 10 nm thick or less. [12] Since the electrochemical reactions for F1.6 were not uniform, the results from the F1.6 specimen only represent the dark (cycled) areas at which the local current density might have been higher. The SEI thickness increased significantly from F1.6 and F2.6 to F3.5. This increase can happen when an SEI layer on an electrode is not electronically insulating or insufficiently dense to prevent electrolyte diffusion towards the electrode surface. In either case the electrolyte continuously decomposes. This result agreed well with SEM images showing larger SEI precipitations at F3.5 than F1.6. On the other hand, the surface film (SEI) resistance of F1.6 from the EIS analysis was higher than that of F3.5, which seems inconsistent with SEM and XPS results. This apparent contradiction can be explained if the SEI is porous. A porous SEI would appear in EIS as a part of the ohmic resistance rather than the surface film resistance. Considering all of the results from EIS, SEM, and XPS, larger electrolyte volume formed thicker SEI layers with some porosity or channels/cracks. The thickness of the SiO_2 layer on Si was not estimated since Li_xSiO_y continuously increased like Si-Si during the depth analysis, which implies that the SiO_2/Si interface was not sharply delineated. Instead, it is possible that Li_xSiO_y was present throughout the Si particles because its CPS even increased continuously at the depth of original diameter of the silicon particle (50 - 70 nm). The spherical shape of silicon particle probably changed to rough shapes, larger surface area, after large volume changes during cycling. The irregularly expended silicon surfaces after lithiation might partially cover Li_xSiO_y and leave or trap it in the inner surfaces during contraction. If this repeats, Li_xSiO_y can be found in side of the silicon although the silicon may not cover it entirely.

The non-uniform SEI was verified from the Si2p peaks in Figure II-36a (0 nm depth) and Si atomic percentages in Figure II-36b. Si^0 (99.6 eV for Si 2p) was clearly detected from the top surfaces of the anode, especially at F3.5, implying SEI did not cover the Si particle surfaces uniformly. It should be noted that the electron escape depth is only 5−10 nm beneath the anode surface. Hence, Si^0 was present not only under the SEI but also on top of the SEI or near the top surface. In Figure II-36a, Li 1s, O 1s and P 2p peaks indicated the amount of dense lithium compounds (e.g., LiF, Li_2O, Li_2CO_3) increased as the analysis depth approached the SEI/Si interface. C 1s, O 1s, and P 2p peaks showed polymeric carbonates and phosphorus compounds mostly distributed in the outer surface of the SEI. The graphite peak intensity (284.5 eV) was not clear after 100 cycles, which also happened in another study. [9] According to the results of XPS survey scans from the top surface (before sputtering) (Figure II-36b), F3.5 showed a higher ratio of carbonate compounds

(C 1s and O 1s) and lower ratio of Li compounds (Li 1s) than F1.6 and F2.6. Hence, F3.5 might have a higher ratio of polymeric compounds than the lower electrolyte volume factor groups.

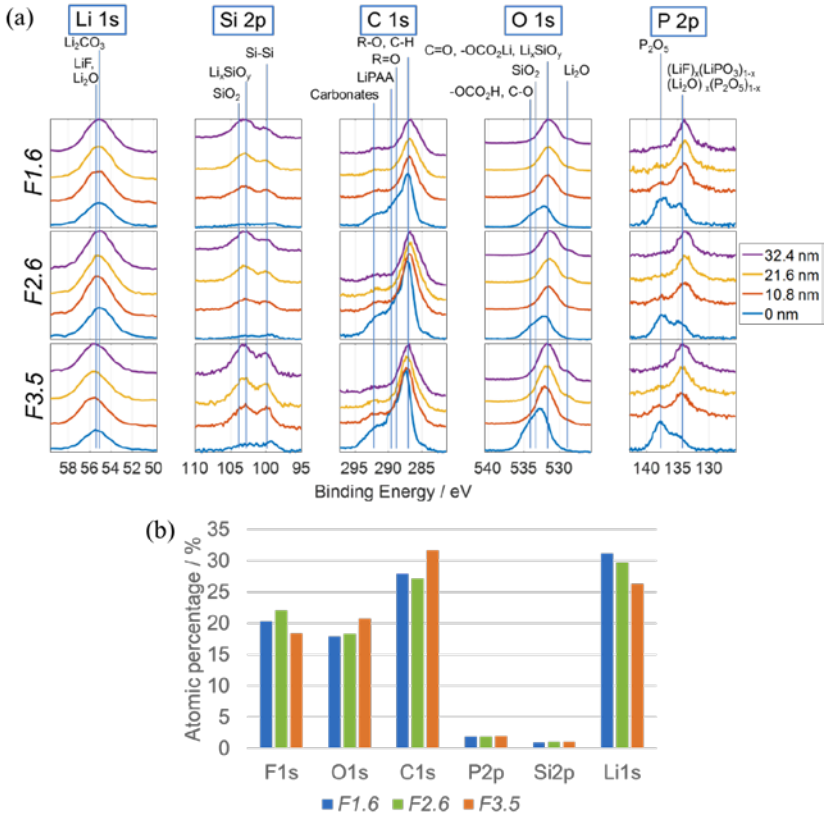

Figure II-36. (a) XPS peaks from depth profiles of F1.6, F2.6, and F3.5 and (b) atomic percentages from the top surface (before sputtering) from XPS survey scans. Depth was calculated based on the sputter rate for SiO2.

In summary, the electrolyte volume effects were investigated with lithium ion batteries in pouch format with 15 wt.% Si-graphite as the anode and $LiNi_{0.5}Mn_{0.3}Co_{0.2}O_2$ (NMC532) as the cathode. The electrolyte was 90 wt.% 1.2 M $LiPF_6$ in EC:EMC with 10 wt.% FEC. This work determined a baseline condition for electrolyte volume when integrating Si into graphite anode, which provided insights on practical cell and pack design. The electrolyte volume to total pore volume needs to be at least 3.1 to achieve the best performance. However, the optimized capacity retention in this study was still lower than that of cells with pure graphite anodes without silicon. Less electrolyte resulted in higher ohmic resistance, larger cell-to-cell capacity variation, and greater capacity fade. HPPC tests demonstrated the lowest resistance for the volume factor 3.1 and 3.5 groups, followed by 2.6, 2.1, and 1.6. For the volume factor 1.6, lithium dendrites were found on the anode surface after cycling. Unlike typical full cells having graphite anodes, significant anode charge transfer resistances were detected in EIS measurements and became more pronounced as the cell voltage decreased. Irreversible capacity loss also continuously increased in all factor groups as cells were cycled. SEM and EDS analysis showed that SEI covering the active particles was bulkier for the volume factor 3.5 compared to 1.6. SEI formed thicker layers on Si-rich areas compared to graphite-rich areas. XPS results also showed SEI thicknesses around 10 to 35 nm after 100 cycles, and the SEI thickness increased as the electrolyte volume factor increased. The XPS elemental analysis along the depth of anode indicated that LixSiOy formed throughout the Si particles rather than just as a surface layer. Considering all of the results from EIS, SEM, and XPS, it was found that the SEI on Si has large pores or channels that are permeable to electrolyte.

Thermodynamic Understanding and Abuse Performance (SNL)

As we develop new materials to increase performance of lithium ion batteries for electric vehicles, the impact of potential safety and reliability issues become increasingly important. In addition to electrochemical performance increases (capacity, energy, cycle life, etc.), there are a variety of materials advancements that can be made to improve lithium-ion battery safety. Issues including energetic thermal runaway, electrolyte decomposition and flammability, anode SEI stability, and cell-level abuse tolerance behavior. Introduction of a next generation materials, such as a silicon-based anode, requires a full understanding of the abuse response and degradation mechanisms for these anodes. This work aims to understand the breakdown of these materials during abuse conditions in order to develop an inherently safe power source for our next generation electric vehicles.

The effect of materials level changes (electrolytes, additives, silicon particle size, silicon loading, etc.) to cell level abuse response and runaway reactions will be determined using several techniques. Experimentation will start with base material evaluations in coin cells and overall runaway energy will be evaluated using techniques such as differential scanning calorimetry (DSC), thermogravimetric analysis (TGA), and accelerating rate calorimetry (ARC). The goal is to understand the effect of materials parameters on the runaway reactions, which can then be correlated to the response seen on larger cells (18650). Experiments conducted showed that there was significant response from these electrodes. Efforts to minimize risk during testing were taken by development of a smaller capacity cylindrical design in order to quantify materials decision and how they manifest during abuse response.

The effect of materials level changes (electrolytes, additives, silicon particle size, silicon loading, etc.) to cell level abuse response and runaway reactions will be determined using several techniques. Experimentation will start with base material evaluations in coin cells and overall runaway energy will be evaluated using techniques such as differential scanning calorimetry (DSC), thermogravimetric analysis (TGA), and accelerating rate calorimetry (ARC). The goal is to understand the effect of materials parameters on the runaway reactions, which can then be correlated to the response seen on larger cells (18650). Experiments conducted showed that there was significant response from these electrodes. Efforts to minimize risk during testing were taken by development of a smaller capacity cylindrical design in order to quantify materials decision and how they manifest during abuse response.

This work continues the efforts from last year, which aimed to evaluate electrochemical and abuse response for electrodes provided from the CAMP facility at Argonne National Laboratory. This included evaluation of anodes containing between 0 and 15 wt% silicon from NanoAmor. Investigations were completed on coin cell and 1.25 Ah 18650 form factors. Several experiments showed a high level of gas generation and overall runaway for cells containing silicon electrodes. To further understand the response of these materials, this work focused on understanding the effect of several factors to runaway response and gas generation including solvent selection, electrode processing, silicon content, and the effect of water. The primary reaction believed to be resulting in significant contribution to runaway reaction is the water reaction. This is particularly interesting in systems using polyacrylic acid (PAA) binders as one of the products during degradation of PAA is water, which could lead to increase runaway energetics. During degradation of PAA, water is evolved at the expected temperature of 100°C as well as a second peak around 250°C, which is presumably from polymer degradation reactions.

In order to investigate the effect of binder during runaway, electrodes were prepared with several processes to identify the contribution to overall runaway enthalpy based upon water content during processing and during high temperature breakdown. Figure II-37 shows the electrodes used to evaluate runaway energetics. Electrodes were made with nanoamor 70-130 nm silicon, Hitachi Mag-E graphite, Timcal C45 carbon, and several different binders in weight percentage ratios of 15/73/2/10 respectively. Electrodes parameters were 45 µm thickness, 45% porosity, and areal capacity of 1.9 mAh/cm^{-2}.

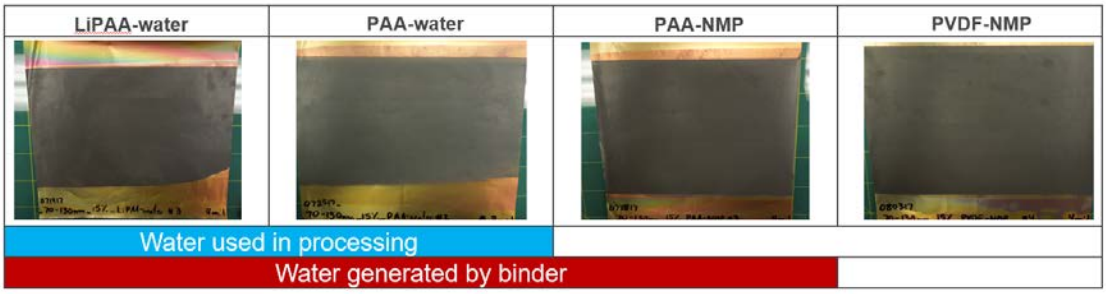

Figure II-37. Prepared electrodes processed with water (blue) and that will have water present during runaway reactions (red) in comparison to normal non-aqueous systems (right).

Coin cells were assembled and formation cycling was conducted on all electrodes. After 5 cycles, each cell was held at 100% state of charge and disassembled for differential scanning calorimetry (DSC) to evaluate the head generated during thermal abuse conditions. Each sample had an additional amount of electrolyte added to make a 1:1 wt% ratio between active material and electrolyte. All cells performed similarly under formation conditions, as seen in Figure II-38 left, with the exception of the PVDF, which was expected as it is known to be a slightly lower performing binder for the silicon system. DSC results can be seen in Figure II-38 right, which all show similar responses with a slight exotherm around 225°C with full material runaway occurring near 275°C.

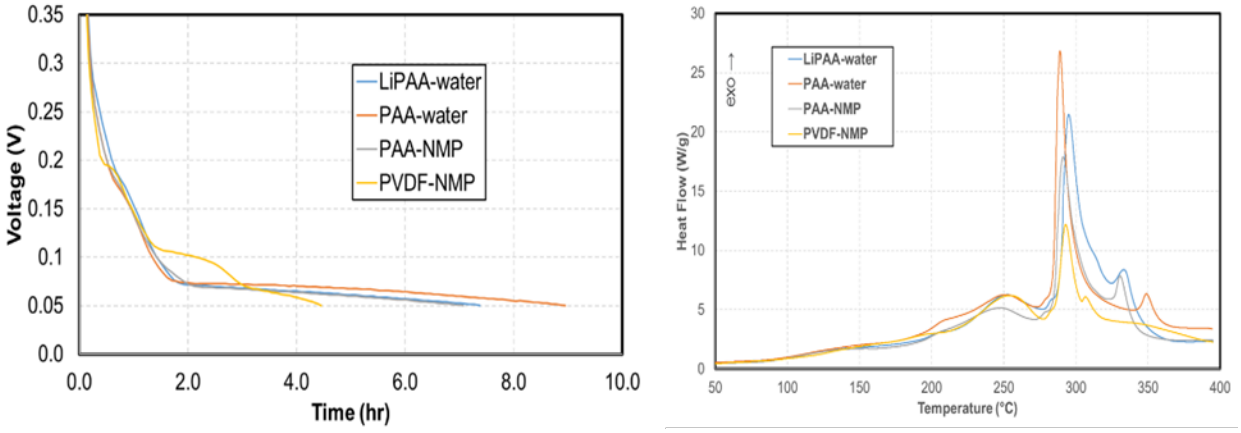

Figure II-38. (left) Half-cell formation lithiation. (right) DSC results from extracted material.

Normalization of heat flow to mass of active material shows fairly consistent results for overall runaway energy of between 40 - 55 W/Ah peak heating rates. While the reaction with water, both residual from processing and produced during runaway, plays a role in runaway it is not the sole contributing factor. Previous work has shown clear correlations to silicon content, silicon particle size, and state of charge.

Full cells were built using the 0, 5, 10, and 15 wt% silicon electrodes and built into 18650 format cells for larger cell evaluation of decomposition and abuse response. To mitigate potential safety issues, electrodes were made to be approximately half the normal length for construction into an 18650 cell. The resulting void volume within the case was taken up by either a tube of copper or a length of current collector foil wrapped to make the right jelly roll diameter. Either case, the extra copper component was then attached to the copper current collector of the anode to ensure proper electrical continuity to the negative case. All cells were formed with five formation cycles, held at 100% SOC, and then evaluated using ARC.

No clear trend was observed for electrodes of half-length using both extra current collector (Figure II-39, yellow and blue) or solid copper tubing inserts (Figure II-39, green and pink). To make sure that the differences seen were not due to residual electrolyte degradation for extended periods of time, inspection of ARC data between 50 and 150°C shows no appreciable difference between the two cells types, as seen in Figure II-39, right panel.

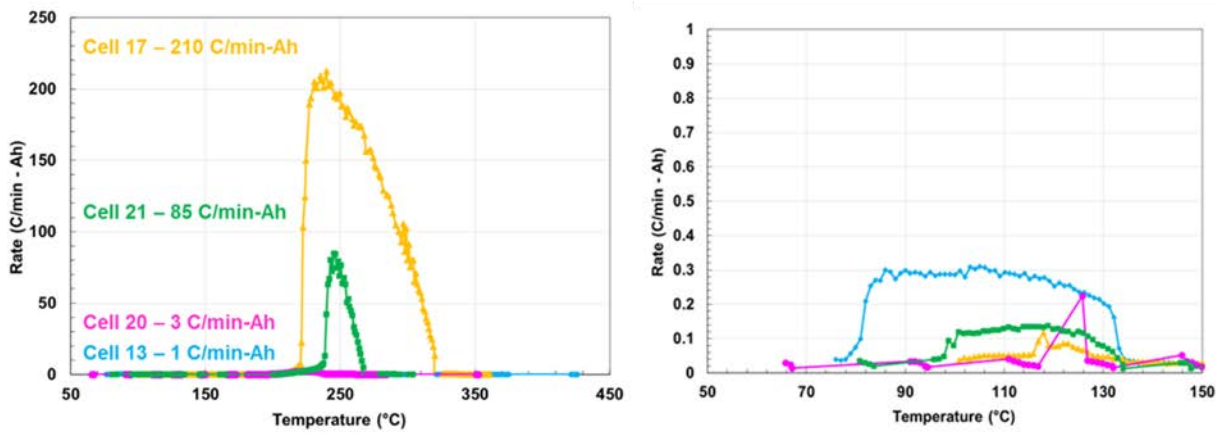

Figure II-39. ARC evaluations for several sample 18650 cells containing undersized electrodes.

During ARC evaluations, a gas samples system was assembled that would actuate a valve at 275ºC to open and take a grab sample of vapor. This would then allow for isolation after full runaway of the cell, which was sent for gas sampling evaluation and chemical analysis. This was done for baseline NMC 523 vs Conoco Phillips G8 graphite using a standard sample bottle, 15 wt% Nanoamor silicon using a standard sample bottle, and 15 wt% Nanoamor silicon using a cleaned and sealed sample vial. Figure II-40 shows the results of analysis for organic components (Figure II-40A), hydrocarbons (Figure II-40B), and gases (Figure II-40C).

The primary differences seen in the gas sampling data are that there is a significantly larger amount of ethanol in the baseline samples without silicon but a significantly larger amount of ethane in the samples that do contain silicon. This is particularly interesting in light of the significant gas generation seen previously for larger cells evaluated with ARC. These evaluations were done by an independent lab, which requires transportation time for the samples. Many of the reactive species that could be present during cell runaway are likely to have already reacted in this scenario. Efforts will continue to work towards the ability to analyze gas generation in real time for a more complete understanding of reaction chemistry during runaway for these next generation materials.

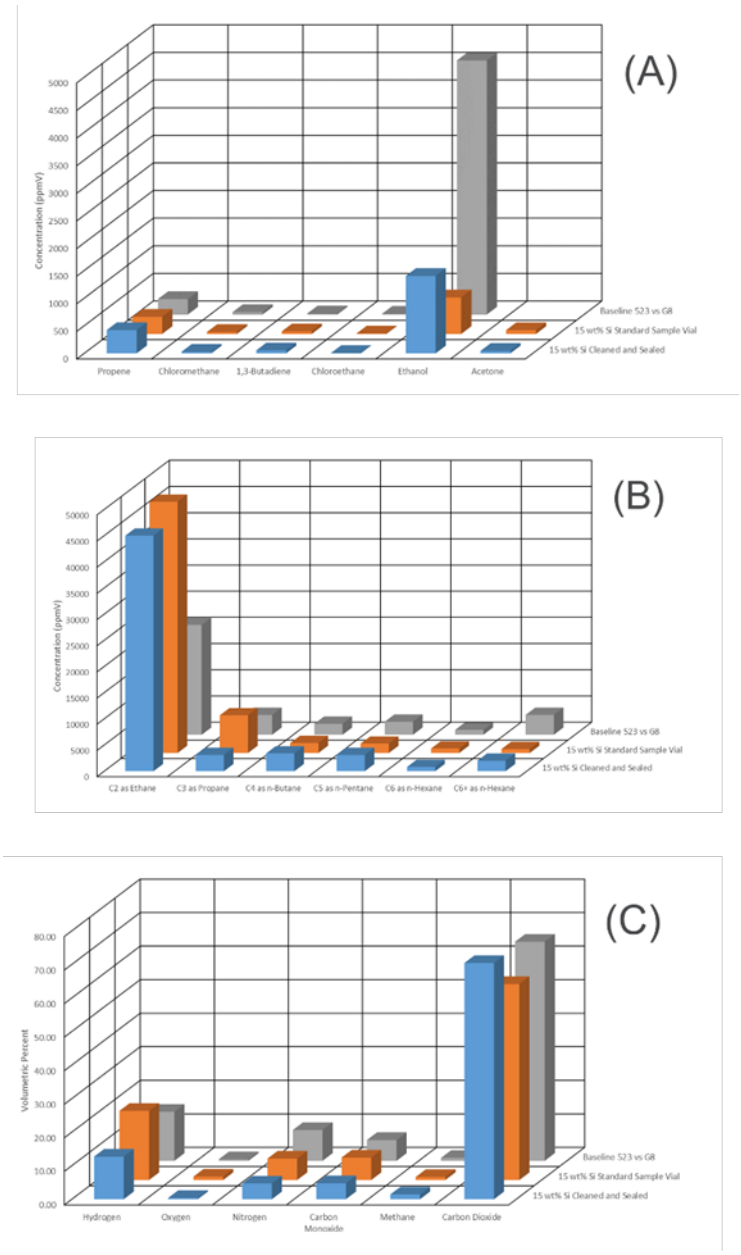

Figure II-40. Gas sampling results for electrodes containing baseline G8 graphite and 15 wt% silicon using both standard sample vials and cleaned and sealed bottles. Data is shown for analysis completed on organic species (A), hydrocarbons (B), and gases (C).

Conclusions

Recent efforts to develop new baseline electrodes have identified a promising U.S. silicon supplier, Paraclete Energy, as a source for silicon materials. Paraclete has provided multiple samples for evaluation and screening. Encouraging aspects of working with Paraclete Energy are that they have demonstrated their ability to control particle size and customize processing steps to target surface chemistries. Electrochemical data is comparable to our best electrode performance and more importantly the silicon source provides a dependable and repeatable silicon powder from batch to batch.

Water-based processing studies of silicon containing anodes have identified the reaction of silicon with water as a degradation mechanism that can lead to processing issues and impact final electrode performance. These include significant hydrogen generation during processing and conversion of silicon to silica on the silicon particle surface. Further, the role of electrode drying temperature on anode performance was examined in detail. Electrodes cast in water (LiPAA binder) with lower residual water content cycle better than the NMP cast PAA electrodes (with higher water content). Interestingly, the PAA performance is dramatically influenced by drying temperature. This is consistent with the previous TGA data which showed significant water loss above 140ºC due to dehydration. At higher temperatures, the decomposition of the PAA produces a far worse binder.

The electrolyte volume effects were investigated with lithium ion batteries in pouch format using baseline electrodes. The relationship between electrolyte volume, electrochemical performance, and properties of the solid electrolyte interphase in pouch cells with Si-graphite composite anodes and NMC532 cathodes was examined. We conclude that a minimum electrolyte volume factor of 3.1 times the total pore volume of cell components (cathode, anode, and separator) is needed for better cycling stability. Less electrolyte causes increases in ohmic and charge transfer resistances. Lithium dendrites are observed when the electrolyte volume factor is low. The resistances from the anodes become significant as the cells are discharged. However, solid electrolyte interphase thickness grows as the electrolyte volume factor increases and is non-uniform after cycling.

Thermodynamic understanding and abuse performance studies demonstrate that there is an impact on safety response with nanoscale silicon materials compared to graphite-based anodes. Changes to material and cell level properties can have impact on safety and thermal response characteristics. We have reported thermal runaway properties of cells (coin cells and cylindrical cells) containing nanoscale silicon up to 15 percent by weight. We continue to develop the understanding of abuse response for these anodes to better understand how these next generation negative electrode materials will impact cell and battery-level abuse tolerance.

Key Publications

1. Eric Allcorn, Ganesan Nagasubramanian, Kyle Fenton. "Materials Safety Study of Practical Nano-Silicon + Graphite Anodes for Lithium-Ion Batteries." Prime 2016, Honolulu, HI, Oct. 2 - 7, 2016.
2. Kyle Fenton, Chris Orendorff, Ganesan Nagasubramanian, Josh Lamb, Eric Allcorn. "Impact of next Generation Electrode Materials on Abuse Response." Prime 2016, Honolulu, HI, Oct. 2 - 7, 2016.
3. L, Zhang, Y. Liu, B. Key, S. E. Trask, Z. Yang and W. Lu, " Si nanoparticles: stability in aqueous slurries and the optimization of oxide layer thickness for optimal electrochemical performance", submitted.
4. L. Zhang, Y. Liu, S.E. Trask, Z. Yang and W. Lu, "Silicon and silicon monoxide as the anode for lithium-ion batteries", presentation given at energy storage seminar at Argonne National Laboratory, January 2017.
5. L. Zhang, Y. Liu, S.E. Trask, Z. Yang and W. Lu, "Silicon and silicon monoxide as the anode for lithium-ion batteries", invited talk given at University of Loyola Chicago, January 2017.
6. L. Zhang, Y. Liu, S.E. Trask, Z. Yang and W. Lu, "The effect of oxide layer thickness on the electrochemical performance of silicon anode for lithium-ion batteries", selected talk given at Gordon research seminar, March 2017.
7. L. Zhang, Y. Liu, S.E. Trask, Z. Yang and W. Lu, "The effect of oxide layer thickness on the electrochemical performance of silicon anode for lithium-ion batteries", poster given at Gordon research seminar and Gordon research conference, March 2017.

8. L. Zhang, Y. Liu, S.E. Trask, Z. Yang and W. Lu, "Optimization of oxide layer thickness for silicon as the anode for lithium-ion batteries", CSE postdoc seminar at Argonne National Laboratory, May 2017.
9. "Next Generation Anodes for Lithium-Ion Batteries: Overview," 2017 U.S. Department of Energy Vehicle Technologies Office Annual Merit Review and Peer Evaluation Meeting, June 5-9, 2017, Washington, DC.

References

1. *Alloy Negative Electrodes for Li-Ion Batteries*. M.N. Obrovac and V.L. Chevrier, Chem, Rev. 2014, 114, 11444-11503.
2. *Modeling the Performance and Cost of Lithium-Ion Batteries for Electric-Drive Vehicles*. Second Edition, Argonne National Laboratory Report, ANL-12/55.
3. *Performance of Full Cells Containing Carbonate-Based LiFSI Electrolytes and Silicon-Graphite Negative Electrodes.* S.E. Trask, K.Z. Pupek, J.A. Gilbert, M. Klett, B.J. Polzin, A.N. Jansen, and D.P. Abraham, Journal of The Electrochemical Society, 163 (3) A345-A350 (2016).
4. Yoshida, S.; Masuo, Y.; Shibata, D.; Haruta, M.; Doi, T.; Inaba, M., Adsorbed Water on Nano-Silicon Powder and Its Effects on Charge and Discharge Characteristics as Anode in Lithium-Ion Batteries. *J. Electrochem. Soc.* **2017,** *164*, A6084-A6087.
5. Buchholz, F. L.; Graham, A. T., *Modern Superabsorbent Polymer Technology*. Wiley-VCH: 1997.
6. McNeill, I. C.; Sadeghi, S. M. T., Thermal Stability and Degradation Mechanisms of Poly(Acrylic Acid) and its Salts: Part 1 Poly(Acrylic Acid). *Polym. Degrad. Stabil.* **1990,** *29*, 233-246.
7. McNeill, I. C.; Sadeghi, S. M. T., Thermal Stability and Degradation Mechanisms of Poly(Acrylic Acid) and its Salts,: Part 2 Sodium and Potassium Salts. *Polym. Degrad. Stabil.* **1990,** *30*, 213-230.
8. An, S. J.; Li, J.; Daniel, C.; Meyer, H. M.; Trask, S. E.; Polzin, B. J.; Wood, D. L., Electrolyte Volume Effects on Electrochemical Performance and Solid Electrolyte Interphase in Si-Graphite/NMC Lithium-Ion Pouch Cells. *ACS Applied Materials & Interfaces* **2017,** *9*, 18799-18808.
9. Bareño, J.; Shkrob, I. A.; Gilbert, J. A.; Klett, M.; Abraham, D. P., Causes and Mitigation of Capacity Fade in NCM523/Si-Gr Lithium-ion Cells. *J. Electrochem. Soc.* **2017**, Under review.
10. Philippe, B.; Dedryvère, R.; Allouche, J.; Lindgren, F.; Gorgoi, M.; Rensmo, H.; Gonbeau, D.; Edström, K., Nanosilicon Electrodes for Lithium-Ion Batteries: Interfacial Mechanisms Studied by Hard and Soft X-ray Photoelectron Spectroscopy. *Chem. Mater.* **2012,** *24*, 1107-1115.
11. Nie, M.; Abraham, D. P.; Chen, Y.; Bose, A.; Lucht, B. L., Silicon Solid Electrolyte Interphase (SEI) of Lithium Ion Battery Characterized by Microscopy and Spectroscopy. *J. Phys. Chem. C* **2013,** *117*, 13403-13412.
12. An, S. J.; Li, J.; Sheng, Y.; Daniel, C.; Wood III, D. L., Long-Term Lithium-Ion Battery Performance Improvement via Ultraviolet Light Treatment of the Graphite Anode. *J. Electrochem. Soc.* **2016,** *163*, A2866-A2875.
13. An, S. J.; Li, J.; Mohanty, D.; Daniel, C.; Polzin, B. J.; Croy, J. R.; Trask, S.; Wood, D. L., Correlation of Electrolyte Volume and Electrochemical Performance in Lithium-ion Pouch Cells with Graphite Anodes and NMC532 Cathodes. *J. Electrochem. Soc.* **2017,** *164*, A1195-A1202.

14. Young, B. T.; Heskett, D. R.; Nguyen, C. C.; Nie, M.; Woicik, J. C.; Lucht, B. L., Hard X-ray Photoelectron Spectroscopy (HAXPES) Investigation of the Silicon Solid Electrolyte Interphase (SEI) in Lithium-Ion Batteries. *ACS Appl Mater Interfaces* **2015,** *7*, 20004-20011.

15. Philippe, B.; Dedryvère, R.; Gorgoi, M.; Rensmo, H.; Gonbeau, D.; Edström, K., Role of the LiPF6Salt for the Long-Term Stability of Silicon Electrodes in Li-Ion Batteries – A Photoelectron Spectroscopy Study. *Chem. Mater.* **2013,** *25*, 394-404.

II.B.2 Next Generation Anodes for Lithium-Ion Batteries: Characterization, Diagnostics, and Analysis (ANL)

Dennis Dees, Principal Investigator
Argonne National Laboratory
9700 South Cass Avenue
Argonne, IL 60439
Phone: 630-252-7349
E-mail: dees@anl.gov

Peter Faguy, Technology Manager
U.S. Department of Energy
Phone: 202-586-1022
E-mail: Peter.Faguy@ee.doe.gov

Start Date: October 1, 2015 End Date: September 30, 2019
Total FY17 Project Cost: $3,600,000 DOE FY17 share: $3,600,000 Non-DOE share: $0

Project Introduction

Silicon has received significant attention as a viable alternative to graphitic carbon as the negative electrode in lithium-ion batteries due to its high capacity and availability [1]. Elemental silicon can theoretically store >3500 mAh/g, nearly an order of magnitude higher than graphite (372 mAh/g and 818 mAh/mL, respectively). However, several problems have been identified that limit its utility including large crystallographic expansion (~320%) upon lithiation which translates to particle cracking, particle isolation, and electrode delamination issues. Further, there are fundamental and volume change related SEI stability issues, which affect cycling efficiency. The wealth of previous studies in this area is both a testament to its potential and the size of the challenge that must be overcome, requiring a great amount of innovation on multiple fronts.

Next Generation Anodes for Lithium-Ion Batteries, also referred to as the Silicon Deep Dive Program, is a five National Laboratory consortium assembled to tackle the barriers associated with development of an advanced lithium-ion negative electrode based upon silicon as the active material. This research program baselines promising silicon materials that can be developed or obtained in quantities sufficient for electrode preparation within the consortium facilities. Composite electrode and full cell development leverages recent investments made by DOE-EERE-VTO in electrode materials and characterization. The primary objective of this program is to understand and eliminate the barriers to implementation of a silicon-based anode in lithium-ion cells. The Labs are focused on a single program with continuous interaction, clear protocols for analysis, and targets for developing both the understanding and cell chemistry associated with advance negative electrodes for lithium-ion cells. First and foremost, this undertaking is a full electrode/full cell chemistry project leveraging baseline electrodes prepared at the consortium facilities. All efforts are directed to understanding and developing the chemistry needed for advancing silicon-based anodes operating in full cells. Materials development efforts include active material development, binder synthesis, coatings, safety, and electrolyte additives. Efforts include diagnostic research from all partners, which span a wide range of electrochemical, chemical and structural characterization of the system across length- and time-scales. Specialized characterization techniques developed with DOE-EERE-VTO funding, include neutrons, NMR, optical, and X-ray techniques being employed to understand operation and failure mechanisms in silicon-based anodes. In addition, several strategies to mitigate lithium loss are being assessed. The project is managed as a single team effort spanning the Labs, with consensus decisions driving research directions and toward development of high-energy density lithium-ion batteries. A detailed list of participants is given in Figure II-41.

Figure II-41. Program participants including Laboratories, research facilities, and individual contributors.

Objectives

- Understand and overcome the science and technology barriers to the use of silicon-based anodes in high-energy density lithium-ion batteries for transportation applications.
  - Stabilize the SEI
  - Stabilize the electrode
- Demonstrate functional prototype lithium-ion cell chemistries which meet the DOE/USABC performance targets.

Approach

Sandia National Laboratories (SNL), Oak Ridge National Laboratory (ORNL), National Renewable Energy laboratory (NREL), Lawrence Berkeley National Laboratory (LBNL), and Argonne National Laboratory (ANL) have teamed together to form an integrated program. Technical targets have been developed and regular communications have been established. Throughout the program, there is a planned focus on understanding, insights into, and advancement of silicon-based materials, electrodes, and cells. All anode advancements will be verified based on life and performance of full cells. Toward that end, baseline silicon-based materials, electrodes, and cells have been adopted, along with full cell testing protocols.

The fundamental understanding of silicon-based electrode active materials is based on extensive electrochemical and analytical diagnostic studies on components, electrodes, and cells conducted within the program. This effort contains in-situ and ex-situ studies on full and specialty cells, including reference electrode cells. Overall, the diagnostic studies are intended to help establish structure-composition-property relationships, including lithium-alloying surface and bulk transport and kinetic phenomena. Further, they

should form the basis for accurately assessing component and electrode failure modes and lay a path for advancements.

Communication of programmatic progress to battery community is critical. This will generally be accomplished through publications, presentations, reports, and reviews. Further, the program is open to industrial participation and/or collaboration that does not limit program innovation or the free flow of information. Finally, this program is highly integrated with our sister program on SEI-Stabilization, called SEI-Sta for short. In general, SEI-Sta is focused on the development and characterization of model systems, thin-film well-defined active area electrodes on which it is easier to extract fundamental information on lithium-silicon phase formation, lithium transport, and interfacial phenomena (e.g., SEI formation and growth).

Results

Characterization of Si from NMP and water-based slurries (ORNL)

Si slurry was collected from the mixing vessels in both water and NMP experiments. The slurries were dried and the powders were collected for X-ray, ATR FTIR and NMR characterization studies. Figure II-42 shows comparison X-ray diffraction data collected for the Si before and after processing. From this data one notices a significant broadening of the Si peak after milling in water due to the decrease in Si particle sizes from 71 nm to 53 nm. Smaller changes are observed in NMP processed electrodes. This means that the observed gassing reaction is actively consuming the silicon in the nanoparticles. This is critical because the loss of silicon, and the resulting formation of an oxide coating reduces the theoretical capacity of the electrode.

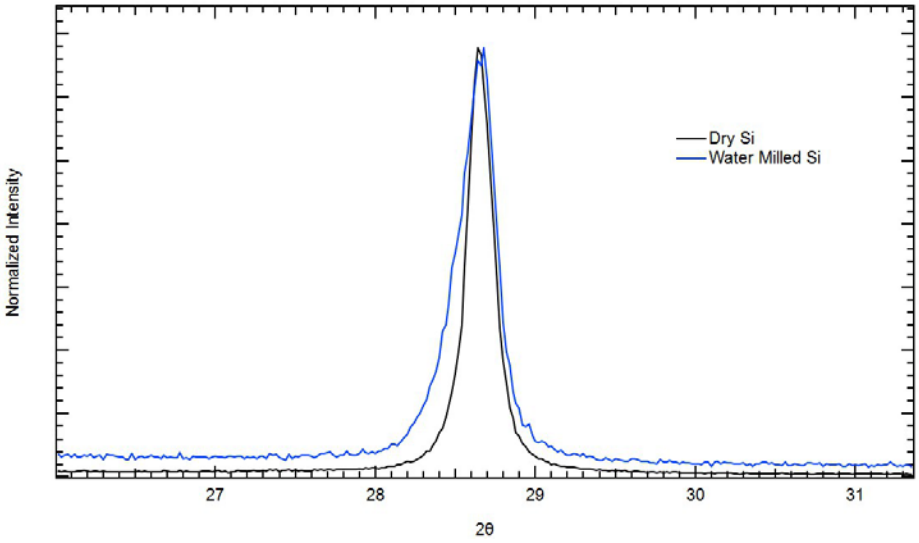

Figure II-42. Powder X-ray diffraction data collected for the raw and post-processed silicon powders.

In collaboration with Baris Key (ANL) the silicon was further with ^{29}Si NMR to determine the difference in the elemental Si to SiO_x ratio (Figure II-43). Figure II-43-Top shows the intensity of the NMR spectra was normalized to a shift at -120 ppm relating to SiO_X. A decrease in the Si peak at -80 ppm indicates more Si was converted to SiO_x during processing. NMP processed Si showed the least SiO_x production, while water processed showed the most consistent with the X-ray data. Interestingly aqueous-based LiPAA proved effective in passivating most of the additional oxidation of the silicon caused by water processing pointing to an interesting processing pathway which may yield more reproducible electrodes. ^{1}H-^{29}Si cross polarization NMR was used to observe differences in the surface environment of water processed Si against Si milled free of any solvents (Figure II-43-Bottom). “Dry” Si has an abundance of Si-H and (SiO)2 – Si – (OH)2 (labeled Q2) coordinated sites, which disappear in the water processed sample. The Q3 and Q4 sites, which represent (SiO)3 – Si – (OH) and (SiO)4 – Si respectively remain relatively constant between both milling methods. This

result indicates that the processing changes the Si surface chemistry which will influence SEI formation and binder affinity in ways that have not been explored, but are proposed as future research directions depending on funding.

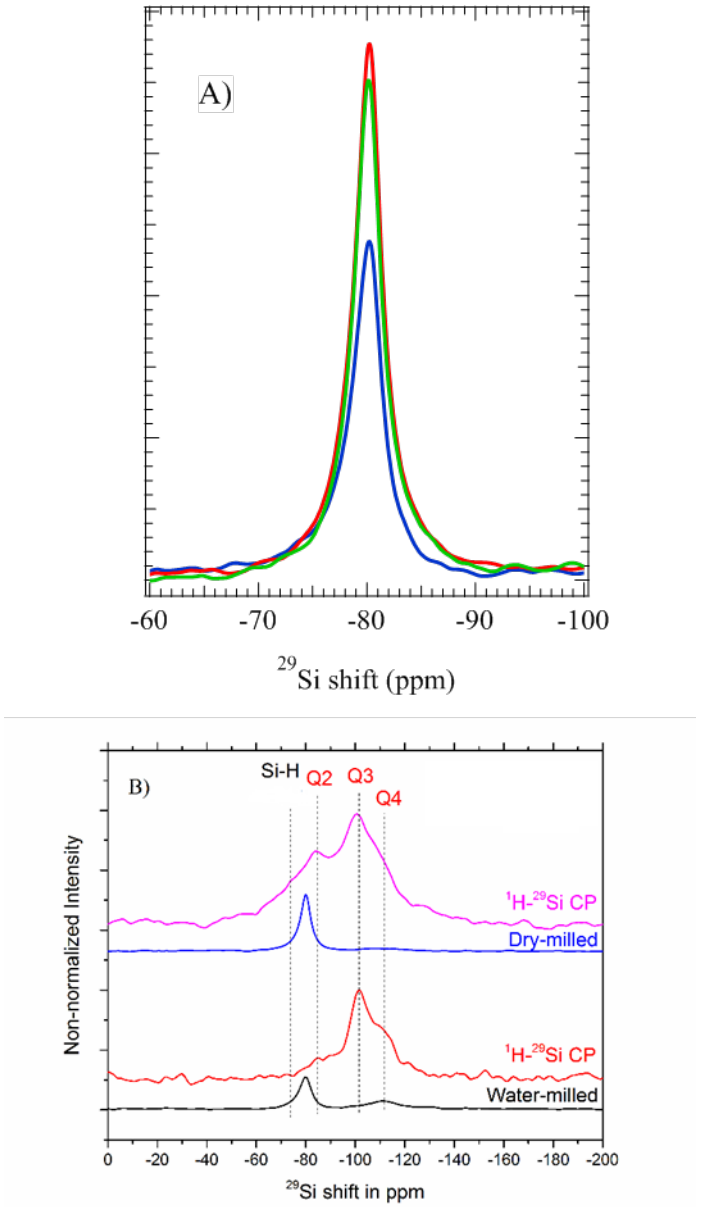

Figure II-43. (Top) ^{29}Si NMR of Nanoamor (70-130) Si powder processed in NMP (red trace), water with LiPAA binder (green trace), and water (blue trace). All spectra have been normalized to Si-O shift at -120 ppm. (Bottom) - ^{1}H-^{29}Si cross polarization NMR and accompanying ^{29}Si NMR of dry milled Si (fuchsia trace and blue trace) and water milled Si (red trace and black trace). Vertical lines designate Si coordinated sites.

There are also major differences in the FTIR absorbance spectra of the Si samples, Figure II-44. Each show the broad band of the Si-O-Si stretching in the range of 900 – 1200 cm^{-1}, but the NMP processed Si has additional bands absent in the water processed Si. Bands at 2900 cm^{-1}, 1275 cm^{-1}, and 880 cm^{-1} in the NMP processed Si can be linked to methyl groups on Si surface. Three intense bands in the NMP processed Si at 1670 cm^{-1}, 1580 cm^{-1}, and 1430 cm^{-1} have yet to be identified, but show there is a strong difference in the surface functionalization of these two Si powders. This result indicates that the processing changes the Si surface

chemistry which will influence SEI formation and binder affinity in ways that have not been explored, but are proposed as future research directions depending on funding.

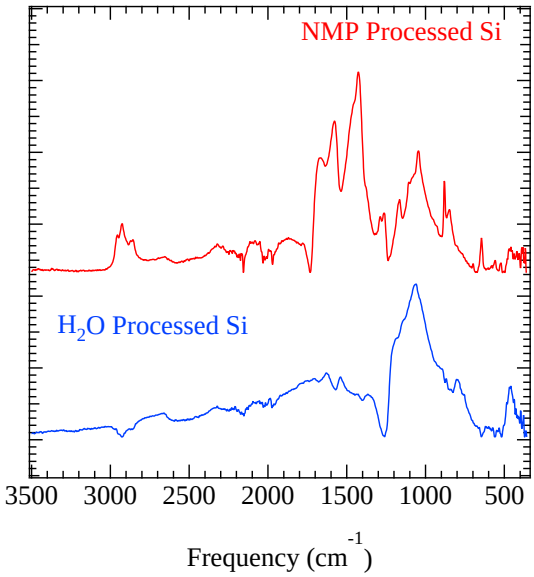

Figure II-44. Absorption spectrum from ATR-FTIR of NMP processed Si and water processed Si.

The selection of slurry solvent plays a major role in the performance of full cell batteries utilizing Si-graphite composite anodes. When completed in water, mixing needed to break up agglomerations of Si can result in additional oxidation. This can be minimized in NMP, but NMP radically changes the surface chemistry of the Si, the consequences of which are not fully understood. Also, the solvent can dictate the choice of binder, as LiPAA is not soluble in NMP. Though LiPAA-based Si-graphite electrodes must be coated using aqueous slurries, their respective full cell batteries still perform better than their NMP counterparts. PAA binder does not perform well because of its low degradation temperature, making it difficult to drive off all absorbed water. Furthermore, it is believed that this PAA is not electrochemical stable, slowly converting to LiPAA and contributing to a poor Coulombic efficiency. A better understanding of how slurry solvents interact with the surface of Si will be needed to further progress Si-based electrodes, as these functionalizations play a key role in binder selection and may change SEI contributions over long term electrochemical cycling.

NMR Studies of Composite Silicon Electrodes (ANL)

Solid state (NMR) have been instrumental in understanding lithiation and delithiation mechanism and SEI composition of silicon electrodes in the last decade [2-6]. The summarized results indicate formation of complex amorphous phase compositions upon lithiation of silicon and local formations of reactive overlithiated phases that lead to significant and complex side reactions in the electrolyte. The extent of these reactions, coupled with large volume changes, is believed to be responsible for poor cyclability of silicon electrodes.

The type of local order determines key electrochemical performance metrics in intermetallic anode systems such as silicon anodes. The study focused on characterization of the baseline commercial materials and their evolution and degradation on extended electrochemical cycling. Correlations between structure and activity relationships are drawn to help the team to optimize powders used in composite electrodes as well as detailed characterization of cycled electrodes to identify key reactions.

A multinuclear solid state NMR method has been used on pristine commercial silicon powders. Local 29Si, 13C, 1H, 7Li order is probed to gain comprehensive insights into pristine commercial powder compositions. By optimizing the 29NMR signal and quantification of the silicon content in elemental silicon and silicate

phases, average silicate shell thicknesses were estimated from NMR and results were found to corroborate well with complementary methods.

Solid State Magic Angle Spinning (MAS) NMR spectroscopy has also been used to qualitatively and quantitatively probe the silicon ordering in the pristine and treated powder samples. NMR spectroscopy has previously been shown to effectively resolve elemental silicon from silicates regardless of sample crystallinity [7]. Figure II-45 shows 29Si MAS NMR spectra collected for the pristine and treated powders. For each spectrum, the sharp resonance at -80 ppm is due to elemental silicon and the broad resonance at -110 ppm is assigned, according to literature [7], to amorphous SiO_2 on the outer shell (based on TEM and XRD findings) of largely spherical particles. With heat treatment, an increasing trend in the intensity of the -110ppm resonance was observed. Using the fully quantitative relative ratios of areas under the Si vs. SiO_2 resonances, the following average silicon molar contents have been extracted from spectra deconvolutions; 79:21 for pristine sample, 72:28 for 400ºC treated sample and 56:44 for 600ºC sample, respectively. Based on these ratios, an average of 6.1nm, 8nm and 12nm amorphous SiO_2 shells were estimated for pristine, 400ºC and 600ºC samples, respectively. The referenced paper also shows favorable electrochemical performance for the 400ºC sample over the baseline and 600ºC sample with a much thicker shell. It must be noted that NMR is an averaging bulk technique and perfectly spherical particles with 80nm diameters was assumed. Therefore it is possible to have an under or overestimation of the modelled thicknesses depending on the mean particle size distribution.

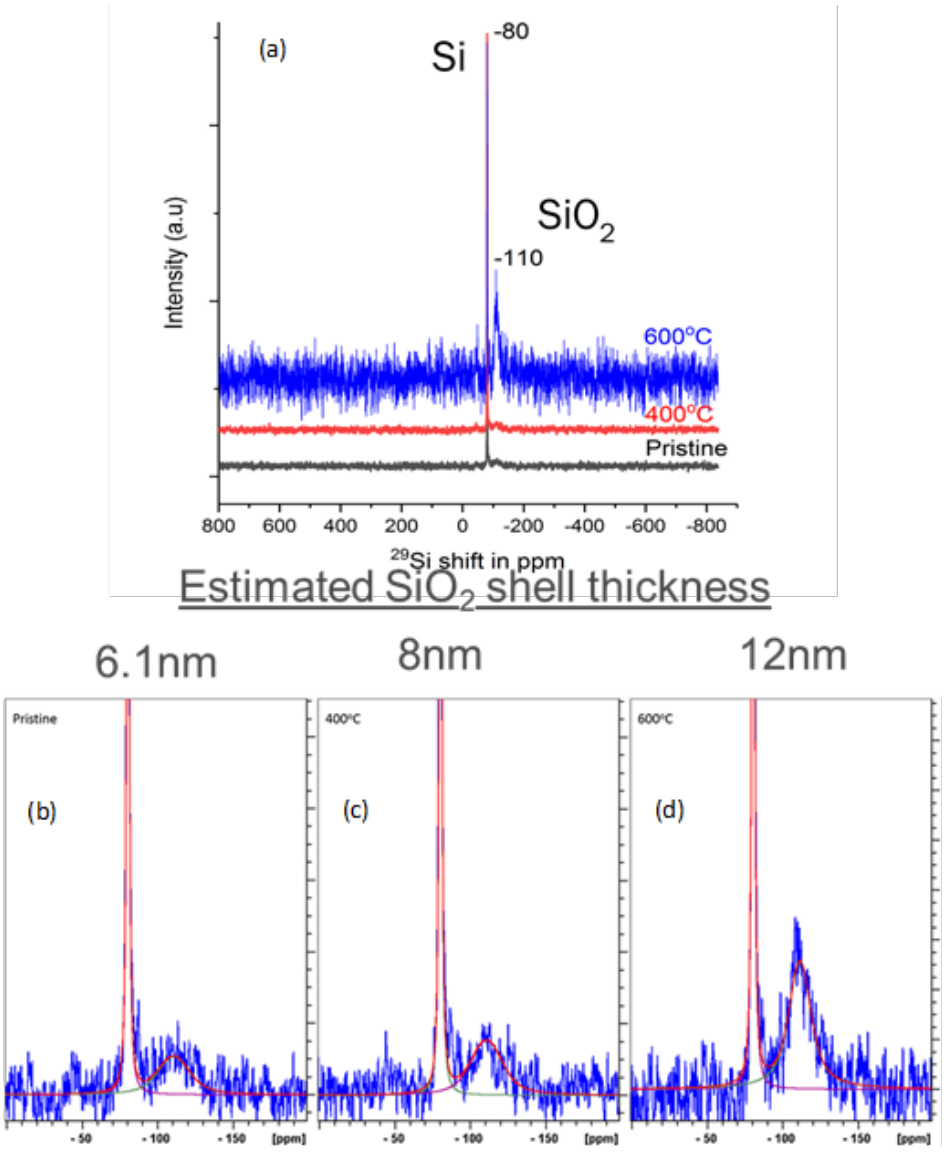

Figure II-45. 29Si MAS NMR and deconvolutions (b to d) of pristine and treated commercial HydroQuébec80nm silicon powders. (ANL, Linghong Zhang et al., ACS Applied Materials & Interfaces, 2017, just accepted manuscript)

When compared to other commercial powders such as NanoAmor 70-130nm or Paraclete silicon powders only slight variations in Si:SiO2 contents were found, the latter mainly correlated inversely with increasing average particle size. Different commercial batches, due to their production and processing variations vary in particle size distribution and morphology, and marginally in performance. The surface termination of the commercial powders mainly found to vary in -OHs and aliphatic proton content. The aliphatics were further confirmed by 1H-13C CP MAS NMR as shown in Figure II-46 for Paraclete and NanoAmor commercial powders. In addition, depending on manufacturer processing the "coating" on the particles contained hydroxly or ether organic groups, and in the case of NanoAmor powders, carbonyl and or ester groups. The CAMP full cell data on the Paraclete samples with varying "coatings" has been shown to demonstrate slightly different electrochemical performance metrics, with sample D performing marginally better. The stability of this surface treatment on the particles is currently under investigation. Furthermore, typical water treatment of the pristine commercial powders in electrode making, such as slurry making with LiPAA binder, has been shown to increase the thickness of the SiO_2 shell considerably (15-25%) while generating H_2 gas and negatively impacting electrode performance.

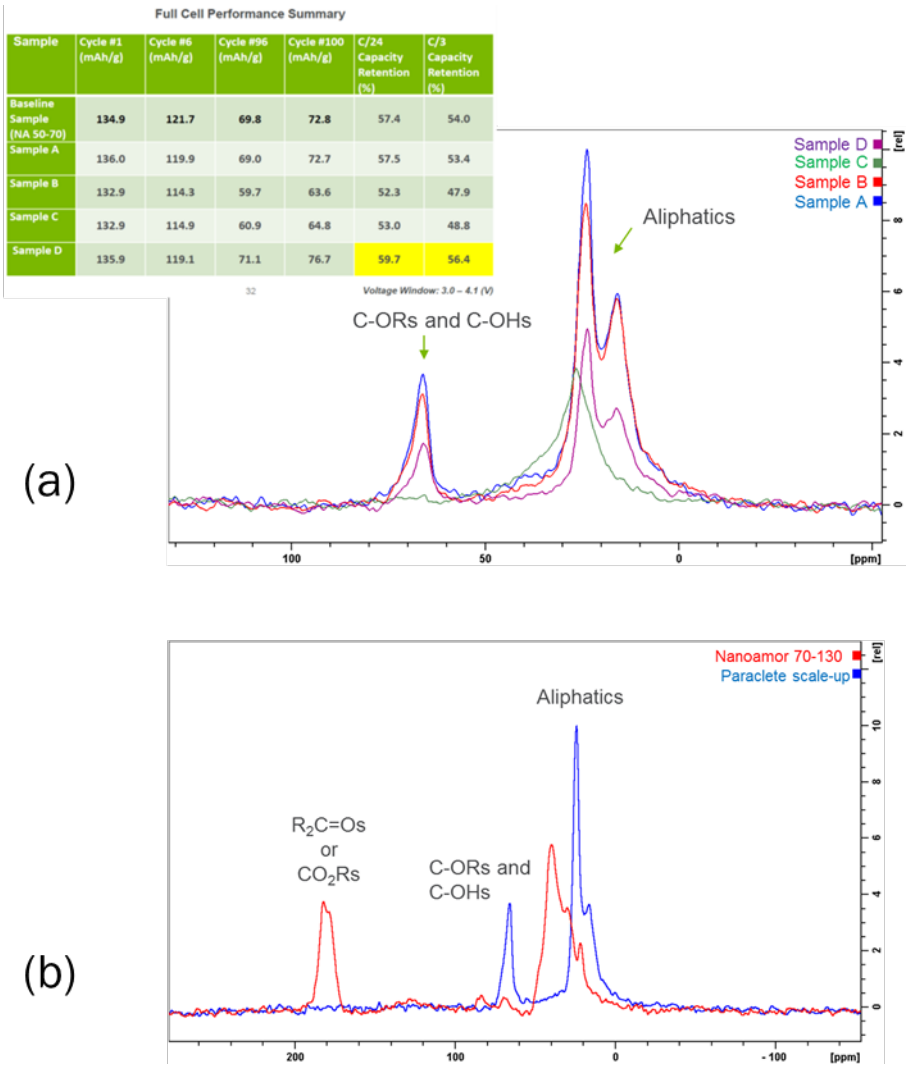

Figure II-46. (a) 1H-13C CP MAS NMR of Paraclete silicon powder batches and corresponding electrochemical performance metrics (b) 1H-13C CP MAS NMR of Paraclete powder and NanoAmor 70-130nm powder. (ANL, unpublished work)

Silicon Nanomaterials: Stability in Aqueous Slurries and Optimization of Oxide Layer Thickness for Electrochemical Performance (ANL)

When silicon is in contact with air, a native oxide layer of several nanometers will form. As the size of the silicon particle becomes smaller, this oxide layer takes up a larger volume and weight and thus plays a more and more important role. The actual thickness of the oxide layer may also vary due to the manufacturing processes and storage history. While the use of Si nanoparticles largely mitigates the particle pulverization problem observed in micron-sized Si particles, the impact of oxide layer on the electrochemical performance of Si nanomaterials becomes non-marginal. Xun and coworkers reported that the presence of oxide layer harms the initial performance of the silicon anodes in a non-aqueous system [8, 9]. When the oxide layer was partially etched away by HF, improved initial reversible capacity as well as decreased initial irreversible capacity loss per surface area was observed. Recently, Touidjine and coworkers reported that the native oxide layer around silicon is not thick enough to prevent further reaction of water with the inner silicon core [10]. This wet oxidation reaction forms porous silicon oxide, which is accompanied by the generation of hydrogen gas, and also harms the reversible capacity of the material. With the current trend going towards water-based laminate making processes due to both better electrode performance and economic reasons, the presence of

oxide layer in the silicon electrodes is inevitable. Therefore we need to consider the Si electrode materials (especially Si nanomaterials) used with aqueous binders as Si core materials with a thin SiO_2 shell, and understand its stability and electrochemical performance as a whole. The purpose of this work is to understand how the oxide layer thickness affects the stability of the Si nanoparticles in aqueous slurries, and furthermore to optimize the oxide layer thickness to achieve optimal initial electrochemical performance as well as cycle performance.

In this work, we investigated the effect of oxide layer on the electrochemical performance of silicon anodes by growing the oxide layer of Si nanoparticles in a controlled manner. Si nanoparticles with an average size of 80 nm were used. Lithium polyacrylate (LiPAA) with a pH of ~7 and carbon black (C45) were mixed with the Si material to fabricate the electrodes. Brunauer-Emmett-Teller (BET) surface analysis, transmission electron microscopy (TEM) as well as Fourier-transform infrared spectroscopy (FTIR) were performed to characterize the silicon nanoparticles. Finally, the electrochemical performance of the silicon anodes of different oxide layer thicknesses was analyzed and the oxide thickness is optimized based on the electrochemical performance.

Figure II-47a shows the SEM image of the as-received Si nanoparticles. The particles are spherical shaped with most particles in the ~100 nm range. Some larger particles with diameters of several hundred nanometers can also be observed. Figure II-47b shows the mass change of silicon particles after heat treatment at different temperatures. As the heating temperature increases, the mass change increased from 1.9% at 300℃, to 35% at 700℃, in an exponential manner, showing that the oxidation process is kinetically-controlled.

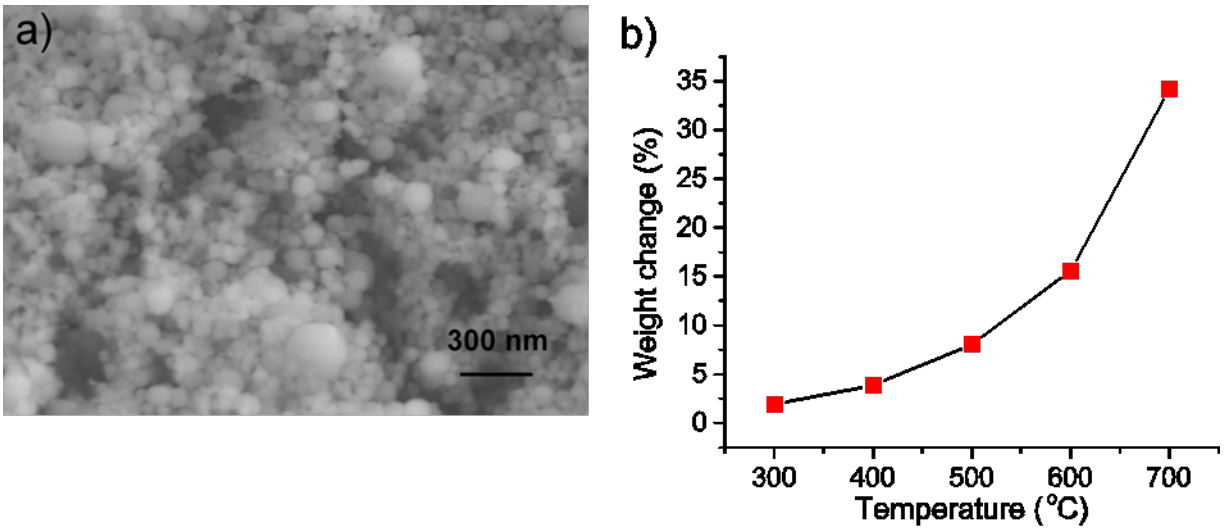

Figure II-47. a) Scanning electron microscopy image of silicon nanoparticles b) Mass change of the Si nanoparticles after heat treatment at different temperatures.

Fourier-transform infrared spectroscopy is a powerful technique to characterize the IR-active species on surface as well as in bulk. Figure II-48 shows the FTIR spectra of the pristine and treated Si nanoparticles measured in the attenuated total reflection mode. The pristine Si nanoparticles showed a broad feature containing peaks from surface Si-O-Si stretching (1250 cm-1 – 850 cm-1) and bending vibrations (850 cm-1 – 750 cm-1) in the 1250 cm-1 – 700 cm-1 region. The peaks are broad due to the random packing of the tetrahedral unit of Si-O in the amorphous SiO_2 layer. As the treatment temperature increases, the peaks become narrower and less convoluted, indicating the packing form of the Si-O tetrahedral unit becomes more ordered. Noticeably for the 600℃ and 700℃ treated Si nanoparticles, an additional sharp peak around 1120 cm-1 appeared. This peak is assigned to oxide in bulk Si by Mawhinney and co-workers, indicating that at elevated temperatures, oxygen may further diffuse into bulk silicon to form oxide inside bulk silicon [11]. A more-ordered packing structure of the SiO_2 layer as well as existence of oxide in bulk silicon could all affect the

resistivity and lithium ion diffusivity of the SiO_2 layer, and further affect the electrochemical property of the whole particle.

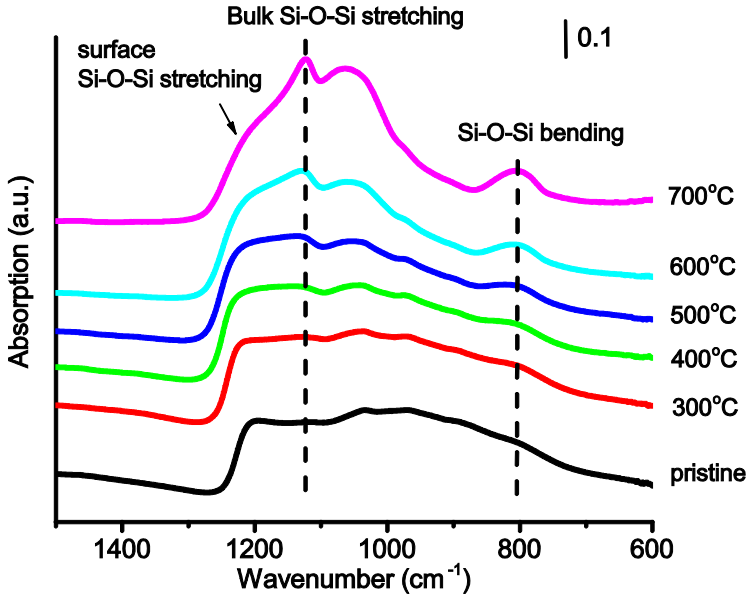

Figure II-48. FTIR spectra of pristine Si nanoparticles and Si nanoparticles treated at different temperatures.

The reaction between Si nanoparticles and water generates H_2 gas. To test the stability of our silicon samples in aqueous slurries, we monitored the gas formation after the Si nanoparticles were mixed into the slurry at both room temperature and elevated temperature of 75℃, at which the laminates are usually dried.

Three samples were chosen for this test: pristine, 400℃-treated and 600℃-treated Si samples, as they represent different oxide layer thicknesses. The Si samples were mixed with LiPAA, C45 and 18 MΩ de-ionized water using a centrifugal mixer (Thinky Mixer) at 2000 rpm to obtain good slurry property. The slurries were then transferred into pouches and the pouches were vacuum-sealed immediately. The whole process took about 20 minutes. The pouches were then placed at room temperature and monitored for 2 weeks for possible swelling behavior that could be caused by gas generation. We did not observe any pouch swelling during the 2 week period. Since previous reports observed significant H_2 formation within the first 2 hours at room temperature, we conclude that in our case we did not observe significant reaction between water and our silicon samples under room temperature. Our laminates are usually dried at 75℃ for 4 hours, therefore we further tested the stability of the slurries at elevated temperature of 75℃. We observed significant swelling for the pristine Si sample, slight swelling for the 400℃-treated sample and no swelling for the 600℃-treated sample.

To conclude, all of our silicon samples are fairly stable in room-temperature aqueous slurries. There is no significant wet oxidation and corresponding gas generation when the silicon nanoparticles are subject to lab-scale mixing and sitting at room temperature for 2 weeks. At elevated temperature of 75℃, pristine Si nanoparticles showed significant gas generation corresponding to wet oxidation. However, heat-treated Si samples with even slightly thicker oxide layer showed significant improvement on the stability in aqueous slurries. Our results suggest two scenarios:

a) For small lab-scale slurry making process, a small slurry of several grams is usually produced at a time and the heat dissipation is relatively good. In this case the temperature rise of the slurries as well as the time the slurries stay at elevated temperatures is usually limited. In this case, there may not be significant amount of wet oxidation to significantly change the overall oxide layer of the silicon nanoparticles.

b) Large-scale slurry making process usually involves mixing of slurries on the kilogram scale. It usually requires much harsher mixing conditions such as intensive high energy ball milling for an extended amount of time. During this process significant temperature rise may happen to the slurries. The slurries may also stay at higher temperature for much longer time. This can result in significant wet oxidation reaction between silicon and water. In this case, the stability of Si particles at elevated temperatures should be taken into consideration.

To obtain initial electrochemical performance information of heat treated Si nanoparticles, we cycled the assembled half cells between 10 mV and 1.5 V at C/10 rate for 3 cycles. Figure II-49 compares the electrochemical performance of the initial formation cycles for the Si electrodes with Si nanoparticles of different treatments. Si nanoparticles treated at 700°C did not show any reversible capacity from silicon and is therefore not shown in Figure II-49.

Comparing the performance of 500°C and 600°C-treated Si nanoparticles with the pristine Si nanoparticles, we observed decreased specific capacity and coulombic efficiency. The decreased specific capacity is mostly likely caused by the significant decrease of the active Si from the heat treatment processes, and the decreased coulombic efficiency is likely due to the increased parasitic reactions from the irreversible reactions between SiO2 and lithium ions.

On the other hand, the Si nanoparticles after 300°C and 400°C heat treatment showed comparable specific capacity and coulombic efficiency during the formation cycles. While the pristine Si nanoparticles started with slightly higher reversible capacity, the heat-treated samples retained their capacity better during the 3 formation cycles, which resulted in very comparable reversible capacity at the 3rd formation cycle. This better capacity retention at formation cycles suggests that the mechanical integrity of the Si nanoparticles may be improved after the treatment. In conclusion, the initial electrochemical performance comparison of different Si samples shows that while too thick of an oxide layer may decrease the initial coulombic efficiency and reversible specific capacity of the material, a slight increase of the oxide layer thickness does not harm the initial performance.

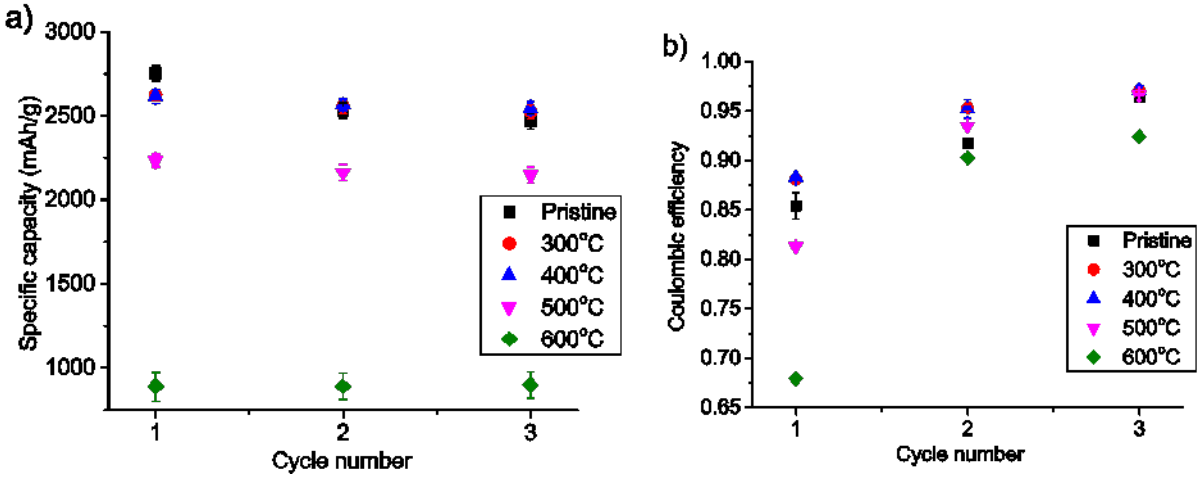

Figure II-49. a) Specific capacity and b) coulombic efficiency comparison of initial electrochemical performance of Si nanoparticles after different treatments.

It was noted by Xun and coworkers that when comparing the initial performance, irreversible capacity loss per surface area should be taken into consideration as treatment may change the surface area significantly and affect the surface area available for parasitic reactions [8]. Here we measured the BET surface area of our silicon samples and calculated irreversible capacity loss per surface area for the 1st cycle. BET surface area measurements show that our oxidation treatment did not result in any significant decrease of the surface area. The calculated irreversible capacity loss per surface area shows that treating the silicon nanoparticles at 300°C and 400°C resulted in slightly decreased irreversible capacity loss per surface area, whereas treating the

nanoparticles at 500℃ and 600℃ increased irreversible capacity loss per surface area. For 600℃-treated Si, the result from initial formation cycles done at C/100 is shown since we observed an interesting capacity increase over cycles when the electrodes were cycled at C/10, indicating the electrode was not fully activated at the first three cycles at C/10 rate.

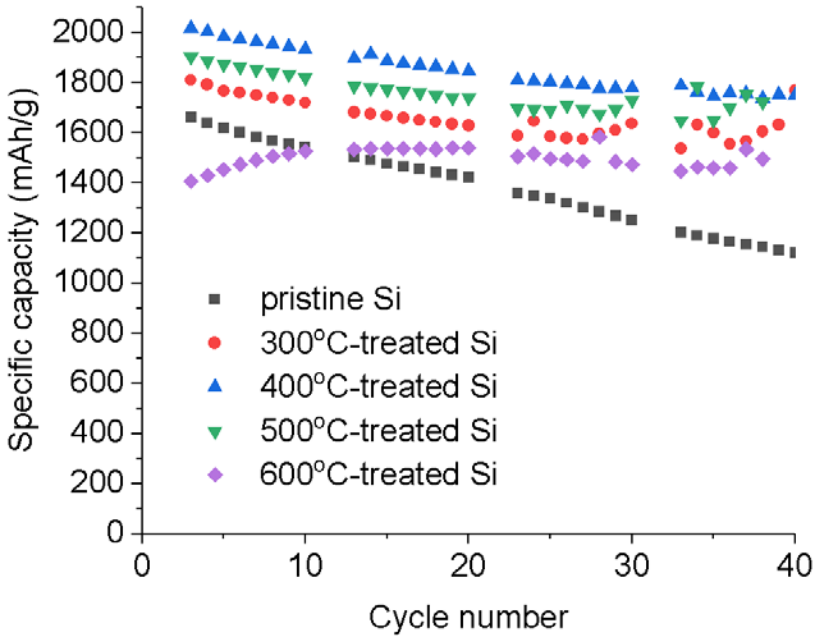

Figure II-50. Half cell cycle performance for 500℃ -treated and 600℃ -treated Si nanoparticles.

Figure II-50 shows half cell cycle performance for pristine, 300℃-treated, 400℃-treated, 500℃-treated and 600℃-treated Si electrodes for 40 cycles. The cells went through initial formation cycles (C/10 rate between 1.5 V and 10 mV for 3 cycles) and rate cycles (delithiation rate at C/5, C/3, C/2, 1C and 2C for 3 cycles each while lithiation rate set to C/5 for all cycles) before subjecting to cycle tests. For half cell cycle tests, the cells were cycled between 1.5 V and 10 mV at C/3 rate with a HPPC cycle at every 10th cycle. We observed improved capacity retention with all treated samples. The 400℃-treated Si electrode showed the highest specific capacity with improved capacity retention. For 500℃-treated and 600℃-treated Si electrodes, although the reversible capacity is compromised in both cases in the initial formation cycles, both treated samples showed improved capacity retention during the 40 cycles of cycle test. This supports that a thicker oxide layer improves the mechanical stability of the particles during cycling, thus improving the capacity retention.

We further compared the cycle performance of the 400℃-treated Si nanoparticles with the pristine silicon nanoparticles in a full cell configuration with $LiNi_{0.5}Co_{0.2}Mn_{0.3}O_2$ (NCM523) used as the cathode. To get full cell cycle performance information, we cycled the assembled full cells at C/3 rate for 50 cycles after three formation cycles at C/10 rate. Figure II-51 a-b shows the cycle performance of the 400℃-treated and the pristine silicon nanoparticles between 2.5 V and 4.3 V. The anode capacity is used here since the performance of anodes is compared in this study. The specific anode capacity in full cell tests appears lower than the specific capacity in half cell tests. This is because in full cell tests, an N/P ratio of 1.1-1.2 is utilized so that anode has some extra capacity and lithium plating on the anode can be prevented. The presence of extra silicon in the anode leads to the lower specific anode capacity. Compared to pristine silicon nanoparticles, the 400℃-treated Si nanoparticles showed an improvement of capacity retention from 52.91% (3 cell average) to 59.70% (3 cell average) when cycled under the same voltage window. It should also be noted that a significant improvement in capacity retention was observed for both sets of cells when we raised the lower cutoff voltage from 2.5 V to 3.2 V, as shown in Figure II-51c-d. In this case, about 17% less lithium was cycled compared to the case where the cells were cycled between 2.5 V- 4.3 V due to the smaller cycling voltage window.

Compared to the pristine silicon cells, the 400℃-treated Si full cells showed an improvement of capacity retention from 72.23% (3 cell average) to 78.31% (2 cell average) when cycled under the same voltage window. At the end of the 50 cycles, the specific capacity of the cells cycled with 3.2 V lower-cutoff voltage retains a larger specific capacity than the cells cycled with a 2.5 V lower-cutoff voltage. The much better capacity retention with a 3.2 V lower-cutoff voltage can be explained by the higher coulombic efficiency observed over cycling, as shown in Figure II-51b and Figure II-51d. This higher coulombic efficiency can be caused by the better structural stability when less lithium is cycled. Another likely reason for the higher coulombic efficiency is the better electrochemical stability of the solid electrolyte interphase layer of silicon. When the 2.5 V lower-cutoff voltage is utilized, the solid electrolyte interphase of silicon is more likely to be subject to a more oxidizing potential and therefore is more likely to be oxidized. This oxidation and subsequent re-formation of the SEI layer at each cycle leads to extra irreversible lithium consumption which leads to poor capacity retention.

Note that for pristine and 400℃-treated Si nanoparticles, better capacity retention is observed in half cells compared with full cell testing results. In half cell tests, the lithium inventory is unlimited, therefore the effect of irreversible lithium consumption caused by parasitic reactions (such as new SEI formation) on capacity fading is not properly reflected. Full cell testing results better reflect the capacity retention in practical applications.

The coulombic efficiency comparison in Figure II-51b and Figure II-51d shows that the initial coulombic efficiency of the 400℃ treated Si full cells is on average higher than the coulombic efficiency of the pristine Si full cell for both voltage windows. However, when cycled between 2.5 V and 4.3 V, the coulombic efficiency decreased for 400℃-treated Si full cells before it rose again as the cells cycle. This phenomenon was not observed for the 400℃-treated Si full cells cycled between 3.2 V and 4.3 V. This suggests that the lower cutoff voltage may degrade the oxide layer in some way. More study need to be conducted to fully understand this phenomenon.

The improved cycle performance we observed agrees with the previous work conducted by Sim and coworkers, where they studied the impact of SiO_2 coating thickness on the capacity retention of 1.4 um Si particles, and found that with a thicker SiO_2 layer, the capacity retention is improved [12]. They attributed the improvement to the suppression of the volume expansion by the SiO_2 coating to the particles. In our case, the capacity retention improvement may also be attributed to the improved mechanical integrity of the particles, as better mechanical property makes particles less likely to crack during the cycling, thus less lithium consumption caused by SEI formation.

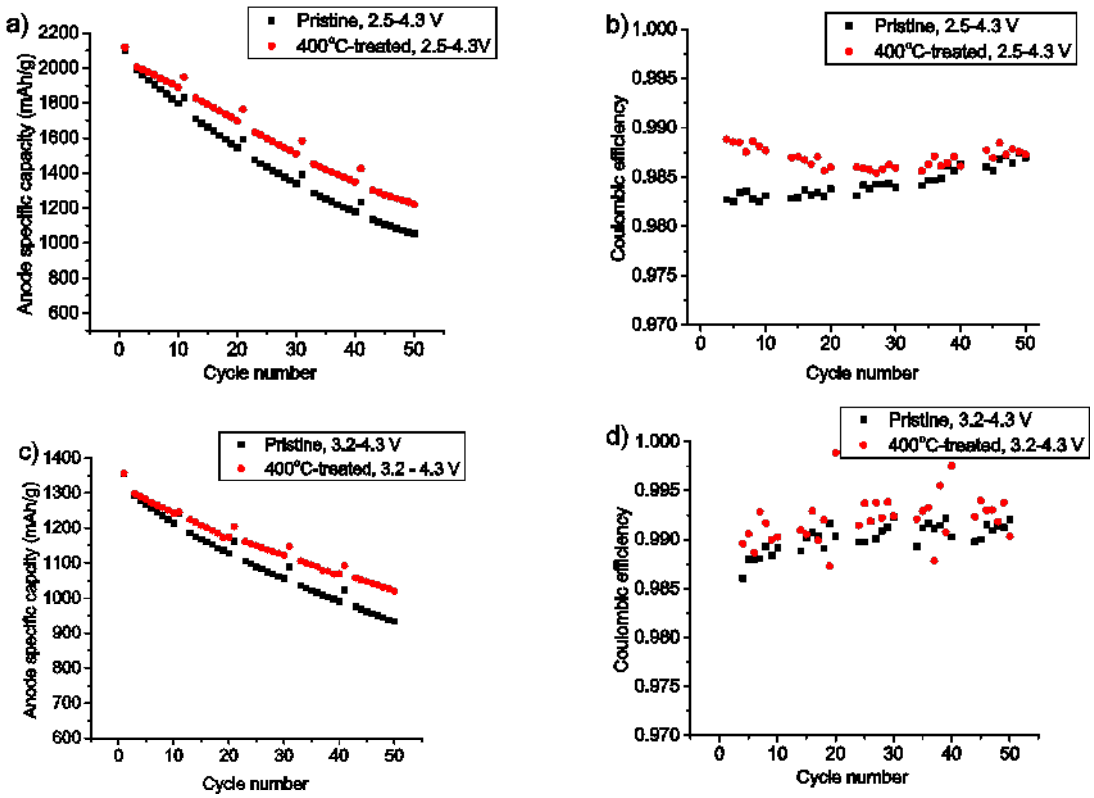

Figure II-51. a,b): capacity retention and coulombic efficiency of pristine and 400°C -treated Si nanoparticles cycled between 2.5 V and 4.3 V c,d): capacity retention and coulombic efficiency of pristine and 400°C -treated Si nanoparticles cycled between 3.2 V and 4.3 V.

Characterizing Electrode Heterogeneity as a Function of Processing (ORNL)

With all of the processes that are occurring chemically during the processing of the silicon electrode another issue is whether or not the electrodes are cast with the best structure. We note that the change in surface chemistry, particle sizes and gas evolution will all impact the electrode and how uniform it is. To investigate these we have been performing extensive characterization studies of the cast electrodes. Electrode homogeneity is also key to improving performance and extending cycle life. Figure II-52 shows Raman maps of the Si-Gr anodes before and after cycling. To visualize anode heterogeneity, Raman maps were analyzed using a combination of cluster and basis analysis. Silicon, graphite, and carbon all have strong Raman-active modes, making Raman microspectrometry and mapping well-suited to characterize the composite anodes. The lithiation of Si can easily be followed across the electrode by monitoring the transition from crystalline silicon (c-Si) to amorphous silicon (a-Si). Raman maps (50 x 50 μm, 2500 spectra) were collected on Si-Gr composite anodes after 1, 2, and 100 cycles (Figure II-52). The maps were analyzed by treating each spectrum in the composite as a linear combination of the individual components (c-Si, a-Si, graphite, and carbon black). In the pristine anode, much of the map is dominated by c-Si as expected. After cycling, a-Si is found across large areas of the electrode, but some c-Si remains even after 100 cycles. The presence of c-Si was further verified with XRD. This indicates that parts of the electrode remain electronically or ionically isolated and unable to participate in the alloy reaction with lithium.

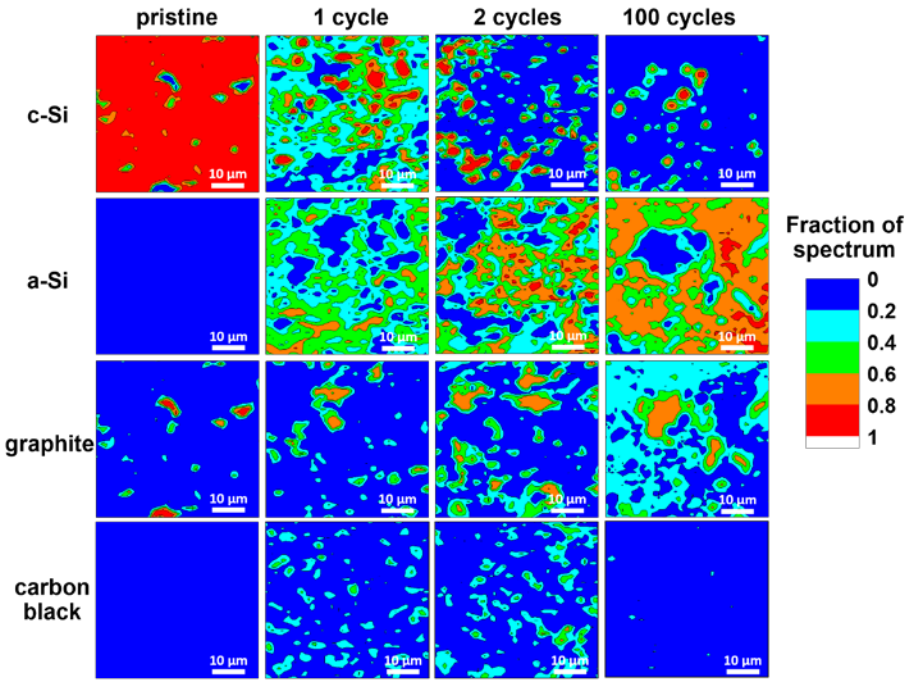

Figure II-52. Raman maps of Si-Gr anodes taken before cycling (pristine), after 1 formation cycle, after 2 formation cycles, and after the full cycling protocol (100 cycles). Raman maps were generated by deconvoluting each composite spectrum into the sum of the four components (c-Si, a-Si, graphite, and carbon black).

Similar to the Raman maps, XPS data was collected on silicon electrodes cast at ORNL, SNL and ANL for comparison. Figure II-53 shows representative Si 2p XPS data collected for several of these samples. The data was all normalized to the Si^0 species to highlight the changes in oxidized silicon. There are several unique features in this data. First, there is clear evidence for the Si in the spectra which is surprising given the predicted thickness of the polymer binder on the electrode surface which is estimated to be at least 15-20 nm thick. A layer of this thickness would totally attenuate the photoelectrons generated from the Si. This means that the binder is not homogenously coating the Si despite the beliefthat PAA/LiPAA adheres to the Si surface strongly. This heterogeneity leaves extensive tracks of Si exposed to the electrolyte where it can react or become isolated with cycling. The second this these XPS results show is that the relative concentration of Si^{4+} is changing significantly depending on the processing consistent with the previous NMR data. These results point to the need to dramatically improve the processing of the electrodes to enable total Si utilization. We proposed to investigate the processing of these electrodes with future funding including evaluating solvent choice, order of reagent addition, and other processing conditions.

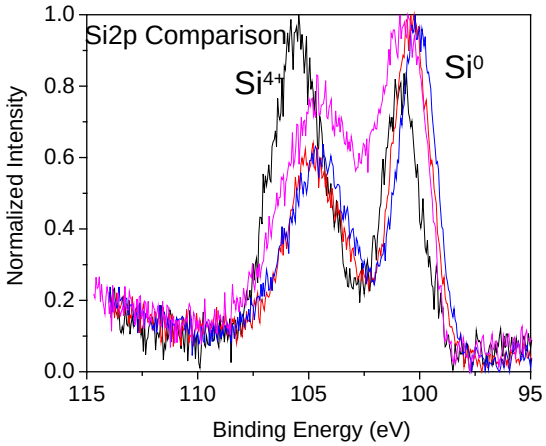

Figure II-53. Representative normalized Si 2p XPS data collected on 4 different Si-Gr-CB-PAA electrodes produced at ORNL, SNL and ANL.

Capacity Fade and Its Mitigation in Li-ion Cells with Silicon-Graphite Electrodes (ANL)

Previous research on Si electrodes implicates erosion of silicon particles by hydrofluoric acid (HF) as one of the leading causes of performance deterioration, as this acid readily reacts with the SiO_2 shell and silicon core of the particles. This acid is generated when the conventional $LiPF_6$ salt is hydrolyzed by moisture. The latter can have several origins, but the most likely source is the negative electrode itself, as it is often processed from an aqueous slurry. Indeed, the coupling of silicon and graphite is not an easy one, as the Si/SiO_2 particles are strongly hydrophilic, whereas Gr and carbon particles are strongly hydrophobic. For Gr electrodes, the binder is typically PVdF (polyvinylidene fluoride), a hydrophobic and inert polymer, and the organic solvent is N-methyl-2-pyrrolidone. For Si and Si-Gr electrodes, carboxylated polymers (such as lithiated polyacrylic acid, LiPAA, and carboxymethylcellulose, CMC) have been used as the binder, as they form strong contacts with all of the particles present in the matrix, and the solvent is often water. While residual water from the electrode fabrication process has less effect on the performance of Gr electrodes, it has significant effect on the performance of Si electrodes. The role of this residual water in cell capacity fade is an important consideration in our study.

Our approach was to examine performance and longevity of full cells, prepared using electrodes fabricated (with commercially available materials) by the Cell Analysis, Modeling, and Prototyping (CAMP) facility at Argonne. The positive electrode (NCM523) contained 90 wt% $Li_{1.03}(Ni_{0.5}Co_{0.2}Mn_{0.3})_{0.97}O_2$, 5 wt% carbons and 5 wt% PVdF binder. The negative electrode (SiGr) contained 73 wt% graphite, 15 wt% nanosilicon (50-70 nm), 2 wt% carbons, and 10 wt% LiPAA binder (450 kDa); the silicon-free graphite (Gr) negative electrodes contained 88 wt% graphite, 2 wt% carbons, and 10 wt% LiPAA. The baseline (Gen2) electrolyte was 1.2 M LiPF6 in a 3:7 w/w mixture of ethylene carbonate (EC) and ethyl methyl carbonate (EMC) solvents; cells with this electrolyte are the Gen2 cells. Some cells contained 10 wt% fluoroethylene carbonate (FEC) added to the Gen2 electrolyte; these are referred to as the FEC-cells.

The causal mechanisms for capacity fade in these full cells were inferred from data obtained by electrochemistry, microscopy, spectroscopy and thermogravimetry techniques. The cell cycling protocol consisted of three (formation) cycles at a nominal C/20 rate, 94 (aging) cycles at a C/3 rate, and three (final) cycles at a C/20 rate, for a total of 100 cycles in the 2.5-4.1 V voltage range at 30°C. This protocol was repeated multiple times for cells tested beyond 100 cycles. Scanning electron microscopy (SEM) images were obtained with a Hitachi S-4700-II microscope to observe changes to the bulk morphology of the electrodes before and after cycling. XPS (surface analysis) data were obtained on electrode samples with a PHI 5000 *VersaProbe II* system from Physical Electronics; the samples were inserted into the XPS analysis chamber through the glovebox, without exposure to ambient air. Thermogravimetry was carried out in helium flow

using a Perkin Elmer Pyris 1TGA thermogravimetric analyzer coupled to a Perkin Elmer Clarus 680 gas chromatograph – mass spectrometer.

Electrochemical characterization of NCM523/SiGr and NCM523/Gr cells: Figure II-54 shows cell discharge capacities as a function of cycle number. The Gen2 and FEC cell capacities are comparable during the early (to ~10) cycles. Subsequently, the Gen2 cell shows rapid capacity decrease, whereas the FEC cell shows a more gradual (yet significant) capacity decrease. After 100 cycles, the specific capacity and capacity loss for the Gen2 cell are 13 mAh/g and 91.8%, respectively, and the corresponding values for the FEC cell are 72 mAh/g and 53.5%, respectively. These results show that while the addition of FEC slows the capacity fade, it does not prevent it fully. In contrast, NCM523/Gr full cells containing the FEC electrolyte show only ~9% capacity loss after 100 cycles. The only difference between these NCM523/Gr and NCM523/Si-Gr cells is the presence of 15 wt% Si nanoparticles in the negative electrode, which implicates the silicon as the dominant contributor to capacity fade.

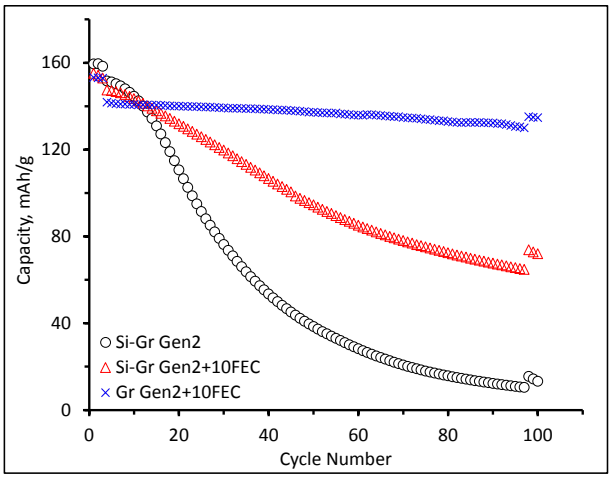

Figure II-54. Capacity versus cycle number plots for full cells containing the SiGr negative electrode with Gen2 electrolyte (black), SiGr negative electrode with Gen2+10 wt% FEC electrolyte (red), and Gr negative electrode with Gen2 +10 wt% FEC electrolyte (blue). It is obvious that cells containing the 15 wt% Si show faster capacity decline.

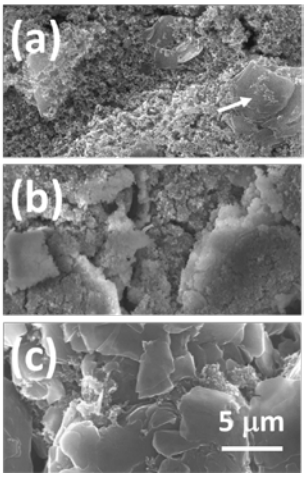

Figure II-55. SEM images of the negative electrode. (a) Pristine Si-Gr electrode showing large graphite flakes (arrow) in contact with Si and carbon nanoparticles in the matrix. (b) The same electrode harvested after 100 cycles from a cell containing Gen2 electrolyte. The graphite particles are completely covered by electrolyte breakdown deposits. In contrast, panel (c) shows a Gr electrode (no Si) harvested from a Gen2 cell after 100 cycles. The graphite flakes and the C45 carbon particles are still clearly observed, as the SEI is relatively thin.

SEM images from Graphite (Gr), and 15wt% Si-Gr (SiGr) electrodes: Figure II-55a and Figure II-55b show SEM images of a SiGr electrode before and after one hundred 2.5-4.1 V cycles in a full cell configuration. The graphite, nanosilicon and C45 (nano)carbons are evident in the pristine electrode (Figure II-55a). In the cycled SiGr electrode, the SEI deposits form a thick covering on both silicon (and carbon) nanoparticles and the micron-size graphite flakes. In contrast, the graphite flakes can be readily distinguished in images of Gr electrodes (Figure II-55c) harvested from NCM523/Gr cells cycled under similar conditions. Figure II-55 is a graphic illustration of the difference between the Gr and SiGr electrodes from cycled cells. For the SiGr electrodes, the SEI deposits becomes so extensive that they fill up the electrode pores, eventually isolating the active material from lithium-ions in the electrolyte and/or electronic contact with the current collector. The Gr electrodes, on the other hand, show much less (and thinner) SEI deposits and function well for hundreds of additional cycles.

X-ray photoelectron spectroscopy (XPS) data on positive and negative electrode samples: Electrodes for XPS analyses were harvested from full cells held at 2.5 V for 24 h before disassembly. Hence, the negative and positive electrodes are expected to be in the delithiated and lithiated states, respectively. Data from electrodes harvested from a 3-cycle NCM523/Gr cell are included for comparison. Figure II-56 to Figure II-58 show XPS plots for C 1s, O 1s, F 1s, Si 2p, Li 1s and P 2p regions for both negative electrodes (anodes) and positive electrodes (cathodes). The scattered open symbols in these plots indicate the background-corrected XPS data, whereas the smooth lines are the least-squares fits of these data. Note that the ejected photoelectrons arise from the top five to ten nanometers of the electrode. As the graphite and silicon particles become covered with decomposed electrolyte, these thick deposits are the main contributors to the overall XPS spectra for the aged electrodes. We begin our discussion with data from the negative electrodes (Figure II-56a-d, Figure II-57a,b).

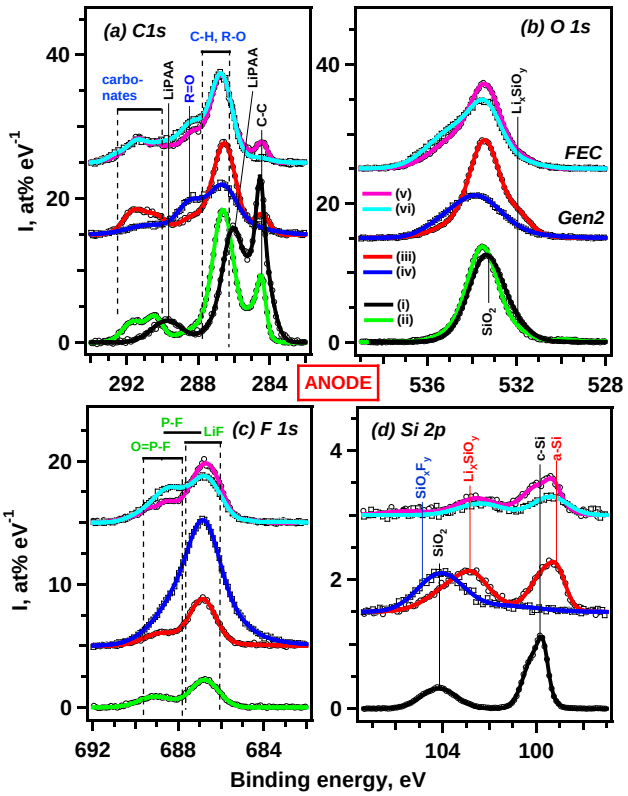

Figure II-56. XPS spectra from pristine SiGr electrode (i) and from negative electrodes harvested from the following full cells: (ii) NCM523/Gr cell, after three formation cycles in Gen2, (iii) NCM523/SiGr cell, after three formation cycles in Gen2, (iv) NCM523/SiGr cell, aged in Gen2, (v) NCM523/SiGr cell, three formation cycles in Gen2 containing FEC, (vi) NCM523/SiGr cell, aged in Gen2 containing FEC.

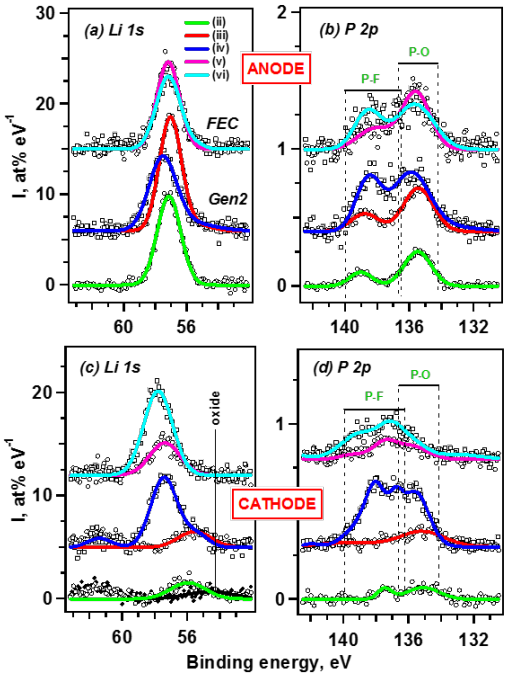

Figure II-57. XPS spectra in (a,c) Li 1s and (b,d) P 2p bands from harvested (a,b) negative electrodes and (c,d) positive electrodes from disassembled cells: (ii) NCM523/Gr cell, after three formation cycles in Gen2, (iii) NCM523/SiGr cell, after three formation cycles in Gen2, (iv) NCM523/SiGr cell, aged in Gen2, (v) NCM523/SiGr cell, three formation cycles in Gen2 containing FEC, (vi) NCM523/SiGr cell, aged in Gen2 containing FEC.

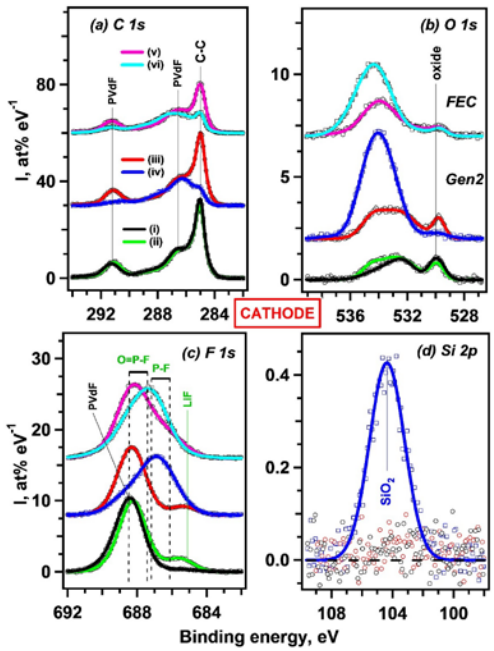

Figure II-58. XPS spectra of harvested positive electrodes from cells (i) to (vi) (see inset in panel 'a' for the color table): (i) pristine Si-Gr cell, (ii) Gr cell, after three formation cycles in Gen2, (iii) Si-Gr cell, after three formation cycles in Gen2, (iv) Si-Gr cell, aged in Gen2, (v) Si-Gr cell, three formation cycles in Gen2 containing FEC, (vi) Si-Gr cell, aged in Gen2 containing FEC. The spectral regions are indicated in the panels.

The C 1s spectrum (Figure II-56a) of the pristine Si-Gr electrode (trace i) show intensities arising from the graphite (284.5 eV) and LiPAA binder (286.0, 289.5 eV). The graphite peak intensity decreases significantly after formation cycling and is not seen after 100 cycles for either cell (traces iv and vi), confirming our SEM observation that graphite in the Si-Gr cells is buried under the overlying SEI deposits. A similar observation can be made about the LiPAA peaks, which are not observed even after formation cycling and indicating that the binder is covered by the SEI. Peak intensities centered around 286.5 eV (R-O), 288.5 eV (R=O), and in the 290-292 eV range (R-OCO_2), where R=C_xH_y, are observed in the cycled electrodes; these signals arise from electrolyte decomposition products that could include alkyl carbonates (such as ethylene dicarbonate from EC reduction) and alkyl fluorophosphates. Overlapping with these R-O peaks are the C-H peaks from the polymeric component. For Gen2 cells, the decrease in 286.5 eV and 290-292 eV intensities and increase in 288.5 eV intensity for the 100 cycle electrode (relative to the 3-cycle electrode) suggests that the alkyl carbonates are being covered by compounds that include fluorophosphates, as cell aging proceeds. The FEC cells (traces v and vi) also show the 288.5 eV intensity increase suggesting an increase in the phosphate content, but without a corresponding decrease in the alkyl carbonate intensities.

The Si 2p spectrum from the pristine electrode (trace i in Figure II-56d) shows two strong peaks near 100 eV (Si) and 104 eV (SiO_2), which reveals that the silicon nanoparticles have a SiO_2 shell. From an examination of the XPS spectrum, and from an analysis of the Si-Gr half cell electrochemistry data, we conclude that the SiO_2 shell thickness is less than 5 nm. After 3 cycles, both the Gen2 and FEC cells show intensities around 99.5 eV, which arises from the delithiated amorphous silicon. For the Gen2 cell (trace iii), strong intensities are also seen in the 102 – 105 eV range, suggesting the presence of Li_xSiO_y (102.8 eV, strong), SiO_2 (104 eV, weak) and SiO_xF_y (105 eV, weaker) phases. The FEC cell (trace v) shows relatively weaker Li_xSiO_y intensities, and negligible SiO_2 and SiO_xF_y intensities. After 100 cycles, the Gen2 cell (trace iv), shows negligible intensity in the 98.5-100.5 eV range indicating complete coverage of the silicon nanoparticles by SEI deposits that include SiO_2 and SiO_xF_y species formed by progressive substitution of the oxide anions by F- anions. In contrast, the FEC spectrum (trace vi) shows weak Si and Li_xSiO_y intensities and negligible SiO_xF_y signals.

Parallel developments are seen in the F 1s spectra (Figure II-56c). The pristine electrode does not show fluorine signals, which is as expected. After 3 cycles both Gen2 and FEC electrodes (traces iii and v) display intensities display intensities in the 686-688 eV range (LiF and P-F bonds in $Li_xPF_yO_z$) and in the 688-690 eV range (O=P-F bonds in $Li_xPF_yO_z$). Previous studies have shown LiPF6 exists in equilibrium with LiF and PF5. Hydrolysis of the PF_5 results in a variety of $Li_xPF_yO_z$ compounds, including POF_3, $PO_2F_2^-$ and $PO_3F_2^-$ species; the greater extent of hydrolysis leads to the increasing oxygen-rich species content. After 100 cycles the Gen2 sample (trace iv) shows a large increase in both 686-688 and 688-690 eV ranges indicating substantial hydrolysis of the $LiPF_6$ salt. The FEC electrode (trace vi) shows an increase in the 688-690 eV signals but a small decrease in the 687-688 eV signals, indicating slower generation of the F-rich species, and more conversion to the O-rich $Li_xPF_yO_z$ compounds. This observation suggests that the FEC-generated SEI is more protective than the EC-generated SEI.

Signals consistent with increasing $LiPF_6$ salt hydrolysis on aging are also seen in the P 2p spectra (Figure II-57b). For the Gen 2 samples (traces iii and iv), both P-F signals (137-139 eV) and P-O signals (around 134-136 eV) increase on aging. Smaller changes are seen for the FEC samples, again indicating a more protective SEI. The Li 1s spectra (Figure II-57a) and O 1s spectra (Figure II-56b) also show changes on aging; these plots are harder to interpret as multiple species contribute to the spectral features. For both Gen2 and FEC samples, changes in the O 1s spectra reflect the decrease in alkyl carbonate content (533.5 eV) as these compounds are increasingly buried under the salt decomposition and hydrolysis products (535.5 eV). The Li 1s spectra indicate changes in Li-speciation for the Gen2 samples, and less so for the FEC samples.

The XPS spectra for the NCM523 positive electrodes are shown in Figure II-57c, d and Figure II-58a-d. The C 1s spectra (Figure II-58a) from the pristine electrode (trace i) shows show intensities arising from the C45 carbon black (285 eV) and PVdF binder (286.3 and 291 eV). On cycling the intensities arising from both graphite and PVdF decrease, indicating coverage by mostly inorganic surface species. Although weak, the

graphite and PVdF intensities are still observed even after 100 cycles (see traces iv and vi) indicating a relatively thin or non-uniform surface coverage.

The reduction in PVdF intensities on aging are also observed in the F 1s spectra (Figure II-58c). The pristine electrode contains a peak at 688.5 eV arising from C-F bonds in PVdF. After 3 cycles (traces iii and v), additional intensities around 685 eV signify the presence of LiF. After 100 cycles (traces iv and vi), strong intensities in the 686-687 eV range indicate the presence of LixPFyOz compounds, which are the products of LiPF6 decomposition and hydrolysis. Corresponding intensity increases on aging are also seen in the Li 1s spectra (Figure II-57c) and P 2p spectra (Figure II-57d).

Perhaps the most significant observation is the presence of silicon (~3 at%) on the positive electrode of the aged Gen2 cell. Judging from the binding energies, this signal at 104 eV (Figure II-58d, trace iv) stems from silicon dioxide (or lithium silicate). None of the other positive electrodes examined showed noteworthy Si 2p intensities, indicating that (i) the deposition is enhanced by cycling, and (ii) the FEC additive hinders Si loss from the Si-Gr electrode. The presence of SiO2 could also partially explain the increased intensities on aging in the O 1s spectra (Figure II-58b) for the Gen2 cell (traces iii and iv) compared to those of the FEC cell (traces v and vi). Yet, even after 100 cycles, weak intensities around 529.8 eV, arising from O2- anions in NCM523, indicates that the coverage is thin enough ($\lesssim$ 5 nm) to allow photoelectrons emitted from the oxide below it to pass through.

Characterization of water loss from LiPAA using thermogravimetry: To quantify water loss from LiPAA, an aqueous solution containing 10 wt% LiPAA was first evaporated to a thick slurry and then water was removed at 120ºC over 5 h in a vacuum oven. The material was subsequently equilibrated with water vapor for 40 h under the ambient conditions. The hydrated LiPAA gel initially contained ~2.2 water molecules per monomer unit, and one-half of this water was quickly lost as the temperature increased to 150ºC (Figure II-59). For the next 3 h, the loss followed t1/2 behavior that is typical for diffusion-limited mass loss and then it settled into the exponential mode with 1/e time constant of 11 h. As seen from the plot, after 3-4 h at 150ºC, ~ 0.1 mol.eq of water was retained in the sample, and 0.02 mol.eq was retained even after 10-15 h. Note that that the water loss was quantified for the pure LiPAA binder; water loss from the composite material can be still slower, as water molecules can form H bonds both with silanol groups on the silica surface and the carboxylate anions adhering and interacting with this surface.

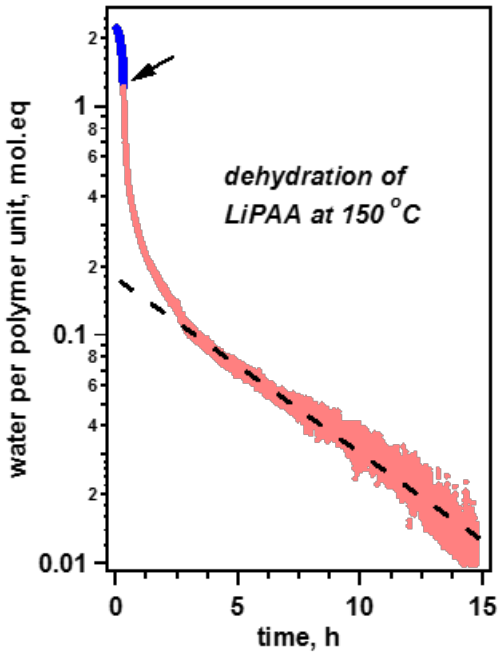

Figure II-59. Water loss from hydrated LiPAA binder as observed by thermogravimetry. Note the logarithmic vertical scale. The first section of the plot (indicated with the arrow) corresponds to heating of the sample from 50 to 150°C at 6°C/min, whereas the scattered dots indicate the 150°C isotherm. After the first 3 hours, the mass loss settles into the exponential regime (dashed line).

Why residual water in the SiGr electrode matters: The as-received Si nanoparticles have a SiO_2 shell, which is lined with silanol (≡Si-OH groups). After cycling we note the gradual disappearance of Si and Li_xSi signals in the Si 2p XPS spectra and the concomitant increase in the SiO_xF_y, SiO_2 and Li_xSiO_y signals; continuous increase in the LiF and $LiPO_xF_y$ signals in the F 1s and P 2p spectra is also seen. The oxide-by-fluoride (O-by-F) substitution, and the gradual conversion of nonfluoride lithium salts to LiF can be rationalized through reactions of hydrolytically generated HF. Specifically, LiPF6 disproportionates to LiF and PF_5, and the pentafluoride hydrolyses to POF_3 releasing two molecules of HF in the process. Further hydrolysis can yield $PO_2F_2^-$ and PO_3F^- anions releasing more HF. The latter can react with silica, silicon, lithium salts (such as alkoxides and alkyl carbonates) in the negative electrode, and (lithiated) transition metal oxides and hydroxides on the positive electrode, forming the fluorides. A schematic of these concepts is shown in Figure II-60.

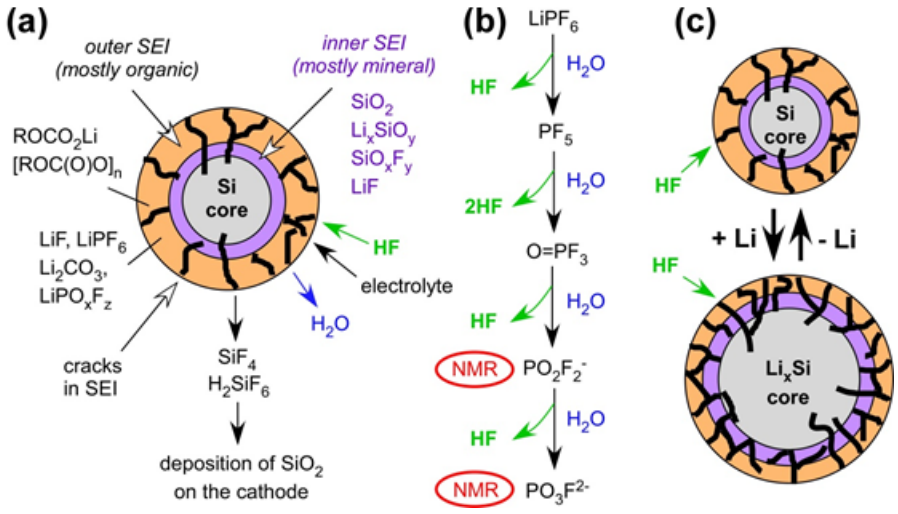

Figure II-60. (a) Schematic representation of a Si particle in the advanced stages of aging, with the inner and outer SEI layers formed around the Si core. Mineral compounds derived from Si prevail in the inner SEI while various organic compounds (including alkyl carbonates and inner-carbonate polymers) prevail in the outer SEI, with insoluble salts trapped in the semisolid matrix. Electrolyte and HF molecules can diffuse through the pores and cracks in the outer SEI and react with the particle interior, releasing SiF_4 and water molecules back into the electrolyte. This water joins the hydrolytic cycle for LiPF6 (shown in panel b). In the latter, water sequentially hydrolyzes PO_xF_y species, consuming five water molecules and releasing five HF molecules in total; the released HF can react with Si particles, continuing the hydrolytic cycle. The two species at the end of this sequence can be observed using NMR spectroscopy in the fluids collected from the aged cells. (c) As the Si particles repeatedly expand and contract during lithiation/delithiation, deep cracks develop allowing access of HF to the core, resulting in its digestion and additional SEI formation.

For example, reaction 1 illustrates interaction of the surface silanol groups on silica with HF yielding fluorinated species and releasing a water molecule, which can cause further hydrolysis of LiPF6.

$$\equiv Si\text{-}OH + HF \rightarrow \equiv Si\text{-}F + H2O \quad (1)$$

Another possibility is that the residual bound water in the binder matrix transforms to LiOH during the first cycle. Subsequent hydrolysis (or basic hydrolysis) of LiPF6 occurs according to the net equation

$$LiPF_6 + 2\ LiOH \rightarrow LiPO_2F_2 + 2\ LiF + 2\ HF \quad (2)$$

releasing HF that reacts with the various electrode components forming fluorides and releasing water (e.g., via reaction 1) which enters the hydrolytic cycle.

At the advanced stage of this O-by-F substitution, tetrafluorosilane (SiF_4) and/or hexafluorosilicic acid (H_2SiF_6) can be generated. These are highly soluble compounds that can diffuse out of the negative electrode and into the electrolyte before they hydrolyze there to the silicic acid (H_4SiO_4). The SiF_4 or H_2SiF_6 could also reach the positive electrode and react with the lithiated metal oxides (either directly or via hydrolysis) forming the corresponding fluorides and converting to SiO_2 (such reactions of transition metal oxides are used for ore refinement). In this manner, silicon is transferred from the negative to the positive electrode and becomes deposited at the layered oxide surface where it can be observed in XPS spectra.

EQCM Studies of Silicon Anodes (ANL)

Silicon electrodes for LIB systems are a leading contender for the next generation of anode material. The ten-fold increase capacity seen for silicon-based systems vs graphitic carbons could have a significant impact on overall electrochemical cell storage market if issues related to their cycling stability can be addressed. We have

focused on determining the interfacial properties of a charged silicon electrode, the silicon oxide passivation layer, and explored this interface using simple film forming additives that mediate lithium transport.

The natural passivation layer of silicon is generally related to its handling on formation. The natural passivation layer is usually found to be approximately a 2-3 nm thick layer of silica. A combination of experimental and theoretical work has shown that this passivation silica layer reacts with electrolyte decomposition products around 900 mV to form lithium silicate. Previously we demonstrated that the lithium silicate formed is a kinetic product and on cycling it loses the equivalent of a lithia molecule and reverts to the more stable lithium orthosilicate. In the past year Baris Key extended this work to show that the lithium orthosilicate eventually diffuses away from the interface and gets incorporated into the SEI layer. Last year we re-established our EQCM spectroscopic effort to determine how the passivation layer reactivity is affected by the addition of small amounts of the common electrolyte additive FEC to the Gen2 electrolyte system. Without FEC the system was found to form a relatively porous SEI layer that got thicker as a function of state of charge. Addition of FEC (1-5 wt%) to the electrolyte was found to create a much denser SEI layer than the SEI formed in Gen2 electrolyte. In a continuation of these studies we evaluated the role of higher amounts of FEC on the system and looked at the role of the salt counter-ion, as PF_6 anion has been implicated in some of the decomposition pathways by also evaluating systems using the TFSI anion.

Utilizing thin film model silicon electrodes, the role of surface passivation, electrolyte additives, and electrolyte can be investigated as a function of state of charge. The thin film electrode format is conducive to a variety of spectroscopic studies and utilizing a combination of 29-Si, 7-Li, and 19-F NMR (with Baris Key (ANL)) combined with electrochemical quartz crystal microbalance (EQCM) the interfacial properties can be correlated with the observed electrochemical performance.

The interface between the silicon electrode and electrolyte is a key point of contact in the electrochemical cell. Silicon is well known to have an unstable SEI layer due in part to its reactivity at high states of charge and lack of dimensional stability on cycling, as opposed to graphitic carbon which has exceptional dimensional stability [1, 13]. As part of this effort we have utilized a combination of EQCM spectroscopy and film forming additives to study the role of film thickness and density on the electrochemical properties of a silicon anode. Last year we reported the densification of the SEI on addition of FEC and the role silica passivation played in SEI formation. This is speculated to result from the breakdown of the FEC molecule happening at a higher voltage than the similar molecule EC and utilizing a different pathway that yields a different and denser polymer coating [14]. Building on this study, we evaluated the role of the amount of the film forming additive FEC in the electrolyte and, as seen in Figure II-61, there are several changes that are observed. As the film thickness increases (approximated by %FEC added) the silicon reduction peak sharpens and moves to lower potential, indicative of better lithium diffusion at the particle-electrolyte interface, additionally the samples with highest amount of FEC (20%) have much broader peaks that can be tied to higher viscosity, interfacial resistance, and lower electrolyte conductivity. Since addition of FEC to electrolytes is typically done as an additive rather than a salt/solvent mixture, addition of 20% FEC to Gen2 results in a drop in salt concentration from 1.2M to 0.96M and movement off the peak in electrolyte conductivity.

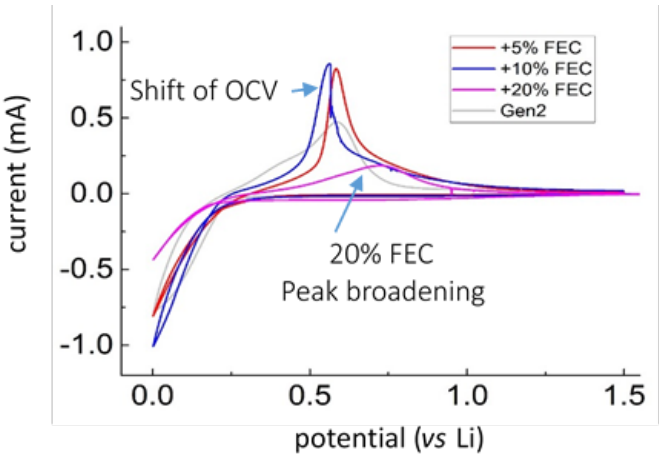

Figure II-61. Electrochemical reduction of a silicon thin film in a Gen2/FEC electrolyte mixture.

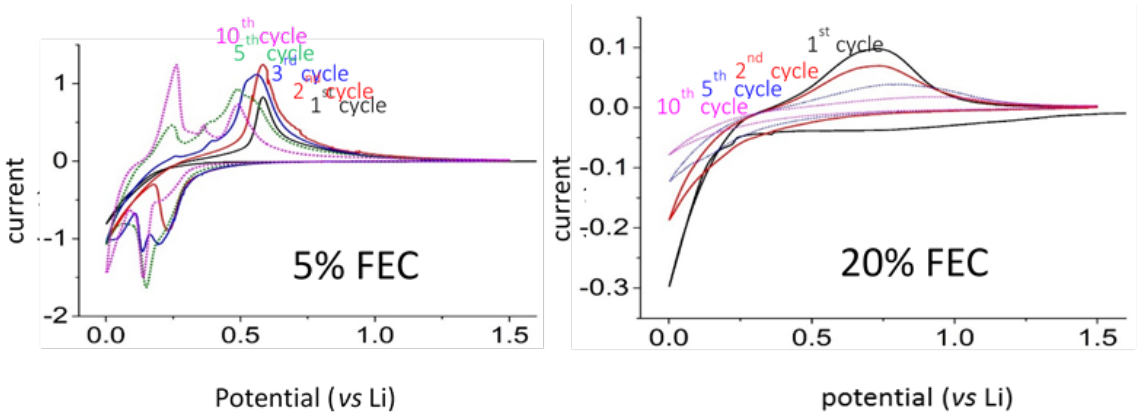

Figure II-62. CV comparison of 5% FEC and 20% FEC addition to Gen2 on the cycling of a silicon electrode.

Additional EQCM studies have shown that the role of film stability and electrochemical properties. Whereas the FEC forms a dense polymeric film on the surface of the electrode, the propensity of the silicon electrode to crack (Si film thickness ≈ 50 nm) on cycling leads to active material isolation and electronic isolation. This can be seen (Figure II-62) in a comparison to an electrode cycled in 5% FEC/Gen2 vs 20% FEC/Gen2. The sample(s) with lower amounts of FEC additive show a new peak growing in around 250 mV (vs Li) [15]. This peak, assigned in the literature to either electrode degradation (Si isolation) or Cu diffusion into the charged electrode (from Cu current collector) grows in rapidly when the FEC film is thinner. This is consistent with either mechanism or a combination as the copper solubility and lattice expansion are both maximized at low voltage (maximum lithiation). Efforts to assess the copper loss from the current collector (e.g., pitting) are planned.

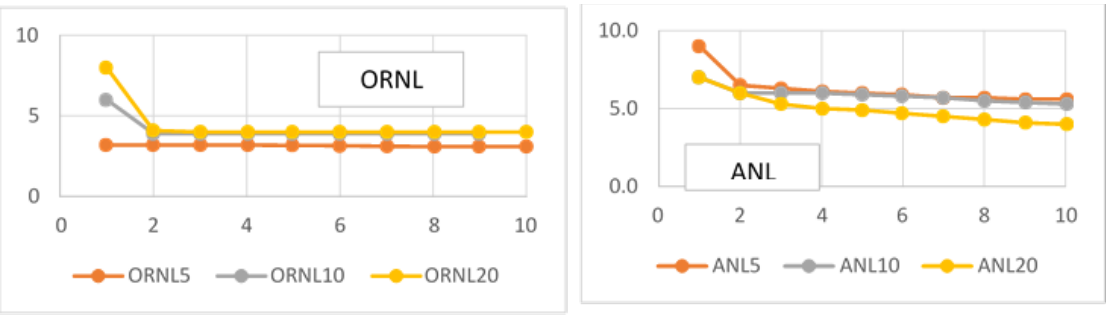

Figure II-63. A comparison of the cycling performance of a silicon thin film electrode versus surface passivation layer thickness.

In addition we also assessed the issues associated with the silica passivation coating in association with Gabe Veith as ORNL. As part of the SEISta Round Robin effort, we were provided with a series of silicon thin film electrodes for evaluation. After several weeks of aging these electrodes had thicker and more uniform silica passivation layers than our 'fresher' films and thus were good choices to assess the role of the interfacial silica on FEC film formation [16]. Electrochemical evaluation of the films was consistent with the earlier work noted. The aged electrodes had a higher silica content (nominally both had the same amount of Si/cm3). From the data shown in Figure II-63, the ORNL samples have much more cycling stability, albeit at a lower capacity. Both of these are consistent with the role proposed for the silica passivation layer as the silica acts to buffer the surface but also consumes silicon to make the buffer. The FEC appears to have a positive impact, notably for the ANL samples, which show better cycling stability than the cells cycled with no FEC additive. Both sets of materials show increasing first cycle irreversibility, consistent with the irreversible electrochemical reduction of FEC, which has been shown to take several cycles depending on concentration.

Understanding Capacity Losses with Silicon Anodes (ORNL)

Analysis of Coulombic Inefficiencies of PAA-based Si-Graphite Half Cells

PAA based full cells also display a first cycle Coulombic efficiency ~5% worse than LiPAA-based cells. The electrochemical reduction of additional water in the cells accounts for some Coulombic losses, but there are continuous losses through the first 40 cycles, summing up to a difference between the two systems of 71 mAh g^{-1}. Lucht et. al., has previously proposed the reduction of the acidic proton on the carboxylic acid of PAA to form LiPAA, following reaction 3. [17]

$$(3) \qquad \text{–COOH} + \text{Li}^+ + e^- \rightarrow \text{–COOLi} + \tfrac{1}{2}\,\text{H}_2$$

To verify these observations, PAA was mixed with 17% carbon black and coated on Cu foil. The coatings were dried at 120° C or 220°C, above and below the decomposition temperature of PAA. A modified pouch cell was produced with Li foil as the counter electrode and 1.2 M $LiPF_6$ in 3:7 (w:w) EC:EMC. The cell was held at 1 V vs Li metal for 1 week and analyzed for gassing by the Archimedes method. [18] The PAA coating was removed, rinsed in DEC, and scraped from the Cu foil for ATR FTIR. The resulting spectra (Figure II-64) show new peaks at 1567 cm^{-1} and 1416 cm^{-1} for the 220° C PAA sample, closely matching the carboxyl stretch of LiPAA. The 120°C PAA sample also displays a change in the spectra, but with a broad range of peaks from 1670 cm^{-1} to 1580 cm^{-1}. While the exact reason for this is still unclear, it is recognized the symmetric and asymmetric carboxyl stretches can vary based on the coordinating environment of the carboxylate ion. [19] For both drying temperatures of PAA, a peak at 1700 cm^{-1}, from the carboxylate stretch of PAA, shows that not all the PAA has been converted to LiPAA, likely due to the poor electrical conductivity of the binder. This observation closely matched the gradual Coulombic efficiency gains of the PAA-based cells through the first 40 cycles compared to the LiPAA-based cells. After the voltage hold, the volume increased within the cell by 130 µl, presumably due to H_2 generation from the reduction of PAA. A more detailed gas analysis is needed to identify the content of the gassing, but the volume produced here is on the right order expected for H_2 generation based on reduction of PAA.

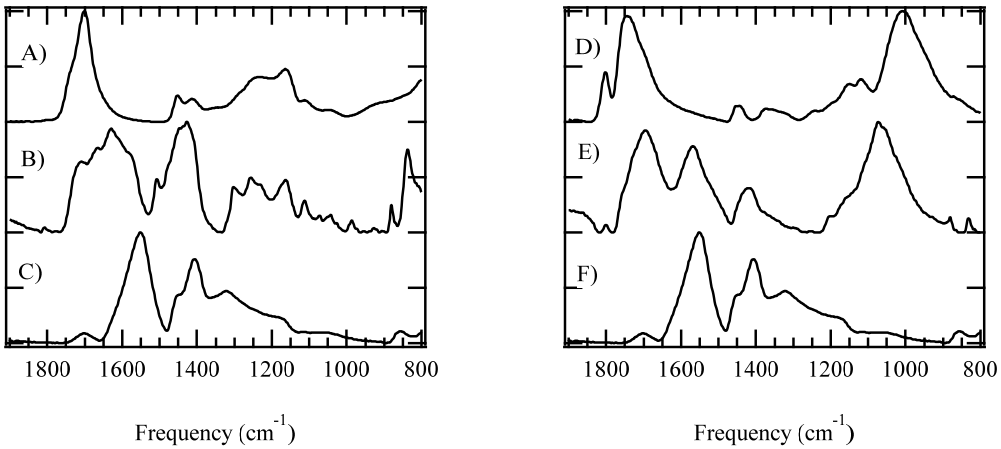

Figure II-64. ATR FTIR spectra of A) PAA dried at 120°C, B) PAA dried at 120°C, electrochemically reacted with Li metal, C) LiPAA dried at 120°C, D) PAA dried at 220°C, E) PAA dried at 220°C, electrochemically reacted with Li metal, and F) LiPAA dried at 220°C.

Analysis of Coulombic Inefficiencies of PAA Based Si-Graphite Full Cells

FTIR and Raman spectroscopy provide highly complementary information about the chemical changes that occur in Si anodes during battery cycling. FTIR is sensitive to changes in the binder and SEI chemistry, while Raman spectroscopy probes structural changes in the active materials. Despite the power of these techniques, Raman and FTIR are generally only applied to electrodes cycled in half cells for a few cycles. The mechanisms that lead to cell failure are often very different in half cells compared to full cells, [20] and some of these processes may not be evident after only a few cycles. Therefore, we carried out detailed vibrational analysis of Si-Gr composite anodes cycled in full cells with NMC532 cathodes. The anodes were analyzed after formation cycling and after long-term cycling when significant capacity fade had occurred.

Single-layer pouch cells were built at the ORNL BMF with silicon-graphite composite anodes (A-A006A) and $LiNi_{0.5}Mn_{0.3}Co_{0.2}O_2$ cathodes (A-C013A) coated by the CAMP facility at ANL. The electrolyte was 90 wt.% Gen 2 and 10% wt.% FEC and the electrolyte volume factor was 3.5-4.5. Cells were cycled between 3.0 and 4.1 V using the standard ANL protocol for a total of 100 cycles. Anodes were harvested after 1 formation cycle, 2 formation cycles, and the full cycling protocol. Anodes were analyzed by FTIR spectroscopy without air exposure. To gain insights into the SEI composition, FTIR spectra of cycled anodes were compared to a library of reference spectra of common SEI components.

The FTIR spectra of the Si-Gr composite anodes change significantly after one electrochemical cycle (Figure II-65). The broad SiO_2 band from 1000 – 1250 cm^{-1} largely disappears consistent with the electrochemical reduction of the oxide. Broad overlapping bands between 650 and 1100 cm^{-1} emerge that are a good match for lithium silicates (Li_xSiO_{2y}). The vibrational signatures of the LiPAA binder also change after one cycle. The pristine anode shows a broad shoulder near 1700 cm^{-1} that can be assigned to the carbonyl stretch of the acid (COOH) groups in LiPAA. This mode disappears after cycling indicating that the acidic protons in the binder are reduced according to the following reaction: [17, 21]

$$\text{-COOH} + Li^+ + e^- \rightarrow \text{-COOLi} + \tfrac{1}{2}\, H_2$$

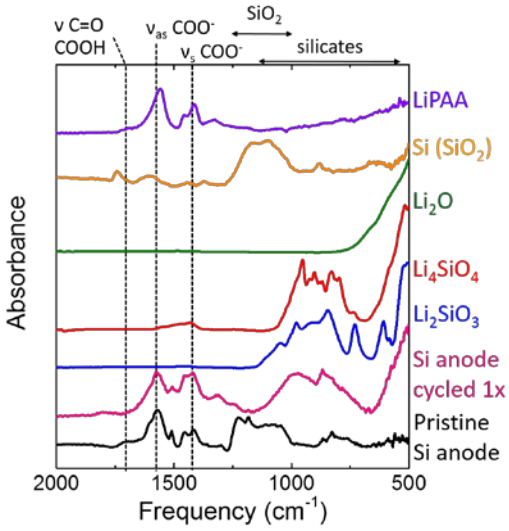

Figure II-65. FTIR spectra of the pristine Si anode and the Si anode after one formation cycle. FTIR spectra of Li_2SiO_3, Li_4SiO_4, NanoAmor silicon, and LiPAA are also shown for comparison.

This result is consistent with the half-cell data presented previously. Hydrogen evolution has been observed with silicon anodes using mass spectrometry and is typically attributed to residual water or FEC reduction. [22] The reduction of acid groups in the binder is another important mechanism that has received relatively little attention.

The SEI on the Si-Gr composite anodes continues to evolve with extended cycling (Figure II-66). After 100 cycles, the mode near 1400 cm^{-1} increases in intensity significantly. This is most likely due to the build-up of Li_2CO_3, which may form as an innate component of the SEI or as a reaction production from residual water. Further evidence for the growth of the SEI layer comes from the EC signal (ν(C=O) near 1800 cm^{-1}) that remains after 100 cycles. The EC is likely trapped in a thick SEI and cannot be removed by washing. All the reactions characterized by FTIR (silicate formation, carbonate formation, and binder decomposition) consume lithium ions and contribute to capacity fade. FTIR is therefore an excellent tool to evaluate the stability of the SEI formed on composite anodes and ultimately improve performance.

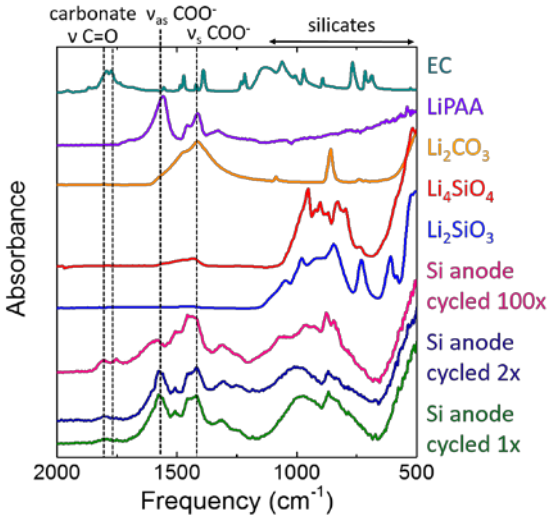

Figure II-66. FTIR spectra of the Si anode after one formation cycle, after two formation cycles, and after 100 cycles. FTIR spectra of Li_2SiO_3, Li_4SiO_4, Li_2CO_3, LiPAA, and EC are also shown for comparison.

In the future, FTIR will be combined with gas analysis to fully characterize the reactivity of binders with carboxylic acid groups. Factors that influence silicon passivation (electrolyte additives, nature of the oxide layer) will be systematically studied by monitoring the changes in SEI chemistry with FTIR. Raman mapping of electrode homogeneity and measurement of inactive silicon will characterize improvements in electrode formulation and processing. Insitu Acoustic Time of Flight (ToF) analysis of Si/Gr-NMC full cells during formation as well at various SOCs combined with EIS and microstrcutural analysis will be reported in coming quarters. This will provide more fundamental insights on the amorphization and alloying of semi-crystalline silicon during lihitation (delithiation).

Quantification of the Li Losses During Full Cell Cycling

Capacity fade of Si-based electrode in Li-ion cells has been ascribed to (1) electrical disconnection from structural degradation and (2) active lithium loss from SEI destruction/re-construction, and (3) our recently identified PAA titration. To explore the SEI component three-electrode cell analysis was performed to elucidate the SEI destruction/re-construction is the dominant factor leading to capacity fade. The electrodes used in three-electrode conflact cell were received from CAMP facility. Anode is made of 73 wt% Hitach MAGE, 15 wt% NanoAmor silicon (50–70 nm), 2wt% C-45 carbon (Timcal) and 10wt% LiPAA (LiOH titrate) with a loading of 3.28 mg/cm^2. Cathode is made of 90 wt% $LiNi_{0.5}Mn_{0}.3Co_{0.2}$ (TODA), 5 wt% C-45 carbon (Timcal), 5 wt% PVDF (Solvay 5130) with a loading of 11.32 mg/cm^2. A Li ring was used as reference electrode.

For the first 100 cycles, constant current cycling at C/3 was applied between cathode and anode in Figure II-67 (left). The cell showed a rapid capacity fade after 100 cycles. Then the constant current cycling was applied between cathode and Li ring (so-called cathode half-cell) in Figure II-67 (middle) at slow rate of C/50 since they are not facing each other. The open circuit potential of NMC cathode is close to 4.0 V, indicating the cathode is lithium deficit at oxidation state. During the first charge, only a small fraction of capacity (0.27 mAh compared to 1.7 of original capacity) can be obtain. This means limited active lithium was left due to the consumption of active lithium during SEI destruction/re-construction at the anode side. During discharge, 1.3 mAh capacity is re-gained, meaning the NMC cathode can be replenished from Li ring. Figure II-67 (right) shows the anode half-cell can be cycled close to its original capacity. This means the capacity fade is not from electric disconnection of the active material, but rather the active lithium loss. That is because the capacity cannot be regained if the fade is from electric disconnection due to structural degradation. Figure II-68 further demonstrates the argument which shows the capacity can always be re-gained close to its original value by Li replenishment from reference Li ring.

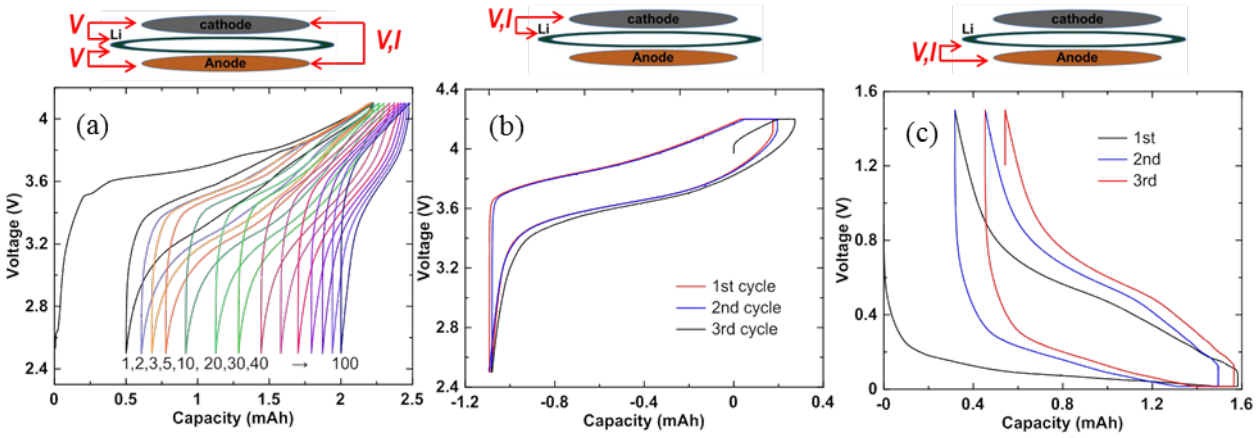

Figure II-67. (a) Voltage curve of the cathode/anode cycling at C/3, (b) Voltage curve of the cathode/Li ring cycling at C/50, and (c) Voltage curve of the anode/Li ring cycling at C/50.

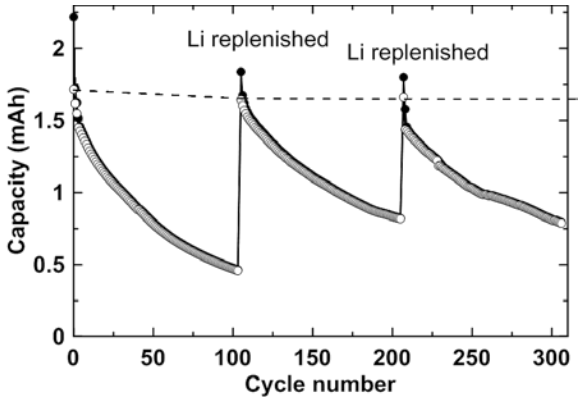

Figure II-68. Capacity cycling of the three electrode cell with Li replenished from Li ring every 100 cycles.

The voltage curves of the cathode and anode versus reference electrode during capacity fade at C/3 cycling are shown in Figure II-69. During discharge, the cathode voltage curve overlaps with each other for the top part. However, the elbow at the end of discharge gradually increases in voltage with less and less lithium can be re-intercalated into the cathode during cycling. Meanwhile, the cathode voltage during charge starts at higher voltage with less capacity available during cycling. This means the cathode is cycling in the top part of the voltage curve due to disappearance of bottom part of the voltage curve from lithium loss at the anode side. For the anode side, the end of charge voltage is also increasing with cycle number due to less active lithium available to further intercalate into graphite and lithiation of silicon.

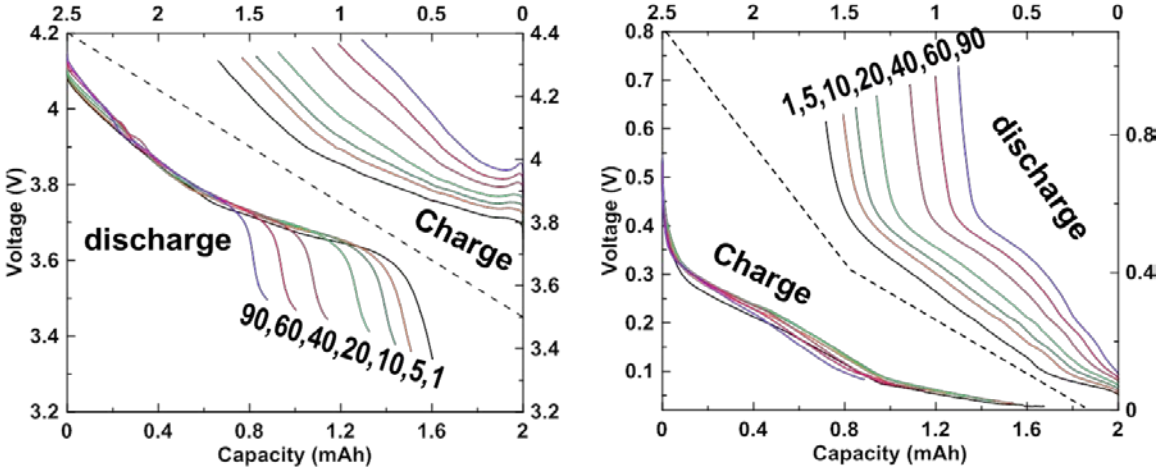

Figure II-69. a) Cathode and (b) anode voltage curve versus reference electrode during capacity fade at C/3 cycling.

Cell Modeling Silicon Alloy Electrodes (ORNL)

Si alloys, where Si is diluted by inactive component, are being investigated. The inactive component buffers the volume expansion and is also beneficial to the electrochemistry of Si, which could suppress the formation of $Li_{15}Si_4$. The cycling performance is improved because there is no particle fracture induced by a two-phase reaction front. A typical formula is written as $Si_x[M]_{1-x}$, where x is the "atomic ratio of active Si" and M is "inactive phase in the alloy" such as Fe, Ni, Mo, etc. Two questions need to be answered: 1) what is the best way to incorporate Si alloys in anode coatings; and 2) how much energy density improvement in a lithium-ion full cell can be achieved? Such information is not included in the latest version of BatPac.

In the study by Du et al., electrodes with good cycle life, high energy density, and low volume expansion were obtained when alloys were blended with graphite and calendered to high densities [25], which has been shown to be the most beneficial way to implement Si in practical Li-ion cells. [26, 27] This model is based on the well-studied conclusions: (1) lithiation of silicon alloys follows Vegard's law (molar volume of lithium requires 9 mL/mol) [23]; (2) the porosity in the Si alloy/graphite coating remains constant during charge/discharge; and (3) the volumetric capacity and energy density have to be calculated at fully expanded (lithiated) state.

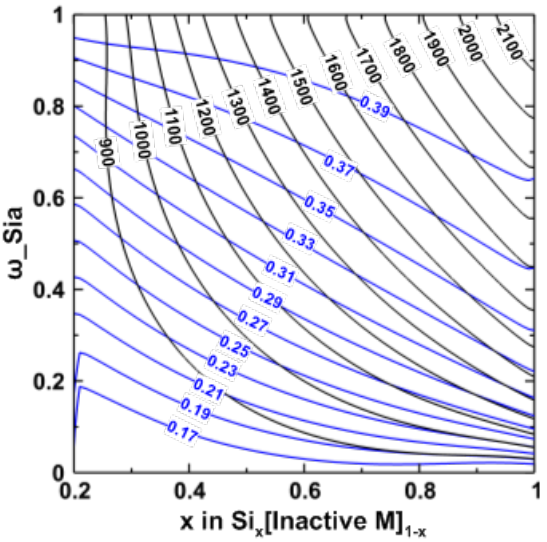

Figure II-70. Contour mapping of volumetric capacity [Ah/L, black lines] and average delithiation voltage [V, blue lines] of the Si alloy/graphite versus the composition of Si alloy and weight ratio of Si alloy/graphite. Black lines are in 100 Ah/L increment and blue lines are in 0.02 V increment.

It has been shown that the most likely way to implement Si alloys in practical Li-ion cells is blending with graphite, [24, 25, 26] which introduces a variation of ω_{Sia}, which is the weight ratio of Si alloy in the mixture. In Figure II-70, the volumetric capacity is shown to increase with an increase in either ω_{Sia} (more Si alloy), or x (more active component in Si alloy), or both. Another important factor for anode design is the average delithiation voltage. It has been pointed out by Obrovac and Chevrier that the anode voltage has more effect on volumetric energy density than the anode volume, [26] because active anode materials occupy a rather small portion of the total cell volume, while the cell energy is proportional to the cell voltage. The anode voltage should be as low as possible to get high voltage output when paired with the cathode. Since graphite has much lower voltage compared to Si, the average voltage of the Si alloy/graphite decreases with increasing graphite content as shown in Figure II-70. Therefore, a competing trend exists in the Si alloy/graphite coating design for high energy density cells: increasing active Si content in the coating increases the volumetric capacity while decreasing the anode voltage requires more graphite in the coating.

One of the most important anode metrics for new material implementation is the associated cell volumetric energy density. A contour plot of volumetric energy density is shown in Figure II-71 for cells with Si-alloy/graphite composite anodes and $LiNi_{0.5}Mn_{0.3}Co_{0.2}O_2$ (NMC532) cathodes. It is seen that the baseline cell with pure graphite (0% Si alloy) has about 740 Wh/L energy density. The energy density gradually increases from the bottom left corner (low ω_{Sia}, low x) to the upper right corner (high ω_{Sia}, high x). One macroscopic issue associated with the volume expansion of Si alloy is the dimensional change in Li-ion cells. Conventional Li-ion cells with pure graphite electrode have about 3-4% thickness change during charge/discharge due to inter-plane distance change between graphene layers. It is understood that cell expansion is much greater when Si alloy particles are incorporated into the anode, but, so far, there is no published analysis considering how

the large volume needed for the expansion of these anodes can be accommodated by the cell during initial assembly. This volume change should be kept as small as possible for practical cell and battery pack design.

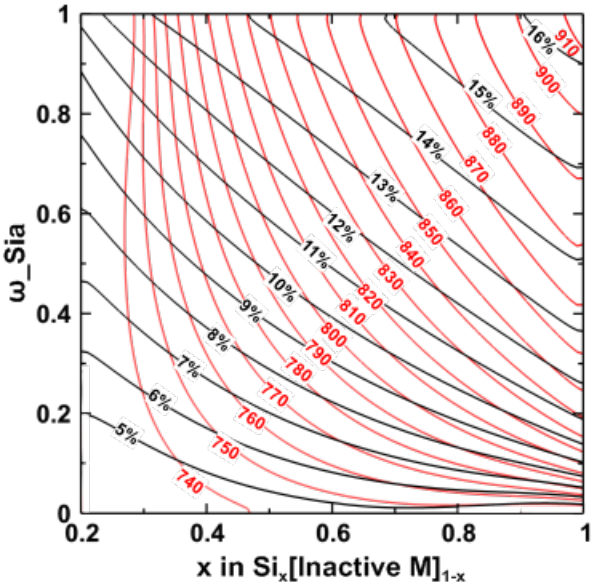

Figure II-71. Contour mapping of cell stack energy density [Wh/L, red lines] using Si alloy/graphite electrode and volume expansion ratio of the cell stack [black lines]. The increment between adjacent red lines is 10 Wh/L and the increment between adjacent black lines is 1%.

The result of the degree of cell stack expansion is shown in Figure II-71, and it is seen that to achieve the same energy density of the cell and minimize the cell stack expansion, the preferred strategy is using a high capacity (greater x) Si alloy. This strategy increases the content of graphite in the coating (lower ω_{Sia}), which contributes to the total energy density but has a low particle expansion rate (10% for graphite particles).

Figure II-72 shows the contour plots volume expansion of the Si alloy particles together with energy density of the cell stack. The volume expansion of Si alloy tends to affect the SEI layer which has little elasticity since the components in SEI are decomposition products of reactions between solvents, salts, lithium ions, and impurities in the electrolyte. [28, 29] The SEI layer on Si alloys is unstable because it can be easily broken by the large Si volume changes during lithiation/delithiation. The fresh Si surface exposed to electrolyte will form new SEI, which further consumes cell lithium inventory, leads to reduced coulombic efficiency (CE) and results in a high rate of capacity fade in full cells. Meanwhile, the ever-thickening SEI layer eventually fills pore volume in the anode, leading to the electrode failure due to blocking of Li^+ diffusion pathways. Therefore, Si alloy particles with smaller volume expansion (smaller x) are preferable in terms of less active lithium loss during new SEI formation. Figure II-71 and Figure II-72 together suggest competing strategies for maximizing the cell energy density with respect to the volume change issue. To achieve the same energy density improvement, Figure II-71 suggests using high capacity (greater x) Si alloy to minimize the expansion of the cell stack. However, Figure II-72 suggests using Si alloy particles with relatively low capacity (smaller x for smaller volume expansion) to alleviate the SEI instability.

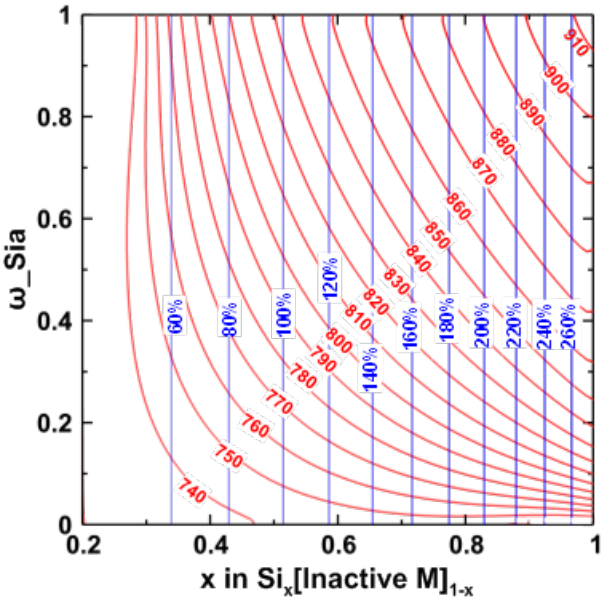

Figure II-72. Contour mapping of cell stack energy density [Wh/L, red lines] and volume expansion ratio [blue lines] of Si alloys. The increment between adjacent red lines is 10 Wh/L and the increment between adjacent blue lines is 20%.

Conclusions

Developing the initial particle size and morphology, as well as surface characteristics, of the silicon that will be compatible to processing and stable during cycling is critical for the program success. To this end, the development of techniques to characterize the silicon materials that allow the dynamics of processing and cycling to be understood is an important first step. Silicon NMR results suggest that very small average particle sizes (<50nm) result in large compositions (up to 40%) of silicon oxide type order that could be significantly detrimental in electrochemical performance. Raman maps and XPS data of cycled electrodes present clear evidence of nonuniformity during cycling associated with processing. NMR and ATR-FTIR studies indicate the selection of slurry solvent in electrode processing plays a major role in the performance of full cell batteries utilizing Si-graphite composite anodes. When completed in water, mixing needed to break up agglomerations of Si can result in additional oxidation. This can be minimized in NMP, but NMP radically changes the surface chemistry of the Si, the consequences of which are not fully understood. A better understanding of how slurry solvents interact with the surface of silicon will be needed to further progress silicon-based electrodes. Partial oxidation of silicon nanoparticles was examined to minimize the interaction of silicon with aqueous slurries. The oxidized silicon nanoparticles demonstrated improved stability in aqueous slurries at elevated temperatures. We also found that with a slightly increased oxide layer thickness to ~3 nm, the initial electrochemical performance was not compromised. Furthermore, an improvement in rate performance and full cell cycle performance can also be achieved.

Electrochemical and analytical studies on baseline cells subjected to 100 cycles and the harvested electrodes indicates extensive SEI formation in the negative electrode (with or without FEC) and Si deposition on the positive electrode (without FEC) were observed. The chemical patterns of these changes were consistent with advanced HF acidolysis of Si/SiO_2 particles. Once water becomes inadvertently introduced into the Si-containing electrode, it continuously cycles through the system, yielding HF acid. This HF acid causes considerable damage to Si particles, while hydrolysis of $LiPF_6$ keeps on supplying fluoride anions for this cycle. Given that HF plays such pivotal and dramatic roles in this capacity fade, it is noteworthy that a part of the problem is the presence of water in electrodes that are processed from aqueous solutions of polycarboxylate binders. This is especially vexing because it might be impossible to remove all of this matrix-trapped water, as high temperatures are needed to shift the hydration equilibria and release the water from the

hydrates, whereas at such temperatures the residual $–CO_2H$ groups in the polycarboxylate binder decompose, releasing more water. If water cannot be removed from the matrix, then using lithium salts that do not hydrolyze and yield HF can be a way to address this problem; however, most of such salts are known to corrode aluminum current collectors; finding alternatives to $LiPF_6$, thus, remains a continuing challenge for lithium-ion cells.

The role of interfaces in developing a better understanding of the silicon electrode in a lithium-ion battery configuration by comparing the results of using a polymer coating on the surface and varying the amount of silica. Electrochemical quartz crystal microbalance (EQCM) and CV studies have identified the role of FEC in forming films of varying thickness and the role these films play in impedance and cycling stability. Adding silica as the interfacial phase was found to increase first cycle irreversible capacity as expected and had minimal impact on the samples with denser silica layers. Samples with less dense layers showed a larger benefit from the FEC additive, in terms of increase cycling stability over the first 10 cycles, maximized at 10wt% FEC. Above this amount increased film thickness and lower electrolyte conductivity counteract any benefit of increased amounts.

Electrochemical and analytical studies on materials, electrodes, and cells were utilized to understand capacity losses with silicon anodes. Analysis of coulombic inefficiencies in PAA binder-based Si-graphite full cells identified the importance of using the lithiated binder. FTIR was used to identify SEI reaction products and was shown to be an excellent tool to evaluate the stability of the SEI formed on composite anodes and ultimately improve performance. Three electrode full cells were used to examine electrode shifts with cycling and clearly demonstrated that capacity losses occurred at the anode. Also, the third electrode of lithium was used to replenish the lithium in the full cell, effectively increasing cycle life and suggesting the importance of lithium inventory issues.

An engineering model was developed to study silicon alloy/graphite electrodes. The analysis of silicon containing electrodes indicates that optimum electrode characteristics will be a balance of composition, loading, porosity, and SEI stability. The model should help determine electrode limitations and how best to take advantage of electrode improvements.

Key Publications

1. J. Bareño, I.A. Shkrob, J.A. Gilbert, M. Klett, D.P. Abraham, “Capacity Fade and Its Mitigation in Li-ion Cells with Silicon-Graphite Electrodes”, J. Phys. Chem. C, Accepted for Publication (2017).

2. M. Klett, J.A. Gilbert, K.Z. Pupek, S.E. Trask, D.P. Abraham, “Layered Oxide, Graphite and Silicon-Graphite Electrodes for Lithium-ion Cells: Effect of Electrolyte Composition and Cycling Windows”, J. Electrochem. Soc. 164 (2017) A6095.

3. M. Klett, J.A. Gilbert, S.E. Trask, B.J. Polzin, A.N. Jansen, D.W. Dees, D.P. Abraham, “Electrode Behavior RE-Visited: Monitoring Potential Windows, Capacity Loss, and Impedance Changes in Li1.03(Ni0.5Co0.2Mn0.3)0.97O2/Silicon-Graphite Full Cells”, J. Electrochem. Soc. 163 (2016) A875.

4. C.D. Malliakas, K. Leung, K.Z. Pupek, I.A. Shkrob, D.P. Abraham, “Spontaneous aggregation of lithium ion coordination polymers in fluorinated electrolytes for high-voltage batteries”, Phys. Chem. Chem. Phys. 18 (2016) 10846-10849.

5. I.A. Shkrob, J.F. Wishart, D.P. Abraham, “What Makes Fluoroethylene Carbonate Different?”, J. Phys. Chem. C 119 (2015) 14954.

6. D.P. Abraham, K. Kalaga, S.E. Trask, “Passivation of the Silicon-Graphite negative electrode during Aging of Lithium-ion Full Cells”, International Society of Electrochemistry (ISE) Fall meeting, Providence, RI, Aug 28-Sept. 1, 2017.

7. D.P. Abraham, Invited Speaker, “Designing Silicon-containing Lithium-ion Cells”, Case Western Reserve University, Cleveland, OH, October 20, 2016.

8. D.P. Abraham, “Electrochemical Diagnostics in the Silicon Deep Dive Program”, DOE Program Update, Argonne National Laboratory, October 18, 2016.

9. D.P. Abraham, “A Closer Look at Silicon-Graphite (SiGr) Composite Electrodes During Cycling in NCM523/SiGr Full Cells”, Advanced Automotive Battery Conference (AABC 2016), Detroit, MI, June 14-17 2016.

10. D.P. Abraham, “Designing high-energy lithium-ion cells with Si-containing electrodes”, Gordon Research Conference on Batteries, Ventura, CA, February 21-26, 2016.

11. “Next Generation Anodes for Lithium-Ion Batteries: Overview,” 2017 U.S. Department of Energy Vehicle Technologies Office Annual Merit Review and Peer Evaluation Meeting, June 5-9, 2017, Washington, DC.

References

1. *Alloy Negative Electrodes for Li-Ion Batteries*. M.N. Obrovac and V.L. Chevrier, Chem, Rev. 2014, 114, 11444-11503.

2. B. Key, R. Bhattacharyya, M. Morcrette, V. Seznec, J-M. Tarascon, C. P. Grey, J. Am. Chem. Soc., 2009, 131 (26), pp 9239–9249

3. B. Key, M. Morcrette, J-M. Tarascon, C. P. Grey, J. Am. Chem. Soc., 2011, 133 (3), pp 503–512

4. A. L. Michan, M. Leskes, C. P. Grey, Chem. Mater., 2016, 28 (1), pp 385–398

5. A. L. Michan, D. Divitini, A. J. Pell, M. Leskes, C. Ducati, C. P. Grey, J. Am. Chem. Soc. 2016, 138, 7918−7931

6. A. L. Michan, B. S. Parimalam, M. Leskes, R. N. Kerber, T. Yoon, C. P. Grey, B. L. Lucht, Chem. Mater., 2016

7. Multinuclear Solid-State Nuclear Magnetic Resonance of Inorganic Materials, Volume 6, 1st Edition, Authors: Kenneth MacKenzie M.E. Smith

8. S. Xun et al., "The effects of Native Oxide Surface Layer on the Electrochemical Performance of Si Nanoparticle-Based Electrodes", Journal of the Electrochemical Society, 2011, 158(12)

9. S. Xun et al., "Imptoved Initial Performance of Si Nanoparticles by Surface Oxide Reduction for Lithium-Ion Battery Application", Electrochemical and Solid-State Letters, 2011, 14(5)

10. A. Touidjine et al., "Partially Oxidized Silicon Particles for Stable Aqueous Slurries and Practical Large-Scale Making of Si-Based Electrodes", Journal of the Electrochemical Society, 2015, 162(8)

11. Mawhinney et al., " Ftir Study of the Oxidation of Porous Silicon", Journal of Physical Chemistry B, 1997, 101(5)

12. Sim et al., "Critical Thickness of SiO2 Coating Layer on Core@Shell Bulk@Nanowire Si Anode Materials for Li-Ion Batteries", Advanced Materials, 2013, 25(6)

13. X. Su, Q. Wu, J. Li, X. Xiao, A. Lott, W. Lu, B. W. Sheldon, Ji Wu Adv. Energy Mater., 4, 1300882 (2014).

14. Roland Jung, Michael Metzger, Dominik Haering,Sophie Solchenbach, Cyril Marino, Nikolaos Tsiouvaras, Christoph Stinner, Hubert A. Gasteiger Journal of The Electrochemical Society, 163 (8) A1705-A1716 (2016)

15. Zhijia Du, Hui Liu,S. N. Ellis, R. A. Dunlap, M. Zhu, M. N. Obrovac Journal of The Electrochemical Society, 163 (7) A1275-A1279 (2016)

16. Aude A. Hubaud, ZhenZhen Yang, David J. Schroeder, Fulya Dogan, Lynn Trahey, John T. Vaughey Journal of Power Sources 282 (2015) 639-644

17. Nguyen, C. C.; Yoon, T.; Seo, D. M.; Guduru, P.; Lucht, B. L., Systematic Investigation of Binders for Silicon Anodes: Interactions of Binder with Silicon Particles and Electrolytes and Effects of Binders on Solid Electrolyte Interphase Formation. *ACS Appl. Mater. Interfaces* **2016,** *8*, 12211-12220.

18. Aiken, C. P.; Xia, J.; Wang, D. Y. H.; Stevens, D. A.; Trussler, S.; Dahn, J. R., An Apparatus for the Study of In Situ Gas Evolution in Li-Ion Pouch Cells. *J. Electrochem. Soc.* **2014,** *161*, A1548-A1554.

19. Deacon, G. B.; Phillips, R. J., Relationships between the Carbon-Oxygen Stretching Frequencies of Carboxylato Complexes and the Type of Carboxylate Coordination. *Coordin Chem Rev* **1980,** *33*, 227-250.

20. Dupre, N.; Moreau, P.; De Vito, E.; Quazuguel, L.; Boniface, M.; Bordes, A.; Rudisch, C.; Bayle-Guillemaud, P.; Guyomard, D., Multiprobe Study of the Solid Electrolyte Interphase on Silicon-Based Electrodes in Full-Cell Configuration. *Chem. Mat.* **2016,** *28*, 2557-2572.

21. Bachman, G. B.; Astle, M. J., The Dropping Mercury Electrode in Acetic Acid. I. Discontinuous Current-Voltage Curves1. *J. Am. Chem. Soc.* **1942,** *64*, 1303-1309.

22. Jung, R.; Metzger, M.; Haering, D.; Solchenbach, S.; Marino, C.; Tsiouvaras, N.; Stinner, C.; Gasteiger, H. A., Consumption of Fluoroethylene Carbonate (FEC) on Si-C Composite Electrodes for Li-Ion Batteries. *J. Electrochem. Soc.* **2016,** *163*, A1705-A1716.

23. Obrovac, M. N.; Christensen, L.; Le, D. B.; Dahn, J. R., Alloy Design for Lithium-Ion Battery Anodes. *Journal of The Electrochemical Society* **2007,** *154*, A849-A855.

24. Du, Z.; Liu, H.; Ellis, S. N.; Dunlap, R. A.; Zhu, M.; Obrovac, M. N., Electrochemistry of CuxSi1−x Alloys in Li Cells. *Journal of The Electrochemical Society* **2016,** *163*, A1275-A1279.

25. Du, Z.; Dunlap, R. A.; Obrovac, M. N., High Energy Density Calendered Si Alloy/Graphite Anodes. *Journal of The Electrochemical Society* **2014,** *161*, A1698-A1705.

26. Obrovac, M. N.; Chevrier, V. L., Alloy Negative Electrodes for Li-Ion Batteries. *Chemical Reviews* **2014,** *114*, 11444-11502.

27. Zhao, H.; Yuan, W.; Liu, G., Hierarchical electrode design of high-capacity alloy nanomaterials for lithium-ion batteries. *Nano Today* **2015,** *10*, 193-212.

28. Arora, P.; White, R. E.; Doyle, M., Capacity Fade Mechanisms and Side Reactions in Lithium-Ion Batteries. *Journal of The Electrochemical Society* **1998,** *145*, 3647-3667.

29. Nie, M.; Abraham, D. P.; Chen, Y.; Bose, A.; Lucht, B. L., Silicon Solid Electrolyte Interphase (SEI) of Lithium Ion Battery Characterized by Microscopy and Spectroscopy. *J. Phys. Chem. C* **2013,** *117*, 13403-13412.

II.B.3 Next Generation Anodes for Lithium-Ion Batteries: Materials Advancements (ANL)

Dennis Dees, Principal Investigator
Argonne National Laboratory
9700 South Cass Avenue
Argonne, IL 60439
Phone: 630-252-7349
E-mail: dees@anl.gov

Peter Faguy, Technology Manager
U.S. Department of Energy
Phone: 202-586-1022
E-mail: Peter.Faguy@ee.doe.gov

Start Date: October 1, 2015 End Date: September 30, 2019
Total FY17 Project Cost: $3,600,000 DOE FY17 share: $3,600,000 Non-DOE share: $0

Project Introduction

Silicon has received significant attention as a viable alternative to graphitic carbon as the negative electrode in lithium-ion batteries due to its high capacity and availability [1]. Elemental silicon can theoretically store >3500 mAh/g, nearly an order of magnitude higher than graphite (372 mAh/g and 818 mAh/mL, respectively). However, several problems have been identified that limit its utility including large crystallographic expansion (~320%) upon lithiation which translates to particle cracking, particle isolation, and electrode delamination issues. Further, there are fundamental and volume change related SEI stability issues, which affect cycling efficiency. The wealth of previous studies in this area is both a testament to its potential and the size of the challenge that must be overcome, requiring a great amount of innovation on multiple fronts.

Next Generation Anodes for Lithium-Ion Batteries, also referred to as the Silicon Deep Dive Program, is a five National Laboratory consortium assembled to tackle the barriers associated with development of an advanced lithium-ion negative electrode based upon silicon as the active material. This research program baselines promising silicon materials that can be developed or obtained in quantities sufficient for electrode preparation within the consortium facilities. Composite electrode and full cell development leverages recent investments made by DOE-EERE-VTO in electrode materials and characterization. The primary objective of this program is to understand and eliminate the barriers to implementation of a silicon-based anode in lithium-ion cells. The Labs are focused on a single program with continuous interaction, clear protocols for analysis, and targets for developing both the understanding and cell chemistry associated with advance negative electrodes for lithium-ion cells. First and foremost, this undertaking is a full electrode/full cell chemistry project leveraging baseline electrodes prepared at the consortium facilities. All efforts are directed to understanding and developing the chemistry needed for advancing silicon-based anodes operating in full cells. Materials development efforts include active material development, binder synthesis, coatings, safety, and electrolyte additives. Efforts include diagnostic research from all partners, which span a wide range of electrochemical, chemical and structural characterization of the system across length- and time-scales. Specialized characterization techniques developed with DOE-EERE-VTO funding, include neutrons, NMR, optical, and X-ray techniques being employed to understand operation and failure mechanisms in silicon-based anodes. In addition, several strategies to mitigate lithium loss are being assessed. The project is managed as a single team effort spanning the Labs, with consensus decisions driving research directions and toward development of high-energy density lithium-ion batteries. A detailed list of participants is given in Figure II-73.

Figure II-73. Program participants including Laboratories, research facilities, and individual contributors.

Objectives

- Understand and overcome the science and technology barriers to the use of silicon-based anodes in high-energy density lithium-ion batteries for transportation applications.
  - Stabilize the SEI
  - Stabilize the electrode
- Demonstrate functional prototype lithium-ion cell chemistries which meet the DOE/USABC performance targets.

Approach

Sandia National Laboratories (SNL), Oak Ridge National Laboratory (ORNL), National Renewable Energy laboratory (NREL), Lawrence Berkeley National Laboratory (LBNL), and Argonne National Laboratory (ANL) have teamed together to form an integrated program. Technical targets have been developed and regular communications have been established. Throughout the program, there is a planned focus on understanding, insights into, and advancement of silicon-based materials, electrodes, and cells. All anode advancements will be verified based on life and performance of full cells. Toward that end, baseline silicon-based materials, electrodes, and cells have been adopted, along with full cell testing protocols.

Supported by the diagnostic studies, materials development on silicon-based materials, electrodes, and cells is being conducted to enhance interfacial stability, accommodate intermetallic volume changes, and improve overall performance and life. Key to this effort is the development and testing of coatings and additives designed to modify and stabilize the dynamic silicon-electrolyte interface. Further, functional polymer binders designed to accommodate volume changes, increase conductivity, and improve adherence are being developed and analyzed. Finally, the program is exploring active material development. Alternative high-energy silicon-alloy/composite materials are being considered. Also, strategies for introducing additional lithium inventory into the cell are being developed.

Communication of programmatic progress to battery community is critical. This will generally be accomplished through publications, presentations, reports, and reviews. Further, the program is open to industrial participation and/or collaboration that does not limit program innovation or the free flow of information. Finally, this program is highly integrated with our sister program on SEI-Stabilization, called SEI-Sta for short. In general, SEI-Sta is focused on the development and characterization of model systems, thin-film well-defined active area electrodes on which it is easier to extract fundamental information on lithium-silicon phase formation, lithium transport, and interfacial phenomena (e.g., SEI formation and growth).

Results

Polymer Binders for Silicon Anodes (ORNL)

A high-performance polymer binder can mitigate the volume expansion stress and maintain the electrical contact with conductive additive and current collector to achieve long-term cycling capacity. Recent progress in the field of polymer binders for silicon-based anode has clearly demonstrated the importance of adhesion strength and mechanical property of the polymeric materials. The graft polymers have been attracting significant attentions due to their efficient control over the structure and the corresponding properties of obtained materials. [2-5] The graft copolymer with chemically distinguished grafted side chains and polymer backbones can retain their desired properties from both polymer components, and enable efficient control of both chemical/physical interaction and mechanical performance, [3, 5] which are extremely important for polymer binder applications. The PAA grafted polyvinylidene fluoride (PVDF) and NaPAA grafted CMC are reported to exhibit improved cycling performance compared with linear analogues, while their architecture effect on polymer binder performance were not investigated due to the limitation of synthetic strategy which do not allow a defined polymer architecture.

To elucidate the architecture effect of synthetic polymers on the polymer binder performance, ORNL team (Saito, Cao) synthesized a novel graft block copolymer with readily tunable architecture parameters such as side chain length and grafting density (Figure II-74) and tested as the polymer binder for the high-mass loading silicon (15wt%)/graphite (73wt%) composite electrode (active materials > 2.5 mg/cm2).

The novel graft copolymer glycol chitosan-g-lithium polyacrylate (GC-g-LiPAA) with GC as backbone and LiPAA as side chains was obtained by amidation reaction and RAFT polymerization (Figure II-74). The (g) signifies grafted. The side chain length and the degree of grafting density were tailored by changing the feed ratio during the reaction. For example, 22.1% of the GC repeating units was functionalized, which corresponds to 88 arms per graft copolymer. RAFT polymerization of acrylic acid from the macro GC22%-RAFT allows the growth of polymer side chains. Followed by neutralization with LiOH, the synthesized GC-g-LiPAA resulted in the GC22%-g-LiPAA62 where 62 represents the chain length and is a measure of the degree of polymerization (DPn).

The composite electrode with 73% graphite and 15% silicon as the active materials at a loading of active materials > 2.5 mg/cm2; thickness > 30 µm was fabricated. The theoretical specific capacity is calculated to be 875 mAh/g. Moreover, the good water solubility of the obtained graft copolymer GC22%-g-LiPAA62 allows to use water as the solvent. Energy-dispersive X-ray spectroscopy mapping showed the homogenous distribution of silicon and formation of a uniform porous structure.

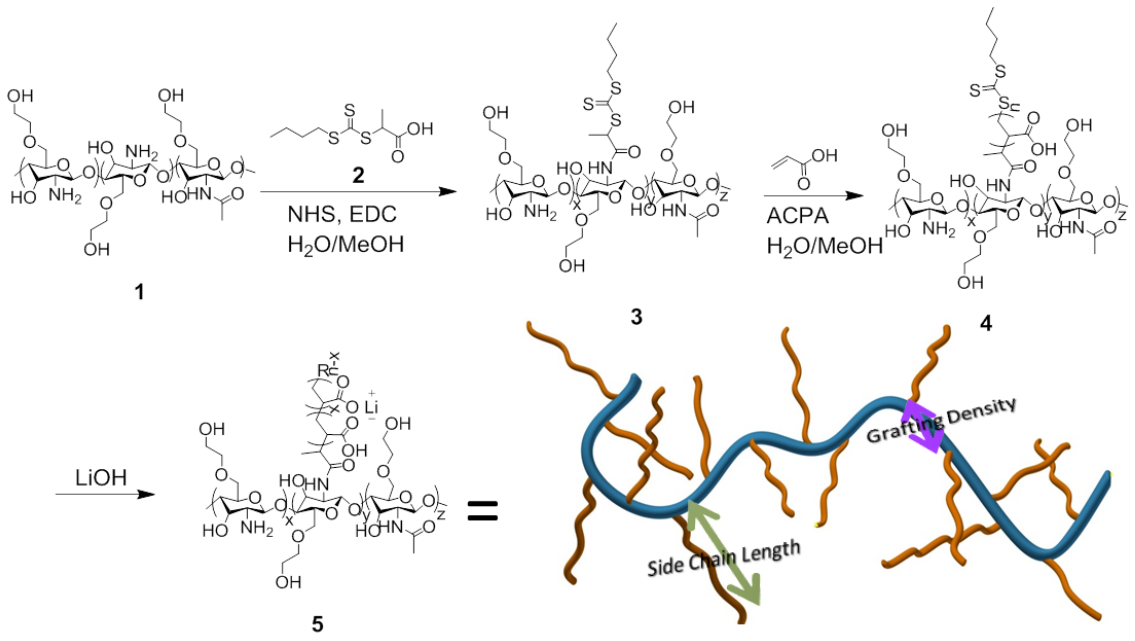

Figure II-74. Synthesis of graft copolymer GC-g-LiPAA via RAFT polymerization.

The architecture effect of synthetic polymer binders on the electrochemical performance of silicon/graphite electrode was investigated by comparing the synthesized graft copolymer with the linear analogues. Pure GC and physical mixture (indicated by "m") of GC and LiPAA (GC21%-m-LiPAA76) were utilized as the linear analogues for comparison purpose. As illustrated in Figure II-75(A), the electrodes based on PVDF and GC showed acceptable de-lithiation capacities at the first cycle. However, a rapid capacity loss was observed for the subsequent cycles, and only less than 300 mAh/g capacity was retaining, which is mostly contributed by the graphite. Addition of neutralized linear LiPAA to the GC can promote the physical interaction with the silicon materials and provide extra lithium-ion access to mitigate the de-activation of silicon particles. [6-9] As expected, the electrodes with the physical mixture of LiPAA and GC (GC21%-m-LiPAA76) as the binder showed higher initial de-lithiation capacity and better cycling performance (356 mAh/g after 100 cycles) than GC and PVDF. The electrodes with graft copolymer GC22%-g-LiPAA62 showed high initial de-lithiation capacity (745 mAh/g) and significantly improved cycling performance with a de-lithiation capacity of 495 mAh/g after 100 cycles. Moreover, as illustrated in Figure II-75(B), the graft copolymer GC22%-g-LiPAA62 exhibited higher initial coulombic efficiency than its linear analogues (90.3% vs 62.8%, 76.1%, and 88.1%). The interesting phenomenon that worth our attention is the significantly improved cycling performance of GC22%-g-LiPAA62 compared with that of GC21%-m-LiPAA76 in both retaining capacity and coulombic efficiency. With the same chemical composition and functional-group ratio, the significantly improved cycling performance clearly suggests the advantage of a multi-grafted architecture over the physical mixture which may be contributed by the formation of a better interfacial architecture.

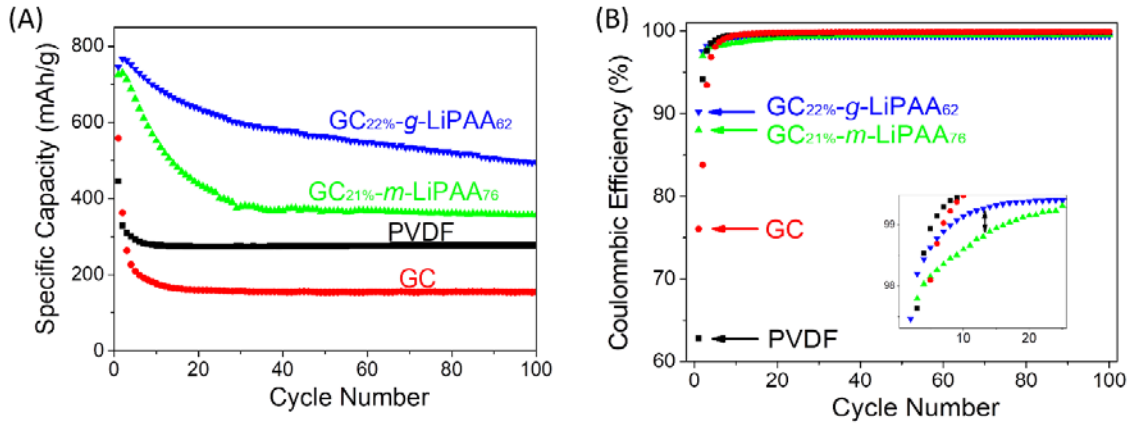

Figure II-75. (A) Cycling performance silicon/graphite electrodes from the polymer binder of PVDF, GC, GC21%-m-LiPAA76 and GC22%-g-LiPAA62 at a current rate of C/10; (B) Coulombic efficiency of the electrodes from different polymer binders, inset is the zoom-in area showing the comparative efficiency of electrodes from GC21%-m-LiPAA76 and GC22%-g-LiPAA62 in the first 30 cycles;

The improved binder performance of graft copolymer GC22%-g-LiPAA62 can be explained as follows. First, the incorporation of numerous LiPAA side chains in the graft copolymer allows more efficient interaction with the SiNPs, which can efficiently prevent the isolation of SiNPs from the surrounding conductive network. The significantly higher peeling force of the electrode made from GC22%-g-LiPAA62 (~0.75 N/cm) compared with that from GC22%-m-LiPAA76 (< 0.1 N/cm) confirms improved adhesion strength of GC22%-g-LiPAA62 with the electrode composite. Secondly, the enhanced interaction and extra lithium-ion source should help forming a stable solid electrolyte interphase (SEI) layer on SiNPs. Lastly, the comparative higher solution viscosity of the graft copolymer may also contribute to the formation of a homogenous electrode film due to the reason pointed out above.

The side chain length of grafted copolymer is adjusted by changing the feeding ratio of monomer (acrylic acid) to macro RAFT-CTA (GC22%-RAFT, 4). Significant improvement was observed when the side chain length of GC22%-g-LiPAAx increased from DPn=17 to DPn=27 in terms of both first-cycle de-lithiation capacity and long cycling performance. Comparable initial discharge capacity was obtained when further increasing the side chain length from DPn=27 to DPn=62. In terms of long-term cycling performance, the electrode made of GC22%-g-LiPAA62 showed better performance than that with the GC22%-g-LiPAA27, while this difference is much less significant comparing with that when the DPn of side chain increased from 17 to 27 (See Figure II-76).

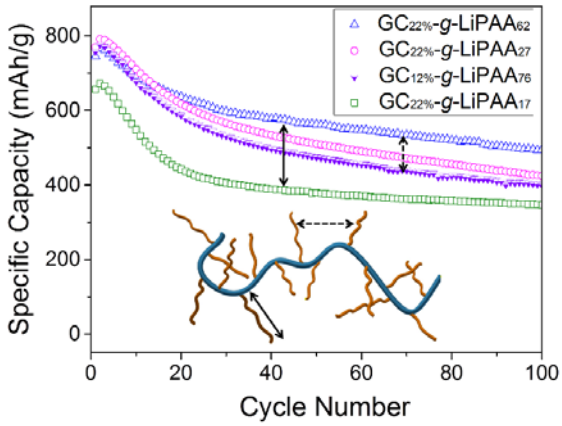

Figure II-76. Cycling performance of silicon/graphite electrodes from the polymer binder of GC22%-g-LiPAA17, GC22%-g-LiPAA27, GC22%-g-LiPAA62, and GC12%-g-LiPAA71 at a current rate of 0.1 C.

The galvanostatic result showed that the electrode with GC12%-g-LiPAA76 exhibited comparable initial delithiation capacity with that from GC22%-g-LiPAA62 (758 mAh/g vs 745 mAh/g) (Figure II-76). However, after 10 cycles, the graft copolymers with higher grafting density start showing the advantage in the long-term cycling performance (67% retaining capacity for GC22%-g-LiPAA62 vs 54% retaining capacity for GC12%-g-LiPAA76 at 100th cycle). The better cycling performance of the graft copolymer with higher grafting density should be mainly attributed to the increased number of anchoring points (88 arms vs 48 arms) that interact with the active material and conduction network. Similar to the explanation above, the higher peeling strength and increased solution viscosity (23.1 mPa.S to 195 mPa.S) suggest that the enhanced interaction of the high grafting-density graft copolymer with electrode composite is responsible for the improved binder performance.

Advanced Polymer Binders

Saito and Cao have designed a cross-linked catechol group functionalized chitosan as the polymer binder for SiNPs-based anode for further improving the adhesion and the mechanical stability. In this project, a nature-derived polymer, chitosan was functionalized by catechol groups (Chitosan-CG) as shown in Figure II-77. Then after mixing the Chitosan-CG with SiNPs and carbon black, different weight percents of glutaraldehyde (GA) was added as the cross-linker. The synthesized polymer binders not only provide strong adhesion to silicon surface by catechol groups, but also resist the deformation of the anode during lithiation/delithiation process by cross-linking.

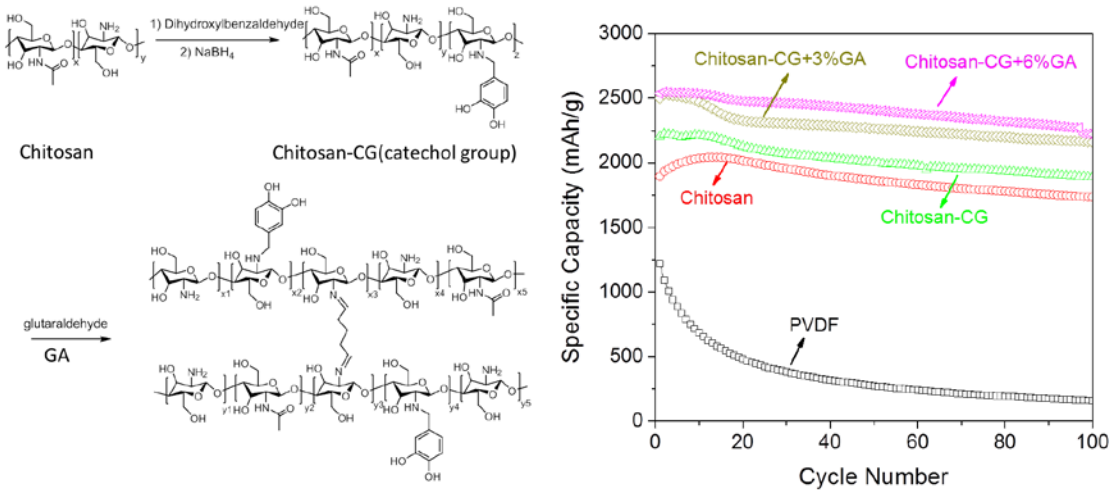

Figure II-77. Synthesis scheme of cross-linked catechol groups functionalized chitosan; cycling performance of different polymer binders. (silicon-based anode: 60% SiNPs, 20% polymer binder and 20% carbon black).

The cycling performance of different polymer binders was shown in Figure II-77. It can be seen that the chitosan showed better cycling performance than typical polymer binder PVDF. After functionalization by catechol groups, the cycling performance of the fabricated anode improved due to the physical interaction of the catechol groups with the SiNPs. In-situ cross-linking will further provide the mechanical robustness of the polymer binders which can resist the deformation of SiNPs during the lithiation and de-lithiation process. Therefore, with 6w% of GA added, the silicon-based anode with Chitosan-CG+6%GC exhibited excellent long-term stability with retaining capacity over 2350 mAh/g after 100 cycles. This is an extremely promising research direction we propose to continue to investigate depending on funding availability in FY18.

Polymer Binder Development for Silicon Anodes (ANL)

A series of new polymeric binders have been developed by utilizing flexible backbones and incorporating hydrophilic groups that could improve the desired properties, and some examples include carboxymethyl cellulose (CMC), alginate, and poly(acrylic acid) (PAA), etc. With some success, many of those binders provided much improved cycling performance for silicon anodes. However, those improvements are still far from enough for practical applications and significant capacity losses were still observed during extended cycling tests. As one of the most important components that directly works with silicon particles, those binders still need significant improvement in terms of physical, electrochemical as well as mechanical properties, including adhesion, cohesion, elasticity, conductivity, electrochemical stability, yield strength, tensile strength, fatigue strength, and crack resistance, etc. There are still many blanks that need to be filled in the binder field. In this project, we are trying to improve the cycling performance of silicon-based anodes by re-engineering the best performing exiting binders, such as PAAs.

Crosslinked Poly(acrylic acid) Binders for Silicon Anode

Polymeric materials can be divided into three categories based on their overall structures: linear, branched and crosslinked polymers. And those structures have huge impact on the polymer properties, especially on physical and mechanical properties. Most binders that have been studied are linear polymers, and only a few examples of novel binders have used branched or crosslinked polymers and very little has been done to systematically study the impact of those structural changes on polymer properties and more importantly on cycling performance. [10] Here we proposed and started to develop new polymeric materials by re-design the promising linear polymeric binders into crosslinked structures, hoping to understand the associated property changes and improve the cell cycling performance by pushing those properties to the desired directions. In this report, we used PAAs as the base material and adapted two approaches to crosslink those linear polymers.

To prepare the crosslinked PAA (cPAA) binders, two approaches have been proposed and conducted (See Figure II-78): firstly, commercially available PAA polymers were reacted directly with crosslinkers that have two or more linking groups, such as ethylene glycol diglycidyl ether (EGDGE). The epoxy groups in EGDGE can efficiently react with carboxyl groups at room temperature and form a bridge between two carboxyls. This allows quick screening of the cross-linkers and finding the optimal molar ratios for a better performance. Secondly, acrylic acid (AA) monomers were co-polymerized with the vinyl type cross-linkers, such as poly(ethylene glycol) diacrylate (PEGDA). Reversible Addition-Fragmentation chain Transfer (RAFT) was used to prompt higher molecular weights and low polydispersity index (PDI). This approach has a better control of the crosslinking reaction sites as well as the molecular weights of cPAAs.

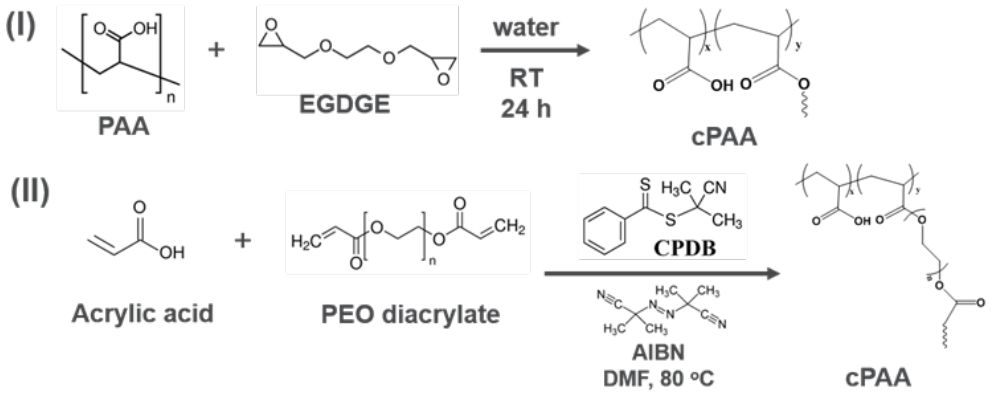

Figure II-78. Approaches for synthesizing crosslinked PAA binders.

For cycling characterization, half cells containing the new developed binders were used. Two types of silicon electrodes were used to evaluate those binders in this report, including silicon/graphite composite electrode, which contains 15% silicon particles, and high capacity silicon electrode, which contains 70% silicon particles.

Five cPAAs have been synthesized and their characterization results are summarized in Table II-6. Two binders, cPAA1 and cPAA2, were synthesized via approach I, and a PAA polymer with number average molecular weight (Mn) around 30 k were used as the precursor to react with EGDEG crosslinkers at different concentrations. By design, if crosslinking happened, a much increased Mn for cPAA1 and cPAA2 should be expected. However, we were surprised to see that cPAA1 and cPAA2 demonstrated very similar Mn values, which is also close to that of the precursor PAA polymer. This unexpected result may indicate that the crosslinking reaction didn't occur as hoped to bridge two PAA chains but rather connect two carboxyl groups from a single PAA chain, leading to no crosslinking but intramolecular bridging. In that case, the more crosslinker added, the more constrained conformation should be expected considering more intramolecular bridges formed. The two cPAAs were evaluated in half cells and the specific capacity profiles are compiled in Figure II-79. As shown in the left, for silicon/graphite composite electrode, cPAA1 seems to work well and affords comparable cycling performance to that of PAA cells but no obvious improvement was observed either. The cell containing cPAA2, on the other hand, delivered much worse initial capacity as well as capacity retention (see Table II-6). The results actually are supporting our speculation on the intramolecular crosslinking reactions. With low content of EGDEG, as those crosslinkers were attached to each individual PAA chain but no crosslinking between different chains occurred, cPAA1 should still behave very much the same as linear PAAs. For cPAA2, the higher content of EGDEG may lead to more constrained conformation by those intramolecular linking, which may account for the much worse performance. However, this conformation change is a good new for high capacity silicon anodes. As shown in the Figure II-79(right), for the high capacity silicon anode test, the cPAA2 binder delivered much better initial capacity and capacity retention compared to those of linear PAA cells. We suspected that the conformation changes may lead to better adhesion of cPAA2 binder to silicon particles, accounting for the improved cycling performance.

Overall, approach I could produce cPAAs in a very efficient way but due to the abundant caroxylic acid groups, there is very little control of the crosslinking sites on PAA polymers and therefore the majority of crosslinkers only attached to each PAA chains by linking adjacent carboxyl groups instead of bridging different chains. A better control of the crosslinking reactions should be needed.

Table II-6: Summary of synthesized cPAAs.

Approach	Polymer	Crosslinker[a]	Crosslinker %[b]	DP[c]	Mn[d]	PDI	Initial capacity (mAh/g)	Capacty retention
I	cPAA1	EGDEG	0.01%	404	34.3 K	2.66	722	39%
	cPAA2	EGDEG	0.1%	404	38.3 K	2.36	474	31%
II	cPAA3	PEGDA1	0.05 %	690	50.3 K	1.50	704	28%
	cPAA4	PEGDA2	0.2 %	631	44.1 K	1.77	751	76%
	cPAA5	PEGDA2	0.1 %	736	64.8 K	1.45		

a) The number average molecular weights (Mn) of PEGDA1 and PEGDA2 are 8,000 and 250 Da, respectively.

b) This value is the weight percentage of the crosslinkers to the PAA polymers.

c) DP (degree of polymerization) is the number of repeating units of the polymer.

d) Mn is the number average molecular weight of the methylated crosslinked PAA, characterized by gel permeation chromatography (GPC).

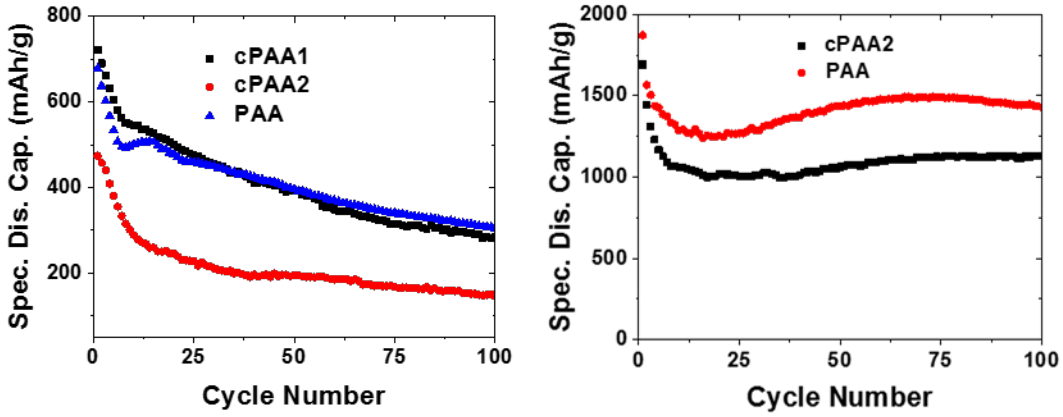

Figure II-79. Specific discharge capacities of half cells of (left) silicon/graphite composite electrodes (15% silicon) and (right) high capacity silicon electrodes (70% silicon) using PAA-based binders during the course of 100 cycles under C/3 rate.

Approach II was proposed to produce cPAAs by co-polymering the monomers and crosslinker molecules. cPAA3, cPAA4, and cPAA5 were synthesized by heating the mixture of acrylic acid (AA), 2-cyano-2-propyl benzodithioate (CPDB, RAFT agent), azobisisobutyronitrile (AIBN, initiator) as well as poly(ethylene glycol) diacrylate (PEGDA, crosslinker). The RAFT agents (CPDB) help to control the molecular weight and polydispersity (PDI) of the produced polymers. Since the crosslinking reactions occurs as the chain grows, there should be a good chance for the crosslinkers to bridge two chains instead of growing on the same chain. Two PEGDA (PEGDA1, 8000 Da and PEGDA2 250 Da) were used in the synthesis. As shown in Table II-6, all three polymers were produced with reasonable PDI values. The different percentage of crosslinker doesn't seem to impact the overall molecular weights very much and all three cPAAs have similar Mn values. Figure II-80 plots the specific capacity as a function of cycle numbers for the half cells containing cPAA3, cPAA4 and liner PAA binders. The cycling test of cPAA5 is ongoing. For silicon/graphite composite electrodes, cPAA3 cell delivered reasonable initial capacity but worst capacity retention, possibly due to the large Mn of the crosslinker used. On the other hand, cPAA4 binder demonstrated a strikingly attractive cycling performance with the highest initial capacity and capacity retention values among the results of this report.

Even though the cycling was not complete and only at 86th cycles, the 76% capacity retention still puts cPAA4 among the most promising binders that have ever been reported for silicon/graphite composite electrodes. Currently, more detailed study regarding further optimizing the crosslinker content as well as electrode loading is ongoing. As shown in Figure II-80(right), cPAA4 also demonstrated improved cycling performance for the high capacity silicon electrode, where better initial capacity and capacity retention were observed.

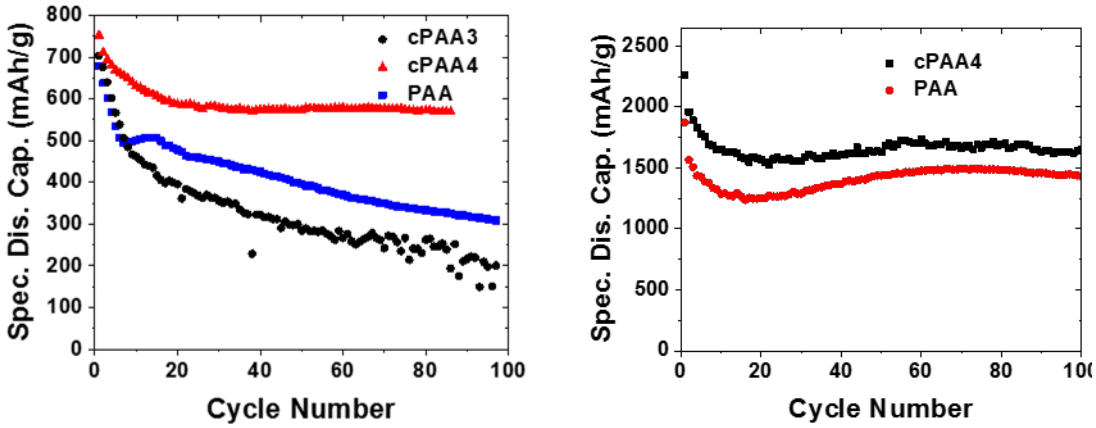

Figure II-80. Specific discharge capacities of half cells of (left) silicon/graphite composite electrodes and (right) high capacity silicon electrodes using PAA-based binders during the course of 100 cycles under C/3 rate.

Engineered Stiff PAA Based Binders for Silicon Anode

As the most promising silicon binder, PAAs offer attractive properties, such as good aqueous and nonaqueous solubility, excellent chemical stability, tunable acidity for improved adhesion, etc. However, as one kind of soft polymers, PAA-based binders often suffer performance degradation possibly due to the related weak mechanical properties. Here we report a new family of PAA-based binders, poly(4-vinylbenzoic acid) (P4VBA) (see Figure II-81), by introducing stiffness enhancing moieties into PAA structures. P4VBA binders have an extra benzene ring in the repeating units compared to those of PAAs, and it is believed that such modification should lead to enhancements of the mechanical properties. [11]

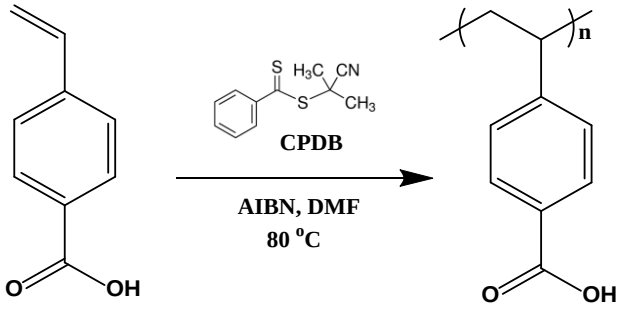

Figure II-81. Synthetic route for P4VBA binders.

P4VBA binders are not commercially available and have been synthesized using reversible addition-fragmentation chain-transfer (RAFT) polymerization method, which can afford good control of the molecular weight of the synthesized polymers.

For cycling characterization, half cells containing silicon/graphite composite electrode were used to evaluate the new developed binders, which contains 73 wt% graphite flakes, 15 wt% silicon particles, 2 wt% C45 and 10 wt% binder. The slurry was processed using water or N-Methyl-2-pyrrolidone (NMP) solvent.

P4VBA binders were synthesized by polymerization of 4-vinylbenzoic acid monomers, which contain not only all the functionality of PAAs, such as flexible poly(ethylene) backbone and pedant carboxyl groups but also have an additional benzene ring in the repeating units, which is believed to prompt the mechanical properties, such as yield strength, tensile strength, fatigue strength, and crack resistance, etc. Two P4VBA binders with different number average molecular weights (Mn) have been synthesized and their characterization results are summarized in Table II-7. By using RAFT method and controlling reaction time, we can control the molecular weight of the synthesized polymers. The Mn of P4VBA1 is controlled at lower range at 7.4 K while P4VBA2 is at 55.4K. To fairly compare the performance, two PAA binders with similar degree of polymerization (DP) were used as control materials. P4VBA binders are soluble in NMP but not in water, therefore NMP was used to prepare the slurry. NMP and water were both used to prepare the slurries of PAA binders.

Table II-7: Summary of P4VBA and PAA binders cycled.

Polymer	DP[a]	Mn[b]	PDI	Initial Capacity (mAh/g)	Capacty Retention
P4VBA1	46	7.4 K	1.31	648	40%
P4VBA2	342	55.4 K	2.37	786	36%
PAA1	42	3.6 K	1.89	603	41%
PAA2	338	29.1 K	3.11	676	32%

(a) DP (degree of polymerization) is the number of repeating units of the polymer.
(b) Mn is the number average molecular weight of the methylated crosslinked PAA, characterized by gel permeation chromatography (GPC).

As shown in Figure II-82, specific capacity profiles of cells using P4VBA and PAA binders were compiled. For those low DP binders shown in the left, the cycling performance of the cell containing P4VBA is very similar to that of the cell fabricated using PAA1 water solutions. But for the cell that used PAA1 solution in NMP, the cycling was actually worse. For the high DP materials shown in the right, the P4VBA2 cell showed significant improvement over the cell of PAA2 (water) in terms of initial capacity and capacity retention. On the other hand, the cycling performance of the PAA2 (NMP) cell was much worse.

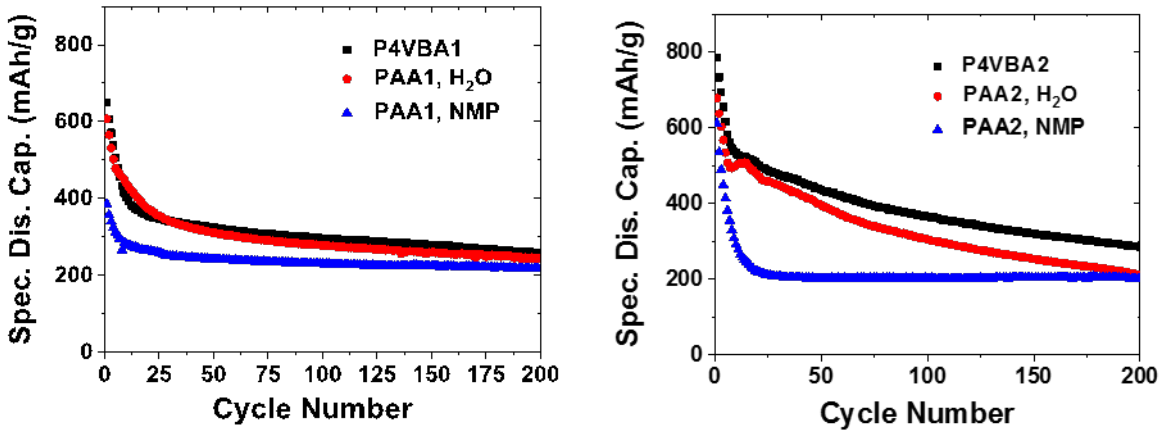

Figure II-82. Specific capacity profiles of cells containing P4VBA and PAA binders.

Development of Binary Polymeric Binder Systems Capable of in-situ Crosslinking

We are working on development of binary polymeric systems able to in-situ crosslinking during the process of electrode laminate manufacturing. The two components of the system need to be stable and non-reactive during aqueous slurry preparation process to allow for casting but should undergo rapid thermally induced crosslinking during laminate drying. The selection of proper components for the binary system needs to take

under consideration several criteria required for binder for LIBs electrode. The components of the binary system need to be soluble or forming stable emulsion in water, the cross- linked polymer needs to be chemically compatible with electrolyte and other electrode materials and electrochemically stable during cycling of the batteries. The polymer needs to be characterized by good adhesion to the current collector and good cohesion between particles of the composite anode.

The intra- and extra-molecular crosslinking will result in a flexible 3D mesh holding silicon and graphite particles together preventing loss of electrical contact and mechanical degradation of the electrode during cycling. Interaction of the backbone polymer with Si surface may further strengthen the structure and improve performance (Figure II-83).

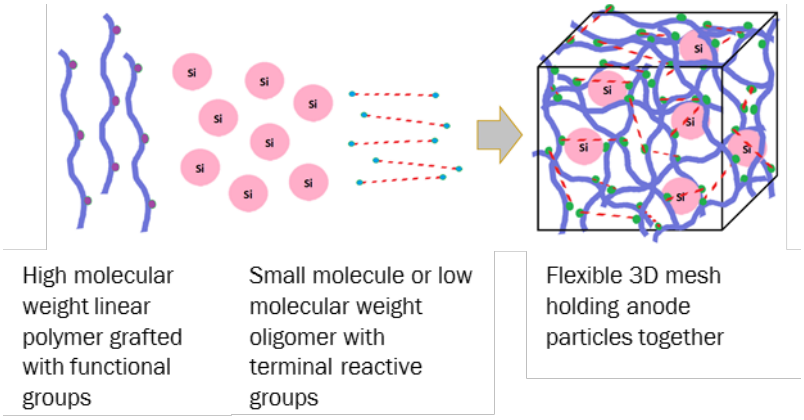

Figure II-83. In situ formation of 3D mesh from polymer and reactive small molecules.

We selected commercially available poly(ethylene-alt-maleic anhydride), Mw = 100 - 500 kD and poly(methyl vinyl ether-alt-maleic anhydride), Mw = 216 kD as a starting material for synthesis of backbone polymers (Figure II-84). The anhydride moiety in the starting materials were hydrolyzed to the corresponding poly(acid) co-polymer (R= H, OCH_3) (Figure II-85). The acids were used in a series of “proof-of-concept” experiments to investigate in-situ cross linking (Figure II-86).

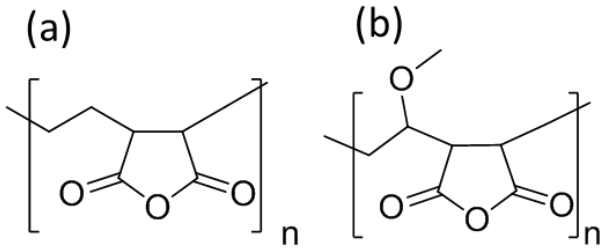

Figure II-84. (a) poly(ethylene-alt-maleic anhydride) and (b) poly(methyl vinyl ether-alt-maleic anhydride).

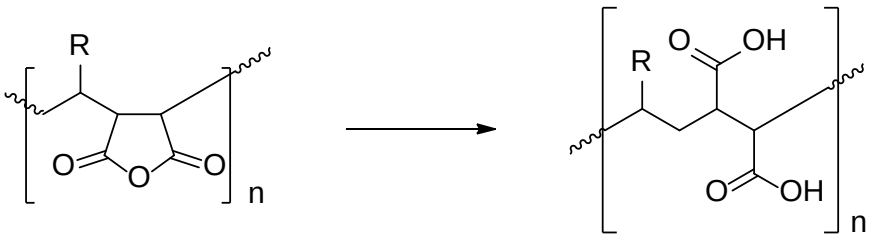

Figure II-85. Hydrolysis of poly(anhydride) to poly(acid).

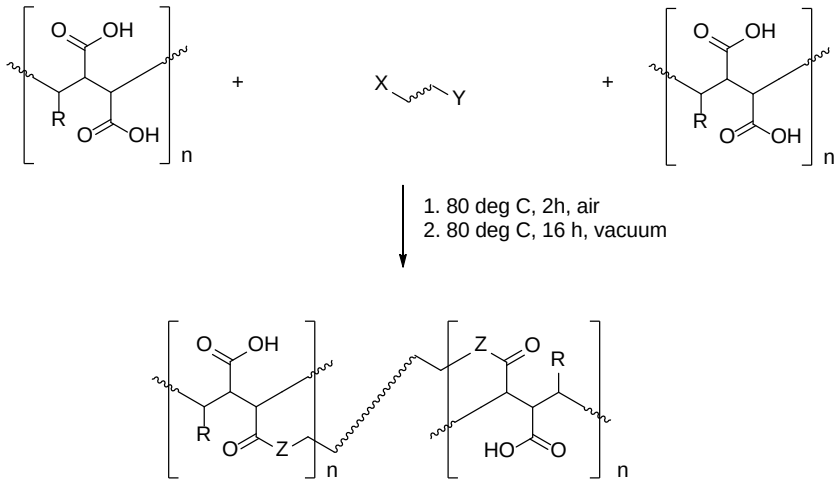

Figure II-86. General scheme of in-situ crosslinking of poly(R=H or OCH_3-alt-maleic acid) and small molecule, 80:20 (X, Y = OH or NH2, Z = O or NH).

The following small molecule linker were used in the experiments: triethylene glycol, PEG400, PEG1000, 1,4-butanediol, and 4-aminobutan-1-ol. FTIR analyses of the resulting materials revealed, in each case, formation of the expected crosslinks as evident by presence of ester or/and amide bonds. Small amount of anhydride in the product was also observed.

We also synthetized a series of poly(R=H or OCH_3-alt-maleic acid) derivatives that possess capability of intra- and intramolecular crosslinking via condensation reaction. An example of a synthesis of the linear polymer and self-crosslinking product is represented on Figure II-87. The following linear polymer derivatives were synthetized: poly(ethylene-alt-maleic anhydride) with ammonia (1:1 mol/mol), poly(ethylene-alt-maleic anhydride) with 6-aminohexan-1-ol (1:1 mol/mol), poly(ethylene-alt-maleic anhydride) with 6-aminohexan-1-ol and ammonia (1:0.05:0.95 mol/mol), poly(methyl vinyl ether-alt-maleic anhydride) with 4-butan-1-ol and ammonia (1:0.1:0.9 mol/mol).

Investigation and Development of Aqueous Based Polymer Binders (LBNL)

This work is part of the polymer binder group research on understanding and developing new polymer binders for Si-based materials. This is a first year of a multi-year project to develop aqueous-based emulsion binders for Si-based materials. This year work is on investigation of the stability of the conductive polymer binders, synthetically introducing new anthracene-based conductive moiety to the methacrylate backbone, and decipher the formulation of aqueous-based emulsion of Si-based electrode systems.

Characterization of the stability of the Polymethacrylatepyrene (PPy) type of binders in Si composite electrode

PPy type of conductive polymer binder and Si graphite materials are fabricated into composite electrode based on ANL baseline composition. The performance characteristics of the electrode are compared with the ANL baseline performance. At C/10 rate, the cycling of PPY-based electrode is very stable and at theoretical gravimetric capacity. The analysis of the electrode after cycling demonstrate the both chemical and electrochemical stability of the PPY binder. Although the electrode is extensively washed after the cycle test by DMC, the FTIR spectra shows the stable PPY binder on the surface of the composite electrode (Figure II-88). The electrode also has similar adhesion strength before and after the electrochemical test, demonstrating the superb adhesion properties of the PPY binder materials [12].

Synthesis of a group of conductive polymer binder and test its performance.

After confirmed the stability of the PPy binder, a series of conductive polymer binders based on methacrylate polymer backbone is synthesized to demonstrate the versatility of this side chain conducting mechanism, and

its utilization as a binder in the Si-based electrode. We have developed two new polymer binder materials, of anthracene methyloxide side chains homopolymer – P(Ant), and its copolymer with triethyleneoxide methylether P($Ant_{0.7}$-co-$TEG_{0.3}$) (Figure II-89). Anthracene has delocalized pi bonds, similar to the pyrene structure. The polymer molecular weight is around 20K with a PDI of 2.2, which are similar the PPY binder developed previously in our lab. The P(Ant) binder is combined with Si nanoparticle to formulate into electrode, shown in Figure II-90. As demonstrated in the binder testing with the Si materials, the P(Ant) conductive polymer binder works effectively as both binder and conductive agent for the Si electrode.

Si electrode fabrication based on aqueous-based SBR binder, and investigation of its performance. SBR water emulsion is used as aqueous-based binder for the Si and graphite composite electrode. We are using the commercial SBR and CMC to develop Si and graphite-based electrode, and testing the electrode performance. The goal of this effort is to gain experience of fabrication of the electrode based on the aqueous emulsion system. As demonstrated in Figure II-91, the electrode capacity is consistent across 3 cells, and the cycling is stable at C/3 cycling in the first 30 cycles. The first cycle efficiency is also very consistent among all 3 cells.

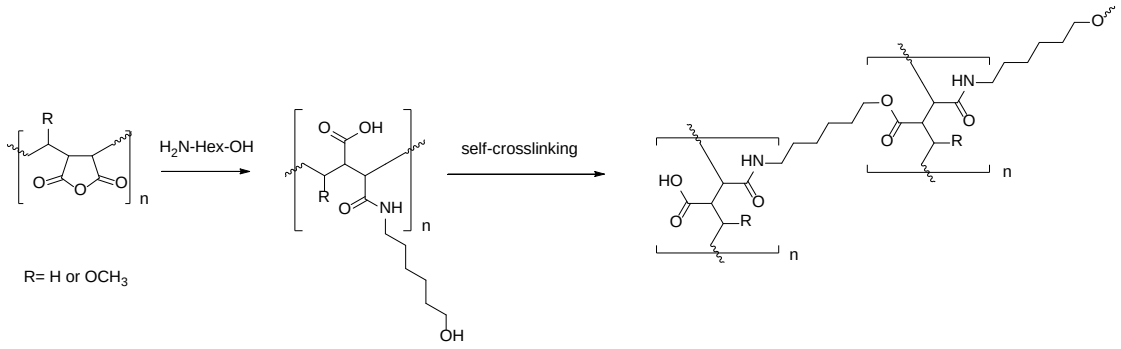

Figure II-87. An example of a synthesis of the linear polymer and self-crosslinking product.

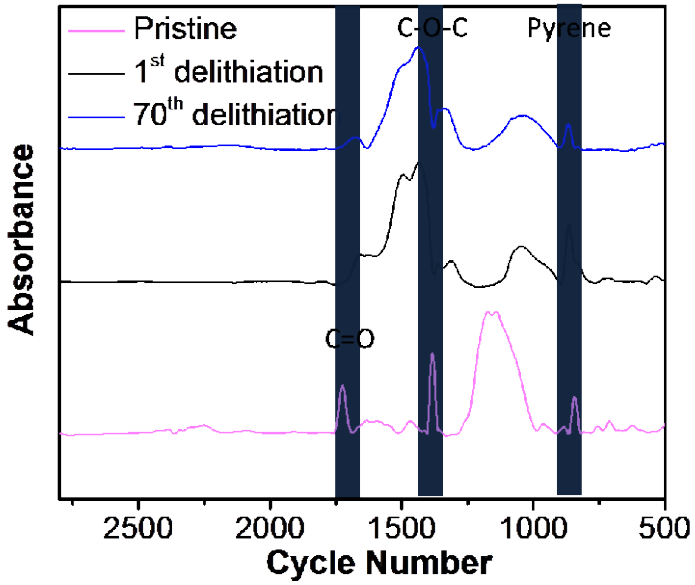

Figure II-88. Fourier transform infrared (FTIR) spectra of the PPy-based pristine and delithiated electrodes.

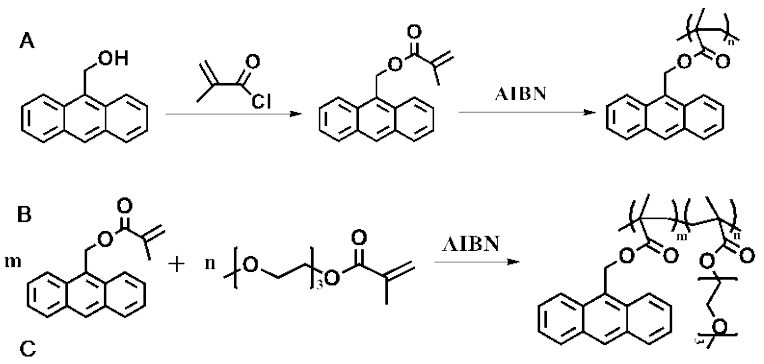

	M_n	M_w	M_p	PDI
P(Ant)	17000	36000	25000	2.2
P($Ant_{0.7}$-*co*-$TEG_{0.3}$)	19000	43000	31000	2.3

Figure II-89. Synthesis of anthracene-based polymers. A. anthracenemethyleneoxide methacrylate polymer – P(Ant). B. Copolymer with Triethyleneoxide - P($Ant_{0.7}$-co-$TEG_{0.3}$). Molecular weights and polydispersity (PDI) of the P(Ant) and P($Ant_{0.7}$-co-$TEG_{0.3}$) polymers.

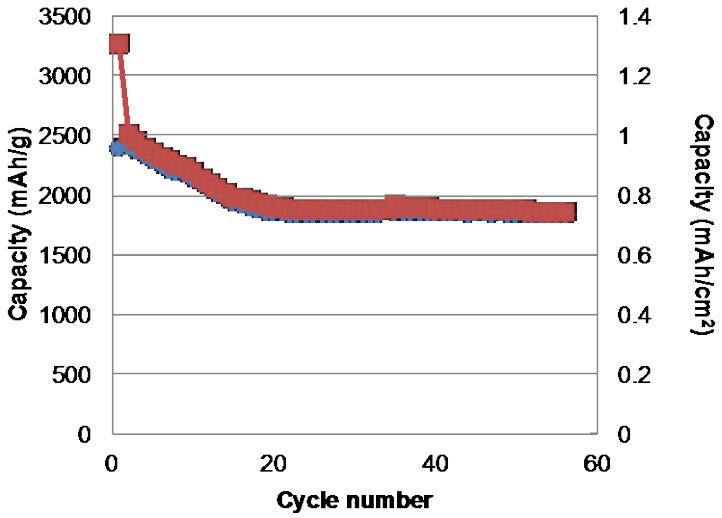

Figure II-90. Si nanoparticle cycling with the P(Ant) binder. (Electrode composition is 90% nano Si particles, and 10% binder, 0.4 mg/cm² of Si materials, cycling rate C/10).

A

Electrode: magE/nanoSi/C45/CMC/SBR = 90/10/2.5/3/2.4	Mass Loading (mg/cm²)	Thickness (µm)	1st Cycle Effic ency
Cell 1	2.60	30	0.890
Cell 2	2.85	33	0.894
Cell 3	2.63	27	0.905

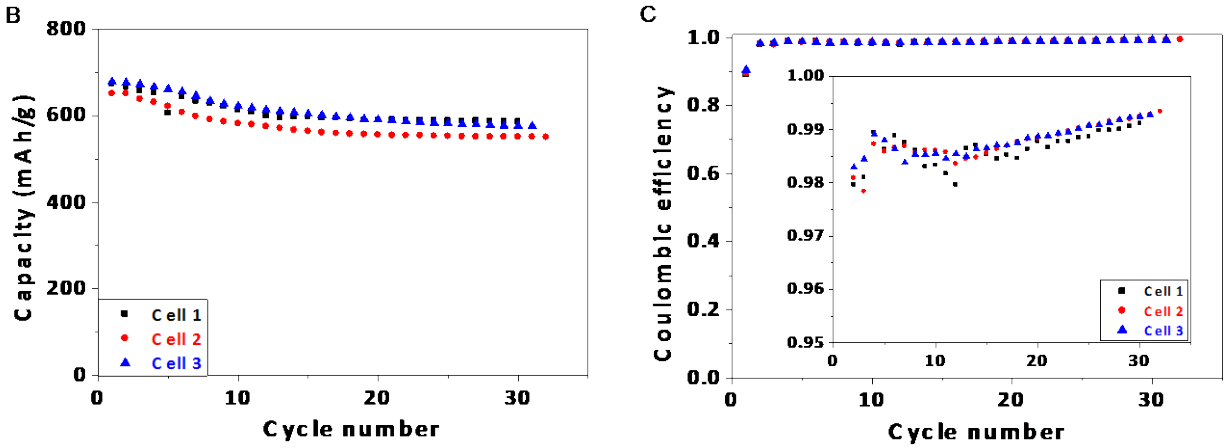

Figure II-91. Si nanoparticle and graphite composite electrode cycling with commercial SBR binder. A. Electrode composition and the mass loading of 3 cells made of the same laminate against Li metal electrode. B. Cycling performance of 3 cells at C/3 rate. C. The coulombic efficiencies of the cells.

All the synthetized polymer are investigated for physicochemical properties required for a binder. Selected materials will be used to manufacture composite silicon (Paraclete Energy, nSiO and SM-Silicon™ powders)/graphite electrode.

Silicon Surface Modification Using Molecular Layer Deposition (NREL)

The overall goal of this project is to develop sustainable high-energy density of Si-based nanocomposite electrodes for use in vehicular applications. In this work, surface modifications, which chemically or physically change the surface of electrode components, has been applied to improve the interphase chemistry, conductivity, and mechanical integration in Si-based electrodes. It is the nanostructured architecture that greatly increases the overall capacity; however, decreasing the particle size also increases both the surface area and electrolyte-reduction reactions resulting in the formation of solid-electrolyte-interphase (SEI) layer and the associated irreversible loss of Li. Surface modifications on both active particles and laminated electrodes have the capability to modify the solid-electrolyte-interphase (SEI) through the control of composition, thickness and mechanical properties.

Unlike other electrode materials, Si particles are covered by an insulating oxide layer, but also suffer from the morphological changes during Li cycling. Therefore, besides the requirement for the chemical stability, a functional coating is required with the control of thickness and mechanical properties. Molecular layer deposition (MLD) will be used to produce a conformal surface coating composed of an elastic aluminum alkoxide polymer with a tunable elastic modulus and chemical reactivity, depending on composition. Based on low-temperature, sequential and self-limiting surface reactions, MLD can also apply to the laminate electrodes (summarized in FY16) and the particles (FY17 focus area), resulting in conformal coatings with atomic-level control of film thickness while maintaining the electrode architecture and inter-particle electronic path.

ALD technique has proven itself to be the *best method to deposit continuous, conformal and pinhole-free films*. Our recent work has proven ALD as an important tool in mitigate the parasitic side reactions between the liquid electrolyte and electrode surface, leading to the improved performance of LIBs electrodes. But the rigid inorganic coatings, such as Al_2O_3 coating, are not robust enough to provide structural support when applied to large-volume-expansion materials such as Si. In order to address the challenge of Si's dramatic volumetric change, NREL have utilized MLD to grow a mechanically robust, flexible coating as a surface modification for high capacity Si nanocomposite anodes. Based on the similar mechanism of ALD, MLD method allows for the integrating the organic fragments into metal oxide matrix, leading to the formation of hybrid organic-inorganic materials. The thin, conformal, and flexible MLD coating is able to penetrate the electrode's porous structure and covalently bind to available surfaces. This creates a strong, flexible network within the electrode that binds the materials and ensures sufficient contact area throughout cycling.

Addition of 15 wt.% of Si into the graphite-based electrode results in the increase of specific capacity from 372 mAh/g to 918 mAh/g, and improved Coulombic efficiency (CE). This is an eclectic approach as the electrode solely made of Si particles rapidly fails due to the enormous volume changes of Si with lithiation. FY17, the research has been focused on demonstration of the composite electrodes, comprised of the graphite and the silicon particles. Both NanoAmor Si particles and Alfa Si particles were used to identify the coating effects on the electrochemical properties. Different from the previous study, poly acrylic acid has been used as the polymer binder additive—instead of polyvinylidene fluoride used in FY16—to enhance the mechanical integrity, increase the mass loading thereby improve the area capacity. This research elucidates the important role of the surface modification in stabilizing the cycling performance, but also shed light on the interaction between the graphite and the Si particles.

Molecular Layer Deposition

Alumium alkoxide (AlGL) films were grown directly on the particles or the laminated electrodes using trimethylaluminum and glycerol precursors at 180˚C for the particles, and at 150 ˚C for the particles. The typical growth rate for the AlGL chemistry is 2.5 Å per cycle. The typical AlGL reaction sequence was: i) Dose trimethylaluminum for 2 seconds, ii) hold trimethylaluminum pressure static for 90 seconds, iii) flow purge for 180 seconds, iv) 5 cycles of argon static purge, v) dose glycerol for 2 seconds, vi) hold glycerol pressure static for 120 seconds, vii) flow purge for 240 seconds, viii) 7 cycles of argon static purge. Flow purge is performed by pumping out excess precursors and reaction byproducts while flowing argon through the reactor. Argon static purge is performed by dosing argon for 20 seconds, holding argon pressure static for 5 seconds, pumping for 45 seconds, and flow purging for 20 seconds. This sequence constitutes of one AB cycle of AlGL. The electrodes were coated with 10 cycles of AlGL. Pulse dosing was also used to enhance the completion of the reactions, see details in the result section.

Preparation of electrodes and coin cells

Standard types of 2032 half coin cells with Li metal foil as counter electrodes were prepared for these experiments. The anode mixture was composed of Si, graphite, carbon black and poly acrylic acid (PAA) binder with a wt.% ratio of 15%-73%-2%-10%, and mixed with using 1-methyl-2-pyrrolidinone (NMP) solution. The mixture was coated on Cu foil and then dried under air. Before assembling the cells the 1.4 cm punched electrodes were dried overnight (120˚C) in a vacuum oven. 1.2 M $LiPF_6$ in ethylene carbonate, diethyl carbonate (3:7 wt%) and fluoroethylene carbonate (10%) was used as the electrolyte. Cells were assembled in an Ar filled glove box and tested at room temperature. Constant current (CC) is applied during discharge and charge between the voltage range of 0.01 V and 1.0 V.

Development of the MLD alucone coating for silicon particles

The research in FY16 was directed towards understanding the impact of MLD coating on the various electrodes made of different Si particles and binders. Significantly improvements have been achieved for the Si electrode (made of 60 wt.% 50nm Si from Alfa, 20 wt.% PVDF and 20 wt.% carbon black) coated with MLD aluminum glycerol (AlGL) ultrathin film. Then, the same MLD coating chemistry has been applied to the electrodes made with the functional binders, including lithiated polyacrylic acid (LiPAA) and carboxymethyl

cellulose (CMC). Both binders were believed to have the chemical interaction with the surface of Si particles, resulting in enhanced mechanical integrity, thus improved cycling reversibility. The Si-LiPAA electrode provided by CAMP is consisted of 15 wt.% Si (50-70nm from NanoAmor), 73 wt.% Hitachi Mag-E graphite and the LiPAA binder. The Si-CMC electrode is made here with 60 wt.% Si (50nm from Alfa), 20 wt.% carbon black and 20 wt.% CMC binder. Surprisingly, cycling behavior of MLD coated electrodes shows no difference compared with the uncoated electrodes. Note that both binders have the strong chemical interaction with the surface of silicon particles. Therefore, the surface of silicon particles has been already covered/modified by the functional binders, which blocks the direct contact and prevents the reactions between MLD precursors and the Si particles. It is believed that the interaction between the binders and Si particles negates the coating effects. Therefore, in FY17, we have modified the MLD coating technology to coat both particles and the laminated electrodes. The coated particles can be used to make electrodes with different functional binders.

Si particles (70-130 nm) from NanoAmor AlGL were selected as our new baseline material, because Si particles (30-50nm, NanoAmor) were discontinued. Then, the Si particles from both Alfa (50nm) and NanoAmor (70-130nm) have been coated with MLD AlGL chemistry. The films were grown on nano-Si powder in an ALD fluidized bed reactor. Si particles were heated to 180°C and dried under a low-pressure nitrogen flow. The pressure drop across the powder bed was determined at various nitrogen gas flow rates in order to determine an appropriate gas flow rate for fluidizing the powder. The AlGL reaction sequence was the following: i) dose TMA until the mass spectrometer indicates saturation of the TMA surface reaction; ii) purge with nitrogen; iii) dose glycerol until the mass spectrometer indicates saturation of the TMA surface reaction; iv) purge with nitrogen. This sequence constitutes of one cycle of the AlGL MLD process. The growth rate is ~2.3Å per cycle. 10 MLD cycles were applied to Si nanoparticles from Alfa, while 5 MLD cycles were performed for NanoAmor Si particles.

Real time residual gas analyzer mass spectrometry has been equipped into the MLD process, in order to measure the composition of the gas flow. The changes in composition of the gas flow can be used to determine the completion of MLD reactions.

TMA ($Al(CH_3)_3$) and glycerol ($C_3H_5(OH)_3$) were used as precursors to form aluminum glycerol (AlGL)16 coating and the reactions are as follow:

Step A: $R\text{-}OH^* + Al(CH_3)_3 \rightarrow R\text{-}O\text{-}Al(CH_3)_2^* + CH_4$

Step B: $R\text{-}O\text{-}Al(CH_3)^* + C_3H_5(OH)_3 \rightarrow R\text{-}O\text{-}Al\text{-}OC_3H_5(OH)_2^* + CH_4$

where asterisks indicate surface species and R represents the Si. Mass spectrometer was used to monitor the reaction process and determine the completion of the reaction. Figure II-92 exhibits the intensity of the residue gas as a function of reaction time. The cumulative intensity of the product (hydrocarbon, m/z 15, methane) was observed along the TMA dose and glycerol dose. During either TMA or glycerol does, the intensity of methane keep increasing linearly with time. After couple TMA/glycerol doses, the intensity of the product starts decreasing, while the excess TMA/glycerol was observed in the gas flow. It indicates the completion of the half-cycle reaction.

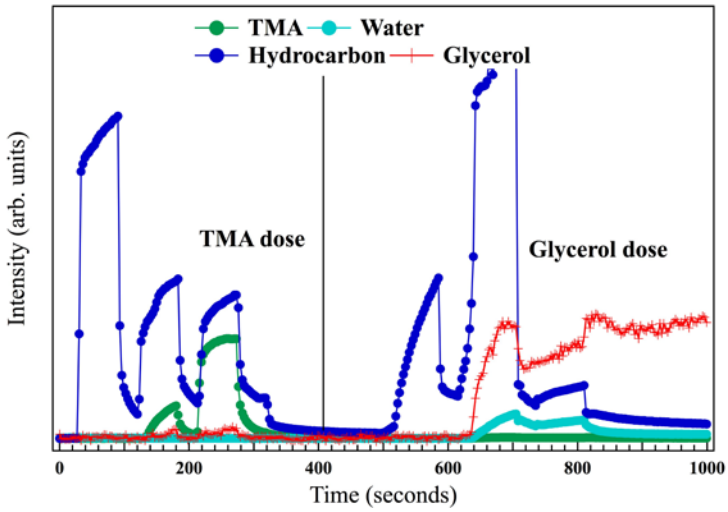

Figure II-92. Mass spectra of one MLD cycle including TMA and glycerol doses. Pulse dosing was used for both precursors to enhance the reactions.

Si particles from NanoAmor show quite different morphology compared with the particles purchased from Alfa. Figure II-93a and Figure II-94 a-c show the morphology of the as-received particles. The particles from Alfa have uniform and spherical morphology, however, the particles from NanoAmor have irregular shaped morphology. After MLD coating, uniform coating with a thickness of ~5nm has been successfully obtained for the Alfa Si particles. In contrary, it is hard to identify the coating layer for the NanoAmor particles. We expect that the ball milling process—used in NanoAmor sample preparation—results in surface amorphization. It causes the difficulty to identify the coating layer after MLD reaction, as displayed in Figure II-94 (d-f). Besides, the high content oxide and organic impurities were expected for the NanoAmor silicon particles—reported by other team members. The impurities can limit the growth of MLD coating materials.

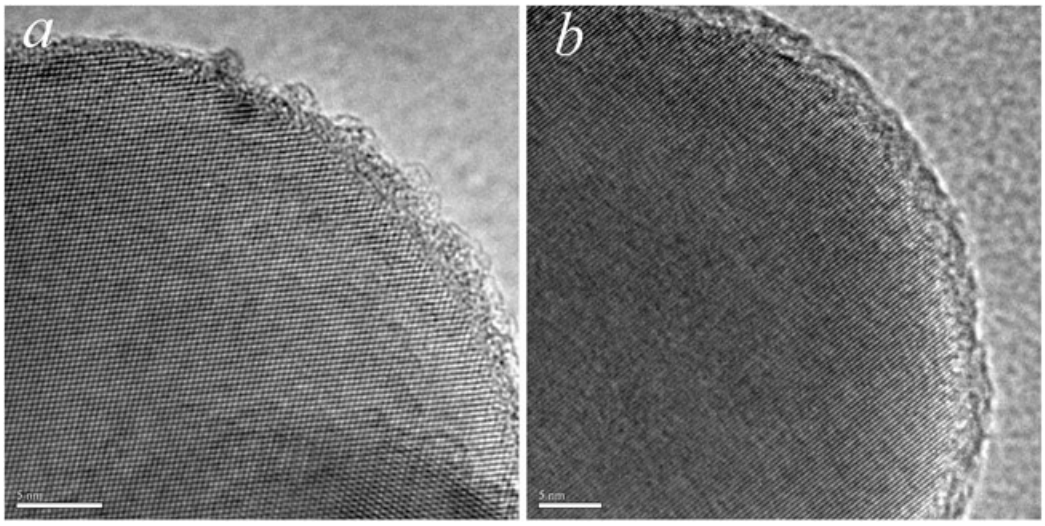

Figure II-93. TEM images of the uncoated Si particle (a) and the MLD coated Si particle (b). The particles have the size about 50 nm, were purchased from Alfa.

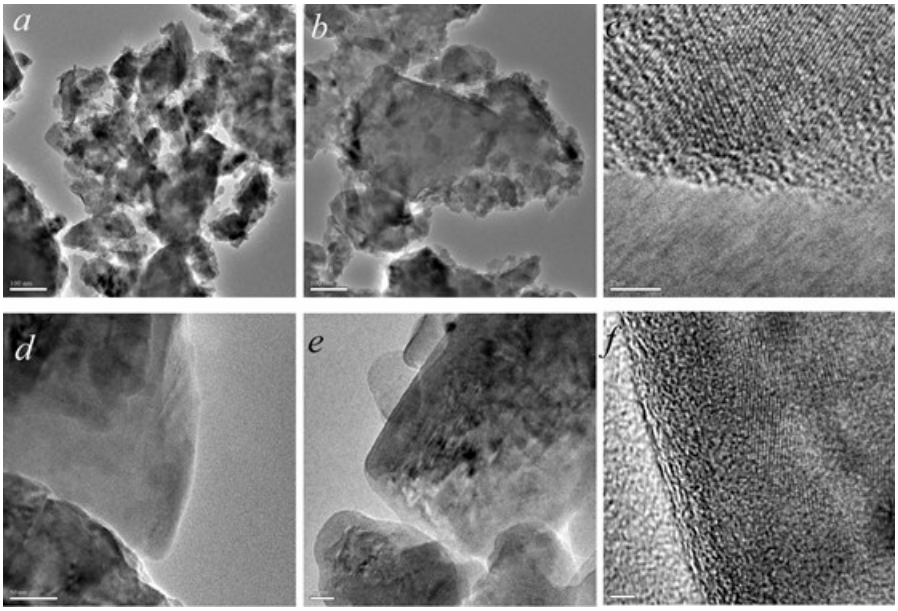

Figure II-94. TEM images of uncoated Si particles (a-c), and MLD coated Si particles (d-f). The Si particles were from NanoAmor, has been used as the new baseline material.

Impact of the coating on the electrochemical performance of the composite electrode

The electrodes were fabricated at NREL, with the 73 wt% graphite, 15 wt% Si (Nano & Amor, 70-130nm), 10 wt% lithiated poly acrylic acid (LiPAA) and 2 wt% Timcal C45. The MLD alucone coating was applied on both particles (purchased from Alfa and NanoAmor). 10 MLD alucone coating was initially applied on the particles from Alfa. However, the thick coating has significantly affected the electronic conductivity, thereby, very low capacities were obtained for the coated particles. Therefore, thin alucone coating obtained by 3 MLD cycle was performed later and the electrochemical performance is shown here. The electrochemical properties of the electrodes made with NanoAmor silicon particles were shown in the Figure II-95. Based on the electrochemical cycling data, there is no major difference between the as-received particles and the coated particles, except for the improved Coulombic efficiency (CE) for the coated particles. Combining the morphologic analysis for the NanoAmor silicon particles, we believe that the alucone coating was not fully covered the particles. The poor coating quality can be attributed to the organic impurities on the surface of silicon particles. And, the shapeless morphology, as shown in Figure II-94 may cause the difficulty to form uniform and conformal coating on the surface of the particles.

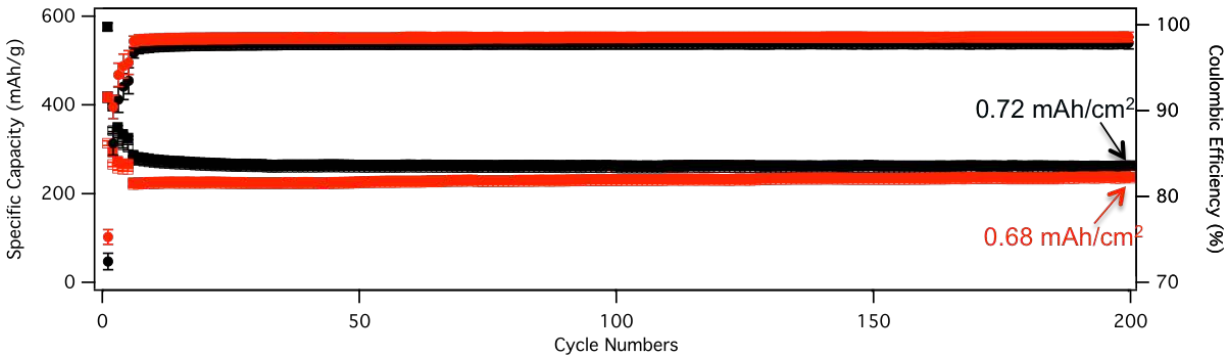

Figure II-95. Specific capacity of the uncoated electrode (plotted in black) and the electrode fabricated by using the coated Si particles (plotted in red). The electrode is fabricated by using 73 wt% graphite, 15 wt% Si (NanoAmor, 70-130 nm), 10 wt% poly acrylic acid and 2 wt% Timcal C45. No major difference in electrochemical performance was observed for the coated particles.

In contrary, significant improvement was observed for the coated Alfa particles. The electrochemical cycling performance of the alucone coated Alfa silicon particles was plotted in Figure II-96a. The alucone-coated particles have shown highly reversible capacity for over hundred cycles, as compared to the fast capacity degradation in the uncoated particles. PAA has been used as polymer binder additive, to enhance the mechanical integrity. Unexpectedly, the decay in electrochemical performance was shown in the uncoated particles after 50 cycles.

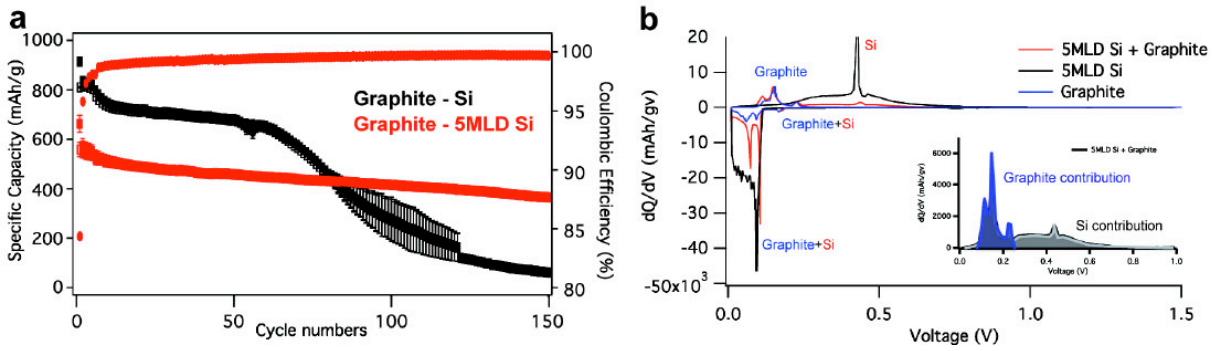

Figure II-96. (a) Specific capacity of the uncoated electrode (plotted in black) and the electrode fabricated by using the coated Si particles (plotted in red). The electrode is fabricated by using 73 wt% graphite, 15 wt% Si (Alfa, 50 nm), 10 wt% poly acrylic acid and 2 wt% Timcal C45. Improved electrochemical performance was achieved for the coated particles. (b) Different capacity (dQ/dV) curves of the electrodes made with the graphite, the MLD coated Si and the graphite-coated Si. The inset plot illustrates the capacity contribution from each component.

Addition of 15 wt.% of Si into the graphite-based electrode results in the increase of specific capacity from 372 mAh/g to 918 mAh/g, and improved Coulombic efficiency (CE). This is an eclectic approach as the electrode solely made of Si particles rapidly fails due to the enormous volume changes of Si with lithiation. Figure II-96a shows the cycling performance of the composite electrode. Fast capacity degradation is observed after 60 cycles and the composite electrode loses the entire reversible storage capability after 150 cycles. This indicates that even small portion of Si materials in the graphite-based electrode can negatively affect the reversible lithiation/delithiation in the composite electrode. Without the addition of Si particles, the graphite anode has shown reversible capacity for hundreds of cycles (not shown here).

In order to understand the failure mechanism in the composite electrodes, we have studied the differential capacity (dQ/dV) plots for the graphite anode (Si not added, Graphite-CB-PAA, 88 wt.% - 2 wt.% - 10 wt.%), the Si anode (graphite not added, Si-CB-PAA, 70 wt.% - 15 wt.% - 15 wt.%), and the composite electrode (Graphite-Si-CB-PAA, 73 wt.% - 15 wt.% - 2 wt.% - 10 wt.%). Note that the anodic potential peaks occurred at 0.25-0.5 are due to the delithiation of Si anode, while the delithiation of graphite usually completes before 0.3 V. However, it is hard to distinguish the cathodic potential peaks of the Si component from the lithiation peaks of the graphite anode. Therefore, we used the delithiation dQ/dV (cathodic) curves to evaluate the reversibility of the Si component, as shown in the Figure II-96b. Inset of Figure II-96b displays the contribution of delithiation capacity from the each component, the graphite and the Si particles respectively. The graphite-coated Si composite electrode has the sustainable cycling performance, although the initial reversible capacity of the graphite-coated Si composite electrode is lower than that of the graphite- uncoated Si composite electrode. Figure II-97 and Figure II-98 present the voltage profile and the dQ/dV curves of the graphite-uncoated Si composite electrode and the graphite-coated Si composite electrodes, respectively. The dQ/dV curves for the 1st and 100th cycle have been plots for these two electrodes. Both electrodes show similar behavior at the 1st cycle, with the equal capacity contribution from both components. In both the graphite-uncoated Si electrode and the graphite-coated Si electrode, the delithiation peaks from the Si component become broadened and the peak currents gradually decrease for both cells. However, at 100th cycle, the peaks from the graphite component disappear in the cell with the graphite-uncoated Si composite electrode. When using coated Si in the composite electrode, the delithiation peaks from the graphite component are well

maintained. For the electrode made with the uncoated Si particles, the capacity fading in both graphite and Si components leads to the performance decay. Interestingly, the electrochemical behavior of Si in the composite electrode affects the cycling performance of the other component (graphite).

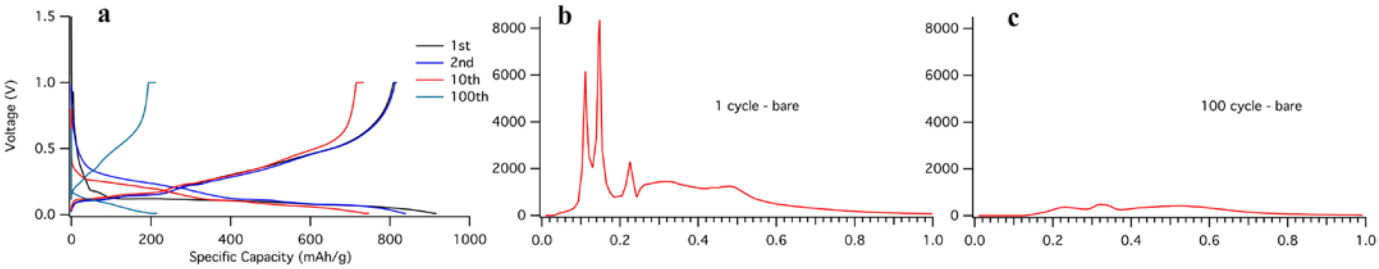

Figure II-97. a) Voltage profile of the graphite-uncoated Si composite electrode cycling between 10 mV and 1 V; (b) Differential capacity (dQ/dV) plots during delithiation at the first cycle; and (c) at the 100th cycle.

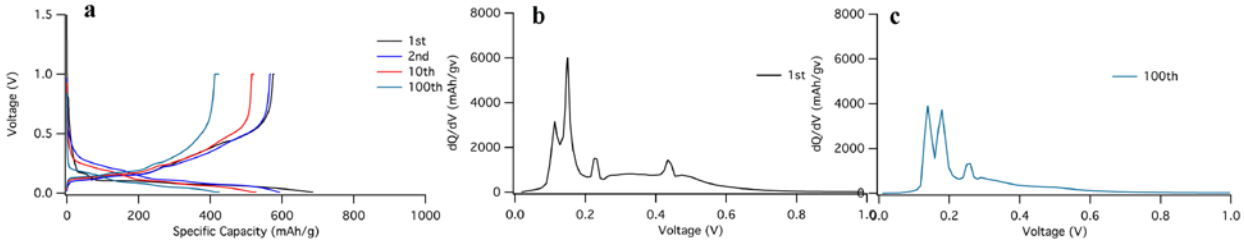

Figure II-98. (a) Voltage profile of the graphite-coated Si composite electrode cycling between 10 mV and 1 V; (b) Differential capacity (dQ/dV) plots during delithiation at the first cycle; and (c) at the 100th cycle.

Impact of the coating on the electrode structure

The cross-sectional SEM images of the composite electrodes—the graphite-uncoated Si electrode and the graphite-coated Si electrode—reveal the similar porous structure of the electrodes, as shown in 27a. The electrode has the average thickness of 30 μm. After one hundred cycles, the electrode made with the uncoated silicon particles experienced dramatic volume expansion at the thickness direction, as indicated in Figure II-99b. It is not surprising that the Si-based electrodes have the volumetric expansion, due to the volumetric fluctuation of Si particles along with the electrochemical reactions. But the large volumetric changes are not expected for the electrode with such a low content of Si particles (only 15%). It is very possible that the original electrical paths have been damaged/blocked after the large volume changes. On the contrary, the electrode made with the coated Si particles shows the original morphology with a limited volumetric expansion, which greatly help maintaining the initial electrical matrix for conducting the electrons.

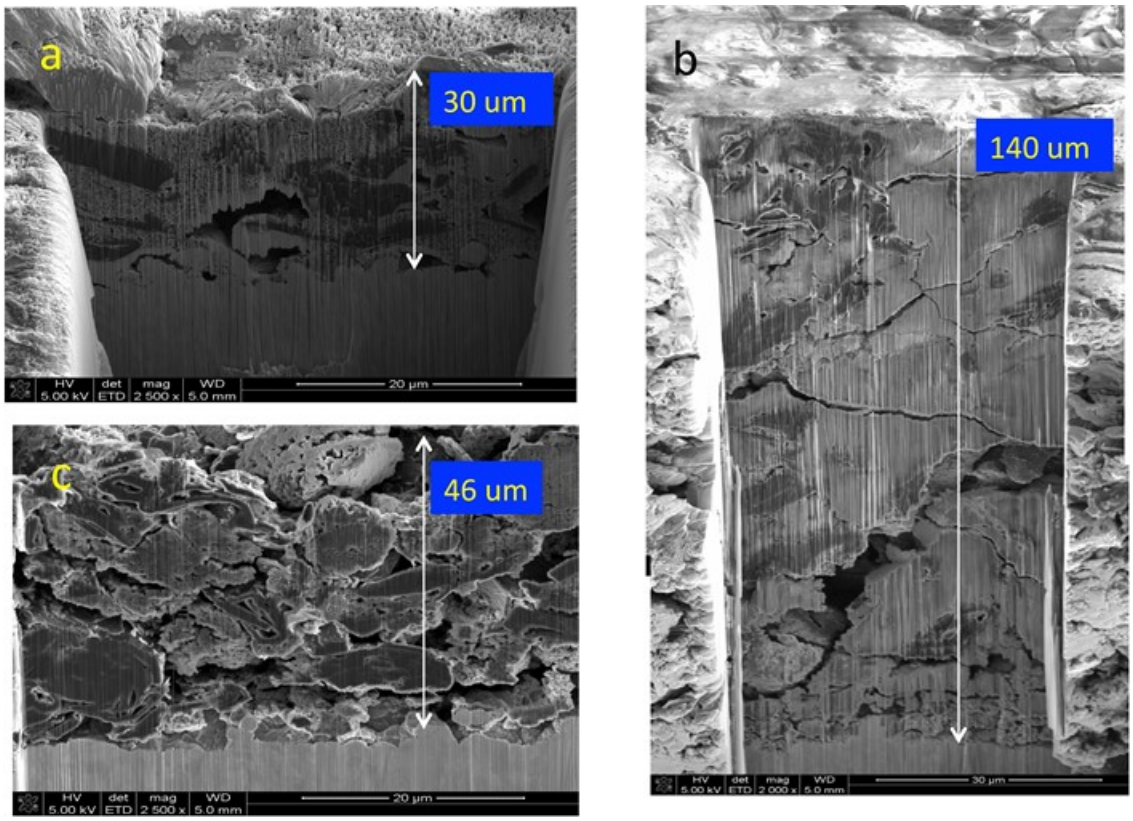

Figure II-99. Cross-sectional SEM observation of (a) the as-prepared electrode made with the uncoated silicon particles; (b) the uncoated electrode after 100 electrochemical cycles; (c) the electrode made with the coated Si particles, after 100 electrochemical cycles.

SEM images are presented in Figure II-100 for the surface morphology of the cycled electrodes, including the graphite-uncoated Si electrodes, and the graphite-coated Si electrodes. After 100 cycles with the uncoated silicon particles, a large number of cracks with different sizes were formed on the electrodes. The surface of the electrodes seems to be heavily covered, mostly likely by the formed solid electrolyte interface (SEI) layer. By coating the silicon particles with 5 MLD alucone (about 1nm), the amount of crack was significantly reduces as shown in Figure II-100 (c) and (d). It is worthy to mention that the 15 wt.% Si particles (50nm) have much higher surface area than those of graphite particles (more than 30 μm), thereby dominates the surface area of the electrode. The formation of the thick SEI for the uncoated silicon particles can cause the high impedance, and exacerbate the volume expansion, finally lead to the loss of the electron conductive paths. As a consequence, the capacity starts fading after 60 cycles for the electrode made with the uncoated Si particles.

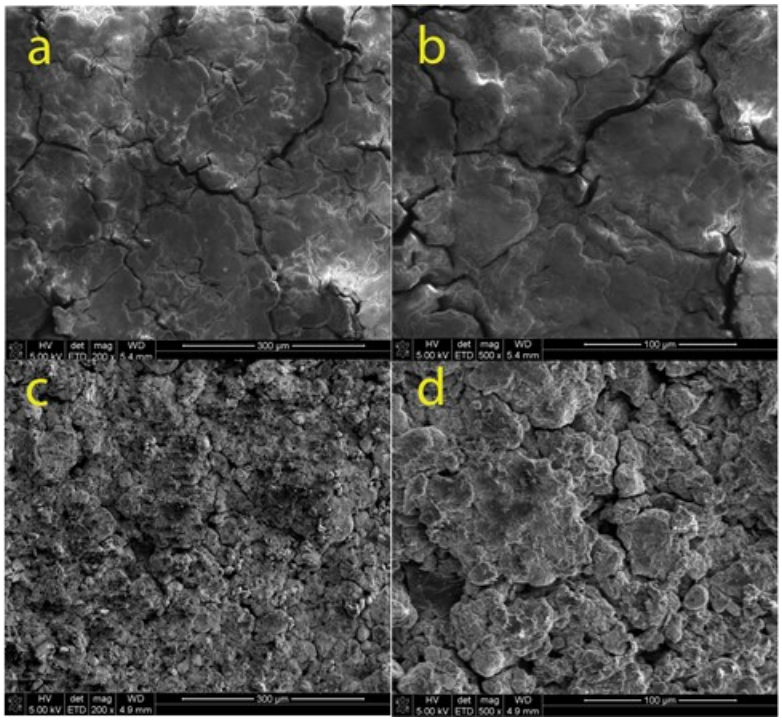

Figure II-100. SEM images of the surface of (a) and (b) the graphite-uncoated Si electrode after 100 electrochemical cycles; (c) and (d) the graphite-coated Si electrode after 100 electrochemical cycles.

Interfacial Modification of Si Anode – Surface Modification (ANL)

The chemical and electrochemical reaction on the surface of the silicon (Si) and lithiated silicon (Li_xSi) with electrolyte solvent/additive plays a significant role in the battery performance of silicon anode. The non-volatile reaction products deposit on the particle and form the so-called solid-electrolyte-interface (SEI). For the traditional graphite-based anode, this exclusively Li^+-conducting SEI layer passivates the surface of the lithiated graphite and prevents the further reactions with electrolyte thus enables the reversible lithiation/delithiation chemistry of lithium ion battery. However, due to the huge volume expansion/contraction of silicon-based anode, the surface passivation is not established since the SEI cracks and reforms with cycling which consumes considerable amount of active lithium resource from the cathode leading to the rapid capacity decay.

The overall goal of this project is to develop sustainable high-energy density of Si-based nanocomposite electrodes for electric vehicle application. Specifically, in this work, we try to engineer the Si surface chemistry through different approaches with a target to stabilize the interface affording a Si anode with extended cycle life. The first approach is to develop new electrolyte/additive that could chemically/electrochemically decomposes and deposits on the lithiated Si surface forming a resilient SEI layer that stabilizes the interfacial reactivity of Li_xSi and electrolyte. Fundamental understanding of how the reactivity of electrolyte/additive with Si anode and how the chemical composition of SEI affects the cell performance will be systematically performed. The second approach is to functionalize the surface of Si particles through organic silane chemistry with a target to stabilize the interface affording a Si anode with extended cycle life.

Small-Molecule Functionalized Silicon Nano Particles (NP)

When exposed to air, a native oxide layer of up to 5-7 nm will form on the surface of silicon particles and the surface functionalities are vary with storage history and handling process. Figure II-101a shows the pictures of the nano silicon particles from Nano Amor and Alfa Aesar dispersed in ethyl alcohol. The color of the two materials are very different, and the surface functionalities are quite different as well based on the FT-IR

results shown in Figure II-101b. Silanol group -Si-OH is universally present on the surface of Si NPs. To obtain Si particles with homogeneous distribution of surface silanol as a reaction platform, a –Si-OH enrichment reaction was performed on the pristine Nano Amor silicon NPs with an average particle size of 70-130 nm. The -Si-OH enriched Si NPs are further reacted with alkoxysilanes through a hydrolysis/ condensation reaction. Ethyl alcohol (Et-OH) and dry tetrahydrofuran (THF) were used as solvents to synthesize silane-functionalized Si nanoparticles.

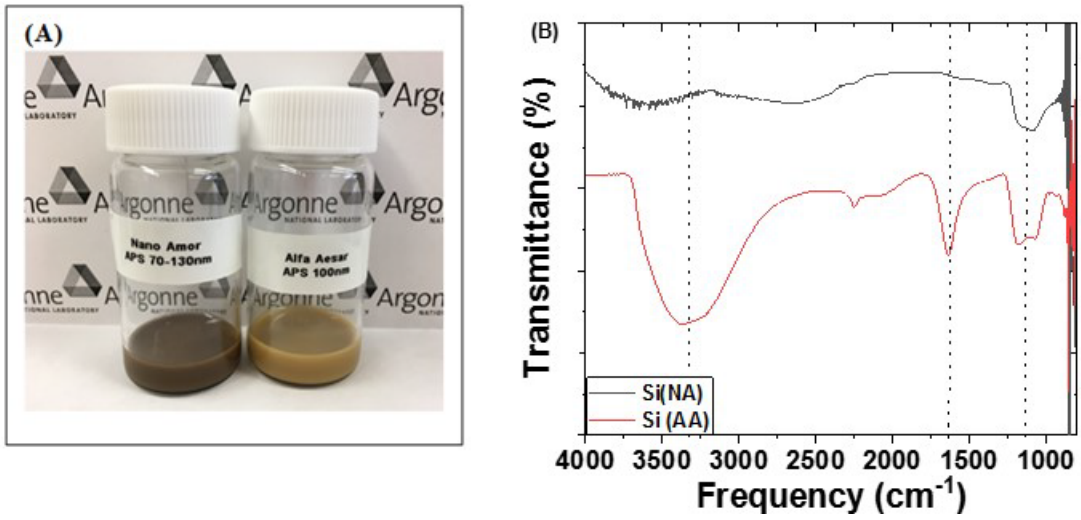

Figure II-101. (A) Pictures of dispersions of Si NPs in ethanol and (B) FTIR spectra of Si NPs from Nano Amor (black) and Alfar Aesar (red).

Figure II-102 shows the FTIR spectra of the synthesized Si NPs with vinyl and methyl methacrylate groups. In Figure II-102, the peaks around 1000-1200 cm^{-1} corresponds to the vibrational Si-O-Si bond, which is evident that the surface of the pristine Si NPs is oxidized to SiO_x to some extent. After the -Si-OH group enrichment, the peaks at 3000-3500 cm^{-1}, an area of typical -OH vibration, becomes larger and broader than that of the pristine Si particles, indicating the increased concentration of Si-OH group on the surface of the treated Si NP. Figure II-102a shows the FTIR spectra of the vinyl-Si-Et-OH (iii) and MP-Si-Et-OH (iv) as well as the pristine (i) and oxidized silicon NPs (ii). Only one new peak at 1650 cm^{-1} (-C=C-) appeared for vinyl-Si-Et-OH (iii) and MP-Si-Et-OH (iv) functionalized silicon. However, the vinyl-Si-THF (iii) and MP-Si-THF (iv) synthesized using THF as a solvent showed a new peak at 2900 cm^{-1} (Figure II-102b) which is the typical of C-H bond vibration on $-CH_2=CH-$ group. In addition, the peak at 1750 cm^{-1} confirms the presence of carbonyl (C=O) group for the MP-Si-THF (iv) sample. It is evident that the surface functionalization process is successful when the dry THF is used as a solvent.

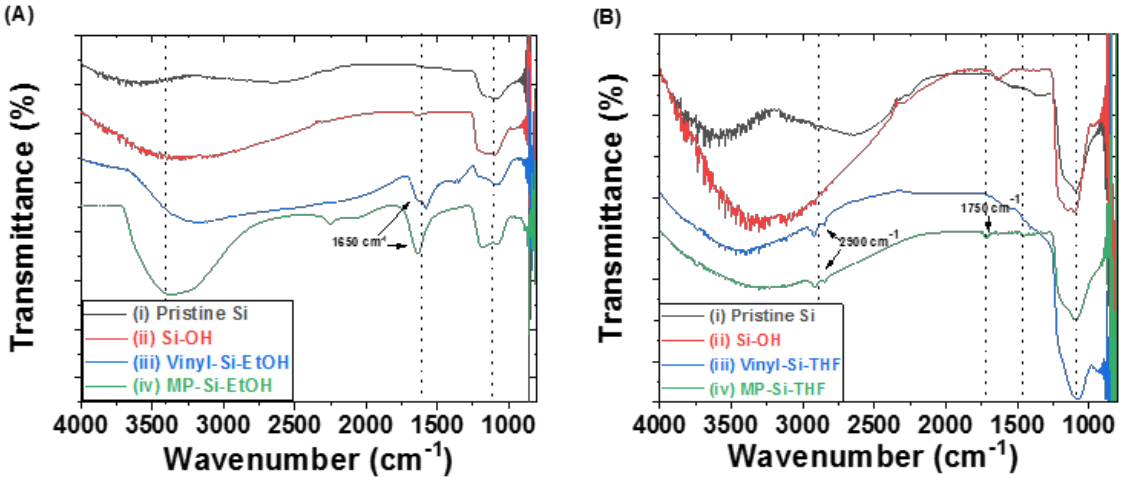

Figure II-102. FTIR spectra of silicon nano powders. (a) Pristine Si, -Si-OH enriched Si, vinyl-Si-Et-OH and MP-Si-ET-OH, and (b) pristine Si, -Si-OH enriched Si, vinyl-Si-Et-THF and MP-Si-ET-THF.

Figure II-103 shows the TGA profiles of the surface enriched Si NPs, vinyl-Si-THF and MP-Si-THF as well as the pristine silicon. For the surface enriched Si NPs, it only showed a 0.5% weight loss at the end of the heating temperature 800°C, while a much higher weight loss was observed for the two functionalized Si NPs with 1.5% loss for vinyl-Si-THF and 3.75% loss for MP-Si-THF, respectively. The weight retention confirmed the attachment of different surface structure on the Si NPs. The electrochemical properties of these functionalized Si NPs will be studied in the near future.

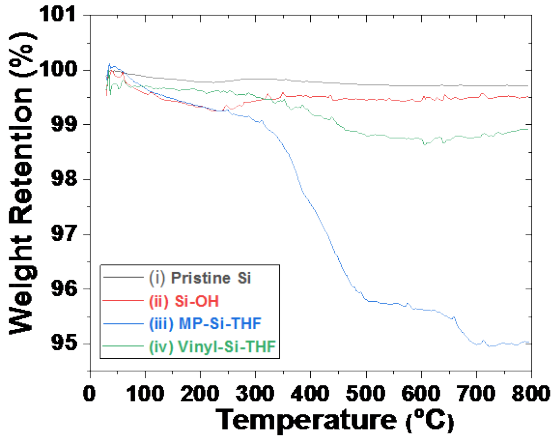

Figure II-103. TGA profiles of (i) pristine Si NPs, (ii) oxidized Si NPs, (iii) vinyl-Si-THF and (iv) MP-Si-THF.

Electrolyte Additive Electrochemistry and Working Mechanism

SEI formation process involving FEC additive and the FEC/hexamethyldisilazane (HMDS) additive is quite different evaluated by the Si-graphite/Li half cells. Figure II-104a shows the expanded voltage profiles where the SEI formation occurs. The addition of silazane additive alters the reduction of the electrolyte and chemical composition of the SEI. Figure II-104b-Figure II-104c shows the differential capacity voltage profiles (dQ/dV) for the first three cycles. In contrast to results reported by other groups, the crystalline $Li_{4.4}Si$ phase exists for each cycle for the FEC/HMDS additive cell, while FEC-additive-only cell did not show this phase. At this stage, it is not fully understood yet whether the appearance of the $Li_{4.4}Si$ phase is correlated with the cell performance. Figure II-105 summarizes the cycling data and the Coulombic efficiency of Si-graphite/Li half cells with Gen 2 electrolyte, Gen2+10% FEC and Gen2+10% FEC+1% HMDS. The capacity retention of the

FEC/HMDS mixture additive cell is significantly improved compared with the baseline electrolyte and the FEC-only-additive cells. The working mechanism of the mixture additive is illustrated in Figure II-106. It is evident that the HMDS is reactive with moisture from the electrolyte and absorbed by the Si particles within the electrode. Further, the reaction of HMDS with silanol group (-Si-OH) on the Si NPs forms a trimethlysilyl-terminated surface functionality that can act as an artificial SEI that could prevent the side reaction of the lithiated Si with electrolyte.

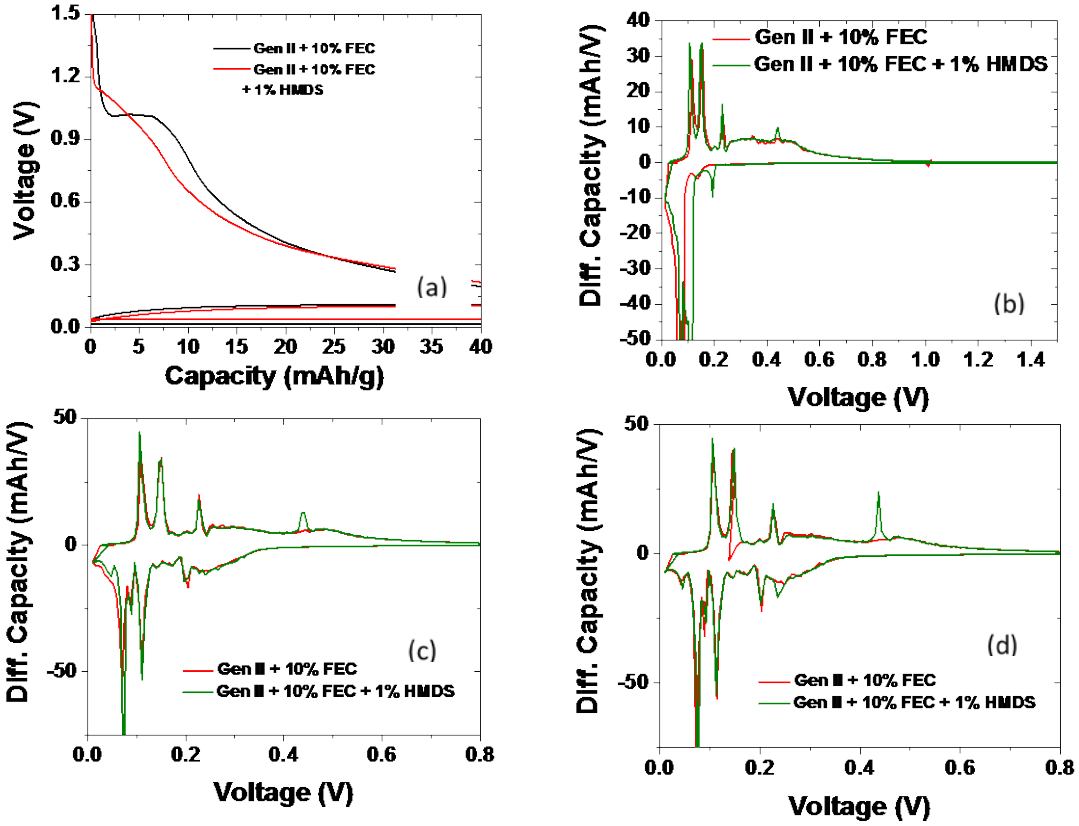

Figure II-104. (a) Expanded voltage profile for SEI formation, and (b-d) dQ/dV profiles for the 1st, 2nd and 3rd cycle for the Si-graphite composite anode with Gen2+10% FEC and Gen2 +10% FEC +1% HMDS.

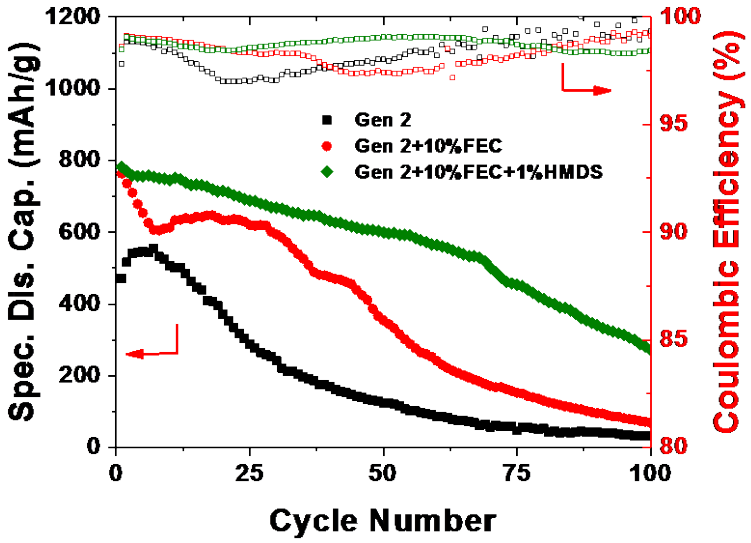

Figure II-105. Capacity retention and Coulombic efficiency of Si-graphite/Li half cells with Gen 2 electrolyte, Gen2+10% FEC and Gen2+10% FEC+1% HMDS.

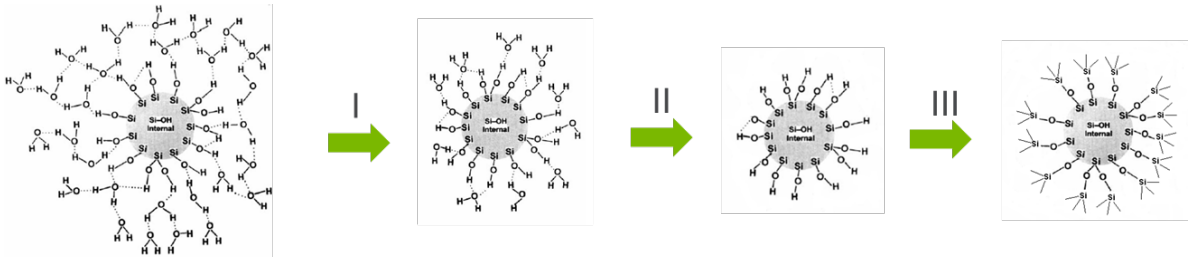

Figure II-106. Proposed surface reaction of HMDS with -Si-OH on the surface of Silicon nanoparticles.

Development of High Energy Metals (LBNL)

Dahn's group identified amorphous Si-Sn films with Sn content lower than 40 mol% as the ideal compositions in thin film batteries, for example, $Si_{0.64}Sn_{0.36}$ showed a large reversible capacity of ~ 1900 mAh/g and low irreversible capacity of ~ 100 mAh/g during the 1st cycle. [13] Ahn et al., later confirmed amorphous Si-Sn nanocomposite electrode films produced by magnetron co-sputtering method demonstrated improved cycling performance compared to amorphous Si film at a similar thickness. [14] Sputtered films with phase separated amorphous Si embedded in the Sn matrix also delivered a reversible capacity of 1400 mAh/g with good cycling stability at Si/Sn ratio close to 1. [15] Attempt to prepare nanocomposites of Si/Sn-based nanoparticles enwrapped in porous carbon nanofibers led to an initial specific capacity of 1347 mAh/g and 1073 mAh/g was retained at the 50th cycle. [16] Kwon et al., reported a sophisticated synthesis of carbon-coated $Si_{70}Sn_{30}$, the composite electrode exhibiting a high reversible capacity of 2032 mAh/g and excellent capacity retention (97% after 60 cycles). [17] All the previous work showed promising electrochemical performance within Si-Sn system, it would be interesting to apply a facile and scalable method to capitalize on the large theoretical capacity of Si, high electrical conductivity of Sn, as well as potential improvement in structural stability of the host electrode. [1]

We explored the synthesis of Si-Sn nanocomposites via mechanical milling method that is cost-effective, facile, and scalable. Using the base $Si_{0.66}Sn_{0.34}$ identified from the previous work [13], we have investigated the effect of milling method on the phase formation and electrochemical properties as well as the introduction of

graphite during the synthesis. In addition, we also explored the synthesis of Sn, Si-Sn nanoparticles by chemical reduction method.

In FY16, the synthesis of Si-Sn nanocomposites was first explored on both Retsch planetary and Spex shaker mill. We explored the effect of milling energy and time as well as the addition of graphite on the phase formation and electrochemistry. The best sample, Si-Sn-C nanocomposites, delivered an initial reversible capacity of about 1000 mAh/g with the 1st cycle coulombic efficiency of 80.2%. The capacity retention of Si-Sn-C nanocomposites was about 80% at Cycle 50. To investigate the origin of the capacity loss, SEM images were collected on the Si-Sn-C electrodes at pristine state, the 50th lithiation, and the 50th delithiation (Figure II-107). Comparing Figure II-107 a, e, i, we noticed the change in morphology on the electrode after 50 cycles, and some cracking occurred at the electrode level after the 50th delithiation. Electrode cracking was mainly due to the fact that both Si and Sn experiences volume changes during lithiation-delithiation process. Such volume change was even more pronounced at higher magnifications. According to Figure II-107 d, h, l, the volumes of the particles significantly increased after lithiation, and the volumes cannot fully resumed back upon delithiation. Instead, the electrode became pulverized and led to additional side reactions between electrode and electrolyte, which largely accounted for the capacity loss over the extended cycles even at a lower electrode loading. This is believed to be a major contributing factor for capacity decay, given the presence of a number of defects generated by high energy milling process.

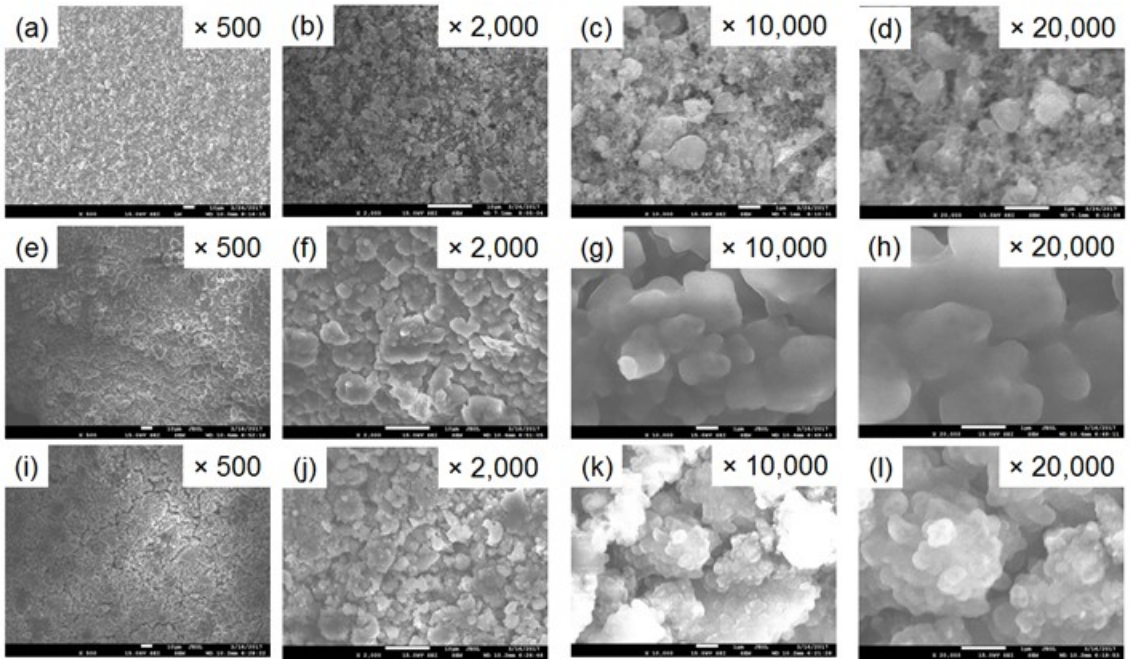

Figure II-107. SEM images of Si-Sn-C electrodes at (a – d) pristine state, (e - h) the 50th lithiation, and (i - l) the 50th delithiation.

According to the previous studies on Si-Sn nanocomposites, a proper control of the morphology, particle size and homogeneity is of critical importance for the electrochemical performance, ideally, mixed Si and Sn at an atomic level. However, inhomogeneous particle size distribution was noticed (Figure II-108 a, b). Moreover, uneven elemental distribution of Si and Sn in the particle was also revealed (Figure II-108 c) with some relatively large Si particles (yellow color) being clustered and embedded in the Sn matrix (blue color). Therefore, we investigated the synthesis by Cryomill, which was tailored for cryogenic grinding by enabling continually cooled grinding jar via liquid nitrogen during milling, thus offering the potential to break down particle size, achieve good mixing, and avoid Sn melting. As shown in Figure II-108 d-f, Si-Sn sample prepared by Cryomill has a more uniform particle size distribution, meanwhile, much more homogeneous Si,

Sn mixing was achieved by Cryomill. However, the as-prepared sample by Cryomill did not exhibit improved cycling performance, likely due to the insufficient mechanical energy input.

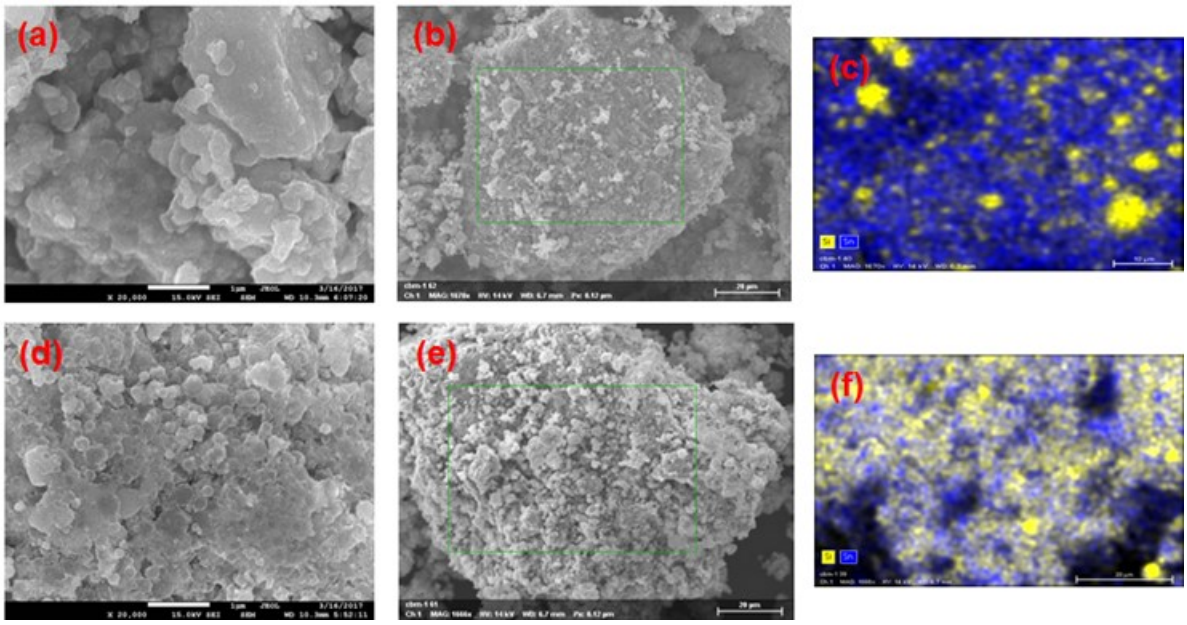

Figure II-108. (a, b) SEM image, (c) Si, Sn EDS mapping of the selected area (green box in (b)) in Si-Sn sample prepared by high energy mill and (d, e) SEM image, (f) Si, Sn EDS mapping of the selected area (green box in (e)) in Si-Sn sample prepared by Cryomill.

Therefore, we explored chemical reduction method, which can enable the design of materials with controlled surface and bulk composition, i.e., core-shell structure, which will allow the in-depth understanding of the reaction mechanism of Si-Sn phases with lithium. This synthesis process typically involves reduction of metal salts (metal chlorides, metal nitrates etc.) using borohydride reducing agent (sodium borohydride, potassium borohydride) to precipitate the homogeneous or heterogeneous mixtures of un-reacted, nanoscale elemental constituents. In our studies, we first prepared Sn nanoparticles by reducing $SnCl_2$ in $NaBH_4$ solutions for 5 min and 150 min. As shown in Figure II-109 a-d, both samples demonstrated a similar morphology, with the particle size varying between 100 nm and 1 μm. Effective Sn metal reduction was confirmed by XRD (Figure II-110 a). We also investigated elemental distribution in the Sn sample prepared by 5 min reduction to investigate the completion of reaction. It can be seen in Figure II-109 e-h that Sn, Cl, and O were observed in the final product, the atomic ratio of O and Cl was estimated to be ~ 15.7% and 7.4%, corresponding to 75 mol% Sn, 20 mol% SnO, and 5 mol% $SnCl_2$.

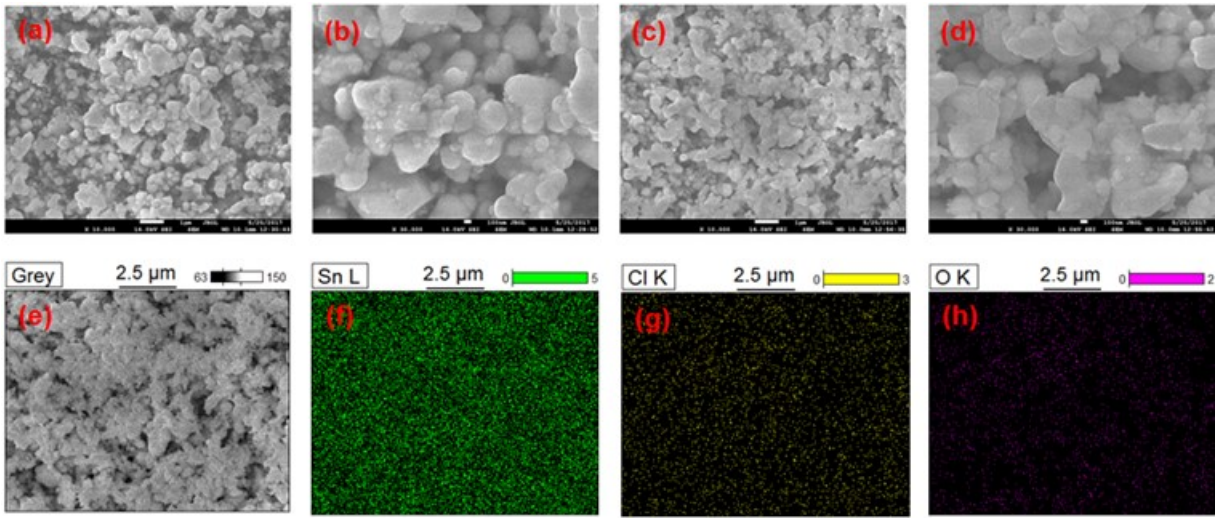

Figure II-109. (a, b) SEM image, (c) Si, Sn EDS mapping of the selected area (outlined by green lines in (b)) in Si-Sn sample prepared by high energy mill. (d, e) SEM image, (f) Si, Sn EDS mapping of the selected area (outlined by green lines in (e)) in Si-Sn sample prepared by Cryomill.

After evaluating the effectiveness of Sn metal reduction, we prepared Si-Sn samples using chemical reduction method. We first added Si nanoparticles into $NaBH_4$ solution and ultrasonically mixed them to facilitate Si dispersion, followed by adding $SnCl_2$ solution into the $NaBH_4$ solution with Si nanoparticles at a speed of 0.2 mL/sec and mixing for two extreme durations, 5 min and 15h. Afterward, we removed the supernatant and centrifuge the insoluble materials, washed and dried the final product under vacuum. Formation of Si-Sn nanocomposites in both samples was revealed by XRD (Figure II-110 a). From the preliminary electrochemical evaluation (Figure II-110 b), the sample prepared by 15h reduction exhibited an initial capacity of 1060 mAh/g at a low electrode loading (0.82 mg), increasing electrode loading to 1.43 mg led to a reduction of the initial capacity to 984 mAh/g. Both samples showed capacity fade when cycled at C/3 after the first three formation cycles, with the capacity of ~ 750 and 400 mAh/g remained in the early cycles. As a comparison, the sample prepared by 5 min reduction showed a relatively higher capacity (1327 mAh/g) compared to that reduced for 15h, but followed by a faster capacity decay. These preliminary results demonstrated that the chemical reduction is effective in preparing metals by reducing salts, but a proper control of reacting conditions to drive complete reaction, avoid oxide impurity formation, while remain efficient control of the particle size and morphology of the final product, is critical to produce metal anodes by chemical reduction method.

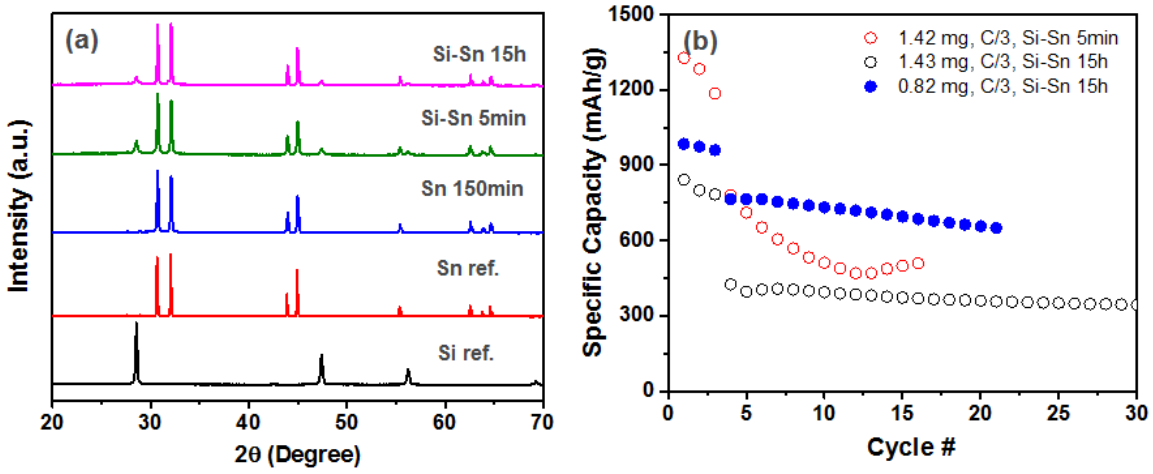

Figure II-110. (a) XRD patterns and (b) cycling performance of Si-Sn samples produced by chemical reduction method. Cells were cycled between 1.5 and 0.05 V at room temperature.

Exploring Li Inventory Strategies (ANL)

Lithium inventory control is an issue that is part of the Si deep dive (DD) project. Si/graphite blended electrodes require careful cell-capacity balancing to begin to enable the technology. Typically this requires much thicker (and heavier) cathodes to account for first cycle irreversible capacity losses (ICL). In addition, due to electrode voltage slippage, the SOC is hard to control, and cell capacity can be compromised. The usable capacity begins to shrink in the cell, and eventually Li-trapping in the Si material wins out, and lifetime is exhausted. The behavior must be understood and then addressed by the lithium inventory team as part of the overall project.

Cycling Si-based electrodes is complicated by destruction and reformation of the SEI on the Si electrode surface. Unfortunately the Li is siphoned from the full cell as a result which causes stresses on the cathode and loss of capacity. Thus an analysis of lithium inventory is needed in order to track the losses in the cell. Certainly, the SEI problems arising from excessive Li_xSi volume changes is problematic, but how the lithium loss as a function of cycle life occurs, and if there is a specific voltage window (or Li_xSi alloy phase) that predominates Li loss is unknown. Furthermore, for a Si-graphite blended cell, does the graphite experience particle electrochemical grinding from Li_xSi volume changes? Such processes need to be determined and once knowledge gained, solutions found.

A combination of specially designed full cells, examination of pre-lithiation additives, cycling results, and SEM, Raman, and Li-NMR are needed to follow Li inventory in Si containing cells. We will pursue these research strategies for analysis of these electrochemical and chemical processes.

SiO_x/NCM-LFO Cell Results

This past year we synthesized new batches of LFO, blended them with NCM523 powder, made electrodes that were balanced with a SiO_x anode and cycled the full cells. The extra lithium delivered from the LFO portion (~40 mAh/g) ensured that the LFO would provide pre-lithiation property to the Si-containing cell.
Figure II-111 shows the voltage profiles of SiO_x anode together with individual NCM523 cathode (left) or a NMC:LFO (100:7 w:w) (right) blended electrode (80:10:10 active:PVDF:C45). The voltage profiles are shown between 4.3 to 3 V and the electrolyte was Gen 2 (w/ FEC). The blended electrode enables the NCM523 to access its full capacity without overcharge. The lithium inventory is controlled from a pre-lithiation approach. As a result better utilization of the cathode is realized as is presented in Figure II-112. The left hand side of the Figure II-112 is a graph of the capacity of the cathode as a function of cycle number to 50 cycles. Note that the capacity delivered is higher with LFO (black filled squares) than without (red filled circles). The right hand

side shows that the rate capability of the blended electrode - NMC-LFO, is not limiting. The Li half-cell is cycled at C/3 with HPPC tests done intermittently.

In addition to full cell cycling diagnostic analysis experiments described above, complementary work focused on synthesis scale-up with MERF using iron oxide and iron oxalate precursors at 50 g scale. The scale-up synthesis of the material is then to be used in CAMP facility for electrode making. We are now in the process of testing the material in CAMP electrodes.

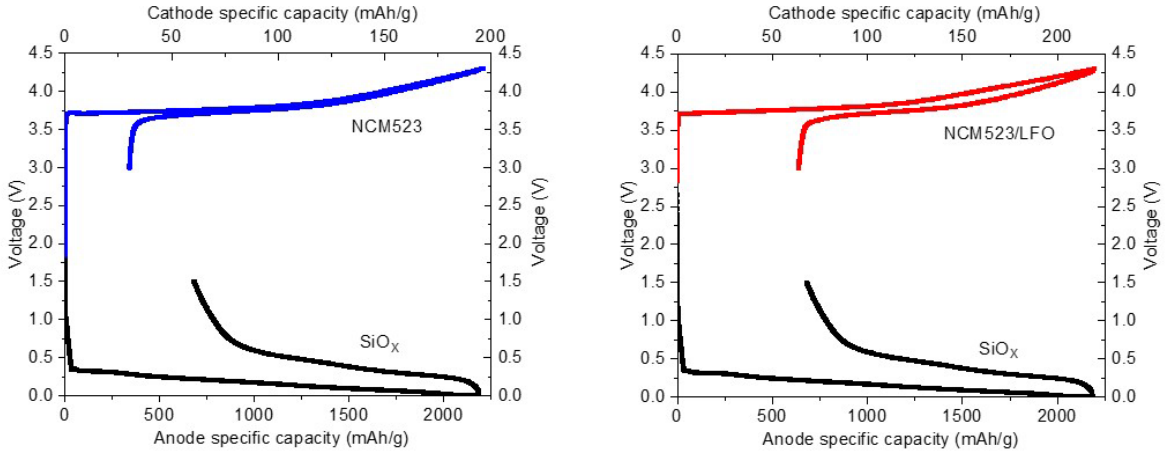

Figure II-111. Voltage profiles of (left) Li/NCM523 and Li/SiOx cells, and (right) Li/NCM523-LFO and Li/SiOx cells. The utilization of the NCM electrode is greater as a result of the extra pre-lithiation capacity imparted in the cell from the additive, LFO.

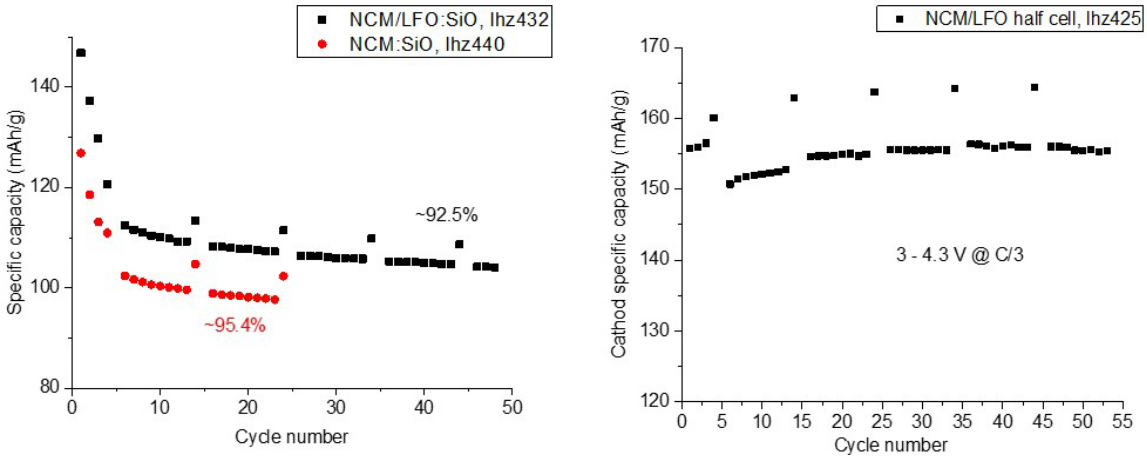

Figure II-112. (left) Capacity versus cycle number for SiO_x/NCM523 cells (red filled circles; 2.5 to 4.3 V, C/10), and SiO_x/NCM523-LFO cells (black filled squares; 2.0 to 4.3 V, C/10). (Right) capacity versus cycle number for NCM523-LFO half cells.

Lithium Inventory and Tracking of 15%Si-Graphite Anode

The CAMP NCM523 cathode (electrode library ID: A-C013A) is known to drop 20% of its capacity (3 to 4.1 V cycling voltage window) over 100 cycles when paired with a 15%Si-graphite CAMP anode (electrode library ID: A-C013A). This was documented in last year's Si DD annual report (page 9). The resultant cathode capacity at 100 cycles is below 80 mAh/g. This deleterious behavior has to be understood and improved. The main failure mechanism is thought to be the poor coulombic efficiency caused by lack of formation of robust SEI layer on the Si material. As a result, cyclable Li is extracted irreversibly from the NCM523 cathode

leading to capacity loss. To probe this behavior, we decided to replace the NCM523 electrode with a high-capacity LiFePO4 (LFP) cathode, and employ the electrode as a reference/counter electrode in the cell. To this end this strategy allows us to (1) establish a stable dQ/dV plot to track the lithium inventory that occurs at the 15%Si-graphite anode, (2) provide an excess of Li that will replenish Li to the cell, and (3) keep the cathode from being overcharged. By controlling these three parameters, we should be able to track the lithium inventory. Figure II-113 shows the voltage profiles of the (a) Li/LFP half-cell showing over 4 mAh capacity, and (b) the Li/15%Si-graphite half-cell. Notably, the capacity of this cell is a lower 1 mAh.

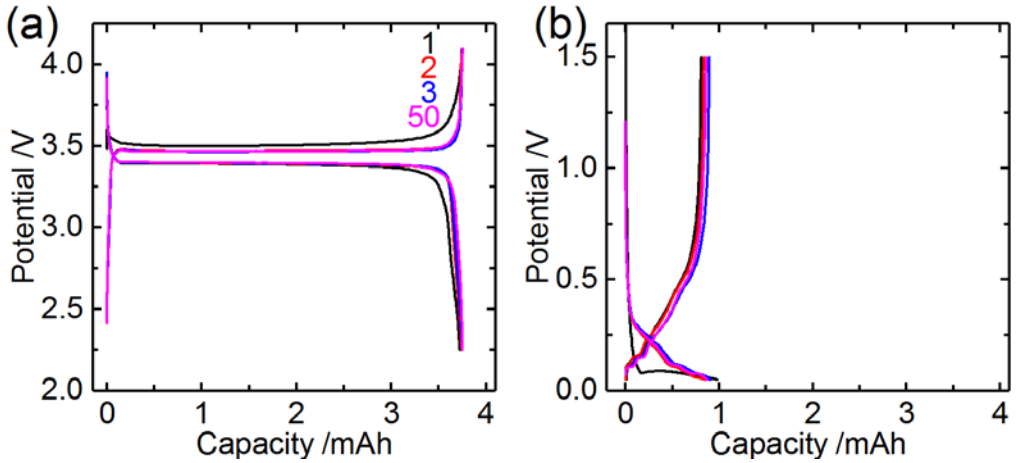

Figure II-113. (Representative potential profiles for the (a) high capacity $LiFePO_4$ reference/counter electrode against Li metal, and (b) 15%Si-graphite electrode against Li metal. In the full/reference cell, as the Si irreversibly consumes Li the $LiFePO_4$ electrode has ample Li inventory to continue to supply capacity to the cell.

The full cell voltage profiles of 15%Si-graphite/LFP are provided in Figure II-114. As noted earlier, the use of a high capacity LFP reference electrode makes extended cycling of a Si-containing electrode possible. To this end, the cell tested at a 1C rate was cycled 1000 times. After 100 cycles the cell cycles with efficiencies >99.5%, and therefore consumes little Li each cycle and the LFP Li inventory is not exhausted. On cycle 1000 the cell is cycling between (approx.) 2.79 and 3.29 mAh on the LFP electrode. The capacity retention, measured at C/10 every 100 cycles, decays approximately linearly and is 74% after 100 cycles, 57% after 500 cycles, and 41% after 1000 cycles. The cycle efficiency on the C/10 cycles improves with cycling; 96.8% on cycle 100, 98.5% on cycle 500, and 99.0% on cycle 1000. The improving cycling metrics observed here are consistent with current Si failure models. In later cycling the SEI growth and delamination fill the pores, and mechanical stresses and particle agglomeration densify the electrode structure. This likely impedes Li diffusion and limits it to regions nearest the separator and/or other accessible surface regions, thereby decreasing the lithiation capacity. Consequently, the volume expansion would be less and the SEI cracking and number of freshly exposed surfaces reduced. This would lead to lower capacity fade and higher cycle efficiencies, as observed in this study.

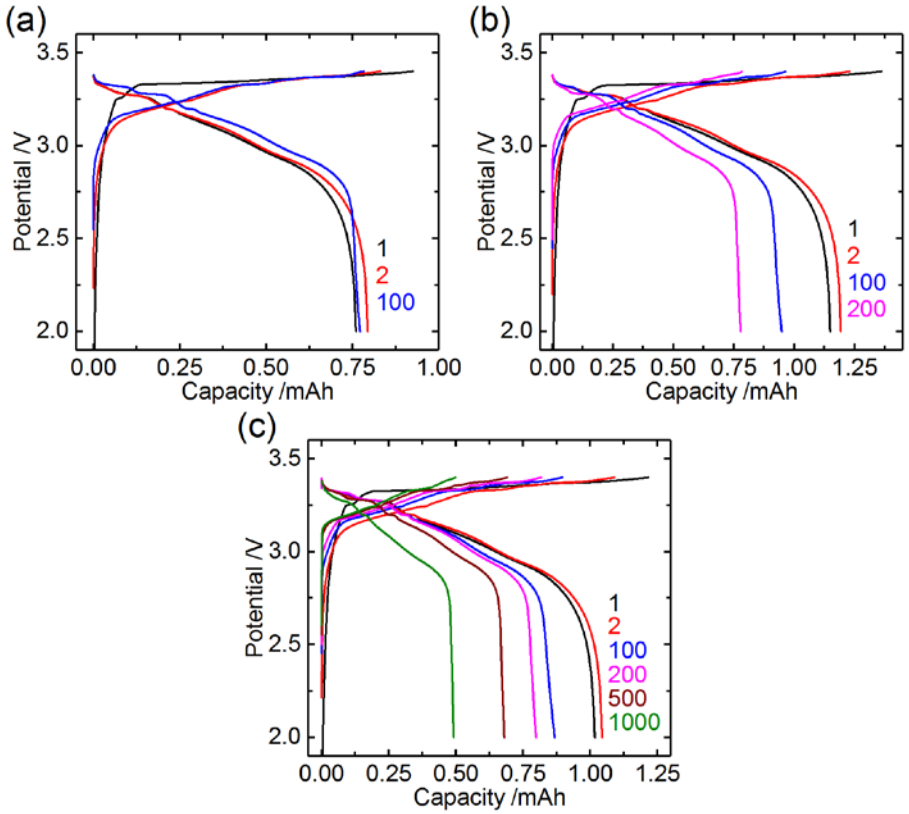

Figure II-114. Representative electrochemical profile versus capacity with cycle number of Si-graphite cycled against a LiFePO4 reference electrode at (a) C/10, (b) C/5, and (c) 1C. In (b) and (c) the first and last 3 cycles of each set of 100 cycles were performed at C/10 while the intermediate cycles were performed at C/5 and 1C, respectively.

Figure II-115 considers a breakdown of the delithiation capacity delivered above and below 3.185 V. From the dQ/dV (Figure II-116) it is clear that graphite is the main contributor to the capacity at potentials higher than 3.185 V (0.205 V versus Li^0), although Si may also make a contribution. Below 3.185 V the capacity is solely from Si delithiation. Therefore, Figure II-116 shows an approximation of the relative capacity retention of the Si and graphite components in the blended electrode. Capacity fade of Si is most rapid in the first 400 cycles, dropping to 61 %, and thereafter decreasing steadily to 46% after 1000 cycles. Meanwhile, the capacity above 3.185 V is >80% after 400 cycles, but begins to decrease approximately linearly to be around half its initial value after 1000 cycles. The most severe losses are from the graphite process at 3.372 V.

The potential at which the dQ/dV intensity begins to rise in region A changes gradually between cycle 20 and cycle 100, increasing by ~40 mV. This is likely caused by gradual ionic isolation of Si particles, particularly those closest to the current collector which makes the lithium mobility to these particles kinetically limiting and more difficult (resistance increases). The two minor Si lithiation processes at 3.27 and 3.30 V (B and B', 0.20 and 0.17 V versus Li^0) and the process at ~3.35 V (C, ~0.12 V versus Li^0) are related to lithiation of the larger Si clusters, which causes them to be further broken down to smaller clusters. Conspicuously, minimal capacity fade is noted in region C after 100 cycles. Between cycle 20 and 100 the potential at which this process occurs steady increases, however, suggesting the over-potential for this process increases with cycling. The 1C cycling data shows the potential rise is greater at higher cycling rates and the trend continues beyond 100 cycles.

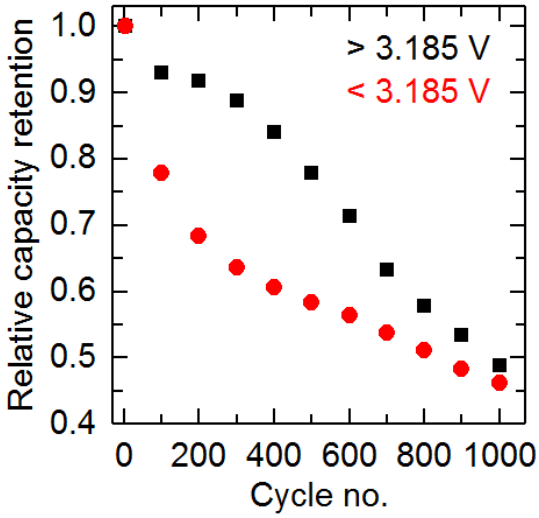

Figure II-115. Relative capacity fade above and below 3.185 V with respect to cycle number for Si-graphite cycled against a LiFePO4 reference electrode at 1C. The first and last 3 cycles of each set of 100 cycles were performed at C/10 while the intermediate cycles were performed at 1C.

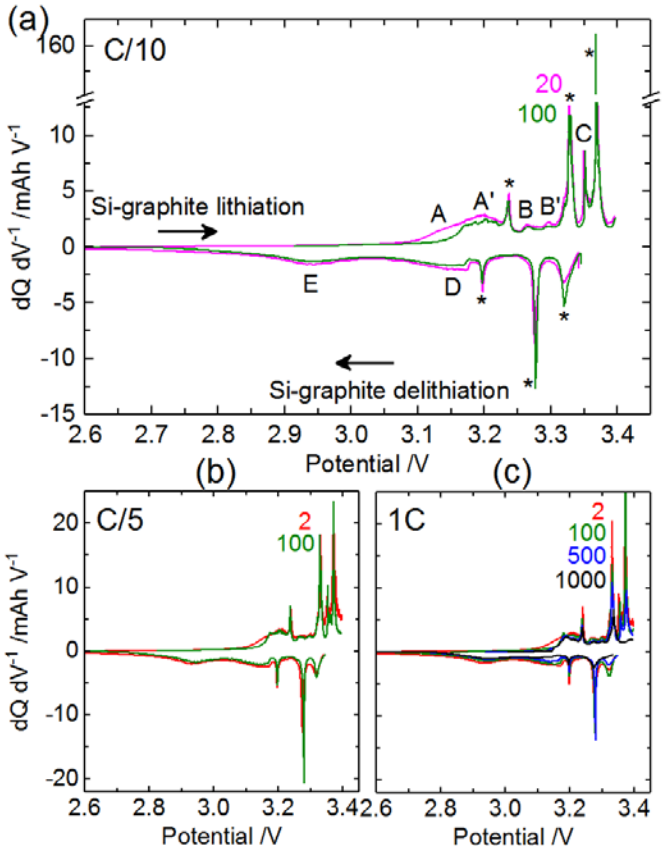

Figure II-116. Representative differential capacity dQ/dV plots for Si-graphite cycled against a LiFePO4 reference electrode at (a) C/10, (b) C/5, and (c) 1C. In (b) and (c) the first and last 3 cycles of each set of 100 cycles were performed at C/10 while the intermediate cycles were performed at C/5 and 1C, respectively. In (a) the * marks (de)lithiation processes attributed to graphite, letters A-C mark lithiation processes of Si, and letters D-E mark delithiation processes of Si.

To understand the rate of capacity loss in regions A-E, the dQ/dV intensity at 3.14 (A), 3.20 (A'), 3.27 (B) and 3.30 V (B') on lithiation, and 3.16 (D) and 2.94 V (E) on delithiation vs. cycle number for the C/10 cell was analyzed (not shown). Firstly, there is a significantly greater rate of capacity loss in region A (3.14 V, or 0.33 V versus Li^0) compared to other regions. The rate of loss is around three times greater and is highly linear with respect to cycle number. This suggests a continual degradation rather than a catastrophic failure mechanism, consistent with Li trapping at or near the surface of Si grains. It also demonstrates that the greatest losses occur on lithiation as amorphous Si is broken down to form silicon clusters. Losses are less severe and less linear with cycle number during lithiation at other potentials. Rates of loss on delithiation are just slightly higher in region D (3.16 V or 0.23 V versus Li^0) relative to region E (2.94 V or 0.45 V versus Li^0).

SEM images reveal the differences that exist in the topography of pristine Si-graphite blended electrodes and those cycled at C/5 for 100 cycles. As Figure II-117a illustrates, two domains can be clearly distinguished in the uncycled electrode, the darker regions corresponding to graphite particles of micrometer size and the lighter areas due to the mixture of nanosized silicon and conductive carbon. Conversely, in the cycled electrodes (Figure II-117b) such domains disappear in favour of the formation of a homogeneous surface where particle-like aggregates are found. Based on this, it seems likely that the aggregate growth initiates around the graphite domains encountered in the pristine electrode as a result of the volume expansion/ contraction suffered by Si during cycling, which contributes to silicon covering the entire surface of the electrode. Conversely, EDS mapping of the cross-section of the pristine (Figure II-117c) and cycled electrodes (Figure II-117d) manifests no divergences between them. The presence of carbon domains (graphite) and Si is observed in both, revealing that in the expansion and contraction of Si the graphite particles are simply buried beneath the electrode surface.

The Raman spectra is shown in Figure II-117f, (as compared to uncycled pristine electrode in Figure II-117e). The results show the expected crystalline Si to amorphous structural change. The large graphite domains are no longer clearly observed. The graphite domains do have a similar Raman spectrum to those in the pristine electrode as previously indicated in the EDS map cross-section. However, the D band (disorder mode) is broader and may imply the graphite particles are broken into smaller pieces, by Si during repeated cycling. Si aggregation is also evident after cycling, as reported in the literature and tends to occur on or near the graphite particles.

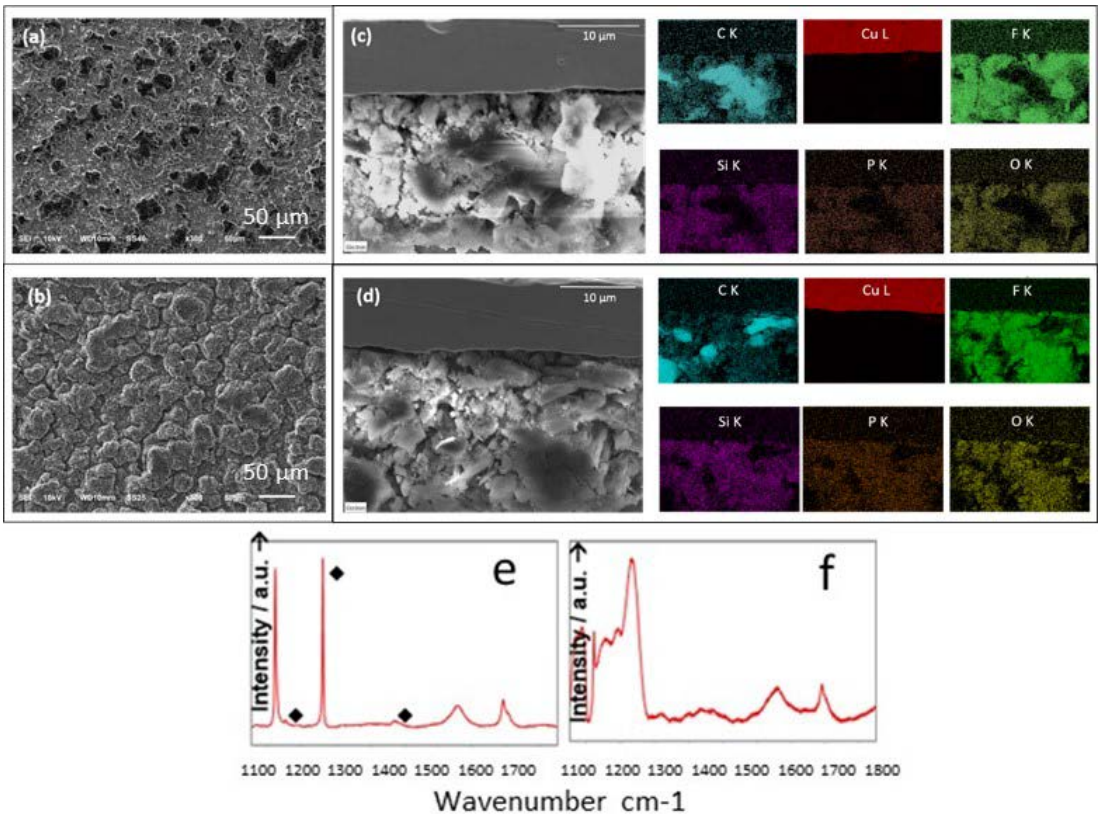

Figure II-117. SEM (a-d) and Raman spectra (e-f) of the pristine Si-graphite electrode (a,b,e) and after 1000 cycles at 1C against a LFP reference electrode (c,d,f). Cross-section images of Si-Gr (c) pristine electrode and (d) cycled and the EDS mapping of C K (cyan), Cu L (red), F K (green), Si K (violet), P K (orange) and O K (yellow) associated to them. Note that the pristine electrode has been extracted from a half cell assembled against metallic lithium and the cycled electrode belongs to the Si-Gr/LFP full cell cycled at C/5 for 100 cycles.

Conclusions

The development of high-performance polymer binders for silicon-based electrodes is being pursued. These binders are designed to mitigate the volume expansion stress and maintain electrical contact with conductive additive and current collector to achieve long-term cycling capacity. Several different approaches are being explored. Graft copolymers (i.e., GC-g-LiPAA via RAFT polymerization) show improved of cycling performance over PVDF and GC binders. Improving on these binders, crosslinked catechol group functionalized chitosan was designed and developed as a polymer binder to further improve adhesion and the mechanical stability. Early cycling results with these materials are promising.

A series of cPAA binders has been developed via two approaches. Approach I allows quick and efficient synthesis but with no control of the crosslinking sites and approach II prompts the intermolecular crosslinking by incorporating the crosslinking reaction into the chain growth process. The cPAA1 and cPAA2 binders obtained by approach I demonstrated no improvement on the cycling performance of silicon/graphite anodes possibly due to the intra-molecular crosslinking and the resultant constrained conformations. cPAA3 and cPAA4 were synthesized by copolymerization of AA monomers and crosslinker molecules. cPAA4 demonstrated a much-improved cycling performance in the half cell of the silicon/graphite electrode. The initial capacity and capacity retention are 751 mAh/g and 76% at the 86th cycle, and both are much higher than those of the linear PAA cell. cPAA4 is so far the best performing binder within this class and is worthy of more detailed investigation. Both cPAA2 and cPAA4 delivered surprisingly improved cycling performance of

high capacity silicon anodes (70% silicon). More systematical investigations of those crosslinked PAA binders are currently on going, including optimizing crosslinking reactions, and electrode post-characterizations.

A new family of PAA-based binders was developed. The incorporated arene ring is expected to afford additional stiffness that could benefit the cell performance. P4VBA binders with two different molecular weights were synthesized and characterized. The improved cycling performance of P4VBA2 may indicate that the incorporated benzene ring of the repeating unit of P4VBA2 may contribute to the improved the desired mechanical properties. Detailed characterization regarding the mechanical properties of these binders is ongoing.

Binary polymeric systems able to crosslink in-situ during electrode processing is being explored. Specific components are being identified that allow casting but undergo rapid thermally induced crosslinking during laminate drying.

Finally, development of conductive polymer binders is continuing with work focused on investigation of the stability of the conductive polymer binders, synthetically introducing new anthracene-based conductive moiety to the methacrylate backbone, and decipher the formulation of aqueous-based emulsion of Si-based electrode systems. Analysis of the electrode stability of the Polymethacrylatepyrene (PPy) type of binders after cycling demonstrate both chemical and electrochemical stability of the PPY binder. After confirmation of the stability of the PPy binder, a series of conductive polymer binders based on methacrylate polymer backbone were synthesized that works effectively as both binder and conductive agent for the Si electrode.

The alucone MLD coating has been developed on the Si particles. The TEM images confirmed that the conformal coating was achieved for the Si particles from Alfa, but failed on the Si particles from NanoAmor. For the electrodes made with the NanoAmor Si particles, the coating impact is negligible in terms of the electrochemical cycling performance. It is believed that the oxide and organic impurities on the surface of Si particles negatively affect the growth of the coating materials. The poor coating quality and coverage is not sufficient to affect the electrochemical properties of the silicon particles; thereby, there is no major difference in the electrochemical cycling behavior.

The greatly improved reversibility was obtained for the Alfa Si particles. After the MLD coating (1nm), the electrodes made with the coated Si particles shows highly reversible cycling performance over hundreds cycles, as compared with the electrodes comprised of the uncoated Si particles. PAA was used here to enhance the mechanical integrity for the electrodes, thereby enable the high mass loading for high area capacity. In all of the cells, a high mass loading of (>3mg/cm2) was used. Due to the low conductivity of the pristine alucone coating, the electrodes made with the coated Si particles always show lower reversible capacity. Although the electrodes made with the uncoated Si particles offer higher reversible capacity, but much low capacity retention after 50 cycles. The study of capacity contribution from each component has revealed that the capacity fading has been observed for the active components, graphite and Si particles. When combining with the coated Si particles, the graphite offers stable cycling performance. The SEM analysis supported the effectiveness of the surface protection strategy. The alucone coating suppressed the growth of the SEI layer, reduced the impedance and help maintaining the original electrode structure. Furthermore, the flexible alucone coating can also accommodate the volume changes, and further secure the stability of the entire electrode and therefore improve the cycling performance.

A fundamental understanding of the reactivity of the electrolyte with silicon-based anodes and how the chemical composition of the SEI affects cell performance is being systematically performed through organic-based interfacial modifications. Specifically, in this work, we engineer the silicon surface chemistry through two approaches targeted at stabilizing the interface affording extended cycle life. The first approach is to develop new electrolyte/additive that chemically/electrochemically decomposes and deposits on the lithiated Si surface forming a resilient SEI layer that stabilizes the interfacial reactivity of LixSi and electrolyte. The second approach is to functionalize the surface of Si particles through organic silane chemistry with a target to

stabilize the interface affording a Si anode with extended cycle life. Both approaches have been shown to effectively modify the SEI and early promising cycling results have been observed.

We explored the synthesis of Si-Sn nanocomposites via mechanical milling method that is cost-effective, facile, and scalable. We completed the post-mortem analysis on the spatial distribution of the phases in the pristine and cycled Si-Sn-C electrodes using SEM and EDS. Change in morphology on the electrode along with some cracking at the electrode level was observed after 50 cycles. Meanwhile, we explored Cryomill and chemical reduction methods. Cryomill demonstrated effectiveness in preventing particle agglomeration. Chemical reduction method was effective to produce Sn metal by reducing Sn salts, even by 5 min. From our preliminary studies, Si-Sn samples produced by this method delivered an initial capacity of over 1000 mAh/g without further synthesis optimization. The necessity of optimizing the reaction conditions to achieve complete reduction, avoid oxide impurity, and optimize particle size and morphology was revealed by EDS. In next year, we will focus on the production of Si-Me anode using splat quenching method, which is a commonly used method in metallurgy and well suited for preparation of metal/alloy materials that are near-amorphous, non-crystalline.

Lithium inventory control in Si-graphite/NCM cells is critically important to the success of such advanced cells in EV transportation applications and we are tasked from DOE to understand and solve this problem. In summary, two tasks were completed this past year. First, LFO pre-lithiation additive was shown to improve the cycling and utilization of a full SiOx/NCM523-LFO full cell. Second, a Si-graphite blended electrode has been paired with a high capacity LFP reference electrode. LFP provides a stable reference potential and abundant Li inventory to understanding the irreversibility and capacity fade in Si-based electrodes during extended cycling. The losses in capacity observed in the different potential plot (dQ/dV) have been related to the evolution in the Si local structure, electrode morphology and mechanical properties during (de)lithiation. Extended cycling of the Si-graphite electrode showed slowing capacity fade and increasing cycle efficiencies, particularly after 100 cycles, consistent with current Si-containing electrode failure mechanisms. Further work is required to more fully understand the interactions between Si and graphite components in the blended electrode, and the role graphite plays in Li diffusion to the bulk of the electrode and capacity retention.

Key Publications

1. Hu, B.; Zhang, J.; Jiang, S.; Zhang, Z.; Zhang, L, "Cross-linked Poly(Acrylic Acid) Binder for Silicon Anode of Lithium-Ion Batteries". ABAA-10, poster, Oct 1-4, 2017, Oakbrook, IL.
2. Hu, B.; Zhang, J.; Jiang, S.; Zhang, Z.; Zhang, L., "Cross-linked Poly(Acrylic Acid) Binder for Silicon Anode of Lithium-Ion Batteries". Manuscript in preparation.
3. Hu, B.; Zhang, L.; Zhang, S.; Zhang, J.; Zhang, Z.; Lu, W.; Zhang, L; "Understanding Molecular Weight Effect of Poly(Acrylic Acid) Binders for Silicon Anode of Lithium-Ion Batteries", to be submitted.
4. Hu, B.; Zhang, J.; Shkrob, I. A.; Zhang, Z.; Zhang, L. "Poly(4-vinylbenzoic acid) binders for the silicon lithium-ion batteries", invention report, IN-17-019.
5. Hu, B.; Zhang, J.; Shkrob, I. A.; Zhang, Z.; Zhang, L. Poly(4-vinylbenzoic acid) binders for the silicon anode of lithium-ion batteries. Manuscript in preparation
6. S. Son and C. Ban, “Systematic Investigation of the Alucone-Coating Enhancement on Silicon Anodes with Polyvinylidene Fluoride as Binder”, ACS Applied Materials & Interfaces, Accepted.
7. 231st ECS Meeting in New Orleans, LA, 2017, “Nanostructure Silicon-Based Hierarchical Architectures for High-Performance Lithium-Ion Battery Anode”.
8. 231st ECS Meeting in New Orleans, LA, 2017, “An in-Depth Investigation of the Alucone Coating Impact on the Performance of the Silicon Anode”.

9. C. Ban, C. Jiang, ECS PRIME, 2016, “Examining Electrical Properties of Solid Electrolyte Interface on Silicon Electrodes”.

10. C. Ban, 18th International Meeting on Lithium Batteries 2016, “Surface Modification of Silicon Anodes for Durable and High-Energy Lithium-Ion Batteries”.

11. J. Xu, M. Ling, L. Terborg, H. Zhao, F. Qiu, J. J. Urban, R. Kostecki, G. Liu, W. Tong*, “Facile Synthesis and Electrochemistry of Si-Sn-C Nanocomposites for High-Energy Li-ion Batteries,” Journal of the Electrochemical Society, 164, A1378-A1383 (2017).

12. Wesley M. Dose, Premkumar Senguttuvan, James Blauwkamp, Christopher S. Johnson, The Effect of Pre-lithiation Chemistry on Li Inventory in High-Energy Li-ion Cells, 232nd The Electrochemical Society Meeting, National Harbor, MD, Oct. 1-5, 2017

13. W. M. Dose, V. A. Maroni, M. J. Piernas-Muñoz, I. Bloom, C. S. Johnson, Capacity loss in silicon-graphite blended anodes upon extended cycling: a new approach to Li inventory, Advanced Batteries for Automotive Applications (ABAA10), Oak Brook, IL Oct. 22-25, 2017

14. “Next Generation Anodes for Lithium-Ion Batteries: Materials Advancements,” 2017 U.S. Department of Energy Vehicle Technologies Office Annual Merit Review and Peer Evaluation Meeting, June 5-9, 2017, Washington, DC.

References

1. *Alloy Negative Electrodes for Li-Ion Batteries*. M.N. Obrovac and V.L. Chevrier, Chem, Rev. 2014, 114, 11444-11503.

2. Shi, H.; Zhao, Y.; Dong, X.; Zhou, Y.; Wang, D., Frustrated crystallisation and hierarchical self-assembly behaviour of comb-like polymers. *Chem. Soc. Rev.* **2013,** *42*, 2075-2099.

3. Liang, H.; Cao, Z.; Wang, Z.; Sheiko, S. S.; Dobrynin, A. V., Combs and Bottlebrushes in a Melt. *Macromolecules* **2017,** *50*, 3430-3437.

4. Daniel, W. F. M.; Burdynska, J.; Vatankhah-Varnoosfaderani, M.; Matyjaszewski, K.; Paturej, J.; Rubinstein, M.; Dobrynin, A. V.; Sheiko, S. S., Solvent-free, supersoft and superelastic bottlebrush melts and networks. *Nat. Mater.* **2016,** *15*, 183-189.

5. Zhang, J.; Schneiderman, D. K.; Li, T.; Hillmyer, M. A.; Bates, F. S., Design of Graft Block Polymer Thermoplastics. *Macromolecules* **2016,** *49*, 9108-9118.

6. Song, J.; Zhou, M.; Yi, R.; Xu, T.; Gordin, M. L.; Tang, D.; Yu, Z.; Regula, M.; Wang, D., Interpenetrated Gel Polymer Binder for High-Performance Silicon Anodes in Lithium-ion Batteries. *Adv. Funct. Mater.* **2014,** *24*, 5904-5910.

7. Magasinski, A.; Zdyrko, B.; Kovalenko, I.; Hertzberg, B.; Burtovyy, R.; Huebner, C. F.; Fuller, T. F.; Luzinov, I.; Yushin, G., Toward Efficient Binders for Li-Ion Battery Si-Based Anodes: Polyacrylic Acid. *ACS Appl. Mat. Interfaces* **2010,** *2*, 3004-3010.

8. Pieczonka, N. P. W.; Borgel, V.; Ziv, B.; Leifer, N.; Dargel, V.; Aurbach, D.; Kim, J.-H.; Liu, Z.; Huang, X.; Krachkovskiy, S. A.; Goward, G. R.; Halalay, I.; Powell, B. R.; Manthiram, A., Lithium Polyacrylate (LiPAA) as an Advanced Binder and a Passivating Agent for High-Voltage Li-Ion Batteries. *Adv. Energy Mater.* **2015,** *5*, 1501008-n/a.

9. Li, J.; Le, D.-B.; Ferguson, P. P.; Dahn, J. R., Lithium polyacrylate as a binder for tin–cobalt–carbon negative electrodes in lithium-ion batteries. *Electrochim. Acta* **2010,** *55*, 2991-2995.

10. Koo, B.; Kim, H.; Cho, Y.; Lee, K. T.; Choi, N.-S.; Cho, J., A Highly Cross-Linked Polymeric Binder for High-Performance Silicon Negative Electrodes in Lithium Ion Batteries. Angewandte Chemie International Edition 2012, 51 (35), 8762-8767.

11. Odian, G., Principles of Polymerization, 4th Edition. Willey-Interscience, New York: 2004; p 832.

12. Ling, M.; Liu, M.; Zheng, T. Y.; Zhang, T.; Liu, G., Investigating the Doping Mechanism of Pyrene Based Methacrylate Functional Conductive Binder in Silicon Anodes for Lithium-Ion Batteries. J. Electrochem. Soc. 2017, 164 (4), A545-A548.

13. T. D. Hatchard and J. R. Dahn, *Journal of The Electrochemical Society*, 2004, **151**, A1628-A1635.

14. H.-J. Ahn, Y.-S. Kim, K.-W. Park and T.-Y. Seong, *Chemical Communications*, 2005, DOI: 10.1039/B407264B, 43-45.

15. X. Xiao, J. S. Wang, P. Liu, A. K. Sachdev, M. W. Verbrugge, D. Haddad and M. P. Balogh, *Journal of Power Sources*, 2012, **214**, 258-265.

16. H. Wang, H. Huang, L. Chen, C. Wang, B. Yan, Y. Yu, Y. Yang and G. Yang, *ACS Sustainable Chemistry & Engineering*, 2014, **2**, 2310-2317.

17. Y. Kwon and J. Cho, *Chemical Communications*, 2008, DOI: 10.1039/B716694J, 1109-1111.

II.B.4 Silicon Electrolyte Interface Stabilization (SEISta) (NREL, ANL, ORNL)

Anthony Burrell, Principal Investigator
National Renewable Energy Laboratory
15013 Denver West Parkway
Golden, CO 80401
Phone: 303-384-6666
E-mail: Anthony.Burrell@nrel.gov

Brian Cunningham, Technology Manager
U.S. Department of Energy
Phone: 202-287-5686
E-mail: Brian.Cunningham@ee.doe.gov

Start Date: July 1, 2016 End Date: September 30, 2019
Total FY17 Project Cost: $2,650,000 DOE FY17 share: $2,650,000 Non-DOE share: $0

Introduction

The SEISta project was developed to specifically tackle the foundational understanding of the formation and evolution of the solid electrolyte interphase on silicon. This project will have as its primary goal an understanding of the reactivity of the silicon and lithiated silicon interface with the electrolyte in lithium-ion systems. It consists of researchers from multiple national laboratories (ANL, SNL, ORNL, LBNL, and NREL) working toward clear unified goals.

Silicon is a viable alternative to graphitic carbon as an electrode in lithium-ion cells and can theoretically store >3,500 mAh/g. However, lifetime problems have been observed that severely limit its use in practical systems. The major issues appear to involve the stability of the electrolyte and the uncertainty associated with the formation of a stable solid electrolyte interphase (SEI) at the electrode. Recently, calendar-life studies have indicated that the SEI may not be stable even under conditions where the cell is supposedly static. Clearly, a more foundational understanding of the nature of the silicon electrolyte interface is required if we are to solve these complex stability issues. A new multi-lab consortium has been formed to address a critical barrier in implementing a new class of materials used in lithium-ion batteries that will allow for smaller, cheaper, and better performing batteries for electric-drive vehicles. This consortium, nicknamed the Silicon Electrolyte Interface Stabilization (SEISta) project, was formed to focus on overcoming the barrier to using such anode materials. Five national laboratories, led by the National Renewable Energy Laboratory (NREL), are involved: NREL, as well as Argonne (ANL), Lawrence Berkeley (LBNL), Oak Ridge (ORNL), and Sandia National Laboratories (SNL).

Objectives

- Overarching Mission: Develop a stable SEI layer for silicon anodes to enable the use of intermetallic anodes for lithium-ion batteries.
    - Critical Questions:
        - What are the properties of the lithiated silicon electrolyte interface?
        - What is the silicon SEI actually made of and what reactions are contributing to it?
        - How fast does the silicon SEI grow?
        - Does it stop growing?
        - Is it soluble?
        - Can it be stabilized?

- After we solve these critical questions, we need to understand how the following variables affect the SEI layer:
    - Voltage
    - Temperature
    - Electrolyte and additives
    - Cathode transition metals
    - % lithiation
- FY17 Objectives
    - Quarter 1 Milestone:
        - Established protocols for sample synthesis, preparation, characterization, and analysis to ensure compatibility of experimental data from all consortium members. Protocols will be posted on the shared cloud drive and provided to the ANL lead silicon electrode deep-dive.
    - Quarter 2 Milestone:
        - Completed round-robin sample analysis to ensure protocols established in Quarter 1 are functional. Results based upon less than 5% variance in electrochemical performance between laboratories to ensure equivalent starting materials and preparations.
    - Quarter 3 Milestone:
        - Define the relationship between the surface of the lithiated silicon and the nature of the SEI by demonstrating that the chemical or physical properties are or are not affected by the nature of the silicon surface treatment—specifically, by contamination, oxide content, dopant level, or degree of crystallinity.
    - Quarter 4 Milestone:
        - Determine if the nature of the silicon (purity level, doping, and/or structure) have an effect on formation and evolution of the SEI. This will determined by observing measurable chemical and physical changes in the SEI layer between substrates.

Approach

The SEISta team works to ensure that protocols for sample preparation, experimental design and implementation, as well as data reporting are consistent across the whole team. Each laboratory is working toward the same set of quarterly milestones using its own specific talents and capabilities in a concerted effort with the other team members. This joint focus results in multiple researchers interacting to produce and analyze data to ensure that individual experimental variations are not leading to erroneous results. Critical to the success of this effort is the use of standard samples that can be shared by all parties. In the first FY, a round-robin sample test was established to ensure that data could be duplicated at the different laboratories by different researchers. In addition to weekly whole-team video presentations, we have held on-site face-to-face meetings each quarter for all team members, and other interested parties, to brainstorm and sort out issues with existing experiments and jointly develop new experimental plans.

Results

- *In-situ* neutron reflectometry was used to identify and follow the thickness and composition of the SEI layer with fluoroethylene carbonate (FEC) additives.
- Developed tip-enhanced Raman spectroscopy method to characterize the SEI.

- Completed round-robin analysis of vapor-deposited thin films and identified key areas to address.
- Explored the gassing of silicon-based materials and the influence of the surface chemistry of these materials on the reactivity.
- Completed an investigation of the passivating behavior of tin-based model electrodes. The effect of oxygen species and electrolyte formulation has been studied. The reductive decomposition reaction of ethylene carbonate:diethyl carbonate (EC:DEC)-based electrolytes has been revealed, demonstrating that Li2CO3 is the primary product of EC decomposition.
- Determined the role of a dense thermal oxide layer on Si. Relative to the native oxide on the Si surface, the thermal oxide reduces side reactions with the electrolyte and inhibits cracking; but it also impedes lithiation of the underlying Si. There was no evidence of a conversion reaction of the oxide or formation of a known bulk silicate during initial stages of cycling. Thermal oxide coatings to Si anodes could be beneficial with optimization of thickness and morphology of the Si.
- Thin films of Li2O, Li2CO3, and LiF were applied to Si wafer model electrodes as preliminary steps to the development/study of the concept of “artificial SEIs” on the electrochemical properties of Si anodes. The preliminary results were similar to those reported above for the thermal oxide. More work is needed to explore this approach further.
- Conducted comprehensive Fourier transform infrared (FTIR) spectroscopy characterization of solid-phase material to elucidate chemical reactivity of different forms of Si, SiO2, and LixSiOy with electrolyte (EC/LiPF6 and Gen2).
- Determined key process parameter (W/cm3) to tune plasma-synthesized Si nanoparticle phase: a-Si → a-Si:H → c-Si.
- Completed design and testing of scaled-up load-lock collection system for plasma-prepared Si nanoparticles.
- Successfully devised a high-yield synthesis of Li7Si3, an intermediate product in the lithiated silicon system ("Li2.3Si"). About 4 g of product were characterized and passed onto the team via round-robin or reaction studies.
- Showed that even in 3 ppm or less of air or water, the surface of the material will self-discharge to produce Li12Si7 ("Li1.7Si", by X-ray diffraction (XRD), 29Si nuclear magnetic resonance (NMR)) and Li2O/LiOH (via Raman, FTIR).
- Reactivity studies followed by 29Si or 7Li NMR showed significant rapid reactivity of lithiated silicon with the conventional binder PVDF, and limited reactivity with ANL CAMP standard-LiPAA.
- Developed a method, using XRD and NMR, to directly probe and study the inherent reactivity of lithium silicides vs. typical Li-ion battery components.
- Purchased, installed, and tested systems for air-free transfer of samples between Ar glove box, focused-ion-beam mill, Fishione Nanomill, and FEI F20 UT FEG STEM.
- Began electron microscopy analysis of selected Si anode samples.
- Developed scanning spreading resistance microscopy (SSRM), an atomic force microscopy (AFM)-based nano-electrical probe, to map in nm resolutions the three-dimensional electronic resistance of SEI. This was done laterally by the sharp probe and vertically by milling away SEI materials layer by layer.

- The electronic resistance of the SEI was found to be large (up to 10^9 Ohm-cm) but finite, and relatively uniform within one order of magnitude in the lateral direction; but it decreases sharply along the vertical direction from the SEI surface toward the Si.
- The electronic resistance and thickness of the SEI was observed to depend on lithiation/delithiation parameters, most sensitively on the electrolyte.
- Established protocol for sample preparation and testing.
    - Completed round robin on Cu samples
    - Initiated round robin on Si samples
- Established deposition conditions for controlled Li:Si ratio silicates.
    - Deposited Li:Si 0 to over 8
    - Deposited test samples
    - Characterized film evolution on model SEIs in lithiated and nonlithiated states
- Test cells built, tested, and distributed to teams.

Summary of Milestones for FY17

Quarter 1 Milestone
Establish protocols for sample synthesis, preparation, characterization, and analysis to ensure compatibility of experimental data from all consortium members. Protocols will be posted on the shared cloud drive and provided to the ANL lead silicon electrode deep-dive.

This milestone was 100% completed. The project required the development of multiple procedures for shipping, testing, and analysis of samples. All materials were purchased from single sources and distributed by the purchasing laboratory, and then packaged and shipped to partner organizations. SNL purchased copper foil, NREL purchased silicon wafers and electrolytes, and ORNL purchased lithium foil.

Quarter 2 Milestone
Complete round-robin sample analysis to ensure protocols established in Quarter 1 are functional. Results based on less than 5% variance in electrochemical performance between laboratories to ensure equivalent starting materials and preparations. As new samples and partners are added, these protocols need to be updated and added to.

This milestone is 100% complete, although it was delayed from the initial Q2 date until Q4 and we did not achieve the 5% threshold, with a 7% spread in the data being achieved. This difference was due to the unanticipated difficulty in selecting samples and getting delivery, as well as the need for unified testing equipment. The analysis of the data, which was based on thin-film samples all prepared at ORNL is described below, but can be summarized in the following points. 1) Sample preparation adds some variability to the data, but storage time has a more significant impact on the data. 2) Storage and treatment of the samples result in variances that need to be addressed in the next year. 3) Potential issues with cell design have to be addressed moving into FY18 because each laboratory used its own cell configuration (punch size and alignment). 4) The potential for damage to the sample needs to be addressed in future work. Use of the standard cell, which is described below, will help address many of these issues.

Quarter 3 Milestone
Define the relationship between the surface of the lithiated silicon and the nature of the SEI by demonstrating that the chemical or physical properties are or are not affected by the nature of the silicon surface treatment—specifically, by contamination, oxide content, dopant level, or degree of crystallinity.

This milestone is 100% complete. The nature of the silicon has a dramatic effect on the chemical reactivity of the interface even before electrochemistry. This is described below in the different chemical reactivity studies.

Quarter 4 Milestone
Determine if the nature of the silicon (purity level, doping, and/or structure) has an effect on formation and evolution of the SEI. This will be determined by observing measurable chemical and physical changes in the SEI layer between substrates.

This milestone is 100% complete. The nature of the silicon has a dramatic effect on the formation of the SEI. Clear differences between the commercially prepared wafer samples are apparent in the electrochemistry, as well as differences between the sputtered samples and the wafers.

Round-robin analysis of vapor-deposited thin films to identified key areas to address in integrated laboratory experimental work.

As part of the SEISta program, we executed a round-robin evaluation of electrode materials with the goal of identifying reproducibility between labs and reproducibility of producing samples. ORNL prepared 18 sets of identical samples that were distributed to the partner labs. These films consisted of amorphous silicon deposited on battery-grade copper foil (SNL). The films were deposited at an applied power of 90 W at a distance of 7.0 cm from substrate to target. Samples were deposited at 7.0 mtorr of argon pressure, which is the same pressure used to deposit the sample used for the Neutron Reflectrometry (NR) studies. The thickness of the films was determined to be 55 ± 2 nm based on quartz-crystal microbalance and neutron reflectometry measurements. The density of the films was estimated to be 2.1 g/cc from the NR data. The initial and final samples were kept at ORNL; the remaining samples were distributed to the team members to try to identify changes in materials chemistry or surfaces as a function of target aging.

The films were punched into electrodes with diameters from 10 to 15 nm at the various labs and assembled into half-cell-type coin cells using a standard 18-mm Celgard 2325 separator and 200 µL electrolyte/cm2 of electrode. This procedure was provided on the Box site. The electrolyte was purchased in bulk and distributed to each of the team members. There were two base electrolytes: 1.2 M LiPF and 1.0 M LiTFSI in 3:7 wt% ethylene carbonate: ethyl methyl carbonate. Cells were cycled at a rate of C/10 in a constant current/constant voltage-type measurement. The procedure was provided to all the team members via the Box site. The cycled data were aggregated at ORNL.

Figure II-118 shows the data collected for the $LiPF_6$-based electrolyte. From these data, several unique features are observed. First, there appears to be a wide discrepancy in the capacity of the cells measured at each laboratory. Second, there is evidence for an electrochemical transition or reaction at 0.5 V (vs. Li/Li+), which is likely the reduction of EC on the electrode surface.

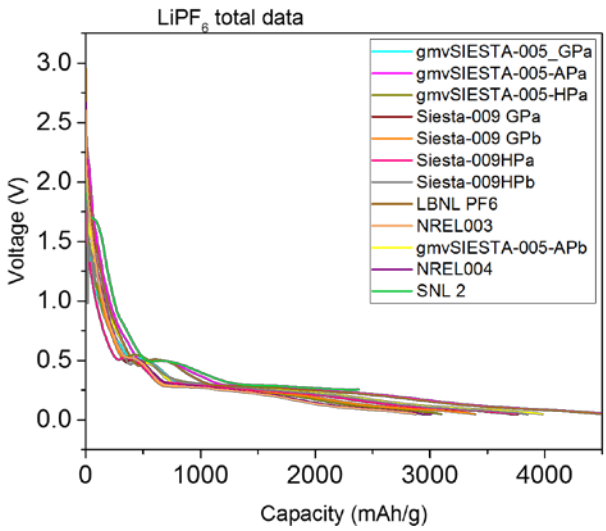

Figure II-118. Raw capacity versus voltage data for cells cycled in the LiPF6 electrolyte.

This 0.5 V transition appeared constant for all the samples evaluated in this study. Given this consistency, all the data were normalized to a point below this transition (0.45 V vs. Li/Li+). This normalized data are shown in Figure II-119. A magnified view of the data above 0.45 V and below 0.45 V is shown in Figure II-120 and Figure II-121, respectively. The data show that most of the differences observed in capacities (Figure II-118) are due to reactions that are occurring at potentials above 0.5 V. Indeed, the average capacity for the electrodes is within 417 mAh/g after shifting to 0.45 V. This is within 7% of the theoretical capacity of the electrodes and close to the 3.2% error associated with the uncertainty in silicon thickness (± 2 nm). The key issue now is identifying the reactions that are occurring above 0.5 V and why they vary between all the electrodes. Potential variables include aging of the sample, storage conditions (air or argon), and sample-handling procedures.

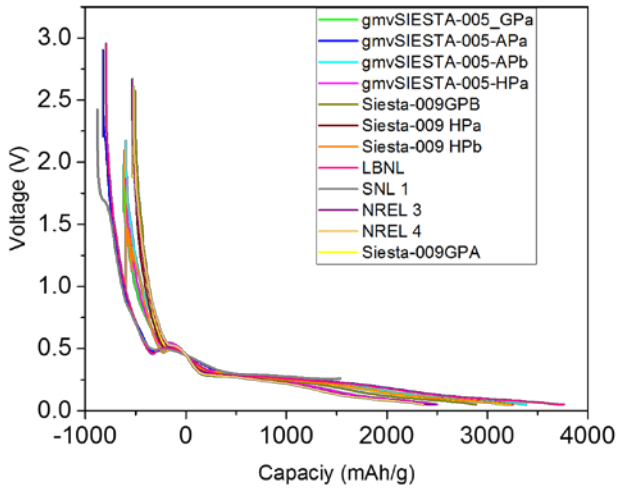

Figure II-119. Capacity versus voltage data for cells cycled in the LiPF6 electrolyte shifted to 0.45 V.

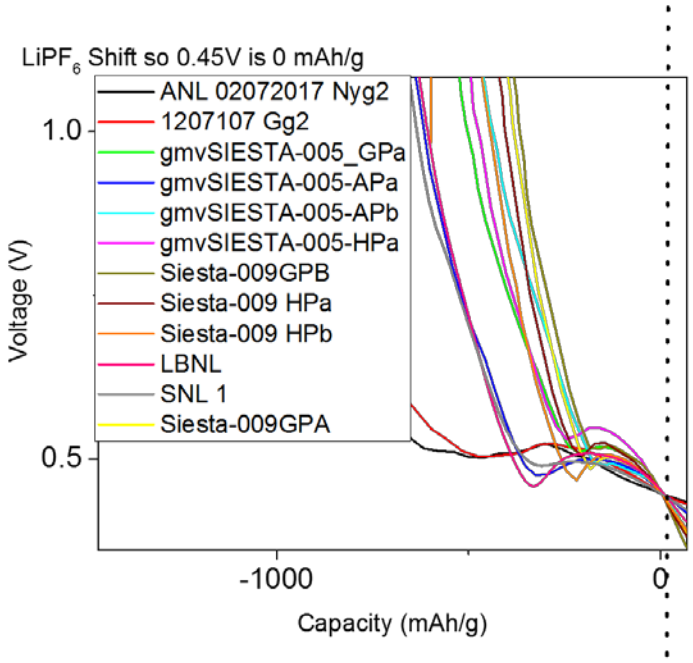

Figure II-120. Magnified view of capacity versus voltage data for cells cycled in the LiPF6 electrolyte above 0.45 V.

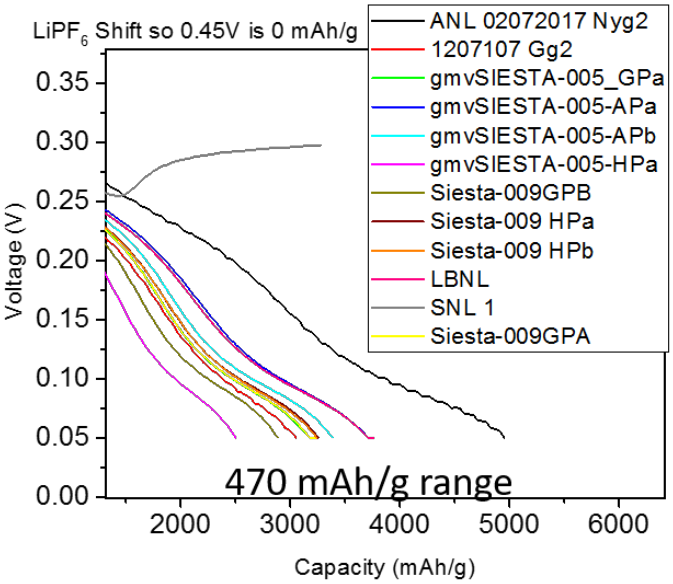

Figure II-121. Magnified view of capacity versus voltage data for cells cycled in the LiPF6 electrolyte below 0.45 V.

Identical electrodes were cycled in an electrolyte with LiTFSI as a salt. The aggregated data is shown in Figure II-122. Again there were large differences in observed capacities along with a plateau at 0.5 V vs. Li/Li+. The consistency of this voltage plateau would confirm the reaction is coming from the reduction of the solvent since it is the same as the LiPF6 electrolyte. Again the data were shifted so that zero capacity is located at 0.45 V vs. Li/Li+. Figure II-123 and Figure II-124 show magnified views of this shifted data above and below 0.45 V respectively. Again the largest variation in capacity is due to the electrochemical reactions that occur above 0.5 V. The capacities below 0.45 V are within 1000 mAh/g, which is a 22% error. This is far

larger than the LiPF6 data but points to a different reaction mechanism with LiTFSI versus LiPF6 likely in the SEI formation. Interestingly the samples with the highest capacities above 0.5 V also had the largest capacities below 0.45 V. This points to a reaction mechanism where whatever changes the surface reactions continues to mediate the reactivity during lithiation. Understanding this correlation will enable a more detailed understanding of the SEI formation mechanism and the role of the salt.

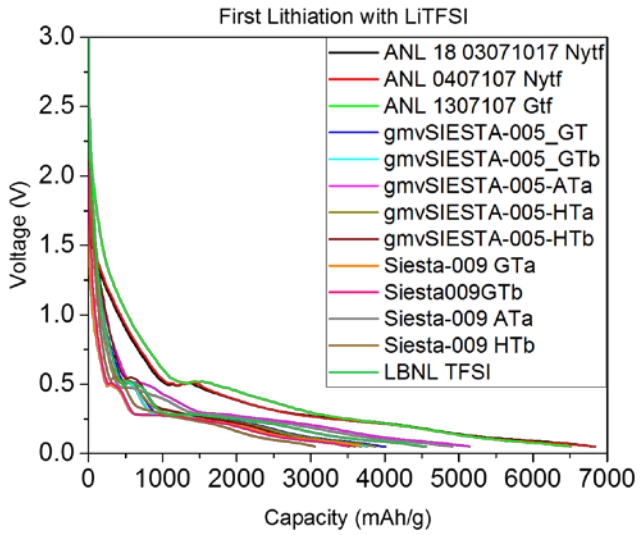

Figure II-122. Raw capacity versus voltage data for cells cycled in the LiTFSI electrolyte.

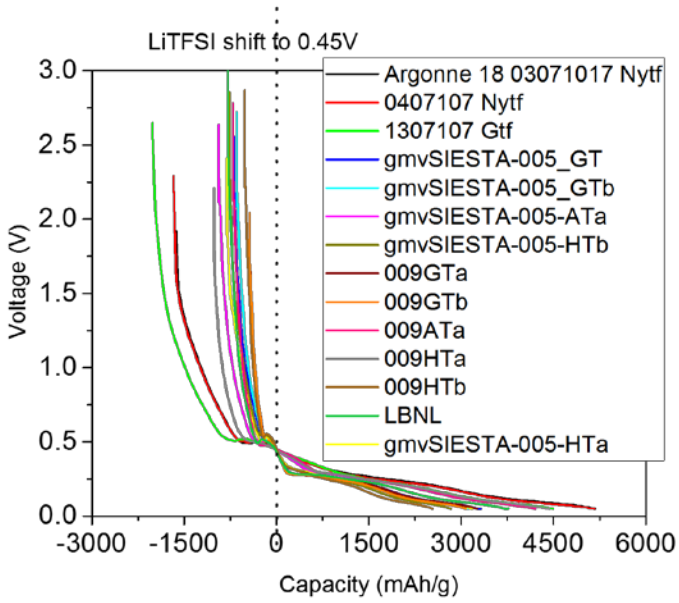

Figure II-123. Capacity versus voltage data for cells cycled in the LiTFSI electrolyte shifted to 0.45 V.

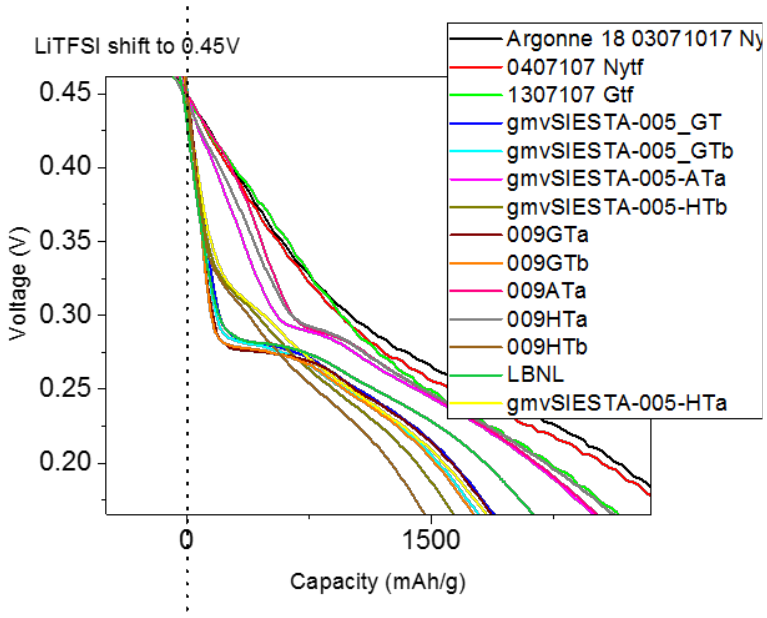

Figure II-124. Magnified view of capacity versus voltage data for cells cycled in the LiTFSI electrolyte below 0.45 V.

To understand the origin of this capacity above 0.5 V, we performed XPS measurements on uncycled Si electrodes stored in air and in an argon-filled glove box. The data from these measurements are presented in Figure II-125, which shows a clear change in the surface Si-O with storage condition. This means that the surface is becoming progressively more oxidized with time in air. This surface oxide may be the cause of the capacity differences. Furthermore, these data indicate that time is a critical variable in the analysis of silicon electrodes. Future studies will include time-dependent data and records to identify these effects.

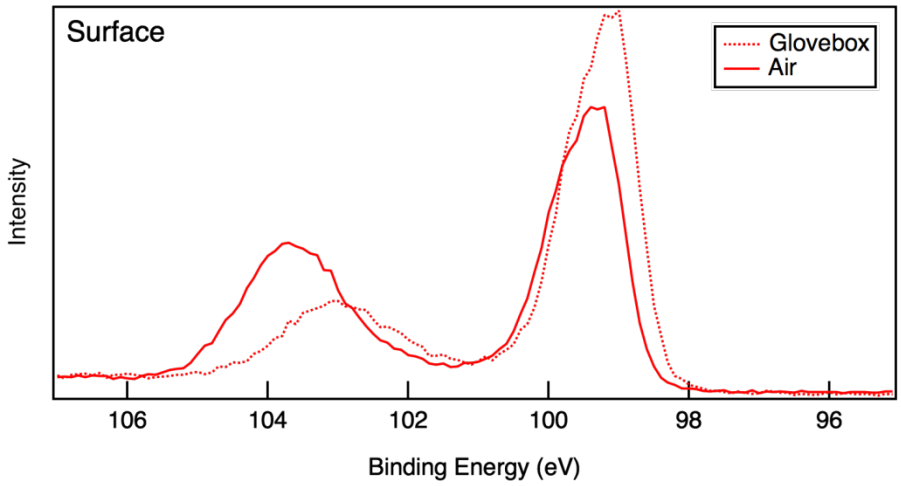

Figure II-125. XPS data collected for an uncycled silicon electrode aged in a glove box and in air for 3 weeks.

Time-of-flight SIMS (TOF-SIMS) depth-profiling measurements were performed on sputter-deposited silicon on copper-foil films prepared at both NREL and ORNL. Some of the profile data sets are shown in Figure II-126. In addition to observed variations in oxygen and fluorine content in the silicon films between the sites (not shown), the figure illustrates that transition-metal impurities were noted in the silicon films deposited at both sites. Because these transition metals are all constituents of stainless steel, it is believed these impurities are coming from the stainless-steel ring that holds the silicon sputter target in place. Although the

SIMS data sets are not quantified, the concentrations of these species likely fall in the 1×10^16–1×10^19 atoms/cm3 range. It remains unclear whether impurities at those levels affect electrochemical performance to a significant degree.

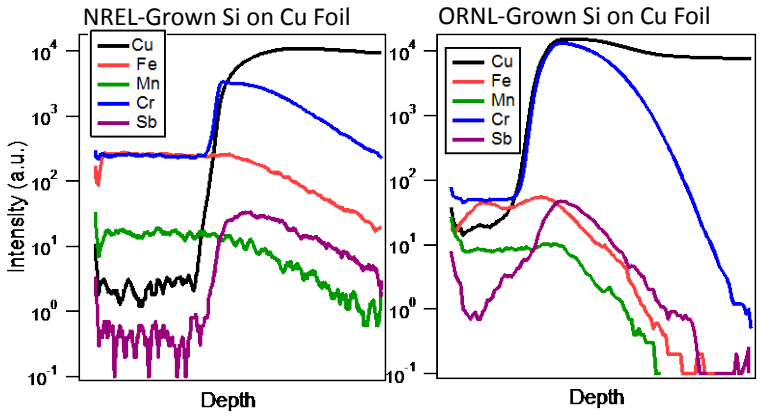

Figure II-126. TOF-SIMS depth profiles of silicon films on copper foil grown at both NREL (left) and ORNL (right). Only composition profile for the transition-metal impurities and the copper substrate are shown.

To assist in understanding the variability in the round-robin tests of sputtered Si films on Cu-foil substrates, in late FY17 we performed initial measurements on samples stored in glove boxes at each site. The aim is to assess whether the variability observed in electrochemical performance is due to surface contamination caused by various glove box ambients, or perhaps due to variability in implementation of the testing protocol.

We have performed TOF-SIMS measurements on samples from two sites so far, NREL and ORNL. Preliminary TOF-SIMS and XPS analyses of the ORNL samples suggest there are some changes to the samples upon long-term storage in the ORNL glove box. We observed lower surface coverages of fluorine and chlorine for the three ORNL samples, as shown in Figure II-127. In addition, we noted the presence of a high-intensity peak at mass 147, which we attribute to pump oil (C8H3O3) on the sample that was in the glove box for 3 months. This peak was clearly not present in the sample exposed to air for 2 weeks, or in the sample that was in the glove box for 2 weeks. Thus, we tentatively conclude that introduction of large amounts of surface contamination from the glove box ambient is not a major source of error, at least for samples in the box for short times at the ORNL location. Analysis of samples from other sites is expected in early FY18.

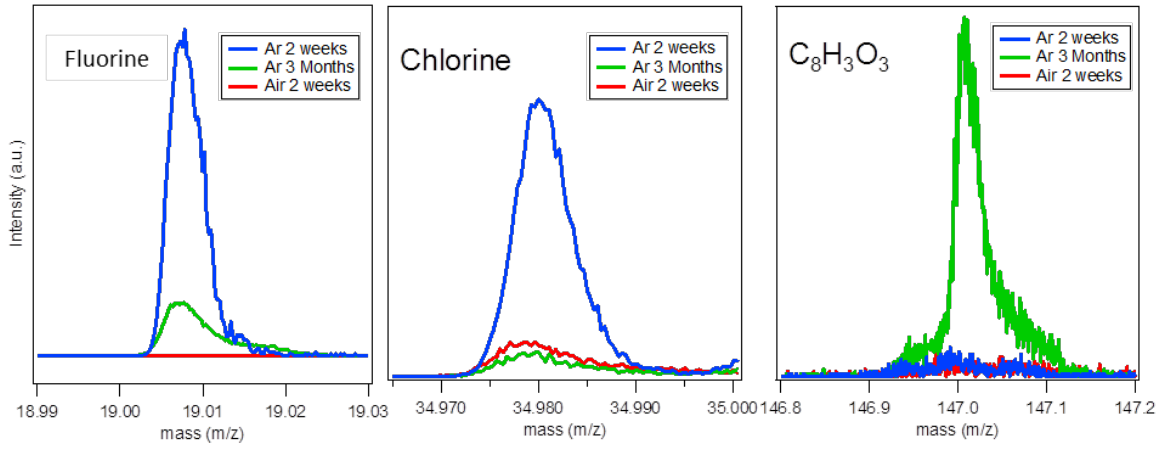

Figure II-127. TOF-SIMS surface spectra of the ORNL films, showing the changes to the sample surface upon long-term exposure in the ORNL glove box, as well as shorter-term exposure to air.

We have concluded that the variation in sample handling and cell assembly may have contributed to the variance in the data; therefore, we implemented a new cell-design project to ensure that this variability was minimized.

In light of the variability of the thin-film samples, a set of wafer samples was selected to duplicate the round robin, and this test is currently beginning for FY18. SEISta initial characterization of the wafer samples was completed in FY17, and the analysis and second round robin for these samples are scheduled for Q1 FY18. In FY17, NREL TOF-SIMS capabilities supported the SEISta Si wafer round-robin study with surface characterization and depth-profiling measurements of the prepared Si wafer surface prior to cycling. The goal of these and other surface-characterization measurements was to document surface cleanliness and correlate with subsequent electrochemical properties and cycling performance. In these studies (summarized in Figure II-128 through Figure II-130), we noted from principal-component statistical analysis of the spectra that samples subjected to RCA cleaning after the native-oxide formation process had much less surface contamination in the form of carbon-containing species, sodium, fluorine, and chlorine.

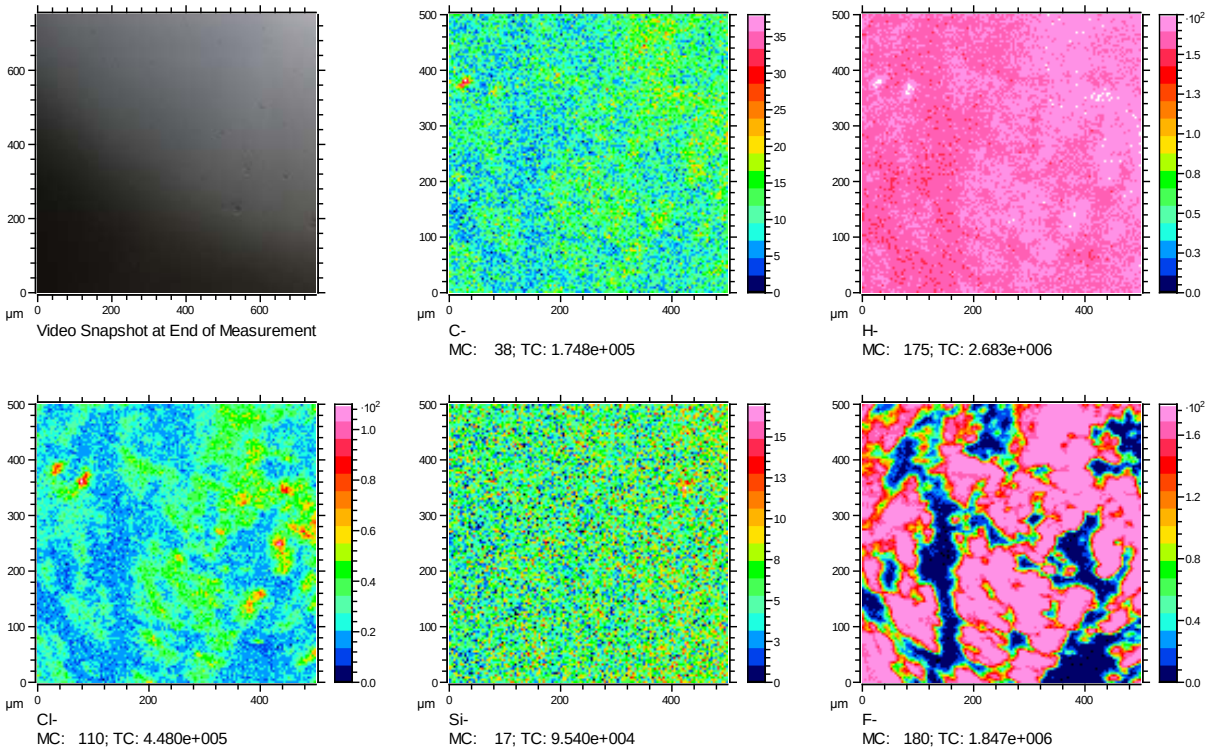

Figure II-128. Optical and negative-polarity TOF-SIMS images from as-received (uncleaned) SEISta round-robin Si(001) wafer sample with native oxide. Mass channel labels are to the lower left of each image. The measurements reveal large amounts of fluorine and chlorine contamination.

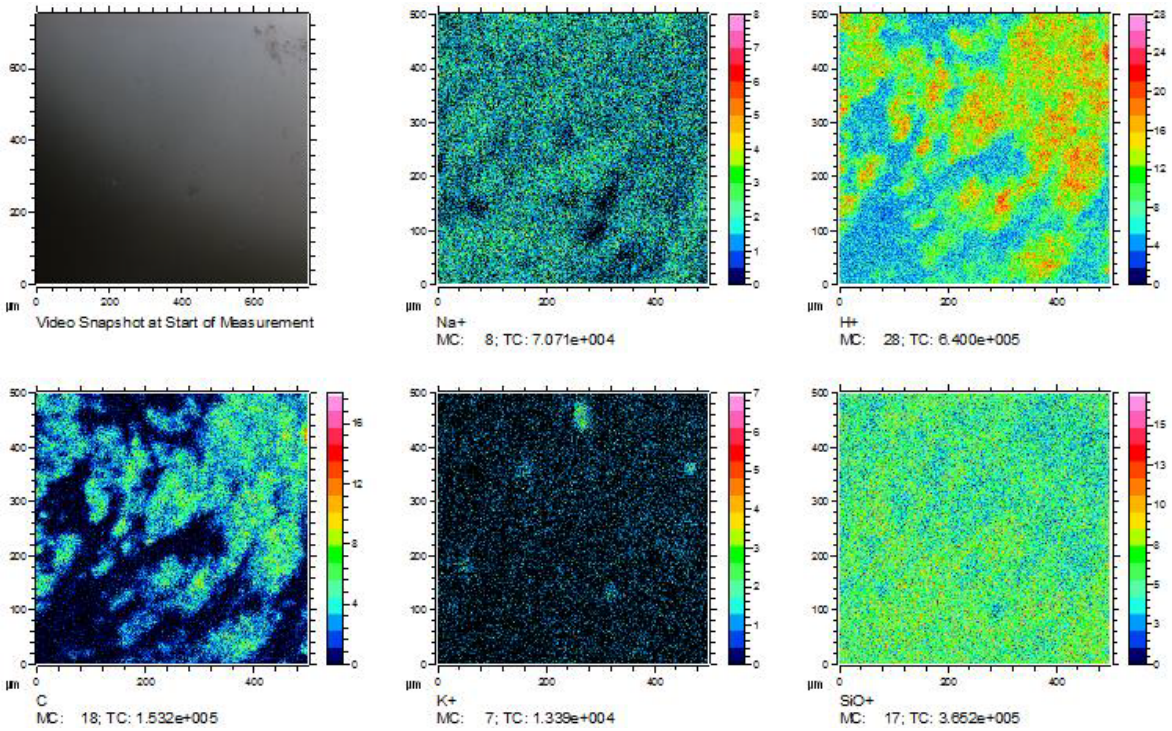

Figure II-129. Optical and positive-polarity TOF-SIMS images from as-received (uncleaned) SEISta round-robin Si(001) wafer with a native oxide. Mass channel labels are to the lower left of each image. The measurements reveal a large amount of hydrocarbon contamination.

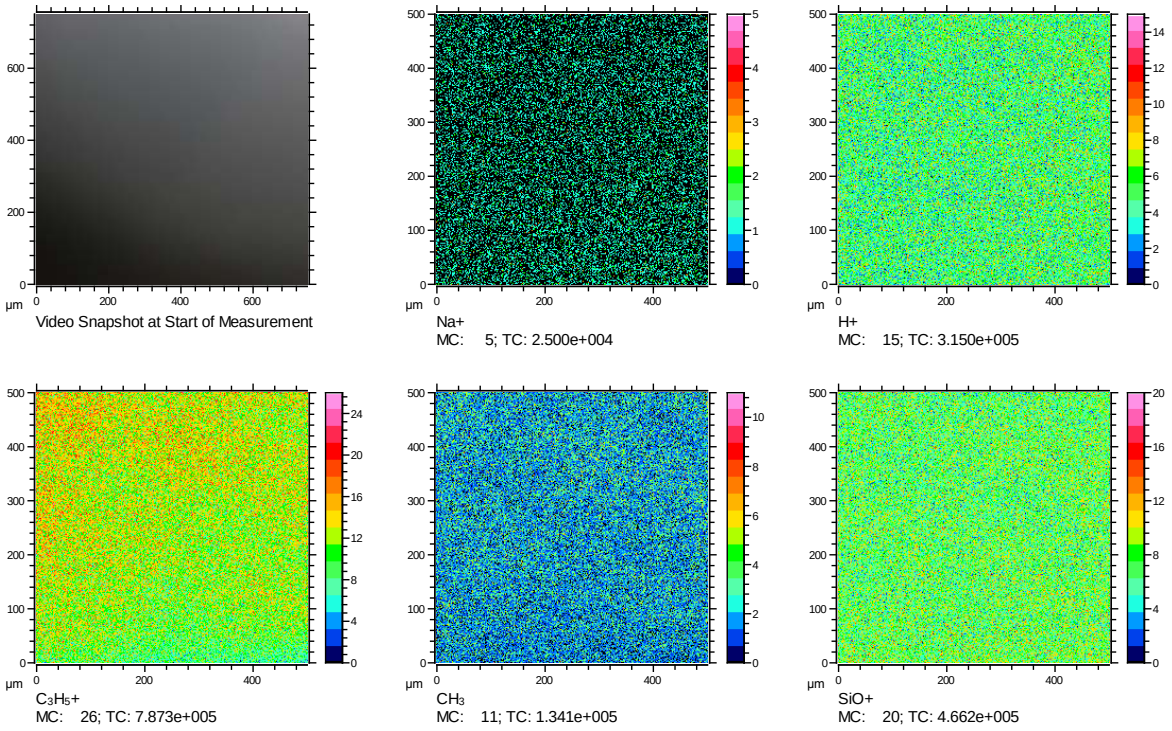

Figure II-130. Optical and positive-polarity TOF-SIMS images from RCA-cleaned SEISta round-robin Si(001) wafer with a native oxide. Mass channel labels are to the lower left of each image. Essentially no hydrocarbon contamination is observed.

TOF-SIMS depth profiling and 3-D tomography measurements were also completed on cycled Si-wafer samples to support the Kelvin probe force microscopy (KPFM) and scanning spreading resistance microscopy (SSRM) experiments also performed at NREL. Surface spectra, standard depth profiling, and 3-D tomography (100-nm lateral resolution) measurements were completed on half-cycle (lithiated) and full-cycle (delithiated) samples. The TOF-SIMS depth profile results support the very interesting observations of SSRM milling experiments that the SEI is substantially thicker for the half-cycle specimen than the full-cycle specimen. The data presented in Figure II-131 show profiles of two species associated with the SEI layer for the two samples taken under identical analysis conditions. The TOF-SIMS sputter-crater depths will be verified by a second set of AFM measurements so that precise determinations can be made for overall SEI thicknesses in the two cases.

TOF-SIMS 3-D tomography at 100-nm lateral resolution can reveal the chemistry and microstructure of the SEI, and representative results for the full-cycle SSRM sample are shown below (Figure II-132 and Figure II-133) for the lithium and hydrocarbon distributions, respectively, within the SEI, which appear to accumulate within the observed cracked areas.

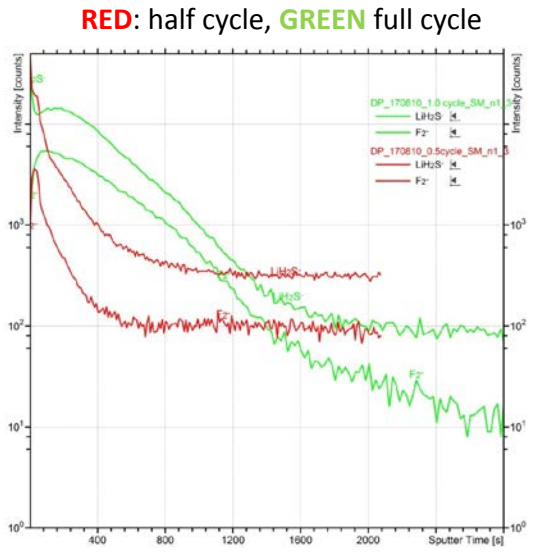

Figure II-131. TOF-SIMS depth profiles of two Si-wafer samples that were also analyzed with SSRM. The red profile is the half-cycle sample, and the green is the full-cycle sample. Consistent with the KPFM data, it appears that the SEI is much thicker for the delithiated sample—an interesting result.

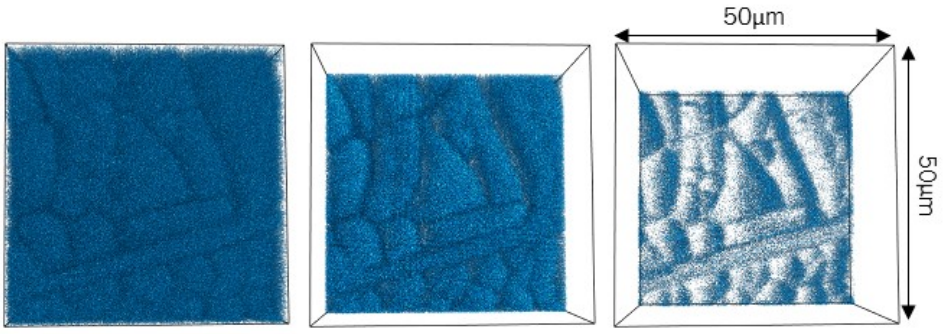

Figure II-132. TOF-SIMS 3-D reconstruction of the lithium distribution in the SEI of the full-cycle KPFM specimen (50 µm x 50 µm area, depth currently unknown). The image at left shows the full dataset; image in the middle shows the data from about halfway through the SEI; image at right shows the lithium distribution at transition between the SEI and the silicon.

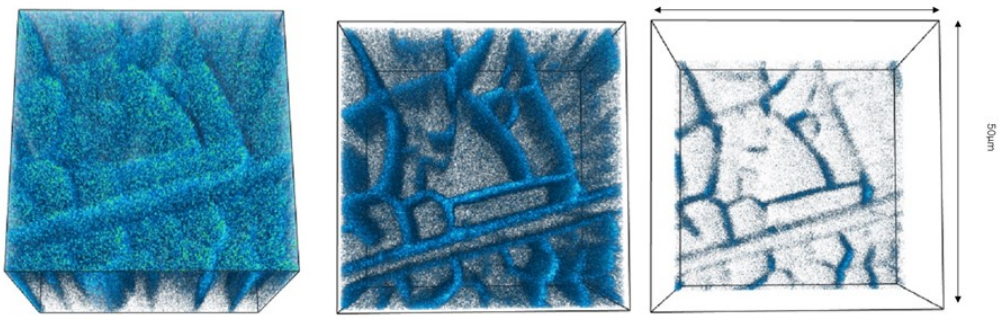

Figure II-133. TOF-SIMS 3-D reconstruction of the C2H- distribution in the SEI of the full-cycle SSRM specimen (50 µm x 50 µm area, depth currently unknown). The image at left shows the full dataset; image in the middle shows the data from about halfway through the SEI; image at right shows the lithium distribution at transition between the SEI and the silicon.

To ensure reliability of data collected with these new wafer samples, the test cell will be used by all partners in future studies. We have begun the implementation of a standardized three-electrode cell that can accommodate the future work in thin films, wafers, and even composite electrodes.

Design of three-electrode electrochemical cell

To diagnose and distinguish the individual electrode performance, it is necessary to use three-electrode cells. The three-electrode cell enables the separate monitoring charge and discharge potentials at the anode and cathode. There are many existing fixtures, including customized and commercially available products that can perform the three-electrode electrochemical characterization. However, there is large cell-to-cell variation in the cells without a good control of the electrode size, distance between electrodes, amount of electrolyte, and position of each electrode. It is extremely important to standardize the cells to obtain reliable and reproducible electrochemical data. More importantly, the SEISTa project is multi-lab research consortium; the research has been performed by more than 20 PIs across five national labs. Reliable and reproducible data are required to conduct the multi-lab research and are requested for achieving an accurate fundamental understanding of electrochemical properties. Therefore, in this study, a three-electrode electrochemical cell was designed, assembled, and used by team members under the SEISTa project.

The electrochemical cell with three electrodes is shown in Figure II-134 and Figure II-135. The counter electrode and the reference electrode were located in the cell cap and locked by a retainer plate against the working electrode located at the bottom. A locate pin was used to help align the electrodes. Stainless steel (316) was used to collect current and was connected to the banana jack for outside wiring. The stainless-steel current collector was pressed to the working electrode, herein, a silicon wafer. A torque screwdriver was used to apply the pressure on the current collector to enhance the sufficient electrical transfer from the current collector to the silicon wafer samples. The three electrodes are connected via electro wiring to a potentiostat that applies voltage between the working electrode and the reference electrode while measuring the current flow between the working electrode and the counter electrode.

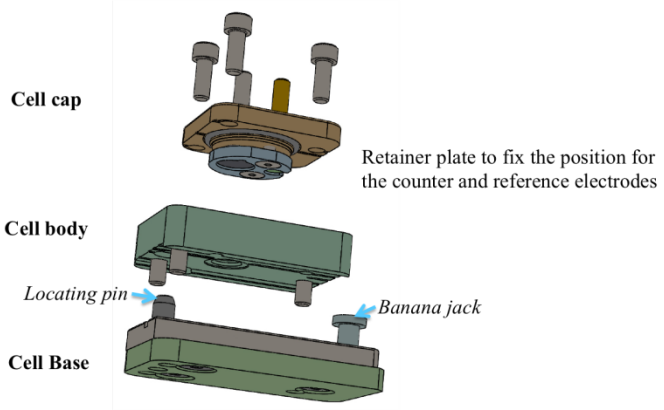

Figure II-134. Schematic sketch of the electrochemical cell: 1) the reference electrode and the counter electrode located in the cell cap (top); 2) cell body (middle); and 3) cell base with the working electrode (bottom).

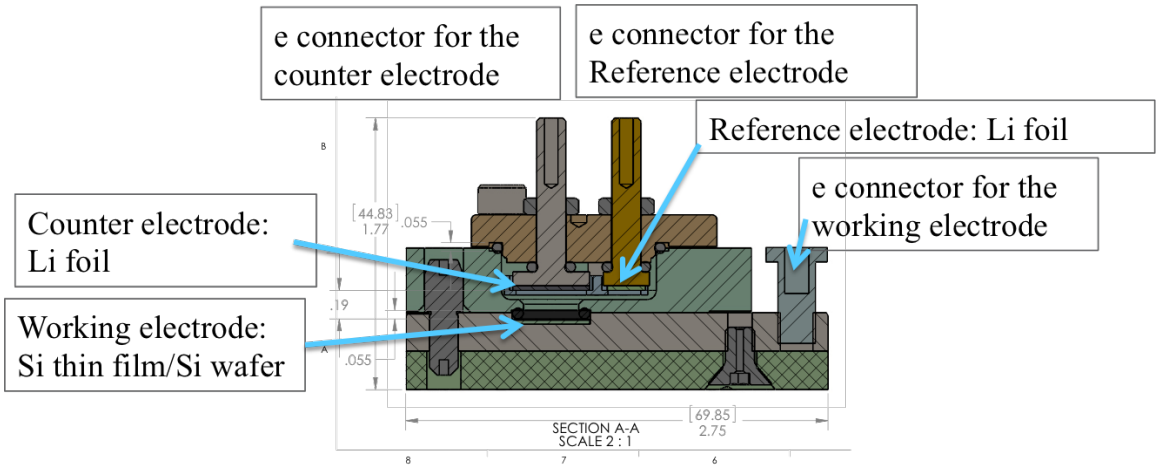

Figure II-135. Cross-sectional sketch of the designed electrochemical cell.

A silicon wafer was selected as the model sample in this project. All of the silicon wafer samples were cut and cleaned by the NREL team, using the standard protocol (described in a previous report). Due to the low conductivity in silicon samples, the pressure between the silicon wafer samples and the stainless-steel current collector is extremely important. As indicated in Figure II-136, the pressure applied on the bottom of the stainless-steel current collector can affect the electrochemical properties. With low pressure (<3 lbs-in), the working electrode experiences a high overpotential, leading to low electrochemical activity with much lower capacity. With high pressure (>5 lbs-in), the brittle silicon wafer samples are easily broken, which generally causes a very noisy electrochemical response, and finally, abnormal electrochemical behavior. When appropriate pressure is applied, reproducible electrochemical behavior can be obtained.

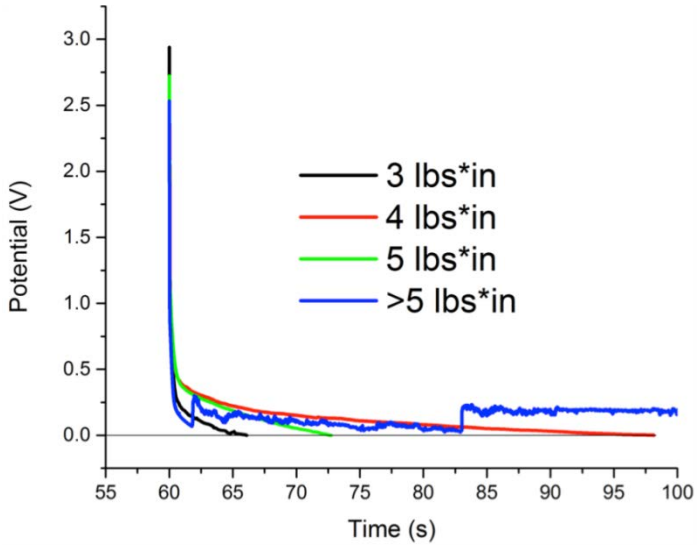

Figure II-136. The voltage profile during lithiation of silicon wafer samples. Increasing pressure was applied on the stainless-steel current collector to ensure sufficient electrical conductivity.

Due to the high reactivity of the organic carbonate electrolyte, any side reactions between the cell components and the electrolyte may cause unexpected electrochemical responses. Therefore, before assembly, it is highly recommended to check all of the components—including the screws, cell body, current collectors, and O-rings—to make sure all components are untouched without color changes, clean and dry, and in their original shape. Here, we have summarized the procedure for cell assembly.

1. Place the stainless-steel spacer directly on the cell base, and put the silicon wafer on the top of the stainless-steel spacer; finally, put the O-ring on the top of the silicon wafer.
2. Put the cell body on the top of the cell base. Use the locate pin to make sure the O-ring is in place, and use the grooves located on the cell body to hold the O-ring.
3. Tighten the screw on the cell body to seal the silicon wafer.
4. Use the torque screwdriver (5716A52, slip-release adjustable torque-limiting screwdriver with bit set) to apply pressure on the screw back of the silicon wafer. Do not apply too much pressure. The torque of 4 lb-in on 18-8SS screw (8/36NF, ¾" long) can offer good sealing and sufficient contact.
5. Add the electrolyte. Now we add 0.7 mL of electrolyte for the vertical position. We need a little more electrolyte for the other position (testing is going on).
6. Place the lithium metal counter electrode and the lithium reference electrode on the current collectors, which are located on the cell cap. Note that we did not use the retainer plate for now due to the corrosion found on the screws for the retainer plate.
7. Once the cell cap was ready, put the cell cap into the cell body and tighten the screws on the cell cap.
8. Connect the cell with the banana plugs.
9. At this moment, to reduce the inferior effects of the poor wetting/bubbles, we use the vertical position to run the cell.
10. Rest the cell for 4 hours, and use 10 μA to run the lithiation for 6 hours and delithiation for 6 hours.

The three-electrode cell has been used to demonstrate the electrochemical behavior of our baseline silicon samples, as shown in Figure II-137. The cell resistances, particularly generated from the contact between the backside of silicon wafer samples and the current collector, result in the ohm drop at the beginning of lithation. In addition to the silicon wafer samples with the native oxide, we plan to investigate the thermal oxide-coated samples. To mitigate the contact resistances, we are currently working with other team members to develop conductive glue and new procedures for enhanced electrical conductivity. In FY18, this cell will continue to be refined and used for both standardization of experiment, but also for spectroscopic measurements.

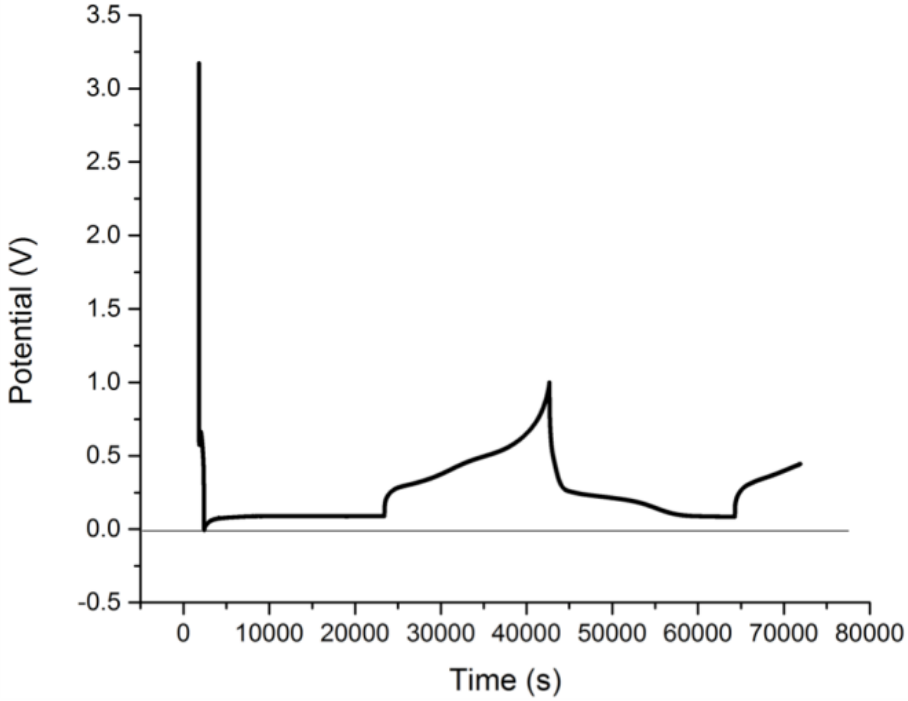

Figure II-137. The voltage profile of the baseline silicon wafer sample, during lithiation and delithiation. The current for both lithiation and delithiation is 10 μA. The reaction duration is limited to 2 hours for both lithiation and delithiation processes.

Methods to Facilitate Accurate Inter-Lab Comparisons of SEI Chemistry Based on XPS Peak Assignments

One the key methods employed in the round-robin studies to examine the nature and variation of the silicon thin-film samples was *situ* X-ray photoelectron spectroscopy (XPS). *Ex-situ* XPS analysis is frequently used to help identify chemical states and phases that are present within an SEI. The validity of these analyses depends critically on accurately measuring core-level binding energies (BEs) and correctly assigning peaks to particular chemical states. This task can be quite challenging, in part because the co-existence of multiple overlapping chemical states is a common situation in a complex SEI. For example, more than ten frequently encountered Li functionalities lie within a range of ~3 eV in the Li 1s core level. Further complicating accurate XPS chemical-state analysis is the fact that many materials relevant for battery applications are poor electronic conductors, and consequently, they suffer from electrostatic charging effects that artificially shift XPS core levels. To attempt to compensate for these effects, many researchers calibrate XPS BEs by shifting the lowest-observed carbon peak to 284.8 eV (or a similar value, e.g., 284.6 eV), indicative of C-C bonding. This approach often works well, but can lead to inaccuracies in reported core-level BE values if the amount of surface species characterized by C-C bonding is minimal and difficult to detect (a possibility when air-free transfers are employed to minimize effects on highly reactive battery materials), or if another lower-BE functionality is also present in the C 1s region (e.g., carbonate). A result of these complicating factors is that binding energies reported using C-C as a calibration, especially for battery materials, can be highly inaccurate. For example, the literature reported that BEs for a metallic Li vary over a range of nearly 7 eV.

To overcome these issues, we have developed an XPS analysis methodology that can reliably correct for lab-to-lab variability in XPS BE calibration procedures that are exacerbated by charging effects on electronically insulating materials. The approach developed relies on two basic guidelines:

- Each chemical phase should be characterized by a well-defined BE separation between individual elemental core levels associated with that phase. For example, if Li2O is thought be a component of the SEI, the BE difference between the O 1s and Li 1s peaks should be constant regardless of charging effects.

- Elemental ratios must be appropriately constrained during peak fitting. This means that if components of a specific spectrum are thought to arise from Li2O, then a 2:1 Li to O ratio of relative intensities should be observed/fit.

The inability to achieve adequate fits to a subset of XPS spectra while simultaneously applying appropriate elemental-ratio and BE separation constraints described above is generally a strong indication that one or more phases have not been correctly identified. Further, if during peak fitting only one of these two rules is found to be true, then other possibilities should be investigated. For example, possibly both Li2O2 and Li2O are present on the surface rather than just Li2O and it should be fit accordingly in both core levels. To demonstrate validity of the BE separation rule, a literature survey was completed for available XPS data sets and core-level BEs were plotted (Figure II-138) for inorganic SEI phases. Each of these plots demonstrates a strong linear (unity slope) correlation, as expected if the primary sources of BE errors are simple offsets caused by electrostatic charging. We speculate that outliers in the compiled data sets in Figure II-138 are likely incorrect peak assignments. To confirm some of the BE separation values—and, when possible, identify absolute Bes—specific functional groups were synthesized *in-situ* in the XPS chamber, preventing additional contamination that could cause inaccuracies in the measurements. In these experiments, it was also possible to use the Li 1s and valence-band maximum values from sputter-cleaned metallic Li foils as absolute BE calibrations. Additionally, measurements on thin overlayers (e.g., Li2O) on metallic Li are much less susceptible to charging phenomena. Data sets obtained in this manner were in good agreement with BE separations calculated from the linear regression of reported literature values (Figure II-139, and blue squares in Figure II-138).

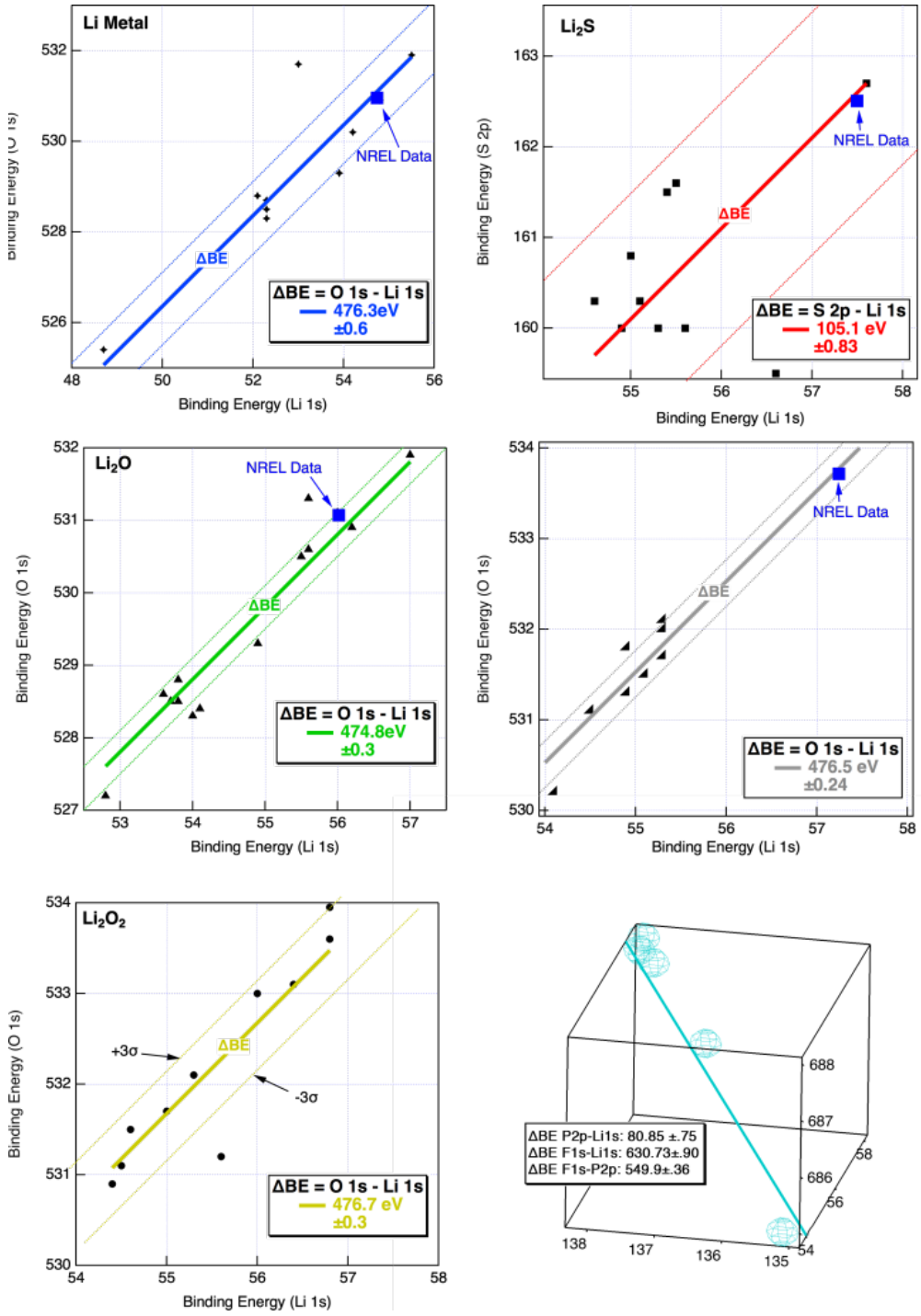

Figure II-138. Summary of binding-energy separations for common inorganic SEI constituents. Reported literature values for specific phases plotted vs. BEs of relevant core levels. Best-fit lines with unity slopes were used to determine average BE separations. In each case, values extracted from NREL datasets are shown as a blue square.

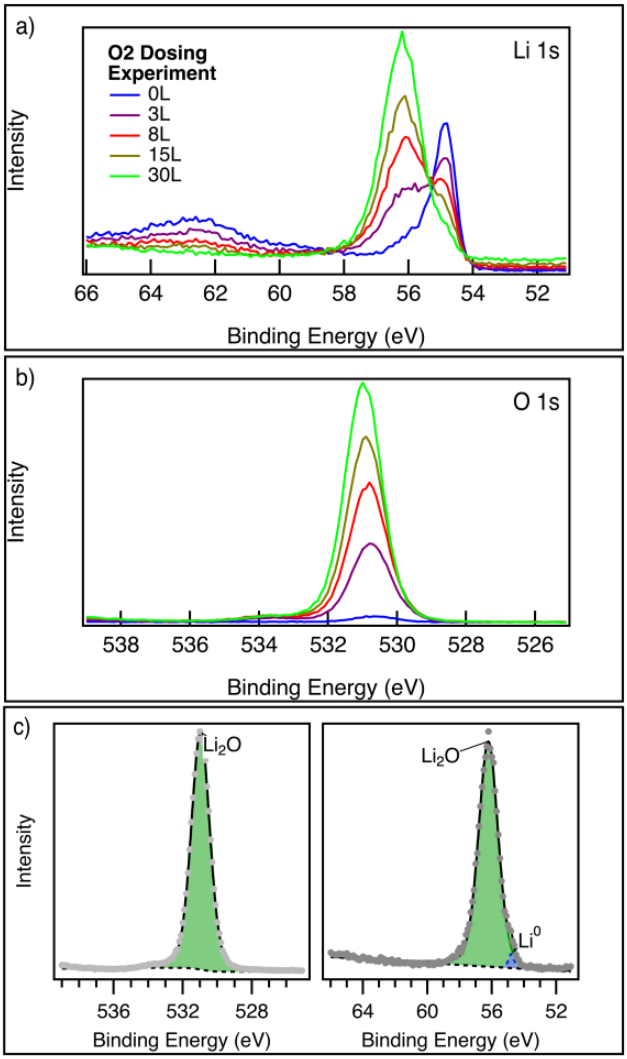

Figure II-139. Time-resolved XPS spectra showing *in-situ* oxygen exposure to form a pristine layer of Li2O on sputter-cleaned Li metal. BE separation for this phase was found to be 476.85 eV, in good agreement with the prior figure.

Using Computational Methods to Understand the Silicon-Electrolyte Interface

Within the bulk anode, we are interested in dopants or additives to Si that favorably impact its properties. Such properties include a more uniform discharge profile, higher voltage, volumetric expansion, and higher discharge rate. Literature reports show that conversion electrodes lose crystallinity as they charge and become amorphous. The anode will thus be modeled as an amorphous material. As a precursor to additives, amorphous Si with a native oxide layer will be benchmarked to ensure a fundamental understanding of the thermodynamics and kinetics of lithiation of the amorphous electrode.

To generate amorphous configurations, a random liquid configuration of the desired composition is generated using Packmol and the system is brought to equilibrium at high temperature. Snapshots of the resultant melt are then quenched using simulated annealing to generate amorphous phases that preserve the short-range order of the liquid state. Diffusivity calculations are performed in a similar manner using *ab initio* molecular dynamics (AIMD) to simulate elevated temperatures. Equilibrium structures give a glimpse of the thermodynamics of the system, while diffusion captures the kinetics of the system.

We perform classical molecular dynamics simulation (MD) to characterize the solvation structure, self-diffusion coefficient, and other macroscopic properties of the bulk electrolyte (1.2M LiPF6 in EC, EC/EMC, and EC/FEC). We used two sets of potentials: Optimized Potential for Liquid Simulation (OPLS) and General AMBER Force Field (GAFF). The calculated property results are compared with the experimental results to validate the potentials for MD simulation. With the calculated solvation structure, the 6-31++g* level quantum chemical calculation is conducted to get the IR spectrum result. The calculated and experiment-obtained IR spectra are compared to assign peaks with certain species so that solvation structure information can be deciphered accordingly.

Classical MD is also used to find possible reaction pathways to SEI formation. Si anode at the initial state before charging is modeled with a crystalline structure and an amorphous native silicon oxide layer on top of it. A constant-potential method (CPM) is used with charge fluctuation at the electrode surface to simulate experimental conditions. Harnessing CPM with classical MD, compared to time-consuming AIMD, enables us also to extend the time scale of simulation long enough to explore the dynamics of electrolyte molecules at the charge-fluctuating electrode surface.

Calculated equilibrium phase diagrams (Figure II-140) predict that lithiation of Si will generate lithium silicates (LixSi) that discharge to form Si. SiO2, however, under lithiation is thermodynamically predicted to eventually phase separate into LixSi and Li2O (in deep charge). Upon discharge, the LixSi can reform Si, while the Li2O will stay inactive, contributing to capacity loss. Voltage profiles from the phase diagrams show that the SiO2 (Figure II-141b) initially discharges at a much higher potential than Si (Figure II-141a); however, the potential drops off rapidly and becomes comparable to the Si potential. This is consistent with the phase diagram, showing that silicides are the discharged species at higher lithium concentration. The high potential of the native oxide provides insight into the formation of the SEI and should be compared to experimental results. The larger potential provides a more favorable potential for electrolyte decomposition and electrolyte formation.

Furthermore, kinetics of the model Si anode were evaluated through Li self-diffusivity using *ab initio* molecular dynamics. Figure II-142 shows the diffusivities of the corresponding LixSi and LixSiO2 phases. Most notably in Figure II-142, it is evident that the SiO2 exhibits significantly slower diffusion for Li from the electrolyte/SEI to the bulk of the Si, and hence, it impedes lithiation of the Si anode.

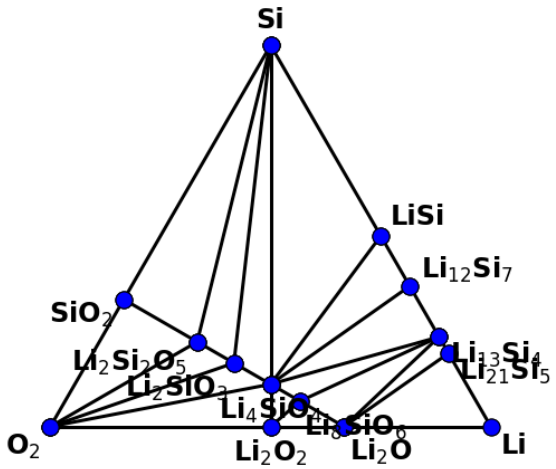

Figure II-140. Ternary phase diagram of the Li-Si-O system.

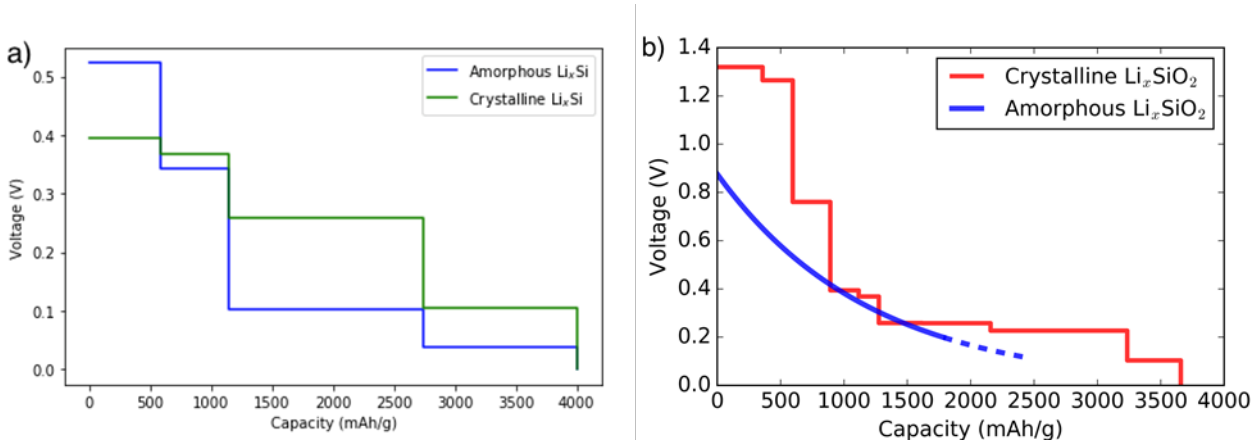

Figure II-141. Voltage profile for a) amorphous and crystalline lithium silicides and b) amorphous and crystalline lithium silicates.

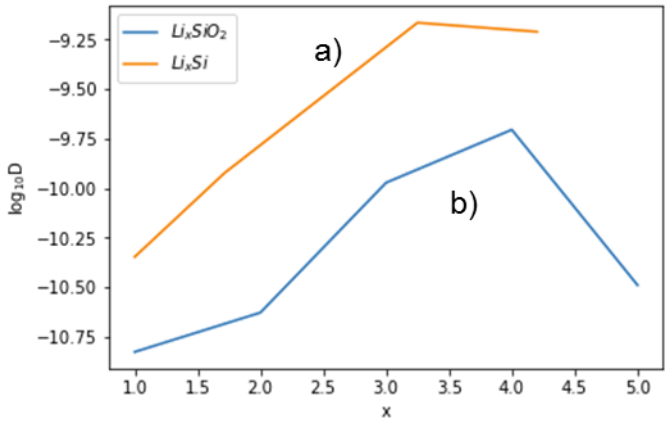

Figure II-142. Diffusivities in a) lithium silicides are greater than diffusivities in b) lithium silicates. Due to high variability in diffusivities, amplified by a log-scale, error bars are not shown.

The bulk properties for pure EC were calculated. For the two sets of potential adopted, OPLS gives better enthalpy and ε results, whereas GAFF underestimates the ε. However, GAFF gives better viscosity results compared to experimental results. Then, 5 ns of NVT run of MD simulation were conducted for 1.2 M LiPF6 in EC. According to the radial distribution functions (RDFs), the total coordination number (CN) for Li ion is around 5.69~5.77 for both OPLS and GAFF, which signifies some over-coordination due to the non-polarizable force fields. Two basic solvation structures are observed (Figure II-143): contact ion pair (CIP) and solvent-separated ion pair (SSIP). For both force fields, the SSIP is the dominating species, with about 20% CIPs. Interestingly, there also exists a small portion of aggregate solvates (AGGs). At 1.0 M, the abundance of CIP has dropped to about 10% of the Li solvation structures.

Peaks of the IR spectrum from experimental results were designated as coordinated ones and uncoordinated ones based on calculation and IR database, which gives us information of solvation structure. By comparing the calculated and experimental results, we can conclude that they have similar shifts for CIP and SSIP, respectively, despite small differences in absolute frequency values. Thus, going forward, we can use the computed values to identify majority and minority solvation species from experimental results. We can also get the ratio of CIP and SSIP by comparing the intensity in future studies, which will, in turn, be compared with the MD results.

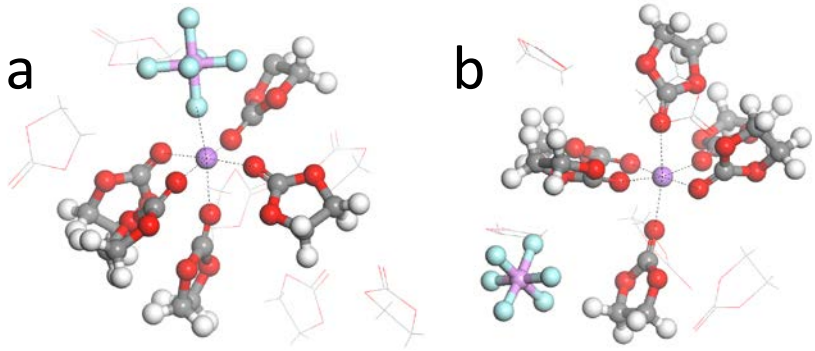

Figure II-143. The (a) CIP and (b) SSIP solvation structures.

Interfacial properties of ions/electrolyte molecules of LiPF6/EC at the Si anode at the initial charging step is being studied via the constant potential method (CPM) in classical MD. We will first investigate the solvation structure of electrolyte molecules at Si anodes. 1 M LiPF6 in EC is employed as the electrolyte, and neat crystalline Si with/without native silicon oxide layer as the anode (Figure II-144). The complicated structure at the electrode surface makes the electric field act heterogeneously on each molecule; thus, the electrode is modeled with CPM, where constant electric potential is applied to the battery cell as in typical experimental conditions. This model will allow us to investigate more realistic structural properties as well as more accurate dynamical properties—e.g., diffusion, ion conduction, and lithiation—because the response of the molecules in the electrolyte phase to an external field can be described explicitly.

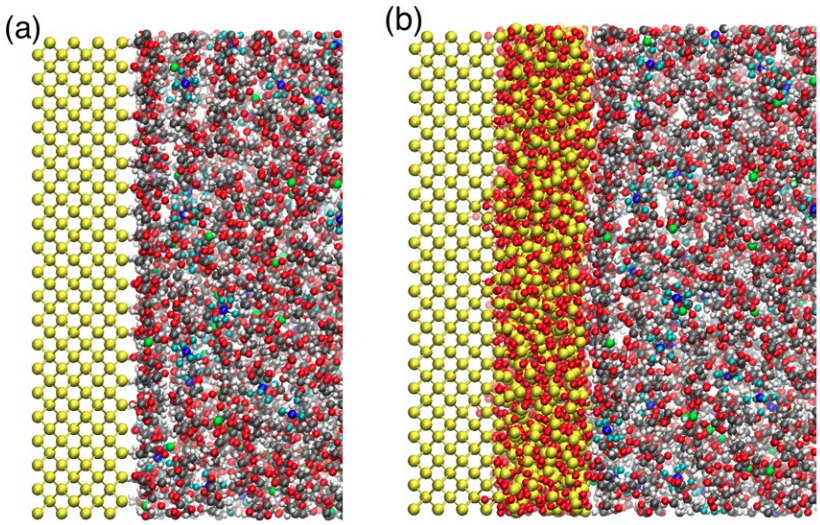

Figure II-144. Snapshot of a classical MD simulation of a model silicon anode with a crystalline structure (a) and amorphous silicon oxide on top of it (b). A constant electric potential is applied to the model battery cell. Si (yellow), Li (green), C (gray), H (white), O (red), P (blue), and F (cyan).

Materials development for bassline materials within SEISta

One key task within SEISta explores plasma-synthesized silicon nanoparticles (Si NPs) as model systems for LixSi anodes. Such plasma-prepared Si NPs are valuable because they feature hydrogen-passivated surfaces and a high surface area resulting from their <10-nm diameter, which makes them well suited for chemical reactivity studies to understand 1) early-stage SEI layer growth, as well as 2) individual SEI component chemical stability. With our existing capabilities, we have determined that the plasma power density can be used to tune the Si NPs from amorphous (a-Si) to hydrogenated (a-Si:H) to crystalline (c-Si), which are each expected to provide different anode characteristics in planned FY18 electrochemical studies. Making larger-diameter (10–200 nm) Si NPs and at a greater scale (>100 mg) additionally required new hardware and plasma-system components. In FY17, we acquired a 12-kg cylinder of 100% silane (SiH4) gas precursor, installed a higher-flow (500 sccm) SiH4 mass flow controller, and have designed and completed testing on a new load-lock collection system capable of collecting ~10 g of Si NPs per reactor run (Figure II-145). An alternate insert within this load lock will facilitate up to five different samples per reactor run, greatly increasing our throughput as we explore the conditions necessary to produce larger-diameter particles.

Figure II-145. Scaled-up plasma reactor, load-lock collection system, and small-diameter (<10-nm) hydrogen-passivated Si NPs.

Next, a comprehensive FTIR characterization of solid-phase material elucidated the chemical reactivity of the small-diameter Si NPs with electrolyte (EC/LiPF6 and Gen2, Figure II-146). Model systems with alkoxide and silyl ester groups (suspected chemical species following carbonate electrolyte decomposition) that were intentionally bound to the surface of Si NPs revealed that the silica (SiOx) formed in the presence of surface-bound alkoxides is relatively robust against dissolution, whereas SiOx on the surface of Si NPs functionalized with silyl esters is susceptible to chemical attack. Similar studies on different forms of commercial SiOx found that fumed SiOx and 30–50-nm NanoAmor Si (which is primarily SiOx) are chemically unstable to EC/LiPF6 and Gen2 electrolytes. In contrast, Stöber SiOx (prepared via a sol-gel process) is virtually unreactive toward these electrolytes. Finally, the reactivity of two types of lithium silicates—Li2SiO3 and Li4SiO4, prepared at ORNL—evoked as SEI components were additionally compared. Interestingly, we found that Li2SiO3 coordinates carbonates whereas Li4SiO4 is relatively unreactive. The attenuated total reflectance (ATR)-FTIR analysis of reacted electrolytes with three different SiOx forms supports reactivity results of each SiOx, and additional characterization of reacted electrolytes with Si NPs or lithium silicates will be performed to complement the previous results. This work provides insight into the types of chemical species present in the SEI layer that either afford stability or lead to its dissolution.

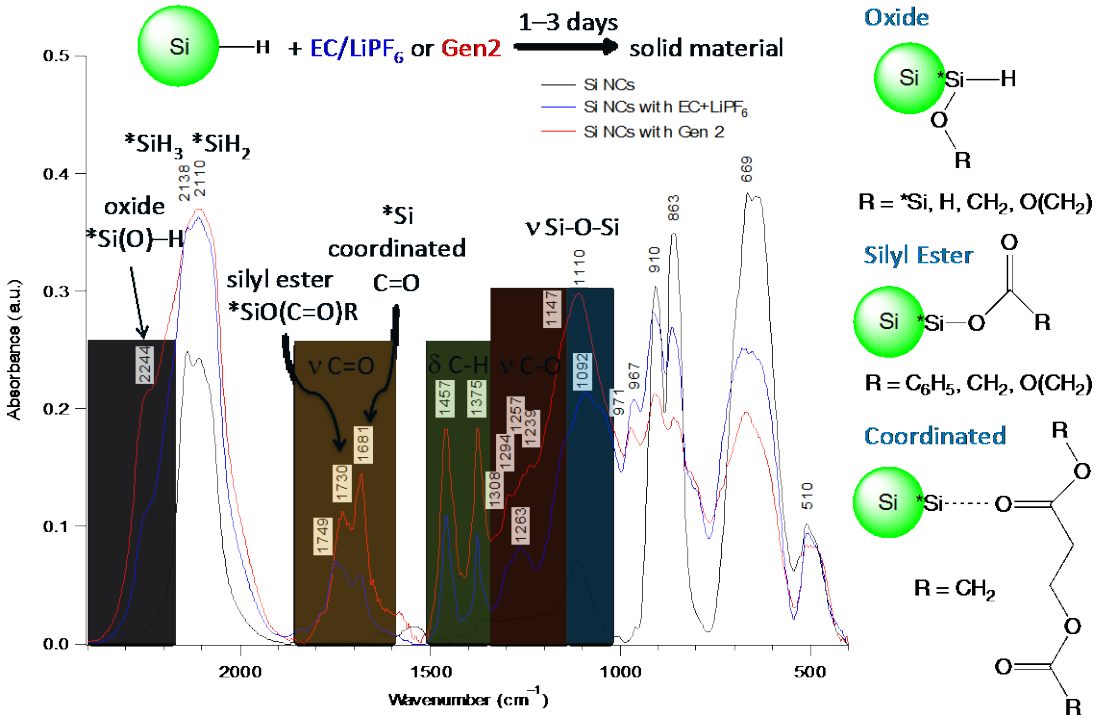

Figure II-146. Example of FTIR data of solid material following reaction of Si NPs and electrolyte.

Complementary studies characterizing the gaseous products from the chemical reactions of Si, SiOx, and LixSiOy with electrolytes were performed (see below) and correlate well with the above solid-phase results. In addition to this work between NREL and ORNL, SEISta-facilitated assistance has been supplied by University of California Berkeley, where density functional theory (DFT) experiments are under way to confirm many of the new vibrational modes that were assigned from these chemical reactivity studies. A publication detailing the combined experimental and computational results will be extremely valuable to the field because currently no such comprehensive spectroscopic characterization of SEI components exists. Additional work in new capability development is planned in FY18 to explore the molecular nature of species dissolved in the electrolyte that would present a complete accounting of all products during early-stage chemical SEI formation.

Reactivity studies of silicon and lithiated silicon samples

The nature of the silicon electrolyte interface is critical in developing the SEI. This interface is complex, and as such, a significant portion of the SEISta team is focused on the reactivity of the silicon, its surface, and the lithiated versions and variants.

Explored the gassing of silicon-based materials and the influence of the surface chemistry of these materials on the reactivity.

As the primary basis for the silicon work, we wanted to understand if the silicon surface had any fundamental limitation in its compatibility with the silicon electrode. Therefore, we began by examining the chemistry of silicon and silicon oxide particles (high surface area for better resolution) with traditional electrolyte components. It has been observed that extensive gassing occurs upon exposure to the baseline electrolyte (EC:DMC 30:70 1.2M PF6). To explore these reactions and identify ways to prevent them, we used an assortment of silicon-based materials to explore different surface influences of the reaction chemistry that may influence the surface reactivity of the materials. The silicon-based materials are a nanocrystalline silicon synthesized from silane (nanocryst – NREL), a nano-amorphous silicon commonly used in making silicon electrodes, both fumed and Stöber-prepared silica, lithium metasilicate, and lithium orthosilicate. The silane-based silicon (nanocryst) has a particle size of 7 nm and is terminated with hydrogens, whereas the

nanoamorphous silicon is 70–130 nm in size and has a known native oxide layer. Samples were dried in the evacuation chamber to the Ar glove box prior to use. All materials were handled in the argon glove box. Electrolyte used for the studies includes 3:7 ethylene carbonate:ethyl methyl carbonate that was either 1.2 M in LiPF6 (Gen 2) or 1.2 M in LiTFSI. All others were made, including the fluoroethylene carbonate, which was simply added to the Gen 2. The LiClO4 salt was 1 M in 3:7 EC/DMC.

To follow the rates in the gassing reaction, kinetic IR experiments were run on an Agilent Technologies Cary 680 FTIR. These studies could track CO, CO2, SiF4, PF3, HF, and electrolyte, but not H2 or O2 gas. In a glove box, a known amount of silicon-based material (~0.2 g) is weighed and transferred onto a boat (40 mm x 13 mm x 2 mm). The boat is inserted into the IR gas cell (Figure II-147)), and the cell is sealed around KBr windows, as well as with a septum (SupleCo GR-2 septum, 6 mm) in the injection port. A small syringe is filled with electrolyte (400 µL), and brought out of the glove box along with the gas cell. The cell is placed on the holder in the IR spectrometer, and a background scan is taken. The electrolyte is injected through the injection port, first making sure that the boat is situated under the port inside the cell. Once the electrolyte is injected, the kinetic experiment is started.

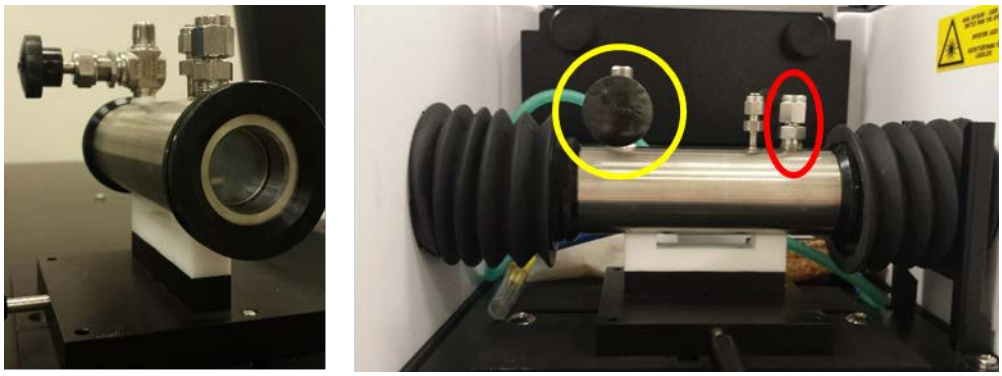

Figure II-147. IR gas cell used for kinetic measurements from two different angles. The path length through the cell is 11 cm, and the KBr windows are 25 mm in diameter by 2 mm thick. The injection port (circled in red) is sealed with a septum, and the outgas port (yellow) can be opened for purging, if necessary.

CO and CO2 calibration curves were constructed by purging the gas cell with Ar gas, with a needle and hose leading through the injection port and leaving the outgas port open. The outgas port was closed and the needle removed to take the background, and then a known concentration of gas was flowed into the gas cell. Scans were taken with the outgas port closed and the injection needle removed so that there was no interference from the incoming gas or escaping gas in the resulting spectrum.

Silicon/silica particles

The Archimedes' principle was employed to evaluate the amount of gas released by the reactions between the silicon materials and the electrolytes. The gas released was followed by the relating change in the buoyancy to the change in gas volume of pouches over time as shown in Figure II-148. All reactions were duplicated to illustrate the reproducibility. The nanocryst Si immediately produced gas upon contact with Gen2 and produced 0.2 mL of gas in 480 minutes (Figure II-148-left). Interestingly, removing the salt from the electrolyte showed that no gas evolved, suggesting that the salt has a major role in the reaction mechanism. Because PF6- anion is known to undergo hydrolysis, we replaced the Gen2 anion with TFSI. The TFSI electrolyte showed slight gassing, with the rate being 115 times slower than Gen2. As the TFSI electrolyte evolved only 0.02 mL of gas, we conclude that the identity of the anion does matter in producing gas. The effect of the standard FEC additive on spontaneous gas production was also measured. A 10% solution of FEC in Gen 2 was prepared, and the pouches produced the same amount of gas for the FEC/Gen 2 sample as for the Gen 2, indicating that either the main gassing reaction does not involve the decomposition of the solvent, or the decomposition is not something that the FEC can prevent. In comparison, the nanoamor (Figure II-148 - right) took much longer (days to weeks) to begin degassing. The reaction with Gen2 produced 4 mL of gas

between 3–5 days. This was an order-of-magnitude more gas produced than with nanocryst, although it was much slower, which suggests that the oxide layer influences the kinetics and mechanism. Here, we saw that the FEC doubled the time delay for gas production, but the same amount of gas was produced. Replacing the PF6- anion with ClO4- prevented the reaction from occurring, again indicating that the LiPF6 salt is an integral part of the reaction.

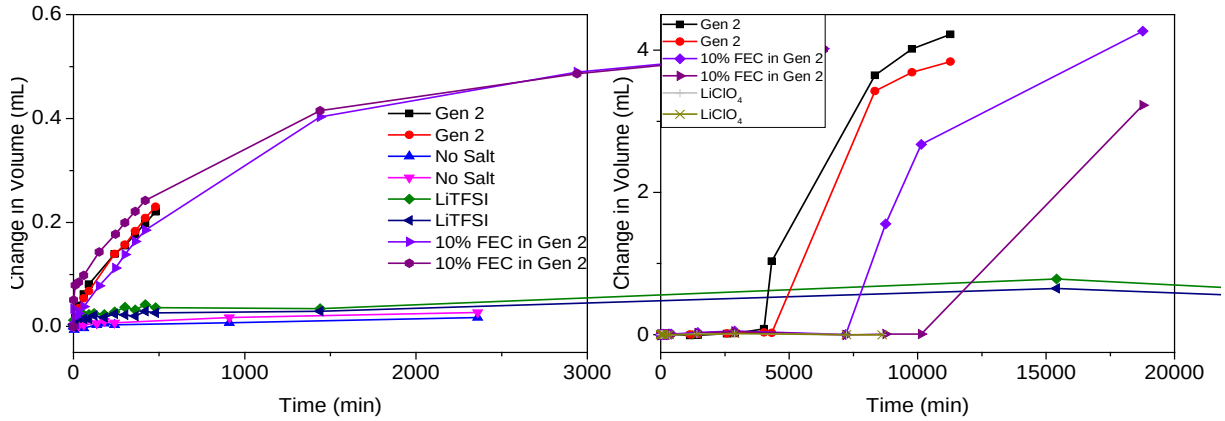

Figure II-148. Plot of change in volume (calculated through buoyancy) of the nanostructured silicon compounds reacting with various electrolytes in pouches. The left plot is of the nanocrystaline and the right is the nanoamorphous.

There are no data on TFSI salt with nanoamor, or on any of the other materials, because the IR experiment of it with nanocryst revealed a large amount of HF gas forming. So the reactions were stopped due to safety concerns.

Mass spectroscopy was conducted on the gases in the pouch cells. Figure II-149-B shows the mass spectroscopy data of the Gen2-nanocryst Si pouch after 480 minutes. The gases evolved in the pouch were found to be O2 (32 amu) and CO/ethylene (28 amu). *In-situ* IR spectra of the air space's evolution were also recorded in real time. Here, the sealed gas cell volume of 36 mL was fixed (Figure II-147). Representative transient spectra are shown in Figure II-149-A, at selected time points, as many more spectra were taken to accurately follow the evolution over time. Within the data, most peaks are attributed to solvent vapor. Because the solvent is volatile, the referenced background was taken to be the first 10 seconds after solvent addition. Peaks that appeared at later times and grew throughout the reaction were attributed to products of the reaction, such as carbon dioxide (2,350 cm-1), carbon monoxide (2,200 cm-1), silicon tetrafluoride (725 cm-1), and phosphorous trifluoride (475 cm-1). The insets on the IR plot give a representative view of the products over time. The CO, SiF4, and PF3 peaks increase in intensity with time, indicating that they are being produced throughout the entire reaction. The CO2 peak went negative before growing, indicating that initial concentrations of the gas were used in the reaction, or simply dissolved into the solution, as CO2 is known to be highly soluble in carbonates [1]. Figure II-149-C shows the integrated IR signal over time for the different gas products. For the first 500 minutes, the only product changing is carbon monoxide. At around 500 minutes, the CO starts to increase, as the CO2 decreases. From 900 minutes, all curves begin to increase, with the CO, SiF4, and PF3 peaks flattening slightly at 1,150 minutes. From this, it can be determined that the evolution of the gases is highly correlated. Further proof of their correlation can be found in the derivative plot, which is an inset of Figure II-149-C. All four curves line up from 650 to 950 minutes, and then they begin to rise at varying slopes from there. There is a spike in CO, SiF4, and PF3 at 1,190 minutes, corresponding to the bump in the integrated signal vs time plot. This indicates that the reaction mechanism is changing with time and that certain products or species are involved in different reactions.

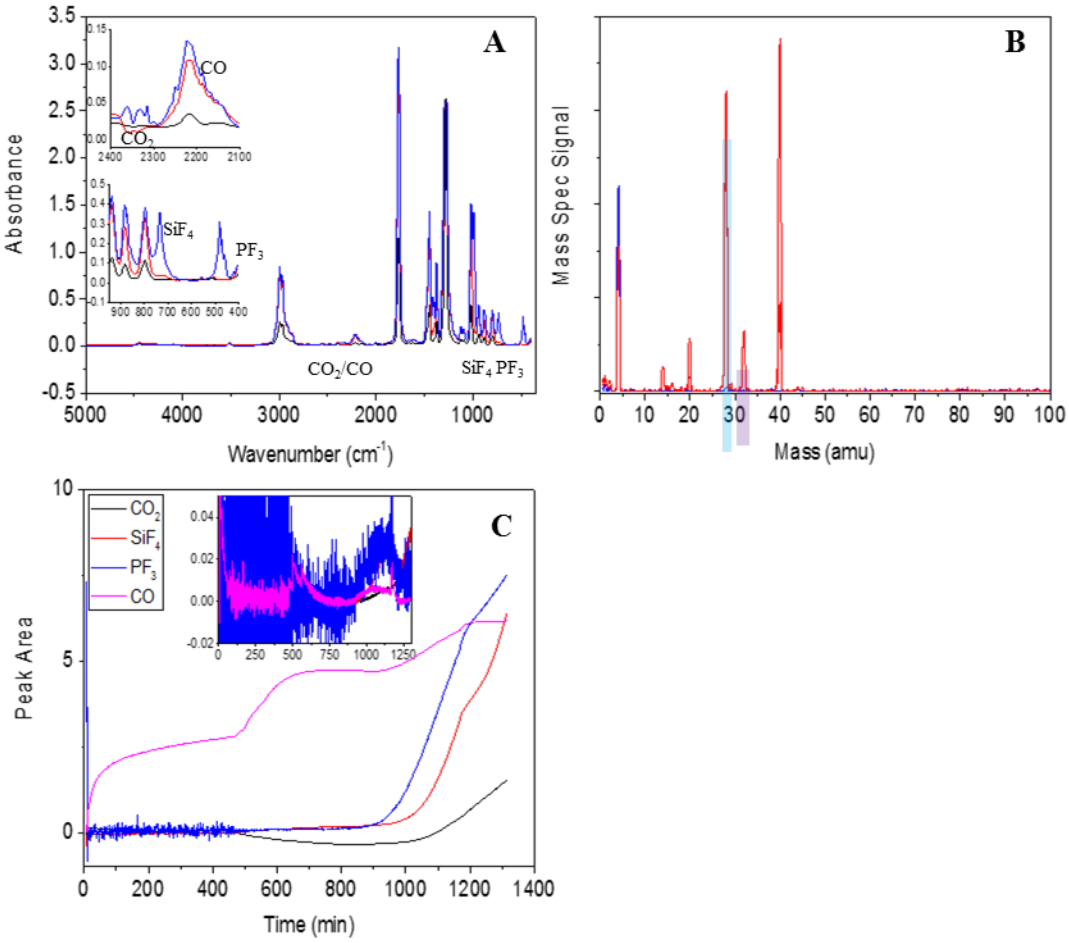

Figure II-149. Characterization data for the gases produced in the reaction between the silicon nanocrystals prepared by silane and the Gen 2 electrolyte. a) Kinetic IR (black = 14 min, red = 752 min, blue = 1,278 min), insets CO2 and CO, and SiF4 and PF3. b) Mass spectrum was taken after 480 minutes (sample is red, helium is blue). Boxes around peaks correspond to various compounds (blue = CO, purple = O2,). SiF4 (104 amu, 85 amu, 86 amu, 87 amu), PF3 (69 amu), CO2 (44 amu), F (19 amu), and H2 (2 amu). c) Peak area vs time plot to illustrate any correlation between the evolution of the different gases. Inset is derivative of plot with respect to time. (In both, black = CO2, purple = CO, red = SiF4, and blue = PF3).

The nanoamor Si showed drastically different results in the MS and IR. Here, the major reaction products are CO2, SiF4, and PF3, and H2 forming (Figure II-150-B). H2 evolution could be attributed to water reacting with silicon (Si + 2H2O → SiO2 + 2H2), or silicon reacting with an H-C-O compound, such as the solvent molecules. The IR spectra show that gases begin evolving immediately upon mixing in the reaction, which is drastically different from the buoyancy experiments.

The PF3 evolves the fastest, but begins to slow down around 100 minutes when the CO2 and SiF4 rate increases. Just after 200 minutes, the CO2 reaction increases in rate again, and the SiF4 decreases until equilibrium is presumably reached. The PF3 gas begins to disappear around 500 min, suggesting its consumption for another reaction. The small amount of PF3 in the MS may be from the continued consumption of PF3 gas for the next two weeks before reaching the point that the mass spectrum was taken. Clearly, the mechanism of electrolyte degradation is different between the two Si particles.

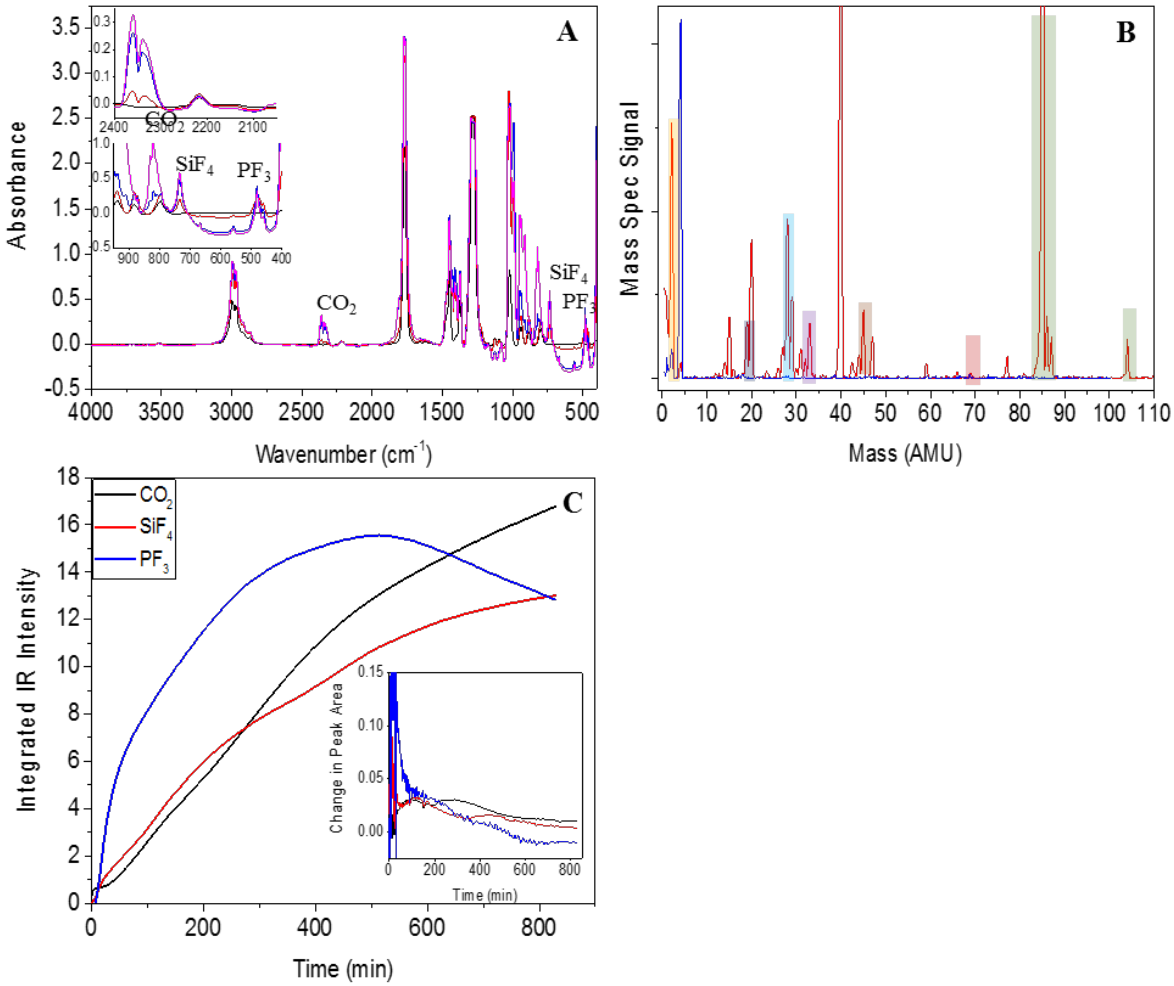

Figure II-150. Characterization data for the gases produced in the reaction between the nanoamorphous silicon and the Gen 2 electrolyte. a) Kinetic IR (black = 0.936 min, red = 126 min, blue = 559 min, purple = 818 min), insets CO2, and SiF4 and PF3. b) Mass spectrum was taken after 14 days (sample is red, helium is blue). Boxes around peaks correspond to various compounds (yellow = H2, black = F, blue = CO, purple = O2, orange = CO2, red = PF3, green = SiF4). SiF4 (104 amu, 85 amu, 86 amu, 87 amu), PF3 (69 amu), CO2 (44 amu), F (19 amu), and H2 (2 amu). c) Peak area vs time plot to illustrate any correlation between the evolution of the different gases. Inset is derivative of plot with respect to time. (In both, black = CO2, red = SiF4, and blue = PF3).

Silica

To test the theory of the importance of the native oxide layer for the production of CO2, multiple silica compounds were tested in the same fashion. First tested was a fumed silica (S5505, Sigma Aldrich), which was dried in a glove box antechamber before use. Figure II-151-B shows the mass spectrum of the gas evolved in the pouch reaction between the S5505 and the Gen 2 electrolyte after 40 days. The products were found to be CO, CO2, H2, PF3, and SiF4 (SiF4 (104 amu, 85 amu, 86 amu, 87 amu), PF3 (69 amu), CO2 (44 amu), O2 (32 amu), CO (28 amu), F (19 amu), and H2 (2 amu).). These indicate that both the decomposition reaction of the solvent and the salt reaction with the silicon substrate are occurring. From the selected plots from the kinetic IR in Figure II-151-A, the reaction clearly produces the CO2, SiF4, PF3, and CO, as seen in the previous reactions. Therefore, the solvent is still reacting to decompose, and the salt has sufficient access to the silicon to react with it, forming SiF4. In Figure II-151-C, the plot of the integrated intensity vs time, the CO2 curve closely resembles that of the silane-sourced silicon. First, the curve is flat, indicating that any CO2 produced is remaining in the solvent or in equilibrium with surrounding CO2 gas dissolving in and out of the solvent. At

750 minutes, the CO2 begins to disappear, again corresponding to the onset of SiF4 production. As the CO2 begins to increase again at 850 minutes, the SiF4 peak has a plateau that jumps again as the CO2 flattens off at 1,150 minutes. The PF3 curve follows the same plateau and increase pattern as the SiF4, indicating that the evolution of all three gases is connected. The carbon monoxide curve behaves the same as in the nanoamor, with the peak growing quickly in the first couple of minutes, and then staying flat around 2.5 intensity units for the rest of the reaction. The derivative plot has peaks around 850 and 1,100 minutes for all three products, corresponding to the increase in the intensity plots. Somehow, the reactions are correlated in this mechanism because they tend to increase alongside each other.

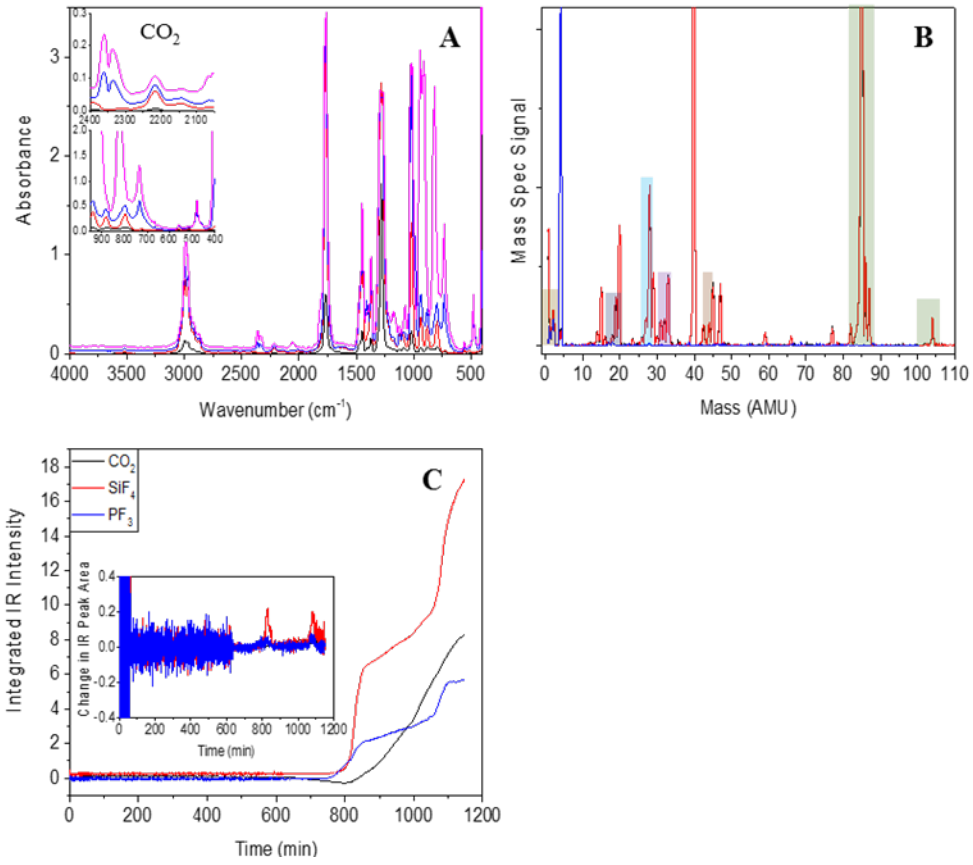

Figure II-151. Characterization data for the gases produced in the reaction between the fumed silica and the Gen 2 electrolyte. a) Kinetic IR (black = 0.3 min, red = 184 min, blue = 1,019 min, purple = 1,147 min), insers CO2, and SiF4 and PF3. b) Mass spectrum was taken after 40 days (sample is red, helium is blue). Boxes around peaks correspond to various compounds (yellow = H2, black = F, blue = CO, purple = O2, orange = CO2, red = PF3, green = SiF4). SiF4 (104 amu, 85 amu, 86 amu, 87 amu), PF3 (69 amu), CO2 (44 amu), F (19 amu), and H2 (2 amu). c) Peak area vs time plot to illustrate any correlation between the evolution of the different gases. Inset: derivative of plot with respect to time of peak area vs time plot. (In both, black = CO2, red = SiF4, and blue = PF3).

Silica prepared by the Stöber method was used as a comparison to determine if morphology influenced the gassing. Figure II-152-B shows the mass spectrum of the reaction with Gen 2, and was taken after the pouch sat reacting for 48 days. The gases evolved were determined to be CO, O2, CO2, SiF4, F, and H2. The CO, O2, CO2, and H2 can all be attributed to solvent decomposition or the reaction of the termination layer on the silica. The excess of CO and O2 compared to the CO2 may indicate the decomposition of the CO2, or simply the solvent molecule decomposing, either the EC or the EMC, prefers to form CO than CO2. The SiF4 results from the reaction between the $LiPF_6$ salt and the silicon in the electrode. Interestingly, there is no PF3 present, a natural product of the reaction generating the SiF4. It is possible that the PF3 formed is used in a further

reaction related to passivation of the silica. As usual, a kinetic IR experiment was performed to follow the changes in the individual gases over time. From the inset plots in Figure II-152-A, the CO2 is decreasing in intensity, indicating that the initial amount present in the background spectrum is either dissolving into the solvent, or reacting to form another product. The CO peak is much stronger next to the decreasing CO2, and the SiF4 and PF3 peaks do not appear to be changing. Figure II-152-C, the IR integrated signal vs time plot, does not indicate there to be any correlation between the gassing of each product relative to the others, which is supported by the derivative plot. The CO2 peak is decreasing, as observed in the IR spectrum. However, as some CO2 is observed in the mass spectrum, it must be produced later than the 12 hours of the kinetic IR experiment could track. The SiF4 peak grows toward the end of the reaction, which would eventually lead to the large amount seen in the mass spectrum. The carbon monoxide trend is consistent with the S5505 and nanoamor peaks—growing to an integrated value of around 2.5 in the first 10 minutes and then staying level for the rest of the experiment. It does not indicate any further correlation between the production of the gases, again indicating that this reaction follows a different mechanism than those prior to it. Another interesting detail from this reaction was that an orange liquid formed in both the pouch and the IR cell. Although it is unclear exactly what this liquid is, some phosphorous compounds such as P2H4 are orange, and the ATR spectrum taken of the liquid line up with signals from Li3F3 and other combinations thereof [2].

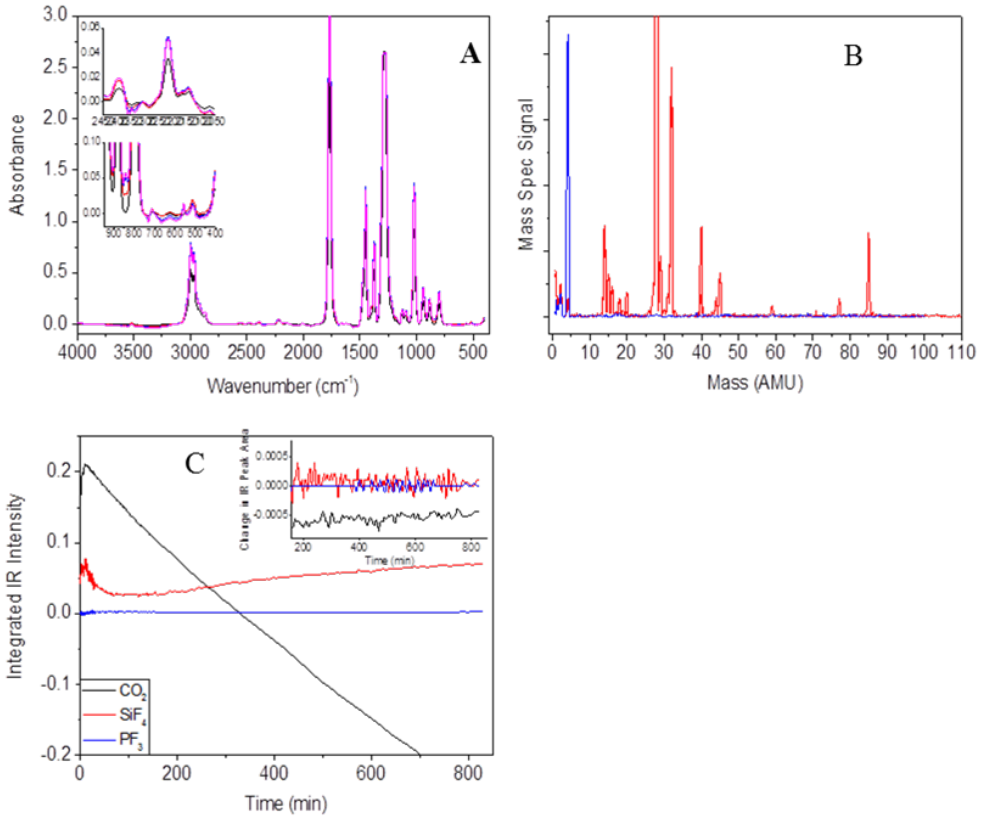

Figure II-152. Characterization data for the gases produced in the reaction between the Stöber silica and the Gen 2 electrolyte. a) In the IR (black = 0.936 min, red = 126 min, blue = 559 min, purple = 818 min), the CO2, SiF4, and PF3 peaks were nonexistent, as identified in the insets. b) The mass spectrum was taken after 48 days, and the reaction gases were present in this spectrum, indicating that the reaction took longer than the IR experiment ran for (sample is red and black, helium is blue). SiF4 (104 amu, 85 amu, 86 amu, 87 amu), PF3 (69 amu), CO2 (44 amu), F (19 amu), and H2 (2 amu). Boxes around peaks correspond to various compounds (yellow = H2, black = F, blue = CO, purple = O2, orange = CO2, red = PF3, green = SiF4). c) From the peak area vs time plot, the three gases produced have inflections in the curves that seem to loosely correlate between the substances, although the derivative plot is difficult to correlate. (In both, black = CO2, red = SiF4, and blue = PF3).

In the pouches, an orange gas is also present that is corrosive and has a negative effect on the mass spectrometer. This would indicate the presence of a fluorinated compound, but it is unclear from the data gathered what the exact composition is.

Lithium silicates

To simulate the gassing reaction with an SEI layer, lithiated silicate compounds were tested. Both lithium metasilicate (Li2SiO3) and lithium orthosilicate (Li4SiO4) were tested (Figure II-153) to see if the ratio of oxygen to silicon made a significant impact.

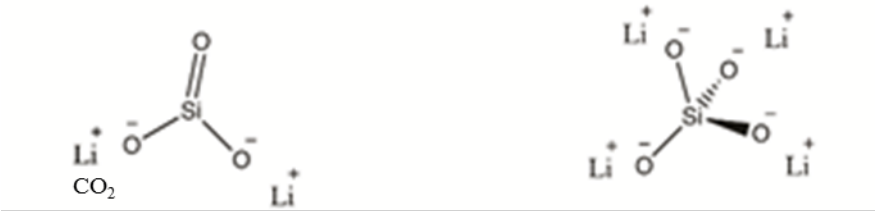

Figure II-153. Structures of lithium metasilicate (Li2SiO3, left) and lithium orthosilicate (Li¬4¬SiO4, right).

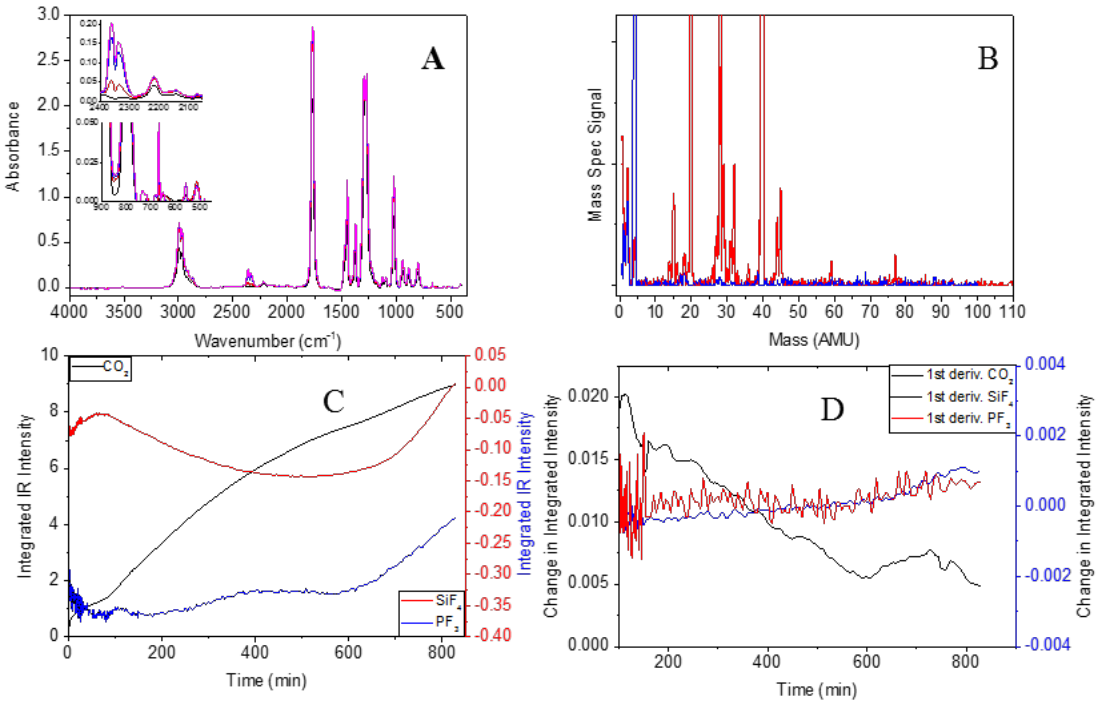

Figure II-154. Characterization data for the gases produced in the reaction between the Li2SiO3 and the Gen 2 electrolyte. a) Kinetic IR (black = 0.936 min, red = 126 min, blue = 559 min, purple = 818 min), insets CO2, and SiF4 and PF3. b) Mass spectrum was taken after 27 days (sample is red, helium is blue). Boxes around peaks correspond to various compounds (yellow = H2, black = F, blue = CO, purple = O2, orange = CO2, red = PF3, green = SiF4). SiF4 (104 amu, 85 amu, 86 amu, 87 amu), PF3 (69 amu), CO2 (44 amu), F (19 amu), and H2 (2 amu). c) Peak area vs time plot to illustrate any correlation between the evolution of the different gases. The double y plot allows for a clearer picture of the SiF4 and PF3 curves as compared to the CO2. d) Derivative of plot with respect to time of peak area vs time plot. (In both, black = CO2, red = SiF4, and blue = PF3). The double y plot allows for a clearer picture of the SiF4 and PF3 curves as compared to the CO2.

In the reaction of lithium metasilicate (Li2SiO3) with Gen 2 electrolyte in the pouches, the mass spectrum (Figure II-154-B) indicated the formation of CO, CO2, H2, and O2, indicating solvent decomposition. The mass spectrum does not indicate the presence of SiF4 or PF3, even after the 28 days of reacting in the pouch. If any had evolved, it must have reacted further during that time. Figure II-154-A, the kinetic IR spectrum, indicated mainly the presence of CO2, with resonance peaks appearing beyond the normal peak at 2,350 cm-1. The peak that appears around 650 cm-1 in the inset usually depicting the SiF4 and PF3 peaks can be attributed to CO2. Very little SiF4 and PF3 evolved in the reaction, which could also be seen in the integrated IR signal vs time plot (Figure II-154-C). The double-y axes allow for the trends between the materials to be compared, even as the change in the CO2 is much greater than that of the other two. The carbon dioxide curve shows an increase in CO2 over time, but the derivative plot shows the rate of evolution to be decreasing throughout the reaction. As with the Stöber, the CO evolution is rapid initially, but remains level at about 2.5 area units for the duration of the reaction. From the low level of gas evolved in the pouch, and the lack of SiF4 and PF3 peaks in the mass and IR spectra, it can be determined that the addition of lithium to the silicate compound helps prevent the reaction of the silicon with the LiPF6 salt.

As with the lithium metasilicate, the lithium orthosilicate mass spectrum, Figure II-155-B, shows the evolution of CO, CO2, and O2 from the reaction with the Gen 2 electrolyte in the pouch after 19 days. There is no

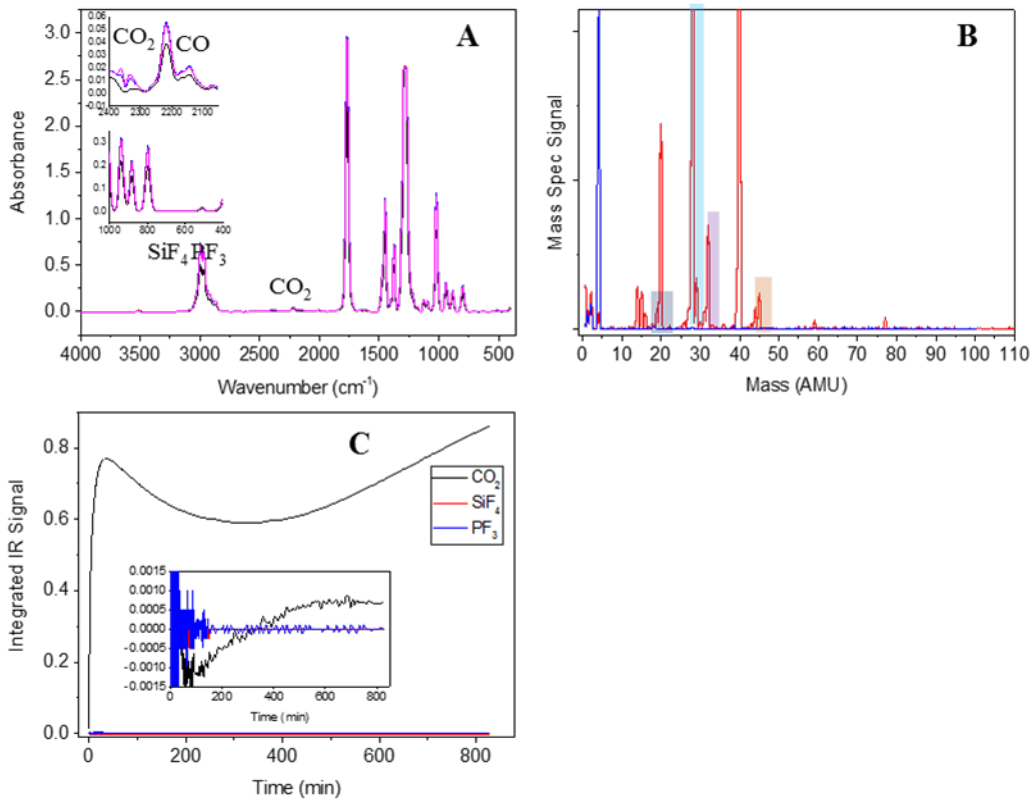

Figure II-155. Characterization data for the gases produced in the reaction between the Li4SiO4 and the Gen 2 electrolyte. a) Kinetic IR (black = 0.936 min, red = 126 min, blue = 559 min, purple = 818 min), insets CO2, and SiF4 and PF3. b) Mass spectrum was taken after 19 days (sample is red, helium is blue). Boxes around peaks correspond to various compounds (yellow = H2, black = F, blue = CO, purple = O2, orange = CO2, red = PF3, green = SiF4). SiF4 (104 amu, 85 amu, 86 amu, 87 amu), PF3 (69 amu), CO2 (44 amu), F (19 amu), and H2 (2 amu). c) Peak area vs time plot to illustrate any correlation between the evolution of the different gases. Inset is derivative of plot with respect to time. (In both, black = CO2, red = SiF4, and blue = PF3).

evidence of SiF4 or PF3 in the mass spectrum, indicating again that only the electrolyte solvent is decomposing. The fluorine peak seen in the mass spectrum is an artifact from the column, as the HF from other pouches started appearing in all spectra. Figure II-155-A shows the spectra from the kinetic IR experiment, where once again the only gases evolving are CO and CO2, not SiF4 or PF3. This trend is further visible in Figure II-155-C, the plot of integrated intensity vs time, where the SiF4 and PF3 curves are flat lines, and the CO2 peak increases to 0.8 area units, and stays relatively constant for the remainder of the reaction. This is also the case with the CO curve as it follows the same trend as in the Li2SiO3 reaction. From the data, it looks like the Li4SiO4 is even better than the Li2SiO3 at preventing gassing reactions. The pouch data show almost no growth over time, and the IR plots show very consistent behavior for each product throughout the reaction time, indicating that there was almost no reaction.

Once the moles of each gas were determined, from the calibration plots, they could be compared across samples by normalizing with respect to the surface area of the material. Figure II-156 shows the amount of gas produced by each material, normalized by amount and surface area of the silicon material. As the lithium silicates have surface areas of around 1 m2/g, the amount of gas produced is the same as if it were calculated per gram of material. This is why the other materials show much less gas evolving per m2, even if the pouches showed much more total gas evolving. However, it is possible to see from the diagram which gases are evolved from which materials, and which are not. The silicon nanocrystals from silane, the nanoamor, and the S5505 silica all produce all three gases in the reaction, but in varying ratios. The S5505 produces almost equivalent amounts of CO2 and SiF4 per m2, while the silicon produced from silane and nanoamor produce a higher amount of SiF4. The PF3 cannot be considered in this ratio, as the value is multiplied by a factor of 100 to make it visible on the plot. The lithium silicates are also interesting to compare, as the Li2SiO3 produced only CO2, while the Li4SiO4 produced much more SiF4 than CO2. The structure of the material must play a significant role in the catalysis of CO2 formation. Interestingly, none of the materials produced no gas, even though some of the pouch curves were flat. This indicates that electrolyte decomposition is easily catalyzed on silicon-based materials, and that the silicon is highly reactive in that environment itself. The mechanisms of all these reactions are not understood yet. Furthermore, it is clear that the reactions are highly correlated. Understanding these reactions will enable us to identify processes or methods to stop them.

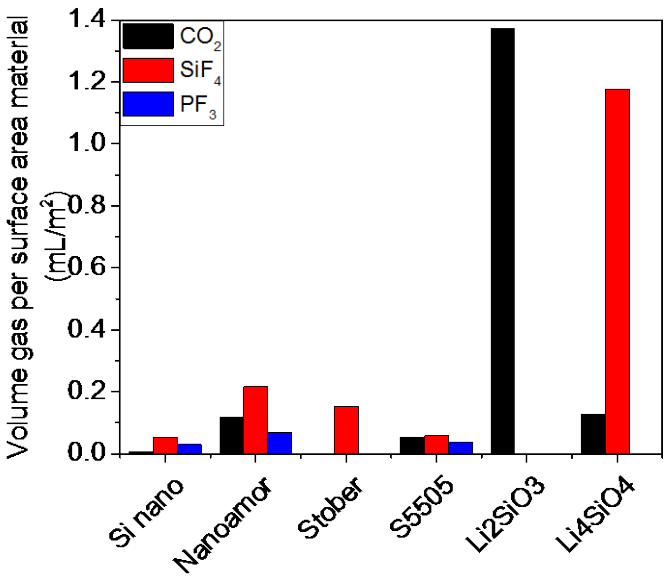

Figure II-156. Chart comparing the volume of each gas produced per surface area of material after reacting for 14 hours between the different silicon materials explored in this paper. The PF3 signal was increased by a factor of 100.

Reactivity of model silicon lithiated materials

Although there is an unexpected reactivity of standard silicon materials, we expected that lithiated silicon and silicon oxides would show enhanced reactivity toward standard electrolytes. One of the most interesting components of the silicon system is LixSiOy, which comes from the lithiation of the native SiOx layer. Study of the native SiOx layer on Si particles has also drawn attention because, on one hand, it confines the volume expansion of Si; on the other hand, it induces interfacial reactions that consume lithium. Lithiation of SiOx is complicated by dependence on the discharge state. At the initial state, SiOx is lithiated to a mixture of LixSiy, Si, and LixSiOy for the first few cycles. Si and LixSiy components progressively disappear when SEI gets thicker [3]. Although it is unclear as to the nature of the lithiated surface on silicon on electrodes, most recent studies focus on lithium silicate as the lithiation product of SiOx [4].

In this work, LixSiOy thin films with different lithium-to-silicon ratios were studied. LixSiy and Si were also studied to provide a baseline for future comparison. LixSiOy can be obtained by simply exposing LixSiy thin film in a low-O ppm glove box. Mechanical and electrical properties are discussed in the following text. A proof-of-concept multilayer thin film was deposited to study the possibility of LixSiOy passivating the Si surface. Although LixSiOy showed ductile behavior, it is still not able to passivate the Si surface because of its high electrical conductivity.

Experimental procedure: The LixSiOy thin film was synthesized by RF magnetron sputtering (13.56 MHz) using a lithium target (Lesker, 99.9%, 2") and silicon target (Lesker, 99.999%, 3" diameter). The chamber geometry is depicted in Figure II-157. The lithium target is 8 cm away from the substrate, and the silicon target is 12 cm from the substrate on axis. Ar (99.999% purity) was introduced to generate a plasma at a constant pressure of 3 mtorr. 30 W RF power was applied on both the lithium and silicon target. The film was deposited at room temperature and turn out to be amorphous, as expected. A combinatorial strategy was applied to screen properties of the lithium silicon compound with different lithium-silicon-oxygen composition. The film will have a higher ratio of Si-Li at the region closer to silicon and vice versa at the region further from silicon.

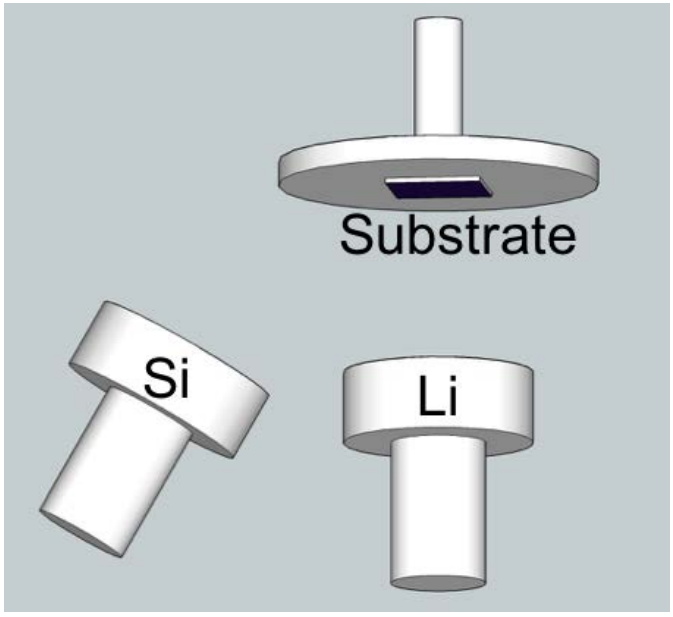

Figure II-157. Chamber geometry used to deposit LixSiOy thin films.

Depth-profile XPS was collected for the lithium-rich region and silicon-rich region. Ar+ ions were used to sputter away the film layer by layer until the copper substrate was revealed. Nanoindentation was applied to determine the mechanical properties. Indentation experiments were performed with a DDESP-10 tip in an argon-filled glove box. Controlling deflection set-points (voltage) applied on the tip allows the force to be controlled. Calibrations were done to quantitatively convert the voltage to load force. A diamond SSRM tip was held to the surface with varied magnitudes of force. Four sites with increasing lithium concentration gradient were indented with varied deflection set-points. Each indentation duration was held for 10 seconds. After unloading the indenter, a tapping mode was used to investigate the indentation depth, and images were also taken with tapping mode nondestructively. Electrochemical properties were investigated by making coin cells. Airless transfer through a vacuum vessel was adopted because of the high reactivity of LixSiOy.

XPS data were collected for the LixSiOy thin film. In Figure II-158, depth-profile core-level spectra are shown for Li1s, Si2p, and O1s. However, keep in mind that these profiles can be affected by a knock-on effect by the sputtering of Ar ions. From the depth profile, significant oxidation is noted at the surface. Due to the extreme affinity of lithium to oxygen and carbon, the surface layer can be easily oxidized into a form, during the transfer process from deposition chamber to XPS chamber, that is assumed to be Li_2CO_3 and Li_2O-based on the XPS carbon spectrum as in Figure II-158.

In the bulk, from the O 1s spectrum in Figure II-159a, only the characteristic peak of LixSiOy at 532 eV was observed. LixSiOy is the only species with oxygen in the film. On the other hand, there are two peaks in the Si 2p spectrum in Figure II-159b—one at 102.5 eV for LixSiOy and one at 99 eV for Si. From the peak intensity ratio, we can easily tell that the Si-rich region contains more Si phase than the Li-rich region. Also, notice that there is a shoulder at the Si peak of the Si-rich region at the lower binding energy, which might come from lithium silicide. This is also true for the Li 1s spectrum in Figure II-159c.

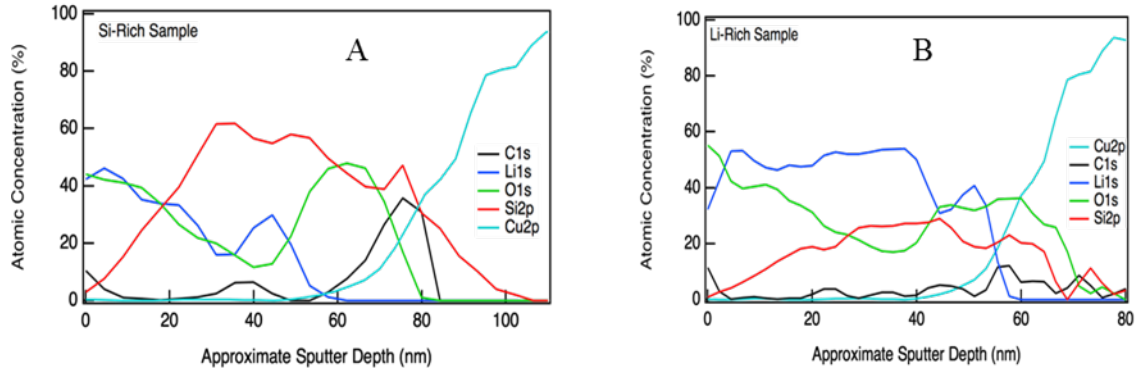

Figure II-158. XPS depth profile analysis of LixSiOy thin film on copper foil. Atomic percentage as a function of sputter depth for a) Si-rich region and b) lithium-rich region.

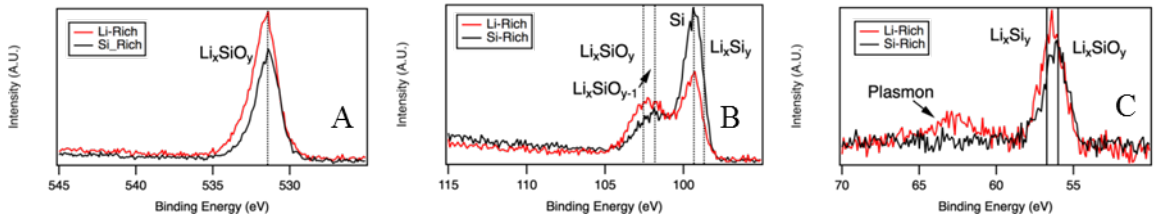

Figure II-159. a) O 1s spectra, b) Si 2p spectra, and c) Li 1s spectra of lithium-rich region and silicon-rich region.

To summarize the XPS results, a mixture of silicon and LixSiOy exists in the bulk with a different ratio with respect to the distance to the lithium target. There is sudden jumps of carbon and oxygen at the surface of copper, and they are suspected to be from the organic species from copper, which was not removed

completely. The lithium-rich region has an approximate formula of Li2SiO, and the silicon-rich region has a formula of LiSi3O with O content normalized throughout the film depth. Because the two regions are deposited at the same time, oxygen levels of the two regions are very close. Different lithium-to-silicon ratios can be referred to different degrees of lithiation of SiOx.

Mechanical behavior measured by AFM nanoindentation
AFM indentation measurements were performed on Si, LixSiy, and LixSiOy thin films. The LixSiOy thin film is just an aged form of LixSiy, which means that AFM was measured after 48 hours after deposition.

For the AFM nanoindentation experiments, the film was deposited on a hard glass substrate. Surface morphology is depicted in Figure II-160a. Surface roughness is on the order of 20 nm in an area 0.5 µm by 0.5 µm. Typical residual indentation imprints were shown in Figure II-160b. An inverted projection image is reflecting the tip geometry imprinted during indentation, as shown in Figure II-160c. As discussed in the XPS atomic profile, there is a lithium concentration gradient throughout the thin film across one direction. A total of four sites with different lithium atomic ratios were measured with various applied loads. It is assumed within each area that the lithium atomic ratio is uniform. Within each region, indentation tests with various applied loads have been performed at small distance intervals from each other, allowing for the visualization of several indentation imprints in the same high-resolution image. Dependence of the indentation depth on the lithium concentration was observed throughout the combinatorial sample.

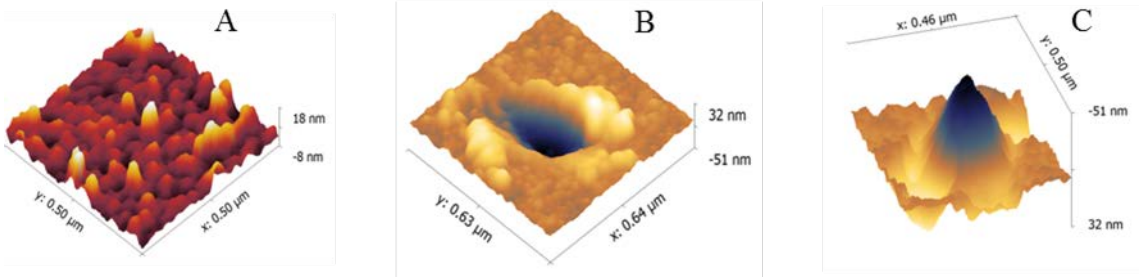

Figure II-160. AFM images of a) as-deposited film, b) indented film, and c) imprinted indented film.

Figure II-161 is a typical residual indentation imprint of film that reflects the film behavior on different force loads. Mechanical response of the lithium-rich area is shown in Figure II-162a, and a linear increase of indentation depth with loads was observed. However, the silicon-rich area shows brittle behavior as exhibited by how the probe easily broke through the film, and the cracks propagate to the substrate. Brittle behavior of the glass substrate also explains why the indentation depth is larger than the film thickness. Another distinct difference between these two behaviors is the following: in the ductile film, the film piles up at the edge of the indentation imprint from the indentation depth curve, whereas in the brittle film, there is no pile-up. The difference between ductile and brittle films are shown in Figure II-162 with AFM height and phase images. Note that we are investigating amorphous film rather than crystalline silicon, which usually cracks along the crystal plane; amorphous film cracks isotopically.

A brief summary on the mechanical response of thin film is shown in Figure II-162e, which plots the indentation depth vs. loads at different sites with increasing lithium atomic ratio. An interesting finding is that LixSiOy has changing properties when x in the formula changes. When x is larger, the indentation depth is larger, which means that the hardness of the film is smaller. This is a qualitative characterization of the film hardness that is adopted in many reported results. When x continues decreasing, the film changes from ductile to brittle. This changing behavior suggests that the initial lithiation product of SiOx is not flexible; it could easily break down upon cycling. When lithium is extracted, it could become less fracture-resistant. As it gradually turns into LixSiOy, as in the lithium-rich area, it is ductile and more resistant to fracturing.

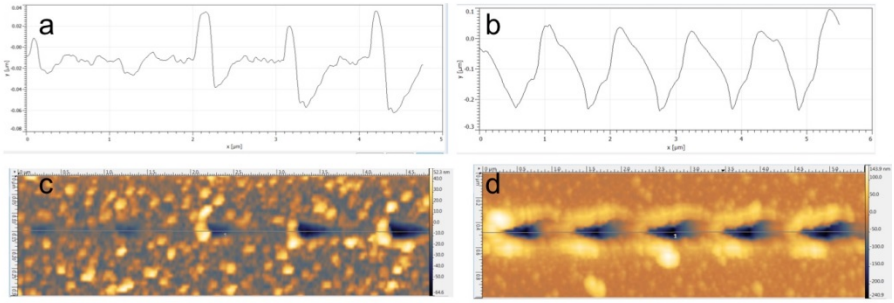

Figure II-161. Indentation depth plotted against the indentation force for the a) lithium-rich region and b) silicon-rich region. AFM images of indented film at c) lithium-rich region and d) silicon-rich region.

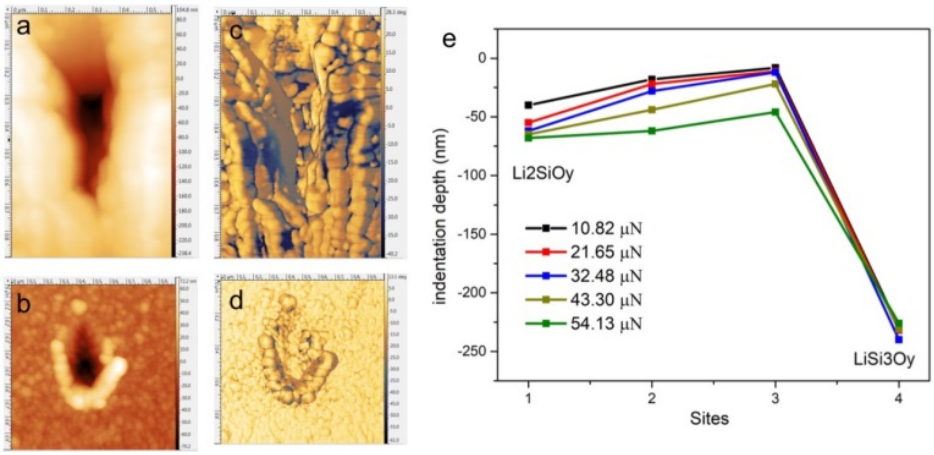

Figure II-162. AFM height image of a) ductile behavior region, b) brittle behavior region; phase image of c) ductile-behavior region and d) brittle-behavior region; and e) plot of indentation depth at different sites.

Figure II-163 is the plot of indentation response from Si, LixSiy, and LixSiOy thin film under the indentation force of 5.4 µN. LixSiy film is fresh film after deposition, whereas LixSiOy film is the oxidized LixSiOy film (48 h after deposition). From the indentation depth, we can easily conclude that hardness of these thin films follows a sequence of Si > LixSiy > LixSiOy because the indentation depth follows the sequence of Si < LixSiy < LixSiOy before cracks occur.

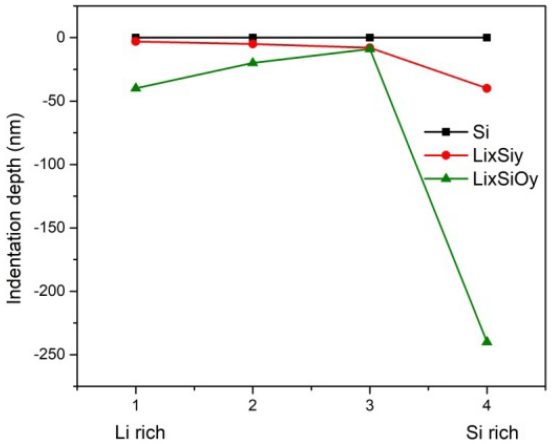

Figure II-163. Indentation depth profiles of Si, LixSiy, and LixSiOy thin film under indentation force of 5.4 µN.

XPS analysis of starting material

In addition to the materials described above, additional samples were prepared and analyzed using depth-profiling XPS to determine the composition and bonding states of the elements as films of varying compositions were exposed to electrolyte for various amounts of times. Samples similar to those used in the round robin were prepared with either a ~50-nm-thick SiO2, or a 50-nm-thick Li:Si 1:1 ratio film (nominally Li2Si2O5). The depth profiles were taken every ~30 A along a profile depth (based on the sputter rate of pure SiO2 as a standard). Composition and bonding states for C, Cu, F, Li, O, Si, and P were collected. The results are shown in Figure II-164 for SiO2 and Figure II-165 for Li2Si2O5.

Between these two films, it is clear that the time evolution of the structure and composition of the film is markedly different, indicating that surface chemistry of the starting film will affect how the SEI forms and its subsequent structure evolves. For the SiO2 film, very little evolution of the surface layer is evident in a short time, whereas the surface layer in the lithiated film more clearly indicates film growth over time. In addition, there is some evidence that fluorine in the films evolved at the surface (penetrating into the film over time), even though this electrolyte does not contain FEC; fluorine here must be coming from the penetration of the salt anion into the film structure, although the phosphorus signal does not indicate phosphorus penetration to the same extent. It is worth noting that these samples were deposited on copper foil, which had a relatively high roughness, which will skew some of the thickness measurements.

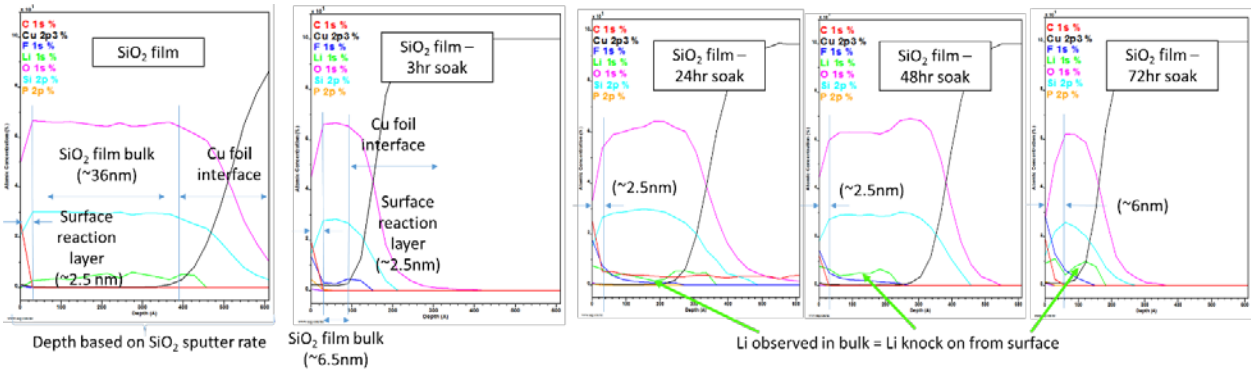

Figure II-164. Time evolution of XPS depth profiles on SiO2 sputtered on Cu foil exposed to electrolyte, from as-deposited (left) to exposed for 72 hours (right). The film evolution and surface is seen to establish rapidly, but affects the SiO2 depth over time.

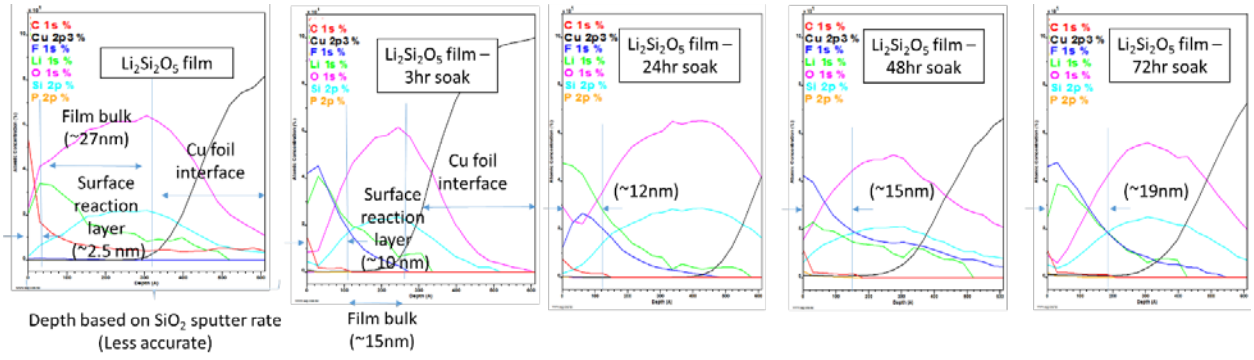

Figure II-165. Time evolution of XPS depth profiles on Li2Si2O5 sputtered on Cu foil exposed to electrolyte, from as-deposited (left) to exposed for 72 hours (right). The time evolution of the film and thickness of the interface layer are markedly different than in the SiO2 case.

A similar trend toward formation of more complex structures can be seen using ATR-IR. Although the two sample sets (SiO2 and Li2Si2O5) look similar in the as-deposited state (except for some expected differences

in the region near 800 cm-1 attributed to the presence of the lithium in the silicate structure), the time evolution of these films on exposure to electrolyte is markedly different. In Figure II-166A, a sample of SiO2 grown on Cu is exposed to the electrolyte for increasing amounts of time, and the ATR-IR spectra are collected on the same sample after exposure. Five regions of interest exist, with the region around 550 cm-1 being attributed to adsorbed or residual LiPF6 from the electrolyte that was not removed upon rinsing. The region from 700 to 900 cm-1 is associated with a number of phosphate and carbonate groups that contain lithium replacements for hydrogen. The region between 1,000 and 1,250 cm-1 is normally associated with O-Si-O stretching of the silicate peak. The region of 1,400 to 1,500 cm-1 is associated principally with a lithiated version of carbonic acid, and the region from 1,700 to 1,800 cm-1 is associated with alkyl carbonates and ethylene carbonate from the electrolyte. As can be seen in the figure, relatively little evolution of the surface is seen until longer times, and what is seen primarily is evidence of salt decomposition due to the formation of the phosphates and residual LiPF6 trapped on the surface. Additionally, some minor decomposition of the EC is visible as a retained product on the surface at long times. Note also the broad peak in the O-Si-O region, indicating that the network is relatively unperturbed up to 72 hours.

Contrast this with a starting film of the 1:1 Li:Si lithium silicate (Figure II-166B). Significant decomposition products appeared in as little as 1.5 hours of exposure to the electrolyte, and the region of salt decomposition products shows much higher levels of salt residuals and phosphate byproducts than in the SiO2 case. The region for stretching of the silicate network has evolved several distinct peaks, which may indicate disruption of the network expected during lithiation. Also note the evolution of the lithiated carbonic acid on the surface, and generation (and possible subsequent extinction) of the alkyl carbonates from the electrolyte decomposition occurring on the surface. Clearly, having lithium in the starting film evokes a much richer time evolution of the SEI formation, even with no active electrochemistry being performed.

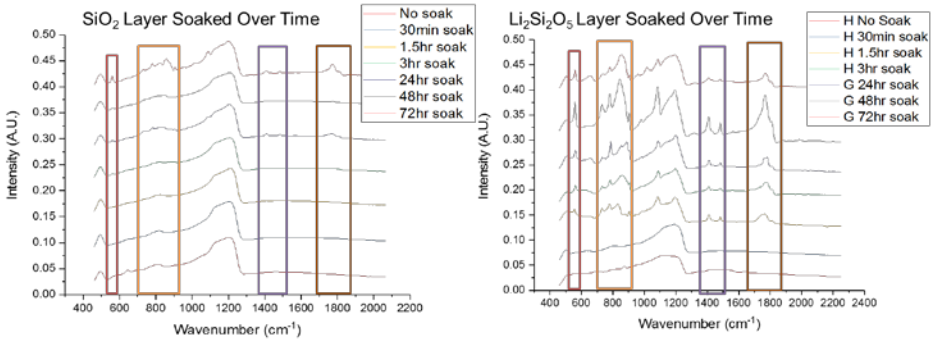

Figure II-166. (left) ATR-IR spectra of SiO2 film sputtered on Cu exposed to electrolyte for various lengths of time. Relatively minor evolution of surface species is noted, and the O-Si-O network is relatively unperturbed. (right) Spectra of Li2Si2O5 film subjected to the same conditions. Although the ATR-IR signals start out similarly, the time evolution of the surface products is very different, with more evidence of salt and electrolyte decomposition being noted.

Scanning spread Resistivity Microscopy

The scanning spread resistivity microscopy technique was applied on LixSiOy thin film. A bias voltage is applied between the STM tip and the sample during contact AFM topography imaging, and the resulting current flowing between the tip and the sample is measured. A surprising result from the SSRM measurements is that LixSiOy has a fairly low resistivity of 10^3 and 10^4 ohms across the whole film with different Li/Si ratios. However, these results were measured at a high bias voltage of -8 V, which might lead to lithium diffusion and cause composition change in the film.

Electrochemical properties

Galvanostatic charge and discharge were performed. 14-mm-diameter thin film was punched out from the silicon-rich region and lithium-rich region. The electrolyte was 1M LiPF6 in a 1:1 (volume) ethylene carbonate

(EC) and dimethyl carbonate (DMC) mixture. Lithium metal was used as the reference electrode. The cells were first charged to 1.5 V and then discharged to 50 mV. Because it is difficult to estimate the density of LixSiOy, we simply plotted the capacity vs. voltage in Figure II-167. A small amount of lithium can be extracted from the film, even up to 1.5 V. This low charge capacity indicates that little LixSiy exists in the film. It also proves that the majority of lithium exists in a form of LixSiOy as detected in XPS.

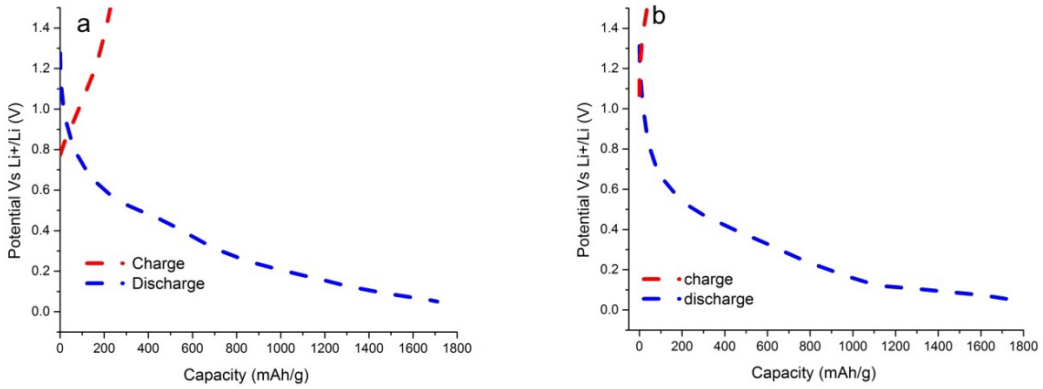

Figure II-167. Charge and discharge profile of a) lithium-rich region and b) silicon-rich region.

Whether a component is beneficial or not as SEI also depends on the chemical reactivity of the material with electrolyte. Here, we did a preliminary measurement of the reaction of LixSiOy with electrolyte by AC impedance at the open-circuit voltage. The electrolyte adopted in the coin cell is a mixture of EC and DMC. As LixSiOy soaked in electrolyte, the surface continuously reacts with electrolyte and the charge transfer resistance is time dependent. The silicon electrode did not show much activity, because the impedance is not time dependent at open-circuit voltage. The reactivity depends on the degree of lithiation. Several papers have discussed [5] possible reduction mechanisms of EC ethylene carbonate on the surface, with different degrees of lithiation due to different mechanisms. A higher degree of lithiated Si was found to be more reactive compared to a low degree of lithiated Si. The difference of reactivity originated from the ability of EC molecules to interact with Li+ ions on the surface. During the lithiation, SiOx becomes increasingly reactive to electrolyte as it takes increasingly more lithium.

Surface reactivity of both silicon-rich and lithium-rich regions were studied by impedance measurement. Impedance evolution was investigated by collecting spectra of a fresh cell and 24 hours later. AC impedance data were collected in a frequency range of 100 KHz to 100 MHz. In Figure II-168, the charge transfer resistance for the fresh cell is much higher than for the bare silicon sample. The higher resistance is suspected to come from the reaction that occurs at the surface of the LixSiOy with the electrolyte. The higher the lithium concentration in the compound, the lower the potential it has versus lithium; thus, the easier it reduces the electrolyte. This would cause a problem when the SiOx is lithiated to LixSiOy; if this layer is not fully covered with the other chemically stable electrolyte decomposition product, it will induce more reduction of electrolyte and eventually it will cause more consumption.

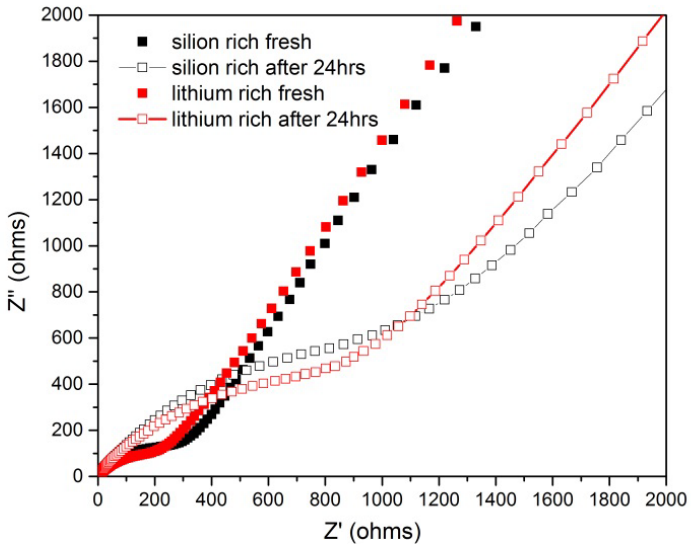

Figure II-168. Impedance spectra of lithium-rich region and silicon-rich region for the fresh cell and cell sitting for 24 hours.

Proof-of-concept of using LixSiOy as SEI

A proof-of-concept multilayer thin film was deposited with LiSiOy on top of a silicon thin film. The thickness of LixSiOy was controlled to 10 nm and the silicon thin film is 50 nm thick. Both silicon and LixSiOy-covered silicon (LixSiOy//Si) were then punched to 14 mm diameter and assembled into a coin cell for the cycling test. From the first cycle-discharge profile, LixSiOy-covered silicon had a lower OCV of only 1.5 V, and it began to reduce electrolyte at a higher potential range as seen in Figure II-169. The lower potential range behaviors for both films are very similar because the same thickness of silicon film was deposited. Galvanocharge and discharge cycling was performed for both the silicon film and LixSiOy//Si film with a current of 5 µA. What was observed in the cycling is LixSiOy//Si showed lower Coulombic efficiency and less stable performance compared to silicon. The lower Coulombic efficiency is consistent with the impedance measurement that LixSiOy continues to react with electrolyte and consumes the electrolyte. Another explanation for this behavior is the low electrical resistivity of LixSiOy and that it does not passivate the reduction of electrolyte.

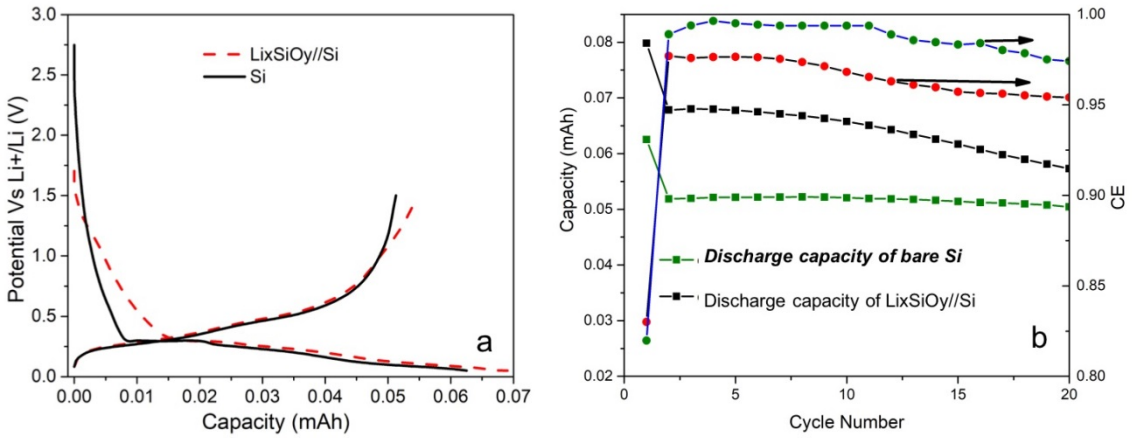

Figure II-169. a) charge and discharge profile of Si and LixSiOy//Si. b) Cycle performance and Coulombic efficiency of Si and LixSiOy//Si.

The mechanical and electrical properties and chemical reactivity of LixSiOy thin film were thoroughly investigated. Highly lithiated LixSiOy film is ductile and more resistant to fracture, but this still does not make

LixSiOy able to passivate the Si surface. Low electrical resistivity explains why LixSiOy is incapable of passivating the Si surface. Mechanical property is not a single criterion to judge whether SEI is stable; low chemical reactivity and low electrical conductivity are also important for SEI stability.

Chemical stability and reactivity of lithiated silicon LixSiy

The natural passivation layer of silicon is generally related to its history, environment, and handling on formation. The natural passivation layer is usually found to be about a 10-Å -thick layer of silica. More aggressive passivation regimes—for example, ozone treatment—can yield denser layers up to 30–50 Å thick. Previous theoretical work has indicated that this passivation silica layer reacts with electrolyte decomposition products around 900 mV to form Li4SiO4, which generally condenses and, over time, diffuses into the SEI layer [6]. Within the SEI layer exist the various breakdown products of the reactivity of the (lithiated) silicon surface with its environment. Besides silicates and siloxanes, various salt, binder, and solvent-based species have been identified. However, the lithiated silicon electrode is relatively nonhomogenous, on charge or discharge, and correlating the formation of specific species in the SEI with specific species in the silicon Zintl anode (or even local potential) is difficult because many species may have seen one or more reducing events or reacted with salt breakdown products (e.g., PF5). The structure/property relationships can be more easily determined by testing the reactivity under more-controlled conditions using lithiated silicon samples.

Using lithiated silicon materials as model silicon electrodes, the role of surface passivation, electrolyte additives, and electrolyte can be investigated as a function of state of charge. New insights into how the SEI layer is built and ages can be determined and used to better understand its limitations by the following: testing the reactivity of these model compounds against various cell components, then following the reaction product distribution—using MAS-NMR (29Si, 7Li, 31P) and other spectroscopic techniques—to correlate with state of charge, composition, and the various materials available to react.

The interface between the silicon electrode and electrolyte is a key point of contact in the electrochemical cell.

Silicon is well known to have an unstable SEI layer due, in part, to its reactivity at medium to high states of charge with many of the key components of the laminate and the electrochemical cell altogether. A synthetic effort was undertaken to make key model compounds based on stoichiometries in the Li-Si phase diagram (Figure II-170). We studied the inherent reactivity of the lithium silicides with battery components such as binders, electrolytes, and additives to directly isolate and elucidate some of the reactivity problems associated with Li-Si materials in a Li-ion battery. Synthetically, the materials are unstable to most oxide-based containers at elevated temperature and tantalum was found to be the most stable for use. Single-phase Li7Si3 could be isolated between 650°–760°C in a closed container to limit lithium loss via evaporation with limited time in the liquid region (> 750°C). Based on previous work, lithium and silicon phase identification and common impurities can be assigned effectively [7-9]. Powder X-ray diffraction showed that the samples, isolated from the correct range of temperature, were mainly Li7Si3, with small amounts of Li12Si7 and SiO2 depending on time at temperature, box atmosphere, length of time after cooling to analysis, and purity of silicon (a source of SiO2). Samples were noted by several research teams to self-discharge against small amounts of impurities due, in part, to active lithium availability. Raman and 29Si NMR were able to detect various amounts of amorphous SiO2 that seemed to track sample age and starting materials.

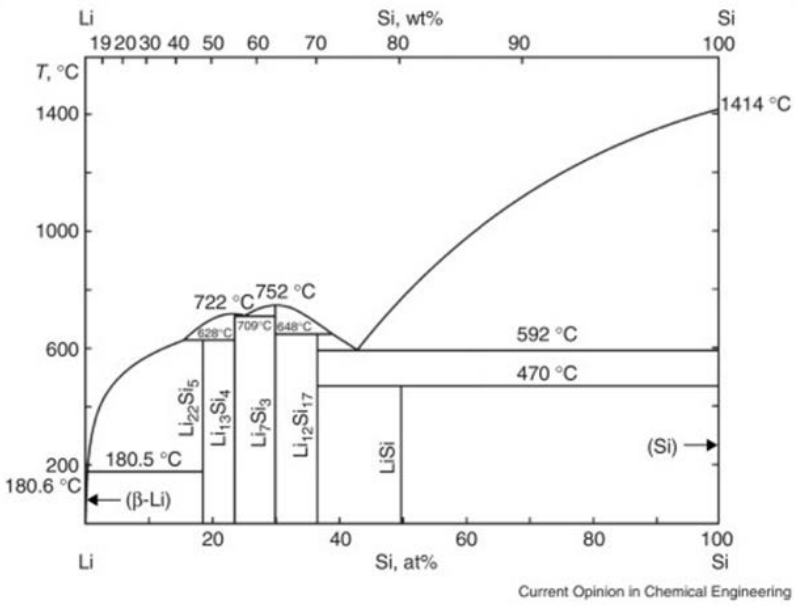

Figure II-170. Phase diagram for the silicon-lithium systems.

To date, X-ray diffraction and solid-state magic angle spinning (MAS) NMR spectroscopy have been used to qualitatively and quantitatively probe reactivity of the model compounds with typical binders used in Li-ion cells. NMR spectroscopy has previously been used [7,8] to effectively study the Li and Si phases in amorphous and crystalline phases of lithium silicides. Using this, the trends in 7Li and 29Si NMR can be used to follow the Li and Si inventory quantitatively pre- and post-treatment. The Li7Si3 model compound was treated with 10 wt.% PVDF (polyvinylidene fluoride) binder in an Ar glove box. Any reaction on the bulk material and the binder was followed by solid-state NMR in Figure II-171. A clear shift was observed for Li in 7Li to less Li per Si consistent with loss from Li7Si3 while affecting mainly the aliphatic carbon and protons of the PVDF binder without affecting the fluorine groups. The Li loss was also found to be consistent in Si NMR. Similarly, Li7Si3 model compound was also treated with 10 wt.% lithiated PAA (polyacrylic acid) binder. Only minor changes were observed in Si NMR and XRD (and Li NMR, data not shown), with a slight shift in the main peak to lower lithium content per Si, as well as a minor formation of Si-rich Li12Si7 phase in Figure II-172. The specific reaction sites on the binder molecules are currently under investigation. Overall, the results for the binder treatments were found to be consistent with the superior electrochemical performance of LiPAA binder over PVDF for silicon anodes, as noted by ANL's Cell Analysis, Modeling, and Prototyping (CAMP) team in their electrochemical evaluation studies.

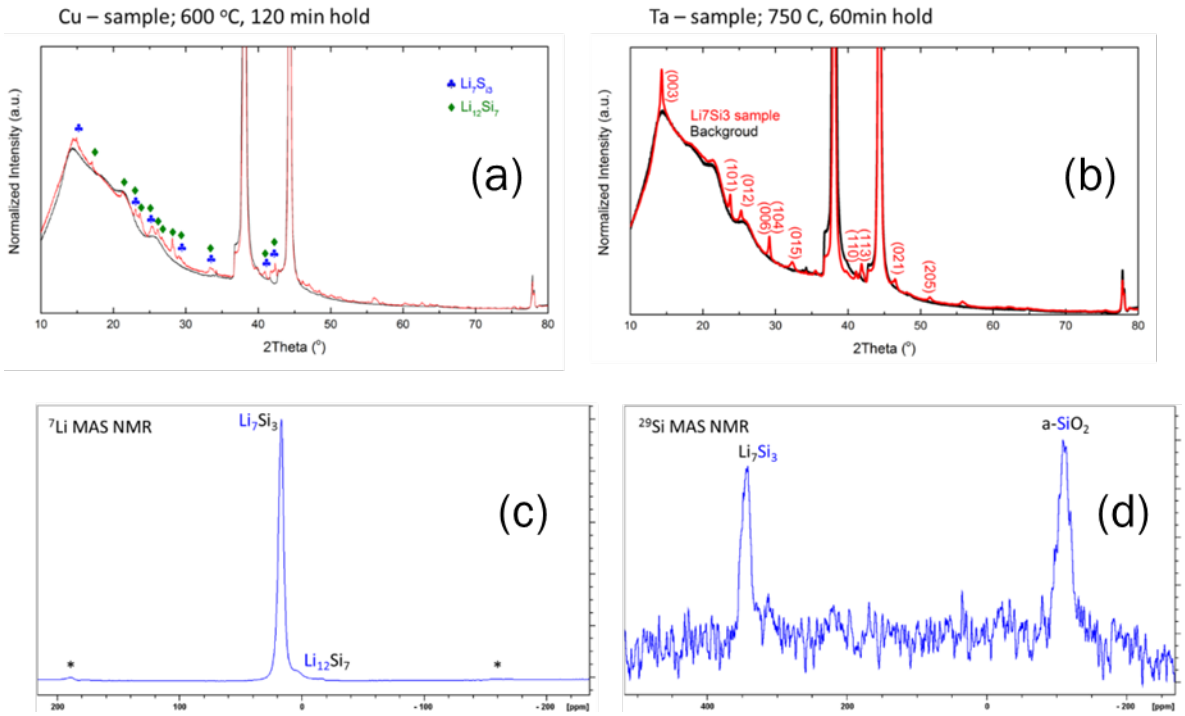

Figure II-171. Long- (XRD), a) and b) and short- (solid state NMR), c) and d) range characterization of Li7Si3 model compound.

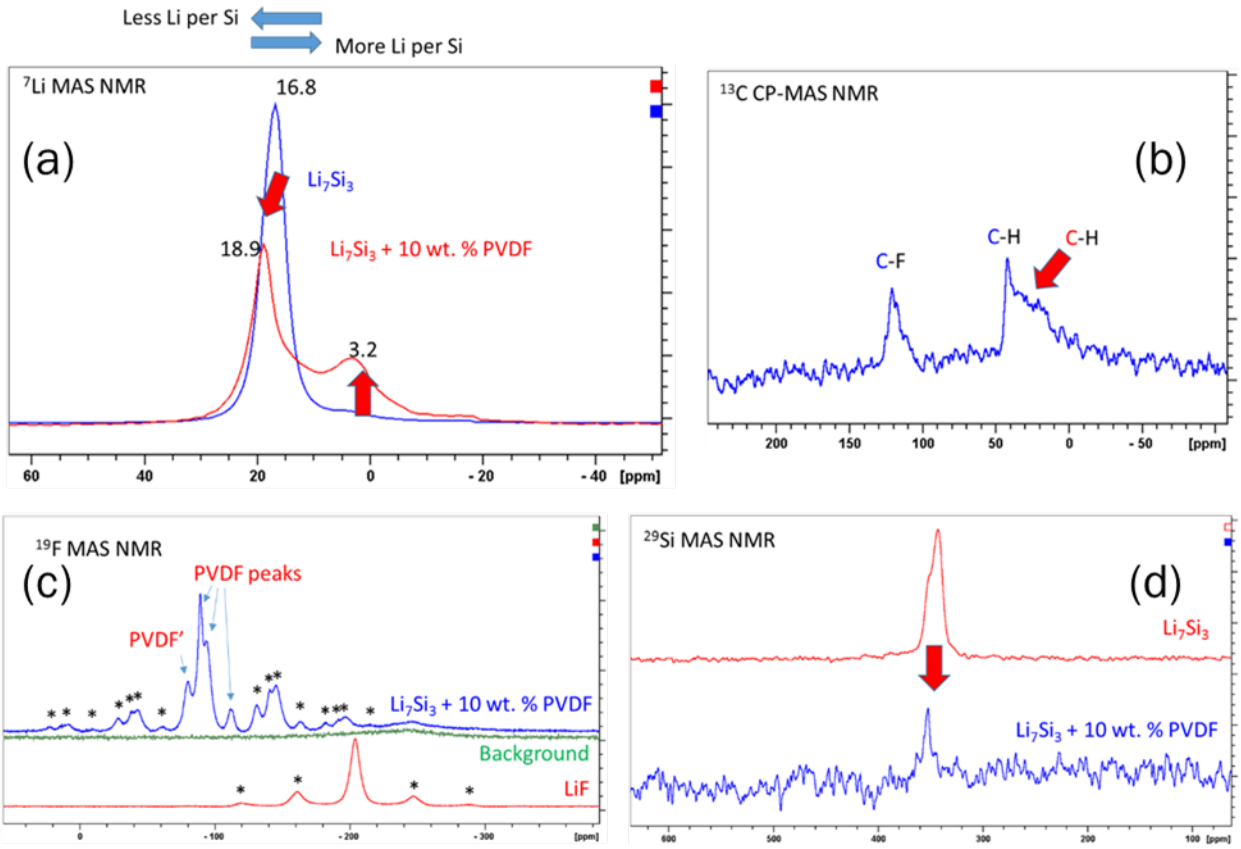

Figure II-172. Multinuclear solid-state NMR data of pristine and PVDF-treated Li7Si3.

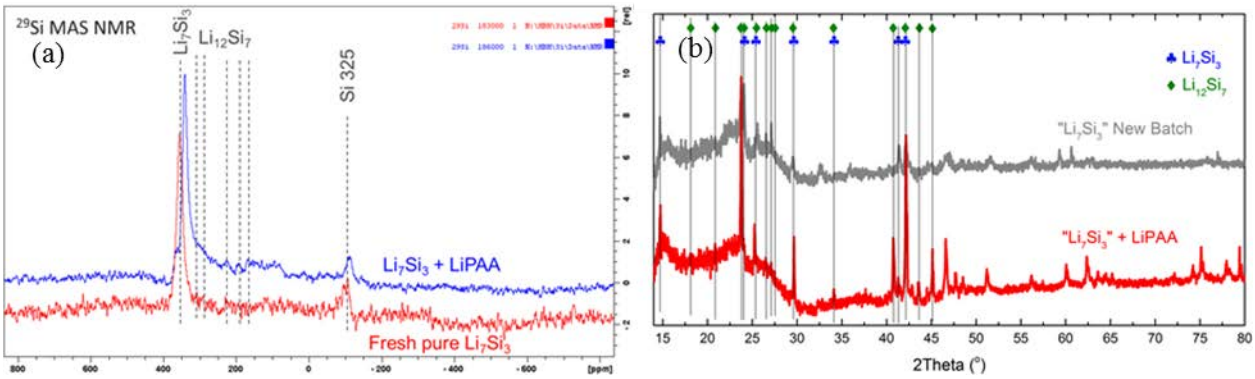

Figure II-173. Solid-state NMR (a) and XRD data (b) of pristine and LiPAA-treated Li7Si3. ANL, unpublished work.

Silicon-rich Li-Si model compounds have been successfully synthesized within bulk and powder forms for investigation of inherent reactivity of lithiated silicon at a single well-defined state of charge. The initial material chosen was Li7Si3, a composition associated with the plateau between 280–300 mV (vs Li). Synthesis and scale-up were carried out in Ta tubes under inert atmosphere using bulk silicon. NMR and XRD results suggest significant reactivity of the compound Li7Si3 vs. PVDF binder and only minor reactivity vs. lithiated PAA binder (Figure II-173). The former reaction is proposed to progress via the aliphatic protons of the binder, as opposed to the fluorine groups, whereas the latter results in minor lithium loss and surprisingly the associated formation of the crystalline Li12Si7 phase, the product of the slight oxidation of the electrode material, but not disproportionation or surface degradation.

Investigating the formation of SEI on model systems

Tin model electrodes

Tin presents a strong catalytic activity toward the organic-based electrolyte being responsible of a poor electrode passivation leading to continuous electrolyte reduction upon cycling [10,11]. A fundamental understanding of the kinetic processes occurring at the Sn/electrolyte interface will begin with a rational and basic study on the SEI components properties. We have undertaken this by designing three types of model electrodes, each differing in the content of oxygen at both bulk and surface level [12]. A schematic representation of the developed systems to be investigated is reported in Figure II-174. The "pristine" electrode consists of a commercially available high-purity tin metal foil, whereas the "melted" version has been obtained by melting the pristine tin foil in inert atmosphere (i.e., glove box environment), thus obtaining a model electrode with a lower content of oxygen dissolved in the bulk and a higher amount of SnO on the electrode surface. The "cleaned" version corresponds to an oxygen-free tin electrode, obtained by removing the SnO layer from the melted electrode by polishing. Chemical composition and structural properties have been confirmed by XRD, XPS, and soft X-ray absorption spectroscopy (sXAS) analysis.

The electrochemical analysis performed in 1M LiPF6 EC:DEC (1:2 wt.%) revealed surprisingly different passivating behavior most likely attributable to the presence of oxygenated species dissolved in the bulk of the model electrodes (see Figure II-174). It appears that a lower content of dissolved oxygen strongly improves the passivating behavior of the electrode, limiting the electrocatalytic activity of tin toward the reductive electrolyte decomposition. These results confirm our earlier observations that the surface film on the pristine Sn cannot prevent continuous electrolyte reduction and that a large fraction of the reaction products dissolves in the electrolyte.

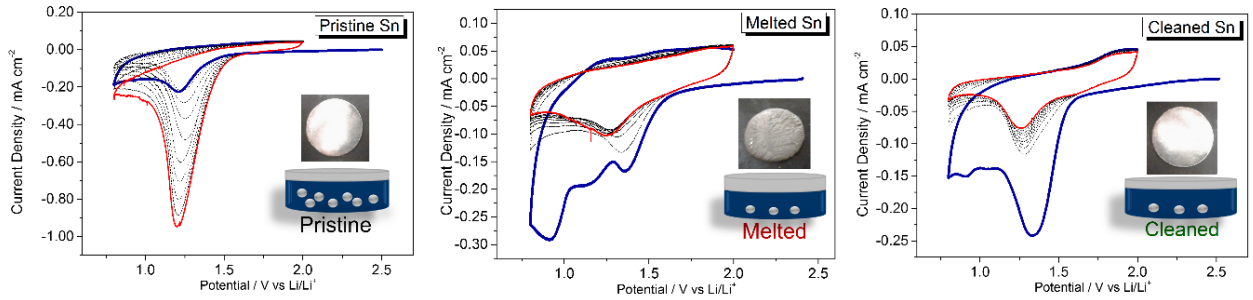

Figure II-174. Cyclic voltammetry of pristine, melted, and cleaned tin model electrodes swept from OCV to 0.8 V and back to 2 V in 1 M LiPF6/EC:DEC (1:2 wt%) electrolyte.

To gain insights into the mechanism of the electrolyte decomposition and SEI layer (re-)formation upon cycling, we investigated the surface layer film by FTIR.

The results, shown in Figure II-175, evidence a different film composition that is most likely responsible of the observed differences in the passivating behavior. Li2CO3 has been identified to be the main component in the surface layer. To investigate the role of Li2CO3 and the corresponding reaction mechanism of the electrolyte decomposition, electrochemical tests have been performed, employing single solvent-based electrolyte, such as 1M LiPF6, DEC. *Ex-situ* FTIR and XAS analysis clearly revealed that the formation of Li2CO3 is the result of the selective decomposition of EC. We observed that the passivating behavior of the tin electrodes can be strongly improved by avoiding the use of EC. In fact, all the three model electrodes cycled in DEC exhibit satisfactory passivating properties. However, despite the deleterious effect of EC, its decomposition and subsequent formation of Li2CO3 is not the ultimate cause leading to the poor passivating properties of the tin electrodes. The improved passivation properties observed for the melted and cleaned electrodes in EC:DEC-based electrodes relies on the presence of other compounds in the SEI as demonstrated in the FTIR spectra. In addition, we demonstrate that the use of additives in the electrolyte and the employment of engineered electrolyte formulations may also be an effective strategy for improving the surface layer stability during cycling. The role of LiF and Li2CO3 used as additives in the electrolyte has been investigated through cyclic voltammetry and *ex-situ* FTIR measurements. These preliminary results show improved passivating behavior of the tin electrodes in the presence of LiF and Li2CO3.

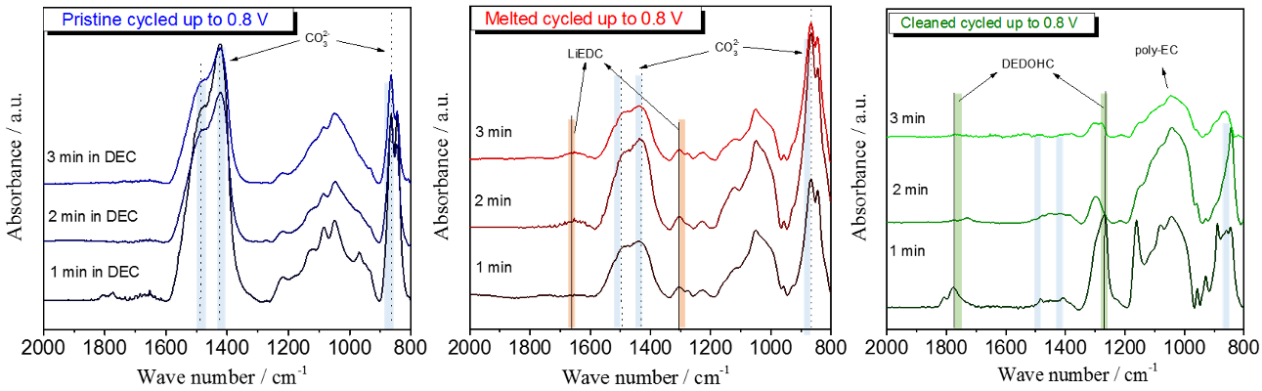

Figure II-175. *Ex-situ* FTIR analysis of pristine, melted, and cleaned tin model electrodes cycled up to 0.8 V in 1 M LiPF6/EC:DEC (1:2 wt%) electrolyte at different washing steps.

The interfacial properties occurring at the electrode/electrolyte interface of Sn, Si, and SiO2 have been analyzed by combining electrochemical investigation and surface chemistry analysis. Our results suggest that the poor passivating behavior of Sn electrodes can be mitigated by reducing oxide species dissolved in the bulk of the electrode and by formulating unique electrolyte compositions.

Artificial SEI Modified Silicon Model Electrodes

We believe that the stabilization of the SEI and the mitigation of the electrolyte reduction upon cycling may be mitigated by designing tailored artificial SEI with a proper thickness and chemical composition. The presence of an artificial SEI layer on model silicon electrodes not only can help improve interfacial properties of Si, but can also lead to a better basic understanding of the interfacial processes occurring at the Si/electrolyte interface. It has been reported that the main components of the silicon SEI are Li2O, Li2CO3, and LiF and contribute to the stability of the passivating film and the lithium-ion transport mechanism through the film [13,14]. To evaluate the effect of Li2O, Li2CO3, and LiF on the reactivity toward the electrolyte, thin films were deposited on p-type-doped Si (100) wafer model electrodes via the pulsed laser deposition (PLD) technique [15]. The main advantages of PLD can be summarized as follows: 1) conceptually simple—a laser beam vaporizes a target surface, producing a film with the same target's composition; 2) versatile—many materials can be deposited in a wide variety of gases over a broad range of gas pressures; and 3) fast—high-quality samples can be grown reliably in 10 or 15 minutes.

LiF, Li2O, and Li2CO3 thin films have a thickness ranging from 40 to 50 nm. Unfortunately, none of the thin films was smooth and perfectly planar. The film surface shows large drop-like features (micrometric dimension). The cyclic voltammetry (CV) measurements are within the 0.01–2.0 V potential range at a scan rate of 0.1 mV sec-1. Figure II-176 exhibits the first CV cycle. The enlarged potential region corresponds to the electrolyte decomposition region.

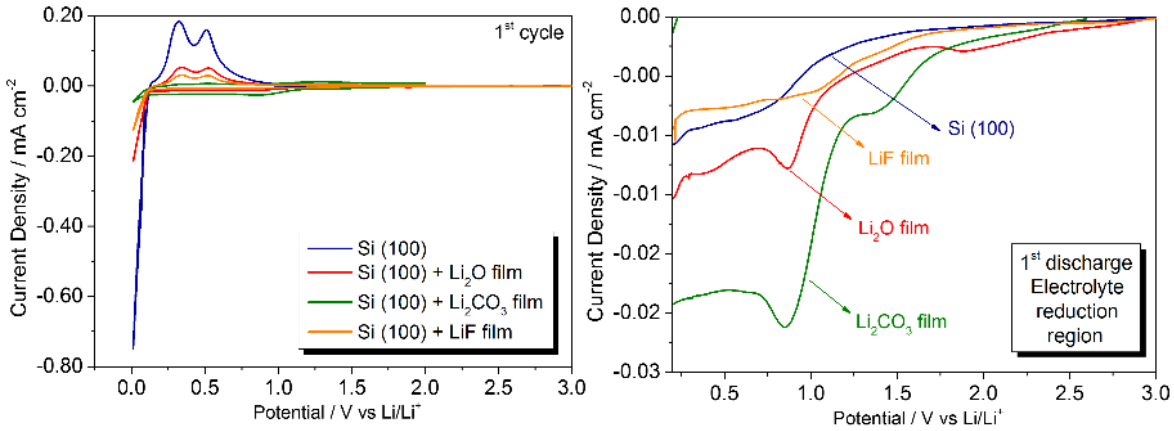

Figure II-176. Cyclic voltammetry of bare Si (100) wafer and comparison with the modified model electrodes with Li2O, Li2CO3, and LiF thin film deposited within the 0.01–2.0 V potential region. Enlarged potential region of the first reduction process.

Clearly, all the Si samples with the LiF, Li2O, and Li2CO3 thin film deposited on the surface inhibit the lithiation process, which is reflected by low lithiation and delithiation currents.

Interestingly, as shown in the enlarged potential region between OCV and 0.2 V, the presence of Li2CO3 and Li2O induces a higher cathodic current and total amount of cathodic charge with respect to the LiF-coated and pristine silicon wafer, most likely attributable to the altered reactivity of silicon toward the carbonate-based electrolyte.

Post-mortem SEM images clearly confirm that the presence of the thin solid films inhibits the (de-)lithiation as documented by fewer cracks in the Si electrodes when compared to the bare silicon wafer (see Figure II-177).

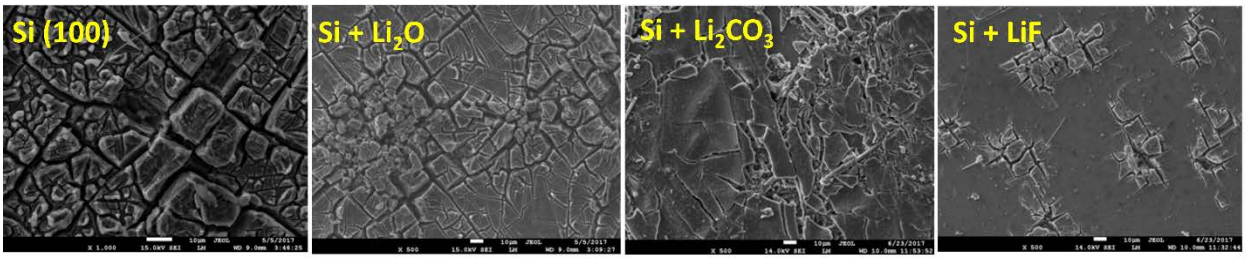

Figure II-177. Post-mortem SEM images of cycled Si (100) electrode the modified model electrodes with Li2O, Li2CO3, and LiF thin film deposited.

This study represents the preliminary step necessary for understanding the single components effect on the Si/electrolyte interfacial processes. Future work is needed to better understand the effect of the thickness on the surface-layer behavior [16].

Silicon oxide-coated model electrodes

The role of a native and artificially grown SiO2 layer on the surface chemistry of a Si electrode has been investigated. For this purpose, we used a Si(100) wafer with different oxide thicknesses (native oxide, 100-nm and 300-nm thermal oxides) as a model electrode. Electrochemical analysis and various spectroscopic and microscopic techniques have been applied to study the effect of the oxide layer on the interfacial processes occurring at the Si/electrolyte, oxide/electrolyte, and Si/oxide/electrolyte interface. The investigation is based on the assumption that the lithiation of the oxide layer may lead to the conversion of the surface oxide to Li2O and Si (Equation 1) or formation of silicate (Equation 2). On the other hand, SiO2 could also act as a barrier for the lithiation of the Si electrode because it is not a good Li+ conductor.

$$SiO_2 + 4\,Li + 4\,e^- \rightarrow Si + 2Li_2O \qquad 1$$

$$SiO_y + XLi^+ + Xe^- \rightarrow Li_xSiO_y \qquad 2$$

To evaluate the feasibility of these assumptions, we studied the lithiation mechanism and the composition and structure at the interface during cycling.

Figure II-178 shows the cyclic voltammetry of Si(100), 100-nm SiO2/Si(100), and 300-nm SiO2/Si(100) electrodes using 1.2 M LiPF6/EC:DEC (3:7 wt%) electrolyte. The results reveal that the cathodic current around 1 V increases and becomes broader as the oxide thickness increases. This may be attributable to both the conversion reaction as shown in Equation 1 and to the interfacial properties of the oxide layers leading to changes of the electrolyte reduction mechanism, similarly to what we observed in the presence of Li2CO3 and Li2O. As the potential is swept in the anodic direction, lower reversible capacity is observed as the oxide thickness increases.

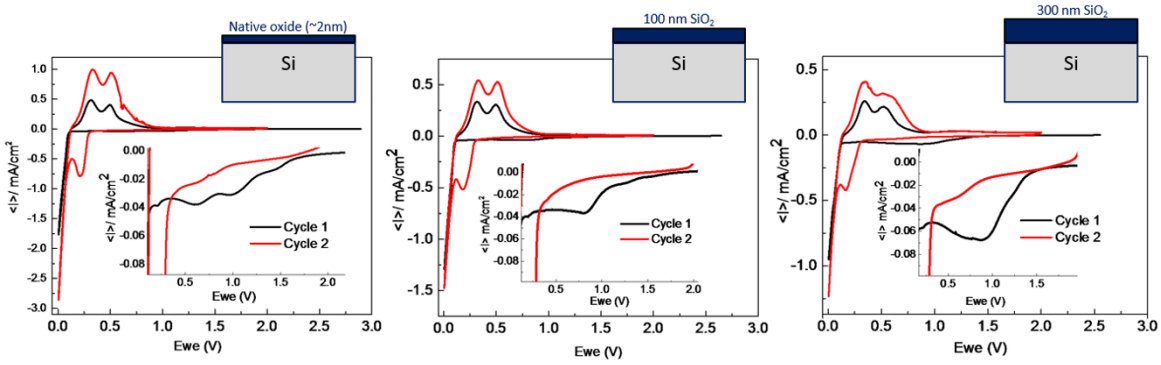

Figure II-178. Cyclic voltammetry of Si(100) wafer, 100-nm SiO2/Si(100), and 300-nm SiO2/Si(100) swept from OCV to 0.005 V and back to 2 V in 1.2 M LiPF6/EC:DEC (3:7 wt%) electrolyte.

Using spectroscopic and microscopic techniques such as attenuated total reflectance-mode Fourier Transform Infrared (ATR-FTIR) spectroscopy, XAS at ALS, XPS, *in-situ* X-ray reflectivity (XRR) at SLAC, and scanning electron microscopy-energy-dispersive X-ray spectroscopy (SEM-EDX), we studied the effect of the oxide layer on the interfacial properties and linked with the electrochemical results. The O K-edge XAS results reported in Figure II-179 shows that there is no formation of Li2O due to the conversion reaction. Although red shift is observed due to the lithiation process, both the Si and O K-edge features are different from the features of Li2SiO3 and Li4SiO4.

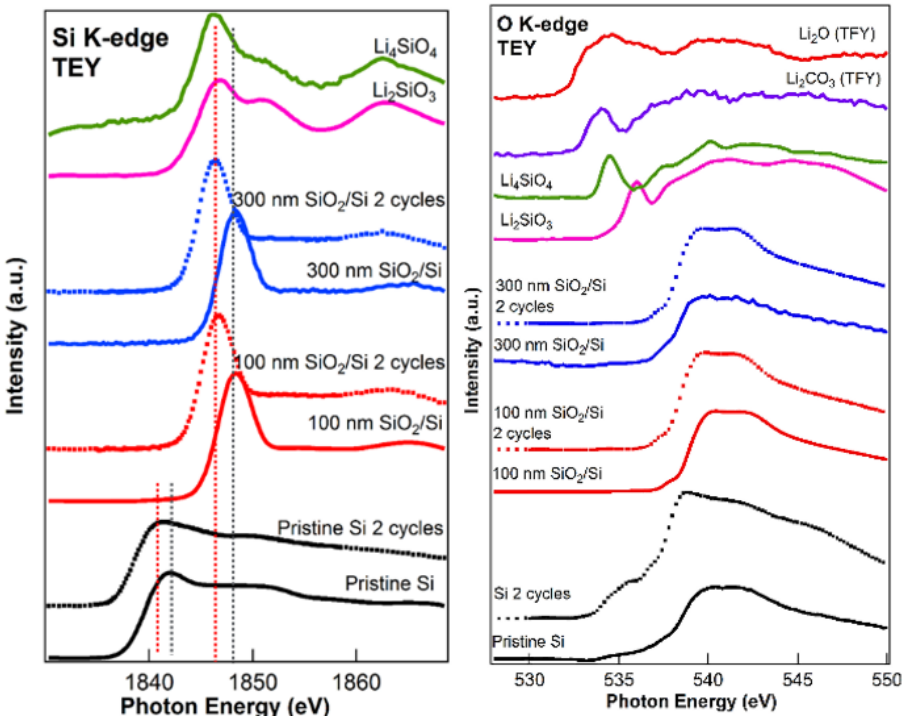

Figure II-179. Si (left) and O (right) K-edge XAS spectra of pristine Si(100) wafer, 100-nm SiO2/Si(100), and 300-nm SiO2/Si(100).

Our result suggests that the thermal oxide acts as a barrier for bulk lithiation and avoids the complete lithiation of the silicon electrode, which leads to the decrease in specific capacity. Hence, thinner oxides (5–20 nm) should be considered for model studies of the effect of the oxide on the interfacial properties.

The initial cycling of a lithium-ion battery results in the formation of a SEI layer between the electrolyte and the anode. This passivating layer, consisting of decomposition products from the electrolyte solution, is critical to the reliability and performance of the battery. The SEI must be both electronically insulating and ionically conductive—permeable to lithium ions yet resistant to electron flow. The mechanisms of SEI formation, stabilization, and evolution are still poorly understood. Moreover, reactivity and diffusivity of lithium present difficulties in SEI characterization, because many sputtering and milling techniques may significantly change chemical composition.

Artificially created simplified interfaces have enabled observation of the effect of SEI single components on the overall behavior of model Si electrodes. The Li2O, Li2CO3, and LiF thin films deposited on Si(100) wafers inhibited the lithiation and delithiation process. The electrolyte decomposition mechanism was also altered by the presence of the thin film and its effect on the Si surface reactivity. We believe that the artificial thin films may affect the charge and mass transfer processes.

In the same way, we demonstrated that the SiO2 film on the surface of silicon model electrodes presents a barrier for lithiation. No signs of conversion reaction could be detected. More work is needed to better understand the effect and role of surface layers on Si electrodes. Thinner oxide layers (5–20 nm) should be considered instead of thick films (100–300 nm) and such an effort is currently ongoing. Accordingly, thinner layers on LiF, Li2O, and Li2CO3 are also being investigated for an improved understanding of the kinetic processes occurring at tailored Si/electrolyte interfaces.

In the past months, we have adapted scanning-spreading resistance microscopy (SSRM) to characterize SEI (Figure II-180). Originally, SSRM was developed as a characterization technique to measure electron-carrier distribution in semiconductor materials. SSRM measures current when applying a bias voltage between the probe tip and sample. When operating the probe at forces that are orders of magnitude greater than other scanning probe techniques, the contribution of the contact resistance between tip and sample becomes minor and the resistance indicates the spreading resistance (Figure II-181), a material property related by the Maxwell equation, $R = \rho/4a$, where R is the resistance measured, ρ is the material-dependent spreading resistance, and a is the electrical radius of the probe. Using SSRM instrumentation on soft materials allows for SEI to be mechanically milled away laterally, giving resistivity measurements for the material located at that depth. Thus, the technique demonstrates high lateral and vertical resolution when characterizing SEI.

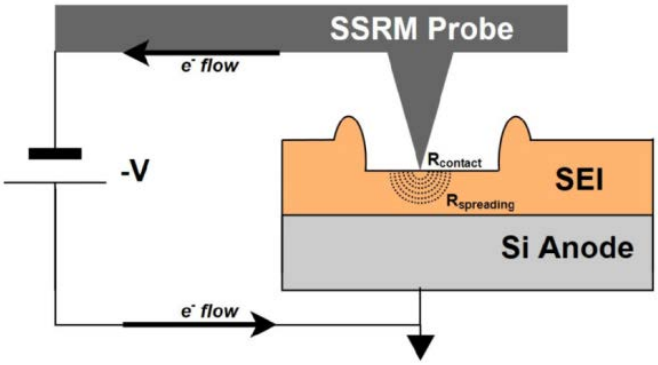

Figure II-180. Schematic depiction of SSRM instrumentation and mechanical milling of a sample.

To date, our characterization of SEI has focused on cycled silicon wafers prepared under varied cycling conditions. Preliminary results show that the SSRM profiling of SEI can quantitatively measure SEI thickness and semi-quantitatively assess lateral and vertical inhomogeneity of SEIs. Recent work depth-profiling SEIs with TOF-SIMS and XPS has shown agreement with conclusions from SSRM studies, and future work will begin to associate resistivity data with known SEI chemical compositions.

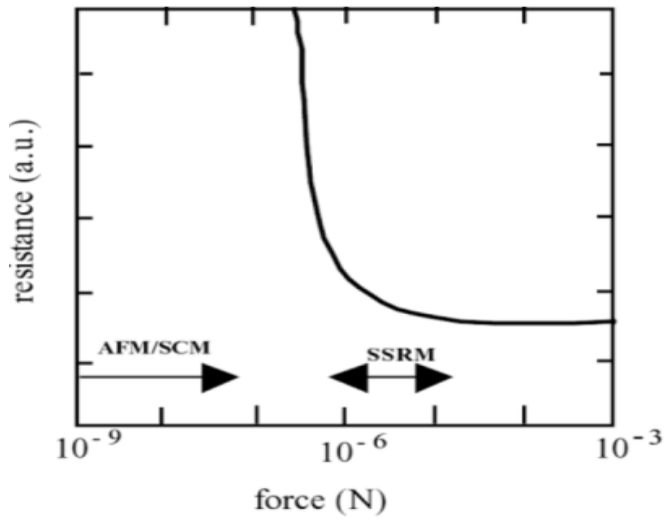

Figure II-181. Contact resistance as a function of applied probe force. Image from Kalanin, S. and Gruverman, A.L., *Scanning Probe Microscopy*, Springer (2007)

Figure II-182 shows an example of the SEI milling and resistance measurement. As milling depth (left panel) increases throughout the SEI layer to the underlying Si, the resistance decreases to the value of Si (higher SSRM signal converts to lower resistance). Figure II-183 shows two series of the SSRM resistance and SEI thickness measurements. The two SEI series show significant differences in both resistance and thicknesses, illustrating that the SEI electronic resistance depends sensitively on electrochemical cycling conditions and electrolyte compositions. Further understanding of SEI resistivity is expected with detailed chemical composition information.

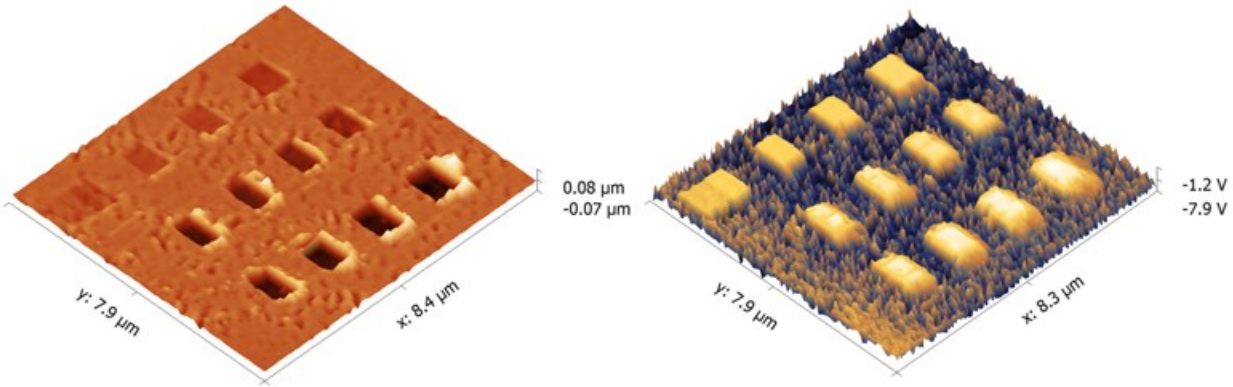

Figure II-182. Height (left) and resistance (right) channels showing the lateral and vertical resolution of the instrument. Deeper milling into SEI carried out under higher probe forces reveals SEI layers of significantly lower material resistance. In the resistance channel image at right, higher voltage is indicative of lower resistance.

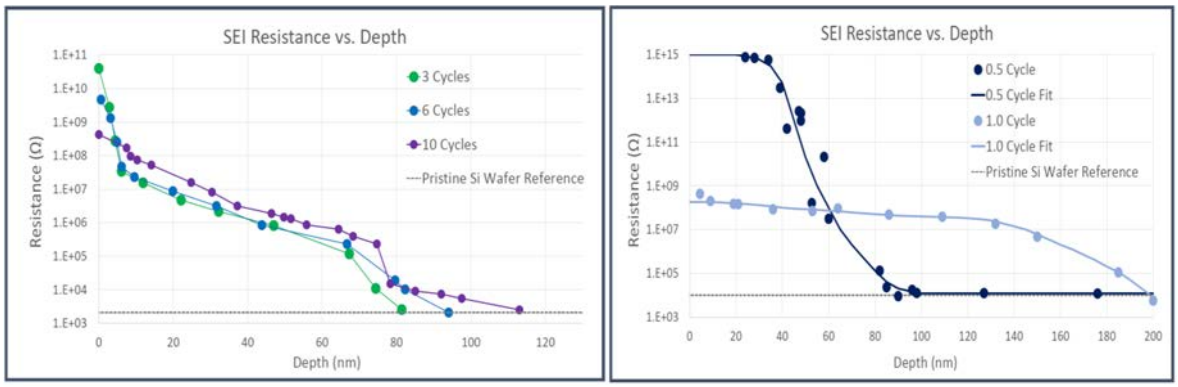

Figure II-183. Studies of resistance vs. depth for different sample series. The plot at left shows how SEI thickness and vertical homogeneity develops over repeated cycles. The plot at right shows the distinct resistance and thicknesses of the lithiated and delithiated phases of SEI formed in the original cycle. Thickness is calculated by measuring the depth at which Si wafer-substrate equivalent resistance is measured.

In-situ neutron reflectometry

In this work, we sought to provide insight into the role of FEC in SEI formation by characterizing the SEI growth *in situ* using neutron reflectometry (NR) and *ex situ* using infrared and X-ray photoelectron spectroscopies. In NR, the specular reflection of neutrons from an interface is measured as a function of the wave vector transfer, $Q = 4\pi\sin(\theta)/\lambda$, perpendicular to the sample surface. The angle of incidence θ is between the incoming neutron beam and the sample surface, and λ is the wavelength of the neutron. Analyzing the neutron reflectivity gives us information about the thickness and composition of the film layers. This ability to follow chemistry and composition has been used to follow the swelling of silicon anodes during alloying/dealloying with Li [17-19]. However, the real power of NR comes from the sensitivity of neutrons to low z components (i.e., H, Li, C, O, F), which makes it a good complementary method to X-rays.

The samples consisted of a 5-mm-thick, 2”-diameter silicon wafer coated with 20 nm of copper, which acts as a contrast layer, diffusion barrier, and current collector, with 50 nm of amorphous silicon deposited on top. These layers were grown following the SEISTa protocols and were demonstrated to cycle with the expected profile of amorphous silicon (see round-robin results). Li-coated TiZr was used as the counter electrode (half-cell-type configuration). TiZr (Ti0.47Zr0.53) was selected as the Li current collector for several reasons. First, TiZr is a null scatterer of neutrons and would not contribute to the NR spectrum. Second, TiZr is stable in contact with metallic Li and does not react electrochemically with Li. Long wires were bound to the Si and TiZr plates using silver epoxy (Illinois Tool Works), which was allowed to dry overnight. The silver epoxy was placed on the edge of the Si wafer to contact the Cu, which was spilled around the wafer during deposition. The epoxy was never in contact with the electrolyte. The components were assembled in a He-filled glove box located at the beamline (H2O < 1 ppm; O2 < 7 ppm). The electrodes were separated by a Teflon-coated Viton O-ring with a 0.8-mm cross-sectional diameter. The total cell volume is about 2.5–2.8 mL depending on the amount of Li on the TiZr. NR measurements were carried out on the liquids reflectometer (LR) at the Spallation Neutron Source (SNS) at Oak Ridge National Laboratory.

Figure II-184 shows representative NR data, along with the fits to the data. From the data in Figure II-184, it is clear that there are significant changes in the reflectivity profile as a function of cycling, as evident by the changes in peak position, corresponding to changes in layer thicknesses and compositions. From the fits, we can estimate layer thickness (based on the separation between the peaks) and layer composition (based on the intensity) and is reported as scattering length density, which is a measure of the nuclear cross-section of the layer. Figure II-185 shows a representation of the refined scattering length density (SLD) profile of the film at different states of charge versus layer thickness. These data show clear changes in layer thickness and composition. Figure II-186 summarizes the electrochemical data (black line) with the resulting Si and SEI

thicknesses and SLD values. The Si thicknesses were estimated from the electrochemical data and were used to confirm the modeling of the NR data. Extensive XPS characterization and IR characterization were performed to provide chemical specificity, and they support the interpretation of the refined SLD data.

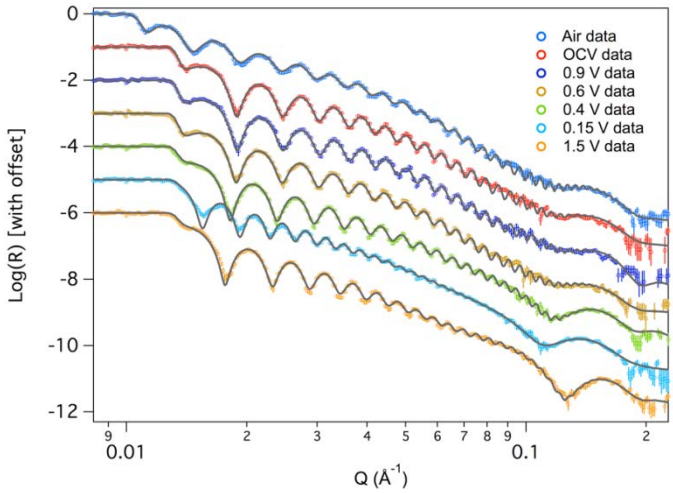

Figure II-184. NR data (data points) and fits (solid line) for representative data sets collected in this study.

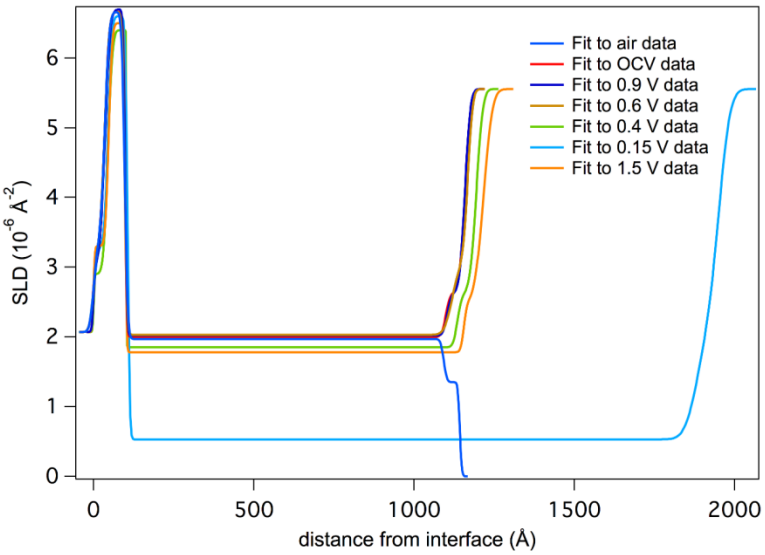

Figure II-185. Plot of the refined SLD profile of the film as a function of distance from the thick Si substrate.

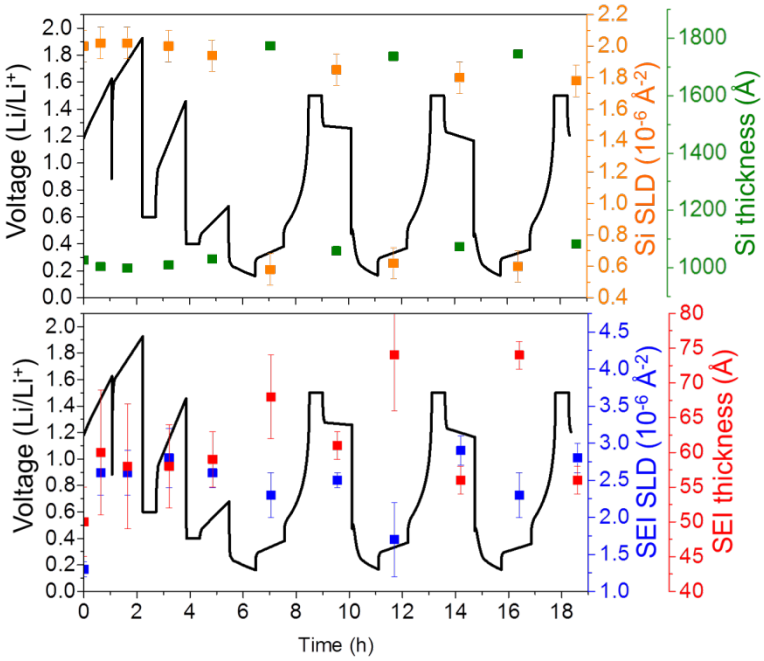

Figure II-186. Plots of SLD values and layer thicknesses as a function of state of charge for silicon (top) and the SEI (bottom).

After cell assembly, the electrode was in contact with the electrolyte for 90 minutes during the setup and alignment procedure. During this time, there is clear evidence for the modification of the silicon surface from the reaction with the electrolyte. Indeed, the SLD of the interface layer increased from 1.3±0.1 to 2.6±0.3 along with a small increase in the layer thickness (50±5 to 60±9 Å). Given that the SLD values of almost all of the components of the electrolyte (D, C, O, P, or F) have high bound coherent scattering lengths (6.6, 6.6, 5.8, 5.1, 5.6 fm, respectively), this layer has to have a high concentration of Li or H (from the FEC) that have negative scattering lengths that would account for the relatively low SLD of the layer.

This change in the surface chemistry is consistent with the measured XPS data where there is a decrease in the concentration of the Si-O bonds at higher binding energies (~104 eV) and C on the surface. In addition, there is an increase in F (Figure II-186), P, and Li, which has to originate from the LiPF6 or FEC (in the case of F) given the lack of binder in these cells. Analysis of the F1s spectra is consistent with the presence of Li-PF6 (690 eV, 6% F species) and Li-P-O-F (687.6 eV, 94% of F species) due to this salt decomposition. In addition there is a change in the C1s spectra (Figure II-187, Figure II-188), from the sample exposed to air, where there is the growth of C=O-type species (287.1 eV) from the decomposition of the solvent or FEC along with the loss of C-O species. Together, these data indicate that the Si-O is being chemically reacted away, likely by the HF originating from the well-documented $LiPF_6$ reaction with water [20]. But this reaction layer is not simply dissolving, it is being replaced with a new reaction layer formed by the decomposition of salt and solvent species. Such a reaction layer has been observed before for Si electrodes in aprotic solvents and likely represents the initial stages of SEI formation [21-24].

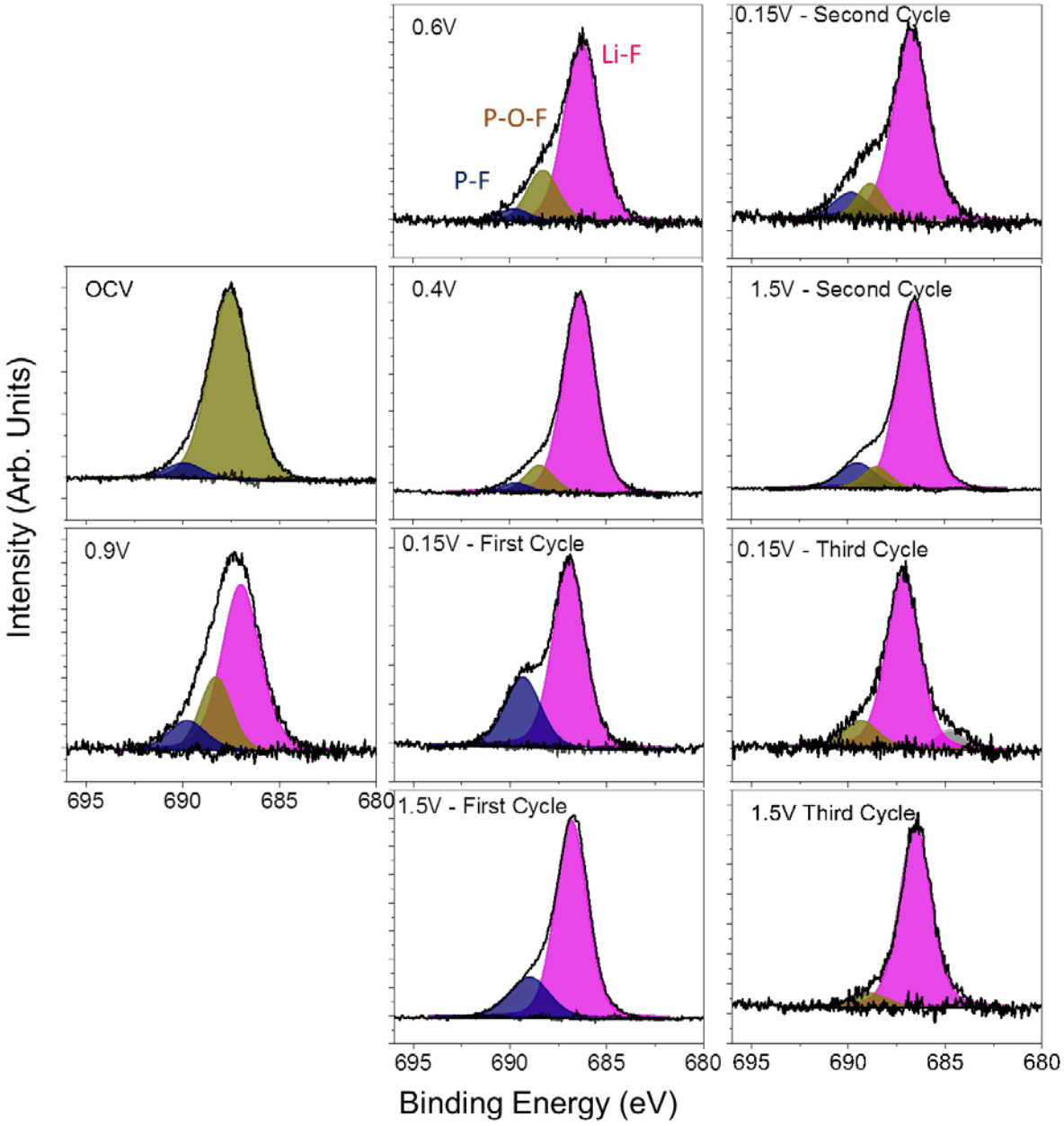

Figure II-187. F1s XPS data collected for the Si electrodes as a function of cycling.

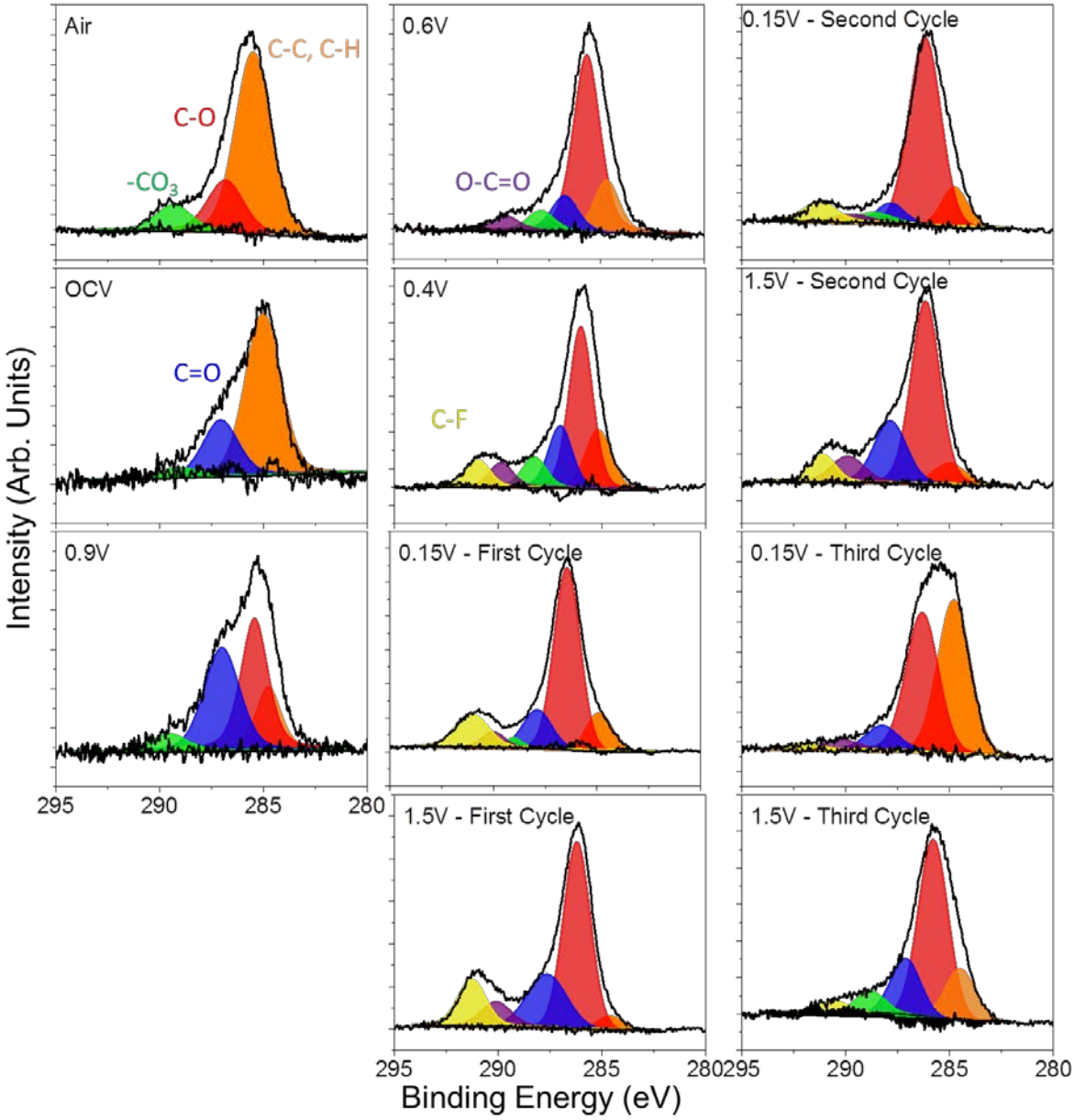

Figure II-188. C1s XPS data collected for the Si electrodes as a function of cycling.

With further lithiation, we start to see evidence of changes in the Si electrode chemistry at potentials less than 0.6 V vs. Li/Li+. Indeed, at 0.6 V, there is a small 8 Å increase in Si thickness (versus as-prepared Si) and a corresponding decrease in the Si layer SLD from 2.0±0.1 to a calculated SLD of 1.93, consistent with Li entering the Si electrode and causing the layer to swell and a decrease in SLD due to the negative SLD of Li (-0.87). At 0.4 V, the thickness increased by 24 Å and the SLD decreased further to 1.85, again consistent with the extent of lithiation and the expected swelling of Li:Si alloys reported by Chevrier [25].

At these stages of lithiation, there is no apparent change in the SEI SLD or thickness based on the NR data. However, there are clear changes in the XPS data, again due to the formation of more C-O species (~285.5 eV) and O=C-O moieties (~288 eV), from the breaking of C=O bonds in the solvent or polymerization of the cyclic carbonates, and additional LiF at the expense of residual Li-P-F and Li-P-O-F species. In addition, we see

evidence for a higher binding-energy C1s species (290 eV) attributed to C-F species due to the reduction of FEC. Interestingly, there is a low-energy Li1s peak (56.2 eV) evident in the XPS data measured for the 0.4-V sample in addition to the main LiF peak at 56.7 eV. This new feature corresponds to Li-Si bonding in the anode that is detectable due to its concentration and the thin SEI (59±4 Å), which does not attenuate the excited photoelectrons. These data support the validity of the SEI thickness derived from the analysis of the NR data, i.e., the SEI is less than 10 nm thick. If the SEI were more than 10 nm thick, it would attenuate and block the XPS signal from the Si. Finally, these data differ from previous XPS reports [26] of FEC-based electrolytes over Si(100) electrodes, which were dominated by C-C/C-H species, not C-O bonds, indicating a different reaction mechanism over crystalline Si versus the amorphous Si here.

Cycling of Li-Si anodes (0.15–1.5 V)

NR data collected for the silicon anode with extensive Li cycling revealed significant and dynamic changes in the SEI thicknesses and composition. The electrodes were repeatedly cycled from a Li-Si stoichiometry close to LiSi to a Li0.1Si. Upon lithiation, the electrode swelled to about 1778±8 Å (from 995±6 Å), causing a significant decrease in the Si SLD; during delithiation, the Si returned to a thickness of 1056±4 Å due to slight irreversibility of the cell. The fitted SLD values and thicknesses determined for the silicon layer were in good agreement with the predicted values based on the electrochemical measurements. Furthermore, the XPS data collected on these electrodes revealed that the Si2p spectra still contained information demonstrating the presence of reduced Si from the electrode. Together, these data confirm that the SEI is less than 10 nm thick and again supports the validity of our NR model.

The more interesting data were obtained for the SEI layer. As demonstrated in Figure II-186, the SEI layer increased in thickness by about 12–13 Å with lithiation, and its SLD decreased to about 2.3±0.3 (from 2.6±0.3). Upon delithiation, the SEI shrunk to its prelithiation thickness and the SLD increased to 2.5±0.1. This swelling and contracting of the SEI layer thickness is consistent with the “breathing” reported for silicon anodes measured by previous NR studies, as well as XPS, TOF-SIMS, and atomic force microscopy studies [21, 22, 27-30]. We should note that in the case of the FEC, the thickness of the SEI “breathes” in the opposite direction of the non-FEC case. The expansion upon lithiation with FEC would indicate that the electrolyte continues to decompose as the layer expands. Given the apparent increase in organic signal and the higher SLD, this would indicate solvent decomposition.

XPS analysis of the Si electrodes at various states of charge revealsignificant changes in the SEI chemistry with cycling that follow the changes in SEI SLD that occur with the electrode “breathing.” Figure II-189 shows a graphical representation of the atomic concentrations of C and F as a function of state of charge and SLD measured for the SEI. The C concentration data are a surrogate for the organic portion of the SEI, while the F signal (originating primarily from LiF) represents the inorganic portion of the SEI. From these data, it is clear that at states of high lithiation (0.15 V), the organic fraction of the SEI increases while the inorganic fraction decreases. Upon delithiation, the concentration of the species reverses and the inorganic fraction of the SEI dominates the SEI layer while the organic content is reduced. These data indicate that the growth in the SEI thickness with lithiation originates from the further decomposition of organic solvent molecules, resulting in a more organic layer as the Si swells. Upon delithiation, this deposited organic layer is decomposed off or dissolves into the electrolyte. The addition of Li and H (from the FEC) drives the SLD of the SEI down during lithiation, while the removal of these species leads to the increase in SLD during delithiation.

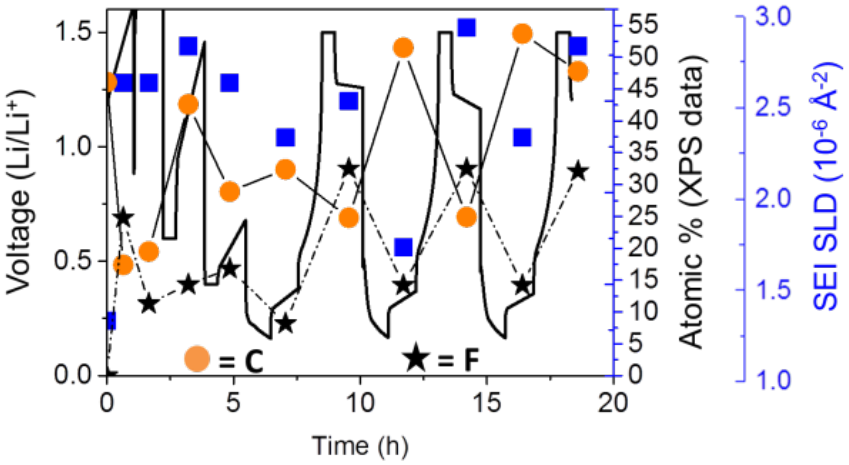

Figure II-189. Plot of C and F atomic concentrations as a function of state of charge and SEI SLD.

Fitting the individual spectra collected for each sample reveals additional changes to the SEI chemistry of both the organic and inorganic components. The C1s data, originating from the organic component (Figure II-188), show that the resulting SEI is still dominated by C-O bonding (~286 eV), from the polymerization of the cyclic carbonates or polymerization of the C=O bonds from the solvent, along with small concentrations of C-F (~291 eV) from the decomposition of the FEC, C=O, O-C=O, -CO3, and C-C/C-D from the decomposition of the solvent. The presence of the carbon-oxygen moieties is supported/confirmed by the O1s data. The spectral contribution from each of these species stays relatively constant with cycling—only the absolute concentration changes. These data confirm the dissolution of the organic species upon delithiation. In addition, the O1s data show for the 0.15 V data the growth of a new species with a binding energy around 530.2 eV attributed to the formation of inorganic Li-O. This Li-O has been reported previously [31]. Interestingly, this Li-O disappears during charging, indicating the possible formation of a reactive oxygen species that is known to decompose organic electrolytes [32, 33].

The F1s data, originating from the inorganic components, show a more dynamic chemistry than the C-containing components. For all the samples, the F1s spectra are dominated by Li-F-type species. However, with lithiation, there appears to be an increase in P-F components due to decomposition and trapping of the LiPF6 salt (evident in the high binding-energy F1s species (~689.5 eV). This is confirmed with the P2p data, which show more P-F species (~137.6 eV) at 0.15 V. Upon charging, the P-F revert to more P-O-F (688.3 eV for F1s and ~135 eV for P2p data). Together, this indicates a continuous decomposition of the Li salt in addition to the solvent molecules described above.

The above data demonstrate the structure and composition of the SEI formed over a silicon anode with lithium cycling in an electrolyte that contains FEC as an additive. At this point, we will compare these data with previously reported NR data collected for electrolytes without FEC in the same electrochemical experiment. The SEI thickness and SLD values for these two samples are summarized graphically in Figure II-190. The OCV for both sets of data show a similar condensed layer with a thickness of about 50 Å, indicating a similar starting point to SEI formation. However, with cycling, the previous non-FEC-containing electrolyte data showed the immediate formation of SEI layer with a thickness between 180 and 250 Å. This SEI layer shows a similar “breathing” as observed for data in this publication; however, the magnitude of the breathing (60 Å) is significantly larger than the 13 Å measured for the FEC-containing electrolyte. The thickness of the SEI measured with NR is less than what was observed for a composite electrode reported by Xu et al., (> 15 nm) during lithiation. However, the SEI was observed to thin upon delithiation [27], similar to what we report here. This may indicate additional reactions promoted by binders and carbon additives influencing SEI chemistry. Reported TOF-SIMS data indicate that the SEI grown over a silicon thin film with FEC when delithiated was about 6.6 nm thick, in good agreement with these results [28]. The TOF-SIMS data for the same electrode

lithiated show an SEI that is 35.1 nm thick [28]. This is consistent with our results, although we note the actual SEI thickness in this report [28] is probably quite a bit thinner than the 35.1 nm. This is evident by examplining the Si2p signal from Si(0) present in their XPS data and is most likely due to an artifact, in there sample, caused by using a different sputter rate for the two SEI layers, resulting in changes in the SEI chemistry organic/inorganic composition.

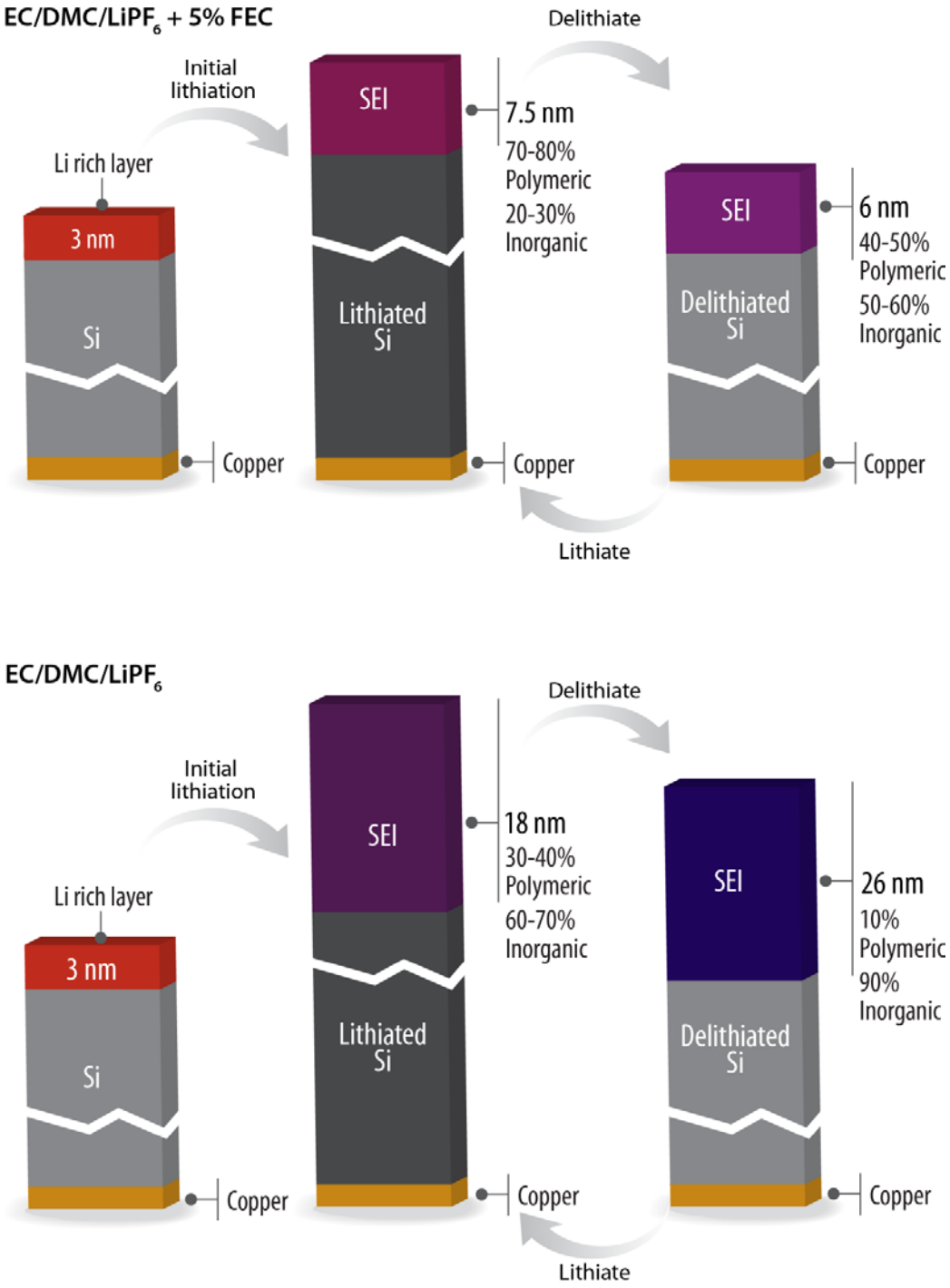

Figure II-190. Graphical summary of SEI layer chemistry grown on silicon with and without FEC.

Comparing the SEI compositions of the two NR studies reveals that the non-FEC-containing electrolyte SEI (at 0.12 V vs. Li/Li+) comprised similar functionality (i.e., C-C/C-H, C-O, C=O, O-C=O, -CO3, LiF, POF, etc.), but the organic content comprised about 4 at% carbon. There was a correspondingly larger increase in inorganic F-containing species (~ 80% LiF) in non-FEC electrolyte. This is significantly fewer organic components than the SEI produced from FEC-containing electrolyte. These results are in good agreement with previous XPS studies that show a more organic SEI with FEC [26-28, 34-38] and NMR studies showing more LiF without FEC [39,40].

Together, these data provide insights into how FEC aids in the cycling of Si anodes for use in Li-ion batteries. The preferential reduction of FEC at potentials greater than 0.9 V (vs. Li/Li+) forms a more organic C=O-containing polymeric surface layer. This layer is not the SEI, but the SEI precursor, which further reacts at 0.6 V to form a layer with more C-O species from the polymerization of cyclic carbonates (likely from FEC) [30, 39-41]. The SEI layer formed during charging from the electrolyte without FEC comprises more inorganic LiF-like components. The polymeric FEC electrolyte effectively keeps the SEI from growing to the ~200 Å level measured for cells without FEC.

Despite this clear improvement in SEI chemistry, problems are still evident with the FEC. In both cases, the "breathing" measured for the SEI originates from the consumption of electrolyte. This consumption lowers the cycle life of the electrode by consuming the electrolyte needed to move Li ions. The thinner FEC SEI and the much reduced "breathing" of the FEC SEI results in less electrolyte consumption, resulting in the reported increase in cycle life of Si-based electrodes. However, even these batteries fail with time as the FEC gets consumed. These data would indicate that a more flexible SEI built from polymeric-like C-O functionality that forms at much higher potentials (vs Li/Li+) may provide a pathway to improve the cycleability of Si anodes.

In summary, following the SEI formation using *in-situ* neutron reflectometry revealed detailed insights to the role that FEC plays in forming a stable SEI over silicon anodes. The FEC selectively binds and reacts to the silicon surface at potentials around 0.9 V, forming a polymer-rich condensed layer on the silicon surface. In contrast, without FEC, the layer becomes more LiF-like. Upon further lithiation, the chemistry evolves from a clear polymerization of the C=O functionality to more Li-O-C-D polymeric species with a low concentration of LiF (~14 at% vs 80% without FEC). Furthermore, the FEC-based SEI is only ~70 Å thick versus ~200 Å without FEC. Together, this indicates that the FEC-based electrolytes are thinner and built from likely more-flexible polymeric components. This thin polymeric layer likely has the flexibility to bend and readjust that LiF-based SEI layers would not. This flexibility ensures a more stable SEI that would more effectively passivate the surface against further reactions. However, the FEC-based SEI is still not perfect because it changes in thickness and composition with cycling (0.15–1.5 V). Specifically, the layer becomes more organic at high states of lithiation and more inorganic at low states of lithiation due to dissolution of the polymer. This points to a potential path to make a more stable SEI through the formation of a more cross-linked, less-soluble polymer SEI, possibly through the design of more elaborate, large-molecule, fluorinated carbonates. It would be interesting to explore this chemistry as a function of oxide surface termination and polymer binders, which likely also participate in the SEI passivation reaction and change the reaction mechanism(s).

Probing the nanoscale heterogeneity of SEI on cycled amorphous silicon using tip-enhanced Raman spectroscopy

SEI on silicon typically is reported to be in the range of tens of nanometers and can be compositionally heterogeneous. Normal vibrational spectroscopy techniques such as micro-Raman and FTIR are widely used, but they only provide chemical information at a relatively bulk scale, typically much greater than 100 nm from the sample surface. This makes it harder for getting information from the real SEI, which can be on the order of tens of nanometers. Tip-enhanced Raman spectroscopy (TERS) is based on the field enhancement of the Raman active signal locally at regions close to the tip. The configuration of the sample and its relative position to the Raman laser and tip is illustrated in Figure II-191. The Raman cross-section is enhanced at least several orders of magnitude due to resonance coupling between surface plasmon modes (of the tip) and the electromagnetic field of the excitation laser. In this report, we provide preliminary results on characterization

of SEI on cycled amorphous silicon using TERS. This method is highly complementary to the IR data collected at LBNL.

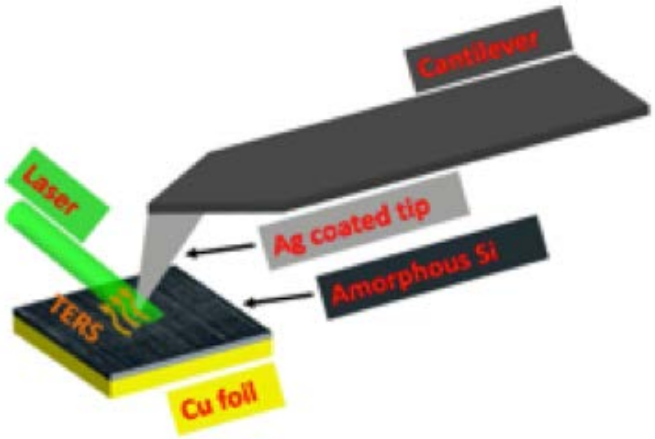

Figure II-191. Schematic picture of the TERS setup for studying SEI on silicon.

An amorphous silicon sample of 80 nm thick on a copper current collector was cycled 5X and 20X times using Gen-2 electrolyte (Sample # Gabe-1609 SiC CHYS, GY-0206 Cell-D-20cyc, 1.5V–0.05V EC/DMC in 1.2M LiPF6). Amorphous Si samples were sputter-deposited at ORNL and cycled as per the procedure finalized by the SEIsta round-robin team. TERS experiments were conducted using a HORIBA Nano Raman Platform integrated with AIST-NT's SPM system, as shown in Figure II-192. The laser wavelength was 532 nm and the objective was 1.5/100X. The setup was modified to work under argon atmosphere for studying SEI on samples under inert condition. A special Ar-compatible antechamber was designed (not shown) for preparing and transferring the sample for TERS experiments. The silicon tip used for TERS is 7 nm in diameter and sputter-coated with 2 nm of chromium as an adhesion layer, followed by a 40-nm Ag layer and 1.5-nm aluminum protection layer.

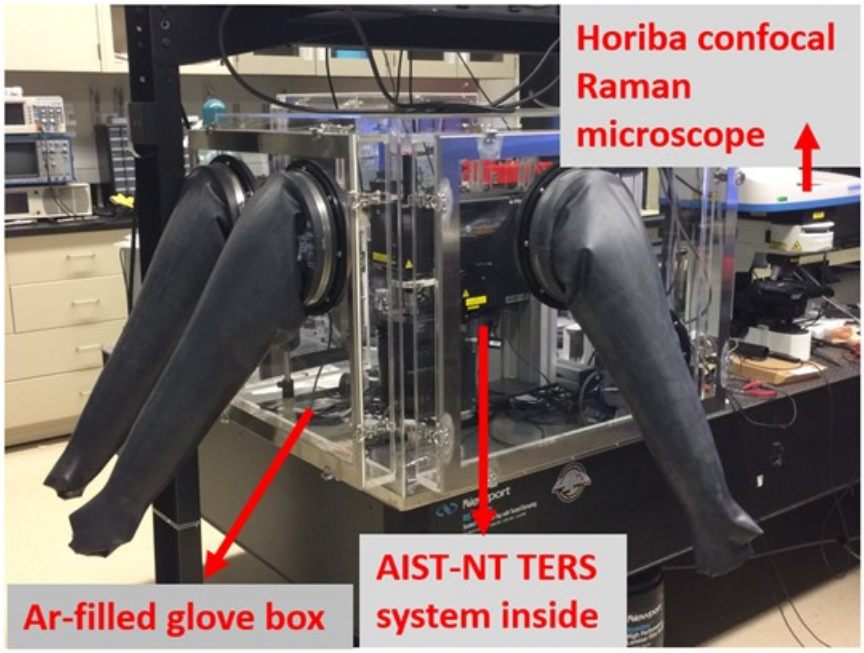

Figure II-192. Image of ORNL's TERS setup operated under argon atmosphere.

As a proof-of-principle example of the usefulness of TERS, we compare below in Figure II-193 a normal micro-Raman signal with TERS for the same sample (cycled amorphous silicon). The standard micro-Raman spectrum (red) shows only the normal silicon Raman bands at 521 nm, whereas the TERS (black) shows several additional peaks coming exclusively from the Raman active SEI on Si. For example, the band at 1,052 cm-1 is assigned to siloxane (Si-O-Si) stretch. Peaks between 1,100 cm-1 and 1,600 cm-1 are most likely from the R-OCOO-M or R-Si (R is methyl group and M is Li+ or Si) [41,42]. The TERS signal shown above has an enhancement factor of around 103. However, under optimized conditions, the enhancement factor would be on the order of 105. Figure II-194 shows the TERS signal from 20X cycled amorphous silicon collected under argon atmosphere. The maximum peak intensity occurs at 1,372 cm-1, which could be assigned to symmetric CH3 stretch. The two peaks at 1,436 and 1,458 cm-1 are due to asymmetric stretch of CH3. The band at 1,552 cm-1 is attributed to -COO asymmetric stretch. The 1,697 cm-1 peak is an overtone of -COO deformation at ~650 cm-1 and CH3 rocking mode (at ~1,050 cm-1). The existence of those bands clearly indicates that these spectral information originate from the SEI on silicon that are otherwise not visible under normal Raman or FTIR. We are currently analyzing the detailed peak positions with their relative enhancement factor, which will be reported shortly as a journal paper.

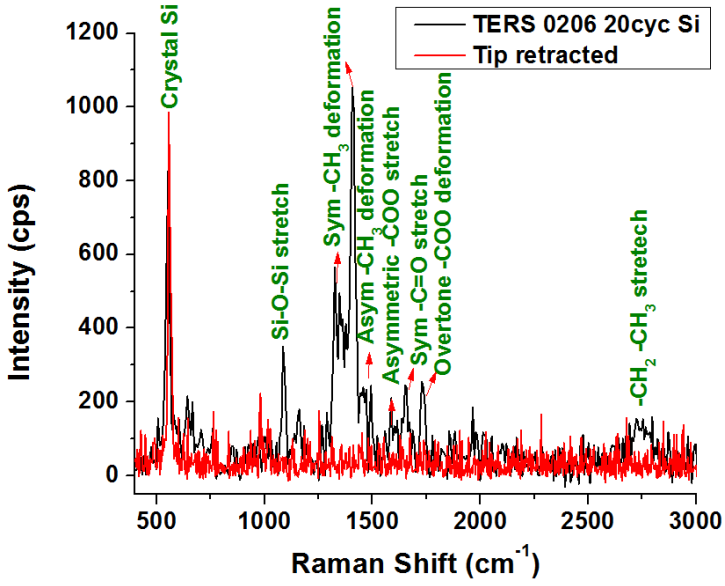

Figure II-193. Comparison of micro-Raman signal with TERS for the same sample (cycled amorphous Si).

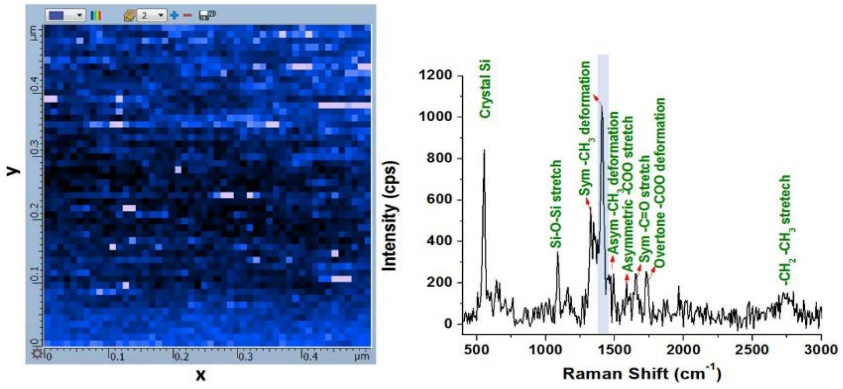

Figure II-194. Shows the TERS results for amorphous silicon cycled 20X. We notice several peaks apart from the silicon coming from the tip centered around 521 cm-1. The peak at 1,372 cm-1 is from CH3 symmetric deformation in CH3-COO components. Using the integration of this peak, the CH3-COO components can be mapped in a 500-nm X 500-nm region.

In the future, TERS analysis will be combined with FTIR, micro-Raman, TOF-SIMS, and XPS analysis to provide a more comprehensive picture of the SEI morphology and its spatial heterogeneity and distribution. This will help to resolve the issue of various chemical phases that preferentially form in the surface region of the SEI versus bulk and their relative abundancies. TERS measurements are being planned on chemically passivated and electrochemically lithiated SiO2/Si wafers in collaboration with LBL and NREL to provide insights into the subsurface chemical structure the SEI and its spatial variability across the thickness.

Conclusions

The first year of the SEISta project has shown that there is a critical need for standardization of research samples and procedures if the understanding of the SEI on silicon is to progress. Even with all team members using the same electrolytes, current collectors, and counter electrodes, getting comparable data is very difficult because of the way the silicon sample is treated, its life history, and minor variations in cell assembly. SEISta will continue to focus on the need for standardization and consistent and repeatable experimental data. In FY18, a standardized cell confirmation will be employed to ensure that some of the variation observed in the FY17 round robin is eliminated. Also, close attention to the experimental timing needs to be a focus for any experiments. The samples that are transported from laboratory to laboratory need to be examined and experiments carried out in timely fashion. The delays caused by minor equipment issues, across the partners, resulted in up to 6 months difference in data collection and contributed to the delay of Milestone 2 and probably added to the variation between samples seen in the round robin. This clearly had an impact on data spread and on the surface chemistry of the sputtered silicon samples.

The unexpected complexity of the basic reactivity of the silicon and silicon oxides with simple organic materials and the salts in the electrolyte has added to the silicon SEI story. All of the silicon samples examined show some form of reactivity with Gen 2 electrolytes. Exploring and understanding the limits of this will be a focus for FY18, specifically understanding what the surface-electrolyte interface looks like before electrochemistry begins so that SEI formation can be better understood.

The nature of the silicon, oxide coatings, and density, for example, clearly have an impact on both the fundamental chemistry of the electrolyte reaction and the ongoing electrochemical behavior of the SEI. In the next year, we will focus on exploring this interaction and the ways it affects the formation and growth/stabilization and solubility of the SEI components in well-characterized systems.

The SEISta team will also be more interactive with the Silicon Deep Dive project using their "top-down" approach and the understanding gained to help tailor both our choice of samples and experiments moving forward.

Key Publications

1. “Fundamental Studies of Silicon-based Electrodes for Li-Ion Batteries – SEISta Program” DOE Hydrogen Program and Vehicle Technologies Program Annual Merit Review, Washington, DC, June, 2017.
2. I. Hasa, T. Otani, T. Homma, P. N. Ross, R. Kostecki, "Surface Reactivity of a Tin Electrode in Organic Carbonate Electrolytes", 2017/9/1, ECS Meeting Abstracts
3. A. M. Haregewoin, L. Terborg, L. Zhang, J. Guo, P. N. Ross, and R. Kostecki, “Fundamental Understanding of the Effect of Polymer Binder on the Interfacial Properties of Si-Electrode Model Systems. 2017/9/1, ECS Meeting Abstract 143
4. Atetegeb Meazah Haregewoin, Lydia Terborg, Liang Zhang, Sunhyung Jurng, Brett L. Lucht, Jinghua Guo, Philip. N. Ross and Robert Kostecki, “The Electrochemical Behavior of Poly 1-Pyrenemethyl Methacrylate (PPy) Binder and its Effect on the Interfacial Chemistry of a Silicon Electrode”, Journal of Power Sources, submitted

5. Coyle, J., Apblett, C. A., Stoldt, C., “Composition and Structure of Lithium Silicate Thin Film Electrolytes Deposited by Radio Frequency Magnetron Sputtering”, 229th ECS, San Diego, CA, May 29-June 2nd, 2016
6. Coyle, J., Stoldt, C., Apblett, C., “Initial Irreversible Capacity Loss Mitigation Through Engineered SEI Layer on Silicon Electrode”, 231st ECS, New Orleans, LA, May 28-June 1st, 2017
7. Coyle, J., Apblett, C., Brumbach, M., Ohlausen, A., Stoldt, C., “Structural and Compositional Characterization of RF Magnetron Co-Sputtered Lithium Silicate Films: From Li2Si2O5 to Lithium-Rich Li8SiO6”, JVST A, JVSTA-A-17-242, accepted.
8. Burrell, AK. "Silicon Where to Now?" Plenary Talk Advance Automotive Battery Conference June 19-2017
9. Burrell, AK. "Silicon Where to Now?" Plenary Talk Power Our Future The 3rd International Forum on Progress and Trends in Battery and Capacitor Technologies, Vitoria, Spain July 2017

References

1. Abramowitz, S.; Acquista, N.; W. Levin, I., Infrared matrix spectra of lithium fluoride. J. Res. National Bur. Stand. 1968, 72A, 487–493.
2. Burtsev, A. P.; Bocharov, V. N.; Ignatov, S. K.; Kolomiitsova, T. D.; Sennikov, P. G.; Tokhadze, K. G.; Chuprov, L. A.; Shchepkin, D. N.; Schrems, O., Integral intensities of absorption bands of silicon tetrafluoride in the gas phase and cryogenic solutions: Experiment and calculation. Opt. Spectrosc. 2005, 98, 227–234.
3. Dupré, N.; Moreau, P.; De Vito, E.; Quazuguel, L.; Boniface, M.; Bordes, A.; Rudisch, C.; Bayle-Guillemaud, P.; Guyomard, D., Chemistry of Materials 28 (8), 2557–2572 (2016).
4. Radvanyi, E.; De Vito, E.; Porcher, W.; Jouanneau Si Larbi, S., Journal of Analytical Atomic Spectrometry 2014, 29 (6), 1120–1131.
5. Martinez de la Hoz, J. M.; Leung, K.; Balbuena, P. B., ACS Applied Materials & Interfaces 2013, 5 (24), 13457–13465.
6. Hubaud, A. A.; Yang, Z. Z.; Schroeder, D. J.; Dogan, F.; Trahey, L.; Vaughey, J., J. Power Sources 2015, 282, 639.
7. Key, B.; Bhattacharyya, R.; Morcrette, M.; Seznec, V.; Tarascon, J.-M.; Grey, C. P., J. Am. Chem. Soc. 2009, 131 (26), 9239–9249.
8. Key, B.; Morcrette, M.; Tarascon, J.-M.; Grey, C. P., J. Am. Chem. Soc. 2011, 133 (3), 503–512.
9. MacKenzie, K.; Smith, M. E., Multinuclear Solid-State Nuclear Magnetic Resonance of Inorganic Materials, Volume 6, 1st Edition.
10. Lucas, I. T.; Syzdek, J.; Kostecki, R., Electrochem. Commun. 2011, 13, 1271–1275.
11. Ayache, M.; Lux, S. F.; Kostecki, R., J. Phys. Chem. Lett. 2015, 6, 1126–1129.
12. Qiao, R.; Lucas, I. T.; Karim, A.; Syzdek, J.; Liu, X.; Chen, W., Adv. Mater. Interfaces 2014, 1, 1–6.
13. Schroder, K. W.; Celio, H.; Webb, L. J.; Stevenson, K. J., J. Phys. Chem. C. 2012, 116, 19737–19747.
14. Sina, M.; Alvarado, J.; Shobukawa, H.; Alexander, C.; Manichev, V.; Feldman, L., Adv. Mater. Interfaces 2016, 3, 1–10.

15. Perea, A.; Gonzalo, J.; Afonso, C. N.; Martelli, S.; Montereali, R. M., Appl. Surf. Sci. 1999, 138–139, 533–537.

16. Li, C.; Gu, L.; Maier, J., Adv. Funct. Mater. 2012, 22, 1145–1149.

17. Wang, H.; Downing, R. G.; Dura, J. A.; Hussey, D. S., Chapter 6: In situ Neutron Techniques for Studying Lithium Ion Batteries. In Polymers for Energy Storage and Delivery: Polyelectrolytes for Batteries and Fuel Cells; ACS Symposium Series, American Chemical Society: 2011; Vol. 1096, pp 91–106.

18. Jerliu, B.; Hüger, E.; Dörrer, L.; Seidlhofer, B. K.; Steitz, R.; Oberst, V.; Geckle, U.; Bruns, M.; Schmidt, H., Volume Expansion during lithiation of amorphous silicon thin film electrodes studied by in-operando neutron reflectometry. J. Phys. Chem. C 2014, 118, 9395–9399.

19. Seidlhofer, B.-K.; Jerliu, B.; Trapp, M.; Hüger, E.; Risse, S.; Cubitt, R.; Schmidt, H.; Steitz, R.; Ballauff, M., Lithiation of crystalline silicon as analyzed by operando neutron reflectivity. ACS Nano 2016.

20. Lux, S. F.; Chevalier, J.; Lucas, I. T.; Kostecki, R., HF formation in LiPF6-based organic carbonate electrolytes. ECS Electrochem. Let. 2013, 2, A121–A123.

21. Fears, T. M.; Doucet, M.; Browning, J. F.; Baldwin, J. K. S.; Winiarz, J. G.; Kaiser, H.; Taub, H.; Sacci, R. L.; Veith, G. M., Evaluating the solid electrolyte interphase formed on silicon electrodes: A comparison of ex situ X-ray photoelectron spectroscopy and in situ neutron reflectometry. Phys. Chem. Chem. Phys. 2016, 18, 13927–13940.

22. Veith, G. M.; Doucet, M.; Baldwin, J. K.; Sacci, R. L.; Fears, T. M.; Wang, Y.; Browning, J. F., Direct determination of solid-electrolyte interphase thickness and composition as a function of state of charge on a silicon anode. J. Phys. Chem. C 2015, 119, 20339–20349.

23. Veith, G. M.; Baggetto, L.; Sacci, R. L.; Unocic, R. R.; Tenhaeff, W. E.; Browning, J. F., Direct measurement of the chemical reactivity of silicon electrodes with LiPF6-based battery electrolytes. Chem. Comm. 2014, 50, 3081–3084.

24. Browning, J. F.; Baggetto, L.; Jungjohann, K. L.; Wang, Y.; Tenhaeff, W. E.; Keum, J. K.; Wood, D. L.; Veith, G. M., In situ determination of the liquid/solid interface thickness and composition for the Li ion cathode LiMn1.5Ni0.5O4. ACS Appl. Mater. Interfaces 2014, 6, 18569–18576.

25. Chevrier, V. L.; Dahn, J. R., First principles model of amorphous silicon lithiation. J. Electrochem. Soc. 2009, 156, A454–A458.

26. Vogl, U. S.; Lux, S. F.; Crumlin, E. J.; Liu, Z.; Terborg, L.; Winter, M.; Kostecki, R., The mechanism of SEI formation on a single crystal Si(100) electrode. J. Electrochem. Soc. 2015, 162, A603–A607.

27. Xu, C.; Lindgren, F.; Philippe, B.; Gorgoi, M.; Björefors, F.; Edström, K.; Gustafsson, T., Improved performance of the silicon anode for Li-ion batteries: Understanding the surface modification mechanism of fluoroethylene carbonate as an effective electrolyte additive. Chem. Mater. 2015, 27, 2591–2599.

28. Schroder, K.; Alvarado, J.; Yersak, T. A.; Li, J.; Dudney, N.; Webb, L. J.; Meng, Y. S.; Stevenson, K. J., The effect of fluoroethylene carbonate as an additive on the solid electrolyte interphase on silicon lithium-ion electrodes. Chem. Mater. 2015, 27, 5531–5542.

29. Shen, C.; Wang, S.; Jin, Y.; Han, W.-Q., In situ AFM imaging of solid electrolyte interfaces on HOPG with ethylene carbonate and fluoroethylene carbonate-based electrolytes. ACS Appl. Mater. Interfaces 2015, 7, 25441–25447.

30. Breitung, B.; Baumann, P.; Sommer, H.; Janek, J.; Brezesinski, T., In situ and operando atomic force microscopy of high-capacity nano-silicon based electrodes for lithium-ion batteries. Nanoscale 2016, 8, 14048–14056.

31. Xu, K., Electrolytes and interphases in Li-ion batteries and beyond. Chem. Rev. 2014, 114, 11503–11618.

32. Younesi, R.; Veith, G. M.; Johansson, P.; Edstrom, K.; Vegge, T., Lithium salts for advanced lithium batteries: Li-metal, Li-O2, and Li-S. Energy & Environmental Science 2015, 8, 1905–1922.

33. Veith, G. M.; Dudney, N. J.; Howe, J.; Nanda, J., Spectroscopic characterization of solid discharge products in Li-air cells with aprotic carbonate electrolytes. J. Phys. Chem. C 2011, 115, 14325–14333.

34. Dalavi, S.; Guduru, P.; Lucht, B. L., Performance enhancing electrolyte additives for lithium ion batteries with silicon anodes. J. Electrochem. Soc. 2012, 159, A642–A646.

35. Bordes, A.; Eom, K.; Fuller, T. F., The effect of fluoroethylene carbonate additive content on the formation of the solid-electrolyte interphase and capacity fade of Li-ion full-cell employing nano Si-graphene composite anodes. J. Power Sources 2014, 257, 163–169.

36. Etacheri, V.; Haik, O.; Goffer, Y.; Roberts, G. A.; Stefan, I. C.; Fasching, R.; Aurbach, D., Effect of fluoroethylene carbonate (FEC) on the performance and surface chemistry of Si-nanowire Li-ion battery anodes. Langmuir 2012, 28, 965–976.

37. Nguyen, C. C.; Lucht, B. L., Comparative study of fluoroethylene carbonate and vinylene carbonate for silicon anodes in lithium ion batteries. J. Electrochem. Soc. 2014, 161, A1933–A1938.

38. Young, B. T.; Heskett, D. R.; Nguyen, C. C.; Nie, M.; Woicik, J. C.; Lucht, B. L., Hard X-ray photoelectron spectroscopy (HAXPES) investigation of the silicon solid electrolyte interphase (SEI) in lithium-ion batteries. ACS Appl. Mater. Interfaces 2015, 7, 20004–20011.

39. Michan, A. L.; Divitini, G.; Pell, A. J.; Leskes, M.; Ducati, C.; Grey, C. P., Solid electrolyte interphase growth and capacity loss in silicon electrodes. J. Am. Chem. Soc. 2016, 138, 7918–7931.

40. Michan, A. L.; Leskes, M.; Grey, C. P., Voltage dependent solid electrolyte interphase formation in silicon electrodes: Monitoring the formation of organic decomposition products. Chem. Mater. 2016, 28, 385–398.

41. Arreaga-Salas, D. E.; Sra, A. K.; Roodenko, K.; Chabal, Y. J.; Hinkle, C. L., Progression of solid electrolyte interphase formation on hydrogenated amorphous silicon anodes for lithium-ion batteries. J. Phys. Chem. C 2012, 116, 9072–9077.

42. Socrates, G., Infrared and Raman Characteristic Group Frequencies: Tables and Charts. John Wiley & Sons: 2004.

II.B.5 Development of Si-based High-Capacity Anodes (PNNL)

Ji-Guang Zhang, Principal Investigator
Pacific Northwest National Laboratory
902 Battelle Blvd, Mail Stop K2-44
Richland, WA 99352
Phone: 509-372-6515
E-mail: Jiguang.Zhang@pnnl.gov

Jun Liu, Co-Principal Investigator
Pacific Northwest National Laboratory
902 Battelle Blvd, Mail Stop K2-44
Richland, WA 99352
Phone: 509-375-4443
E-mail: Jun.Liu@pnnl.gov

Prashant N. Kumta, Co-Principal Investigator
University of Pittsburgh
815C Benedum Hall
3700 O'Hara Street
Pittsburgh, PA 15261
Phone: 412-648-0223
E-mail: pkumta@pitt.edu

Tien Duong, Technology Manager
U.S. Department of Energy
Phone: 202-586-7836
E-mail: Tien.Duong@ee.doe.gov

Start Date: October 1, 2015 End Date: September 30, 2017
Total Project Cost: $1,190,000 DOE share: $1,190,000 Non-DOE share: $0

Project Introduction

Silicon has been extensively studied as a high-capacity anode for next-generation high-energy Li-ion batteries. However, fast capacity fade still greatly limits its practical application. A large volume change during lithiation and delithiation causes pulverization and subsequent loss of electrical contact, repeated breaking/formation of the solid electrolyte interphase (SEI) and continuous consumption of electrolyte.

In this project, we combined micron-sized Si with nanoporosity (mSi-np) generated by a low-cost process with a conformal high quality carbon coating on the surface of porous Si to enable stable operation of a Si-based anode. The mSi-np provides nanoporosity to allow intrinsic volume expansion and still retain a low surface area. Carbon coating enables high first-cycle efficiency (FCE) and high coulombic efficiency (CE). The target capacity is 1000 mAh/g for the Si-based anode (including Si, carbon additive, and binder) in the high loading condition (>3 mAh/cm^2) required for electric vehicle (EV) applications. We take advantage of PNNL's state-of-the-art material synthesis and characterization capabilities to optimize the structure of Si at both the particle level and electrode level. The stability of the SEI layer was systematically investigated by in situ microscopic analysis. Our partner, University of Pittsburgh (UPitt), applied their extensive experience in this field to synthesize Si-based nanocomposites using high-energy mechanical milling and other low-cost methods. The

best Si anode developed in this work was combined with the optimized binder/electrolyte and matched with a high-capacity cathode in a full-cell configuration.

Objectives

The objectives of this project are to advance the fundamental understanding of the degradation mechanism of Si-based anodes, including the mechanical and electrochemical stability, and develop high-energy, long life silicon (Si)-containing anode materials using low-cost synthesis approaches to enable their practical application in Li-ion batteries for plug-in hybrid electric vehicles and EVs.

Approach

- Develop micron-sized Si nanoparticles with nano pores and high quality carbon coating by three approaches:
    - Develop a low temperature (210°C) aluminothermic reduction of SiO_2 using an eutectic salt mixture of $AlCl_3$ and $ZnCl_2$.
    - Synthesize micron-sized porous silica as the precursor of thermic reduction using microemulsion self-assembly to improve the tap density as well as the electrochemical performance of Si anodes.
    - Synthesize a hierarchically structured Si/multi-walled carbon nanotube (MWNT) composite as the precursor of thermic reduction to accommodate the swelling of silicon particles and stabilize its structural and electrolyte integrity.
- Use high-energy mechanical milling of silicon oxides with different reducing agents and electrodeposition to generate Si – lithium conducting nanocomposite material.

Results

1.1 Micron-sized porous Si (p-Si) anodes synthesized by low temperature aluminothermic reduction

A low temperature (210°C) aluminothermic reduction process has been developed to synthesize p-Si with addition of a eutectic salt mixture of $AlCl_3$ and $ZnCl_2$, which not only serves as the mediator to reduce the reaction temperature, but also as reactant that enables reduction through a unique reaction route. The development has two main advantages. First, it greatly reduces the thermite reaction cost by lowering the process temperature. Second, with carbon pre-coating on the porous SiO_2 precursor, the final product of carbon coated porous Si (p-Si@C) can have the desired morphology and porous structure and has good electrochemical performance. Figure II-195 shows the synthesis process, structural characterization, and electrochemical performance of p-Si@C. Pure Si was obtained after the aluminothermic reaction and acid washing. The porous structure of the SiO_2 precursor was maintained in the final product. Scanning electron microscopy (SEM) showed highly porous Si spheres with a pore size of ~30–50 nm. p-Si@C electrodes delivered a high specific capacity of ~2100 mAh/g (based on the active material of Si) after the formation cycles. After 250 cycles, the p-Si@C was able to retain ~86% of its initial capacity at the current density 1.2 A/g and a high specific capacity ~1290 mAh/g at the current density of 8 A/g.

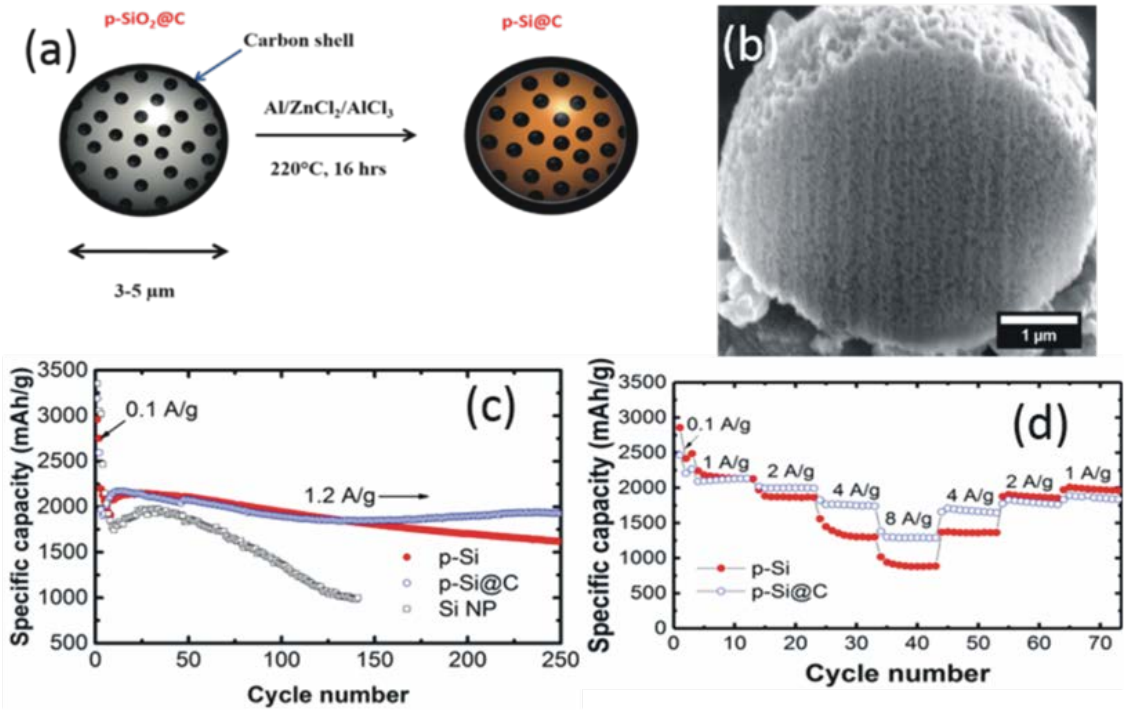

Figure II-195. (a) Schematic illustration of the synthesis of p-Si@C; (b) SEM images showing the morphology and cross section of p-Si@C; (c)-(d) Long-term cycling and rate performance of p-Si (red plot) and p-Si@C (blue plot).

1.2 Porous silicon synthesized using micron-sized silica prepared from microemulsion of silica nanoparticles

In another effort, micrometer-sized porous silicon was synthesized by magnesiothermic reduction using micrometer-sized porous silica as the precursor, which was prepared from nanosized silica using microemulsion. Figure II-196a illustrates the synthesis process of the porous Si microspheres. The step-by-step synthesis products, from SiO2 nanoparticles to SiO2 microspheres, to porous Si spheres, are shown in the SEM images in Figure II-196b-Figure II-196d. The preserved void space and subsequent carbon coating enable good mechanical and electrical stability of the porous Si and enhance its cycle life and rate capability compared to nano-Si. The obtained porous Si (p-Si/C) delivers a high reversible capacity of 1467 mAh/g at 1C with 90% capacity retention over 200 cycles (Figure II-196e). The p-Si/C electrode also shows good rate performance, as shown in Figure II-196f.

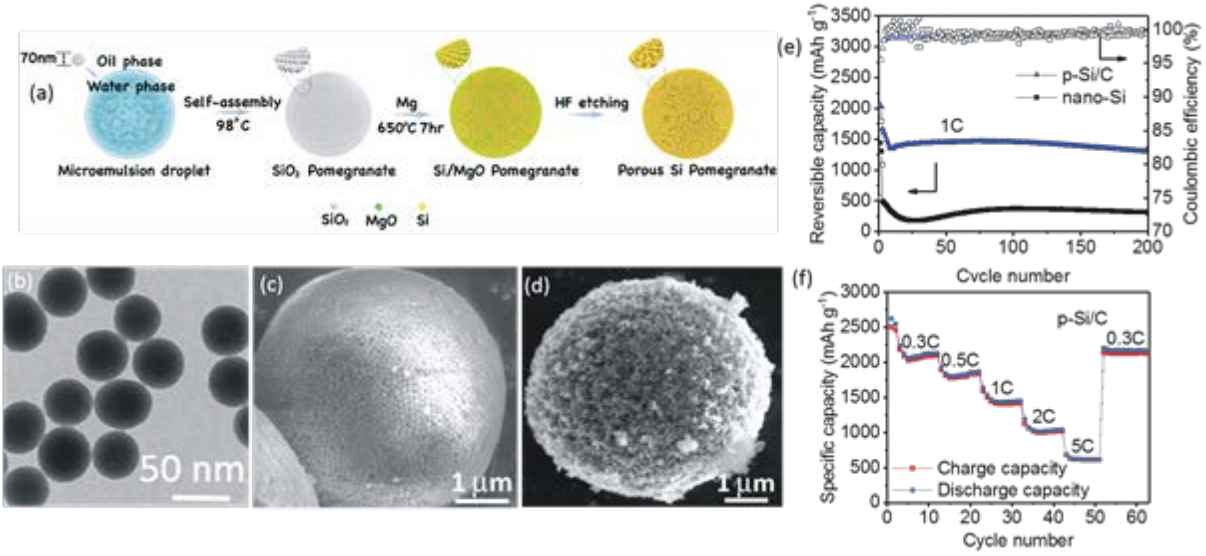

Figure II-196. (a) Schematic illustration of the synthesis of p-Si@C; (b) TEM image of the silica nanoparticles; (c) SEM image of the SiO_2 microspheres by emulsion method; (d) SEM image of the porous Si microsphere; (e) Cycling performance of p-Si/C and nano-Si; (f) rate performance of the p-Si/C.

1.3 Hierarchically structured Si/MWNT composite

Hierarchically structured micron-sized Si/MWNT particles were synthesized by aluminothermic reduction of the microspheres of SiO_2/MWNT, which was prepared by the hydrolysis of tetraethyl orthosilicate on an MWNT surface. The unique structure of Si/MWNT composite provides (1) enough void space to accommodate the volume change so that the swelling of the composite can be reduced; (2) good mechanical structure and electronic conductivity from the MWNT matrix. The in situ transmission electron microscope (TEM) study reveals limited volume changes of this hierarchically structured Si/MWNT composite. With well-controlled porosity, the composite only shows ~30% apparent volume change at full lithiation, $1/10^{th}$ of the expansion of bulk Si or Si nanoparticles. Figure II-197a shows the schematic illustration of the preparation process of the Si/MWNT microspheres. Figure II-197b-d are the step-by-step characterization of the structure of MWNT@SiO_2 coaxial cables, MWNT/SiO_2 microspheres, and the final product of Si/MWNT, which maintained the spherical morphology of the precursor. After Si/MWNT composite was coated with a thin layer of conductive carbon using chemical vapor deposition, the Si/MWNT/C composite demonstrated good electrochemical performance with a theoretical specific capacity of 2200 mAh/g (1C) calculated on the basis of the total composite weight. Figure II-197e shows that the Si/MWNT/C electrode delivers an initial reversible capacity of 1884 mAh/g, very close to the theoretical value. After 300 cycles, the electrode is able to retain ~87% of its highest initial capacity achieved at 1C. Although the Si/MWNT/C has a low FCE of 75%, the CE quickly reaches >99% after 5 cycles and remains stable. The Si/MWNT/C also exhibits good cycling stability for high loading electrodes. Figure II-197f shows the cycling performance of electrodes at different loadings. It is believed that good porosity control is a key reason for the good cycling stability.

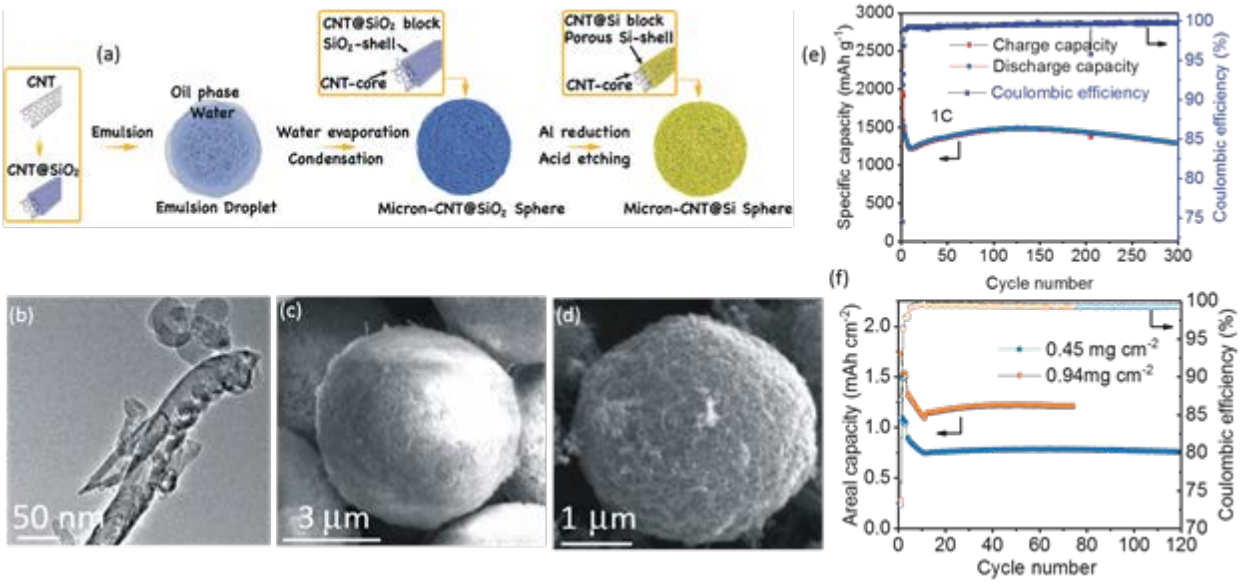

Figure II-197. (a) Schematic illustration of the preparation process of the micro-MWNT-Si composite; (b) TEM image of MWNT/SiO_2 composite (before emulsion); (c) SEM image of MWNT/SiO_2 composite (after emulsion); (d) SEM image of MWNT/Si composite after aluminothermic reaction; (e) long-term cycling performance of Si/MWNTC composite; (f) cycling stability of Si/MWNT/C with different mass loadings at the current density of 0.7 mA/cm^2.

2. Use high-energy mechanical milling of silicon oxides with different reducing agents and electrodeposition to generate Si–Li conducting nanocomposite material

Electrochemically active silicon was obtined by the reduction of silicon precursor (SiX) using inorganic reductants (IR) through low temperature solid-state reduction (LTSR). Figure II-198a shows x-ray diffraction (XRD) patterns of the heat-treated mixture indicating the formation of Si along with different intermeditae phases, but more importantly, showing no peaks corresponding to IR after the reduction of SiX at 200°C for 6 h. The undesired intermediate phases was dissolved in 1 M HCl to obtain Si. The LTSR-derived Si was then embedded in carbon nanofibers (CNF), followed by thermally induced carbonization at 700°C for 1 h and subsequent testing as an anode for Li-ion application. The Si/CNF material showed first-cycle discharge and charge capacities of ~2870 mAh/g and ~2067 mAh/g, respectively, at a current rate of ~50 mA/g, with a first-cycle irreversible (FIR) loss of ~25–30%. During the initial cycles of prolonged testing (Figure II-198b), Si/CNF showed capacities of ~2161 mAh/g and ~1210 mAh/g at current rates of 0.3 A/g and 1 A/g, respectively.

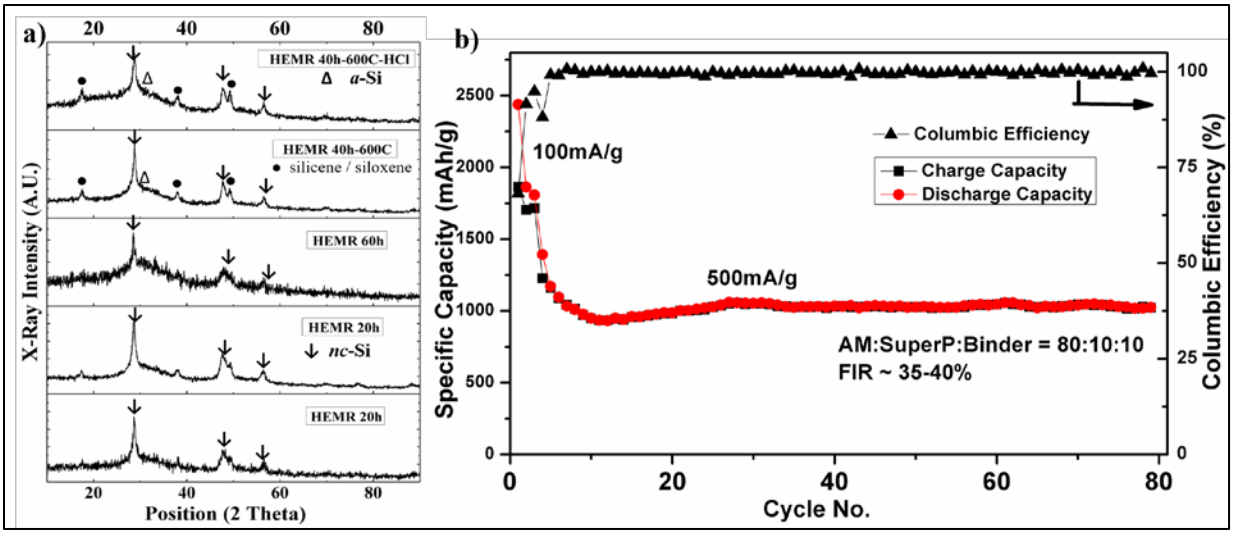

Figure II-198. (a) XRD pattern of LTSR reaction intermediate showing presence of Si, and presence of single-phase elemental Si following HCl treatment. (b) Specific discharge capacity vs. cycle numbers for LTSR-derived Si/CNF nanocomposite. The current rate for the first 3 cycles is 300 mA/g and for the remaining cycles is 1 A/g.

In another effort, a promising anode consisting of amorphous Si deposited on carbon nanotubes (CNTs) was synthesized by a commerically viable facile electrodeposition (ED) process. The SEM image and energy dispersive x-ray spectroscopy (EDAX) mapping (Figure II-199a) of M-Cu (M represents a catalyst) confirmed that a distinct layer (<1 μ) of catalyst M is coated on the Cu foil. The SEM image of CNT/M-Cu (Figure II-199b) shows the formation of CNTs well adhered to the M/Cu substrate. Amorphous Si was deposited on the CNT/M-Cu by a commerically viable electrodeposition process using a nonaqueous ionic electrolyte consisiting of silicon-containing precursors. The SEM analysis of Si-deposited CNT/M-Cu (Figure II-199c and Figure II-199d) shows a uniform deposition of Si on the CNTs, and the size of the silicon particles is < 100 nm. The loading density of ED-Si is ~0.25 mg/cm^2 to 0.31 mg/cm^2. The ED-Si/CNT electrodes show first-cycle discharge and charge capacities of ~3435 mAh/g and ~2050 mAh/g, respectively, with an FIR loss of ~35–45% (Figure II-199e) at a charge/discharge current rate of ~300 mA/g. The ED-Si/CNT also shows excellent capacity retention with a stable capacity of ~1870 mAh/g up to 70 cyles (Figure II-199e).

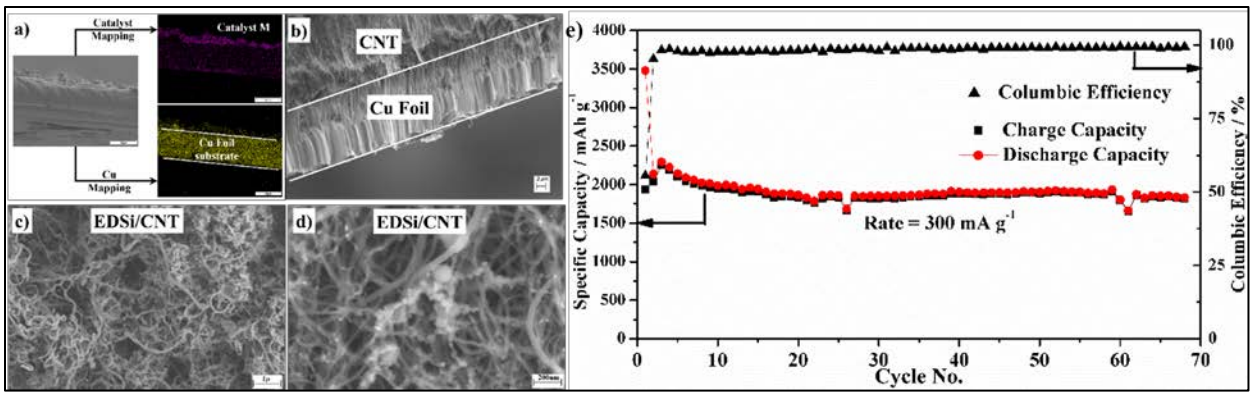

Figure II-199. (a) SEM image and corresponding EDAX mapping of Cu and catalyst layer M of catalyst-coated Cu foil; (b) SEM showing growth of CNT on Cu foil; (c) and (d) low- and high magnification images of electrodeposited Si on CNT/Cu substrates; (e) Specific discharge capacity vs. cycle number for ED-Si/CNT nanostructured binderless electrode tested at 0.3 A/g in Li/Li+ system.

High-energy mechanical reduction (HEMR) of silicon monoxide (SiO) was carried out for 20 h, 40 h, and 60 h using a stoichiometric amount of inorganic reducing agent. The formation of Si from SiO after 20 h and 60 h of HEMR was confirmed by XRD analysis. Additionally, peaks of silicene/siloxene are also observed that result from partial oxidation of the products during HEMR. The composite material obtained after 40 h of HEMR was heat treated (~600°C) for 6 h to achieve complete reduction of SiO, and the undesired oxide matrix was dissolved in HCl to obtain pure nano-Si. The loading density of nano-Si in the electrodes was ~3.5–4.0 mg/cm^2. The electrodes made from the nano-Si showed first-cycle discharge and charge capacities of ~ 2430 mAh/g and ~1870 mAh/g, respectively, with an FIR loss of ~30–40% at a charge/discharge current rate of ~100 mA/g. The obtained nano-Si also shows an excellent capacity retention with a stable capacity of ~1050 mAh/g at the end of 80 cyles at a charge/discharge rate of 500 mA/g. Difficulty in achieving higher loading density and expansion of the slurry-cast Si electrode itself still persisted in slurry-cast elecrodes. To address this issue, a commercial water souble template-based approach was developed to incorporate Si nanoparticles in a porous, electrochemically inactive but electrically conducting metallic foam to maintain the electrical continuity and achieve high loading densities (5–10 mg/cm^2) within the pores, providing free space to counter the volume expansion of the Si electrode. SEM images of the cross section of the nanocomposite foam (Figure II-200a, b) show completely interconnected porosity with pores replacing the sacrificial template upon dissolution of the pre-foamed compact. The electrodes show first-cycle discharge and charge capacities of ~2970 mAh/g and ~1940 mAh/g, respectively, with an FIR loss of ~30–45% (Figure II-200c) at a charge/discharge current rate of ~50 mA/g. The obtained porous nano-Si/conducting foam shows good capacity retention with a stable capacity of ~1025 mAh/g (~4 mAh/cm^2) at the end of 55 cyles at 500 mA/g (Figure II-200c).

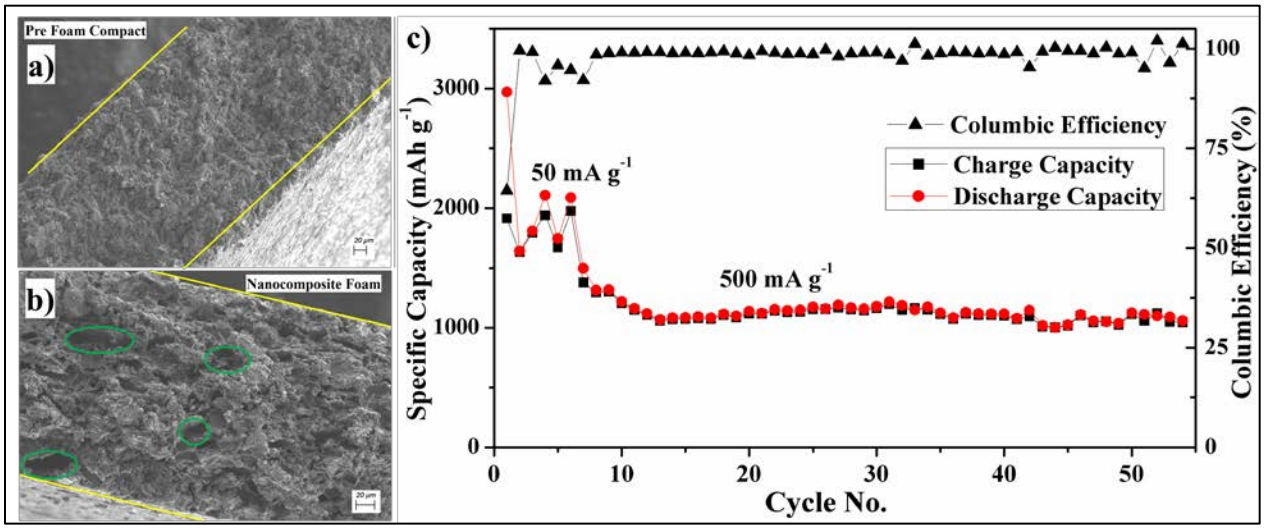

Figure II-200. (a), (b) SEM images of Si-based-nanocomposite conducting porous foams with interconnected porosity; (c) Long-term cycling data of nano-Si conducting foam tested at 50 mA/g for the initial 6 cycles followed by 0.5 A/g in a Li/Li+ system.

Conclusions

We have developed several approaches to synthesize micrometer-sized silicon with nano-porousity and demonstrated their good electrochemical performance. The low temperature thermic reaction (210°C) developed in this work can greatly reduce the production cost. The porous Si (p-Si@C) can have desired morphology and porous structure and has good electrochemical performance. Micrometer-sized porous silicon synthesized from nanosized silica using microemulsion delivers a high reversible capacity of 1467 mAh/g at 1C with 90% capacity retention over 200 cycles. Si/MWNT composite prepared via scalable hierarchical assembly and aluminum reduction demonstrates good electrochemical performance with a reversible capacity of 1290 mAh/g at 1C and a capacity retention of 87% after 300 cycles. In another effort, several scalable

methods were explored to generate nano-Si and Si-based nanostructures by commercially viable low-cost synthesis routes and technologies. The LTSR-derived Si embedded in CNF show a stable discharge capacity of 1210 mAh/g at a current rate of 1 A/g with an FIR loss of ~25–30%. Nano-Si obtained from HEMR was embedded in CNF, and showed a stable discharge capacity of ~1050 mAh/g at a current rate of 0.5 A/g and an FIR loss of ~30–40%. Electrodeposited Si on CNT-Cu foils also showed highly stable performance with a discharge capacity of ~1870 mAh/g, FIR loss of 35–45% at a current rate of 0.3 A/g, and high CE of ~99.95%. Opportunities exist for conducting further optimization studies.

Key Publications/Patents

1. Xiaolin Li, Pengfei Yan, Xingcheng Xiao, Jae Ha Woo, Chongmin Wang, Jun Liu, and Ji-Guang Zhang, Design of porous Si/C–graphite electrodes with long cycle stability and controlled swelling, Energy Environ. Sci., 2017, 10, 1427-1434.

2. Kuber Mishra, Jianming Zheng, Rajankumar Patel, Luis Estevez, Haiping Jia, Langli Luo, Patrick El Khoury, Xiaolin Li, Xiao-Dong Zhou, and Ji-Guang Zhang, High Performance Porous Si@C Core-Shell Structured Anodes Enabled by the Low Temperature Aluminothermic Reduction Reaction, U.S. Patent application filed in March, 2017.

3. Bharat Gattu, Rigved Epur, Prashanth H. Jampani, Ramalinga Kuruba, Moni K. Datta and Prashant N. Kumta, “Silicon-Carbon Core-Shell (C@Si@C) Hollow Nanotubular Configuration - High Performance Lithium-Ion Anodes”, Journal of Physical Chemistry - C, 2017, 121 (18), pp 9662–9671.

4. Bharat Gattu, Prashanth H. Jampani, Moni K. Datta and Prashant N. Kumta, “Water-soluble template derived nanoscale silicon nano-flakes and nano-rods morphologies: stable architectures for lithium ion anodes”, Nanoresearch, 2017, https://doi.org/10.1007/s12274-017-1707-z.

5. Bharat Gattu, Rigved Epur, Pavithra M. Shanti, Prashanth H. Jampani, Ramalinga Kuruba, Moni K. Datta, Ayyakkannu Manivannan, and Prashant N. Kumta, “Pulsed current electrodeposition of silicon thin film anodes for lithium-ion battery applications”, Inorganics, 2017, 5(2), 27.

II.B.6 Pre-Lithiation of Silicon Anode for High Energy Li Ion Batteries (SLAC)

Yi Cui, Principal Investigator
Department of Materials Science and Engineering
Stanford University
McCullough 343, 476 Lomita Mall, Stanford University
Stanford, CA 94305
Phone: 650-723-4613
E-mail: yicui@stanford.edu

Tien Duong, Technology Manager
U.S. Department of Energy
Phone: 202-586-7836
E-mail: Tien.Duong@ee.doe.gov

Start Date: October 1, 2015 End Date: December 31, 2017
Total Project Cost: $300,000 DOE share: $300,000 Non-DOE share: $0

Project Introduction

Rechargeable lithium-ion batteries (LIBs) are widely used for consumer electronics and exhibit great potential for electrical vehicle and grid-scale energy storage. In existing lithium-ion technology, Li is provided by Li-intercalated cathode materials. Graphite is the most commonly used anode material. Various alternative high-capacity anode materials such as silicon, with a theoretical capacity more than ten times of graphite, have been well studied and have already shown promise in potential applications. The formation of a solid electrolyte interphase (SEI) layer on the anode surfaces is a critical process that occurs prior to regular battery operations and consumes a significant amount of Li. Graphite anodes exhibit an irreversible capacity loss of 5–10% from the initial battery charging process, while for high-capacity anode materials, the first-cycle Li loss is even higher (e.g., 15–35% for Si). Low first-cycle Coulombic efficiency leads to the consumption of an excess amount of cathode material solely for the first cycle and thereby, significantly reduces the energy density. It is also challenging to effectively compensate for the Li loss through loading excessive cathode materials as a result of kinetic limitations on the cathode thickness. Accordingly, there is a strong motivation to develop high-capacity materials to prestore a large amount of Li in either cathode or anode to compensate for the initial loss.

Objectives

This study aims to develop high-capacity prelithiation additives that can work as a secondary Li source and compensate the initial Li loss in LIBs. This study pursues two main directions: 1) developing different anode prelithiation additives to increase first-cycle Coulombic efficiency of LIBs, and 2) increase the stability of prelithiation additives in the electrode fabrication environments.

Approach

Usually, prelithiation of cathode materials was previously achieved by treating spinel cathode materials or metal oxides with chemical reagents, like n-butyllithium, LiI, or molten Li. However, the prestored capacity is still relatively low (100–800 mAh/g). Anode materials are more attractive Li reservoirs because of the high specific capacities. In previous studies, there have been three main approaches to realize anodes with prestored Li. One approach is electrochemical prelithiation by shorting electrolyte-wetted anodes with Li foil. Another approach is to incorporate microscale stabilized lithium metal powder (SLMP; FMC Lithium Corp.) into anodes. However, synthesis of SLMP in the research laboratory is difficult. In our previous report, we showed chemically synthesized Li_xSi/Li_2O core shell nanoparticles (NPs) as an effective prelithiation reagent. The NPs maintained their capacities only in the dry air but that their capacities were reduced drastically after exposure to ambient air. In the follow-up study, we showed that using 1-fluorodecane to modify the surface gives rise to an artificial SEI coating consisting of LiF and Li alkyl carbonate. However, these particles maintain their

capacity only in air with low humidity levels (<10% relative humidity (RH)) and their stability in NMP is not possible. The LiF formed at room temperature with this method is amorphous, and the coating consists of side products resulting in a less dense coating which is unable to prevent the penetration of water and NMP. Therefore, we develop a high temperature and gas phase surface fluorination reaction to synthesize LiF-Li_xSi NPs. The dense and crystalline LiF coating improves the stability of Li_xSi NPs in both humid air and regular slurry solvent (NMP), indicating that LiF-Li_xSi NPs are compatible with industrial electrode fabrication processes.

Group IV elements such as Ge and Sn also have relatively high specific capacities (1640 mAh/g for Ge, and 993 mAh/g for Sn) and similar volumetric capacities to Si (2574 mAh/cm^3 for Si, 2275 mAh/cm^3 for Ge, and 2111 mAh/cm^3 for Sn), making them also suitable for pre-storing Li. Therefore, we developed a one-pot metallurgical process to synthesize $Li_{22}Z_5$ alloys (Z = Ge and Sn) and $Li_{22}Z_5$-Li_2O composites by using Z and ZO_2 as the source materials, respectively. Both $Li_{22}Z_5$ alloys and $Li_{22}Z_5$-Li_2O composites are reactive enough to prelithiate various anode materials such as graphite and Sn, thereby achieving high 1st cycle CEs of >100%.

Alloy anodes with much higher capacity have been recognized as promising alternatives to graphites. Without prestored Li in anodes, the energy density is limited by the low capacity of Li metal oxide cathodes. Recently, Li metal has been revived as a high-capacity anode, but faces many challenges resulting from its high reactivity and uncontrolled dendrite growth. Therefore, we develop an air-stable and free-standing Li_xSi/graphene foil as an alternative to Li metal, inheriting the desirable properties of alloy anodes and pure metal anodes.

Results

LiF-coated Li_xSi NPs stable in NMP and humid air

With low solubility in both water and organic solvents, LiF coating could be applicable to Li_xSi NPs to improve the compatibility with industrial electrode fabrication processes. We find the fluoropolymer, CYTOP, gradually decomposes and releases pure F_2 gas upon heating, which reacts with Li_xSi NPs to form a uniform and compact LiF coating. The TEM image in Figure II-201a indicates a uniform and continuous coating with a thickness of 20 nm. After coating, a new XRD peak at 38.7 degree is indexed as LiF (PDF# 00-004-0857), confirming the crystalline nature of the coating (Figure II-201b). The reaction between Li_xSi and NMP as well as the improved stability after LiF coating was studied by gas chromatography (GC, Figure II-201c). After soaking in NMP for 6 h, 20 mg Li_xSi NPs reacted with NMP vigorously to release 18145 ppm H_2 and 938 ppm CH_4. With LiF coating, the reaction with NMP is considerably suppressed. The GC signal of H_2 decreases to only 15% of that of uncoated Li_xSi, and no signal of CH_4 is detected. To confirm the stability of LiF-Li_xSi NPs in the slurry, LiF-Li_xSi NPs were mixed with Super P and PVDF (65:20:15 by weight) in 1,3-dioxolane (DOL) or NMP to form a slurry which was then drop cast on copper foil. Previously, we found that bare Li_xSi is stable in DOL but reacts vigorously with NMP to leave almost no extraction capacity (dashed lines, Figure II-201d). Consistently, LiF-Li_xSi NPs shows a high capacity of 2879 mAh/g using DOL as the slurry solvent, based on the mass of Si in the cell. Replacing DOL with NMP, only a small fraction of capacity (~13%) is sacrificed (Figure II-201d). In contrast to our previous work, Li_xSi directly reacts with F_2 gas at high temperature, forming a dense and crystalline LiF coating which imparts improved stability in NMP. Because of the limited solubility of LiF in water, LiF further improves the stability of Li_xSi NPs in humid air. After being stored in humid air (~40% RH) for 1 day, the capacity is 2328.9 mAh/g, showing a high capacity retention of 85.9% (Figure II-201e). The capacity decay is slow, compared with Li_2O-Li_xSi NPs as shown in the inset of Figure II-201e. The crystalline and dense LiF coating eliminates the side reactions in both NMP and humid air, increasing the feasibility of incorporating LiF-Li_xSi NPs in the commercial electrodes fabrication process. Compared with Si NPs and bare Li_xSi NPs, LiF-Li_xSi NPs exhibit improved cycling performance with 13% capacity decay after 650 cycles (Figure II-201f). Li_xSi NPs are already in their fully-expanded state, which contributes to the excellent cyclability. Void space is created during the delithiation process, which accommodates further volume expansion of subsequent lithiation process. Therefore, each particle does not squeeze against each other to damage the structure of the whole electrode during cycling. The average CE of bare LixSi NPs (from the fourth cycle to the 400th cycle) is 99.79%, lower than the value of the LiF-coated Li_xSi NPs (99.92%, from the third cycle to the 650th cycle). With exceptional chemical stability, the LiF coating

effectively minimizes electrolyte decomposition and side reactions on the electrolyte/electrode interface during cycling, which contributes to the high CE.

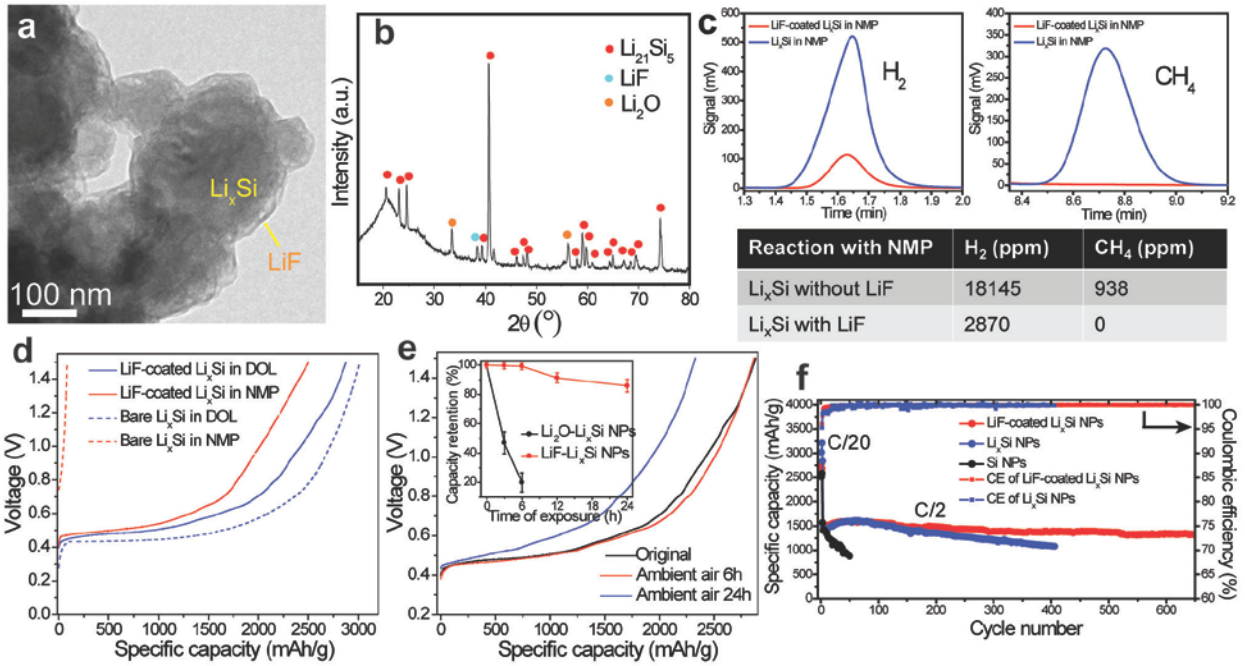

Reaction with NMP	H_2 (ppm)	CH_4 (ppm)
Li_xSi without LiF	18145	938
Li_xSi with LiF	2870	0

Figure II-201. Characterization and stability of LiF-Li$_x$Si NPs. (a) TEM image and (b) XRD pattern of LiF-Li$_x$Si NPs. (c) The amount of gas released for coated (red) and uncoated (blue) Li$_x$Si NPs reacted with NMP measured by gas chromatography. (d) First-cycle delithiation capacities of LiF-Li$_x$Si NPs (solid line) and bare Li$_x$Si NPs (dashed line) using different solvents to form the slurry. (e) The extraction capacities of LiF-Li$_x$Si NPs exposed to ambient air (~40% RH) with varying durations. The inset shows the trend of capacity decay of LiF-Li$_x$Si NPs (red) and Li$_2$O-Li$_x$Si NPs (black) with varying durations. (f) Cycling performance of LiF-Li$_x$Si NPs (red), bare Li$_x$Si NPs (blue) and Si NPs control cell (black) at C/20 for the first several cycles and C/2 for the following cycles (1C=4.2 A/g, and the capacity is based on the mass of Si in the electrodes). The Coulombic efficiency is plotted on the secondary y-axis (LiF-Li$_x$Si NPs: red, and bare Li$_x$Si NPs: blue).

Li$_{22}$Ge$_5$ alloys and Li$_{22}$Ge$_5$-Li$_2$O composites as stable prelithiation reagents

Ball-milled Ge NPs and GeO$_2$ NPs were used as the starting materials to form the Li$_x$Ge alloy and Li$_x$Ge-Li$_2$O composite, respectively. SEM was utilized to characterize the morphology of the Ge and GeO$_2$ NPs before and after lithiation. After ball milling, the size of Ge NPs is in the range of 100~300 nm, while that of GeO$_2$ NPs is in the range of 150~350 nm as shown in Figure II-202a,d. The sizes of the derived Li$_x$Ge alloy and Li$_x$Ge-Li$_2$O composite were larger than those of the starting materials because of the volume expansion and some degree of particle aggregation during the metallurgical process (Figure II-202b,e). XRD confirms the crystalline nature of ball-milled Ge powder (PDF# 00-004-0545) and a small portion of GeO$_2$ (PDF# 00-036-1463) resulting from the high-energy ball-milling process in air (Figure II-202c, upper). XRD confirms the complete transformation of Ge in both Ge powder and the intrinsic oxide GeO$_2$ to crystalline Li$_{22}$Ge$_5$ (PDF# 01-081-6059) during the thermal alloying process (Figure II-202c, bottom). The small peaks of Li$_2$O (PDF# 00-012-0254) come from the conversion of the small amount of intrinsic oxide GeO$_2$. XRD analysis also shows the complete formation of crystalline Li$_{22}$Ge$_5$ and Li$_2$O during the thermal alloying process of GeO$_2$ powder and molten Li. The only difference is the much higher percentage of Li$_2$O in the final product. To measure the prelithiation capacities of the Li$_x$Ge alloy and Li$_x$Ge-Li$_2$O composite, the electrodes were charged to 1.5 V directly at a slow rate of C/20 (1C = 1640 mA/g for Ge and 1126 mA/g for GeO$_2$). The prelithiation capacities were 1335 mAh/g and 892 mAh/g based on the masses of Ge and GeO$_2$ in the electrode, respectively (Figure II-202f). To test the air stability of Li$_x$Ge, Li$_x$Ge NPs was exposed to ambient air (30%~40% RH) for 6 h, exhibiting a high extraction capacity of 947 mAh/g (30% capacity loss, Figure II-202g). Although the specific

capacity is relatively lower, Li_xGe-Li_2O NPs exhibit superior ambient-air stability with a higher capacity retention of 85% (15% capacity loss) compared to bare Li_xGe NPs.

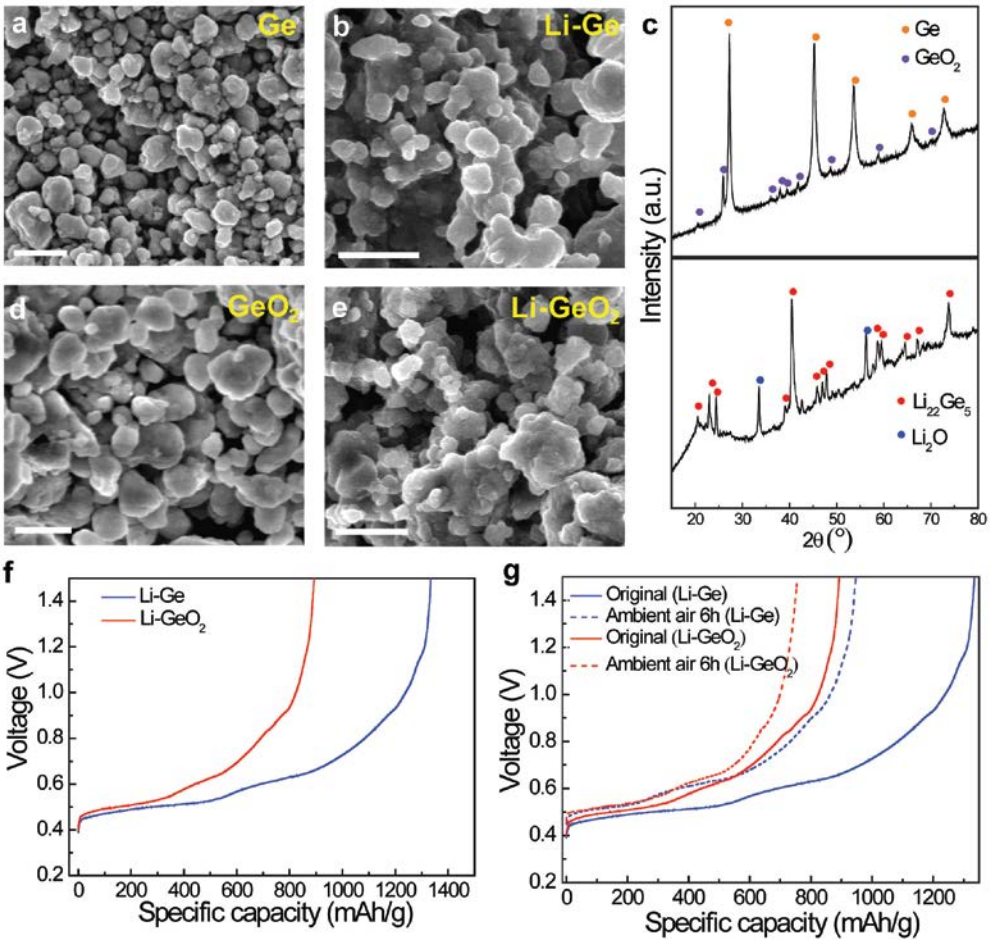

Figure II-202. (a, b) SEM images of Ge NPs (a) before and (b) after thermal lithiation. (c) XRD patterns of Ge NPs before (upper) and after thermal lithiation (bottom). (d, e) SEM images of GeO_2 NPs (d) before and (e) after thermal lithiation. (f) First-cycle delithiation capacities of lithiated Ge NPs (blue) and lithiated GeO_2 NPs (red). The capacity is based on the mass of Ge or GeO_2 in the anode. (g) First-cycle delithiation capacities of lithiated Ge NPs (blue) and lithiated GeO_2 NPs (red) before (solid) and after (dash) exposure to ambient-air condition (30%~40% RH) for 6h.

$Li_{22}Sn_5$ alloys and $Li_{22}Sn_5$-Li_2O composites as stable prelithiation reagents

Sn NPs and SnO_2 nanoclusters were used as the starting materials to form the Li_xSn alloy and Li_xSn-Li_2O composite, respectively. The alloying temperature should be maintained between the melting points of Li metal and Sn NPs to ensure the preservation of the morphology of Sn NPs. SEM was utilized to characterize the morphology of the Sn NPs and SnO_2 nanoclusters before and after lithiation. SEM image confirms that the Sn NPs have sizes less than 200 nm (Figure II-203a). After metallurgical lithiation, the shape of the NPs is retained, whereas the particle sizes are larger due to volume expansion and some aggregation (Figure II-203b). XRD confirms the transformation from Sn (PDF# 00-004-0673) to $Li_{22}Sn_5$ (PDF# 01-081-6569) after thermal alloying with molten Li (Figure II-203c). The small amount of Li_2O arises from the intrinsic oxide SnO (PDF# 04-005-4541) in Sn NPs. The hydrothermal-synthesized SnO_2 nanoclusters are uniform both in size (~50 nm) and shape as confirmed by SEM (Figure II-203d). The monodisperse SnO_2 nanoclusters were utilized as the precursor for the Li_xSn-Li_2O composite. After thermal lithiation, the morphology of SnO_2 nanoclusters was preserved, whereas the size of the clusters slightly increased to 75 nm because of volume expansion (Figure II-203e). XRD of lithiated SnO_2 shows the same final products as lithiated Sn NPs with a higher

percentage of the Li_2O phase. To compare their dry-air stability, different Li_xZ (Z = Si, Ge and Sn) alloys were stored in a dry room (dew point = −50 °C) for 5 days. The remaining capacity of Li_xSn NPs exposed to dry air over many days were studied by charging the Li_xSn NPs electrodes to 2 V at a low rate of C/20 (Figure II-203f). After 5 days' exposure, Li_xSn NPs exhibit a high capacity of 845 mAh/g, corresponding to a capacity retention of 93%. The capacity dacay for Li_xSn alloy and Li_xGe alloy is much slower compared with Li_xSi alloy. Among the Li_xZ alloys, Li_xGe shows the best dry-air stability with negligible (6.5%) capacity decay after 5 days of exposure. No new peaks are present in the XRD pattern of Li_xSn NPs exposed to ambient air (~ 40% RH) for 2 h (Figure II-203g, upper). The XRD pattern reveals small peaks belonging to $Li(OH)•H_2O$ (PDF# 04-010-4336), and $Li_{22}Sn_5$ remains the major component after being exposed to ambient air for 6h (Figure II-203g, bottom). Because of the excellent air stability, the Li_xSn alloy and Li_xSn-Li_2O composites are potentially compatible to the industry battery fabrication process.

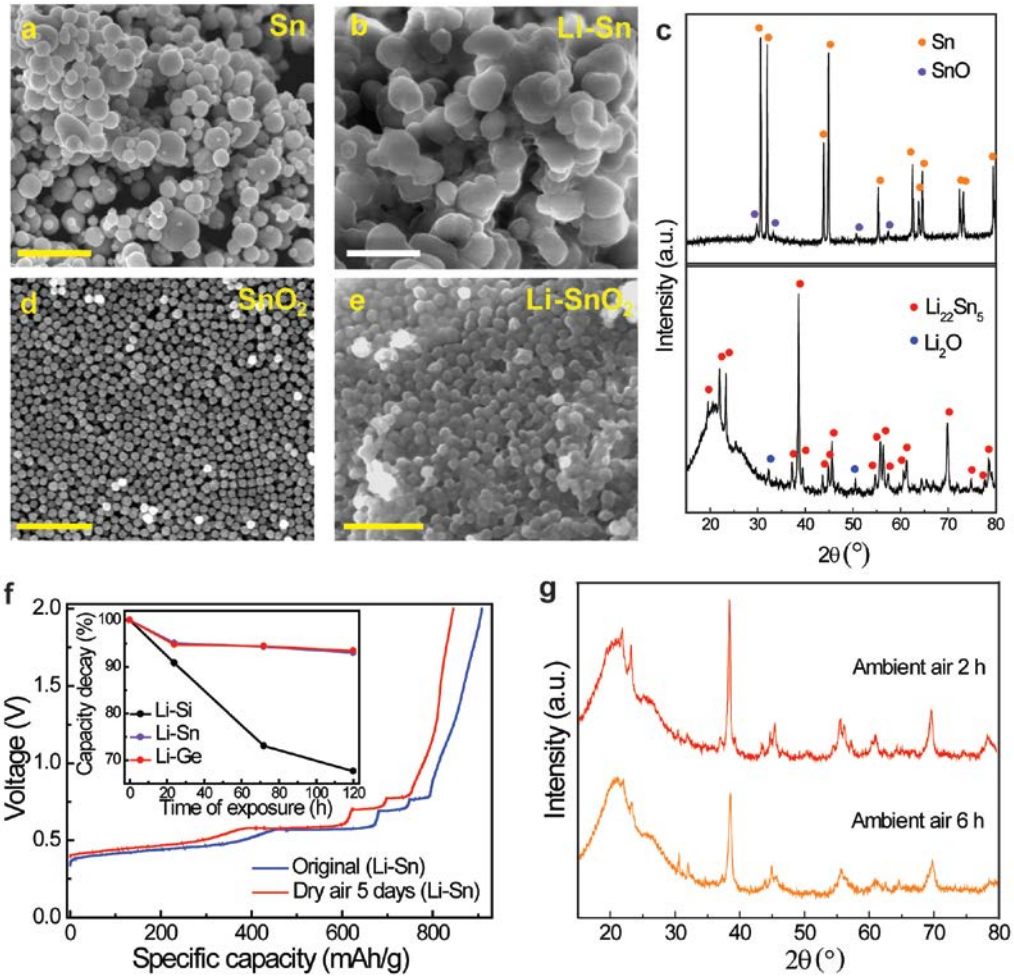

Figure II-203. (a, b) SEM images of Sn NPs (a) before and (b) after thermal lithiation. Scale bar, 500 nm. (c) XRD patterns of Sn NPs before (upper) and after thermal lithiation (bottom). (d, e) SEM images of SnO_2 NPs (d) before and (e) after thermal lithiation. Scale bar, 500 nm. (f) First-cycle delithiation capacities of lithiated Sn NPs before (blue) and after (red) exposure to dry-air condition for 5 days. The inset shows the trend of capacity decay of lithiated Si (black), Sn (purple) and Ge (red) NPs. (g) XRD patterns of lithiated Sn NPs exposed to ambient-air condition for 2h (upper) and 6 h (bottom).

Air-stable and free-standing Li_xSi/graphene foil as an alternative to Li metal

This large-scale freestanding Li_xSi/graphene foil consists of fine nanostructures of densely-packed Li_xSi NPs encapsulated by large graphene sheets. Li_xSi NPs were mixed with graphene sheets and SBS rubber (80:10:10

by weight) in toluene to form a slurry, which was then casted on a PET release film. After drying, it can be easily peeled off. The photograph (Figure II-204a) shows a large Li_xSi/graphene foil with 8 cm width and 24 cm length. The right side of the foil is rolled around a thin tube to illustrate the good flexibility. The superior mechanical property of the Li_xSi/graphene foil is further demonstrated by the uniaxial tensile test, which shows a similar trend to a Li metal foil with much higher stress (Figure II-204d). TEM image with low magnification (Figure II-204b) shows overlapped and interconnected graphene sheets with size up to several microns. A double-layer graphene sheet is clearly observed in Figure II-204c, with the average inter-layer distance of 0.334 nm. XRD pattern (Figure II-204e) of the Li_xSi/graphene foil contains peaks of $Li_{22}Si_5$ (PDF# 01-077-2882), graphitic carbon (PDF# 00-056-0159), and Li_2O (PDF# 04-008-3420). Li_xSi NPs are identifiable underneath the thin graphene sheet (Figure II-204f). After calendared at large stress 40 MPa, Li_xSi NPs are in a densely-packed state as shown in the cross-sectional view of the SEM image (Figure II-204g). With fully-expanded Li_xSi confined in the highly-conductive and chemically-stable graphene matrix, this foil maintains a stable structure and cyclability in half cells. The Li_xSi/graphene foil is successfully paired with high-capacity Li-free cathodes, such as V_2O_5 and Sulphur, to achieve stable full-cell cycling. The Li_xSi/graphene foil is stable in ambient air, owing to the unique structure as well as the hydrophobicity and gas impermeability of graphene sheets.

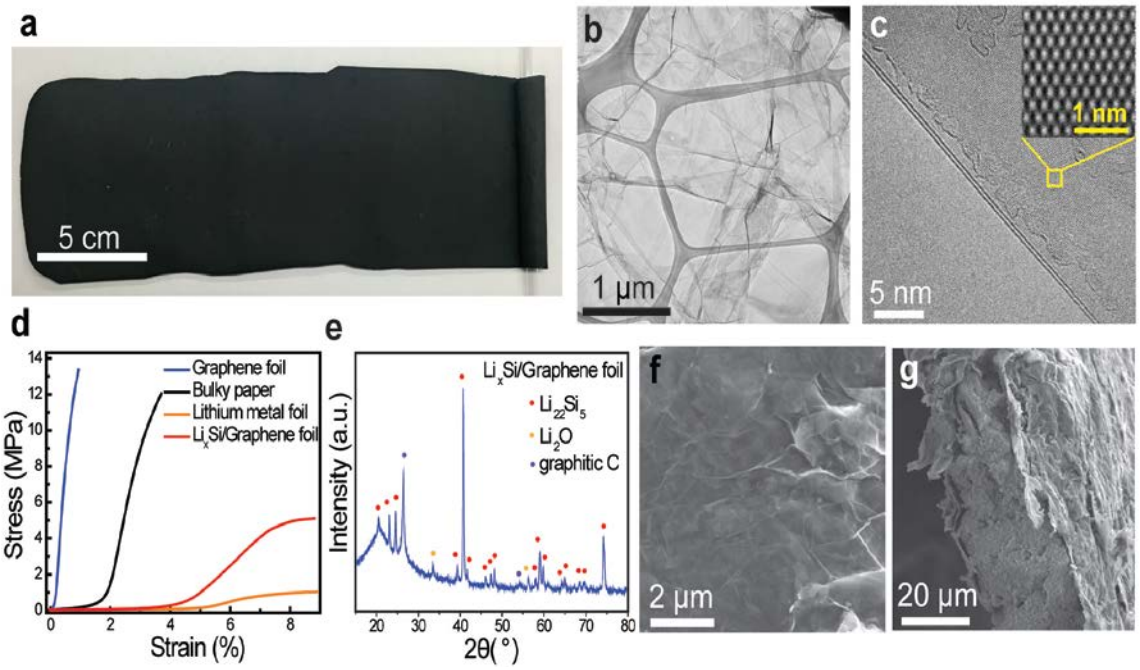

Figure II-204. Characterizations of the Li_xSi/graphene foil. a, Photograph of large Li_xSi/graphene foil with 8 cm width and 24 cm length. b, Low-magnification TEM image of the overlapped and interconnected graphene sheets. c, TEM image shows a double-layer graphene sheet with the inter-layer distance of 0.334 nm. The inset is the atomic resolution image of the graphene sheet. d, Uniaxial tensile test of the graphene foil (blue), bulky paper (black), Li metal foil (orange), and Li_xSi/graphene foil (red). e, XRD pattern reveals the highly crystalline nature of graphitic carbon and $Li_{22}Si_5$. f, Top-view and g, cross-sectional view SEM images of the Li_xSi/graphene foil.

Conclusions

In the past year, we developed a surface fluorination process to form a homogeneous and dense LiF coating on Li_xSi NPs. With this coating, Li_xSi NPs are stable in both humid air and regular slurry solvent (NMP), indicating that LiF-Li_xSi NPs are compatible with industrial electrode fabrication processes. Aside from Si-based prelithiation reagents, we developed $Li_{22}Z_5$ alloys (Z = Ge and Sn) and $Li_{22}Z_5$-Li_2O composites with better air-stability by using Z and ZO_2 as the source materials, respectively. Li-containing anodes afford remarkable battery performance either as anode additive or anode material by itself. The synthesized air-stable and free-standing Li_xSi/graphene foil serves as an alternative to Li metal, inheriting the desirable properties of alloy anodes and pure metal anodes.

Key Publications

1. J. Zhao, L. Liao, F. Shi, T. Lei, G. Chen, A. Pei, J. Sun, K. Yan, G. Zhou, J. Xie, C. Liu, Y. Li, Z. Liang, Z. Bao, and Y. Cui, "Surface fluorination of reactive battery anode materials for enhanced stability", *JACS **139**, 11550 (2017).*

2. J. Zhao, J. Sun, A. Pei, G. Zhou, K. Yan, Y. Liu, D. Lin, and Y. Cui, "A general prelithiation approach for group IV elements and corresponding oxides", *Energy Storage Materials*, in press.

3. J. Zhao, G. Zhou, K. Yan, J. Xie, Y. Li, L. Liao, Y. Jin, K. Liu, P-C Hsu, J. Wang, H-M Cheng, and Yi Cui, "Air-stable and freestanding lithium alloy/graphene foil as an alternative to lithium metal anodes", *Nat. Nanotech*. **12**, 993 (2017).

II.B.7 High Capacity and Long Cycle-Life Silicon Carbon Composite Materials and Electrodes (LBNL)

Gao Liu, Principal Investigator
Lawrence Berkeley National Laboratory
1 Cyclotron Road
Berkeley, CA 94720
Phone: 510-486-7207
E-mail: gliu@lbl.gov

Brian Cunningham, Technical Manager
Phone: 202-287-5686
E-mail: Brian.Cunningham@ee.doe.gov

Start Date: October 1, 2016 End Date: September 30, 2017
Total Project Cost: $565,000 DOE share: $565,000 Non-DOE share: $0

Project Introduction

The low energy density and limited lifetime are two of major drawbacks of the automobile Li-ion batteries for electric vehicle (EV)/plug-in hybrid EV (PHEV) applications. State-of-the-art Li-ion technology is based on a graphite negative electrode and a layered metal oxide, spinel, or olivine phosphate positive electrode system. The theoretical specific capacity of graphite is 372 mAh/g, which is far less than some of the suggested alternative Li-ion storage materials such as tin (Sn) (994 mAh/g) or silicon (Si) (4,200 mAh/g). However, the graphite material has unique advantages in the established Li-ion system: it is structurally stable and incurs only ~10% of volume change during the Li-ion insertion and removal process. This structural stability helps to maintain both electrode integrity and overall cell volume stability. The structural stability is also important to maintain a stable solid electrolyte interface (SEI) layer on graphite to prevent further electrolyte reactions on the surface. The Li-ion electrolyte and additive combinations, which has been developed over the past two and half decades, ensures the formation of electrochemically stable SEI on the graphite surface at very low voltage potential. In order to advance anode chemistry for EV/PHEV applications, any new anode materials need to have a higher capacity than those of graphite, at least the same surface stability of a graphite anode (for long term cycling and storage), and an overall electrode design that is suitable for high-capacity materials.

Si is a naturally abundant material. It possesses the highest capacity of any Li-ion anode material. Si and Li alloys also have a low potential plateau at around 0.45 V (Li/Li^+) during the de-lithiation process. Si anodes, combined with cathode materials at 4 V and above, can offer higher energy density storage for EV/PHEV.

However, despite its remarkable high storage capacity and the intensive research done in this field, applications of Si in Li-ion cells are limited. One reason is that the cycle life of a battery containing Si does not generally exceed 500 cycles. The primary issue is the high-volume change associated with Li-ion insertion into Si. Almost 280% volume expansion occurs as the material transitions from the pure Si phase to the $Li_{15}Si_4$ phase. This high-volume change tends to disrupt the electronic integrity of the composite electrode and induce high and continuous surface side reactions leading to drastic capacity fade.

Si volume expansion, along with the excessive side reactions on the Si surface due to lithiation and delithiation cycling, poses significant challenges to utilizing Si to its highest potential. This project aims to develop high-capacity and long-life Si/C composite anodes to prolong battery cycling and storage lifetime, and to provide an in-depth understanding of Si electrode design strategies to stabilize Si material volume change and to prevent surface side reactions. This work combines novel materials design and innovative synthesis process to synthesize mechanically robust and dimensionally stable Si/C composite materials.

Objectives

This project addresses the low energy density and limited lifetime of the lithium-ion (Li-ion) battery for EV and PHEV applications. This research aims to stabilize Si material volume change to achieve high capacity, stable electrode design and to prevent surface side reactions to prolonged battery cycling and storage lifetime. This project developed synthetic processes to make silicon carbon anode composite materials to reduce volume expansion during charge and discharge process, and applied surface coating to reduce surface side reactions.

Approach

Materials synthesis approach to address the volume expansion and surface reactions is inspired by recent progresses in this field by the LBNL team and other groups, which have shed light on the potential directions for further optimization of the Si materials. First, it was shown that large, secondary-particle-based Si materials allow longer cycle life, higher loading, and improved rate performance. A second key area of recent progress in the field is the development of dimension-stable Si nanotube, which tents to stabilize cycling and reduce side reactions. Si nanotubes with SiO_2 protection layers allow the Si cycling for more than 6,000 cycles with minimum decomposition deposits on the nanotube surface. In this case, the SiO_2 layer is a dense layer, preventing the electrolyte from contacting the Si reactive surface. The Si tubes expand inward during lithiation, so that the surface of the SiO_2 in contact with electrolyte does not change with cycling. Therefore, a physically stable SEI can be formed on the surface of the nanotube. We propose to combine both approaches (large particle size and stable surfaces) to develop both dimension- and surface-stable Si composite materials.

1) Use spray precipitation to synthesize micron size Si/carbon (Si/C) composite particles.

The design approach is a hollow shell-structured Si/C composite particle. The outer diameter of the composite particle has a mean size of 20μ. The inner diameter of the hollow core is approximately 10 μm. The silicon nanoparticles are distributed in the shell of the carbon matrix. The Si nanoparticle size is approximately 10 nm. Sonication spray is a method to generate controlled particle size droplet in the range of 20 μm and above. A sonication spray-precipitation method is used to generate spherical secondary composite particles. Controlled strength of ultrasound dispersion is used during the spray of Si/polymer slurry in solvent A into a solvent B to produce a spherical precipitate. In this case, the polymer binder dissolved in solvent A but precipitated in solvent B. Solvent A and B are miscible. When the slurry droplet is falling into solvent B, the polymer will solidify at the surface of the droplet to form micron-size particles. Solvent A and the polymer will continue transport from the center to the surface of the particles, and precipitate towards the surface where solvent B has a higher concentration. The polymer and solvent A will drag the silicon partials to the outer surface. The net effect of the particle morphology is a hollow core spherical Si and polymer composite particles. By controlling the slurry solvent content and sonication strength, the outer diameter of the particles and the size of hollow core can be controlled. Further sintering these particles around 500-800°C will lead to hollow core spherical Si/C materials. The hollow core of the Si/C secondary particles will accommodate volume expansion of primary Si particles, so the outer surface expansion of the secondary particles is reduced.

2) Secondary particle surface coating to reduce electrolyte side reactions with Si/C composite particles.

Additional coating will be applied to the secondary particle surface either before or after the sintering processing. After the coating, the materials will go through another sintering process to solidify the coatings to form a lithium-ion conducting but electrolyte expelling thin layer in the range of 10-100 nm. Since the existence of the internal void space, the overall volume expansion of the secondary particles will tend to be much lower. The purposes of this costing are two folds. First, it will provide a robust layer to further reduce the outer expansion of the secondary particles. Second, it will isolate the electrolyte interaction with the reactive Si surfaces. The choice of coating materials will be carbon precursors or Li-ion conducting glass ceramics.

This comprehensive design will solve the volume change issues in the secondary particle level. The large particle size will ensure small gravimetric specific surface area for low side reactions. Large pore formation in the electrode will allow for rapid electrolyte ion transport. Since the Si/C composite only expands inwardly, the electrode made by these particles is dimensionally stable. Therefore, the overall cell volume change is very

small. Due to the surface coating layer and the stable secondary particles size, the electrolyte will not contact the Si nanoparticles. Because of the internal void space and carbon clamping, the expansion and contraction will only happen inwardly. This design can solve the most critical issues of continued surface reaction between the high capacity Si and electrolyte.

Results

A sonication spray-precipitation method is developed to generate spherical hollow core composite secondary particles. The process is detailed in Figure II-205. Controlled strength of ultrasound dispersion was used during the spray of Si/polymer composite secondary slurry (in solvent A) into a non-solvent (solvent B) of the polymer to produce a spherical precipitate. By controlling the slurry solvent content and sonication strength, the average size and hollow core of the composite secondary particle precipitated can be controlled. The collected particles will be sintered around 500°C to form Si/C hollow core particles.

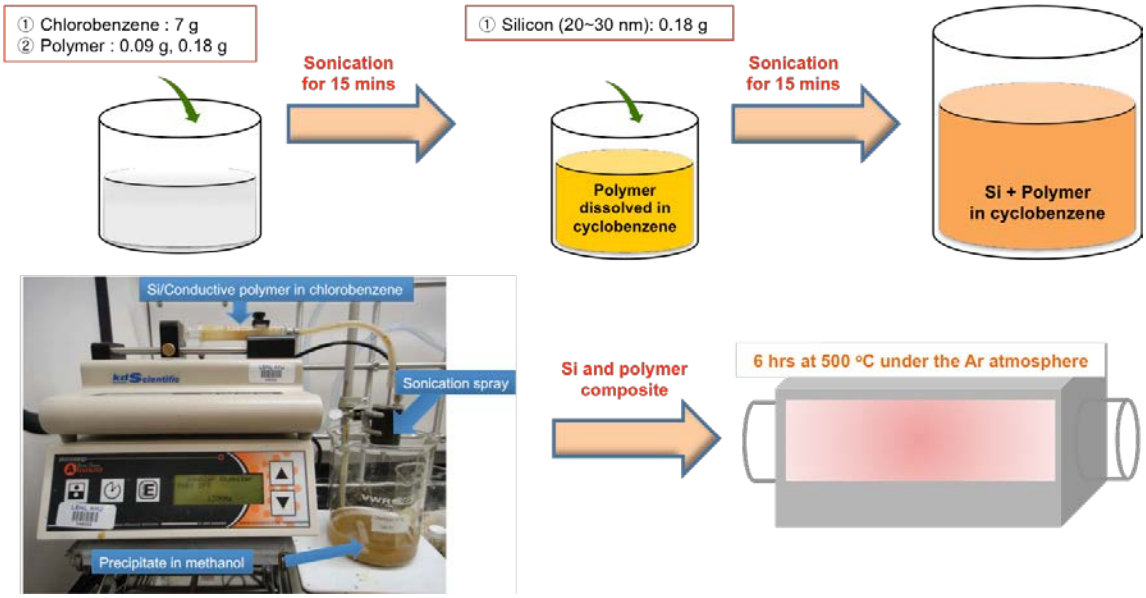

Figure II-205. Schematic process to make hollow core Si/C composite via spray precipitation and post sintering.

Hollow spherical composite secondary particles were fabricated, as shown in Figure II-206. An average particle size of 10 μm in diameter was achieved, as seen in the scanning electron microscope (SEM) image of the particles collected. The initial droplet size from the spray nozzle is controlled by the ultrasonic power at the nozzle. The smallest droplet diameter can be achieved is around 20 μm based on the manufacturer's configuration. Further reduction of composite secondary particle size was achieved by increasing the chlorobenzene (solvent A) content of the slurry. The dried composite secondary particles, ranging from 2 μm diameter to 20 μm diameter, were made when controlled at the smallest spray droplet of 20 μm diameter. The higher the solvent content in the slurry, the further size reduction there is after the droplets precipitate into the non-solvent. When the slurry droplets are sprayed into the non-solvent (solvent B), the migration of slurry solvent (A) from the droplets to the none-solvent (B) starts from the surface of the droplets. The surface polymer solidifies first. Due to the particle size is fixed before the center slurry solvent all migrates out of the spheres, a hollow core forms in the end of the precipitation. These materials have large void space with a diameter of around 10 μm. The void space is expected to accommodate the large volume change of Si during the charging/discharging process. The wall thickness of Si and polymer sample is around 5 μm. The cross-section SEM images of the hollow particles obtained using Focused-Ion-Beam (FIB) milling are shown in Figure II-206d. The cross-section SEM images show large void space in the Si/C composite. Thus, the integrity of the Si/C secondary particles can be maintained during cycling. The distribution of the carbon and

Si is very uniform within the composite, as shown in the EDS mapping image of the elemental Si, carbon (C), and oxygen (O).

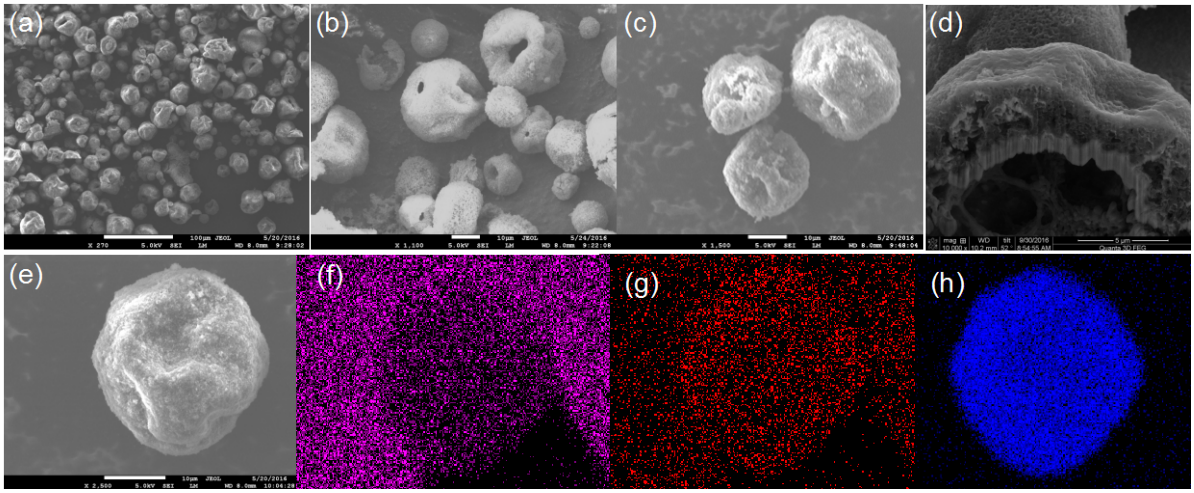

Figure II-206. SEM images of the Si/C composite secondary particles. (a-c) the Si/C hollow secondary particles at different magnifications. (d) FIB cross-section of a hollow Si/C particle. (e-f) A single particle and its EDS mapping image of carbon-(f), oxygen-(g) and silicon-(h). The background carbon tape contains carbon and oxygen elements.

As for the carbon coating to stabilized Si surface, SiO is chosen as active materials. The pyrene-based homopolymer poly(1-pyrenemethyl methacrylate) (PPy) is used as a polymer precursor to generate carbon coating after sintering process. The PPy polymer has layer structure due to the π- π stacking of the pyrene moiety, and forms a graphite-like structure at low sintering temperature. PPy polymer is soluble in organic solvent, and can be coated on the SiO surface easily. A schematic illustration of the process for fabricating the SiO/PPy composite materials is shown in Figure II-207. Typically, SiO micrometer size particles are dispersed in PPy THF solution and sonication for 0.5 h. Then, the solvent were evaporated by rotary evaporator to collect the SiO/PPy precursors. Finally, the sample was sintered at 400, 500, 600°C in an inert gas (sample name: SiO-PPy-T). The obtained final products were uniformly coated with a carbon layer. This carbon coating can effectively prevent the direct contact of SiO with electrolyte and improve the electronic conductivity. Raman spectroscopy is used to obtain the structural information about the SiO-PPy-T composites. A broad peak at 480 cm^{-1} extending asymmetrically down to approximately 430 - 515 cm^{-1} corresponds to the amorphous SiO is observed in all samples. For the SiO-PPy-T composites, the two prominent peaks at 1340 cm^{-1} and 1605 cm^{-1} which correspond to the D band and G band respectively. The intensities of D and G band decrease with the temperature increase. The I_D/I_G ratios are 0.645, 0.580 and 0.561 for SiO-PPy-400, 500 and 600 samples, respectively, indicating the carbon coating graphitic degree increase with increasing the sintering temperature.

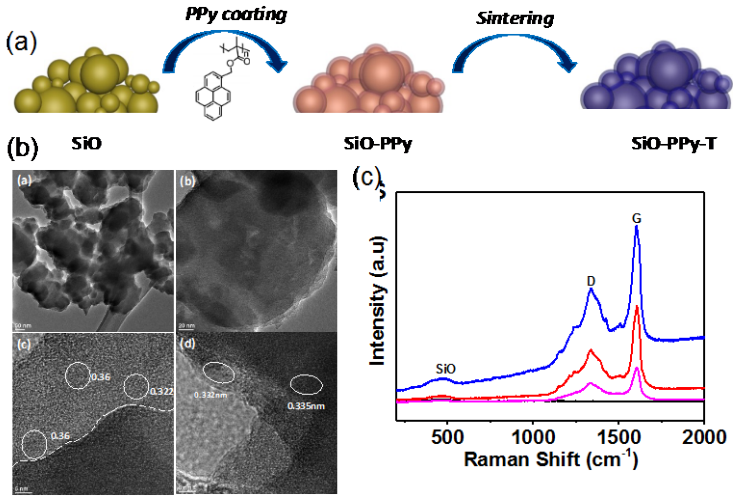

Figure II-207. (a) The process to coat SiO materials using PPy polymer and sintering to form a carbon coating layer on SiO materials (b) TEM images of the carbon coated SiO materials at different magnification, (c) Raman spectra of the SiO and carbon coated SiO sintered at different temperatures, 400°C (red), 500°C (blue), 600°C (magenta).

Galvanostatic charge - discharge curves of pure SiO, and SiO-PPy-400, 500, 600 electrodes cycled ranging from 0.1C to 2C. The SiO-PPy-500 delivers a capacity of 1127.5 mAh/g at the rate of 0.1C, and then gradually decreases to 649.9 mAh/g at the rate of 0.5 C, to 487.0 mAh/g at the rate of 1 C. (See Figure II-208.) Even at high rate of 2C, a reversible capacity of 317.6mAh g^{-1} can be still achieved. Notably, when the rate restored to 0.1C, SiO-PPy-500 composite electrode return of higher capacity of 1145.7 mAh/g, completely recovers its initial capacity. The results are remarkably superior to those of pure SiO, SiO-400 and 600, which show a continuous capacity decrease at each current density in the same range. The results show that the SiO-PPy-500 displays the excellent rate performance with a stable cycling behavior at different current densities. After the first two cycles at 0.05C rate for the formation step, the cells were then cycled at 0.1C over 50 cycles between 0.01-1.0 V. The SiO-PPy-500 electrodes show much higher reversible a specific capacity with 1090.2 mAh/g after 50 cycles than that of the other samples, which is 299.2 mAh/g for SiO-PPy-400 and 846.1 mAh/gfor SiO-PPy-600 and 771.6 mAh/g for uncoated SiO electrode, respectively. The initial coulombic efficiency (CE) of SiO-PPy-500 is 62.2%. In comparison, the SiO-PPy-400, SiO-PPy-600, and uncoated SiO electrodes are only able to demonstrate an initial CE of 30.5%, 55.6%, and 54.8%, respectively. At C/3 rate, the specific capacity of the uncoated SiO electrode after 200 charge/discharge cycles is 534.8 mAh g^{-1} with capacity retention of 65.8%. The SiO/PPy composite sintering at 500°C exhibit improved specific capacity and cycling stability, a higher specific capacity of 793 mAh/g after 200 charge/discharge cycles is achieved. The corresponding capacity retention is as high as 74.5%. When the sintering temperature of the SiO/PPy composite are 400 and 600°C, the reverse specific capacity of the electrode are 264.6 and 396.3 mAh/g at the 200th cycle respectively. These results clearly show that SiO-PPy-500 has the best electrochemical performance and the sintering temperature plays an important role in affecting the structure of the coating layers, obtained from sintering of PPy. The SiO-PPy-500 demonstrates a rapid increase of stabilized efficiency greater than 99.5% after only 5 cycles including the first formation cycle, and very stable in the rest cycles. This high cycling efficiency is quite promising for commercialization of alloy anodes into full-cell systems.

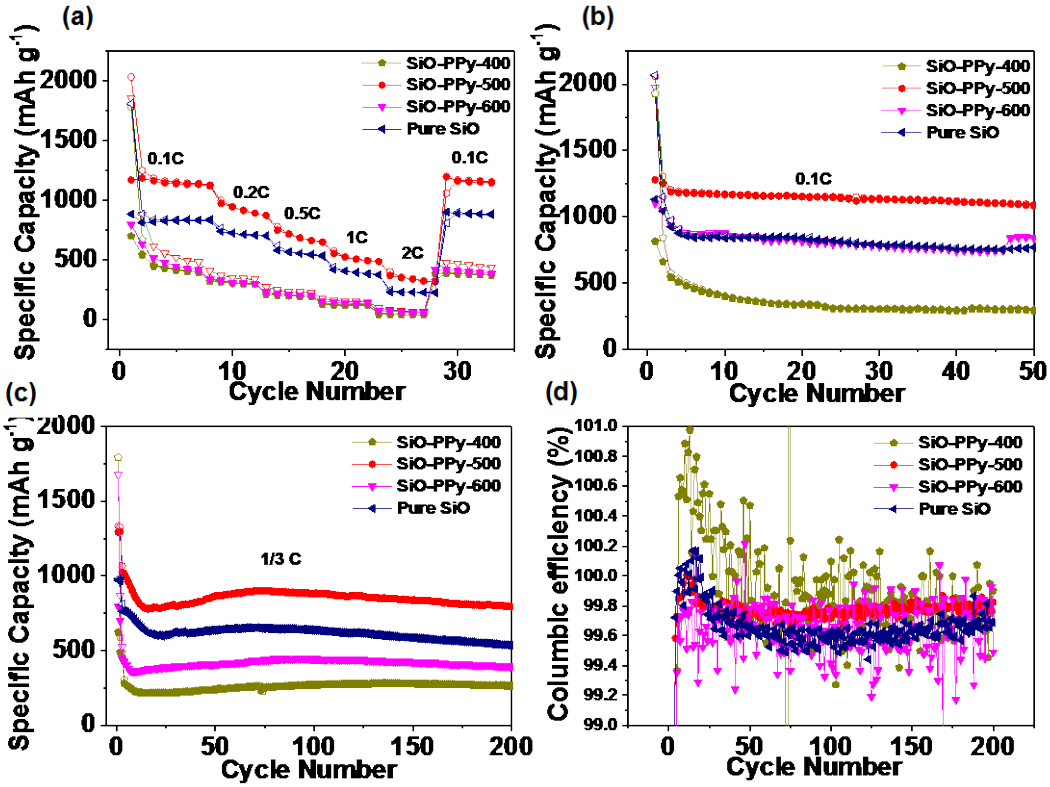

Figure II-208. (a) The Rate capabilities of pure SiO and SiO-PPy sintering at different temperature. (b) Cycling performance at C/10. (c) Cycling performance at C/3. (d) CE for pure SiO and SiO-PPy samples.

Conclusions

The Si/C hollow composite particles are synthesized using sonication spray-precipitation followed by pyrolysis method. The sonication spray of Si and polymer slurry successfully generated Si polymer composite hollow secondary particles. The sintering of the Si polymer composite particles retains the original morphology to yield the Si/C hollow particles. The distribution of carbon and Si is uniform across the secondary particles. An effective and scalable carbon coating process is also developed for SiO materials. The PPy is a very good polymer precursor to form highly graphitic carbon coating on the surface of SiO at a low sintering temperature of 500°C. The carbon coated SiO materials based on PPy precursor demonstrates superb cycling performance and rate capability.

Key Publications

1. Zheng, H. Y.; Qu, Q. T.; Zhu, G. B.; Liu, G.; Battaglia, V. S.; Zheng, H. H. *Acs Applied Materials & Interfaces* **2017,** *9* (14), 12445-12452.

2. Xu, J.; Ling, M.; Terborg, L.; Zhao, H.; Qiu, F.; Urban, J. J.; Kostecki, R.; Liu, G.; Tong, W., *J. Electrochem. Soc.* **2017,** *164* (7), A1378-A1383.

3. Shi, Q.; Liu, W. J.; Qu, Q. T.; Gao, T.; Wang, Y.; Liu, G.; Battaglia, V. S.; Zheng, H. H., *Carbon* **2017,** *111*, 291-298.

4. Self, E. C.; Naguib, M.; Ruther, R. E.; McRen, E. C.; Wycisk, R.; Liu, G.; Nanda, J.; Pintauro, P. N. *ChemSusChem* **2017,** *10* (8), 1823-1831.

5. Ling, M.; Zhang, L.; Zheng, T. Y.; Feng, J.; Guo, J. H.; Mai, L. Q.; Liu, G. *Nano Energy* **2017,** *38*, 82-90.

6. Ling, M.; Liu, M.; Zheng, T. Y.; Zhang, T.; Liu, G. *J. Electrochem. Soc.* **2017,** *164* (4), A545-A548.

7. Higa, K.; Zhao, H.; Parkinson, D. Y.; Barnard, H.; Ling, M.; Liu, G.; Srinivasan, V., *J. Electrochem. Soc.* **2017,** *164* (2), A380-A388.

8. Fang, S.; Tong, Z. K.; Nie, P.; Liu, G.; Zhang, X. G., *Acs Applied Materials & Interfaces* **2017,** *9* (22), 18766-18773.

9. Caihong Feng, Xianpu Meng, Xiaolu Song, Xueting Feng, Yun Zhao and Gao Liu *RSC Advance* **2016**, 6, 110266-110273.

10. Guo Ai, Yiling Dai, Wenfeng Mao, Hui Zhao, Yanbao Fu, Xiangyun Song, Yunfei En, Vincent S. Battaglia, Venkat Srinivasan, and Gao Liu *Nano Letters* **2016**, 16 5365-5372.

11. Jing Mao, Mengze Ma, Panpan Liu, Junhua Hu, Guosheng Shao, Vince Battaglia, Kehua Dai, Gao Liu, *Solid State Ionics*, **2016**, 292, 70–74.

12. Yan Feng, Yuzhen Wei, Zhe Jia, Yuliang Zhang, Vince Battaglia, Gao Liu *Chemistry Select*, **2016,** 1 (2) 309-317.

II.B.8 A Combined Experimental and Modeling Approach for the Design of High Current Efficiency Si Electrodes (GM)

Xingcheng Xiao, Principal Investigator
GM Global Research and Development
30500 Mound Road
Warren, MI 48090
Phone: 248-912-8132
E-mail: Xingcheng.xiao@gm.com

Yue Qi, Co-Principal Investigator
Michigan State University
3509 Engineering Building
East Lansing, MI 48824
Phone: 517-432-1243; Fax: 517-432-1105
E-mail: yueqi@egr.msu.edu

Tien Duong, Technology Manager
U.S. Department of Energy
Phone: 202-586-7836
E-mail: Tien.Duong@ee.doe.gov

Start Date: June 1, 2013 End Date: March 31, 2017
Total Project Cost: $1,318,947 DOE share: $1,318,947 Non-DOE share: $0

Project Introduction

The use of high capacity Si-based electrode has been hampered by its mechanical degradation due to the large volume expansion/contraction during cycling. Nanostructured Si can effectively avoid Si cracking/fracture. Unfortunately, the high surface to volume ratio in nanostructures leads to unacceptable amount of solid-electrolyte interphase (SEI) formation and growth, thereby low current/coulombic efficiency and short life. Based on mechanics models we demonstrate that the artificial SEI coating can be mechanically stable despite the volume change in Si, if the material properties, thickness of the SEI, and the size/shape of Si are optimized.

The real challenges to developing a model that allows us to design high current efficiency Si electrodes with electrochemically and mechanically stable artificial SEI layer are: a) poor understanding of SEI failure mechanisms; b) lack of accurate mechanical properties of the SEI; and c) difficulty in validation of the model. All of these are due to the extreme challenges associated with characterizing the properties of nano-meter thin SEI layer on lithiated Si in real battery systems. Therefore, we will first address these questions based on simpler thin film electrodes

Objectives

The use of high capacity Si-based electrode has been hampered by its mechanical degradation due to the large volume expansion/contraction during cycling. Nanostructured Si can effectively avoid Si cracking/fracture. Unfortunately, the high surface to volume ratio in nanostructures leads to unacceptable amount of solid-electrolyte interphase (SEI) formation and growth, thereby low current/coulombic efficiency and short life. Based on mechanics models we demonstrate that the artificial SEI coating can be mechanically stable despite the volume change in Si, if the material properties, thickness of the SEI, and the size/shape of Si are optimized. Therefore, the objective of this project is to develop an integrated modeling and experimental approach to understand, design, and make coated Si anode structures with high current efficiency and stability.

Approach

- Combine simulation with experiments to obtain critical material properties of SEI layer and lithiated Si, with in-situ electrochemical characterization capabilities developed at GM R&D Center.
- Develop a multi-scale model to establish correlation between coulombic efficiency and mechanical degradation of SEI on Si;
- Use the validated model to guide synergetic design of surface coating with Si size/geometry/architecture.

Results

Further explored Li diffusion through the SEI layer/intrinsic passivation layer (SiO_2) on Si

The mixed LiF/SiO2 Reactive MD simulations were performed to investigate the effect of composite coating on LiF. Previously, we have shown that Li diffuses very fast through the SiO2 coating by lithiating it first (Figure II-209b) and LiF acts as a barrier for Li diffusion (Figure II-209d). For a SiO_2-LiF mixed coating (50 Volume % for each phase), we noticed that Li diffusion through the composite coating is almost as slow as that in LiF coating. Lithiation of SiO_2 was observed, but few Li atoms were able to diffuse through. One possible reason is that lithiated SiO_2 in the composite coating was under large compressive stress, as the LiF phase prevented its volume expansion. Therefore lithium diffusion through the SiO_2 is hindered dramatically.

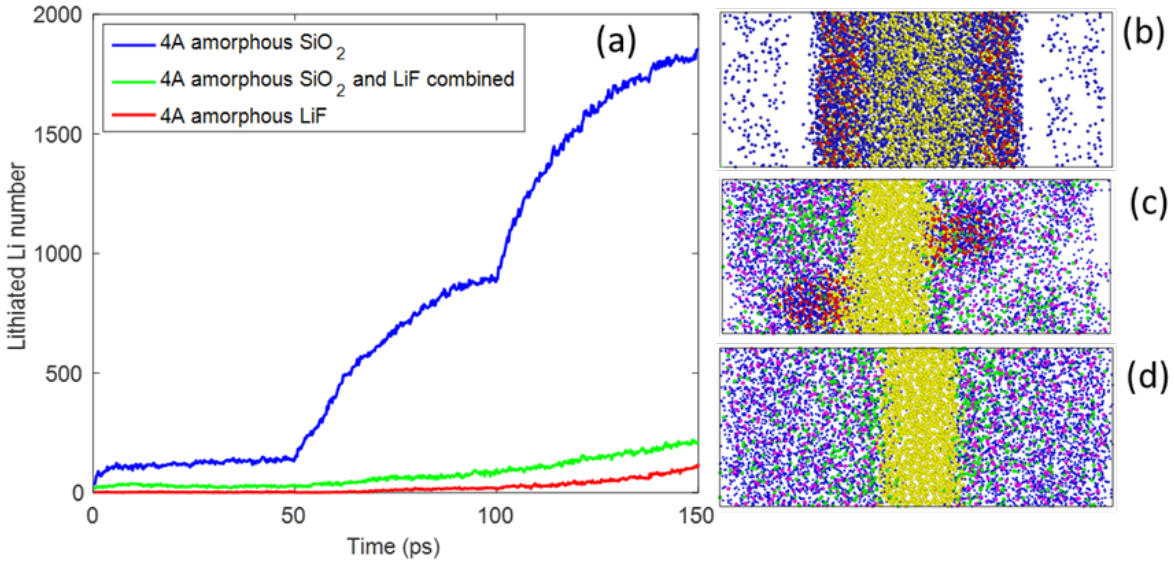

Figure II-209. (a) The number of Li atoms reached Si thin film after 150ps MD simulations and the corresponding structure of Si initially coated with (b) SiO2, (c)SiO2-LiF, and (c) LiF.

Further elaborated the failure mechanism of SEI layer on Si electrode

The comparisons between continuous Si thin films and patterned Si islands made it possible to measure the excess Li consumption due to the strain in the SEI. Figure II-210 schematically shows how SEI evolved with mechanical strain caused by Si volume changes during lithiation and delithation process. The key direct observation from this study is that large in-plane strains in the SEI layer lead to substantial increases in the formation of inorganic Li-containing constituents, without significantly altering the overall SEI thickness. By combining in situ AFM observations with electrochemical lithium loss measurements, an irreversible capacity vs. strain map was obtained to correlate the extra capacity losses resulting from SEI break/repair effect at different SOC. More generally, the experimental approach in our work provides a useful tool for evaluating the relationships between capacity loss and mechanical deformation of the SEI. The correlation between irreversible capacity and strain will depend on several different properties in the SEI. Improved understanding

of these phenomena can provide important insight into designing improved SEI films that can minimize capacity losses.

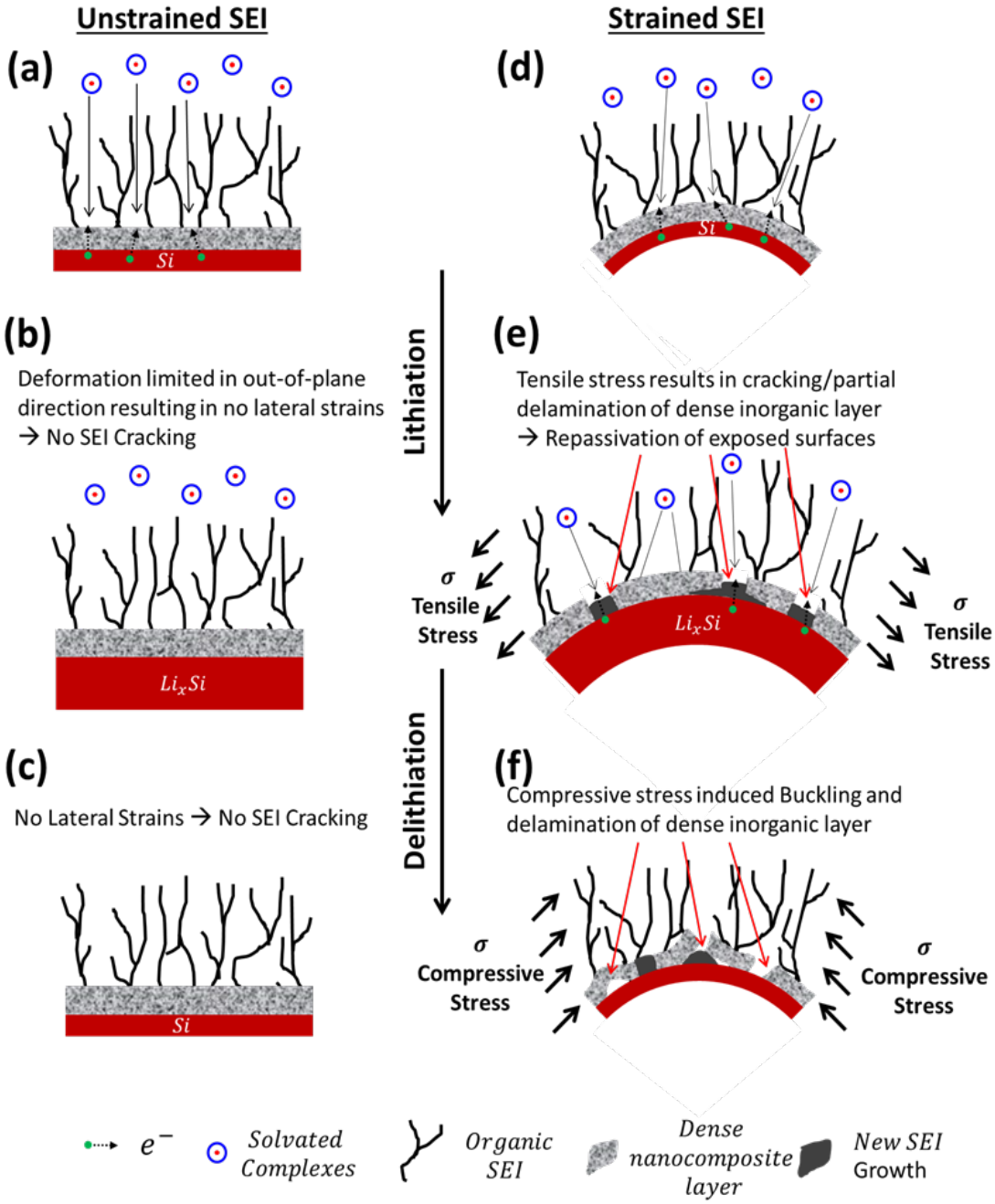

Figure II-210. Schematic representation of the SEI Evolution with (d, e, f) and without strain (a, b, c). In practical electrode geometries such as silicon particles, expansion (contraction) of the underlying Si stretches (compresses) the SEI layer and causes in-plane tensile (compressive) stress in the film.

Explored the mechanical integrity using in situ measurements of lithium-induced stresses in silicon nanoparticle-based composite electrodes

The effects of silicon nanoparticle loading and two different binders on the stress buildup in porous composite electrodes were investigated, as shown in Figure II-211. The in-situ stress evolutions in these electrodes were

measured by monitoring the changes in the curvature of an elastic substrate. The stress measurements of reference carbon black electrodes (CB/CMC: 80/20 wt%) show an approximately linear and reversible stress change which is consistent with an elastic response. However, the stress response of Si electrodes exhibit several stages during both lithiation and delithiation. For the 20 wt% Si-NP electrodes, compressive stress develops during lithiation which increases rapidly with capacity up to ~200 mAh/gSi, and then exhibits a clear transition (softening) after which it continuously increases at a slower rate. The maximum average composite stress at the full-lithiation reaches -35 to -50 MP in these electrodes. In comparison, the 60wt% Si electrodes exhibit an additional hardening behavior towards later stages of lithiation which reflects the complex ways in which the particles interact with each other and the binder. At full lithiation, average in-plane nominal stresses in these electrodes range from -100 to -150 MPa. The stress measurements also indicate that the Na-Alginate leads to higher stresses than the CMC binder. This implies that the deformation of the entire composite electrode is directly impacted by the binder mechanical properties. The thickness changes measured using FIB cross-sections suggest that part of the volume expansions in these electrodes is accommodated by decreasing the porosity. Therefore, porosity plays a key role in suppressing the volume expansion and need to be optimized to get long-term performance. Simple cell models with periodic arrays of spherical core-shell particles (core: active particle, shell: binder) were constructed to visualize the structural changes in these electrodes. In absence of rigorous microstructural models, they provide an initial basis for understanding particle interactions and internal changes.

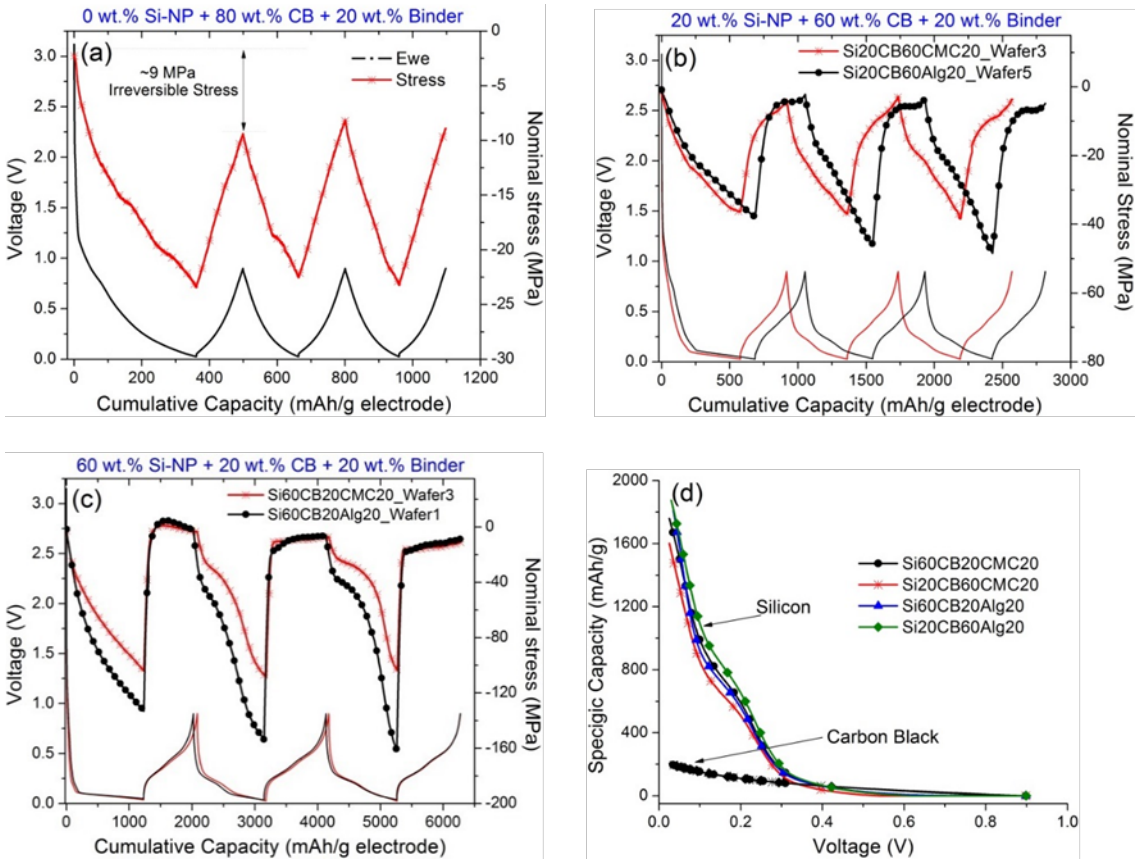

Figure II-211. Potential and nominal stress response of composite electrodes with a) 0wt% Si (CB/CMC: 80/20) b) 20 wt% Si (Si/CB/Binder: 20/60/20) and c) 60 wt% Si (Si/CB/Binder: 60/20/20). Si-containing electrodes were prepared with two different binders; Na-Alginate and CMC and their electrochemical and mechanical response are compared in panels b) and c). Specific capacity of silicon and carbon black particles in Si-containing electrodes during 2nd cycle lithiation d).

A new strategy has been developed to stabilize the SEI and Si-based electrode

By controlling the cycle potential window, we have demonstrated the excellent cycle performance of columnar Si film electrode paired with Li Ni0.6Mn0.2Co0.2O2 counter electrode. It has been demonstrated that the controlled potential window leads to half of the mechanical stress and it was retained at compressive state, when the Li-Si electrode is operated between 0.13 and 0.55 V versus a Li reference. The deformation of Si electrode is maintained at elastic region and no plastic flow is observed during cycling. (Figure II-212) The combining effects can mitigate the mechanical degradation therefore leading to significantly improved cycle life. The full cells have 90% capacity retention of the initial cell capacity even after 400 cycles, as shown in Figure II-213 left plot. Figure II-213 also shows the cross-section of Si film electrode after different cycles. Although the thickness has increased to 10 microns from 3 microns, the film still retains the mechanical integrity and good adhesion to current collectors. The constraint from the current collector leads to Si expansion along the thickness direction. The SEI has been observed along the boundary of the columnar structure, indicating Si has become porous which can effectively accommodate the volume expansion and reduce the stress. In addition, the thickness of Si film electrode does not show significant changes after first 10 cycles, which provides the very useful information for battery cell design.

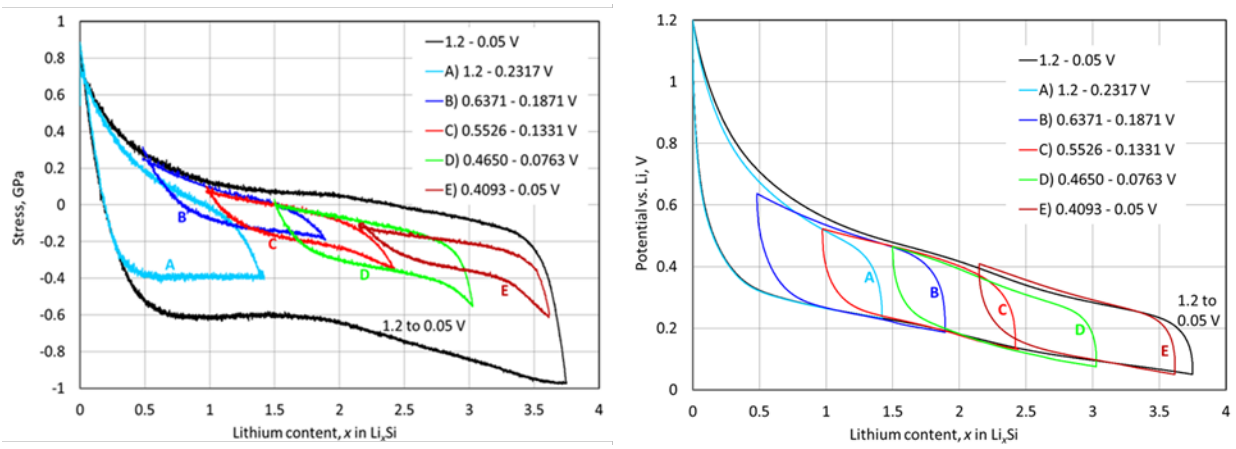

Figure II-212. Left plot: stress measured over the full potential range and for A through E. Right plot: corresponding potential measurements

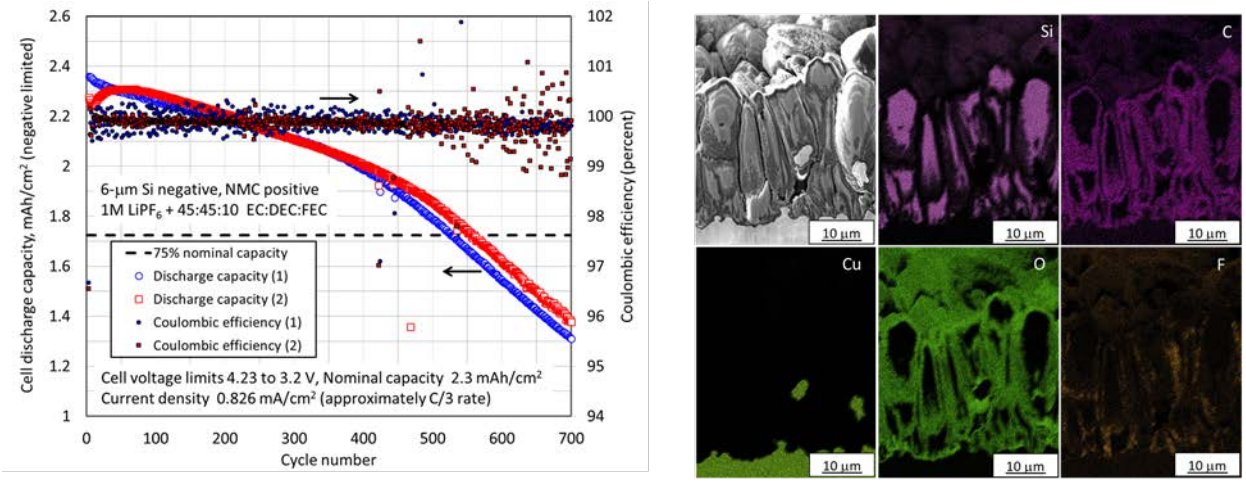

Figure II-213. Left plots: Full-cell (Si-NMC) discharge capacity and Coulombic (or current) efficiency versus cycle number. Results for two cells are plotted (denoted by 1 and 2). The current density and voltage limits are indicated. Upon reaching a voltage limit, the polarity of the current was immediately changed (i.e., no voltage holds). Right image: Secondary-electron micrograph (upper left) and elemental maps of the electrode cross-section for Si, C, Cu, O, and F after 395 cycles.

Conclusions

By using combined in-situ electrochemical experiments and modeling techniques, we were able to identify SEI failure modes. The in-plane strains in the SEI layer lead to substantial increases in the amount of inorganic phase formation, without significantly affecting the overall SEI thickness. Better understanding of these phenomena can provide important insight into designing desirable SEI films that can minimize capacity losses.

Tailoring the nanostructure and architecture to control stress/strain distribution in Si base active materials can sufficiently mitigate the mechanical degradation and stabilize SEI layer. With the optimized SEI formation protocols and electrolyte additives (FEC), high cycle efficiency was achieved (>99.8% with first cycle CE>94%)]

Key Publications

1. R Kumar, A Tokranov, BW Sheldon, X Xiao, Z Huang, C Li, T Mueller, In situ and operando investigations of failure mechanisms of the solid electrolyte interphase on silicon electrodes, ACS Energy Letters 1 (4), 2016, 689-697

2. M. Verbrugge, X. Xiao, Q. Zhang, M. Balogh, K. Raghunathan, D. Baker, Fabrication and Characterization of Lithium-Silicon Thick-Film Electrodes for High-Energy-Density Batteries Journal of The Electrochemical Society 164 (2), 2017, A156-A167

3. Q. Zhang, L. Han, J.Pan, Z. Chen, and Y. Cheng, Chemically stable artificial SEI for Li-ion battery electrodes, Appl. Phys. Lett. 110, 133901 (2017).

4. X. Su, K. Guo, T. Ma, P.A. Tamirisa, H. Ye, H. Gao, and B. W. Sheldon. Deformation and Chemomechanical Degradation at Solid Electrolyte–Electrode Interfaces. ACS Energy Letters 2 (2017): 1729–1733

5. K.J. Kim, J. Wortman, S. Y. Kim, Y. Qi, Atomistic Simulation Derived Insight on the Irreversible Structural Changes of Si Electrode during Fast and Slow Delithiation, Nano Letters. 2017, 17, 4330-4338

6. Y. Wang, Q. Zhang, D. Li, J. Hu, D. Dang, X. Xiao, and Y. Cheng, “Mechanical Property Evolution of Silicon Composite Electrodes Studied by Environmental Nanoindentation.” Advanced Energy Materials, DOI: 10.1002/aenm.201702578 (2017)

7. R. Kumar, J. Woo, X. Xiao, B.W. Sheldon, Internal Microstructural Changes and Stress Evolution in Silicon Nanoparticle Based Composite Electrodes Batteries and Energy Storage, J. Electrochem. Soc. 2017 164(14): A3750-A3765

8. F. M. Hassan, Q. Hu, J. Fu, R. Batmaz, J. Li, A. Yu, X. Xiao, and Z. Chen, Hot-Chemistry Structural Phase Transformation in Single-Crystal Chalcogenides for Long-Life Lithium Ion Batteries, ACS Appl. Mater. Interfaces, 2017, 9 (24), pp 20603–20612

9. X Li, P Yan, X Xiao, JH Woo, C Wang, J Liu, JG Zhang, Design of Porous Si/C-Graphite Electrodes with Long Cycle Stability and Controlled Swelling, Energy & Environmental Science, 2017, 10.1039/C7EE00838D